frontiers | Research Topics

Paleolimnology: Insights from sedimentary archives

Edited by
Adriana Aránguiz-Acuña, Kunshan Bao and Xiaofeng Cao

Published in
Frontiers in Ecology and Evolution

ISSN 1664-8714
ISBN 978-2-8325-4279-8
DOI 10.3389/978-2-8325-4279-8

About Frontiers

Frontiers is more than just an open access publisher of scholarly articles: it is a pioneering approach to the world of academia, radically improving the way scholarly research is managed. The grand vision of Frontiers is a world where all people have an equal opportunity to seek, share and generate knowledge. Frontiers provides immediate and permanent online open access to all its publications, but this alone is not enough to realize our grand goals.

Frontiers journal series

The Frontiers journal series is a multi-tier and interdisciplinary set of open-access, online journals, promising a paradigm shift from the current review, selection and dissemination processes in academic publishing. All Frontiers journals are driven by researchers for researchers; therefore, they constitute a service to the scholarly community. At the same time, the *Frontiers journal series* operates on a revolutionary invention, the tiered publishing system, initially addressing specific communities of scholars, and gradually climbing up to broader public understanding, thus serving the interests of the lay society, too.

Dedication to quality

Each Frontiers article is a landmark of the highest quality, thanks to genuinely collaborative interactions between authors and review editors, who include some of the world's best academicians. Research must be certified by peers before entering a stream of knowledge that may eventually reach the public - and shape society; therefore, Frontiers only applies the most rigorous and unbiased reviews. Frontiers revolutionizes research publishing by freely delivering the most outstanding research, evaluated with no bias from both the academic and social point of view. By applying the most advanced information technologies, Frontiers is catapulting scholarly publishing into a new generation.

What are Frontiers Research Topics?

Frontiers Research Topics are very popular trademarks of the *Frontiers journals series*: they are collections of at least ten articles, all centered on a particular subject. With their unique mix of varied contributions from Original Research to Review Articles, Frontiers Research Topics unify the most influential researchers, the latest key findings and historical advances in a hot research area.

Find out more on how to host your own Frontiers Research Topic or contribute to one as an author by contacting the Frontiers editorial office: frontiersin.org/about/contact

Paleolimnology: Insights from sedimentary archives

Topic editors

Adriana Aránguiz-Acuña — University of Tarapacá, Chile

Kunshan Bao — South China Normal University, China

Xiaofeng Cao — Tsinghua University, China

Citation

Aránguiz-Acuña, A., Bao, K., Cao, X., eds. (2024). *Paleolimnology: Insights from sedimentary archives*. Lausanne: Frontiers Media SA.

doi: 10.3389/978-2-8325-4279-8

Table of contents

frontiers | Frontiers in Ecology and Evolution

TYPE Editorial
PUBLISHED 04 January 2024
DOI 10.3389/fevo.2023.1352925

OPEN ACCESS

EDITED AND REVIEWED BY
Laura Parducci,
Sapienza University of Rome, Italy

*CORRESPONDENCE
Kunshan Bao
kunshan.bao@m.scnu.edu.cn

RECEIVED 09 December 2023
ACCEPTED 18 December 2023
PUBLISHED 04 January 2024

CITATION
Bao K, Aránguiz-Acuña A and Cao X (2024) Editorial: Paleolimnology: insights from sedimentary archives.
Front. Ecol. Evol. 11:1352925.
doi: 10.3389/fevo.2023.1352925

Editorial: Paleolimnology: insights from sedimentary archives

Kunshan Bao[1]*, Adriana Aránguiz-Acuña[2] and Xiaofeng Cao[3]

[1]School of Geography, South China Normal University, Guangzhou, China, [2]Laboratorio de Ecología Acuática, Departamento de Recursos Ambientales, Facultad de Ciencias Agronómicas, Universidad de Tarapacá, Arica, Chile, [3]Center for Water and Ecology, State Key Joint Laboratory of Environment Simulation and Pollution Control, School of Environment, Tsinghua University, Beijing, China

KEYWORDS

paleolimnology, lake sediments, peat, Holocene, Anthropocene, paleoecology, geochemistry, pollution

Editorial on the Research Topic
Paleolimnology: insights from sedimentary archives

In the past century, global changes characterized by warming and intense human activities have led to unprecedented changes in lake and wetland ecosystems worldwide (Smol et al., 2005). The series of ecological and environmental issues that have arisen have attracted widespread attention from governments and the scientific community in various countries. Scientifically assessing the impact of climate change and human activities on lake and wetland ecosystems has become one of the important scientific topics that are currently being prioritized (Long et al., 2021). It is also the key content of research in related disciplines such as paleolimnology, Quaternary science and past global changes (PAGES).

The study of paleolimnology interprets lake and wetland sedimentary profiles which are terrestrial archives that can record natural and human-induced changes in the environment, preserved in biological, sedimentological, and geochemical components of the sediment (Frey, 1988). The global occurrence, high accumulation rates and a wealth of microfossils and biogeochemical tracers of lake and wetland sediments allow developing the past environmental change history of sub-decadal to millennial scales. This can place the present-day observed change into the context of long-term natural environmental variability, and provides a potential means for the investigation of the interactions between past climatic dynamics and anthropogenic activities, in the absence of long-term instrumental monitoring programmes (Moser et al., 2019; Bao et al., 2023).

Over the past 40 years, the field of paleolimnology has made significant progress in contributing to our knowledge of long-term climate change (i.e., Villacis et al., 2023), altered biogeochemical cycles (i.e., Bao et al., 2021), environmental pollution (i.e., Kissinger et al., 2023), variations in dust composition and deposition (i.e., Chen et al., 2020), and species invasions and biodiversity (i.e., Cuenca-Cambronero et al., 2022). An overview of the importance of sediment records from continental aquatic ecosystems, especially lakes,

was given out to provide long-term insights needed to ensure the maintenance of ecological products and services by adapting to current and future environmental changes (Saulnier-Talbot, 2016). Recently there are series of Research Topics on paleolimnology to be published in different journals. In 2020 *Lake and Reservoir Management* presented a Research Topic on paleolimnology and lake management which includes studies from lakes across North America and shows the value of paleolimnology in making decisions regarding aquatic ecosystem restoration and management approaches (Paterson et al., 2020). In 2022 the Research Topic, entitled"Paleolimnology and Paleoecology in a Rapidly Changing Asia", was publish on *Journal of Paleolimnology* and summarized the key advances in the fields of lake development, ecological shifts and anthropogenic forcing in the different parts of East Asia (Chen et al., 2022). In 2023, Tunno et al. provided an overview of new methodologies recently applied to the field of paleoecology which was published on *Frontiers in Ecology and Evolution*. These all show a flourishing paleolimnology decipline, with continuously increasing numbers of paleolimnological investigations and updating proxy analysis technologies. However, paleolimnological studies in the tropics still lag far behind efforts at higher latitudes, and there will now be calls to encourage more paleolimnological research at low latitudes (Escobar et al., 2020).

Therefore, the objective of this Research Topic is to further address key aspects of global paleolimnological research in dealing with lakes and wetlands records of climate change and anthropogenic impacts and to facilitate knowledge dissemination. A total of 12 papers is presented in this Research Topic. The papers cover multiple themes, including chronological techniques and model applications, comprehensive interpretation of multiple alternative indicators, historical reconstructions of the past climatic, environmental and ecological evolution throughout the Holocene, and the human traces for the global Anthropocene definition. Geographically, these case studies include a variety of lakes and wetlands from 83°N to 34°S and from 170°E to 120°W. They are of mountain lakes and peatlands as higher up to 4000 m above the sea level, arctic lakes and ponds, and coastal wetlands.

Accurate and precise dating of sediments and peats is fundamental for to provide quantitative measurements of change rates, which require a relatively large number of dates to build a chronology of sufficient resolution for proxy interpretation and paleolimnological records comparison between sites. In this Research Topic, all studies used the radiocarbon dating to understand the Holocene environmental changes and the ^{210}Pb and ^{137}Cs dating to reconstruct the history of Anthropocene environmental changes. It is quite crucial to ensure a certain abundance of different sources of carbon that can be extracted from sediments for radiocarbon dating analysis. A pilot study was conducted at two contrasting lake basins on the eastern side of the Sierra Nevada (California) to present an improved method for extracting, sorting and dating pollen from lake sediment cores (Tunno et al.). This new technique combines an optimized pollen extraction protocol (without using strong chemicals, e.g., hydrofluoric acid), sorting by flow cytometry, and standard graphitization and AMS radiocarbon measurement methods. This is a very valuable contribution to the chronological methodology for the paleolimnology.

The basic paradigm of combining the past and the modern in the paleolimnology study is to use the past pattern to discuss the modern situation and to use the modern process to prove the past change. With the development of the paleolimnology, there is an increasingly urgent to the integration of modern environment/ecology into paleoenvironment/paleoecology (Goodenough and Webb, 2022). Modern processes mainly include the regional environmental factors survey and typical lakes and wetlands ecological monitoring. In this Research Topic, 3 papers explored surface-sediment taxa-environment relationships and their spatial changes of pollen in East Siberia (Geng et al.), diatom along the ice-free margin of Greenland (Weckström et al.) and zooplankton Bosminidae in the middle and lower reaches of the Yangtze River (Cheng et al.). These modern spatio-environmental studies of different proxies are an essential part of the paleolimnological approach, which is helpful for the quantitative reconstruction of the past environmental changes.

The Holocene is a typical interglacial period and generally characterized by a relatively warm and stable climate, but it is constantly interrupted by a series of rapid (or extreme) climate change events, threatening the development of human civilization. As a result, the Holocene climate and environmental changes history has always been keynotes of the paleolimnology and well comparatively documented by comprehensive interpretation of multiple alternative indicators. The sedimentary environment and hydroclimate evolution since the last glacial maximum were reconstructed from a mountain peat core of the southern margin of the Sichuan Basin based on concentrations in major and trace elements, total organic carbon (TOC), total nitrogen (TN) and the stable carbon isotope composition of organics (δ^{13}Corg) (Huang et al.). Another high-altitude lacustrine record in the semiarid Andes (29°S) was reconstructed from a multiproxy approach including organic/inorganic matter content and trace elements along with biological proxies such as pollen, diatoms and chironomids, which illustrated the climate-driven changes at millennial to sub-centennial timescales during the past 2400 years in the semiarid Andes of central Chile (Martel-Cea et al.). In addition, two paleolimnological studies from estuarine environments in China (Ling et al.) and in South Africa (Kirsten et al.) interpreted the observed changes in the geomorphic settings in the context of sea-level rise and anthropogenic factors since the mid-Holocene. Both studies obtained a series of sediment cores representing contrasting estuarine habitats and applied for multiple proxy analyses including a range of physicochemical characteristics (organic matter content, magnetic susceptibility, particle size, organic δ^{13}C and selected elements) and paleoecological parameters (pollen, Dinoflagellate, and Foraminiferal organic linings).

To understand fully current trajectories of the Earth system driven by the Great Acceleration since the mid-20th century

(Steffen et al., 2018), we need to increasing studies trying to provide more evidence for better understanding of the global definition of the Anthropocene and the decipher of human-climate interaction. Recent developments in multi-proxy paleolimnological approaches and short-time-scale chronological methods (i.e., ^{210}Pb and ^{137}Cs) have substantially advanced our ability to make robust inferences about past century's environment change. In this Research Topic, a representative subalpine lake (Cuoqia Lake) in the southeast of Tibetan Plateau was chosen as a monitor of regional environmental and ecological changes over the past two centuries based on ^{210}Pb and ^{137}Cs dates and multiproxy data including brGDGTs, n-alkane, and fatty acids (Yan et al.) and geochemistry, stable isotopes and sedimentary pigments (Zhang et al.). Statistical analyses and scenario ecosystem process-based modelling quantified the synergistic impacts of climate warming and anthropogenic activities on the algal proliferation and community succession in remote alpine lakes on the Tibetan Plateau (Zhang et al.). Multi-proxies records (black carbon, 16 priorities of PAHs and δ^{13}C) from a ^{210}Pb dated peat profile in Altay Mountain of northwest China indicated an increase of black carbon emission in 1950–1980 probably due to the agricultural exploration and a decrease after 1980 probably related to the increasing environmental protection (Luo et al.). In addition, Jaque et al. used different proxies (magnetic properties, geochemical analysis, loss on ignition, satellite image processing, and reflectance spectrum) on a reservoir sediment record in the Aconcagua River Valley to unravel the environmental and/or climatic history in central Chile between 1975 and 2019, and thus to evaluate the effects of climate drought events and regional polluting industrial activities.

In summary, the articles collected in this Research Topic provide insight into some of the most recent advances in dating methods, contemporary ecological processes, Holocene climate change and Anthropocene environmental pollution. They underlined the importance of the application of new tools and multiply proxies, and thus a comprehensive understanding of paleoenvironmental changes and their interactions with human-climate system. Paleolimnological studies are presenting a thriving development trend and provide a broad suite of information on the occurrence of ecological conditions, climate events and anthropogenic disturbances, especially for missing long-term monitoring data in remote regions. We hope that the data, insights, and recommendations offered in the present Research Topic will be of use to our readers and to paleolimnological communities at large.

Author contributions

KB: Funding acquisition, Writing – original draft, Writing – review & editing. AA-A: Writing – review & editing. XC: Writing – review & editing.

Funding

The author(s) declare financial support was received for the research, authorship, and/or publication of this article. KB acknowledges support from the National Natural Science Foundation of China (Grant Number 41971113) and the Scientific Research Foundation for Young Talents of South China Normal University (118/8S0593).

Acknowledgments

The authors are grateful to Scott Andrew Mensing (University of Nevada, United States), Franco Biondi (University of Nevada, Reno, United States), Chuanxiu Luo (Chinese Academy of Sciences (CAS), China), Olga Solomina (Institute of Geography (RAS), Russia) and Laura Parducci (Sapienza University of Rome, Italy) for helpful edits on some of the papers. Also, we thank all of the reviewers whose comments and suggestions helped the authors improve their papers.

Conflict of interest

The authors declare that the research was conducted in the absence of any commercial or financial relationships that could be construed as a potential conflict of interest.

Publisher's note

References

Bao, K., Liu, T., Chen, M., Lin, Z., Zhong, J., and Neupane, B. (2023). Peat records of atmospheric environmental changes in China: A brief review and recommendations for future research perspectives. *Catena* 229, 107234. doi: 10.1016/j.catena.2023.107234

Bao, K., Zhang, Y., Zaccone, C., and Meadows, M. E. (2021). Human impact on C/N/P accumulation in lake sediments from northeast China during the last 150 years. *Environ. pollut.* 271, 116345. doi: 10.1016/j.envpol.2020.116345

Chen, F., Chen, S., Zhang, X., Chen, J., Wang, X., Gowan, E. J., et al. (2020). Asian dust-storm activity dominated by Chinese dynasty changes since 2000 BP. *Nat. Commun.* 11, 992. doi: 10.1038/s41467-020-14765-4

Chen, G., Yang, X., and Smol, J. P. (2022). Linking paleoecology with paleolimnology: evaluating ecological shifts, human impacts and monsoon climate from sediment signals in East Asia. *J. Paleolimnol.* 68, 1–6. doi: 10.1007/s10933-022-00242-z

Cuenca-Cambronero, M., Courtney-Mustaphi, C. J., Greenway, R., Heiri, O., Hudson, C. M., King, L., et al. (2022). An integrative paleolimnological approach for studying evolutionary processes. *Trends Ecol. Evol.* 37 (6), 488–496. doi: 10.1016/j.tree.2022.01.007

Escobar, J., Serna, Y., Hoyos, N., Velez, M. I., and Correa-Metrio, A. (2020). Why we need more paleolimnology studies in the tropics. *J. Paleolimnol.* 64, 47–53. doi: 10.1007/s10933-020-00120-6

Frey, D. G. (1988). What is paleolimnology? *J. Paleolimnol.* 1, 5–8. doi: 10.1007/BF00202189

Goodenough, A. E., and Webb, J. C. (2022). Learning from the past: opportunities for advancing ecological research and practice using palaeoecological data. *Oecologia* 199, 275–287. doi: 10.1007/s00442-022-05190-z

Kissinger, J. A., Gregory, B. R. B., Clarkson, C., Libera, N., Eickmeyer, D. C., Kimpe, L. E., et al. (2023). Tracking pollution from fur farms using forensic paleolimnology. *Environ. pollut.* 335, 122307. doi: 10.1016/j.envpol.2023.122307

Long, K. E., Schneider, L., Connor, S. E., Shulmeister, N., Finn, J., Roberts, G. L., et al. (2021). Human impacts and Anthropocene environmental change at Lake Kutubu, a Ramsar wetland in Papua New Guinea. *PNAS* 118 (40), e2022216118. doi: 10.1073/pnas.2022216118

Moser, K. A., Baron, J. S., Brahney, J., Oleksy, I. A., Saros, J. E., Hundey, E. J., et al. (2019). Mountain lakes: Eyes on global environmental change. *Global Planetary Change* 178, 77–95. doi: 10.1016/j.gloplacha.2019.04.001

Paterson, A. M., Koster, D., Reavie, E. D., and Whitmore, T. J. (2020). Preface: paleolimnology and lake management. *Lake Reservoir Manage.* 36 (3), 205–209. doi: 10.1080/10402381.2020.1805998

Saulnier-Talbot, E. (2016). Paleolimnology as a tool to achieve environmental sustainability in the Anthropocene: an overview. *Geosciences* 6, 26. doi: 10.3390/geosciences6020026

Smol, J. P., Wolfe, A. P., Birks, H. J. B., Douglas, M. S. V., Jones, V. J., Korhola, A., et al. (2005). Climate-driven regime shifts in the biological communities of arctic lakes. *PNAS* 102 (12), 4397–4402. doi: 10.1073/pnas.0500245102

Steffen, W., Rockstrom, J., Richardson, K., Lenton, T.M., Folke, C., Liverman, D., et al. (2018). Trajectories of the earth system in the anthropocene. *PNAS* 115, 8252–8259. doi: 10.1073/pnas.1810141115

Villacis, L. A., Moreno, P. I., Vilanova, I., Henriquez, C. A., Henriquez, W. I., Villa-Martinez, R. P., et al. (2023). A freshwater diatom perspective on the evolution of the southern westerlies for the past ~14 000 years in southwestern Patagonia. *Quaternary Sci. Rev.* 301, 107929. doi: 10.1016/j.quascirev.2022.107929

frontiers in Ecology and Evolution

METHODS
published: 25 May 2021
doi: 10.3389/fevo.2021.668676

An Improved Method for Extracting, Sorting, and AMS Dating of Pollen Concentrates From Lake Sediment

Irene Tunno[1], Susan R. H. Zimmerman[1], Thomas A. Brown[1] and Christiane A. Hassel[2]*

[1] Center for Accelerator Mass Spectrometry, Lawrence Livermore National Laboratory, Livermore, CA, United States, [2] Flow Cytometry Core Facility, Indiana University Bloomington, Bloomington, IN, United States

High-resolution chronologies are crucial for paleoenvironmental reconstructions, and are particularly challenging for lacustrine records of terrestrial paleoclimate. Accelerator Mass Spectrometry (AMS) radiocarbon measurement of terrestrial macrofossils is the most common technique for building age models for lake sediment cores, but relies on the presence of terrestrial macrofossils in sediments. In the absence of sufficient macrofossils, pollen concentrates represent a valuable source of dates for building high-resolution chronologies. However, pollen isolation and dating may present several challenges, as has been reported by different authors in previous work over the last few decades. Here we present an improved method for extracting, purifying and radiocarbon-dating pollen concentrates using flow cytometry to improve the extraction efficiency and the purity of the pollen concentrates. Overall, the nature of the sediments and the abundance of the pollen represent major considerations in obtaining enough pollen grains and, consequently, enough carbon to be dated. Further, the complete separation of pollen from other forms of organic matter is required to ensure the accuracy of the dates. We apply the method to surface samples and sediment cores recovered from two contrasting lake basins on the eastern side of the Sierra Nevada (California), and describe the variations that may be used to optimize pollen preparation from a variety of sediments.

Keywords: radiocarbon, AMS, pollen separation, flow cytometry, high-resolution chronology, lake sediment, Sierra Nevada

OPEN ACCESS

Edited by:
Scott Andrew Mensing,
University of Nevada, United States

Reviewed by:
Brendan Culleton,
Pennsylvania State University (PSU), United States
John Southon,
University of California, Irvine, United States
Thomas A. Minckley,
University of Wyoming, United States

****Correspondence:***
Irene Tunno
tunno1@llnl.gov

Specialty section:
This article was submitted to Paleoecology, a section of the journal Frontiers in Ecology and Evolution

Received: *16 February 2021*
Accepted: *28 April 2021*
Published: *25 May 2021*

Citation:
Tunno I, Zimmerman SRH, Brown TA and Hassel CA (2021) An Improved Method for Extracting, Sorting, and AMS Dating of Pollen Concentrates From Lake Sediment. Front. Ecol. Evol. 9:668676. doi: 10.3389/fevo.2021.668676

INTRODUCTION

Lakes are archives that can record natural and human-induced changes in the environment, preserved in biological, sedimentological, and geochemical components of the sediment. In order to interpret and compare paleorecords between sites, a reliable chronology is fundamental for each paleorecord, and a relatively large number of dates may be required to build a chronology of sufficient resolution for proxy interpretation (Blaauw et al., 2018; Zimmerman and Wahl, 2020). Among the techniques for building chronologies, AMS radiocarbon-based age-depth models are the most widely used for sediment cores recording the last ∼35,000 years. The selection of the organic material for dating is extremely important in order to obtain reliable radiocarbon dates and build an accurate age model. The optimal organic materials that can be measured for ^{14}C are short-lived terrestrial plant macrofossils, such as leaves, needles, and twigs. Such macrofossils are often

not abundant in lake-sediment cores, and this has been viewed as forcing reliance on bulk-sediment measurements, which can lead to age models of uncertain accuracy. AMS measurements on bulk sediments may include samples where different types of organic matter have been homogenized and dated together. Such material can often include carbon recycled by aquatic plants and algae from dissolved organic and inorganic carbon sources.

In cases when terrestrial macrofossils are rare or absent, pollen may be a valuable resource for building a high-resolution age model. In addition, in cases where precise dating of a significant shift in a proxy is desired, pollen dates can allow close bracketing of the event. Pollen is formed by terrestrial plants from atmospheric CO_2, and is often abundant in sediment cores, and so radiocarbon chronologies based on pollen can help to reduce the uncertainties related to the presence of very few macrofossils in a core. Previous studies demonstrated that pollen concentrates can be dated through AMS measurements (Brown et al., 1989, 1992; Newnham et al., 2006; Fletcher et al., 2017), but two main challenges remain: separating sufficient pollen for a radiocarbon date and isolating the pollen from other carbon-bearing material. Through the last three decades, several studies have developed methods to separate and concentrate the pollen including heavy-liquid separation (Barss and Williams, 1973; Regnéll and Everitt, 1996), sieving (Brown et al., 1989), micromanipulator (Long et al., 1992), and mouth pipetting (Mensing and Southon, 1999). The purity of the pollen concentrates remains a key for obtaining reliable dates, as it has been reported that radiocarbon measurements on pollen resulted in dates too old in comparison with independent estimations of the sediment age (e.g., Kilian et al., 2002; Piotrowska et al., 2004).

Recently, flow cytometry sorting has been tested as a technique to isolate pollen from other possible sources of contamination (Byrne et al., 2003; Tennant et al., 2013; Zimmerman et al., 2018). These pilot studies identified the main challenge of pollen AMS dating as maximizing the amount of pollen in a sample to reduce analytical uncertainties, while at the same time minimizing the time (and thus expense) required for sorting by producing the cleanest possible pollen extract. Here we present an improved method for extracting, sorting and dating pollen from lake-sediment cores, which combines an optimized pollen extraction protocol (without using strong chemicals, e.g., hydrofluoric acid), sorting by flow cytometry, and standard graphitization and AMS radiocarbon measurement methods.

STUDY AREAS

Mono Lake

Mono Lake (ML) is a hydrologically closed lake located on the eastern side of the central Sierra Nevada (38.00°N, 119.00°W), at ∼1945.5 m elevation (**Figure 1**). The average depth of the water is 17 m (maximum = ∼48 m) and the surface area is 183 km^2. The main water source is provided by meltwater from the snowpack in the Sierra Nevada, which form the western side of the lake basin. The modern lake is an evaporative remnant of a much deeper glacial-age lake (Zimmerman et al., 2011), and consequently is highly saline (88 g/L) and alkaline (pH = 10). The watershed of the lake is ∼2070 km^2, and spans an elevation range of >1800 m. The lake is surrounded by desert shrubs such as bitterbrush (*Purshia tridentata*), sagebrush (*Artemisia tridentata*), greasewood (*Sarcobatus vermiculatus*), and desert peach (*Prunus andersonii*). The mountains are dominated by pinyon-juniper woodland (*Pinus monophylla, Juniperus osteosperma*) on the western side of the basin and Jeffrey pine forest (*Pinus jeffreyi*) on the southern side of the basin. The north and the east sides are dominated by the alkali sink plant communities, mostly represented by the above-mentioned desert shrubs.

Fallen Leaf Lake

Fallen Leaf Lake (FLL) is a small (5.7 km^2 surface area) and deep (>120 m maximum depth) subalpine lake in the northern Sierra (38.9024° N, 120.0615° W) located ∼2 km south of Lake Tahoe (**Figure 1**). The lake elevation is 1942 m, 45 m above Lake Tahoe; the watershed is 42 km^2. The principal inflow is Alpine Creek from the south, while surface outflow in Taylor Creek and groundwater flow through recessional end moraines connect FLL to Lake Tahoe to the north (Kleppe et al., 2011; Maloney et al., 2013). FLL is a freshwater, meso-oligotrophic organic- and diatom-rich lake with circumneutral pH (Noble et al., 2013, 2016). The surrounding vegetation is dominated by pine (*Pinus jeffreyi* and *Pinus ponderosa*) and by quaking aspen (*Populus tremuloides*) along the creeks.

FOSSIL AND MODERN POLLEN MATERIALS

Pinus pollen type was the main target during the pollen extraction, because it is the most abundant pollen in both lakes. Pine is in fact an ideal pollen type for radiocarbon dating: it is produced in large quantities and efficiently transported by wind. For these reasons, pine is often very abundant in sediments, especially in the western U.S., where the vegetation is dominated by several pine species.

Sediment-Core Samples

Samples for pollen extraction were collected from the Holocene sections of three sediment cores. UWI-MONO15-1C and -1D (Hodelka et al., 2020) were collected in 2015 from the western embayment of Mono Lake, in ∼18 m water depth, and BINGO-MONO10-4A in 2010 from the western embayment in 2.8 m water depth (Zimmerman et al., 2020), from a location very close to that of the core analyzed by Davis (1999). The BOLLY-FLL10-1A and -2D cores were recovered from the center of the southern basin of Fallen Leaf Lake in 2015 (Noble et al., 2016). As a test of the potential fidelity of pollen-based radiocarbon ages, the depths of the Fallen Leaf Lake pollen samples were chosen to be paired with macrofossil dates used by Noble et al. (2016) to develop the age model for the Fallen Leaf Lake cores. In two cases the pollen sample was separated from the centimeter just above the level of the macrofossil. All the cores are archived at the National Lacustrine Core Repository at the University of Minnesota (LacCore) and were sampled there. The samples were

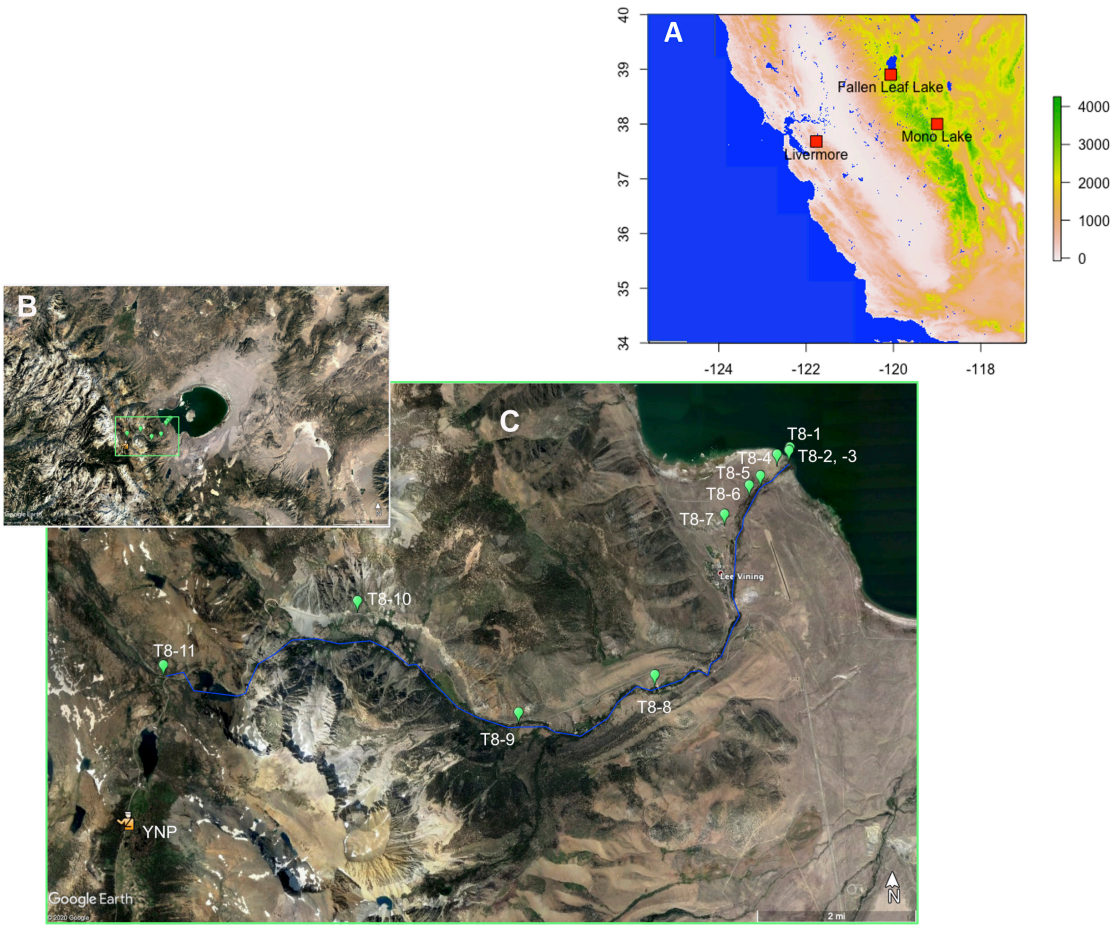

FIGURE 1 | (A) Map of California, United States, showing the locations of the Mono Lake, Fallen Leaf Lake, and Livermore sites. **(B)** Google Earth image of Mono Lake, showing the exposed glacial-age lake bed surrounding the modern lake, and the stream canyons supplying mountain snowmelt from the Sierra Nevada to Mono Lake. **(C)** Detail of **(B)** showing transect #8 (T8), with green markers show the sampling points along the transect. Samples T8-2 and T8-3 were taken at the same coordinates, with T8-2 taken at the lake shore, and T8-3 slightly inland. The location of Lee Vining Creek is shown roughly by the blue line; all sampling locations were on the north side of the creek. The east entrance to Yosemite National Park is indicated for reference (YNP).

stored in polyethylene containers and kept at 5°C until extraction at the Center for Accelerator Mass Spectrometry (CAMS) of Lawrence Livermore National Laboratory.

The main differences between the sediments from the two lakes are their heterogeneity and their pollen concentration, stemming from the contrasting watersheds and lake chemistries. Fallen Leaf Lake sediments are dominated by olive to dark-gray diatom-rich clay throughout the Holocene, with homogeneous, laminated, and mottled textures, and characterized by high content of organic matter and diatoms (Noble et al., 2016). Pollen concentration in the BOLLY-FLL10 cores varies between 170,000 and 1,420,000 grains/cm^3 (Noble, pers. comm., 2017), consisting mostly of pine pollen. The sediments of the two Mono Lake cores are quite heterogeneous, composed of sand- and silt-sized sediment, laminated dark-brown and olive-colored mud, interbedded tephra layers and variable amounts and forms of authigenic carbonate. In the pollen analysis of Davis (1999), pine also dominated, but pollen concentration was reported to vary between 1,200 grains/cm^3 and 180,000 grains/cm^3 over the Holocene. Pollen analysis is underway for the UWI-MONO15 cores. The heterogeneity of the sediments between the two lakes and along the Mono Lake cores required processing modifications during the pollen extraction.

Pollen was initially extracted from samples of 1–2 cc. The volume of the sediment used was increased up to 4 cc when necessary to obtain enough carbon for the AMS measurements. The extraction was performed on 20 samples from BOLLY-FLL10, 26 samples from UWI-MONO15 and 18 from BINGO-MONO10. Of the 64 core samples extracted, 12 were not sorted because the pollen concentration was too low (all from BINGO-MONO10); consequently only 52 samples appear in **Table 1**. In general, the lower limit for reportable ^{14}C measurements at CAMS is 0.020 mg C and samples smaller than that size did not produce a ^{14}C result (**Tables 1**, **2**).

Surface Samples

In June 2017, 38 surface samples were collected along six transects from the shore of Mono Lake toward the mountains,

TABLE 1 | Fossil samples from Mono Lake and Fallen Leaf Lake.

Lab ID	Sediment description	# Pollen grains	Hours of sorting	Pollen %	C (mg)	^{14}C measurement	Separation and/or drying method
Mono Lake							
1C-2U-1 53	Dark-olive to brown, laminated	7,610	1.25	49%	0.013	–	Lyophilizer
1C-2U-2 3.2	Dark brown, laminated	8,038	1.25	29%	0.005	–	Lyophilizer
1C-3U-2 7.5	Very fine alternated dark- and light-gray laminations	7,840	1.75	30%	–	–	Lyophilizer
1C-3U-2 57.9	Alternated dark- and light-gray laminations	10,805	1.5	39%	0.008	–	Lyophilizer
1C-4U-1 49.4	Light-brown with one grayish colored lamina, carbonate rich	13,635	2.5	25%	0.005	–	Lyophilizer
1C-4U-1 99.4	Dark-gray clay	27,166	3.5	24%	0.033	–	Lyophilizer
1C-4U-2-38.5	Dark and yellowish irregularly laminated	133	1.25	2%	–	–	
1C-4U-2 39.5	Very dark with a yellowish lamina	16,016	2.25	18%	0.045	Good	Jouan
1C-4U-2-40.5	Dark gray, finely laminated	–	–	Low	–	–	
1C-5U-1 29	Very dark, homogeneous	4,165	2	6%	–	–	
1C-5U-1 78.6	Very dark, homogeneous	1,973	1.25	5%	–	–	
1C-6U-1-113.5	Dark and light gray, irregularly laminated	–	–	Low	–	–	
1C-6U-1-113.5 +116	Dark gray sediment	–	1	1%	–	–	Lyophilizer, combined samples
1C-6U-1 115.2	Dark and gray irregularly laminated	2,511	1.25	9%	–	–	
1C-6U-1-116	Light- and dark-gray irregularly laminated	–	–	Low	–	–	
1D-2U-1 62.5	Laminated, carbonate rich sediment	4,640	1	30%	–	–	
1D-2U-2 42.4	Laminated, carbonate rich sediment	16,757	2	43%	0.060	Good	Jouan
1D-2U-2 43	Laminated green and light-yellow sediment	18,457	6.5	8%	0.058	Good	Jouan
1D-3U-2 31	Brown sediment	43,550	4.75	27%	0.088	Good	Jouan
1D-4U-1 102.7	Gray, homogeneous	2,721	1.25	14%	–	–	
1D-5U-1 56.2	Dark, homogeneous	<7,000	1	Low	–	–	
1D-5U-2-43	Gray, homogeneous	12,264	7.5	6%	–	–	
1D-5U-2 45.3	Gray, homogeneous	1,232	1.25	8%	–	–	
1D-5U-2-46	Gray, homogeneous	4,174	2.25	14%	–	–	
1D-5U-2 95.3	Gray, homogeneous	<7,500	0.5	Low	–	–	
1D-5U-2-94.5	Dark- to light-gray laminations	19,317	6	22%	0.055	Good	Lyophilizer
4A-1N-2-12	Gray clay lamination	67,456	5	48%	0.020	–	Lyophilizer
4A-1N-2-13	Light brown carbonate-rich	68,774	6.25	38%	0.028	Good	Lyophilizer
4A-1N-2-14	Carbonate-rich sediment	42,428	3	37%	0.160	Good	Jouan
4A-1N-2-20+21	Gray to dark brown to light-yellow colored fine laminations	68,220	8	46%	0.256	Good	Lyophilizer, combined samples
4A-1N-2-48	Light brown, high carbonate-rich sediment	48,719	6.75	35%	–	–	
4A-1N-2-49	Light brown, high carbonate-rich sediment	21,864	3.25	44%	0.035	Good	Lyophilizer

(Continued)

TABLE 1 | Continued

Lab ID	Sediment description	# Pollen grains	Hours of sorting	Pollen %	C (mg)	^{14}C measurement	Separation and/or drying method
Fallen Leaf Lake							
1A-1K-1-54	Olive clay, homogeneous	50,483	4.25	46%	0.083	Good	Sonicator, lyophilizer
1A-1K-1-78	Olive clay, homogeneous	51,519	4.5	38%	0.013	Good	Sonicator, lyophilizer
1A-1K-5-22	Olive clay, mottled	61,763	3.25	64%	–	–	Sonicator, lyophilizer
1A-1K-5-142	Olive clay, mottled	67,242	3.5	53%	0.326	Good	Sonicator, lyophilizer
1A-1K-6-149	Olive clay, mottled	50,000	14	62%	0.020	Good	Sonicator, lyophilizer
1A-1K-7-5	Alternating with yellowish olive and darker gray clay	53,936	2.5	65%	0.016	Good	Sonicator, lyophilizer
1A-1K-7-79	Alternating with yellowish olive and darker gray clay	53,936	2.5	66%	0.073	Good	Sonicator, lyophilizer
1A-1K-8-55	Olive green–greenish gray, homogenous	56,250	3.25	58%	0.015	Good	Sonicator, lyophilizer
1A-1K-8-63	Olive green–greenish gray, homogenous	54,742	2.5	67%	–	–	Sonicator, lyophilizer
1A-1K-8-84	Mottled olive green to olive gray silty clay	52,089	3.25	55%	0.010	–	Sonicator, lyophilizer
2D-1K-1-54	Olive homogeneous silty clay	53,699	2.75	57%	0.266	Good	Jouan
2D-1K-2-38	Olive clay, homogeneous	56,250	2.5	68%	0.055	Good	Jouan
2D-1K-2-48	Olive clay, homogeneous	55,438	2.5	65%	0.256	Good	Jouan
2D-1K-2-78	Olive clay, homogeneous	55,636	2.75	62%	0.283	Good	Jouan
2D-1K-3-25	Yellowish olive clay	55,354	3	66%	0.271	Good	Jouan
2D-1K-3-46	Yellowish olive clay	56,250	3	60%	0.266	Good	Jouan
2D-1K-6-50	Olive and yellowish olive clay	56,250	2.75	73%	0.263	Good	Jouan
2D-1K-6-77	Olive clay, homogeneous	56,250	3.25	54%	0.256	Good	Jouan
2D-1K-8-7	Olive clay with minor silt fraction	56,250	2.75	66%	0.256	Good	Jouan
2D-1K-9-123	Laminated olive silty clay	56,250	2.75	71%	0.263	Good	Jouan

Mono Lake and Fallen Leaf Lake samples were collected from the sediment core UWI-MONO15, BINGO-MONO10, and BOLLY-FLL10. The section and the depth for each sample are showed in the Lab ID column. "# pollen grains": number of particles selected as "pollen grains" by COPAS during sorting (see section "Flow Cytometry Sorting" for discussion of sorting); "hours of sorting": hours that each sort required to obtain the related # pollen grains; "% pollen": the percentage of particles identified as "pollen grains" from the total events recorded by COPAS during sorting of the sample; "C (mg)": the mg of carbon in each sample (measured during the graphitization process);"14C measurement": the samples marked as "good" produced a reliable 14C measurement.

TABLE 2 | Modern samples from surface transect T8 (**Figure 1**) and fresh pinecones.

Lab ID	Sample type	# pollen grains	Hours of sorting	Pollen %	C (mg)	^{14}C measurement	Separation and/or drying method
T8-1-1	Coarse sediments	25,263	3.5	18%	0.035	good	Lyophilizer
T8-2-1	Very coarse sediments	–	0.75	5%	–	–	
T8-3-1-1	Very coarse sediments	10,222	4.75	7%	0.020	–	Lyophilizer
T8-3-1-2	Very coarse sediments	48,419	3.75	38%	0.185	Good	Jouan
T8-4-1-1	Fine sediments	18,638	5.5	6%	0.013	–	Lyophilizer
T8-4-1-2	Fine sediments	20,487	3	18%	0.088	Good	Jouan
T8-5-1	Organic rich	–	–	Low	–	–	
T8-6-1-1	Coarse sediments	<10,000	0.5	Low	–	–	
T8-6-1-2	Coarse sediments	7,770	1.25	24%	–	–	
T8-7-1	Mineral soil -dry	44,548	2.75	55%	0.070	Good	Lyophilizer
T8-8-1-1	Mixed coarse and fine sediments	–	1	Low	–	–	
T8-8-1-2	Mixed coarse and fine sediments	50,975	5.75	41%	0.163	Good	Jouan
T8-9-1-1	Fine organic rich	6,602	1.25	32%	–	–	
T8-9-1-2	Fine organic rich	–	0.75	Low	–	–	
T8-10-1-1	Clay and charcoal rich sediments	<5,000	1	3%	–	–	
T8-10-1-2	Clay and charcoal rich sediments	31,250	2.25	48%	0.201	Good	Jouan
T8-11-1-1	Fine organic rich sediments	22,700	9	10%	0.015	–	Jouan
T8-11-1-2	Fine organic rich sediments	50,000	3	58%	0.160	Good	Jouan
Pinus-1-1	Fresh pinecones	50,000	2.5	61%	0.170	Good	Lyophilizer
Pinus-1-2	Fresh pinecones	137,592	2.5	61%	0.481	Good	Lyophilizer
Pinus-2-1	Frozen pinecones	50,000	2	74%	0.105	Good	Jouan
Pinus-2-2	Frozen pinecones	100,000	3.5	74%	0.376	Good	Jouan
Pinus-2-3	Frozen pinecones	150,000	5.75	74%	0.246	Good	Jouan
Pinus-3-1	Frozen pinecones	50,000	2.75	74%	0.306	Good	Jouan
Pinus-3-1-1	Frozen pinecones	50,000	1.75	74%	0.293	Good	Jouan
Pinus-3-2-1	Frozen pinecones	100,000	3.25	74%	0.549	Good	Jouan
Pinus-3-3-2	Frozen pinecones	150,000	5.25	74%	0.772	Good	Jouan

*See **Table 1** caption for explanation of columns.*

following the main creeks present in the basin (**Figure 1C**). Due to an exceptionally wet winter, the tributary creeks were unusually high, and the surface samples consisted of surficial (1–2 cm depth) soil (above creek level) or sediment (alongside the creek bed) collected within a few meters of the creek, and they vary widely in organic matter content and grain size. The samples were collected in 250 ml Nalgene bottles for the sediments and in 118 ml *Nasco* Whirl-Pack bags for the soil, sealed and stored at 5°C until the extraction. Because the surface samples presented variable organic content and grain size, different amounts (4–8 cc) of sediment were used for each pollen extraction. The results from transect #8 (T8) are presented here. Eleven samples were collected along this transect between the lake shoreline at Lee Vining Creek (T8-1, 1944 m elevation) and the proximity of Ellery Lake, along Route 120 (T8-11, 2921 m elevation) (**Table 2**).

Modern Pine Samples

Fresh male cones were collected from two pine trees (*Pinus* cf. *contorta*) growing in Livermore CA, in June 2017 and March 2018. Cones were collected from the trees, sealed in plastic bags and stored at –20°C until the pollen extraction. A total of nine samples from fresh cones were extracted, sorted, and dated (**Table 2**).

POLLEN EXTRACTION PROTOCOL

Core- and Surface-Sediment Samples

The pollen extraction protocol applied for radiocarbon dating is different from the standard extraction method for pollen analysis (Faegri and Iversen, 1985) because the goal is to yield the largest amount of carbon for dating, without regard for preserving the varieties of pollen present and their proportions, and without adding carbon during the processing. The optimal pollen extraction will also eliminate most of the non-pollen organic and inorganic particles, as a cleaner sample minimizes the sorting time and consequently the cost of the flow cytometry process. The main steps are summarized in **Figure 2**, with sieving and heavy-liquid separation using non-toxic sodium polytungstate (low-carbon SPT – SPT-O, Geoliquids, Inc.) being two important steps in separating pollen from the non-pollen matter. The use of any carbon-based chemical was avoided to prevent contamination. For this reason, acetolysis, commonly

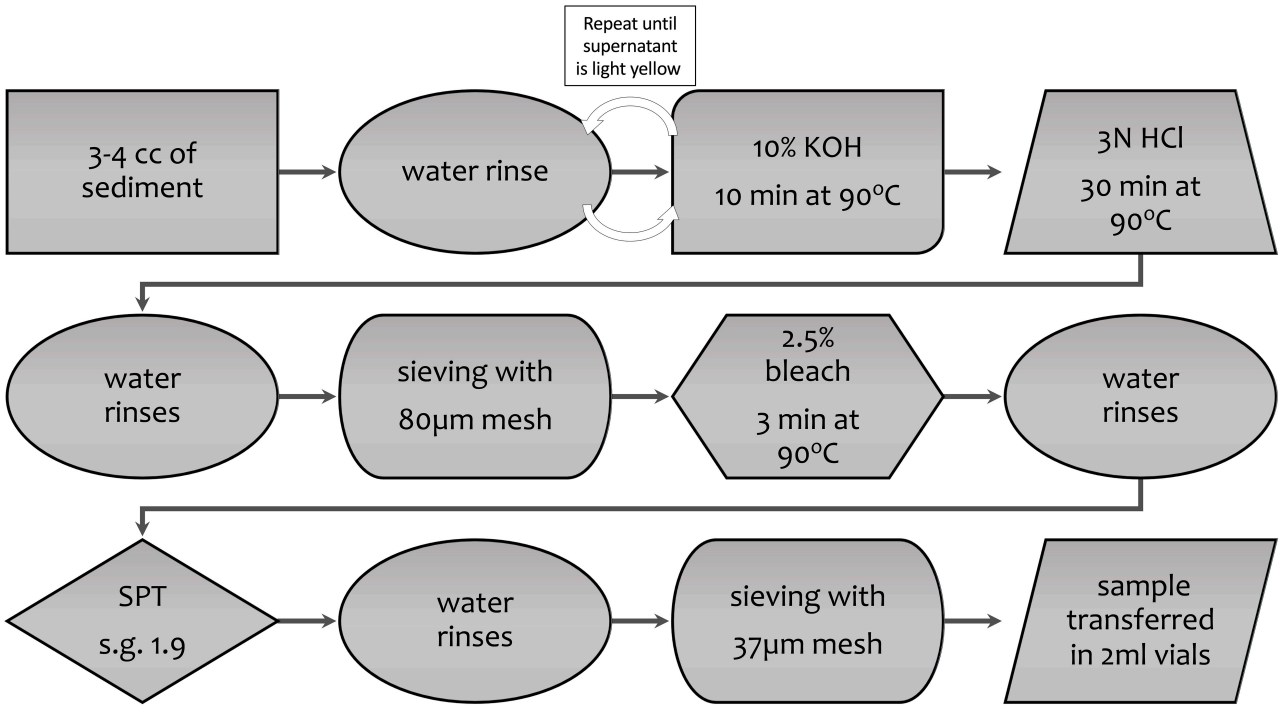

FIGURE 2 | Main steps of the pollen extraction protocol before flow cytometry, including base, acid, bleach, and heavy-liquid steps. Water rinses are indicated by ovals; note that there is no water rinse between the base and acid steps. Size of meshes used for the various steps must be tested and modified depending on the sample and pollen types and other material included in the samples; in every case, the size fractions should be examined to determine into what fraction the pollen appears.

performed during standard extraction for pollen analysis, was not performed. Sieving was performed with sieves of different materials (metal and nylon) and sizes. Both nylon mesh and SPT were discarded after use, to prevent contamination between samples. All steps involving the centrifuge were performed at 2,500 rpm (=3800 RCF using a Thermo Scientific Sorvall ST 8 compact centrifuge). Soft brake function for slow acceleration and braking was applied for the SPT and sodium hypochlorite steps to avoid the resuspending of the sediment and the sinking of the pollen due to the regular brake of the centrifuge.

All samples were first transferred to labeled 50 ml test tubes, rinsed and centrifuged for 2.5 min, and then a series of chemical and physical separation techniques were applied following the final protocol below described. Description of the various tests performed to improve the method, including SPT specific gravities and sieve mesh sizes, is given in Section "Discussion."

Pollen Extraction Protocol

(1) About 30 ml of 10% (by weight) potassium hydroxide (KOH, prepared mixing 59 g of KOH – 86% KOH by weight of dry pellets) and 461 ml MilliQ (MQ) water was added to each test tube and heated at 90°C for 10 min. This was repeated until the supernatant was clear or light-yellow colored.

(2) After the KOH was poured off, about 30 ml of 3 N hydrochloric acid (HCl) was added to each tube to dissolve carbonates, with no water rinses between the KOH and HCl steps. The samples were heated at 90°C for 30 min or until the reaction stopped, and then rinsed of the HCl with MQ water.

(3) Samples were sieved to eliminate the coarser fraction of the sediments without losing pollen grains; 125, 80, and 63 µm sieves were used during this step, depending on the size of the coarser debris. The <125, <80, and <63 µm fractions were kept for the further steps; the coarser fractions were stored in weakly acidified MQ water to preserve the samples in case further analyses were needed.

(4) A 2.5% sodium hypochlorite (NaOCl) solution was added to each sample and heated at 90°C for 3 min to disaggregate and remove the organic material left in the samples. This solution was obtained by diluting an 8% NaOCl unscented commercial bleach. The samples were rinsed with water and centrifuged two times.

(5) After carefully pouring off as much as water possible without disturbing the settled material, about 20 ml of low-carbon 1.9 specific gravity SPT were added to each sample, followed by centrifuging for 20 min to separate the inorganic material. At this stage, the inorganic material sank, and the pollen floated. The supernatant containing the pollen was separated, diluted with water, and centrifuged again; in this lower specific-gravity solution, the pollen completely sank to the bottom of the test tubes. Several water rinses were then performed in order to eliminate the residual SPT from the samples. The tests that led to choosing the value of 1.9 specific gravity for the SPT are discussed in section "Density Separation."

(6) The samples were sieved with either 37 or 20 μm nylon mesh supported by a modified lidded plastic container. The smaller fraction was discarded, after checking under the microscope to be sure no pollen was included in that fraction. The largest fraction was checked under a microscope for purity, collected and concentrated into 2 ml Nalgene vials and shipped to the Flow Cytometry Core Facility, Indiana University, Bloomington to be sorted using flow cytometry.

Modern Pine Samples

Three batches were prepared using 15 and 50 ml test tubes and 50 ml Falcon plastic tubes. The cones were ground with mortar and pestle and sieved at the beginning with a 125 μm sieve to eliminate the coarse fragments of cone. For the first two batches the pollen was extracted following the same protocol applied to the sediment samples, to test for any possible contamination from the chemicals, the plastic tubes, and the processing. The last batch was extracted as follows: approximately 10 ml 3N HCl was added to the solution containing the <125 μm fraction of pollen concentrates to facilitate the precipitation of the grains during the initial centrifuging steps; ∼10 ml for the 15 ml tubes and ∼ 25 ml for the 50 ml tube 10% (by weight) KOH was then added to the sample and heated at 90°C for 10 min; this step was performed twice, until the supernatant was light-yellow colored. A rinse with 3N HCl at 90°C for 30 min followed this step. Then, after a water rinse, the sample was sieved with 80 μm nylon mesh and the >80 μm fraction was discarded to eliminate the coarse organic fraction, mostly represented by bigger fragments of cone. After one rinse with MQ water, 2.5% sodium hypochlorite (NaOCl) solution was added and heated at 90°C for 3 min. Following a water rinse, the sample was finally sieved with 37 μm nylon mesh; the >37 μm fraction was allowed to settle and excess water was removed, and then the sample was shipped to the flow cytometry facility in Indiana. Based on observation of the previous batches, there was no advantage in performing the heavy-liquid separation due to the absence of inorganic material in the sample.

Flow Cytometry Analysis and Pollen Sorting

Flow cytometry sorting was performed using a COPAS *SELECT* large-particle sorter (Union Biometrica) with Advanced Acquisition Package, using a 488 nm laser excitation source. The COPAS was specifically selected for its ability to separate larger particles, but it is possible to use different instruments such as the FACSAria to sort pollen smaller than pine (e.g., *Quercus* spps., *Alnus* spps., etc.). Flow cytometry is used to detect both light-scatter and fluorescence characteristics of particles using laser excitation in a fluidics-based system. These characteristics (scatter and fluorescence) are used to separate the pollen (autofluorescent) portion of the sample from other materials (non-fluorescent). Following the protocol established by Zimmerman et al. (2018) to check for possible radiocarbon contamination, the instrument was swiped before each batch of pollen sorting, and AMS measurements were performed on the swipes before the pollen samples were handled at CAMS. No elevated-^{14}C contamination has been detected on any swipes from the IUB facility.

Concentrated samples were first diluted with MQ water at a final volume of 10 ml per sample. Samples were briefly analyzed by light microscopy to judge the proportion of pollen versus other material in the sample. If many small particles (<30 micron) were seen, the sample was also filtered through a 30 μm CellTrics filter (Sysmex) and the >30 μm particles collected for analysis and sorting. Sample was then added to MQ water in a 250 ml sample cup and analyzed by the sorter. Particles were selected as pollen by first using a gate region on a plot of TOF (Time Of Flight, relative length) vs. EXT (Extinction, relative structure) parameters (**Figure 3**). Particles falling within that gate were selected based upon autofluorescence, which is detected in the RED parameter at an emission of 610/20 nm, versus TOF (**Figure 3**). A test sort was performed to check that ten particles sorted as pollen were indeed pollen (confirmed by light microscopy). Samples were sorted in aliquots based on machine conditions and the selected fractions were collected into sterile petri dishes. These were transferred to 15 ml Falcon tubes and allowed to settle, then fractions of a single sample were re-combined and transferred to a sterile cryogenic tube. To minimize potential contamination from atmospheric carbon, approximately 20 μl of 1N HCl was added to each sorted sample; the samples were then frozen and shipped to CAMS on dry ice and stored at−20°C until pretreatment for AMS was begun.

Over the course of the project, the particles that were not selected by the sorter were periodically collected in the recovery cup and checked under the microscope to verify that the rejected fraction did not contain undesirably large fractions of pollen.

Graphitization and AMS Measurement

In order to be combusted to carbon dioxide (CO_2), the pollen samples needed to be concentrated, dried and weighed into quartz tubes. The sorted samples were allowed to thaw completely at room temperature at CAMS and to settle undisturbed for 24 h, and then as much liquid as possible was pipetted out from the cryo-tubes without disturbing the pollen settled at bottom of each vial. In all cases, no more than 1 ml of solution, containing the pollen concentrate, was transferred by pipetting from the cryo-vial to the standard quartz tube used for graphitization at CAMS (inner diameter = 6 mm). The time required for drying the samples varied depending on the amount of solution transferred into the quartz tube and the technique used for drying. Three different approaches were used: heat block and oven, lyophilizer, and Jouan concentrator centrifuge (model Jouan RC 10.10 – heated/under-vacuum centrifuge). For the first approach, the tubes were placed on a heating block at ∼80°C and then transferred to a 40°C oven to complete the desiccation process, which required 2–3 days to be completed. For the lyophilizer, the quartz tubes containing the pollen concentrates were frozen in liquid nitrogen and freeze-dried for ∼24 h. Finally, for the third approach, the Jouan was used to dry the samples. In this case the quartz tubes were centrifuged at 65°C until the samples were completely dried. This step required approximately 2–6 h. Based on several tests conducted using these three different methods,

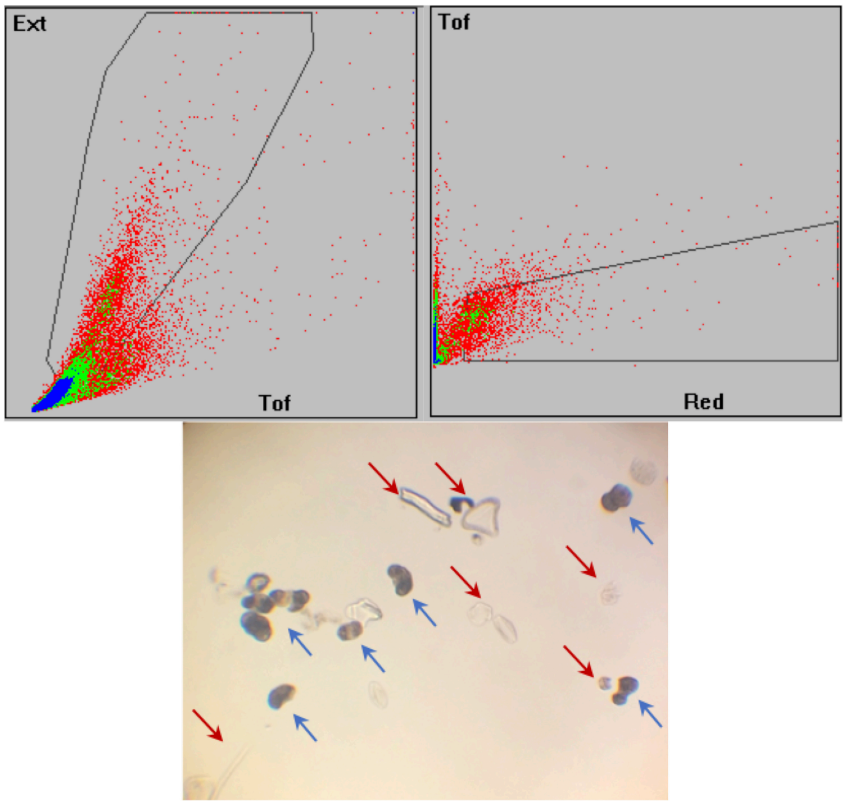

FIGURE 3 | Flow cytometry plots of sample 1D-5U-2-46, as an example of the gates used to separate the pollen grains. The gates are the black polygons, showing the selected areas in which the ideal particles are included; each dot represents a particle that traveled through the COPAS laser. The gates are drawn by the operator based on optical density (Ext = extinction), size (Tof, time of flight), and fluorescence (Red). Photograph below shows the 1D-5U-2-46 sample after extraction and before sorting. The blue arrows indicate some examples of pollen grains, while the red arrows point out non-pollen particles, such as diatoms and organic fragments, that survived chemical digestion and sieving during pollen extraction.

the Jouan gave the most reliable sample handling, and greatly reduced the drying time compared to both the lyophilizer and the heat-block methods. Consequently, most of the samples were processed with the Jouan.

Copper oxide (CuO) and silver powder (Ag) were added to each tube after the sample was completely dry. The samples were then sealed under vacuum with an H_2/O_2 torch and combusted at 900°C for 4 h to oxidize the carbon of the purified pollen to CO_2. The CO_2 was then reduced to elemental carbon in the presence of a low-carbon, reduced-Fe catalyst and a stoichiometric excess of ultrapure hydrogen, similar to the methodology described in Vogel et al. (1984, 1987).

For these samples, which were anticipated to be of suboptimal masses (i.e., 20–40 μg C), the amount of Fe catalyst was decreased compared to larger (>100 μg C) samples, to 2.5 mg (compared to 5.7 mg for larger samples). Radiocarbon data are corrected for the contribution of modern and dead carbon added during combustion and graphitization following Brown and Southon (1997). Coal backgrounds and modern (OX2) standards were handled similarly and analyzed in order to determine the modern (0.3 ± 0.1 μgC) and dead (0.15 ± 0.1 μgC) contributions, respectively. Due to the small size of the pollen samples and static charge, in most cases it was not possible to measure the mass of the samples accurately, even on a high-precision balance. While this prevented estimation of the % carbon content of many of the purified pollen samples, the sample carbon masses needed for the above-mentioned corrections were obtained from known-volume pressure measurements of the CO_2 gas during the graphitization process.

After graphitization, all samples were pressed into sample holders designed for the CAMS high-intensity sputter source and the samples' ^{14}C contents were measured during routine radiocarbon runs. Due to the very small size of some of the samples, the ion source parameters were modified to extend the length of time small samples could be sputtered.

Between July 2017 and September 2019, 102 final samples were extracted from fresh cones, surface transect and sediment-core samples. AMS measurements were conducted on 56 samples, 44 of which produced reliable dates (**Tables 1**, **2**).

DISCUSSION

Pollen Extraction

The density separation and the sieving were the main steps during the pollen extraction to separate the pollen grains from

other organic particles that may represent a contamination source for AMS analysis (**Figure 2**). The pollen concentrates were mostly pine pollen together with some organic particles, such as charcoal, micro plant remains and diatoms in different amounts, depending on the characteristics of the sediment samples (**Figure 4**). Occasionally, different types of pollen (e.g., *Artemisia* type) were observed in the final concentrates.

The samples were initially processed in 50 ml glass and polypropylene (Falcon) centrifuge test tubes because of suspicion that the chemical steps might leach petroleum-based (i.e., ^{14}C-dead) carbon out of the plastic. Comparison of the ^{14}C Fraction Modern of the fresh pine pollen processed in glass and polypropylene tubes (4x each) showed no contamination from the polypropylene during our processing. Therefore, 50 ml Falcon tubes were preferred to glass tubes because they were easier to handle in the centrifuge.

The first critical goal during the pollen extraction is to obtain enough pollen to have a sufficient amount of C to date. This step may represent a major challenge if pollen concentrations in the different layers of the core are not known. This information is very helpful to determine the adequate amount of sediment for the extraction. For all the samples (ML, FLL and surface-transect samples) about 2–4 cc of sediment was processed during the pollen separation, providing extremely variable results (**Table 1**, columns 4–6). As expected from the preliminary pollen analysis, FLL samples showed a very high pollen concentration, and it was relatively easy to separate abundant pollen in all the samples that were extracted. For the ML cores the pollen concentrations were not available and, due in part to the heterogeneity of the cores, it was often difficult or impossible to extract sufficient pollen for dating. Based on the results obtained in this study, 4 cc of raw sediment per sample was the preferable volume to produce a minimum amount of ∼30,000 grains of pollen, with an optimum of 50,000 grains desired. The amount of pollen required for AMS analysis and the amount of sediment required to yield that amount of pollen will vary based on the sediment and pollen type.

The first pollen extractions attempted on many modern samples did not provide the expected results, mainly due to the diverse nature and composition of the sediment. The modified and improved extraction protocol given in Section "Core and Surface Sediment Samples" was applied and reliably produced a pollen concentrate that could be easily dated from most samples. The composition of the sediment of some modern samples did not provide enough pollen grains for dating even with the improved method, leading to the conclusion that certain sediment does not preserve or hold pollen like other types (e.g., coarse or sandy versus fine or clayey sediment, **Table 2**, Column 3).

In general, for samples dominated by a single pollen type (as our samples were), there should be a strong linear correlation between the number of grains sorted and the mg of carbon in the AMS sample. Our results show a weak linear correlation between the number of pollen grains and the C amount for samples dried in the Jouan (**Figure 5** and **Table 1**). Deviation from this trend may result from several parts of the process. To begin with, handling thousands of pollen grains through the many steps required introduces opportunities for loss of grains, until a workable protocol is developed for each lab and handler. Further, the number of "pollen grains" is in reality a number of events identified by the sorter as fitting the gates established by the operator (discussed below in Section "Flow Cytometry Sorting"), and there may be variations in size and condition of the pollen grains. Finally, there may be small but real differences in the amount of carbon contained in each grain, due to the size of the grains, thickness of the exine, and presence or absence of cytoplasm in the grain (especially for fresh pollen).

Chemical Treatment

The base treatment (KOH) is applied to remove as much organic material and humic acid as possible from the sediment. In a standard extraction for pollen analysis, acetolysis is usually used for this particularly important step, but it is not appropriate for AMS measurement due to carbon contamination from the chemicals. Instead, 10% KOH solution was applied. The main concern of using basic solutions during the chemical digestion for radiocarbon dating is the possible contamination by absorption of modern carbon from atmospheric CO_2 by the KOH. To avoid this contamination, the following precautions were followed: (i) the 10% KOH solution was freshly prepared and stored in a screw-top bottle for no longer than a month; (ii) multiple rinses with a shorter exposure to the base were preferred to a prolonged exposure (e.g., three times 10 min with fresh solution instead of a single time for 30 min); (iii) the base treatment was followed by the acid treatment with HCl without water rinses in between the two steps.

To remove as much organic matter as possible NaOCl was used in place of the acetolysis; exposure to NaOCl was limited to 3 min at 90°C because prolonged exposure may result in damage to the pollen grain walls. Other chemicals can be used in place of NaOCl, such as nitric acid (HNO_3) (Tennant et al., 2013) or sulfuric acid (H_2SO_4) (Piotrowska et al., 2004), but in this study NaOCl was preferred because it is easily accessible, less hazardous and equally effective. The 2.5% solution was freshly prepared and stored tightly closed for no longer than a month to maintain the effectiveness of the solution.

The sediments from Fallen Leaf Lake and Mono Lake presented substantially different characteristics that required modification and adjustments during the pollen extraction. The significant organic component required a prolonged base treatment for FLL. All the samples from the core BOLLY-FLL10 required 3 KOH rinses to obtain a light-yellow colored supernatant, starting from a dark-brown initial color. In contrast, ML samples showed very little reaction to the KOH and only 1 base rinse was necessary for most of the samples.

The second remarkable difference between the samples from the two lakes was the HCl reaction. ML samples strongly reacted to the acid treatment due to the high presence of carbonates in the cores. A prolonged acid treatment was required for several samples until the end of the reaction (40–60 min). FLL sediment did not present any visible reaction with HCl (bubbling), consistent with the low presence of carbonates in the core. For FLL the samples were treated with HCl with the standard duration of 30 min at 90°C.

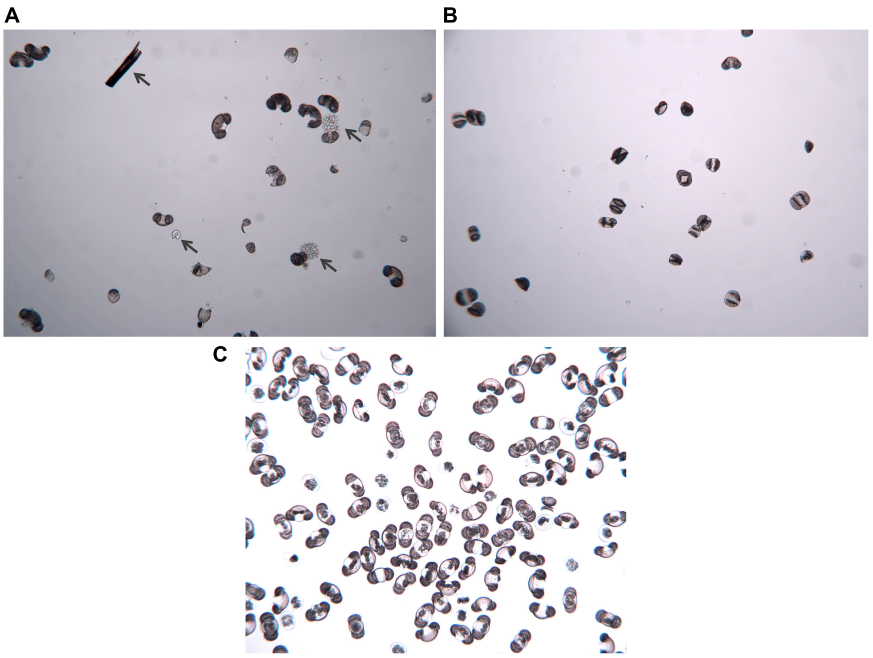

FIGURE 4 | Photos of pollen separates under 100x magnification before and after cytometric sorting. **(A)** Fossil sample before the sorting, with dark gray arrows highlighting organic particles that survived chemical digestion and physical sieving during pollen extraction. **(B)** Fossil sample after sorting, illustrating the greatly increased purity of the sample. **(C)** Modern pinecone sample before the sorting, illustrating the general purity of the sample, even with reduced preparation steps.

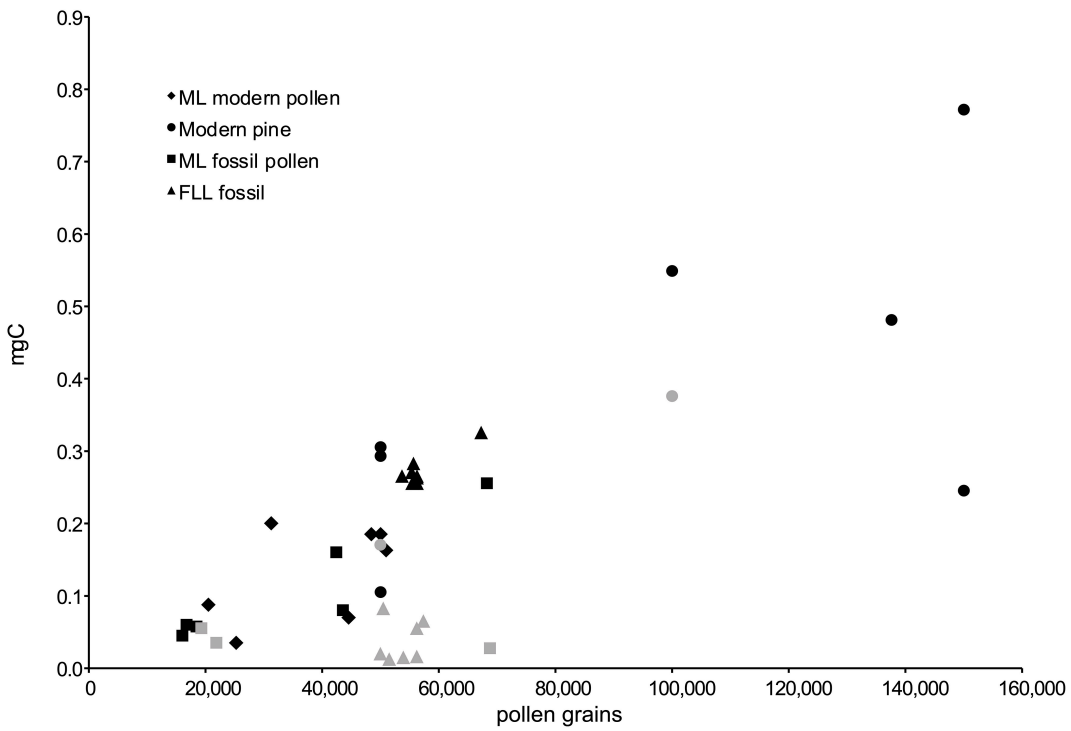

FIGURE 5 | Amount of carbon (mg C) vs. pollen grains in sample, showing only the samples that have been successfully dated. Symbols in gray show the samples that were processed with the lyophilizer, illustrating the significant loss of pollen after sorting and before graphitization. The amount of carbon (mg C) is calculated from the amount of CO_2 after the sorted pollen sample was combusted for graphitization, and the number of pollen grains is the number of "accepted" events counted by the sorter during sorting of the sample.

Physical Separation

The physical separation of the pollen grains from other particles that survived the chemical treatment is crucial to obtain a sample as clean as possible and to reduce the time and the cost of the sorting process. The most appropriate size of the meshes to use is determined by the size of the targeted pollen type. In this study pine pollen was the most abundant in both cores and consequently the desired fraction based on our various experiments was >37 μm and <80 μm. Every fraction was checked under the microscope to avoid a loss of pollen grains.

Sieving was performed with metal sieves (125 and 63 μm) and nylon mesh (80, 37, and 20 μm), targeting pine pollen. Sieving at 125 μm was not necessary for the sediment core samples but was crucial for the modern samples (pinecones and surface transects) to eliminate larger organic debris and small rocks. The 80 and 63 μm sieved samples were cleaner and lacked big fragments that were detected under the microscope in the 125 μm sieved samples. To eliminate smaller particles, initially the final sieving was performed with a 20 μm nylon mesh. However, because of the low percentages of sorted pollen in some batches (**Tables 1**, **2**), the samples were re-sieved at 37 μm. Microscope examination showed that the 20–37 μm fraction contained a large amount of non-pollen material and very little pollen. Thus, the final sieving step was changed from 20 to 37 μm, resulting in higher percent sorted pollen in later batches (**Tables 1**, **2**). For the same reason, the 80 μm mesh was preferred to the 63 μm. Such checks will be required to determine the most efficient mesh sizes for a particular sediment and pollen type.

In an experiment to optimize the sieving process, 10 samples from FLL were sieved in an ultrasonic bath. The use of the sonicator sped up the sieving steps significantly, but, based on the results (**Table 1**, columns 4–6 and **Figure 5**, gray symbols), the effect on pollen grains is unclear at this point.

Density Separation

The heavy liquid separation was performed with SPT to separate the organic from the inorganic material. This step can be alternatively performed with hydrofluoric acid (HF), but we preferred SPT in this study, as it is significantly less hazardous to use and dispose of, and is still highly effective.

A specific gravity of 2.1 for SPT is recommended for pollen analysis extraction (e.g., Munsterman and Kerstholt, 1996; Vandergoes and Prior, 2003); however, it allows small organic particles to separate with pollen grains, which should be avoided in preparation for AMS measurements. Several tests were performed using different specific gravities (1.9, 2.0, 2.1, 2.2) in order to eliminate non-pollen particles in the floating layer. The floating material was decanted in a new, clean tube. Adding water to this solution allowed the pollen grains and the organic particles to settle at bottom of the tube. If the organic material separated with the pollen grains was excessive, the specific gravity was reduced. The purity of the pollen concentrates increased significantly with a lower specific gravity and 1.9 was shown to be the most effective specific gravity for using SPT to separate pollen from other organic material without losing pollen in the settled fraction. Specific gravities >1.9 allowed a significant amount of other organic particles to separate with the pollen grains. A minimum of 3–4 rinses was required to clean the samples from the SPT, although this step appeared to be different for each batch of samples. The heavy liquid separation was not required for the pinecones due to the absence of inorganic material in the samples.

A heavy liquid with low-C content is required to avoid C contamination, and for this reason the SPT-O (from Geoliquids, Inc.) was preferred. The heavy liquid can be challenging to eliminate and for this reason only the necessary amount of SPT was added to the samples, which for the 50 ml test tubes was found to be ∼20 ml. To avoid cross-contamination between samples, the SPT was not reused.

The density separation was effectively applied for all the fossil and modern surface samples, allowing the pollen grains to float and the inorganic particles to sink. Thus, no further steps were required to separate the organic and inorganic matter. However, in FLL samples a considerable number of diatoms fragments were detected in the floating section during the heavy liquid separation for a few samples. Diatoms frustules are composed of silica and do not represent a source of contamination for AMS measurements, but a high abundance of diatoms may increase the time and cost for the sorting process. In the case of high concentration of diatoms, a HF rinse would dissolve the frustules, and thus it may be preferred for some samples. In spite of the presence of the diatoms, the sorting time for FLL was efficient and remained under 4.5 h (**Table 1**, Column 5). Thus, the use of the HF was not necessary in our study.

Flow Cytometry Sorting

The highest percentage of pollen sorted by the flow cytometer (COPAS) was ∼74% of the total particles introduced to the sorter, from fresh cone samples and some FLL fossil samples (**Tables 1**, **2**). This percentage does not seem particularly high, especially as the samples extracted from the fresh cones were characterized by extremely high purity. As we initially expected results closer to 100% for the fresh cones, we examined the sorting process to determine the source of the discrepancy.

The COPAS allows the recovery of the material rejected by the sorter, after the sorting into the recovery cup and before the disposal into the waste container. Several samples were collected during this step and analyzed by light microscopy. The light-microscopic observation revealed that a considerable amount of pollen was rejected during sorting. Most of this pollen was clusters of several grains, or broken or folded grains; however, a few whole, regular-shaped grains were detected as well. These might have been included in the final sample if the gates had been larger; however, larger gates would also increase the likelihood that non-pollen material would be included in the final sample. By selecting a smaller gate, a larger number of pollen grains may be excluded during the sorting (**Figure 3**), but the purity of the sample is improved. The gated region thus has a major role in the results of the pollen percentage and purity, and additional tests of this component of the preparation are planned.

Handling Sorted-Pollen Concentrates

After the sorting by flow cytometry, the samples were transferred into 3.5 ml cryo-tubes and the supernatant was allowed to settle

for at least 2 h to overnight. The samples were then frozen at −18°C and shipped with dry ice to CAMS. Freezing the samples is important to preserve the samples undisturbed as much as possible, to reduce possible loss of pollen grains that may get attached the lid or the internal walls of the vials.

Before proceeding with combustion and graphitization, the samples were allowed to thaw at room temperature and settle overnight, as thawing induces the resuspension of the pollen grains in the solution. Once the pollen had settled, as much of the liquid as possible was removed by pipetting without disturbing the pollen concentrates at the bottom of the vials. The samples were then transferred into quartz tubes and then placed in the Jouan to dry. The Jouan was preferred to the lyophilizer after comparison of the AMS results showed better preservation of pollen concentrates (as indicated by higher C amount in the samples during the graphitization process (**Table 2**, Column 7 and **Figure 5**). This identified a likely loss of pollen during the drying process in the lyophilizer. No additional rinsing or pretreatment was necessary due to the extensive pollen extraction process, and post-sorting storage in slightly acidic water.

COMPARISON OF POLLEN AND MACROFOSSIL DATES FROM FALLEN LEAF LAKE

For 12 of the 15 pollen-macrofossil pairs from the Fallen Leaf Lake cores, the macrofossil and pollen ages agree within the combined 2-sigma uncertainty, and within 1-sigma for ten of the pairs (**Table 3** and **Figure 6**). Of the remaining three pairs, the pollen date for sample 2D-1K-8-7 (CAMS 181806) is 145 years older than the macrofossil, just outside the 130-year combined uncertainty. For samples 2D-1K-3-25 and 2D-1K-6-50, the pollen dates (CAMS 181802, 181804) are significantly younger than the macrofossil dates, by 345 and 285 years, respectively. Although there could be several reasons for the disagreement, one possibility is that the macrofossils were pre-aged on the landscape; in such a case, the pollen dates might be a more accurate representation of the age of the sediment. In this case, the macrofossil material dated at 2D-1K-3-25 was a leaf, making pre-aging a somewhat unlikely possibility for that sample. Finding similar disagreement between pollen and leaf dates from Lake Sugeitsu, Tennant et al. (2013) suggested that the small size (0.4 mg) of the pollen sample might be the cause; however, here, the two 'young' dates are 0.26–0.27 mg, the same as the other FLL pollen samples and well within the range of the routine small-sample correction at CAMS. Overall, these pollen-macrofossil pairs indicate that dating of pollen separates can produce dates with equal accuracy as macrofossils. However, we acknowledge that Fallen Leaf Lake is an ideal case, where pollen dates are unlikely to be needed except where very high precision is required (e.g., during the extreme climatic swings of the last deglaciation).

CONCLUSION

In the absence of sufficient macrofossils for radiocarbon dating in sediment cores, purified pollen represents a potentially valuable source for obtaining a reliable and high-resolution chronology based on radiocarbon measurements. Completely isolating enough pollen grains in order to have enough carbon for the AMS measurements is the dominant challenge, along with preventing adsorption or addition of carbon during the processing. The method for extraction and concentration of pollen that we present here demonstrates that pine pollen can

TABLE 3 | Comparison between macrofossils and pollen dates on FLL core samples.

		Macrofossils					Pollen				
Sample ID	**CAMS ID**	**Fraction Modern**	**±**	**^{14}C age**	**±**	**AGE DIFFERENCE**	**^{14}C age**	**±**	**Fraction Modern**	**±**	**CAMS ID**
2D-1K-1-54	152547	0.9094	0.0032	765	30	−65	830	30	0.9016	0.0033	181798
1A-1K-1-54*	152537	0.7778	0.0028	2020	30	−35	2055	45	0.7742	0.0039	179554
1A-1K-1-78^	152538	0.7633	0.0080	2170	90	−80	2250	140	0.7561	0.0126	179555
2D-1K-2-38	152685	0.6888	0.0065	3000	80	85	2915	45	0.6959	0.0037	181799
2D-1K-2-48	152686	0.6805	0.0026	3090	35	−45	3135	30	0.6769	0.0025	181800
2D-1K-3-25	152687	0.5995	0.0022	4110	30	345	3765	35	0.6257	0.0024	181802
2D-1K-3-46	152688	0.5987	0.0022	4120	30	−85	4205	35	0.5923	0.0024	181803
1A-1K-5-142	152696	0.4365	0.0016	6165	30	−25	6190	60	0.4628	0.0032	181808
2D-1K-6-50	152701	0.4285	0.0016	6660	30	285	6375	35	0.4523	0.0018	181804
2D-1K-6-77	152702	0.3674	0.0017	6805	35	15	6790	35	0.4294	0.0018	181805
1A-1K-6-149	157543	0.3608	0.0016	8045	40	55	7990	180	0.3696	0.0081	179556
2D-1K-8-7	152703	0.0014	0.0014	7885	30	−145	8030	35	0.3679	0.0015	181806
1A-1K-7-5	152544	0.0018	0.0018	8190	45	170	8020	350	0.3684	0.0157	179557
2D-1K-9-123	152704	0.0055	0.0055	9050	140	60	8990	35	0.3265	0.0013	181807
1A-1K-8-55	152545	0.0011	0.0011	10335	35	−285	10620	510	0.2667	0.0167	179559

*The section and the depth for each sample are showed in the Sample ID column. All macrofossil dates were originally published by Noble et al. (2016). *Macrofossil from core depth 53 cm. ^Macrofossil from core depth 77 cm. Uncertainties are quoted at 1-sigma.*

be successfully and reliably extracted, purified and dated from widely varying sediment types.

Pollen concentrations may vary along the cores; thus, having additional information on the type of pollen and characteristics of the sediments can be important for improving the efficiency and the timing of the extraction and sorting method. Pollen concentration in the sediments depends on the characteristics of the sediments and lake basin, and the grain size, organic matter type and concentration, and carbonate content directly impact the variations required to execute the entire process successfully. If available, a pollen analysis is extremely helpful in identifying the dominant pollen type and the amount of raw sediment required to provide sufficient pollen for dating. Further, the dominant pollen type will determine the size of the meshes to be used during the sieving process, in particular during the last sieving step in which the smaller particles are discarded before the cytometric sorting.

The content of organic matter/humic acid and carbonates affects the number of KOH rises and the duration of the HCl treatment for each sample. Organic-rich sediments may require several rinses with KOH that should be performed until the supernatant appears light-yellowish colored. Carbonate-rich sediments may require a prolonged or multiple HCl treatments, based on the observation of the reaction of the samples to the chemicals.

Reducing the potential carbon contamination is crucial for the reliability of the AMS measurements; thus, it is important to identify and limit the potential sources of carbon contamination. In this context, it is recommended to store the KOH in a bottle with a tight lid and store the solution for no longer than a month to reduce the absorption of modern carbon from the atmosphere. After that time, the solution should be discarded, and a fresh bottle prepared. For the same reason, performing the HCl treatment after KOH without a rinse between is highly recommended. A low-carbon heavy liquid is required to prevent contamination related to the presence of carbon in the chemical. Although somewhat expensive, the heavy liquid and the nylon meshes should be disposed of and not reused for multiple samples.

Limiting the loss of pollen grains after the sorting is crucial to having the largest sample possible. Checking the discarded solutions after the sieving steps and the SPT is highly recommended to assure that the pollen has been isolated in the desired fraction. These checks should be included in the preparation whenever sediment from a new site or time period is being prepared, as the types of pollen may be quite different, and when new chemical or physical methods are introduced into an established protocol. Shipping the samples frozen and letting the samples thaw upright reduces the chance of pollen grains being lost in the vial. In addition, settling after thawing reduce the chances of losing pollen grains before the graphitization.

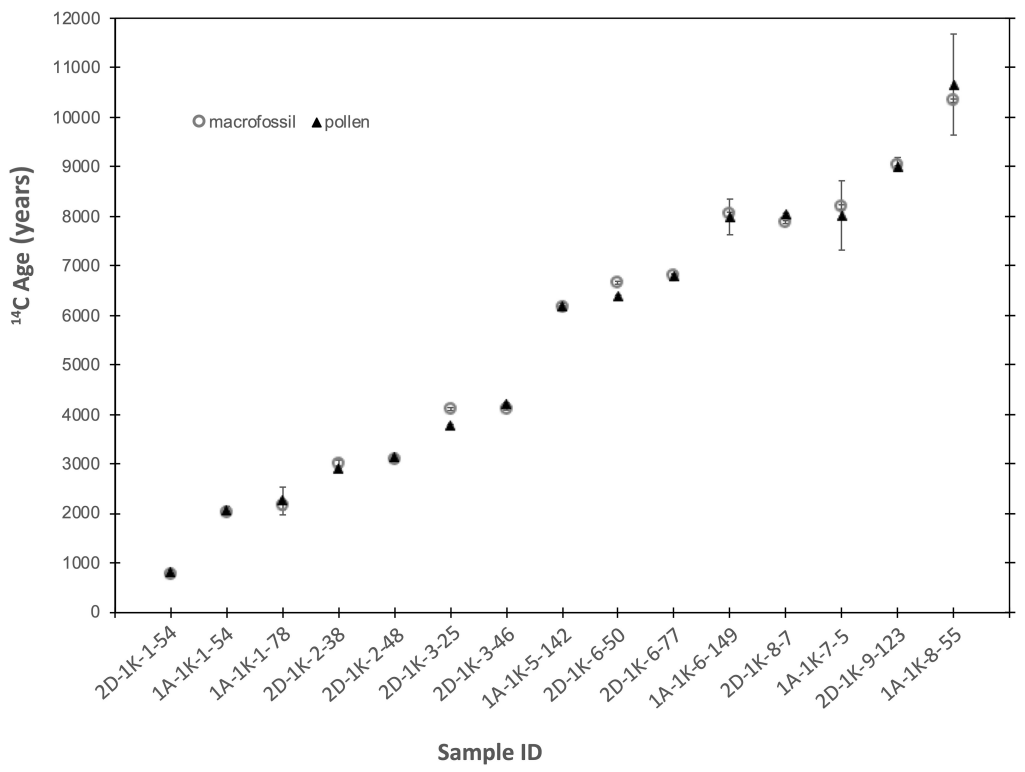

FIGURE 6 | Comparison between macrofossil and pollen dates from FLL sediment core. Samples names refer to the core section and the section depth of the sample.

Excellent agreement between purified pollen dates and macrofossils from the Holocene section of Fallen Leaf Lake shows that pollen dates can be used, at least in some cases, interchangeably and confidently with macrofossil dates. Overall, the method of separating pollen for AMS dating presented here shows that pollen can be reliably separated from a wide variety of lacustrine and surface samples, the first step toward using pollen radiocarbon dates for building high-resolution chronologies for lake-sediment records.

OUTLOOK FOR THE FUTURE

Although we have successfully applied the method and variations presented here on a wide variety of sediment types and demonstrated fidelity between pollen and macrofossil dates at Fallen Leaf Lake, additional work remains to establish purified pollen dating as a routine technique.

First, pollen materials of known age need to be established to monitor for addition of modern and radiocarbon-dead carbon during the processing of pollen, as has been done for wood, shell, bone and other materials. While most labs or investigators should be able to establish a modern pollen reference material by sampling modern vegetation of a relevant type, the development of a radiocarbon-dead pollen material to monitor for addition of modern carbon is more difficult. The ideal pollen must be unequivocally too old to contain original radiocarbon; no more difficult to separate from the geological matrix than most samples of interest; and available in large enough quantities that it can be measured routinely for many years. The first two qualifications were met by ∼90 ka pollen prepared as background by Howarth et al. (2013), but the restricted amount available in a core is less than ideal.

We have focused on pine pollen in this study because it is large and abundant in our study area, but additional work must be done to establish working parameters for deposits dominated by other types of pollen. The size and shape of different pollen types will require different mesh sizes, and affect the number of grains needed to successfully date a sample. Whereas for pine grains we found that 40,000–50,000 grains were ample for a radiocarbon date, for smaller pollen types (e.g., *Betula*, *Alnus*, *Quercus*) the work of Tennant et al. (2013) suggests that an order of magnitude more grains may be necessary to achieve the amount of carbon measured on the FLL samples in this study. In the case of the smaller pollen grains, a sorter such as the Aria II instrument used by Tennant et al. (2013) and also available in the core facility at IUB is more suitable.

Additional testing of the parameters used for gating the events on the flow cytometer is needed to find if different pollen fractions can be separated by the cytometer. For example, Tennant et al. (2013) demonstrated the gate locations of different genera of pollen sorted on the Aria II, but the samples used were modern pollen collected separately; thus far, this separation has not been demonstrated on sediment samples. This would be extremely useful in situations where the sources of material to the pollen fraction are variable, such as where erosion supplies materials with differential preservation in soils (Howarth et al., 2013), and from distinct assemblages from the surrounding watershed (Nambudiri et al., 1980). Perhaps more difficult, but equally useful in some situations, would be the ability to distinguish reworked pollen of the same type as the dominant type, such as pine grains that are torn, crumpled, or otherwise degraded by reworking from an older deposit.

Further, if the application of pollen dating to development of chronologies is to become available to interested paleo scientists, good three-way communication is necessary to successfully move samples from raw mud to a radiocarbon measurement. At least in the United States, flow cytometers tend to be housed in university core facilities that accept outside samples, and are operated by cytometry experts. As the number of AMS facilities and flow cytometry facilities is relatively small compared to the number of chemical laboratories able to chemically concentrate pollen, it seems likely that a key relationship can be established between those two facilities, streamlining the process for investigators wanting to apply pollen dating to their studies.

Finally, as pollen dating is applied more widely, there will be a need to explore the occurrence of pollen in many different kinds of lake systems. While some lakes may present relatively simple results (e.g., Tennant et al., 2013 and the FLL results in **Figure 6**), in other lakes complications may arise that are specific to the dynamics in that particular basin. Basins where regression has exposed old lake sediments (Zimmerman et al., 2018), where deep soils develop and are periodically eroded into the lake (Howarth et al., 2013); and where the potential for unusual carbon dynamics exists (Schiller et al., 2021) demonstrate the need to understand each lake basin as an individual, until enough lakes have been characterized to understand the variety of locations where pollen dating is likely to be successful.

DATA AVAILABILITY STATEMENT

The raw data supporting the conclusions of this article are presented in the tables included in the published article.

AUTHOR CONTRIBUTIONS

SZ and TB designed the study and secured the funding. IT and SZ did the field and core sampling. IT performed the pollen extraction, pretreatment, and graphitization with assistance from SZ and TB. CH performed the flow cytometry sorting in consultation with IT and SZ and contributed to analysis of the flow cytometry data. IT, TB, and SZ analyzed the data. All authors contributed to the writing of the manuscript and approved the submitted version.

FUNDING

This work was performed under the auspices of the U.S. Department of Energy by Lawrence Livermore National Laboratory under contract DE-AC52-07NA27344. This work was supported by the LLNL LDRD grant 17-ERD-052. Contribution: LLNL-JRNL-790160.

ACKNOWLEDGMENTS

We thank Paula Noble for providing the samples from Fallen Leaf Lake core; Kimber Moreland for the help in developing the map with the three different site locations; Alexandra Hedgpeth, Bruce Buchholz, and Tom Guilderson for the support during the lab work; Dave Marquart (Mono Lake Tufa Natural Reserve) for providing information and helping with permits for field work.

REFERENCES

Barss, M. S., and Williams, G. L. (1973). *Palynology and Nannofossil Processing Techniques. Geological Survey of Canada, Paper*, Vol. 73. Ottawa, Ont: Department of Energy, Mines and Resources, 1–26. doi: 10.4095/102534

Blaauw, M., Christen, J. A., Bennett, K. D., and Reimer, P. J. (2018). Double the dates and go for Bayes – Impacts of model choice, dating density and quality on chronologies. *Quat. Sci. Rev.* 188, 58–66. doi: 10.1016/j.quascirev.2018.03.032

Brown, T. A., Farwell, G. W., Grootes, P. M., and Schmidt, F. H. (1992). Radiocarbon AMS dating of pollen extracted from peat samples. *Radiocarbon* 34, 550–556. doi: 10.1017/S0033822200063815

Brown, T. A., Nelson, D. E., Mathewes, R. W., Vogel, J. S., and Southon, J. R. (1989). Radiocarbon dating of pollen by accelerator mass spectrometry. *Quat. Res.* 32, 205–212. doi: 10.1016/0033-5894(89)90076-8

Brown, T. A., and Southon, J. R. (1997). Corrections for contamination background in AMS 14C measurements. *Nucl. Instrum. Methods Phys. Res. B* 123, 208–213. doi: 10.1016/S0168-583X(96)00676-3

Byrne, R., Park, J., Ingram, L., and Hung, T. (2003). "Cytometric sorting of Pinaceae pollen and its implications for radiocarbon dating and stable isotope analyses," in *Paper Presented at the 20th Annual Pacific Climate Workshop*, Asilomar, CA.

Davis, O. K. (1999). Pollen analysis of a late-glacial and Holocene sediment core from Mono Lake, Mono County, California. *Quat. Res.* 52, 243–249. doi: 10.1006/qres.1999.2063

Faegri, K., and Iversen, J. (1985). *Textbook of Pollen Analysis*, 4th Edn. New York, NY: Hafner Press.

Fletcher, W. J., Zielhofer, C., Mischke, S., Bryant, C., Xu, X., and Fink, D. (2017). AMS radiocarbon dating of pollen concentrates in a karstic lake system. *Quat. Geochronol.* 39, 112–123. doi: 10.1016/j.quageo.2017.02.006

Hodelka, B. N., McGlue, M. M., Zimmerman, S., Ali, G., and Tunno, I. (2020). Paleoproduction and environmental change at Mono Lake (eastern Sierra Nevada) during the Pleistocene-Holocene transition. *Palaeogeogr. Palaeoclimatol. Palaeoecol.* 543:109565. doi: 10.1016/j.palaeo.2019.109565

Howarth, J. D., Fitzsimons, S. J., Jacobsen, G. E., Vandergoes, M. J., and Norris, R. J. (2013). Identifying a reliable target fraction for radiocarbon dating sedimentary records from lakes. *Quat. Geochronol.* 17, 68–80. doi: 10.1016/j.quageo.2013.02.001

Kilian, M. R., van der Plicht, J., van Geel, B., and Goslar, T. (2002). Problematic 14C-AMS dates of pollen concentrates from Lake Gosciaz (Poland). *Quat. Int.* 88, 21–26. doi: 10.1016/S1040-6182(01)00070-2

Kleppe, J., Brothers, D. S., Kent, G. M., Biondi, F., Jensen, S., and Driscoll, N. W. (2011). Duration and severity of Medieval drought in the Lake Tahoe Basin. *Quat. Sci. Rev.* 30, 3269–3279. doi: 10.1016/j.quascirev.2011.08.015

Long, A., Davis, O. K., and DeLanois, J. (1992). Separation and 14C dating of pure pollen from lake sediments: nano fossil AMS dating. *Radiocarbon* 34, 557–560. doi: 10.1017/S0033822200063827

Maloney, J. M., Noble, P. J., Driscoll, N. W., Kent, G. M., Smith, S. B., Schmauder, G. C., et al. (2013). Paleoseismic history of the Fallen Leaf segment of the West Tahoe-Dollar Point fault reconstructed from slide deposits in the Lake Tahoe Basin, California-Nevada. *Geosphere* 9, 1065–1090. doi: 10.1130/GES00877.1

Mensing, A. M., and Southon, J. R. (1999). A simple method to separate pollen for AMS radiocarbon dating and its application to lacustrine and marine sediments. *Radiocarbon* 41, 1–8. doi: 10.1017/S0033822200019287

Munsterman, D., and Kerstholt, S. (1996). Sodium polytungstate, a new non-toxic alternative to bromoform in heavy liquid separation. *Rev. Palaeobot. Palynol.* 91, 417–422. doi: 10.1016/0034-6667(95)00093-3

Nambudiri, E. M. V., Teller, J. T., and Last, W. M. (1980). Pre-quaternary microfossils – a guide to errors in radiocarbon dating. *Geology* 8, 123–126. doi: 10.1130/0091-7613(1980)8<123:PMGTEI>2.0.CO;2

Newnham, R. M., Vandergoes, M. J., Garnett, M. H., Lowe, D. J., Prior, C., and Almond, P. C. (2006). Test of AMS 14C dating of pollen concentrates using tephrochronology. *J. Quat. Sci.* 22, 37–51. doi: 10.1002/jqs.1016

Noble, P. J., Ball, G. I., Zimmerman, S. H., Maloney, J., Smith, S. B., Kent, G., et al. (2016). Holocene paleoclimate history of Fallen Leaf Lake, CA., from geochemistry and sedimentology of well–dated sediment cores. *Quat. Sci. Rev.* 131, 193–210. doi: 10.1016/j.quascirev.2015.10.037

Noble, P. J., Chandra, S., and Kreamer, D. K. (2013). Dynamics of phytoplankton distribution in relation to stratification and winter precipitation, Fallen Leaf Lake, California. *West. N. Am. Nat.* 73, 302–322. doi: 10.3398/064.073.0301

Piotrowska, N., Bluszcz, A., Demske, D., Granoszewski, W., and Heumann, G. (2004). Extraction and AMS radiocarbon dating of pollen from Lake Baikal sediments. *Radiocarbon* 46, 181–187. doi: 10.1017/S0033822200039503

Regnéll, J., and Everitt, E. (1996). Preparative centrifugation – a new method for preparing pollen concentrates suitable for radiocarbon dating by AMS. *Veg. Hist. Archeobot.* 5, 201–205. doi: 10.1007/BF00217497

Schiller, C. M., Whitlock, C., Elder, K. L., Iverson, N. A., and Abbott, M. B. (2021). Erroneously old radiocarbon ages from terrestrial pollen concentrates in Yellowstone Lake, Wyoming, USA. *Radiocarbon* 63, 321–342. doi: 10.1017/RDC.2020.118

Tennant, R. K., Jones, R. T., Brock, F., Cook, C., Turney, C. S. M., Love, J., et al. (2013). A new flow cytometry method enabling rapid purification of fossil pollen from terrestrial sediments for AMS radiocarbon dating. *J. Quat. Sci.* 28, 229–236. doi: 10.1002/jqs.2606

Vandergoes, M. J., and Prior, C. A. (2003). AMS dating of pollen concentrates – a methodological study of late Quaternary sediments from south Westland, New Zealand. *Radiocarbon* 45, 479–491. doi: 10.1017/S0033822200032823

Vogel, J. S., Nelson, D. E., and Southon, J. R. (1987). 14C background levels in an accelerator mass spectrometry system. *Radiocarbon* 29, 323–333. doi: 10.1017/S0033822200043733

Vogel, J. S., Southon, J. R., Nelson, D. E., and Brown, T. A. (1984). Performance of catalytically condensed carbon for use in accelerator mass spectrometry. *Nucl. Instrum. Methods Phys. Res. B* 5, 289–293. doi: 10.1016/0168-583X(84)90529-9

Zimmerman, S. R. H., Brown, T. A., Hassel, C. A., and Heck, J. (2018). Testing pollen sorted by flow cytometry as the basis for high-resolution lacustrine chronologies. *Radiocarbon* 61, 359–374. doi: 10.1017/RDC.2018.89

Zimmerman, S. R. H., Hemming, S. R., Hemming, N. G., Tomascak, P. B., and Pearl, C. (2011). High-resolution chemostratigraphic record of late Pleistocene lake-level variability, Mono Lake, California. *Geol. Soc. Am. Bull.* 123, 2320–2334. doi: 10.1130/B30377.1

Zimmerman, S. R. H., Hemming, S. R., and Starratt, S. W. (2020). "Holocene sedimentary architecture and paleoclimate variability at Mono Lake, California," in *From Saline to Freshwater: The Diversity of Western Lakes in Space and Time. Geological Society of America Special Paper*, Vol. 536, eds S. W. Starratt and M. R. Rose (Boulder, CO: Geological Society of America). doi: 10.1130/2020.2536(19)

Zimmerman, S. R. H., and Wahl, D. B. (2020). Holocene paleoclimate change in the western US: the importance of chronology in discerning patterns and drivers. *Quat. Sci. Rev.* 246:106487. doi: 10.1016/j.quascirev.2020.106487

Conflict of Interest: The authors declare that the research was conducted in the absence of any commercial or financial relationships that could be construed as a potential conflict of interest.

frontiers | Frontiers in Ecology and Evolution

ORIGINAL RESEARCH
published: 16 June 2022
doi: 10.3389/fevo.2022.837857

Modern Pollen Assemblages From Lake Sediments and Soil in East Siberia and Relative Pollen Productivity Estimates for Major Taxa

*Rongwei Geng[1,2,3], Andrei Andreev[1], Stefan Kruse[1], Birgit Heim[1], Femke van Geffen[1,4], Luidmila Pestryakova[5], Evgenii Zakharov[5,6], Elena Troeva[6], Iuliia Shevtsova[1], Furong Li[7], Yan Zhao[2,3] and Ulrike Herzschuh[1]**

[1] Section of Polar Terrestrial Environmental Systems, Alfred Wegener Institute Helmholtz Centre for Polar and Marine Research, Potsdam, Germany, [2] Key Laboratory of Land Surface Pattern and Simulation, Institute of Geographical Sciences and Natural Resources Research, Chinese Academy of Sciences, Beijing, China, [3] College of Earth and Planetary Sciences, University of Chinese Academy of Sciences, Beijing, China, [4] Institute of Biochemistry and Biology, University of Potsdam, Potsdam, Germany, [5] Institute of Natural Sciences, North-Eastern Federal University of Yakutsk, Yakutsk, Russia, [6] Institute for Biological Problems of Cryolithozone, Russian Academy of Sciences, Yakutsk, Russia, [7] School of Ecology, Sun Yat-sen University, Shenzhen, China

OPEN ACCESS

Edited by:
Franco Biondi,
University of Nevada, Reno,
United States

Reviewed by:
Anneli Poska,
Lund University, Sweden
Vivika Väli,
Estonian University of Life Sciences,
Estonia

***Correspondence:**
Ulrike Herzschuh
ulrike.herzschuh@awi.de

Specialty section:
This article was submitted to Paleoecology, a section of the journal Frontiers in Ecology and Evolution

Received: 17 December 2021
Accepted: 10 May 2022
Published: 16 June 2022

Citation:
Geng R, Andreev A, Kruse S, Heim B, van Geffen F, Pestryakova L, Zakharov E, Troeva E, Shevtsova I, Li F, Zhao Y and Herzschuh U (2022) Modern Pollen Assemblages From Lake Sediments and Soil in East Siberia and Relative Pollen Productivity Estimates for Major Taxa. Front. Ecol. Evol. 10:837857. doi: 10.3389/fevo.2022.837857

Modern pollen–vegetation–climate relationships underpin palaeovegetation and palaeoclimate reconstructions from fossil pollen records. East Siberia is an ideal area for investigating the relationships between modern pollen assemblages and near natural vegetation under cold continental climate conditions. Reliable pollen-based quantitative vegetation and climate reconstructions are still scarce due to the limited number of modern pollen datasets. Furthermore, differences in pollen representation of samples from lake sediments and soils are not well understood. Here, we present a new pollen dataset of 48 moss/soil and 24 lake surface-sediment samples collected in Chukotka and central Yakutia in East Siberia. The pollen–vegetation–climate relationships were investigated by ordination analyses. Generally, tundra and taiga vegetation types can be well distinguished in the surface pollen assemblages. Moss/soil and lake samples contain generally similar pollen assemblages as revealed by a Procrustes comparison with some exceptions. Overall, modern pollen assemblages reflect the temperature and precipitation gradients in the study areas as revealed by constrained ordination analysis. We estimate the relative pollen productivity (RPP) of major taxa and the relevant source area of pollen (RSAP) for moss/soil samples from Chukotka and central Yakutia using Extended *R*-Value (ERV) analysis. The RSAP of the tundra-forest transition area in Chukotka and taiga area in central Yakutia are ca. 1300 and 360 m, respectively. For Chukotka, RPPs relative to both Poaceae and Ericaceae were estimated while RPPs for central Yakutia were relative only to Ericaceae. Relative to Ericaceae (reference taxon, RPP = 1), *Larix*, *Betula*, *Picea,* and *Pinus* are overrepresented while *Alnus*, Cyperaceae,

Poaceae, and *Salix* are underrepresented in the pollen spectra. Our estimates are in general agreement with previously published values and provide the basis for reliable quantitative reconstructions of East Siberian vegetation.

Keywords: modern pollen assemblages, pollen-vegetation-climate relationships, East Siberia, tundra, taiga, relative pollen productivity, quantitative vegetation reconstruction

INTRODUCTION

Palaeoenvironmental studies in Siberia are important to understand climate and vegetation changes in the Northern Hemisphere. Pollen is the most widely used proxy for quantitative reconstructions of vegetation and climate in the past (Abraham et al., 2017; Sun et al., 2019; Chevalier et al., 2020; Liang et al., 2020). However, the number of quantitative climate and vegetation reconstructions available from Siberia is still low (e.g., Andreev and Klimanov, 2000, 2001; Andreev et al., 2001, 2004, 2011, 2014; Andreev and Tarasov, 2013; Tarasov et al., 2013; Klemm et al., 2016; Kobe et al., 2020), partly because of a lack of modern pollen assemblages that provide the basis for the application of the modern analog technique or the generation of pollen–climate transfer functions (Overpeck et al., 1985; Magyari et al., 2014; Birks and Berglund, 2018). The relative pollen productivity (RPP) is an estimated value of pollen productivity relative to a reference taxon, which calibrates the relationship between vegetation cover and pollen data. Therefore, missing RPP estimates affect the ability of models such as the Landscape Reconstruction Algorithm (LRA; Sugita, 2007a,b) and the Multiple Scenario Approach (MSA; Bunting and Middleton, 2009) to make reasonable vegetation reconstructions.

Modern pollen datasets in Siberia have been published in previous studies (Tarasov et al., 2007, 2011; Müller et al., 2010; Klemm et al., 2016) and databases such as Eurasian Modern Pollen Database (Davis et al., 2020). However, compared to other Northern Hemisphere regions, studies on surface pollen are still rare for some regions such as Chukotka and central Yakutia. Moreover, only a few studies of modern pollen assemblages in arctic Siberia (Pisaric et al., 2001; Müller et al., 2010; Klemm et al., 2013, 2016) and southern Siberia (Pelánková et al., 2008) have been carried out that explore the relationships between pollen assemblages and vegetation or establish pollen–climate transfer functions.

Different pollen source areas and taphonomies can cause inconsistency in the pollen signals from different types of archives (Prentice, 1985; Minckley and Whitlock, 2000; Wilmshurst and McGlone, 2005; Klemm et al., 2013). As fossil pollen records in Siberia are mainly obtained from lake sediments, the quantitative reconstructions remain uncertain because the modern pollen datasets underpinning the reconstructions mostly originate from soils (e.g., Pelánková et al., 2008; Zhang et al., 2018; Cui et al., 2019; Geng et al., 2019). Modern pollen assemblages from lake sediments are less abundant (e.g., Clayden et al., 1996; Pisaric et al., 2001; Klemm et al., 2013, 2016; Niemeyer et al., 2015, 2017) despite commonly being used as palaeoenvironmental archives. Since RPP estimates can vary between regions, the vast area of Siberia is still in need of RPP estimates to make better quantitative vegetation reconstructions. Hitherto, only Niemeyer et al. (2015) have provided RPP estimates for common taxa of the Siberian Arctic and investigated the differences between moss and lake pollen. However, Siberia covers a large area and RPP information from forested boreal areas in eastern Siberia and the Far East tundra–taiga transition area in Chukotka are completely lacking. The bias with archive type might be particularly strong in areas where taxa with strongly different transportation characteristics dominate, such as in Siberia. For instance, *Larix*, the dominant tree in East Siberian forests, is rare in pollen assemblages, probably because it is produced in low numbers, is poorly preserved, and poorly transported, while *Alnus* on the other hand is strongly overrepresented in pollen spectra (Niemeyer et al., 2015). The abundance and representation of Poaceae and Cyperaceae are also complex due to their diverse habitats (Bush, 2002; Semeniuk et al., 2006).

Here, we present the results of a pollen analysis of 48 moss/soil and 24 lake samples collected from East Siberia and RPP estimates for major plant taxa based on moss/soil samples in Chukotka and central Yakutia. The main objectives of this work are: (1) to assess how modern pollen assemblages reflect regional vegetation and climate conditions; (2) to compare and understand possible differences of pollen assemblages from lake sediments and surface soils; and (3) to obtain the relevant source area of pollen (RSAP) and RPP estimates of major taxa in East Siberia for future plant cover reconstructions.

MATERIALS AND METHODS

Study Area

The study areas, Chukotka (65.8–68.5°N, 163.4–168.8°E) and central Yakutia (59.9–63.9°N, 112.9–129.7°E), are situated in eastern Siberia (**Figure 1**). The elevations of the sampling sites range from 94 to 843 m above sea level. The climate is characterized by a mean annual temperature (MAT) of -14.3 to –11.7°C in Chukotka and –9.5 to –5.1°C in central Yakutia, with the lowest temperatures in January and the highest in July. The mean annual precipitation (MAP) ranges from 183 to 274 mm in Chukotka and from 240 to 477 mm in central Yakutia (Matsuura and Willmott, 2018a,b).

The main vegetation types are tundra–taiga transition in Chukotka and taiga in central Yakutia. The tundra is covered by mosses, sedges, and lichens with some prostrate and hemi-prostrate low shrubs (*Salix*, *Dryas*, *Betula nana* L., and different ericaceous taxa). Open larch (*Larix gmelinii* [Rupr.] Kuzen., *Larix cajanderi* Mayr) and spruce–larch (*Larix gmelinii* [Rupr.] Kuzen., *Picea obovata* Ledeb.) forests predominate in the taiga zone of central Yakutia. Larch (*Larix cajanderi* Mayr) forests and pine

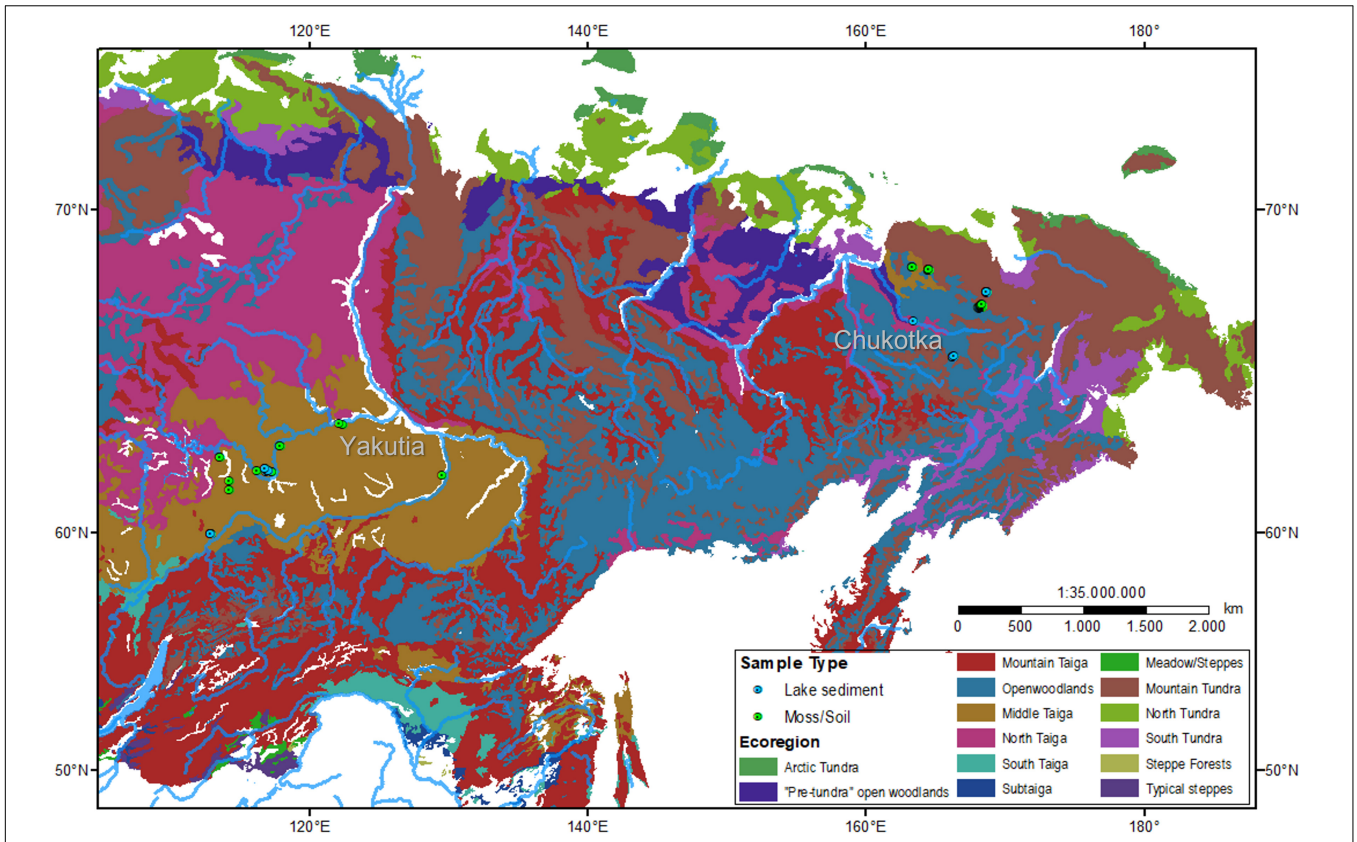

FIGURE 1 | Vegetation map (after Stone and Schlesinger, 2004) and locations of sampling sites in north-eastern and central Siberia.

(*Pinus pumila* [Pall.] Regel) shrubs occupy the Chukotka study regions, while forests with *Abies sibirica* Ledeb., *Pinus sylvestris* L., *P. sibirica* Du Tour, and *Larix gmelinii* (Rupr.) Kuzen. occupy the study area in Yakutia (Safronova and Yurkovsksya, 2019).

Sample Collection

A total of 72 surface samples were collected from both study areas: 30 moss/soil samples and 16 lake surface samples from Chukotka and 18 moss/soil samples and 8 lake surface samples from central Yakutia in July 2016 (Overduin et al., 2017) and in July and August 2018 (Kruse et al., 2019). Coordinates of the sampling sites were obtained by a hand-held Global Positioning System (GPS). Vegetation and major plant taxa were described in the field. Ecoregions, including Floodplain and Anthropogenic Meadows, Mountain Tundra, Open Woodlands, and Middle Taiga, for each sampling site were extracted from a 1:4 million scale vegetation map for the land area of the former Soviet Union. (Stone and Schlesinger, 2004) using ArcGIS 10.3. Detailed information of the 72 sites is presented in **Table 1**.

Pollen Analysis

Pollen samples were taken from the first centimeter of the soil/moss polster below the plant litter, while the lake sediment samples were taken from the uppermost centimeter of the lake cores. The samples were weighed (approximately 1–2 g for moss/soil samples and 3 g for lake samples), and a tablet with *Lycopodium* spores was added to the sample for the estimation of pollen concentrations (Stockmarr, 1971). Each sample was sieved to remove moss/plant residues and coarse particles, and was processed following a modified acetolysis procedure (Faegri et al., 2000), including HCl, NaOH, HF, and acetolysis treatments. The residue was then sieved through a 10 μm mesh. Water-free glycerol was used for sample storage and preparation of the microscopic slides.

At least 300 terrestrial pollen grains were counted and identified in each sample under a microscope at 400X magnification using published pollen atlases and identification keys (Reille, 1992, 1995, 1998; Wang, 1995). Pollen percentages were calculated based on the total number of terrestrial pollen grains. Tilia software (Grimm, 2004) was used to plot the results as a pollen percentage diagram (**Figure 2**).

Vegetation Survey

For the moss/soil samples collected in 2018 ($n = 48$), a vegetation survey around the sampling point was carried out following the steps below. The vegetation within 0-2 m was surveyed in concentric rings of 0.5 m increments. Plant taxa composition was estimated as total cover in percentage. To investigate the vegetation within 2–100 m, vegetation plots were overflown with a consumer grade drone and Survey Red Green Blue (RGB)

TABLE 1 | Information about the 72 sampling sites in East Siberia.

No.	Sample type	Region	Ecoregion from vegetation map	Latitude (°N)	Longitude (°E)	Elevation (m)	MAT (°C)	MAP (mm)
EN18001	Moss/Soil	Chukotka	Mountain Tundra	67.393	168.347	492	–14.49	216.47
EN18002	Moss/Soil	Chukotka	Mountain Tundra	67.387	168.337	416	–14.49	216.36
EN18003	Moss/Soil	Chukotka	Mountain Tundra	67.397	168.347	492	–14.49	216.52
EN18004	Moss/Soil	Chukotka	Mountain Tundra	67.397	168.351	473	–14.49	216.54
EN18005	Moss/Soil	Chukotka	Mountain Tundra	67.420	168.388	597	–14.49	216.90
EN18006	Moss/Soil	Chukotka	Mountain Tundra	67.415	168.403	438	–14.50	216.90
EN18008	Moss/Soil	Chukotka	Mountain Tundra	67.402	168.375	511	–14.50	216.68
EN18011	Moss/Soil	Chukotka	Mountain Tundra	67.404	168.364	611	–14.49	216.66
EN18012	Moss/Soil	Chukotka	Mountain Tundra	67.402	168.378	511	–14.50	216.69
EN18013	Moss/Soil	Chukotka	Mountain Tundra	67.405	168.355	650	–14.49	216.64
EN18015	Moss/Soil	Chukotka	Mountain Tundra	67.420	168.331	663	–14.47	216.70
EN18016	Moss/Soil	Chukotka	Mountain Tundra	67.427	168.390	690	–14.49	216.98
EN18019	Moss/Soil	Chukotka	Mountain Tundra	67.457	168.409	717	–14.47	217.32
EN18021	Moss/Soil	Chukotka	Mountain Tundra	67.392	168.329	504	–14.49	216.39
EN18022	Moss/Soil	Chukotka	Mountain Tundra	67.401	168.348	672	–14.49	216.56
EN18025	Moss/Soil	Chukotka	Mountain Tundra	67.367	168.424	437	–14.54	216.43
EN18026	Moss/Soil	Chukotka	Mountain Tundra	67.396	168.354	473	–14.49	216.54
EN18027	Moss/Soil	Chukotka	Mountain Tundra	67.393	168.359	455	–14.50	216.52
EN18028	Moss/Soil	Chukotka	Open Woodlands	68.468	163.358	305	–12.04	184.59
EN18029	Moss/Soil	Chukotka	Open Woodlands	68.466	163.352	353	–12.04	184.63
EN18030	Moss/Soil	Chukotka	Mountain Tundra	68.406	164.533	283	–12.79	210.39
EN18031	Moss/Soil	Chukotka	Mountain Tundra	68.405	164.545	235	–12.79	210.39
EN18032	Moss/Soil	Chukotka	Mountain Tundra	68.405	164.551	220	–12.79	210.39
EN18033	Moss/Soil	Chukotka	Mountain Tundra	68.403	164.552	220	–12.79	210.35
EN18034	Moss/Soil	Chukotka	Mountain Tundra	68.403	164.548	235	–12.79	210.36
EN18035	Moss/Soil	Chukotka	Mountain Tundra	68.403	164.591	246	–12.77	210.37
EN18051	Moss/Soil	Chukotka	Mountain Tundra	67.803	168.705	631	–12.90	193.82
EN18052	Moss/Soil	Chukotka	Mountain Tundra	67.799	168.708	641	–12.90	193.83
EN18053	Moss/Soil	Chukotka	Mountain Tundra	67.797	168.711	629	–12.90	193.84
EN18055	Moss/Soil	Chukotka	Mountain Tundra	67.791	168.683	843	–12.90	193.77
EN18061	Moss/Soil	Central Yakutia	Middle Taiga	62.076	129.619	217	–9.76	242.29
EN18064	Moss/Soil	Central Yakutia	Floodplain and Anthropogenic Meadows	63.815	122.210	94	–8.88	287.04
EN18065	Moss/Soil	Central Yakutia	Middle Taiga	63.795	122.444	111	–8.81	286.99
EN18067	Moss/Soil	Central Yakutia	Middle Taiga	63.076	117.975	125	–8.20	264.91
EN18068	Moss/Soil	Central Yakutia	Middle Taiga	63.074	117.982	147	–8.20	264.86
EN18071	Moss/Soil	Central Yakutia	Middle Taiga	62.225	116.276	199	–7.34	278.61
EN18072	Moss/Soil	Central Yakutia	Middle Taiga	62.200	117.379	171	–7.23	265.52
EN18073	Moss/Soil	Central Yakutia	Middle Taiga	62.189	117.410	169	–7.23	265.13
EN18074	Moss/Soil	Central Yakutia	Middle Taiga	62.215	117.022	203	–7.18	268.53
EN18075	Moss/Soil	Central Yakutia	Middle Taiga	62.697	113.677	337	–7.92	314.68
EN18076	Moss/Soil	Central Yakutia	Middle Taiga	62.701	113.673	341	–7.92	314.70
EN18077	Moss/Soil	Central Yakutia	Middle Taiga	61.893	114.289	349	–6.27	352.90
EN18078	Moss/Soil	Central Yakutia	Middle Taiga	61.575	114.300	395	–6.36	344.92
EN18079	Moss/Soil	Central Yakutia	Middle Taiga	59.975	112.959	414	–5.40	469.55
EN18080	Moss/Soil	Central Yakutia	Middle Taiga	59.977	112.961	377	–5.40	469.59
EN18081	Moss/Soil	Central Yakutia	Middle Taiga	59.971	112.987	439	–5.41	469.33
EN18082	Moss/Soil	Central Yakutia	Middle Taiga	59.978	112.982	379	–5.41	469.50
EN18083	Moss/Soil	Central Yakutia	Middle Taiga	59.975	113.003	467	–6.15	467.11
EN18205	Lake	Chukotka	Open Woodlands	67.327	168.228	414	–14.47	215.06
EN18213	Lake	Chukotka	Mountain Tundra	67.374	168.420	409	–14.53	216.50
EN18215	Lake	Chukotka	Mountain Tundra	67.385	168.359	407	–14.50	216.42
EN18216	Lake	Chukotka	Mountain Tundra	67.803	168.739	622	–12.91	193.92

(Continued)

TABLE 1 | (Continued)

No.	Sample type	Region	Ecoregion from vegetation map	Latitude (°N)	Longitude (°E)	Elevation (m)	MAT (°C)	MAP (mm)
EN18217	Lake	Chukotka	Mountain Tundra	67.778	168.731	629	–12.90	193.90
EN18219	Lake	Chukotka	Mountain Tundra	67.802	168.712	629	–12.90	193.84
EN18225	Lake	Central Yakutia	Middle Taiga	62.227	117.158	202	–7.19	267.74
EN18226	Lake	Central Yakutia	Middle Taiga	62.233	117.126	198	–7.19	268.16
EN18227	Lake	Central Yakutia	Middle Taiga	62.292	116.881	183	–7.19	270.44
EN18228	Lake	Central Yakutia	Middle Taiga	62.294	116.931	203	–7.19	270.65
EN18229	Lake	Central Yakutia	Middle Taiga	62.200	116.935	182	–7.21	267.68
EN18232	Lake	Central Yakutia	Middle Taiga	59.991	112.984	340	–5.40	469.76
EN18243	Lake	Central Yakutia	Middle Taiga	59.985	112.965	341	–5.40	469.74
EN18247	Lake	Central Yakutia	Middle Taiga	59.984	112.996	344	–5.40	469.56
L01	Lake	Chukotka	Mountain Tundra	67.376	168.254	593	–14.46	215.81
L04	Lake	Chukotka	Mountain Tundra	67.357	168.199	489	–14.43	215.18
L05	Lake	Chukotka	Open Woodlands	67.353	168.172	488	–14.40	214.92
L08	Lake	Chukotka	North Taiga	66.971	163.443	122	–12.07	228.21
L11	Lake	Chukotka	Open Woodlands	65.930	166.378	652	–12.75	286.02
L14	Lake	Chukotka	Open Woodlands	65.917	166.296	658	–12.77	286.32
L15	Lake	Chukotka	Open Woodlands	65.895	166.292	715	–12.78	285.79
L18	Lake	Chukotka	Open Woodlands	65.906	166.341	631	–12.77	285.71
L21	Lake	Chukotka	Mountain Tundra	67.801	168.696	630	–12.90	193.80
L22	Lake	Chukotka	Mountain Tundra	67.805	168.699	625	–12.90	193.81

MAT, mean annual temperature; MAP, mean annual precipitation.

and Red Green Near Infrared (RGN) cameras to obtain spatially mapped detailed vegetation information in 2 and 3 dimensions (2D, 3D) besides the 2018 field vegetation inventories (Kruse et al., 2019; van Geffen et al., 2021a,b). The aerial imagery covered a minimum areal extent of 50 m × 50 m over the vegetation plots. RGB and RGN Structure for Motion (SFM) point clouds were constructed with Agisoft PhotoScan Professional (Agisoft, 2018) according to methods described in Brieger et al. (2019). From each full RGB and RGN point cloud and overhead photo images orthomosaics were created (Kruse et al., 2021). The distribution of plant communities was mapped by a maximum likelihood classification of the layers using the superClass function in the "RStoolbox" package (Leutner et al., 2019) in R (R Core Team, 2019). The training dataset and cover of plant taxa for each community was visually selected and estimated in the field using 2 m × 2 m quadrats. The cover of major taxa was extracted by concentric rings of 1 m increments within the first 25 m and extrapolated to 100 m radius by the averaged taxa cover.

The vegetation within 100–3000 m was inferred from a land-cover classification at a 20 m resolution based on Sentinel-2 satellite image data (European Space Agency, ESA). The training dataset of land-cover types was created based on the 2018 vegetation plots (van Geffen et al., 2021a,b). Plant cover data within the different radii were extracted from these vegetation class maps within a 3000 m radius of each sampling site. Plant taxa composition in each land-cover type was estimated based on the taxa cover extracted from the drone-based orthomosaics. For Chukotka, the classification of the Sentinel-2 satellite data was performed with machine learning algorithms in Python from the SciKit-Learn library (Pedregosa et al., 2011). Several algorithms were trained, including Random Forest, Decision Tree, and Gaussian Naive Bayes, and the best performing algorithms were selected per region based on the mean accuracy over all the classes. For all 35 vegetation plots in Chukotka the vegetation classes were all classified together with an accuracy score of 82% and the K- Nearest Neighbours algorithm. For the vegetation plots in central Yakutia, class variety was more diverse with not enough vegetation plots of the same class for a robust classification. Instead of a supervised trained classification we defined the value ranges of the Normalized Difference Vegetation Index NDVI (Near Infrared – red/Near Infrared + red) and the relative absorption depth (Murphy, 1995) of the red Chlorophyll absorption band (green + Near Infrared/2 × Red) (European Space Agency, 2015) of each of the vegetation classes for assigning classes from the NDVI and pigment absorption depth maps.

To create vegetation input files for the Extended R-Value (ERV) models, the mean absolute cover (in m^2 m^{-2}) of the plant taxa for ERV analysis was calculated for each chosen distance increment. In this study, we used different increments within different distances (1 m increment for the first 25 m radius, 5 m increment for between 20 and 100 m, 10 m increment for 100 to 1000 m, and 50 m increment for 1000–3000 m). We assume homogeneous vegetation cover in each concentric ring, as it is the assumption for data analysis using ERV models and related pollen-dispersal functions.

Climate Data

MAT, MAP, mean summer temperature (MST), mean winter temperature (MWT), mean summer precipitation (MSP), and

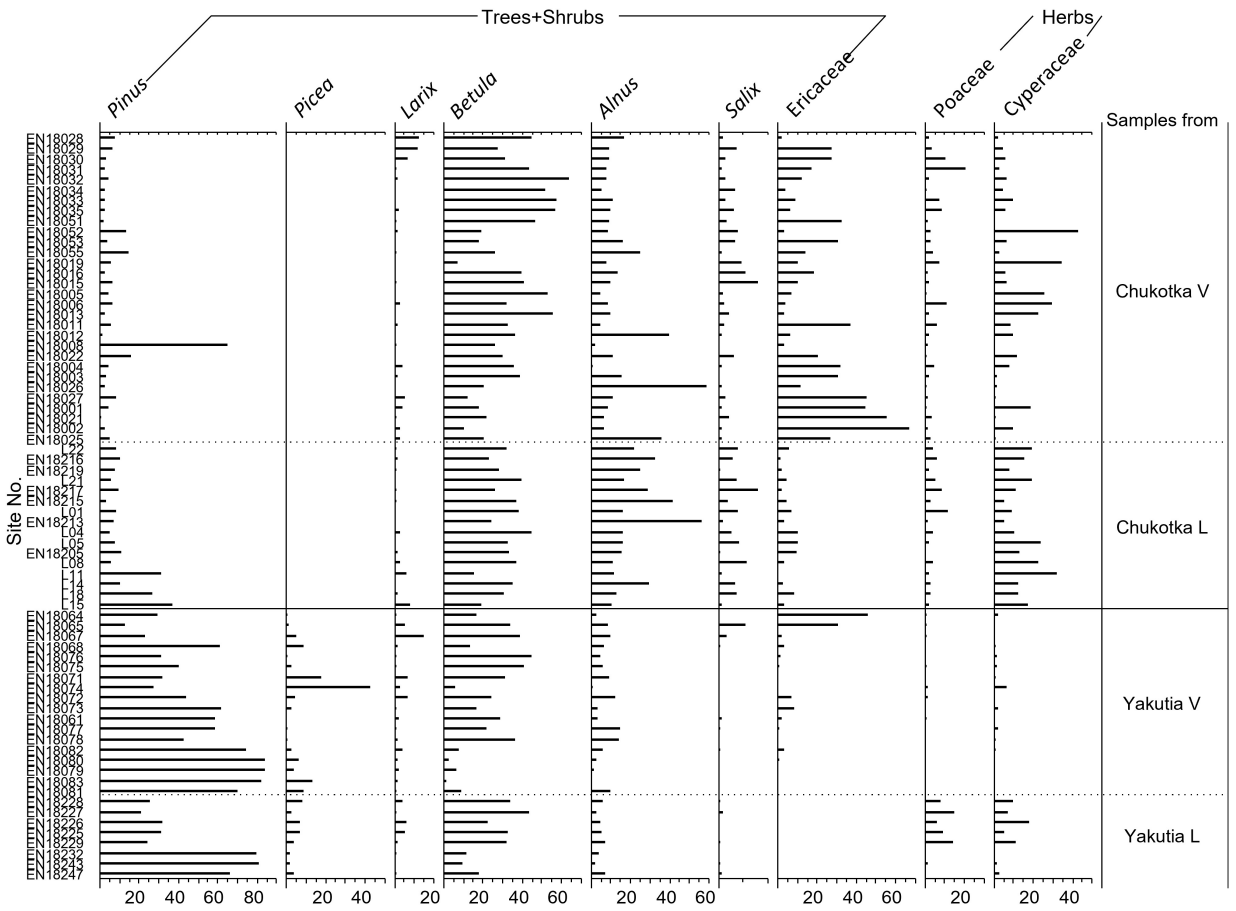

FIGURE 2 | Pollen diagram of the main taxa from 72 surface samples, grouped according to location. Suffix V signifies samples from vegetation plots, i.e., moss/soil samples and suffix L signifies lake sediment samples. Samples in each group are sorted by latitude in descending order.

mean winter precipitation (MWP) over 30 years (1987–2017) and 100 years (1917–2017) were interpolated using the weighted mean method from Terrestrial Air Temperature: 1900–2017 Gridded Monthly Time Series Version 5.01 (Matsuura and Willmott, 2018a) and Terrestrial Precipitation: 1900–2017 Gridded Monthly Time Series Version 5.01 (Matsuura and Willmott, 2018b) in R software.

Numerical Analysis

Taxa that occurred in at least three samples were used in the numerical analysis. A square root transformation of all the data was performed before all the numerical analyses to normalize skewed distributions and reduce the effect of extreme values.

Ordination analyses were used to investigate the main structure in the pollen data and its relation to vegetation type and environmental variables. A detrended correspondence analysis (DCA) was initially performed to estimate the underlying linearity of the data. The results of the DCA showed that the gradient lengths of the first four axes were less than 2.1 standard deviation units, suggesting linear underlying responses. Accordingly, the linear methods Principal Component Analysis (PCA) and Redundancy Analysis (RDA) were chosen to assess how well the pollen assemblages characterize the different vegetation types (Ter Braak and Prentice, 1988). The correlations between pollen assemblages and climate variables are explored in the RDA. Analyses were implemented using the "vegan" package in R (Oksanen et al., 2019).

PROCRUSTES rotation analysis (Peres-Neto and Jackson, 2001) was performed to compare the species scores of the PCA results for pollen data from different sample types using the "vegan" package in R (Oksanen et al., 2019). This analysis was to investigate the similarity and correlation between pollen data from moss/soil and lake samples. The non-randomness (significance) between the tested datasets was assessed by PROTEST (Jackson, 1995; Niemeyer et al., 2017).

Extended *R*-Value Analysis

Besides pollen and vegetation data, other input data required to run the ERV model are fall speed of pollen (FSP) and wind speed. We used a constant wind speed of 2.1 m s^{-1}, which is the mean wind speed calculated from the Global Surface Hourly dataset (1988–2018, Noaa National Centers for Environmental Information, 2001) based on selected weather stations in study area. FSP for the selected taxa (**Table 2**) were taken from the

TABLE 2 | Fall speed of major taxa used to estimate relative pollen productivity (RPP) in this study.

Taxa	Fall speed (m/s)	References
Alnus	0.021	Eisenhut, 1961
Betula	0.019	Li et al., 2015
Cyperaceae	0.035	Sugita et al., 1999
Ericaceae	0.038	Broström et al., 2004
Larix	0.135	Li et al., 2015
Picea	0.056	Eisenhut, 1961
Pinus	0.039	Li et al., 2015
Poaceae	0.035	Sugita et al., 1999
Salix	0.022	Gregory, 1973

literature (Eisenhut, 1961; Gregory, 1973; Sugita et al., 1999; Broström et al., 2004; Li et al., 2015).

ERV.Analysis.v1.3.1. Program (Sugita, unpublished) was used to estimate RPP for the selected taxa in Chukotka and central Yakutia. This program provided 4 pollen dispersal models including Prentice-Sutton distance-weighting method (Prentice's model) which was chosen as the best fit for this study. We ran the ERV analyses using selected moss/soil sampling sites from Chukotka (14 sites) and central Yakutia (17 sites). We selected taxa that occurred sufficiently frequently in both the pollen and vegetation data for most sites and are characterized by between-sample variation in pollen percentages and vegetation abundances (Li et al., 2017). Ericaceae was present at adequate quantities in the pollen assemblages and vegetation of most sites with a wide variation in abundance between sites in both areas. Poaceae is the most common reference taxon in studies of RPPs. Therefore, Ericaceae (Chukotka, Yakutia) and Poaceae (Chukotka) were selected as the reference taxa to run the ERV model and pollen productivity for the other taxa was estimated relative to the productivity of these reference taxa. We ran the ERV model using all sites with available vegetation and pollen data to assess the log-likelihood curves to identify the RSAP and evaluate the pollen–vegetation relationships. The taxa with non-linear relationships and the site outliers in terms of regional vegetation composition and structure were excluded and then a second ERV analysis was conducted. We also explored the effects of including different numbers of taxa in the ERV analysis, repeating calculations with 6, 7, or 8 taxa, and found that the results from the analysis of 6 taxa (*Betula*, Cyperaceae, Ericaceae, *Larix*, Poaceae, *Salix*) for Chukotka and 7 taxa (*Alnus*, *Betula*, Cyperaceae, Ericaceae, *Larix*, *Picea, Pinus*) for central Yakutia are most reasonable.

All three sub-models of the ERV model were tried in the analysis. The input pollen and vegetation datasets for ERV sub-models 1 and 2 were percentages while sub-model 3 used vegetation datasets expressed as absolute abundance (m^2/m^2). ERV sub-model 1 and 2 assumes the background pollen as a constant percentage (Parsons and Prentice, 1981) and a constant proportion of total plant abundance (Prentice and Parsons, 1983). Sub-model 3 assumes that the background pollen comes from beyond RSAP. The RSAP was defined visually from a log-likelihood curve where the values increased with distance and reached an asymptote. The RPP of each taxon was estimated as the average value with all distances greater than the RSAP.

RESULTS

Pollen Assemblages

A total of 46 pollen and spore taxa were identified in the 72 surface samples, 31 of which occurred in at least three samples. The overall dominant taxa are *Alnus*, *Artemisia*, *Betula*, Cyperaceae, Ericaceae, *Larix*, Poaceae, *Pinus,* and *Salix*.

Pollen assemblages from Chukotka are characterized by high percentages of prostrate and hemi-prostrate low shrub taxa (36–94%), with *Betula* ranging from 7.3 to 64.0% and median value 32.2%, Ericaceae (0.3–66.7%, 9.4%, henceforth median value), *Alnus* (1.0–58.6%, 11.2%), and *Salix* (0.0–7.8%, 1.5%). Herb pollen taxa such as Cyperaceae (0.0–42.8%, 9.1%), Poaceae (0.0–20.7%, 2.4%), and *Artemisia* (0.0–18.7%, 1.4%) are also relatively common in some samples. The main tree pollen taxa are *Larix* (0.0–12.0%; 1.0%) and *Pinus* (0.6–65.2%, 5.8%).

Pollen assemblages from central Yakutia are characterized by high proportions of tree taxa (50–99%) especially conifers such as *Pinus* (12.8–84.3%, 43.2%), *Picea* (0.0–42.7%, 3.8%), and *Larix* (0.5–15.2%, 1.5%). Pollen of *Betula* (1.3–44.3%, 22.2%), Ericaceae (0.0–46.0%, 0.3%), *Alnus* (0.3–14.8%, 5.5%), Cyperaceae (0.0–18.3%, 1.0%), and Poaceae (0.0–14.6%, 0.4%) are also common but less abundant than in pollen assemblages from Chukotka.

Vegetation Data

A total of 46 harmonized taxa (some taxa were combined in order to correspond to pollen types) was recorded in the field survey. In the final vegetation dataset employed for the ERV-modeling, 11 land-cover types were included in the application (**Table 3**). For the Chukotka area, graminoid tundra, forest and shrub tundra, and prostrate herb tundra were adopted. The vegetation types of open canopy pine and larch with lichen, open canopy pine, closed canopy pine, open canopy mixed forest, closed canopy mixed forest, open canopy larch, closed canopy larch, and closed canopy spruce were classified in central Yakutia (see example of maps with classifications in **Figure 3**).

Pollen-Vegetation-Climate Relationships of Different Sediment Types

In order to explore the relationships between pollen assemblages, vegetation types, and climate variables, RDA was performed with climate variables as constraining variables (RDA in **Figure 4**). The first two RDA axes explain 50.46% (axis 1: 43.75%, axis 2: 6.709%) of the total variance observed in the pollen assemblages from moss/soil samples while the first two axes of the RDA based on lake samples explain 64.11% (axis 1: 50.29%, axis 2: 13.82%) of the total variance.

The first axes of the lake and moss/soil datasets separate the samples from Chukotka and central Yakutia. The taxa scores of axis 1 reflect the pollen contents of the main taxa for different vegetation types, i.e., *Pinus*, *Picea*, and *Larix* (positive RDA scores) and Ericaceae, *Betula*, *Alnus*, *Salix*, and Cyperaceae (negative RDA scores) in both analyses with different scores.

TABLE 3 | Land-cover types from Sentinel-2 data and their major taxa composition in this study.

ID	1	2	3	4	5	6	7	8	9	10	11
Abies	0	0	0	0.00	0	0	5.92	0.25	0	0	0
Alnus	0.37	2.41	0.17	0.00	0	0	1.91	0.90	0	7.84	0
Betula	7.21	9.95	0.66	0.56	2.77	1.17	0.11	11.13	0.77	16.48	0.26
Cyperaceae	17.44	9.76	0.30	0.39	0	4.58	0.63	0	0.31	0	0
Ericaceae	14.76	29.96	5.65	25.94	39.54	29.69	32.16	2.55	18.86	42.23	9.90
Larix	7.96	18.60	0.17	70.72	37.00	74.00	3.40	41.50	54.67	48.33	36.00
Picea	0	0	0	0.00	0	0	1.72	33.38	0.17	2.74	73.85
Pinus	2.75	11.66	0.30	21.48	37.55	23.87	22.17	1.73	7.23	0.53	0
Poaceae	10.63	3.28	0.30	0.05	0.56	0.12	5.66	0.66	3.17	3.67	3.80
Salix	3.43	6.69	0.52	0.00	0	1.13	1.69	1.92	1.57	0.83	0

Land-cover types: 1 – Graminoid tundra, 2 – Forest tundra and shrub tundra, 3 – Prostrate herb tundra, 4 – Open canopy pine and larch with lichen, 5 – Open canopy pine, 6 – Closed canopy pine, 7 – Open canopy mixed forest, 8 – Closed canopy mixed forest, 9 – Open canopy larch, 10 – Closed canopy larch, 11 – Closed canopy spruce. Types 1–3 occur in Chukotka and 4–11 in central Yakutia.

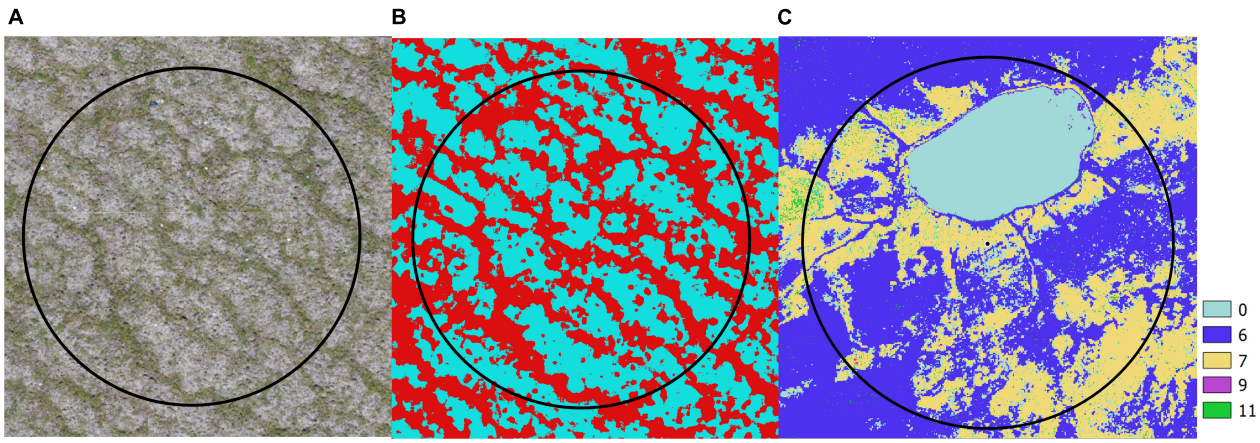

FIGURE 3 | Examples of **(A)** Red Green Blue true-color orthoimage derived from the RGB drone camera with a 15 m radius circle, **(B)** classified vegetation map from orthoimage (barren in blue and shrub tundra in red) with a 15 m radius circle, and **(C)** land-cover map created from Sentinel-2 images with a 3000 m radius circle. The land-cover type IDs are described in **Table 3**: 0 – water body, 6 – Closed canopy pine, 7 – Open canopy mixed forest, 9 – Open canopy larch, 11 – Closed canopy spruce.

All climate variables are positively related to axis 1 with high scores. RDA1 scores of constraining variables are 0.9426 and 0.9327 (MAT) and 0.8948 and 0.9083 (MAP) for moss/soil and lake datasets, respectively. MAT and MAP are shown in the RDA plots (**Figure 4**). The first RDA axis apparently reflects temperature and moisture gradients as shown by the projections in both plots. The RDA plot of moss/soil samples indicates that temperature is the main controlling factor of the changes in pollen assemblages as the arrow of MAT is parallel to the first axis (**Figure 4**). Moreover, the relationship between the climate variables and pollen assemblages of lake samples is stronger than for the moss/soil samples since the first two RDA axes of lake samples explain more of the total variance (64.11%) than the moss/soil samples (50.46%). In general, the samples from Chukotka are associated with lower temperature and precipitation, whereas the samples from central Yakutia are strongly related to higher temperature and precipitation.

PROCRUSTES rotation analyses and PROTEST were performed to find the best fit in a statistical sense between PCA taxa scores of moss/soil and lake samples (**Figure 5**). The results indicate a significant accordance in pollen data between the PCA taxa scores of different sample types. The PROCRUSTES rotation sum of squares(m^{12}) is 0.378 and the root mean square error (RMSE) is 0.1104. Correlation between the two ordination results (r = 0.7887) is high. Pollen taxa residuals of *Rumex*, Poaceae, *Alnus*, *Larix*, and Asteraceae between different sample types are above 0.15 (**Figure 5**) showing a lack of consistency for these taxa in the tested datasets.

Relevant Source Area of Pollen and Relative Pollen Productivity Estimates

Chukotka

Out of the three sub-models, sub-model 1 was excluded at first based on the plots of log-likelihood against distance (**Figure 6**). The RSAP is ca. 500 m with sub-model 3 and ca. 1300 m with sub-model 2 since the log-likelihood approached an asymptote (**Figure 6A**). Ericaceae and *Betula* exhibit a relationship that is

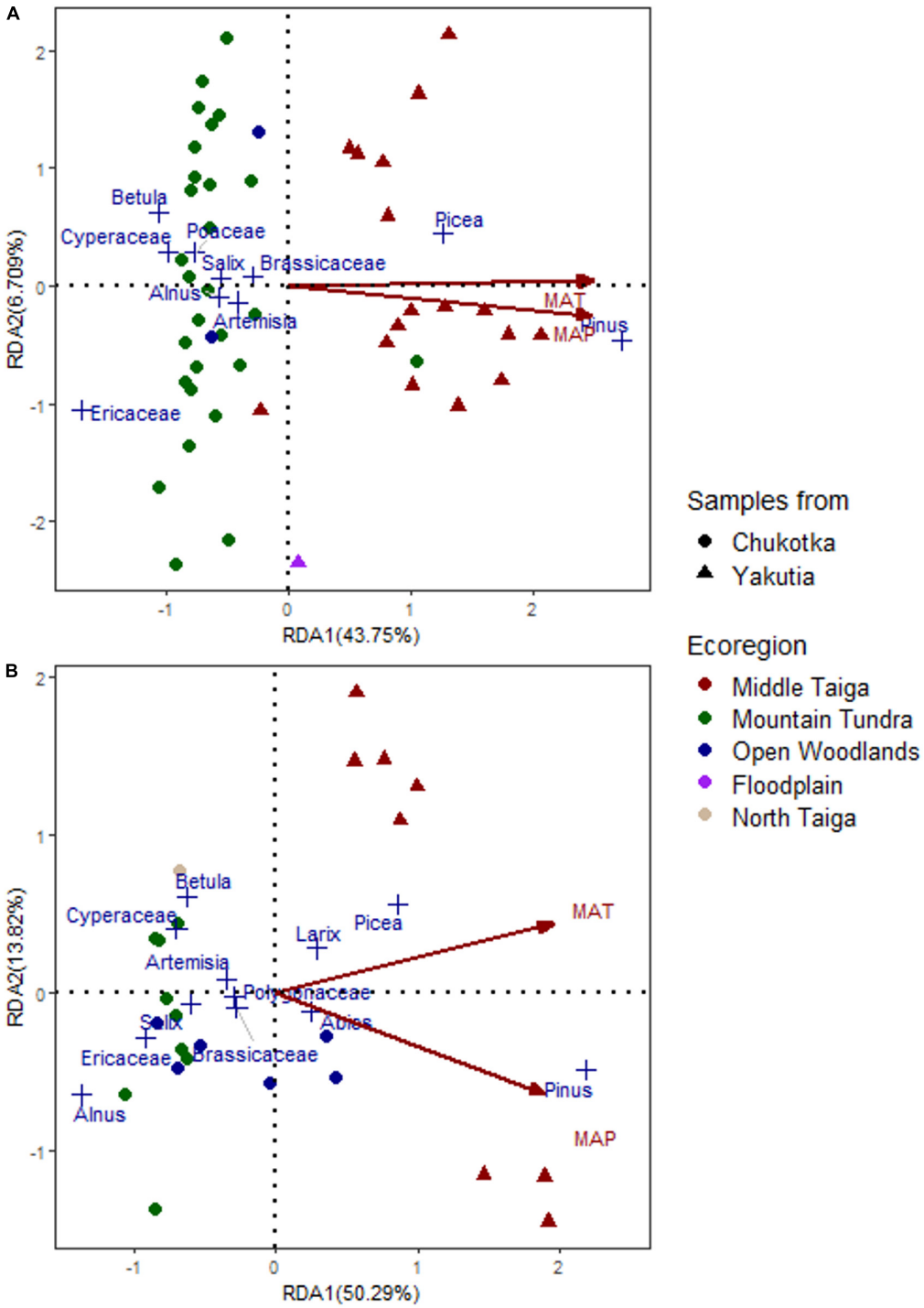

FIGURE 4 | Triplots of redundancy analysis (RDA) based on surface pollen data from **(A)** moss/soil samples and **(B)** lake samples. Climate variables are projected as red arrows in the plots (MAP, mean annual precipitation; MAT, mean annual temperature).

closest to an ideal linear relationship in ERV adjusted pollen proportions and vegetation proportions using sub-model 2 (**Supplementary Figure 1A**).

The RPP estimates relative to both Poaceae and Ericaceae for 6 taxa and their standard deviations (SDs) were calculated using two ERV sub-models (**Table 4**). ERV sub-model 2 mostly produces higher RPPs than sub-model 3 except for Cyperaceae. The ranking of the RPPs is the same for both ERV sub-models: *Betula* > *Larix* > Ericaceae > Poaceae > *Salix* > Cyperaceae with Ericaceae having a RPP of 1 (**Figure 7**). Cyperaceae and *Salix*

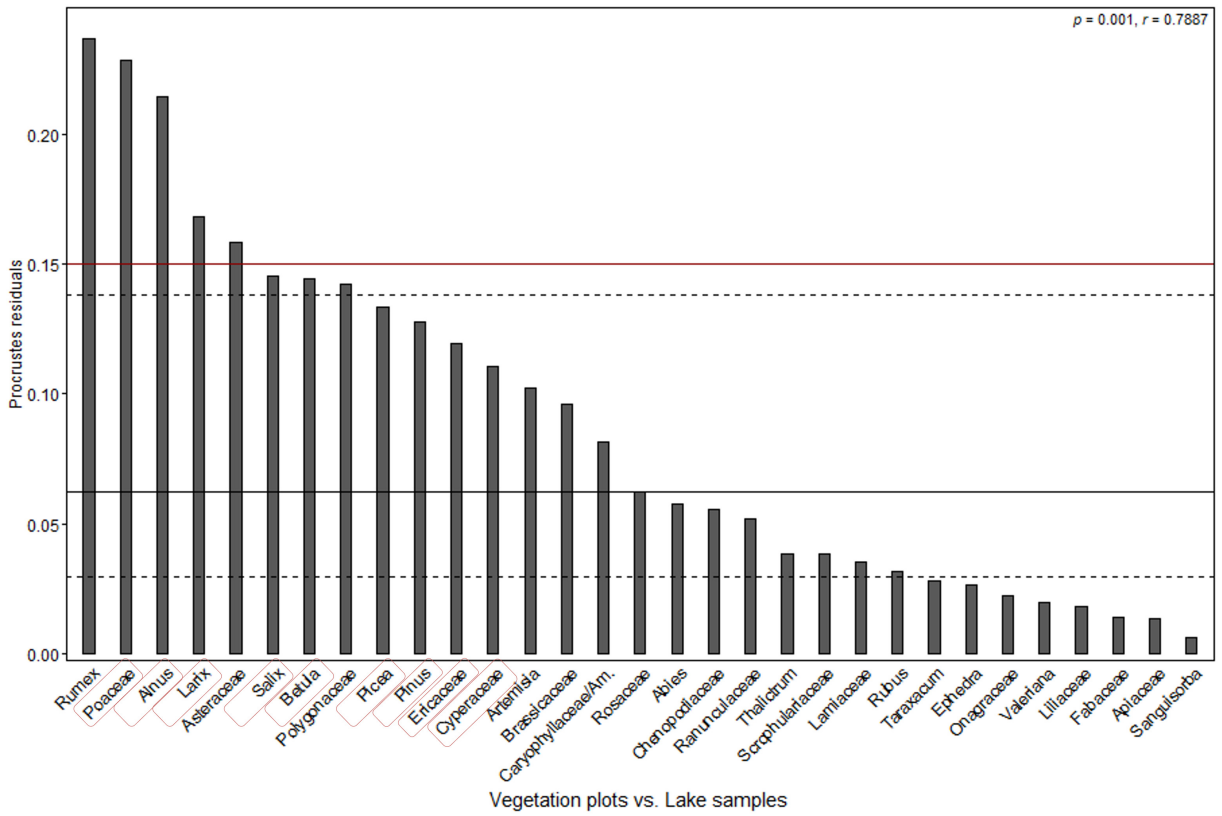

FIGURE 5 | PROCRUSTES residuals plot of comparison between principal component analysis (PCA) taxa scores of moss/soil samples and lake samples (ordered according to the residual scores). Dashed and solid lines are the first, second, and third quartiles. The *p*-value indicates the likelihood of the relationship occurring by chance and the *r*-value reflects the correlation between the two ordination results. Taxa used in ERV model were highlighted in red rectangle.

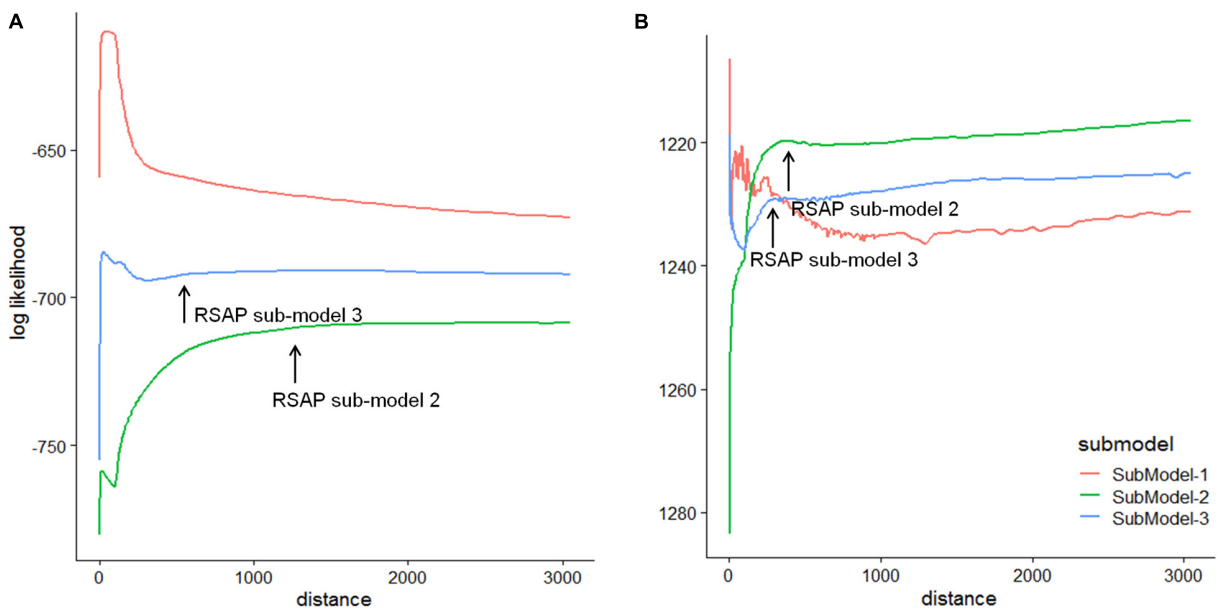

FIGURE 6 | Plots of the log-likelihood against distance from the sampling point using three ERV sub-models for **(A)** Chukotka and **(B)** Yakutia, based on pollen data from moss/soil samples and vegetation data within a 3000 m radius.

TABLE 4 | Relative pollen productivity (RPP) estimates and standard deviations (SDs) for selected taxa in Chukotka and central Yakutia.

	Chukotka (Ericaceae ref.)				Chukotka (Poaceae ref.)				Yakutia (Ericaceae ref.)			
	Submodel 2		Submodel 3		Submodel 2		Submodel 3		Submodel 2		Submodel 3	
	RPP	SD	RPP	SD	RPP	SD	RPP	SD	RPP	SD	RPP	SD
Alnus									**0.54**	0.97	**0.37**	0.26
Betula	**1.80**	0.15	**1.78**	0.13	**2.82**	0.28	**3.27**	0.21	1.02	3.76	**0.49**	0.36
Cyperaceae	0.00001	0.00430	0.00006	0.01680	0.00002	0.00709	0.00009	0.00899	0.01	3.04	0.06	1.63
Ericaceae	1	0	1	0	**1.57**	0.20	**1.84**	0.14	1	0	1	0
Larix	**1.40**	0.24	**1.33**	0.25	**2.18**	0.36	**2.45**	0.46	**4.23**	2.24	**4.27**	1.77
Picea									**2.18**	0.53	**2.76**	0.17
Pinus									**10.38**	3.75	**14.07**	0.96
Poaceae	**0.64**	0.18	**0.55**	0.32	1	0	1	0				
Salix	**0.14**	0.07	0.0006	0.1611	**0.23**	0.11	0.0009	0.0578				

All reliable RPP estimates with smaller SDs are in bold.

have very low RPPs but their large standard deviations suggest that they may not be credible values.

Central Yakutia

Out of the three sub-models, sub-model 1 was excluded at first based on the plots of log-likelihood against distance (**Figure 6**). The RSAP is ca. 250 m with sub-model 3 and ca. 360 m with sub-model 2 since the log-likelihood approached an asymptote (**Figure 6B**). *Picea* and *Pinus* exhibit a relationship that is closest to an ideal linear relationship in ERV adjusted pollen proportions and vegetation proportions using sub-model 2 (**Supplementary Figure 1B**).

The RPP estimates relative to Ericaceae for 7 taxa and their standard deviations (SDs) were calculated using two ERV sub-models (**Table 4**). ERV sub-models 2 and 3 produce similar but varying RPPs. The ranking of the RPPs is the same for both ERV sub-models: *Pinus* > *Larix* > *Picea* > Ericaceae > *Betula* > *Alnus* > Cyperaceae with Ericaceae having a RPP of 1 (**Figure 7**). Cyperaceae and *Alnus* have very low RPPs but their large standard deviations suggest that they may not be credible values. *Betula* also has a very large standard deviation.

DISCUSSION

Pollen-Vegetation-Climate Relationship

Our surface pollen assemblages reflect the vegetation types well in terms of dominant taxa in the study regions. Furthermore, pollen spectra from Middle Taiga and Mountain Tundra are unique as revealed by RDA. *Pinus* and *Picea* have positive RDA scores (**Figure 4**), as do most samples from central Yakutia, reflecting the Middle Taiga ecoregion. Ericaceae, *Betula*, *Alnus*, *Salix*, and Cyperaceae have negative RDA scores, reflecting the ecoregion of Mountain Tundra from Chukotka. The samples from Open Woodlands are scattered around the center of the RDA plots, which is reasonable since this represents a spatially and ecologically transitional vegetation type between tundra and taiga. There are only two sites that are inconsistent with this pattern: EN18008 and EN18065. The vegetation survey of EN18008 found *Pinus pumila* shrubs, which has resulted in a high proportion of *Pinus* in the pollen data and may explain why it was distributed among the samples from central Yakutia in the RDA plot. Our ordination results are similar to other studies. For example, Pelánková and Chytrý (2009) compare proportions of plant species in actual vegetation and their pollen types in surface pollen spectra along transects in the steppe, forest, and tundra of the valleys of the Russian Altai Mountains and conclude that pollen taxa abundances of *Betula nana*, *Larix*, *Picea,* and

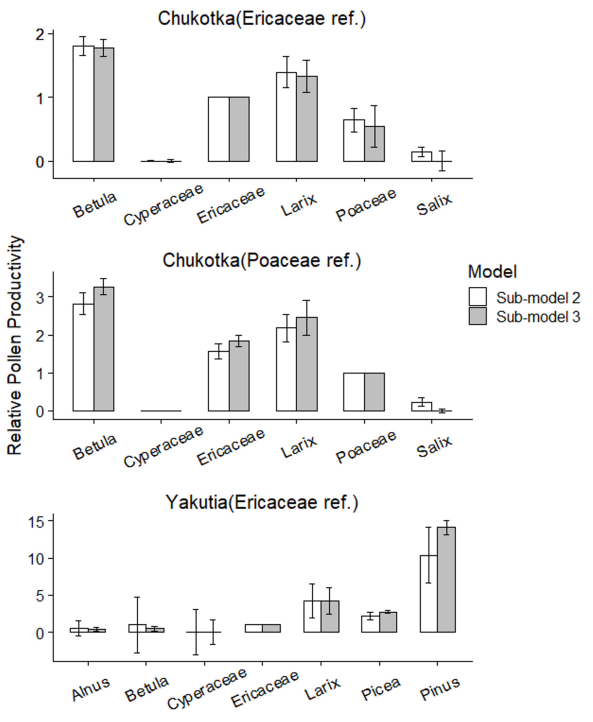

FIGURE 7 | Relative pollen productivity estimates and errors for selected taxa, using plant cover data weighted by two ERV sub-models.

TABLE 5 | Relative pollen productivity (RPP) estimates rescaled relative to Ericaceae (RPPs from Changbai Mt. and Germany were rescaled based on the relationship between their original reference taxa and Ericaceae in this study) in previously published studies for selected taxa that are compared with this study.

Study area	Sample type	Vegetation	RSAP	*Alnus*	*Betula*	Cyperaceae	Ericaceae	*Larix*	*Picea*	*Pinus*	Poaceae	*Salix*	References
Alaska	Moss/soil	Montane tundra	800		20.66	1.89	1				1.89	1.09	Hopla, 2017
Eastern Scotland	Moss/soil	Pine woodland	500		1.19		1		0.48	1.48			Twiddle et al., 2012
Denmark	Lake	Wetland, dryland	1700				1		1.08		0.91		Nielsen, 2004
Northern Finland	Moss/soil	Forest	1000		65.71	0.03	1			120	14.29		Räsänen et al., 2007
Southern Sweden	Moss/soil	Semi-open woodland pasture	200			0.23	1				0.33		Broström et al., 2004
South Norway	Lake	Semi-open landscape	900–1100	3.22		1.57	1		1.38	6.59	1.15	0.71	Hjelle and Sugita, 2012
Germany	Lake	Forest	7000	28.44	17.65		1	16.09	2.91	10.38			Matthias et al., 2012
Changbai Mt.	Moss/soil	Forest	1000		7.47	0.03	1	2.82		12.04	0.64		Zhang et al., 2017
Siberian Arctic	Moss/soil	Arctic tundra and light taiga	10	19.45	5.45	1.61	1	0.0003			3.03	0.09	Niemeyer et al., 2015
Siberian Arctic	Lake	Arctic tundra and light taiga	25000	1430	910	55	1	80			500	3	Niemeyer et al., 2015
Chukotka	Moss/soil	Tundra	1300		1.8	0.00001	1	1.4			0.64	0.14	This study
Central Yakutia	Moss/soil	Taiga	560	0.54	1.02	0.01	1	4.23	2.18	10.38			This study

Salix are significantly correlated to the surrounding vegetation. In a PCA of modern pollen spectra in north-eastern Siberia from Klemm et al. (2013), regional differences between tundra and taiga are reflected.

Betula and Ericaceae in Chukotka and *Picea* and *Pinus* in central Yakutia exhibit relationships that are closest to a perfect linear relationship (**Supplementary Figure 1**). It is common in RPP studies that only a few taxa can fit the theoretical ERV-model linear relationship. A non-perfect relationship might be due to the discrepancy between pollen productivity and pollen dispersion, leading to unevenness in the pollen data and vegetation data (e.g., *Alnus*, *Salix*, Cyperaceae). Other factors influencing the pollen–vegetation relationship may be stochastic pollen dispersal processes, for example by insects rather than wind transport, or pollen transported in clumps rather than as single grains (Tufto et al., 1997; Theuerkauf et al., 2013; Li et al., 2017).

Pollen composition is numerically related to temperature and precipitation (**Figure 4**). *Pinus* and *Picea* are characteristic of the samples from central Yakutia with relatively high MAT, whereas *Betula*, Cyperaceae, and Ericaceae, are indicator taxa in samples from Chukotka and dominate under low MAT. This is in accordance with results from previous studies of Siberian surface pollen spectra (e.g., Pelánková and Chytrý, 2009; Klemm et al., 2013). It suggests that the relationship between pollen assemblages and climate variables is rather tight, and that palaeoclimates can be reasonably accurately reconstructed from fossil pollen records.

Although these correlations may provide climate indicators, the relationships between climate variables and a single taxon can be different in different areas. For example, Pelánková et al. (2008), based on their studies in southern Siberia, suggest that a high proportion of *Pinus* pollen indicates low summer temperatures and higher precipitation and the occurrence of *Larix* pollen indicates low winter temperatures and low precipitation, which contrasts with the positive correlation between MAT and *Pinus* and the insignificant correlation between *Larix* and temperature in this study. This contrast can be attributed to the range of climate variables and vegetation types in geographically different areas.

Pollen Assemblages in Different Sediment Types

PROCRUSTES analysis of PCA taxa scores reveals that pollen data from moss/soil and lake samples have a similar distribution (m^{12} = 0.378, r = 0.7887). However, there are some differences in the representation of several pollen taxa originating from different sediment types as indicated by, for example, the high PROCRUSTES residuals of Poaceae, *Alnus*, *Larix,* and *Salix* (**Figure 5**). The pollen percentages of *Larix* in lake samples from central Yakutia are generally larger than those from the moss/soil samples (**Supplementary Figure 2**). This finding is in accordance with the RPP estimates from moss surface and lacustrine surface-sediment samples in arctic Siberia (Niemeyer et al., 2015). The pollen percentages of Ericaceae from different sample types varied apparently in terms of mean value and variation range (**Supplementary Figure 2**). The variation of pollen assemblages in different sediment types may be attributed to the size of the source area which depends on the diameter of a sampling site (Sugita, 1993, 1994). Pollen data from large lakes show little site-to-site variation even if vegetation is highly

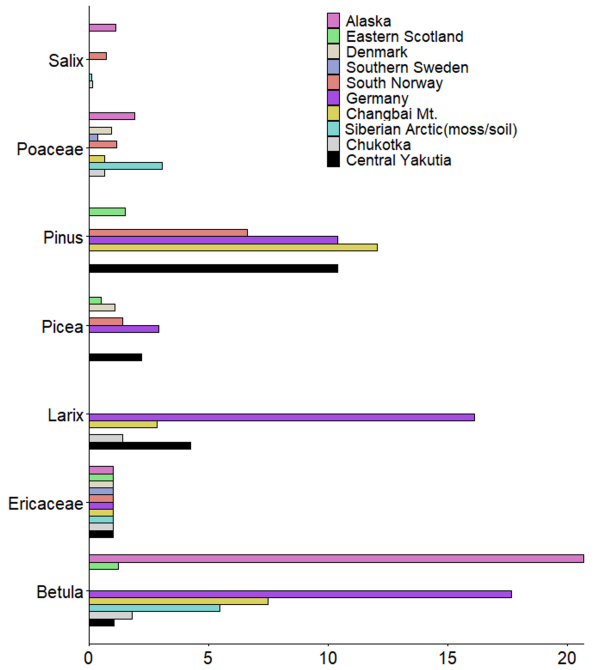

FIGURE 8 | Relative pollen productivity (RPP) estimates of seven selected taxa (*Alnus* and Cyperaceae were excluded because of high standard deviations) compared to RPPs from other studies (Northern Finland and lake samples from Siberian Arctic were excluded as outliers).

heterogeneous compared with pollen data from smaller source area (Sugita, 2007a,b). Therefore, the majority of the pollen in moss/soil samples is likely to originate from local plants, while the lake surface-sediments contain pollen from a larger source area (Bunting, 2002; Zhao et al., 2009). Lisitsyna et al. (2012) state that lake sediment samples from mountain birch woodland tend to overestimate pine and underestimate birch while those from pine forest tend to have higher birch percentages than moss samples, which aligns with our results.

The vegetation type of the sampling sites from central Yakutia is Middle Taiga with more trees and less herbs than the Mountain Tundra and Open Woodlands of sampling sites from Chukotka. Lake samples are characterized by higher amounts of Poaceae and Cyperaceae, especially in samples from central Yakutia (**Supplementary Figure 2**). This might be explained by the higher presence of sedges around the lakes. The Poaceae family includes a number of plant species with very different ecological tolerances. As most fossil pollen records are collected from wet settings, it is difficult but critically important that palynologists recognize whether Poaceae pollen is derived from meadow and marshes that surround their coring site. Interpretations of the pollen signals of Poaceae are likely to overstate "dry" episodes (Bush, 2002).

Relative Pollen Productivity Estimates and Relevant Source Area of Pollen

Based on the plots of log-likelihood against distance from the sampling point (**Figure 6**), sub-model 2 provided a more satisfactory curve and reached an asymptote with the most relatively constant values for both regions. Therefore, sub-model 2 is the most appropriate model to estimate the RSAPs and RPPs for Chukotka and central Yakutia. Estimated RSAPs for moss/soil samples are respectively 1300 and 360 m for the Chukotka tundra and central Yakutia taiga, and are similar to other estimates (see **Table 5**). Several studies (Sugita et al., 1999; Bunting et al., 2004; Broström et al., 2005) suggest that different RSAPs are caused by the distribution and size of the vegetation patches when the basin size is constant. Larger patches and grids will lead to an increase in RSAP (Qin et al., 2020). Other factors such as the taxa included in the analysis and the method used to select sample locations can also influence the estimated RSAP (Broström et al., 2005; Nielsen and Sugita, 2005). Differences in RSAPs may also be due to the number of taxa included and the plant characteristics of the studied landscape (Li et al., 2017). Mixed herb-tree vegetation may have a larger RSAP than all-herb or all-tree vegetation (Bunting and Hjelle, 2010). In our case, taxa included in the ERV analysis of sites from Chukotka are fewer than those from central Yakutia and the vegetation type in Chukotka is mostly tundra with mixed herb and tree taxa while the vegetation in central Yakutia is mainly different types of forest. Moreover, large patch size and the openness can also lead to a relatively larger RSAP in Chukotka.

Our RPPs of *Larix* (RPPchukotka: 1.40 ± 0.24, RPPyakutia: 4.23 ± 2.24), *Betula* (RPPchukotka: 1.80 ± 0.15, RPPyakutia: 1.02 ± 3.76), *Picea* (RPPyakutia: 2.18 ± 0.53), and *Pinus* (RPPyakutia: 10.38 ± 3.75) suggested that they are overrepresented in the pollen spectra, while *Alnus* (RPPyakutia: 0.54 ± 0.97), Cyperaceae (RPPchukotka: 0.00001 ± 0.00430, RPPyakutia: 0.01 ± 3.04), Poaceae (RPPchukotka:0.64 ± 0.18), and *Salix* (RPPchukotka:0.14 ± 0.07) are underrepresented. The RPPs for most taxa in this study compare reasonably well with published studies except *Alnus*, Cyperaceae, and *Salix*.

Even for the same taxa such as *Betula* (RPPchukotka: 1.80 ± 0.15, RPPyakutia: 1.02 ± 3.76) and *Larix* (RPPchukotka: 1.40 ± 0.24, RPPyakutia: 4.23 ± 2.24), the RPP estimates show variation. The reliability of RPP estimates can be assessed by their standard deviations. If the SD is larger than the RPP value, it implies that the estimated RPP is not different from zero and should be considered as unreliable (Li et al., 2017). In our study, the large standard deviations for *Alnus* (RPPyakutia: 0.54 ± 0.97) and *Betula* (RPPyakutia: 1.02 ± 3.76) for Yakutia and for Cyperaceae (RPPchukotka: 0.00001 ± 0.00430, RPPyakutia: 0.01 ± 3.04) for both areas suggest that they may not be credible values. We can also compare the results from sub-model 2 with sub-model 3. Sub-model 2 (Prentice and Parsons, 1983) was developed for datasets where both pollen and vegetation data are available as percentages while sub-model 3 (Sugita, 1994) can be used if absolute vegetation abundance (m^{-2} m^2) is known. Sub-model 2 assumes that the background pollen of each taxon is a constant proportion of total plant abundance (Prentice and Parsons, 1983) and sub-model 3 assumes that the background pollen comes from beyond the RSAP. Large variation in total plant abundance among sites may result in less good estimates from sub-model 2 (Prentice and Parsons, 1983). The taxa with similar RPPs are

Betula, *Larix*, and Poaceae for Chukotka and *Larix*, *Picea*, and *Pinus* for central Yakutia. The RPP of *Salix* (0.14, 0.0006) is significantly different with both sub-models, hence its use should be treated with care.

To compare our results with other studies, RPP estimates in previously published studies were rescaled relative to Ericaceae for major taxa (**Table 5** and **Figure 8**). The large differences between RPP estimates may be due to different species and vegetation types between regions. Differences in methodology for vegetation data collection (Bunting and Hjelle, 2010) and fall speed of pollen can also influence the result of RPP estimates. Our RPP estimates for *Betula* (RPPchukotka: 1.80 ± 0.15, RPPyakutia: 1.02 ± 3.76) and Poaceae (RPPchukotka: 0.64 ± 0.18) are relatively small while our RPP estimates for *Picea* (RPPyakutia: 2.18 ± 0.53) and *Pinus* (RPPyakutia: 10.38 ± 3.75) are relatively large compared with other studies. Even though *Larix* is normally regarded as a very underrepresented taxon, according to our results, the RPP for *Larix* is not as low as the value from moss/soil samples in Niemeyer et al. (2015) and is similar to other studies (e.g., Matthias et al., 2012; Zhang et al., 2017). Besides, RPP estimates for *Larix* (RPPchukotka: 1.40 ± 0.24, RPPyakutia: 4.23 ± 2.24) vary not only in our own study but also in other studies. Nevertheless, most RPP estimates of selected taxa in this study are comparable with published studies except *Alnus*, Cyperaceae, and *Salix*. The large standard deviations and/or the dissimilar values returned by the different sub-models may indicate that our results for these taxa are of limited reliability. Estimates of RPP values can be tested by using them in pollen-based reconstructions of modern or palaeovegetation.

CONCLUSION

Our study reveals that the surface pollen assemblages from Chukotka and central Yakutia numerically reflect the main vegetation types as well as the climate, particularly temperature.

Pollen data from moss/soil and lake samples have a generally similar distribution and significant consistency. Still, for some pollen taxa differences are observed: we find a high abundance of Poaceae and Cyperaceae in lake samples, which at least partly originates from overrepresented wetland taxa in the direct vicinity of the lakes. In contrast to expectation, *Larix* has higher abundances in lake samples than in moss/soil samples. Furthermore, pollen percentages of major taxa in moss/soil samples show a higher variability compared to lake samples.

The RSAP of the tundra-forest transition area in Chukotka and the taiga area in central Yakutia are ca. 1300 and 360 m, respectively. For Chukotka, RPPs relative to both Poaceae and Ericaceae have been estimated while RPPs for central Yakutia are relative to Ericaceae. *Larix*, *Betula*, *Picea,* and *Pinus* are overrepresented while *Alnus*, Cyperaceae, Poaceae, and Salix are underrepresented in the pollen spectra. The RPPs for *Alnus*, Cyperaceae, and *Salix* should be used with caution. Our estimates are in general agreement with previously published values and provide a base for a reliable quantitative reconstruction of East Siberian vegetation.

Our new modern pollen data contribute to the existing modern pollen databases (Davis et al., 2020) and can be used as analogs of tundra and taiga under cold climate conditions. Our results have implications for the interpretation of fossil pollen records and the quantitative reconstruction of past vegetation and climate.

DATA AVAILABILITY STATEMENT

The datasets presented in this study can be found in online repositories. The names of the repository/repositories and accession number(s) can be found below: https://doi.pangaea.de/10.1594/PANGAEA.941577.

AUTHOR CONTRIBUTIONS

RG identified all the pollen samples and wrote the draft. AA helped with identifying pollen, discussed about the results, and revised the draft. SK, BH, FvG, and IS provided and classified the vegetation data. LP, EZ, and ET helped to collect samples and identify the vegetation data. FL helped with running the ERV model. YZ and UH discussed the results and revised the manuscript. All authors contributed to the article and approved the submitted version.

FUNDING

This work was supported by the China Scholarship Council (File No. 201904910635), the ERC consolidator grant Glacial Legacy of Ulrike Herzschuh (Grant No. 772852) the Strategic Priority Research Program of the Chinese Academy of Sciences (No. XDA20070101). The work of AA was financed by Glacial Legacy grant from European Research Council Consolidator Grant 2018-2023. This work has also been supported by the Ministry of Education and Science of the Russian Federation #FSRG2020-0019.

ACKNOWLEDGMENTS

We thank our colleagues from the joint Russian–German expedition 2016 and 2018 for their support in the field. We thank Kathleen Stoof-Leichsenring, Sarah Olischläger, and Antonia Schönberg for support with the laboratory work. Special thanks to Feng Qin, Qiaoyu Cui, and Thomas Böhmer for their help in conducting the analyses. We also thank Cathy Jenks for her help in English writing.

SUPPLEMENTARY MATERIAL

The Supplementary Material for this article can be found online at: https://www.frontiersin.org/articles/10.3389/fevo.2022.837857/full#supplementary-material

REFERENCES

Abraham, V., Novák, J., Houfková, P., Petr, L., and Dudová, L. (2017). A Landscape Reconstruction Algorithm and pedoanthracological data reveal Late Holocene woodland history in the lowlands of the NE Czech Republic. *Rev. Palaeobot. Palynol.* 244, 54–64. doi: 10.1016/j.revpalbo.2017.04.009

Agisoft (2018). *Agisoft PhotoScan User Manual Professional Edition, Version 1.4*. Available online at: https://www.agisoft.com/pdf/photoscan-pro_1_4_en.pdf

Andreev, A., and Klimanov, V. A. (2001). Vegetation and climate in the low reaches of Yana River during Holocene. *Polar Geogr.* 25, 62–71.

Andreev, A. A., and Klimanov, V. A. (2000). Quantitative Holocene climatic reconstruction from Arctic Russia. *J. Paleolimnol.* 24, 81–91. doi: 10.1023/A:1008121917521

Andreev, A. A., Klimanov, V. A., and Sulerzhitsky, L. D. (2001). Vegetation and climate history of the Yana River lowland, Russia, during the last 6400yr. *Quat. Sci. Rev.* 20, 259–266. doi: 10.1016/S0277-3791(00)00118-9

Andreev, A. A., Schirrmeister, L., Tarasov, P. E., Ganopolski, A., Brovkin, V., Siegert, C., et al. (2011). Vegetation and climate history in the Laptev Sea region (Arctic Siberia) during Late Quaternary inferred from pollen records. *Quat. Sci. Rev.* 30, 2182–2199. doi: 10.1016/j.quascirev.2010.12.026

Andreev, A. A., and Tarasov, P. E. (2013). "Northern asia," in *The Encyclopedia of Quaternary Science*, eds S. Elias and C. J. Mock (Amsterdam: Elsevier), 164–172.

Andreev, A. A., Tarasov, P. E., Klimanov, V. A., Melles, M., Lisitsyna, O. M., and Hubberten, H.-W. (2004). Vegetation and climate changes around the Lama Lake, Taymyr Peninsula, Russia during the Late Pleistocene and Holocene. *Quat. Int.* 122, 69–84. doi: 10.1016/j.quaint.2004.01.032

Andreev, A. A., Tarasov, P. E., Wennrich, V., Raschke, E., Herzschuh, U., Nowaczyk, N. R., et al. (2014). Late Pliocene and Early Pleistocene vegetation history of northeastern Russian Arctic inferred from the Lake El'gygytgyn pollen record. *Clim. Past* 10, 1017–1039. doi: 10.5194/cp-10-1017-2014

Birks, H. J. B., and Berglund, B. E. (2018). One hundred years of Quaternary pollen analysis 1916–2016. *Veg. Hist. Archaeobotany* 27, 271–309. doi: 10.1007/s00334-017-0630-2

Brieger, F., Herzschuh, U., Pestryakova, L. A., Bookhagen, B., Zakharov, E. S., and Kruse, S. (2019). Advances in the derivation of northeast siberian forest metrics using high-resolution UAV-based photogrammetric point clouds. *Remote Sens.* 11:1447. doi: 10.3390/rs11121447

Broström, A., Sugita, S., and Gaillard, M.-J. (2004). Pollen productivity estimates for the reconstruction of past vegetation cover in the cultural landscape of southern Sweden. *Holocene* 14, 368–381. doi: 10.1191/0959683604hl713rp

Broström, A., Sugita, S., Gaillard, M.-J., and Pilesjö, P. (2005). Estimating the spatial scale of pollen dispersal in the cultural landscape of southern Sweden. *Holocene* 15, 252–262. doi: 10.1191/0959683605hl790rp

Bunting, M. J. (2002). Detecting woodland remnants in cultural landscapes: modern pollen deposition around small woodlands in northwest Scotland. *Holocene* 12, 291–301. doi: 10.1191/0959683602hl545rp

Bunting, M. J., Gaillard, M.-J., Sugita, S., Middleton, R., and Broström, A. (2004). Vegetation structure and pollen source area. *Holocene* 14, 651–660. doi: 10.1191/0959683604hl744rp

Bunting, M. J., and Hjelle, K. L. (2010). Effect of vegetation data collection strategies on estimates of relevant source area of pollen (RSAP) and relative pollen productivity estimates (relative PPE) for non-arboreal taxa. *Veg. Hist. Archaeobotany* 19, 365–374. doi: 10.1007/s00334-010-0246-2

Bunting, M. J., and Middleton, R. (2009). Equifinality and uncertainty in the interpretation of pollen data: the Multiple Scenario Approach to reconstruction of past vegetation mosaics. *Holocene* 19, 799–803. doi: 10.1177/0959683609105304

Bush, M. B. (2002). On the interpretation of fossil Poaceae pollen in the lowland humid neotropics. *Palaeogeogr. Palaeoclimatol. Palaeoecol.* 177, 5–17. doi: 10.1016/S0031-0182(01)00348-0

Chevalier, M., Davis, B. A. S., Heiri, O., Seppä, H., Chase, B. M., Gajewski, K., et al. (2020). Pollen-based climate reconstruction techniques for late Quaternary studies. *Earth Sci. Rev.* 210:103384. doi: 10.1016/j.earscirev.2020.103384

Clayden, S. L., Cwynar, L. C., and MacDonald, G. M. (1996). Stomate and pollen content of lake surface sediments from across the tree line on the Taimyr Peninsula, Siberia. *Can. J. Bot.* 74, 1009–1015. doi: 10.1139/b96-125

Cui, Q., Zhao, Y., Qin, F., Liang, C., Li, Q., and Geng, R. (2019). Characteristics of the modern pollen assemblages from different vegetation zones in Northeast China: implications for pollen-based climate reconstruction. *Sci. China Earth Sci.* 62, 1564–1577. doi: 10.1007/s11430-018-9386-9

Davis, B. A. S., Chevalier, M., Sommer, P., Carter, V. A., Finsinger, W., Mauri, A., et al. (2020). The Eurasian Modern Pollen Database (EMPD), version 2. *Earth Syst. Sci. Data* 12, 2423–2445. doi: 10.5194/essd-12-2423-2020

Eisenhut, G. (1961). *Untersuchungen über die Morphologie und Ökologie der Pollenkörner heimischer und fremdländischer Waldbäume*. Berlin: P. Parey.

European Space Agency (2015). *Sentinel-2 User Handbook*. Paris: European Space Agency.

Faegri, K., Iversen, J., Kaland, P. E., and Krzywinski, K. (2000). *Textbook of Pollen Analysis*, 4th Edn. Caldwell, NJ: The Blackburn Press.

Geng, R., Zhao, Y., Cui, Q., and Qin, F. (2019). Representation of modern pollen assemblages with respect to vegetation and climate in Northeast China. *Quat. Int.* 532, 126–137. doi: 10.1016/j.quaint.2019.11.003

Gregory, P. H. (1973). *The Microbiology of the Atmosphere*. Aylesbury: Leonard Hill.

Grimm, E. C. (2004). *TGView Version 2.0.2*. Springfield: Illinois State Museum, Research, and Collections Centre. Available online at: www.TiliaIT.com.

Hjelle, K. L., and Sugita, S. (2012). Estimating pollen productivity and relevant source area of pollen using lake sediments in Norway: how does lake size variation affect the estimates? *Holocene* 22, 313–324. doi: 10.1177/0959683611423690

Hopla, E.-J. (2017). *A New Perspective on Quaternary Land Cover in Central Alaska*. Available online at: https://eprints.soton.ac.uk/422162/ (accessed June 21, 2021).

Jackson, D. A. (1995). PROTEST: a PROcrustean randomization TEST of community environment concordance. *Écoscience* 2, 297–303. doi: 10.1080/11956860.1995.11682297

Klemm, J., Herzschuh, U., and Pestryakova, L. A. (2016). Vegetation, climate and lake changes over the last 7000 years at the boreal treeline in north-central Siberia. *Quat. Sci. Rev.* 147, 422–434. doi: 10.1016/j.quascirev.2015.08.015

Klemm, J., Herzschuh, U., Pisaric, M. F. J., Telford, R. J., Heim, B., and Pestryakova, L. A. (2013). A pollen-climate transfer function from the tundra and taiga vegetation in Arctic Siberia and its applicability to a Holocene record. *Palaeogeogr. Palaeoclimatol. Palaeoecol.* 386, 702–713. doi: 10.1016/j.palaeo.2013.06.033

Kobe, F., Bezrukova, E. V., Leipe, C., Shchetnikov, A. A., Goslar, T., Wagner, M., et al. (2020). Holocene vegetation and climate history in Baikal Siberia reconstructed from pollen records and its implications for archaeology. *Archaeol. Res. Asia* 23:100209. doi: 10.1016/j.ara.2020.100209

Kruse, S., Bolshiyanov, D., Grigoriev, M. N., Morgenstern, A., Pestryakova, L., Tsibizov, L., et al. (2019). *Russian-German Cooperation: Expeditions to Siberia in 2018*. Bremerhaven: Alfred-Wegener-Institut.

Kruse, S., Farkas, L., Brieger, F., Geng, R., Heim, B., Pestryakova, L. A., et al. (2021). *SiDroForest: Orthomosaics, SfM Point Clouds and Products from Aerial Image Data of Expedition Vegetation Plots in 2018 in Central Yakutia and Chukotka, Siberia*. Available online at: https://doi.pangaea.de/10.1594/PANGAEA.933263 (accessed July 19, 2021).

Leutner, B., Horning, N., Schwalb-Willmann, J., and Hijmans, R. J. (2019). *RStoolbox: Tools for Remote Sensing Data Analysis*. Available online at: https://CRAN.R-project.org/package=RStoolbox (accessed July 26, 2021).

Li, F., Gaillard, M.-J., Sugita, S., Mazier, F., Xu, Q., Zhou, Z., et al. (2017). Relative pollen productivity estimates for major plant taxa of cultural landscapes in central eastern China. *Veg. Hist. Archaeobotany* 26, 587–605. doi: 10.1007/s00334-017-0636-9

Li, Y., Nielsen, A. B., Zhao, X., Shan, L., Wang, S., Wu, J., et al. (2015). Pollen production estimates (PPEs) and fall speeds for major tree taxa and relevant source areas of pollen (RSAP) in Changbai Mountain, northeastern China. *Rev. Palaeobot. Palynol.* 216, 92–100. doi: 10.1016/j.revpalbo.2015.02.003

Liang, C., Zhao, Y., Qin, F., Zheng, Z., Xiao, X., Ma, C., et al. (2020). Pollen-based Holocene quantitative temperature reconstruction on the eastern Tibetan Plateau using a comprehensive method framework. *Sci. China Earth Sci.* 63, 1144–1160. doi: 10.1007/s11430-019-9599-y

Lisitsyna, O. V., Hicks, S., and Huusko, A. (2012). Do moss samples, pollen traps and modern lake sediments all collect pollen in the same way? A comparison from the forest limit area of northernmost Europe. *Veg. Hist. Archaeobotany* 21, 187–199. doi: 10.1007/s00334-011-0335-x

Magyari, E. K., Kuneš, P., Jakab, G., Sümegi, P., Pelánková, B., Schäbitz, F., et al. (2014). Late Pleniglacial vegetation in eastern-central Europe: are there modern analogues in Siberia? *Quat. Sci. Rev.* 95, 60–79. doi: 10.1016/j.quascirev.2014.04.020

Matsuura, K., and Willmott, C. J. (2018a). *Terrestrial Air Temperature: 1900-2017 Gridded Monthly Time Series*. Available online at: http://climate.geog.udel.edu/∼climate/html_pages/Global2017/README.GlobalTsT2017.html (accessed July 22, 2020).

Matsuura, K., and Willmott, C. J. (2018b). *Terrestrial Precipitation: 1900-2017 Gridded Monthly Time Series*. (accessed July 22, 2020).

Matthias, I., Nielsen, A. B., and Giesecke, T. (2012). Evaluating the effect of flowering age and forest structure on pollen productivity estimates. *Veg. Hist. Archaeobotany* 21, 471–484. doi: 10.1007/s00334-012-0373-z

Minckley, T., and Whitlock, C. (2000). Spatial variation of modern pollen in Oregon and southern Washington, USA. *Rev. Palaeobot. Palynol.* 112, 97–123. doi: 10.1016/S0034-6667(00)00037-3

Müller, S., Tarasov, P. E., Andreev, A. A., Tütken, T., Gartz, S., and Diekmann, B. (2010). Late Quaternary vegetation and environments in the Verkhoyansk Mountains region (NE Asia) reconstructed from a 50-kyr fossil pollen record from Lake Billyakh. *Quat. Sci. Rev.* 29, 2071–2086. doi: 10.1016/j.quascirev.2010.04.024

Murphy, R. J. (1995). The effects of surficial vegetation cover on mineral absorption feature parameters. *Int. J. Remote Sens.* 16, 2153–2164. doi: 10.1080/01431169508954548

Nielsen, A. B. (2004). Modelling pollen sedimentation in Danish lakes at c.ad 1800: an attempt to validate the POLLSCAPE model. *J. Biogeogr.* 31, 1693–1709. doi: 10.1111/j.1365-2699.2004.01080.x

Nielsen, A. B., and Sugita, S. (2005). Estimating relevant source area of pollen for small Danish lakes around AD 1800. *Holocene* 15, 1006–1020. doi: 10.1191/0959683605hl874ra

Niemeyer, B., Epp, L. S., Stoof-Leichsenring, K. R., Pestryakova, L. A., and Herzschuh, U. (2017). A comparison of sedimentary DNA and pollen from lake sediments in recording vegetation composition at the Siberian treeline. *Mol. Ecol. Resour.* 17, e46–e62. doi: 10.1111/1755-0998.12689

Niemeyer, B., Klemm, J., Pestryakova, L. A., and Herzschuh, U. (2015). Relative pollen productivity estimates for common taxa of the northern Siberian Arctic. *Rev. Palaeobot. Palynol.* 221, 71–82. doi: 10.1016/j.revpalbo.2015.06.008

Noaa National Centers for Environmental Information (2001). *Global Surface Hourly Dataset*. Available online at: https://data.noaa.gov/dataset/dataset/integrated-surface-dataset-global (accessed April 9, 2021).

Oksanen, J., Blanchet, F. G., Friendly, M., Kindt, R., Legendre, P., McGlinn, D., et al. (2019). *vegan: Community Ecology Package*. Available online at: https://CRAN.R-project.org/package=vegan (accessed August 3, 2020).

Overduin, P. P., Blender, F., Bolshiyanov, D. Y., Grigoriev, M. N., Morgenstern, A., and Meyer, H. (2017). *Russian-German Cooperation: Expeditions to Siberia in 2016*. Bremerhaven: Alfred-Wegener-Institut, Helmholtz-Zentrum für Polar- und Meeresforschung. doi: 10.2312/BzPM_0709_2017

Overpeck, J. T., Webb, T., and Prentice, I. C. (1985). Quantitative interpretation of fossil pollen spectra: dissimilarity coefficients and the method of modern analogs. *Quat. Res.* 23, 87–108. doi: 10.1016/0033-5894(85)90074-2

Parsons, R. W., and Prentice, I. C. (1981). Statistical approaches to R-values and the pollen— vegetation relationship. *Rev. Palaeobot. Palynol.* 32, 127–152. doi: 10.1016/0034-6667(81)90001-4

Pedregosa, F., Varoquaux, G., Gramfort, A., Michel, V., Thirion, B., Grisel, O., et al. (2011). Scikit-learn: machine learning in Python. *J. Mach. Learn. Res.* 12, 2825–2830. doi: 10.1080/13696998.2019.1666854

Pelánková, B., and Chytrý, M. (2009). Surface pollen–vegetation relationships in the forest-steppe, taiga and tundra landscapes of the Russian Altai Mountains. *Rev. Palaeobot. Palynol.* 157, 253–265. doi: 10.1016/j.revpalbo.2009.05.005

Pelánková, B., Kuneš, P., Chytrý, M., Jankovská, V., Ermakov, N., and Svobodová-Svitavská, H. (2008). The relationships of modern pollen spectra to vegetation and climate along a steppe–forest–tundra transition in southern Siberia, explored by decision trees. *Holocene* 18, 1259–1271. doi: 10.1177/0959683608096600

Peres-Neto, P. R., and Jackson, D. A. (2001). How well do multivariate data sets match? The advantages of a Procrustean superimposition approach over the Mantel test. *Oecologia* 129, 169–178. doi: 10.1007/s004420100720

Pisaric, M. F. J., MacDonald, G. M., Cwynar, L. C., and Velichko, A. A. (2001). Modern pollen and conifer stomates from North-central Siberian Lake sediments: their use in interpreting late quaternary fossil pollen assemblages. *Arct. Antarct. Alp. Res.* 33, 19–27. doi: 10.1080/15230430.2001.12003400

Prentice, I. C. (1985). Pollen representation, source area, and basin size: toward a unified theory of pollen analysis. *Quat. Res.* 23, 76–86. doi: 10.1016/0033-5894(85)90073-0

Prentice, I. C., and Parsons, R. W. (1983). Maximum likelihood linear calibration of pollen spectra in terms of forest composition. *Biometrics* 39, 1051–1057. doi: 10.2307/2531338

Qin, F., Bunting, M. J., Zhao, Y., Li, Q., Cui, Q., and Ren, W. (2020). Relative pollen productivity estimates for alpine meadow vegetation, northeastern Tibetan Plateau. *Veg. Hist. Archaeobotany* 29, 447–462. doi: 10.1007/s00334-019-00751-4

R Core Team (2019). *R: A Language and Environment for Statistical Computing*. Vienna: R Foundation for Statistical Computing.

Räsänen, S., Suutari, H., and Nielsen, A. B. (2007). A step further towards quantitative reconstruction of past vegetation in Fennoscandian boreal forests: pollen productivity estimates for six dominant taxa. *Rev. Palaeobot. Palynol.* 146, 208–220. doi: 10.1016/j.revpalbo.2007.04.004

Reille, M. (1992). *Pollen et Spores d'Europe et d'Afrique du Nord (Pollen and Spores of Europe and North Africa)*. Marseille: Laboratoire de Botanique Historique et Palynologie.

Reille, M. (1995). *Pollen et Spores d'Europe et d'Afrique du Nord, Supplément 1*. Marseille: Laboratoire de Botanique Historique et Palynologie.

Reille, M. (1998). *Pollen et Spores d'Europe et d'Afrique du Nord, Supplément 2*. Marseille: Laboratoire de Botanique Historique et Palynologie.

Safronova, I., and Yurkovsksya, T. (2019). "The latitudinal distribution of vegetation cover in Siberia," in *Results and Prospects of Geobotanical Research in Siberia, Dedicated to the 75th Anniversary of the Laboratory of Ecology and Geobotany of Csbg Sb Ras 2019*, eds N. N. Lashinsky and N. I. Makunina (Les Ulis: E D P Sciences).

Semeniuk, C. A., Milne, L., Ladd, P., and Semeniuk, V. (2006). Pollen in the surface sediments of wetlands in the Becher Point area, southwestern Australia: a baseline for use in interpreting Holocene sequences. *J. R. Soc. West. Aust.* 89, 27–43.

Stockmarr, J. (1971). Tablets with spores used in absolute pollen analysis. *Pollen Spores* 13, 615–621.

Stone, T. A., and Schlesinger, P. (2004). *RLC Vegetative Cover of the Former Soviet Union, 1990*. Oak Ridge: ORNL DAAC.

Sugita, S. (1993). A model of pollen source area for an entire Lake Surface. *Quat. Res.* 39, 239–244. doi: 10.1006/qres.1993.1027

Sugita, S. (1994). Pollen representation of vegetation in quaternary sediments: theory and method in patchy vegetation. *J. Ecol.* 82, 881–897. doi: 10.2307/2261452

Sugita, S. (2007a). Theory of quantitative reconstruction of vegetation I: pollen from large sites REVEALS regional vegetation composition. *Holocene* 17, 229–241. doi: 10.1177/0959683607075837

Sugita, S. (2007b). Theory of quantitative reconstruction of vegetation II: all you need is LOVE. *Holocene* 17, 243–257. doi: 10.1177/0959683607075838

Sugita, S., Gaillard, M.-J., and Broström, A. (1999). Landscape openness and pollen records: a simulation approach. *Holocene* 9, 409–421. doi: 10.1191/095968399666429937

Sun, J., Ma, C., Cao, X., Zhao, Y., Deng, Y., Zhao, L., et al. (2019). Quantitative precipitation reconstruction in the east-central monsoonal China since the late glacial period. *Quat. Int.* 521, 175–184. doi: 10.1016/j.quaint.2019.05.033

Tarasov, P., Williams, J. W., Andreev, A., Nakagawa, T., Bezrukova, E., Herzschuh, U., et al. (2007). Satellite- and pollen-based quantitative woody cover reconstructions for northern Asia: verification and application to late-Quaternary pollen data. *Earth Planet. Sci. Lett.* 264, 284–298. doi: 10.1016/j.epsl.2007.10.007

Tarasov, P. E., Andreev, A. A., Anderson, P. M., Lozhkin, A. V., Leipe, C., Haltia, E., et al. (2013). A pollen-based biome reconstruction over the last 3.562 million years in the Far East Russian Arctic – new insights into climate–vegetation relationships at the regional scale. *Clim. Past* 9, 2759–2775. doi: 10.5194/cp-9-2759-2013

Tarasov, P. E., Nakagawa, T., Demske, D., Österle, H., Igarashi, Y., Kitagawa, J., et al. (2011). Progress in the reconstruction of Quaternary climate dynamics

in the Northwest Pacific: a new modern analogue reference dataset and its application to the 430-kyr pollen record from Lake Biwa. *Earth Sci. Rev.* 108, 64–79. doi: 10.1016/j.earscirev.2011.06.002

Ter Braak, C. J. F., and Prentice, I. C. (1988). "A theory of gradient analysis," in *Advances in Ecological Research*, eds M. Begon, A. H. Fitter, E. D. Ford, and A. Macfadyen (Cambridge, MA: Academic Press), 271–317.

Theuerkauf, M., Kuparinen, A., and Joosten, H. (2013). Pollen productivity estimates strongly depend on assumed pollen dispersal. *Holocene* 23, 14–24.

Tufto, J., Engen, S., and Hindar, K. (1997). Stochastic dispersal processes in plant populations. *Theor. Popul. Biol.* 52, 16–26. doi: 10.1006/tpbi.1997.1306

Twiddle, C. L., Jones, R. T., Caseldine, C. J., and Sugita, S. (2012). Pollen productivity estimates for a pine woodland in eastern Scotland: the influence of sampling design and vegetation patterning. *Rev. Palaeobot. Palynol.* 174, 67–78. doi: 10.1016/j.revpalbo.2011.12.006

van Geffen, F., Geng, R., Pflug, B., Kruse, S., Pestryakova, L. A., Herzschuh, U., et al. (2021a). *SiDroForest: Sentinel-2 Level-2 Bottom of Atmosphere Labelled Image Patches with Seasonal Information for Central Yakutia and Chukotka Vegetation Plots (Siberia, Russia)*. Available online at: https://doi.pangaea.de/10.1594/PANGAEA.933268 (accessed July 19, 2021).

van Geffen, F., Heim, B., Brieger, F., Geng, R., Shevtsova, I. A., Schulte, L., et al. (2021b). SiDroForest: a comprehensive forest inventory of Siberian boreal forest investigations including drone-based point clouds, individually labelled trees, synthetically generated tree crowns and Sentinel-2 labelled image patches. *Earth Syst. Sci. Data Discuss.* [Epub ahead of print]. doi: 10.5194/essd-2021-281

Wang, F. (1995). *Pollen Flora of China*. Beijing: Science Press.

Wilmshurst, J. M., and McGlone, M. S. (2005). Origin of pollen and spores in surface lake sediments: comparison of modern palynomorph assemblages in moss cushions, surface soils and surface lake sediments. *Rev. Palaeobot. Palynol.* 136, 1–15. doi: 10.1016/j.revpalbo.2005.03.007

Zhang, P., Xu, Q., Gaillard, M.-J., Mu, H., Zhang, Y., and Lu, J. (2017). Research of main plant species's relative pollen productivities and relevant source area of temperate coniferous and broad-leaved mixed forest in Northern China. *Quat. Sci.* 6, 1429–1443.

Zhang, Y., Duo, L., Pang, Y.-Z., Felde, V. A., Birks, H. H., and Birks, H. J. B. (2018). Modern pollen assemblages and their relationships to vegetation and climate in the Lhasa Valley, Tibetan Plateau, China. *Quat. Int.* 467, 210–221. doi: 10.1016/j.quaint.2018.01.040

Zhao, Y., Xu, Q., Huang, X., Guo, X., and Tao, S. (2009). Differences of modern pollen assemblages from lake sediments and surface soils in arid and semi-arid China and their significance for pollen-based quantitative climate reconstruction. *Rev. Palaeobot. Palynol.* 156, 519–524. doi: 10.1016/j.revpalbo.2009.05.001

Conflict of Interest: The authors declare that the research was conducted in the absence of any commercial or financial relationships that could be construed as a potential conflict of interest.

frontiers | Frontiers in Ecology and Evolution

TYPE Original Research
PUBLISHED 04 November 2022
DOI 10.3389/fevo.2022.1050429

OPEN ACCESS

EDITED BY
Xiaofeng Cao,
Tsinghua University, China

REVIEWED BY
Shailesh Agrawal,
Birbal Sahni Institute of Palaeosciences (BSIP), India
Mingkun Li,
South China Normal University, China

*CORRESPONDENCE
Chunmei Ma
chunmeima@nju.edu.cn

SPECIALTY SECTION
This article was submitted to Paleoecology, a section of the journal Frontiers in Ecology and Evolution

RECEIVED 21 September 2022
ACCEPTED 17 October 2022
PUBLISHED 04 November 2022

CITATION
Huang M, Deng Y, Peng H, Wen Z, Shang G, Guan H and Ma C (2022) Hydroclimatic changes since the Last Glacial Maximum recorded in mountain peat deposit on the southwestern margin of the Sichuan Basin, China. *Front. Ecol. Evol.* 10:1050429. doi: 10.3389/fevo.2022.1050429

Hydroclimatic changes since the Last Glacial Maximum recorded in mountain peat deposit on the southwestern margin of the Sichuan Basin, China

Ming Huang[1,2], Yunkai Deng[1,3], Haijun Peng[4,5], Zhenming Wen[1], Guangchun Shang[1], Houchun Guan[6] and Chunmei Ma[1,7]*

[1]School of Geography and Ocean Science, Nanjing University, Nanjing, China, [2]Chengdu Institute of Cultural Relics and Archaeology, Chengdu, China, [3]Key Laboratory of Cenozoic Geology and Environment, Institute of Geology and Geophysics, Chinese Academy of Sciences, Beijing, China, [4]State Key Laboratory of Environmental Geochemistry, Institute of Geochemistry, Chinese Academy of Sciences, Guiyang, China, [5]CAS Center for Excellence in Quaternary Science and Global Change, Xi'an, China, [6]Geological Survey of Anhui Province, Hefei, China, [7]Jiangsu Collaborative Innovation Center for Climate Change, Nanjing, China

Knowledge of the hydroclimatic changes in Southwest China since the Last Glacial Maximum (LGM) is crucial for disentangling the long-term evolution of the Asia Monsoon and predicting the future fate of the mountain peat deposit in the Asia Monsoon region. In this study, we obtained a 530-cm-long peat core from the Ganchi wetland in Southwest China and analyzed its geochemical indices, including total nitrogen (TN), total organic carbon (TOC), stable carbon isotope composition of organics (δ^{13}Corg), and the concentration of several major elements, to investigate the sedimentary and hydroclimate evolution since the LGM. We found that the peat strata in the Ganchi wetland have developed gradually from 13.7 cal kyr BP, which is likely ascribed to the warm climate during the Bølling-Allerød (B/A) period. TOC, δ^{13}Corg, K/Ti, and Fe/Mn records showed notable paleoclimate shifts since the last deglaciation. The first warming period after the LGM was observed starting at 18.2 cal kyr BP, which is consistent with other records from Southwest China. The reconstruction results show that the western margin of the Sichuan Basin during the last deglaciation was most affected by the East Asia summer monsoon (EASM), and less affected by the Indian summer monsoon (ISM). The climate of the early Holocene (11.2–7.5 cal kyr BP) was

affected by both the ISM and EASM, resulting in more complex local climatic features. The Holocene Megathermal period observed from 7.5 to 3.5 cal kyr BP, is consistent with the timing detected in other records of Southwest China.

KEYWORDS

Last Glacial Maximum, Southwest China, hydroclimate, Indian summer monsoon, peat record

Introduction

Southwest China is one of the most susceptible areas to climate changes owing to its diverse geomorphology that is adjacent to the Qinghai-Tibetan Plateau (QTP) and influenced by the East Asia summer monsoon (EASM) and the Indian summer monsoon (ISM) (Zhang, 1988; Zheng and Li, 1990; Zhang et al., 2015b; Liu, 2016). The climate of Southwest China, being superimposed by a series of abrupt warming/cooling events at a millennial to centennial timescale, has undergone long-term warming since the Last Glacial Maximum (LGM) (Alley and Clark, 1999; Shakun and Carlson, 2010). Many studies have focused on exploring the duration and mechanisms of warm and cold changes since LGM (Clark et al., 2009; Denton et al., 2010). However, the mechanism of abrupt climate changes in Southwest China since the LGM remains poorly explored due to the low number of geological archives. For instance, it is still debated whether Heinrich 1 (H1), Bøllinge-Allerød (B/A), and Younger Dryas (YD) events have been adequately detected in the paleoclimatic records in Southwest China (Shen and Xiao, 2018). Thus, more archives that cover the LGM from Southwest China are desired for a better understanding of the long-term hydroclimatic changes and driving mechanisms in this region.

Sichuan Basin in Southwest China, located on the southwestern margin of the QTP and adjacent to the Yunnan-Guizhou Plateau, has a population of over 100 million and was the cradle of many ancient Chinese civilizations such as the Sanxingdui culture and the Baodun culture (Huo, 2022). However, most of the paleoclimate reconstructions in Southwest China are concentrated in the Yunnan-Guizhou Plateau. While the majority of these researches were based on lake sediments (Cook et al., 2012; Wang et al., 2014; Xiao et al., 2014a; Wu et al., 2015; Zhang et al., 2015a; Zhang et al., 2017, 2018) and cave stalagmites (Dykoski et al., 2005), studies on peat core records are still minimum (Zhu et al., 2010; Gong et al., 2019; Liu et al., 2022). Besides, most of these researches only cover the last deglaciation or Holocene period, and studies on the LGM are relatively scarce (Devry, 1993; Hong et al., 2014; Peng et al., 2021). The relationship between monsoon evolution and paleoclimatic variability since the LGM in this area is still unclear both temporally and spatially.

Organic matter in peat is mainly derived from the continuous and stable stratigraphic accumulation of local plant residues. Since the vegetation combination varies in response to climate variability, it is thus expected that the development of peatland and its succession processes have recorded changes in the surrounding environment, regional climate, and dominant vegetation (Blackford, 2000; Chambers and Charman, 2004; Xu et al., 2006; Zhao et al., 2011, 2016; Chambers et al., 2012; Zhou et al., 2002). Alpine peat and lake sediment records in the southwest Sichuan Basin have shown several abrupt changes that may associate with the climate changes in the high northern latitudes (Hong et al., 2014; Peng et al., 2021). However, the locations of these records are a bit far away from the Sichuan Basin and are often affected by the local climate of Hengduan Mountain. To investigate the complexity of the climate in the Sichuan Basin since the LGM, more archives that are adjacent to or within the Sichuan basin are needed. Here we present a study of the stable carbon isotope composition of organics (δ^{13}Corg), total nitrogen (TN), total organic carbon (TOC), and element geochemistry of a 26,200 years old peat archive from Dawa Mountain, which is located at the west margin of Sichuan Basin. The objectives of this study are (1) to investigate the environmental evolution of peatland near the Sichuan Basin since the LGM, (2) to reconstruct the LGM hydroclimate of the Sichuan Basin, and (3) to explore the links between abrupt environmental/climate changes and historical civilizations in Southwest China.

Materials and methods

Coring and sampling

Dawa Mountain, located in the southern part of Sichuan Province, China, is situated in the transition zone between the southwest margin of the Sichuan Basin and the Yunnan-Guizhou Plateau. The landform of this region is dominated by scattered karst landforms, such as karst basins and corrosion lakes. The Dawa Mountain region has gentle topographical relief and is not significantly affected by runoff erosion (Luo, 2003; Wang and Chen, 2014). The Ganchi wetland (29°23′ 69The Gan°1′ 54The Ganchi wet1,805 m) was formed due to this

topography and its high precipitation. The peat strata in Ganchi of Dawa Mountain was formed by the paludification of karst wetland, with no riverine input from its surrounding (**Figure 1**).

A 530-cm-long peat core (GC) was collected from the middle of Ganchi wetland using a Russian peat corer. The 50-cm long peat cores were packaged into PVC tubes and transported to the laboratory. These peat cores were sliced into 1-cm intervals, resulting in a total of 530 samples. The strata were divided into five layers based on the sedimentary characteristics: (1) 0–10 cm: dark- brown peat topsoil with abundant grass roots; (2) 10–230 cm: dark-brown peat containing a large number of undecomposed plant roots; (3) 230–380 cm: dark-gray peat with a small number of plant roots; (4) 380–505 cm: gray-black peat mixed with clay; (5) 505–530 cm: Light gray clay mixed with sand and gravel (the bottom of this layer was close to the bedrock).

Methods

Dating

Both plant fragments and pollen residues were extracted from the peat samples for radiocarbon dating. A total of 14 samples were selected from different depths of the GC core for AMS^{14}C dating based on the stratum lithology. Eleven and three samples were tested at the Xi'an Accelerator Mass Spectrometry Center, Institute of Earth Environment, Chinese Academy of Sciences, and Beta analytic Inc., respectively. The age data was then calibrated to calendar ages using Calib7.0.4 (Reimer et al., 2013). The winbacon2.2 R package (Blaauw and Christen, 2011) based on the Bayes formula was used to establish an accurate and complete age-depth model for the GC core and to calculate the deposition rate (**Figure 2**).

Elemental geochemistry

After being transported to the lab, the GC core was first tested using the non-destructive X-ray fluorescence (XRF) core scanning technic, which is a widely used in stratigraphic comparison and paleoclimate research across different depositional environments (Haug et al., 2001; Kido et al., 2006; Cuven et al., 2010; Cheng et al., 2011; Hennekam and de Lange, 2012; Liang et al., 2012; Peros et al., 2017). Major element compositions in the GC core were measured by an Avaa-tech system in the Key Laboratory of Surficial Geochemistry, Ministry of Education, Nanjing University. During the analysis, scanning voltages of 10 KV and 30 KV were selected at a resolution of 1 cm, and the samples were scanned for 10 s to obtain the counts of Ti, K, Si, Al, Fe, Mn, Sr, Zr, Ca, S, and Cl. The elemental concentration results were considered semi-quantitative due to the influence of core water content, grain size, cracks, and surface flatness on the X-ray (Weltje and Tjallingii, 2008).

Total organic carbon, total nitrogen, and $\delta^{13}C_{org}$ analysis

A total of 265 samples were selected at 2-cm intervals for the TOC, TN, and $\delta^{13}C_{org}$ analysis. The pretreatment and measuring were conducted in the Key Laboratory of Surficial Geochemistry, Ministry of Education, Nanjing University. The selected samples were firstly oven-dried, and then grounded and sieved using an 80-mesh sieve. The samples were then treated with 10% HCl for 24 h to remove carbonates. Subsequently, the samples were washed with distilled water to achieve neutrality and dried at low temperature. For TOC and TN measurements, 50 mg of the pre-treated samples were weighed and then tightly wrapped in tin foil and then loaded into the VarioMacro-CHNS elemental analyzer. Phenylalanine was used as the standard sample, and a national standard (GBW04408) was analyzed after 5 samples for quality control of the instrument. The instrument had an analytical accuracy of 0.5%. The ratio of TOC to TN (C/N) was calculated based on the contents of TOC and TN. $\delta^{13}C_{org}$ was determined using a Picarro laser spectrum carbon isotope analyzer (G2131-i). The carbon isotope results are expressed as the per mil (‰) deviation from Vienna Pee Dee Belemnite (VPDB), with a precision of less than 0.3%.

Results

Chronology and sedimentation rate

The AMS^{14}C data of the GC core are shown in **Table 1**, and the age-depth model and sedimentation rate are shown in **Figure 2**. The sedimentation rate of the GC core varied greatly at different depths. The average sedimentation rate of the whole core was 27 cm/kyr. The maximum deposition rate (average of 48 cm/kyr) occurred at 107–226 cm depth, and the minimum deposition rate (average of 8.9 cm/kyr) occurred at 282–365 cm depth. Overall, the sedimentation rate varied significantly during the Holocene, but showed little variability from the LGM to the Holocene.

Scanning X-ray fluorescence results

As shown in **Figure 3**, the variation trends in Al, Ti, and Fe concentrations were similar, while the trends of Si and Mn showed low variability. The changes in these elements and the Al/Si ratio can be divided into three stages. The first stage is the LGM (26.2–18.2 cal kyr BP, 530–372 cm), which can be divided into two sub-stages: Stage I-1 (26.2–25.2 cal kyr BP, 530–505 cm) and Stage I-2 (25.2–18.2 cal kyr BP, 505–372 cm). In Stage I-1, all indexes fluctuated sharply, and in stage I-2, Al, Ti, Mn, and Cl are relatively stable, while other elements and ratios fluctuated slightly. In stage II (18.2–11.2 cal kyr BP, 372–310 cm), Si and Mn remained stable, the strength

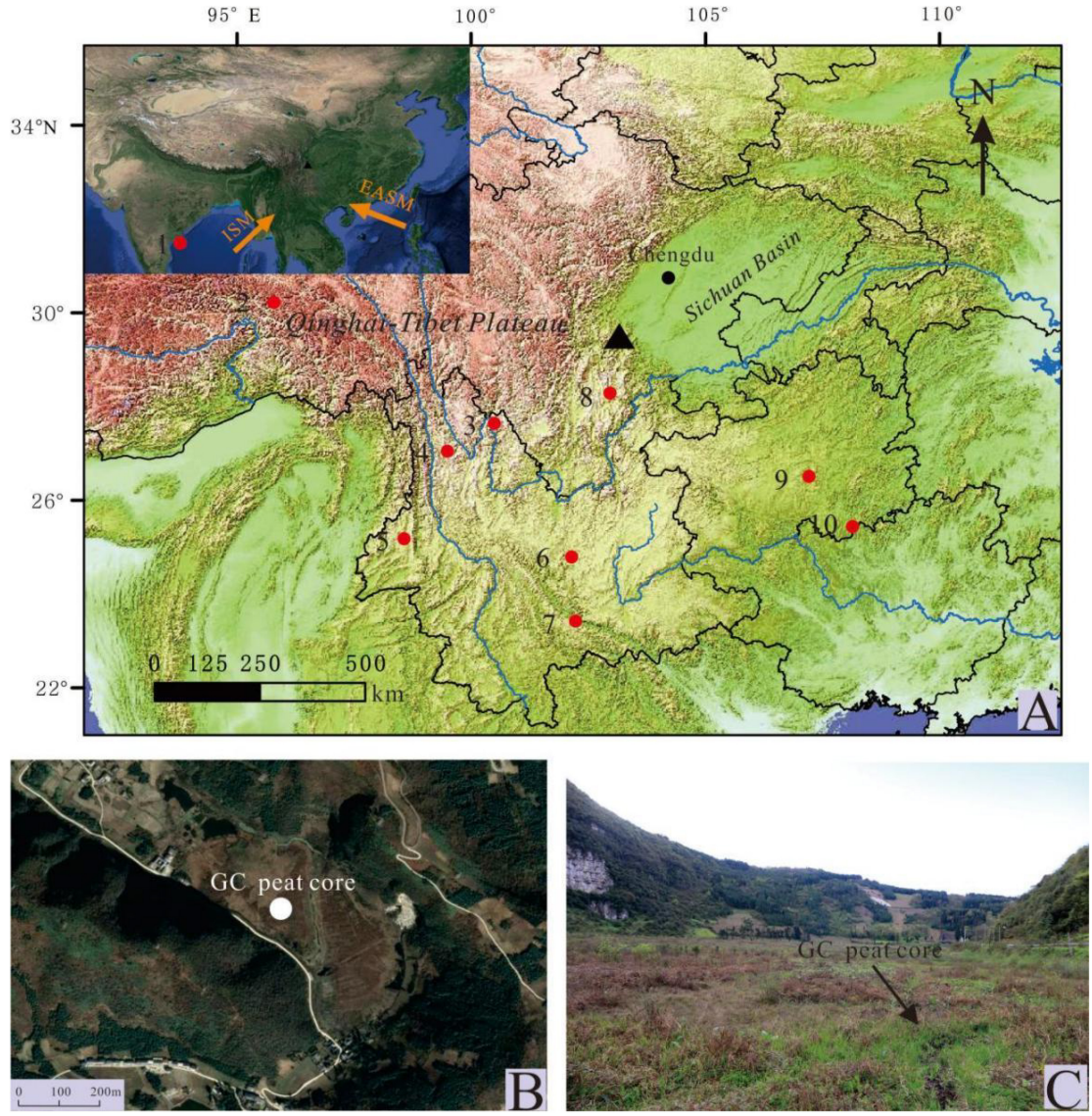

FIGURE 1
Locations of the research area and the related research sites. **(A)** Map of the research area indicating the location of the peat site (black triangle) at the intersection between the Sichuan Basin, Yunnan-Guizhou Plateau, and QTP. The red circles indicate the location of related research sites cited in this study: (1) Core SK218 in the Indian Ocean (Govil and Divakar Naidu, 2011); (2) core NC08/01 in Nam Co Lake on the QTP (Zhu et al., 2015); (3) core LG08 in Lugu Lake, Yunnan Province (Zhang et al., 2018); (4) core TCYL1 in Tiancai Lake, Yunnan Province (Xiao et al., 2014b); (5) core TCK1 in Qinghai Lake, Tengchong County, Yunnan Province (Xiao et al., 2015); (6) core XY08A in Xingyun Lake, Yunnan Province (Wu et al., 2015); (7) core from Yilong Lake, Yunnan Province (Li et al., 2018); (8) Baoan peat core in Sichuan Province (Hong et al., 2018); (9) peat borehole NT03 in Caohai, Guizhou Province (Gong et al., 2019); and (10) stalagmites in Dongge Cave, Guizhou Province (Dykoski et al., 2005). **(B)** Aerial photo of the Ganchi wetland with the location of the GC core shown as a solid white circle; and **(C)** a physical picture shows the geomorphic environment around the sampling site.

of other elements was significantly enhanced, and the Si/Al value gradually increased. In stage III (since 11.2 cal kyr BP, 310–0 cm), the element strength remained relatively stable, but showed great fluctuations at time nodes such as 9.0 kyr BP and 6.0 kyr BP. The Si/Al ratio reaches the maximum value of the profile at this stage.

The correlations between the analyzed elements are shown in Table 2. The correlations between Zr, Sr, Si, Fe, K, Ti, Mn, and Al were generally high, and the correlation coefficients of Zr, Sr, Si, Fe, K, and Ti are above 0.6. While S, Cl, and Ca showed low correlation with other elements, Cl was the only element that negatively correlated with the other elements. The factor analysis results identified three principal components controlling the deposition of chemical elements, with a cumulative contribution rate of 83.5% to the total variance (Figure 4). Factor 1 contributed 57.0% to the total

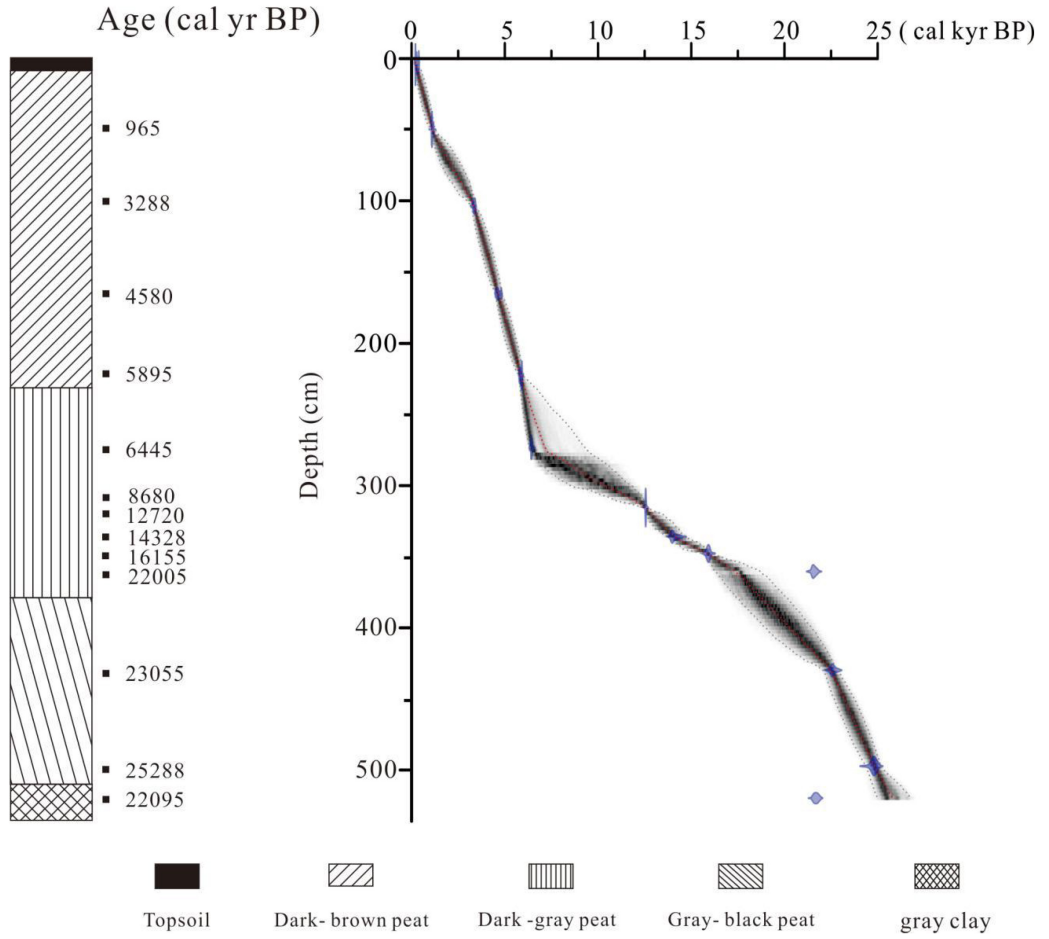

FIGURE 2
Stratigraphy and age-depth model of the GC core.

TABLE 1 AMS^{14}C dating results of the GC core.

Lab. code	Depth(cm)	Materials	^{14}C data (a BP)	Error (±a)	Calibrated age (cal a BP, 2σ)	Mid-point (cal a BP)
XA19958	1	Plant fragments	65	20	–	–
XA19949	49	Plant fragments	1,060	25	930–1,000	965
XA19959	104	Plant fragments	3,070	30	3,210–3,365	3,288
XA19960	167	Plant fragments	4,080	35	4,510–4,650	4,580
XA19961	226	Plant fragments	5,125	30	5,860–5,930	5,895
XA19950	278	Plant fragments	5,655	30	6,390–6,500	6,445
Beta-565627	314	Pollen residue	7,870	30	8,589–8,770	8,680
XA19951	321	Plant fragments	10,820	40	12,680–12,760	12,720
Beta-565624	342	Pollen residue	12,290	60	14,029–14,626	14,328
Beta-565625	354	Pollen residue	13,430	40	15,983–16,324	16,155
XA19952	367	Plant fragments	18,130	65	21,780–22,230	22,005
XA19962	438	Plant fragments	19,105	70	22,770–23,340	23,055
XA19947	507	Plant fragments	20,940	100	25,000–25,575	25,288
XA19948	530	Plant fragments	18,230	75	21,860–22,330	22,095

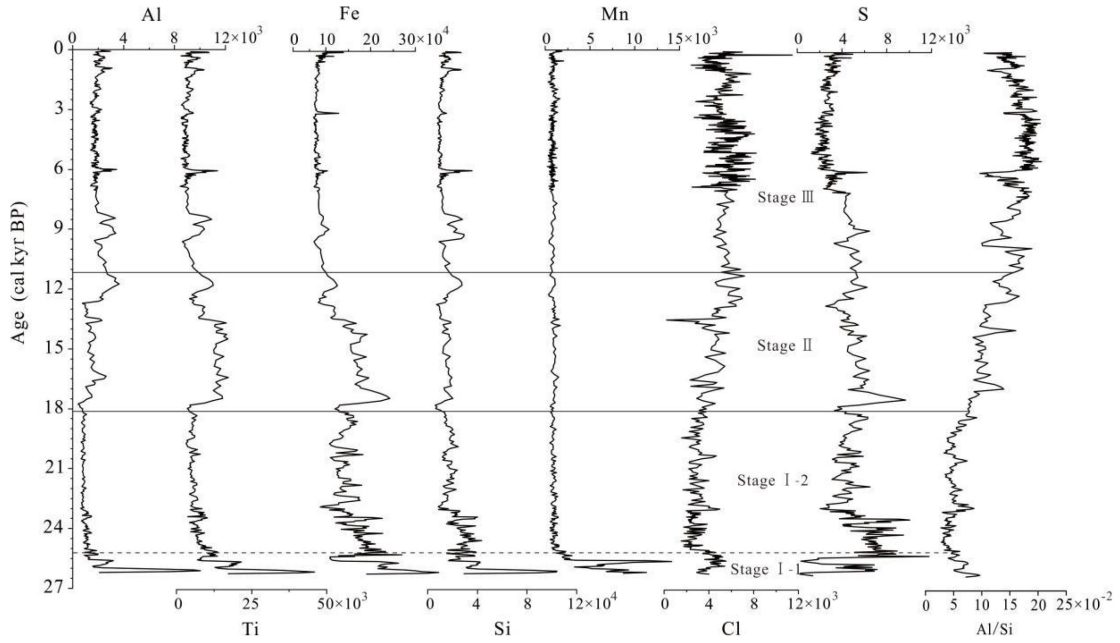

FIGURE 3
Scanning intensity and chromaticity curves of elements from the GC core.

TABLE 2 Correlation coefficients between elements in the GC core.

	Sr	Zr	Al	Si	S	Cl	K	Ca	Ti	Mn	Fe
Sr	1										
Zr	0.900**	1									
Al	0.171**	0.374**	1								
Si	0.612**	0.680**	0.524**	1							
S	0.476**	0.288**	−0.245**	0.399**	1						
Cl	−0.428**	−0.364**	0.248**	−0.372**	−0.364**	1					
K	0.702**	0.821**	0.611**	0.864**	0.143**	−0.277**	1				
Ca	0.512**	0.518**	0.133**	0.374**	0.047	−0.310**	0.526**	1			
Ti	0.836**	0.866**	0.533**	0.804**	0.350**	−0.262**	0.902**	0.396**	1		
Mn	0.497**	0.654**	0.469**	0.636**	−0.014	−0.134**	0.804**	0.494**	0.679**	1	
Fe	0.775**	0.699**	0.073	0.765**	0.682**	−0.474**	0.718**	0.316**	0.805**	0.541**	1

**Significantly correlated at 0.01 level (bilaterally).

variance and was therefore the main influencing factor in the GC core. Factor 2 and Factor 3 contributed 17.4 and 9.1% to the total variance, respectively. S and Fe had a high common factor load in Factor 2, while Ca and Cl had a high common factor load in Factor 3.

Total organic carbon, total nitrogen, and δ^{13}Corg

The GC record can be divided into the same three stages as Figure 3 based on the various characteristics of TOC, TN, C/N, and δ^{13}Corg (Figure 5). In Stage I-1 (26.2–25.2 cal kyr BP, 530–505 cm), the indicators fluctuated sharply, with average TN and TOC values being 0.3 and 4.2%, respectively. The average values of C/N and δ^{13}Corg were 22.7 and –18.6‰, respectively, which were the maximum values in the core. At Stage I-2 (25.2–18.2 cal kyr BP, 505–372 cm), TN was relatively stable, with an average value of 1.1%. TOC and C/N values showed an increasing trend but remained relatively low, with average values of 15.1% and 13.8, respectively. In addition, δ^{13}Corg showed an increasing trend throughout the entire stage, with an average value of –23.4‰.

Stage II represents the last deglaciation (18.2–11.2 cal kyr BP, 372–310 cm), during which the TN, TOC, and C/N values showed an overall increasing trend with average values of 1.3%,

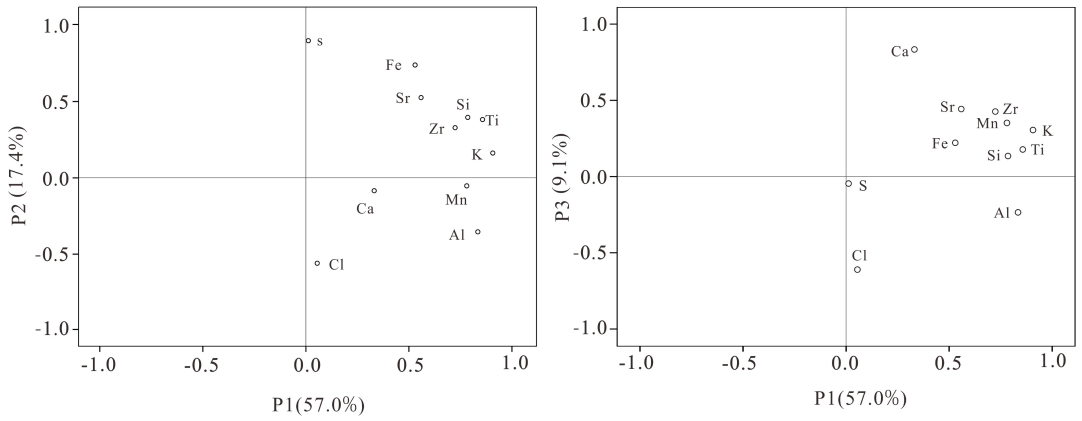

FIGURE 4
Factor analysis component loads of elements in the GC core.

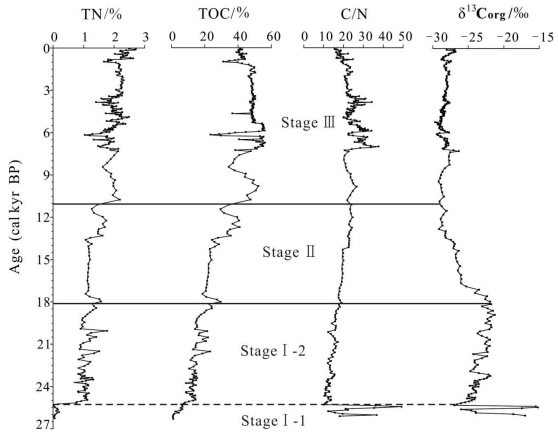

FIGURE 5
δ^{13}Corg, TN, TOC, and C/N curves in the GC core.

28.7%, and 21.1, respectively. The δ^{13}Corg values were generally more negative with an average value of –27‰.

Stage III was the Holocene (since 11.2 cal kyr BP, 310–0 cm), during which the average values of TN, TOC, and C/N were 2%, 47%, and 23.7, respectively; the δ^{13}Corg values were more negative, with an average value of –28.4‰.

Discussion

Sediment and organic matter sources

Lake and wetland sediments have two dominant sources: (1) Exogenous components via erosion in the basin, and (2) endogenous precipitation produced by chemical and biological processes in the lake (Hakanson and Jansson, 2002; Shen, 2013). The correlation between elements is controlled by their geochemical behavior in the supergene environment. The source of substances can therefore be distinguished by the correlation between different elements, where a high correlation indicates similar occurrence conditions and sources of elements (Loring and Asmund, 1996; Ma et al., 2014). Factor analysis can also determine the source and contribution of geochemical elements in the sediments (Lawrence and Upchurch, 1982; Yang and Li, 1999; Zhang et al., 2015c). The loading values of, Al, Mn, Si, K, Ti, and Zr in Factor 1 in the GC core were relatively high, which is consistent with the results of the correlation analysis (**Figure 4**). These elements are rock-forming elements that are mostly transported and deposited in lakes by runoff in the form of terrigenous debris (Cheng et al., 2011; Wu et al., 2011). Therefore, exogenous detritus was likely the main source of the GC core sediments.

TOC generally indicates the level of organic matter in wetland sediments. Moreover, TOC can indicate the productivity of wetlands and their preservation ability in sediments (Meyers and Lallier-Vergès, 1999). TOC sources can be divided into exogenous terrestrial plants and endogenous aquatic plants, which can be roughly determined by the C/N ratio. C/N ratio that is smaller than 10 suggests that organic matter was mainly derived from algae and planktonic organisms and submerged and emergent plants in lakes (Meyers, 1997; Meyers and Lallier-Vergès, 1999); A C/N ratio greater than 20 suggests that the main organic matter source was terrestrial higher plants (Meyers, 1994; Talbot and Laerdal, 2000; Lamb et al., 2006; Morrill et al., 2006; Díaz et al., 2017). Our record higher than 20 for most samples shows that terrestrial higher plants are the dominant source of TOC in the Ganchi wetland.

Different plants exhibit different δ^{13}Corg values. For example, C3 plants exhibit a δ^{13}Corg value between –32 and –20‰, with the highest frequency being –27‰; meanwhile, C4 plants exhibit a δ^{13}Corg value between –15 and –9‰, with the highest frequency being –13‰ (O'Leary, 1981, 1988;

Zhou et al., 2016). The δ^{13}Corg values of submerged plants range from –20 to –12‰, with an average of –15%, which is close to the average δ^{13}Corg value of C4 plants (–14‰). Finally, the δ^{13}Corg values of emergent plants are between –30 and –24‰ (Lei et al., 2014). The δ^{13}Corg value in sediments is therefore sensitive to the changes in organic matter sources and vegetation.

The δ^{13}Corg value during the LGM Stage 1–1 (26.2–25.2 cal kyr BP) was relatively higher values (average value of –18.6‰, **Figure 6**), inferring the dominance of submerged plants. The δ^{13}Corg values of the other stages were relatively more negative (average value of –28.1‰), which is consistent with the sediment isotope values in Caohai (Gong et al., 2019) and Lugu Lake (Zhang et al., 2018). The vegetation features in these areas are dominated by C3 plants, which suggests that the vegetation in Ganchi expands to C3 plants after 25.2 cal kyr BP. The average C/N of the GC core was > 10, especially after ∼13.7 cal kyr BP (∼23.6), which suggests that terrestrial plants were the dominant source of sedimentary organic matter. This also indicates the transition from a lake to a swamp environment in Ganchi after 13.7 cal kyr BP.

The above findings are in good agreement with the results of the major element concentrations. After ∼13.7 cal kyr BP, the intensity of Ti, Zr, and other elements related to exogenous output in Factor 1 gradually decreased (**Figure 3**). Due to the difference in the redox conditions between Fe and Mn, the Fe/Mn ratio can be used to evaluate the redox conditions of sediments. A higher Fe/Mn value indicates an unfavorable redox environment for oxidation, reflecting a deeper water environment. In contrast, a lower value indicates oxidation environments of shallower water levels (Wersin et al., 1991; Meng et al., 2018). We observed a high Fe/Mn ratio before 13.7 cal kyr BP (**Figure 6**), which then decreased sharply, reflecting a significant decline in the water level at approximately 13.7 cal kyr BP. Ti is a representative element of exogenous clastic sediments. The strength of the Ti element also began to decrease significantly during this stage (**Figure 3**), which may be ascribed to the decreased contribution of exogenous clastic sediments after the drying of the lake basin.

As Ganchi has a relatively closed topography without any notable river input, the presence of exogenous clastic sediments in the GC core was likely caused by the fluctuation of the lake water level, which transported exogenous clastic sediments to the coring site. After gradual paludification, the exogenous clastic sediments were likely transported to Ganchi by temporary sheet flow or surface runoff.

Response of total organic carbon and δ^{13}Corg to paleoclimatic changes

In the monsoon climate region, climate changes significantly influence the formation and development of peat. Previous studies have shown that the monsoon and sunlight are important factors affecting the expansion of peatlands in the Hengduan Mountains (Liu et al., 2020), and the humid monsoon climate is also conducive to peatland expansion (Xing et al., 2015). TOC content in peatland sediments is closely related to the accumulation of organic matter, which can reflect the development of peatlands. The TOC records from the Dajiuhu peatland at a latitude similar to Ganchi indicated the close relationship between TOC and EASM strength, with higher TOC correlating with stronger EASM (Zhang, 2017). The TOC records of the Zoige and Hongyuan peatlands in the southeastern margin of the Tibetan Plateau also reflected the Holocene monsoonal changes (Zhou et al., 2002; Wang et al., 2010). The Ganchi sedimentary environment transitioned from a lake to a wetland at ∼13.7 cal kyr BP, resulting in the gradual development of peat, which is consistent with the initial peak timing (14.5–13.0 cal kyr BP) of peat development in the Hengduan Mountain area due to the Bølling-Allerød warm climate (Liu et al., 2022). The variation trend of TOC in the GC core during the last deglaciation is consistent with the variation trend of monsoon intensity, as reflected by sunlight and stalagmite oxygen isotope records from Dongge and Hulu cave (Wang et al., 2001; **Figure 7C**). Therefore, the TOC variation in this study can be used as an indicator of the strength of the monsoon and the resulting paleoclimatic changes.

After 13.7 cal kyr BP, the TOC changes in the GC core were negatively correlated with Ti/Ca, Fe/Mn ratios and terrigenous clastic sediments, but positively correlated with a sedimentation rate (**Figure 6**). During the warm periods of 13.7–12.0 cal kyr BP and 7.5–3.5 cal kyr BP, the TOC and vegetation coverage increased, and the peat accumulation and deposition rates were more rapid (Liu et al., 2020). As the soil and water were effectively conserved, the amount of exogenous clastic sediments entering the dry pool via water inflow decreased. During the cold and dry periods of 12.0–11.2 cal kyr BP, 9.0 cal kyr BP, and 6.0 cal kyr BP, the vegetation coverage, TOC, peat accumulation rate, and deposition rate all decreased. During these cold and dry stages, the increase in detrital sediments in Ganchi may be related to the loss of soil and water and the increase of atmospheric dust deposition (Peng et al., 2021).

The δ^{13}Corg values in wetland sediment core reflect both vegetation evolution and paleoclimatic changes. Moreover, the organic carbon isotope composition of plants reflects the type of photosynthesis, atmospheric CO_2 concentrations (Francey and Farquhar, 1982; Meyers and Ishiwatari, 1993), and climatic conditions (Hong et al., 2010; Xue et al., 2014). Therefore, the environmental signal reflected by the δ^{13}Corg value is complex. In this study, the δ^{13}Corg value was generally more negative during the last deglaciation, which is consistent with the variations in TOC and oxygen isotopes derived from Dongge cave and Hulu cave stalagmites, and with the δ^{13}Corg trend from Baoan peatland, which reflects the variation in the Asian monsoon (**Figure 7**). Therefore, the δ^{13}Corg trend and TOC

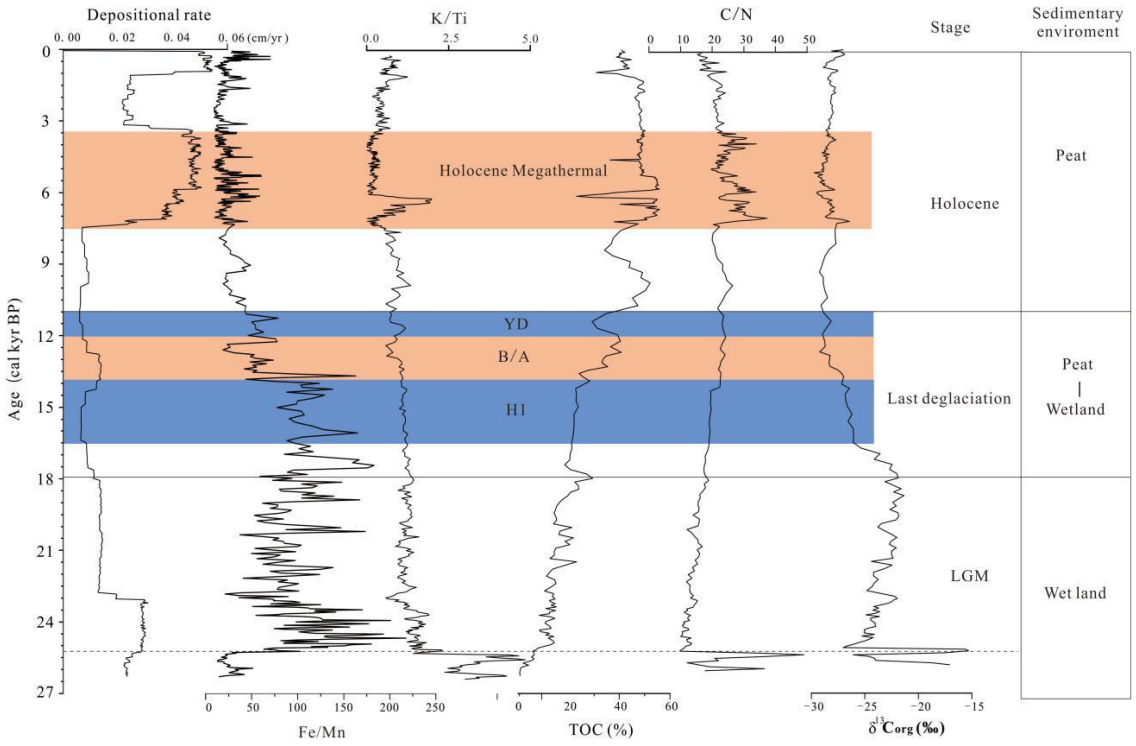

FIGURE 6
Comparison of paleoenvironmental indicators since the LGM in the GC core.

record in the GC core likely reflect monsoon intensity and the subsequent paleoclimate changes. The paleoenvironmental indicators in this study are consistent with the paleoclimate changes recorded by the GC core high-resolution pollen (Deng et al., 2022; **Figure 7A**).

Depositional environmental and vegetation evolution since the Last Glacial Maximum in Ganchi

According to the changes in the paleoenvironmental proxies, the evolution of the depositional environment since the LGM (recorded in the GC core) in Ganchi can be divided into three stages (**Figure 6**): (1) the LGM (26.2–18.2 cal kyr BP), (2) last deglaciation (18.2–11.2 cal kyr BP), and (3) Holocene (since 11.2 cal kyr BP).

Last Glacial Maximum (26.2–18.2 cal kyr BP)

Figure 6 shows that the LGM stage can be divided into two sub-stages. During 26.2–25.2 cal kyr BP, the mean values of TOC, C/N, and δ^{13}Corg were 4.2%, 22.7, and −18.6‰. Organic matter accumulation in the study area was less, mainly in terrestrial higher plants and submerged plants. During 25.2–18.2 cal kyr BP, the TOC value increased, the δ^{13}Corg value reached −23.4‰, and the C/N value was between 10 and 20, which reflected the change of vegetation type in the study area., The contribution of C3 plants gradually increased and become dominant from this stage, but there were also some aquatic plants. The high Fe/Mn ratios indicate a wetland environment. The concentration of Ti, Zr, and other elements indicate the small fluctuation of exogenous clastic sediments, which infers a relatively stable sedimentary environment, with a low and less variable deposition rate.

Last deglaciation (18.2–11.2 cal kyr BP)

In this stage, δ^{13}Corg values showed a more negative trend (mean −27.0u), and TOC and C/N values exhibited increased fluctuations. Particularly from 13.7 cal kyr BP, the average C/N value was greater than 20, TOC increased significantly, and the intensities of Ti and Zr decreased significantly (**Figures 3**, **6**). This indicates that since 13.7 cal kyr BP, the exogenous clastic sediments in the study area decreased significantly; Terrestrial higher vegetation represented by C3 plants further increased, and various algae, phytoplankton, submerged macrophytes, and emergent macrophytes gradually decreased. The Fe/Mn ratio gradually decreased from 13.7 cal kyr BP, indicating a decreasing water level in Ganchi and the transition of the sedimentary environment from wetland to peatland. This is consistent with previous research results on the timing of peat development

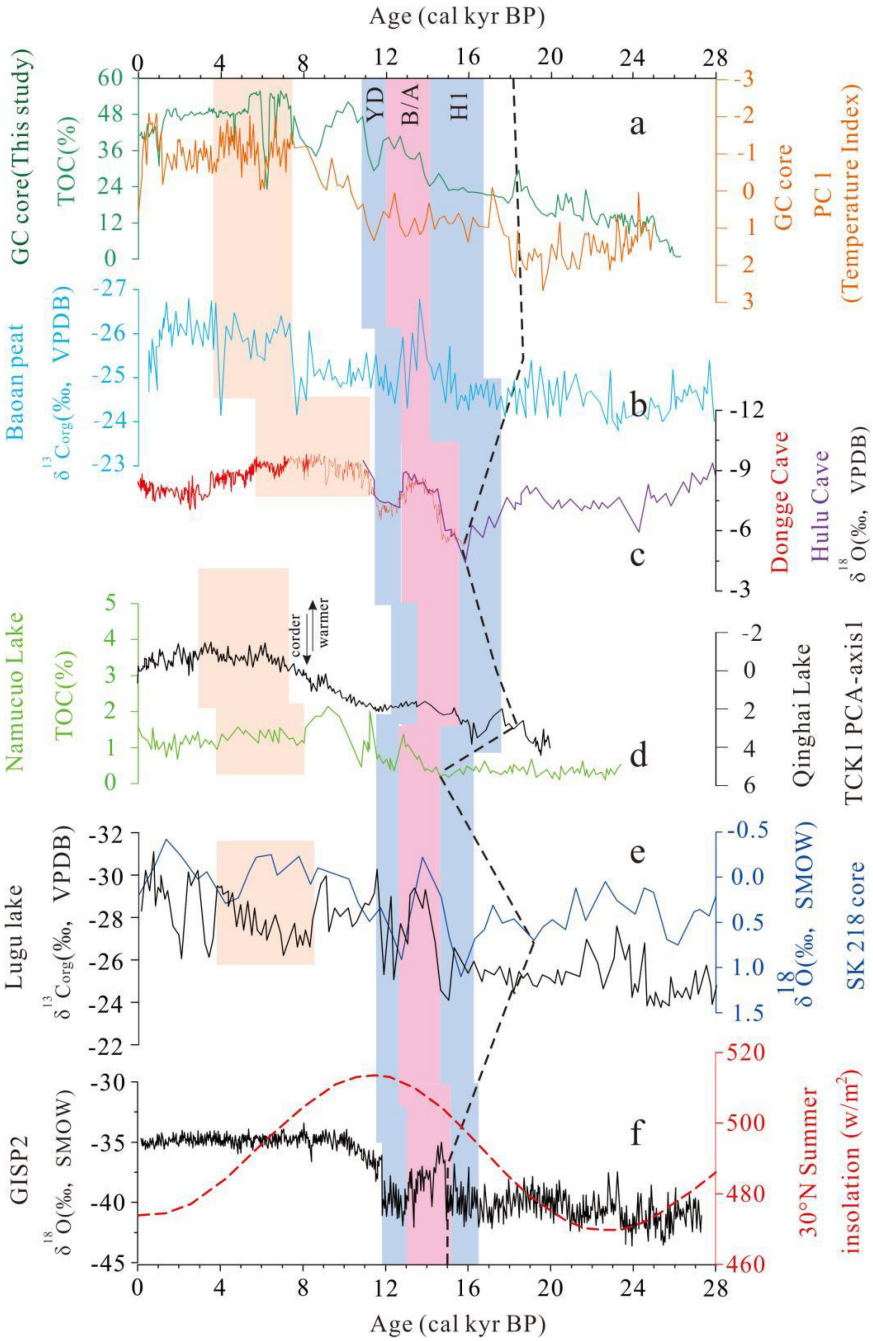

FIGURE 7
Comparison of the paleoenvironmental records in the GC core with that of other areas since the LGM. **(a)** Principal component1 (PC1) scores of the pollen in the GC core (orange curve, Deng et al., 2022), this curve can be used as temperature index, the higher the temperature, the smaller the value. TOC percentage content (green curve) of the GC core (this study); **(b)** δ^{13}Corg records of the Baoan peat (Blue curve, Hong et al., 2018), **(c)** δ^{18}O stalagmite record from Dongge Cave (red curve, Dykoski et al., 2005) and Hulu Cave (purple curve, Wang et al., 2001); **(d)** TOC percentage in sediment core NC08/01 from NamCo Lake, QTP (black curve, Zhu et al., 2015) and the PC1 scores of pollen in core TCK1 from Qinghai Lake, Tengchong (green curve, Xiao et al., 2015); **(e)** sea surface δ^{18}O record from core SK218 in the Indian Ocean (blue curve, Govil and Divakar Naidu, 2011) and δ^{13}Corg record in sediment core LG08 from Lugu Lake, Yunnan Province (black curve, Zhang et al., 2018); **(f)** 30° N summer insolation curve (red dotted line, Berger and Loutr, 1991) and δ^{18}O record from the GISP2 ice core in Greenland (black curve, Stuiver and Grootes, 2000). The black dotted line indicates the first warming period after the LGM at different locations; the blue band indicates the H1 and YD cold events; and the pink band indicates the B/A warm period. The orange band indicates the Holocene Megathermal.

in the southern Hengduan Mountains, which mostly occurred before the Holocene (Liu et al., 2020).

Holocene (since 11.2 cal kyr BP)

During the Holocene, the intensities of Si, Fe, K, and Ti were relatively low, indicating the lower transport of exogenous clastic sediments to the study area. TOC and C/N increased to maximum levels, and the δ^{13}Corg (mean −28.4 ‰) was more negative, which suggests that terrestrial C3 plants were the dominant organic matter sources and that the Ganchi wetland had completely evolved into peatland.

Paleoclimate evolution and driving mechanisms since the Last Glacial Maximum in the southern margin of the Sichuan Basin

First warming period after the Last Glacial Maximum

Studies (Wang et al., 2014; Xiao et al., 2014a; Jin et al., 2015; Zhu et al., 2015; Li et al., 2018) have shown that the LGM climate in Southwest China was generally cold and dry, and the first period of warming after the LGM occurred between 19 and 17 kyr BP (Cook et al., 2012; Wu et al., 2015; Zhang et al., 2018). Similar paleoclimatic changes were recorded in the GC core. During the LGM, due to the cold and dry climate, the organic matter accumulation is less, the TOC was relatively low, and δ^{13}Corg was relatively higher values. Since 18.2 cal kyr BP, the TOC increased significantly, and δ^{13}Corg showed an obvious more negative trend, indicating a warming climate. Therefore, the timing of the first warming period after the LGM in Ganchi (the southern margin of the Sichuan Basin) was 18.2 cal kyr BP, which is consistent with the timing of the first warming period in Southwest China. However, the timing of the first warming in Southwest China notably differed from that recorded in the Northern Hemisphere high latitudes (Johnsen et al., 1992) and the EASM region (Wang et al., 2001), but was similar to that recorded in the Indian Ocean region (Govil and Divakar Naidu, 2011; **Figure 7E**). This suggests that the first warming in Southwest China was not controlled by the changes in the high-latitude ice sheets of the Northern Hemisphere but was likely related to the strengthening of the ISM caused by increasing solar radiation in 30°N since 21 kyr BP (**Figure 7F**), which further affected Southwest China (Shen and Xiao, 2018).

Climate changes during the last deglaciation

The climate was generally warm in the study area during the last deglaciation (18.2–10.9 cal kyr BP), which was superimposed by several abrupt climate change events.

The most notable climate fluctuation occurred during 13.7–12.0 cal kyr BP and 12.0–11.2 cal kyr BP (**Figure 6**). The study area belongs to the carbonatite area. The K, Ca and other soluble elements in the carbonatite are easily leached and migrated, resulting in a relative loss of content, while the Ti element is relatively stable. Therefore, the K/Ti ratio can reflect the chemical weathering intensity of the study area, thus indicating climate change (Qu and Huang, 2019). During 13.7–12.0 cal kyr BP, the TOC increased significantly and the K/Ti ratio decreased, reflecting the warm climate and strong chemical weathering during this period, which likely indicates the Bølling-Allerød warm period in this region.

During the period of 16.5–13.7 cal kyr BP and 12–11.2 cal kyr BP, TOC and δ^{13}Corg were decreased and biased, especially during the period of 12–11.2 cal kyr BP. The K/Ti ratio also increased significantly during 12–11.2 cal kyr BP. The changes in the above indicators reflect that there were relatively obvious climate cooling events in these two periods, which may correspond to H1 and YD events, respectively. Al/Si ratio can be used as an indicator of sediment particle size. In general, with higher Al/Si ratio indicating finer grain size (Bloemsma et al., 2012; Babek et al., 2015). In the above two periods, the Al/Si ratio showed obvious low values, which may mean that the cold and dry climate in these two periods, due to the low vegetation cover, flowing water erosion brought more coarse-grained sediments. These millennial-scale fluctuations are consistent with the δ^{18}O records of the GISP2 ice core in Greenland (Stuiver and Grootes, 2000; **Figure 7F**), the SK218/1 core in the Bay of Bengal (Govil and Divakar Naidu, 2011; **Figure 7E**), and the Hulu cave stalagmite in eastern China (Wang et al., 2001; **Figure 7C**). The significant weakening of the ISM during the H1 and YD periods was also recorded in other lake sediments (Wang et al., 2014; Xiao et al., 2014b; Zhang et al., 2015a) and stalagmites (Dykoski et al., 2005) in Southwest China.

The climate change recorded in the GC core is similar to that observed in the records of Southwest China, except for the precise start and end time of the climate intervals and the degree of change. These differences may be related to the sensitivity of the different regions to climate change as well as the possible uncertainties in chronology (Shen and Xiao, 2018). In addition, due to the topography of the QTP, the climate of different regions in the southwest may be more complex and diverse. For example, the peat records of Caohai, south of the QTP, indicate that the region was sensitive to the B/A warm period but not to the H1 and YD cold events (Gong et al., 2019), which may be more affected by the ISM. However, the signals for H1, YD, and B/A recorded by the pollen of Xingyun Lake, located in the east of the Qinghai Tibet Plateau were relatively weak, which may be more affected by the ISM and EASM (Shen and Xiao, 2018). Therefore, the southwest of the Sichuan Basin may be more affected by the EASM, especially when the ISM is relatively weak.

The gradual temperature rises during the last deglaciation may have been predominantly affected by the gradual increase in low-latitude summer solar radiation since ∼21 kyr BP (**Figure 7E**), which in turn led to the strengthening of the

ISM (Shen and Xiao, 2018). The millennial-scale cooling events (H1 and YD) may have been related to the weakening of the monsoon in response to the weakening of the Atlantic Meridional Overturning Circulation (AMOC), which would have changed the sea surface temperature (Broecker, 2003; Mohtadi et al., 2014, 2016; An et al., 2015). The monsoon began to increase significantly during the B/A, and the emergence of the B/A warm period may be related to the significant increase in radiative forcing produced by greenhouse gases dominated by CO_2 during this period (Clark et al., 2012; Hong et al., 2014).

Holocene climate characteristics

The climate of the Holocene (since 11.2 cal kyr BP) was generally warm and humid, with intensified climate fluctuations. It can be seen from **Figure 6** that TOC increases first and then decreases between 11.2 and 7.5 cal kyr BP, the δ^{13}Corg value showed a gradually higher trend, and the Al/Si ratio fluctuated rapidly, especially reaching the minimum value of about 9.0 cal kyr BP. These changes reflect the climate generally cooled and showed significant fluctuations during the early Holocene (11.2–7.5 cal kyr BP); this is in contrast to the slow and early temperature increase in the Holocene that is reflected by the sporopollen records of Qinghai and Lugu Lake, Yunnan (Xiao et al., 2015; Shen and Xiao, 2018), and to the rapid rise in temperature in the Holocene reflected by the sporopollen records of Wuxu Lake, which is closer to the EASM area (Zhang et al., 2016). Several paleoenvironmental records (Chen et al., 2015; Jia et al., 2015; Zhang, 2017; Kang et al., 2020) in the EASM area indicate a generally warm and humid climate of the early Holocene, which is likely related to the relatively strong EASM during this period. The difference in early Holocene climate characteristics in Southwest China may be related to the relatively strong EASM and the fact that some areas were simultaneously affected by both the EASM and ISM. Therefore, climate change during this period shows regional and complex characteristics.

The Holocene Megathermal is from 7.5 to 3.5 cal kyr BP in the GC records. During this period, the climate was the warmest and wettest, but the climate fluctuation intensified. The environmental indicators in **Figure 6** have obvious responses to climate change in this period. Especially at ∼6.0 cal kyr BP, TOC, δ^{13}Corg, Al/Si, and K/Ti ratio showed the most obvious fluctuations since the Holocene, suggesting that this was the most serious climate fluctuation event during the Holocene Megathermal, which is consistent with the results of the Baoan peat records (Hong et al., 2018; **Figure 7B**) in the adjacent area. The climate cooling in the Middle Holocene is also believed to be closely related to the origin and development of civilization in the Chengdu Plain area in the western Sichuan Basin. Under this climate background, some ancient people from the upper reaches of the Minjiang River migrated to the Chengdu Plain and gave birth to Baodun culture (Huang et al., 2019). The peat records in the east of the QTP also indicate that the 6.0 cal kyr BP climate cooling event is more significant than the 8.2 ka event, which is likely related to the sudden weakening of the EASM around 6.2 kyr BP (Yu et al., 2006). The paleoclimate records of the GC core suggest that the Holocene Megathermal mainly occurred during the mid-Holocene (**Figure 7**), which is consistent with the timing observed in other records of the surrounding ISM areas (Xiao et al., 2015; Zhang et al., 2018; **Figures 7C,E**). The Holocene Megathermal timing in our record also lagged that of most EASM areas, which appeared to have started in the early Holocene (Dykoski et al., 2005; Chen et al., 2015; **Figure 7B**). The Holocene evolution of the EASM and ISM was mainly controlled by the changes in the equatorial Intertropical Convergence Zone (ITCZ), which gradually migrated southward under the control of summer solar insolation in the Northern Hemisphere (Dong et al., 2006). Since the Holocene, the summer solar insolation in the Northern Hemisphere has continually decreased. However, the Holocene Megathermal in Southwest China lags behind the peak solar radiation, which may be related to the continuous melting of glaciers after the solar radiation peak, resulting in a rise in the sea level (Griffiths et al., 2009) and sea surface temperatures (Overpeck et al., 1996). In addition, the research (Yan, 2022) shows that the enhancement of glacier ablation caused by the temperature rise in the middle Holocene exceeded the increase of glacier accumulation caused by the increase of precipitation, which led to the significant retreat of glaciers in Asia's alpine regions during this period. Therefore, during the Holocene Megathermal, the western Sichuan Basin became wetter due to the melting of glaciers on the QTP.

The research area experienced a cooling period in the late Holocene after 3.5 cal kyr BP. TOC and δ^{13}Corg in the GC core recorded a strong cooling event at ∼1.0 cal kyr BP, which was also recorded in the Baoan peatland and Qinghai Lake (**Figure 7**). However, the GC core did not significantly respond to the 4.2 cal kyr BP cooling event, which is the most detected late-Holocene cooling event globally.

Conclusion

The sedimentary environment and hydroclimate evolution of the southern margin of the Sichuan Basin since the LGM were reconstructed from the Ganchi wetland core based on concentrations in major and trace elements, TOC, and δ^{13}Corg. During LGM(26.2–18.2 cal kyr BP), the climate is cold and dry, and the study area was a wetland sedimentary environment. Except for some aquatic plants, C3 vegetation began to dominate from this stage. Since the last deglaciation (18.2–10.9 cal kyr BP), the sedimentary environment of Ganchi transitioned from wetland to peatland, and the C3 vegetation further increased, while the aquatic plants decreased. Peat started to develop in Ganchi at ∼13.7 cal kyr BP, which coincided with the

first peak of peat development in the Hengduan Mountains. During the last deglaciation, the climate in the study area was generally warm but was affected by several abrupt climate events. Similarly, the climate of the Holocene (since 11.2 cal kyr BP) was generally warm and humid, with intensified climate fluctuations.

The hydroclimate in the southwest Sichuan Basin since the LGM showed similar regional evolution characteristics to that observed in Southwest China from the LGM to the Holocene, but exhibited local and more complex climatic characteristics during the Holocene. The climate of the LGM was cold and dry, and the first warming period after the LGM occurred at 18.2 cal kyr BP, which was consistent with the timing of the first warming period in other records of Southwest China. The climate warmed during the last deglaciation, and the abrupt cooling during H1, B/A, and YD was detected in the GC core. Affected by the topography of the QTP, The climate change pattern during the last deglaciation in the southwestern margin of the Sichuan Basin is mainly affected by the EASM and less affected by the ISM. During the Holocene, the climate was generally warm and humid, but the climate fluctuation intensified. The early Holocene climate may have been affected by both the ISM and the EASM, resulting in more complex local climate characteristics. The timing of the Holocene Megathermal (7.5–3.5 cal kyr BP) in our record was consistent with its timing in other records of the ISM region. The climatic cooling event during this period was closely related to the beginning of Baodun Culture in the Chengdu Plain. The research area then entered a cold period during the late Holocene.

Data availability statement

The original contributions presented in this study are included in the article/supplementary material, further inquiries can be directed to the corresponding author.

Author contributions

MH and CM designed the study. MH, CM, HP, YD, and HG analyzed the data. CM and HP performed the analyses and revised the manuscript. ZW and GS did the fieldwork. MH and ZW completed the laboratory analysis. MH wrote the manuscript. All authors contributed to interpreting the results and discussions.

Funding

This research was jointly supported by the National Natural Science Foundation of China (Nos. 41977389 and 42271173), the Frontiers Science Center for Critical Earth Material Cycling Fund (No. JBGS2102), and the National Key Research and Development Program of China (Nos. 2020YFC1521605, 2020YFC1521603, and 2020YFC1521606).

Acknowledgments

We thank Chenglong Li and Bin Zhou from the School of Earth Sciences and Engineering, Nanjing University for their guidance in laboratory analysis. We also thank the Natural Resources Bureau of Jinkouhe District, Leshan City, Sichuan Province for supporting our field sampling.

Conflict of interest

The authors declare that the research was conducted in the absence of any commercial or financial relationships that could be construed as a potential conflict of interest.

Publisher's note

References

Alley, R. B., and Clark, P. U. (1999). The deglaciation of the Northern hemisphere: A global perspective. *Annu. Rev. Earth Planet. Sci.* 27, 149–182. doi: 10.1146/annurev.earth.27.1.149

An, Z., Wu, G., Li, J., Sun, Y., Liu, Y., Zhou, W., et al. (2015). Global monsoon dynamics and climate change. *Annu. Rev. Earth Planet. Sci.* 43, 2.1–2.49. doi: 10.1146/annurev-earth-060313-054623

Babek, O., Grygar, T. M., Famera, M., Hron, K., Novakova, T., and Sedlacek, J. (2015). Geochemical background in polluted river sediments: How to separate the effects of sediment provenance and grain size with statistical rigour? *Catena* 135, 240–253. doi: 10.1016/j.catena.2015.07.003

Berger, A., and Loutr, M. F. (1991). Insolation values for the climate of the last 10 million years. *Quat. Sci. Rev.* 10, 297–317. doi: 10.1016/0277-3791(91)90033-Q

Blaauw, M., and Christen, J. A. (2011). Flexible paleoclimate age-depth models using an autoregressive gamma process. *Bayesian Anal.* 6, 457–474. doi: 10.1214/11-BA618

Blackford, J. (2000). Palaeoclimatic records from peat bogs. *Trends Ecol. Evol.* 15, 193–198. doi: 10.1016/S0169-5347(00)01826-7

Bloemsma, M. R., Zabel, M., Stuut, J. B. W., Tjallingii, R., Collins, J. A., and Weltje, G. (2012). Model-ling the joint variability of grain size and chemical composition in sediments. *Sediment. Geol.* 280, 135–148. doi: 10.1016/j.sedgeo.2012.04.009

Broecker, W. S. (2003). Does the trigger for abrupt climate change reside in the ocean or in the atmosphere? *Science* 300, 1519–1522. doi: 10.1126/science.1083797

Chambers, F. M., Booth, R. K., De Vleeschouwer, F., Lamentowicz, M., Le Roux, G., Mauquoy, D., et al. (2012). Development and refinement of proxy-climate indicators from peats. *Quat. Int.* 268, 21–33. doi: 10.1016/j.quaint.2011.04.039

Chambers, F. M., and Charman, D. J. (2004). Holocene environmental change: Contributions from the peatland archive. *Holocene* 14, 1–6. doi: 10.1191/0959683604hl684ed

Chen, F., Xu, Q., Chen, J., Birks, H. J., Liu, J., Zhang, S., et al. (2015). East Asian summer monsoon precipitation variability since the last deglaciation. *Sci. Rep.* 5:11186. doi: 10.1038/srep11186

Cheng, A., Yu, J., Zhang, L., Liu, Y., and Gao, C. (2011). Analysis of Toson Lake XRF core scanning and application of multivariate statistical methods. *J. Saltlake Res.* 19, 20–25.

Clark, P. U., Dyke, A. S., Shakun, J. D., Carlson, A. E., Clark, J., Wohlfarth, B., et al. (2009). The last glacial maximum. *Science* 325, 710–714. doi: 10.1029/2005GC001226

Clark, P. U., Shakun, J. D., Baker, P. A., Bartlein, P. J., Brewer, S., Brook, E., et al. (2012). Global climate evolution during the last deglaciation. *Proc. Natl. Acad. Sci. U.S.A.* 109, E1134–E1142. doi: 10.1073/pnas.1116619109

Cook, C. G., Leng, M. J., Jones, R. T., Langdon, P. G., and Zhang, E. (2012). Lake ecosystem dynamics and links to climate change inferred from a stable isotope and organic palaeorecord from a mountain lake in Southwestern China (ca. 22.6–10.5 cal kyr BP). *Quat. Res.* 77, 132–137. doi: 10.1016/j.yqres.2011.09.011

Cuven, S., Francus, P., and Lamoureux, S. F. (2010). Estimation of grain size variability with micro X-ray fluorescence in laminated lacustrine sediments, Cape Bounty, Canadian High Arctic. *J. Paleolimnol.* 44, 803–817. doi: 10.1007/s10933-010-9453-1

Deng, Y. K., Ma, C. M., Huang, M., Zhao, L., Shang, G. C., Tang, L. Y., et al. (2022). Vegetation and climate changes since the Last Glacial Maximum inferred from high-resolution pollen records from the Sichuan Basin, Southwest China. *Paleogeogr. Paleoclimatol. Paleoecol.* 606:111231. doi: 10.1016/j.palaeo.2022.111231

Denton, G. H., Anderson, R. F., Toggweiler, J. R., Edwards, R. L., Schaefer, J. M., and Putnam, A. E. (2010). The last glacial termination. *Science* 328, 1652–1654. doi: 10.1126/science.1184119

Devry, I. J. (1993). Pollen evidence of changing Holocene monsoon climate in Sichuan province, China. *Quat. Res.* 39, 325–337. doi: 10.1006/qres.1993.1039

Díaz, K. A., Pérez, L., Correa-Metrio, A., Franco-Gaviria, J. F., Echeverría, P., Curtis, J., et al. (2017). Holocene environmental history of tropical, mid-altitude Lake Ocotalito, México, inferred from ostracodes and non-biological indicators. *Holocene* 27, 1308–1317. doi: 10.1177/0959683616687384

Dong, J., Kong, X., and Wang, Y. (2006). The East Asian Monsoon climate changes at mt. shennongjia and its relation to shift of intertropical convergence zone during the Holocene. *Quat. Sci.* 26, 827–834.

Dykoski, C., Edwards, R., Cheng, H., Yuan, D., Cai, Y., Zhang, M., et al. (2005). A high-resolution, absolute-dated Holocene and deglacial Asian monsoon record from Dongge Cave, China. *Earth Planet. Sci. Lett.* 233, 71–86. doi: 10.1016/j.epsl.2005.01.036

Francey, R. J., and Farquhar, G. D. (1982). An explanation of 13C/12C variations in tree rings. *Nature* 297, 28–31. doi: 10.1038/297028a0

Gong, X., Chen, C., Tang, Y., Huang, K., Yue, Y., Liang, K., et al. (2019). Palaeoenvironment changes during the past 21 kyr inferred from organic geochemical records of Caohai Lake,Guizhou Province. *J. Palaeogeogr.* 21, 1025–1034.

Govil, P., and Divakar Naidu, P. (2011). Variations of Indian monsoon precipitation during the last 32kyr reflected in the surface hydrography of the Western Bay of Bengal. *Quat. Sci. Rev.* 30, 3871–3879. doi: 10.1016/j.quascirev.2011.10.004

Griffiths, M. L., Drysdale, R. N., Gagan, M. K., Zhao, J. X., Ayliffe, L. K., Hellstrom, J. C., et al. (2009). Increasing Australian–Indonesian monsoon rainfall linked to early Holocene sea-level rise. *Nat. Geosci.* 2, 636–639. doi: 10.1038/ngeo605

Haug, G. H., Hughen, K. A., Sigman, D. M., Peterson, L. C., and Röhl, U. (2001). Southward migration of the intertropical convergence zone through the holocene. *Science* 293, 1304–1308. doi: 10.1126/science.1059725

Hennekam, R., and de Lange, G. (2012). X-ray fluorescence core scanning of wet marine sediments: Methods to improve quality and reproducibility of high-resolution paleoenvironmental records. *Limnol. Oceanogr. Methods* 10, 991–1003. doi: 10.4319/lom.2012.10.991

Hakanson, L., and Jansson, M. (2002). *Principles of lake sedimentology*. Caldwell, NJ: The Blackburn Press.

Hong, B., Hong, Y., Uchida, M., Shibata, Y., Cai, C., Peng, H., et al. (2014). Abrupt variations of Indian and East Asian summer monsoons during the last deglacial stadial and interstadial. *Quat. Sci. Rev.* 97, 58–70. doi: 10.1016/j.quascirev.2014.05.006

Hong, B., Hong, Y. T., Lin, Q. H., Shibata, Y., Uchida, M., Zhu, Y. X., et al. (2010). Anti-phase oscillation of Asian monsoons during the Younger Dryas period: Evidence from peat cellulose $\delta^{13}C$ of Hani, Northeast China. *Palaeogeogr. Palaeoclimatol. Palaeoecol.* 297, 214–222. doi: 10.1016/j.palaeo.2010.08.004

Hong, B., Uchida, M., Hong, Y., Peng, H., Kondo, M., and Ding, H. (2018). The respective characteristics of millennial-scale changes of the India summer monsoon in the Holocene and the Last Glacial. *Palaeogeogr. Palaeoclimatol. Palaeoecol.* 496, 155–165. doi: 10.1016/j.palaeo.2018.01.033

Huang, M., Zhu, C., Ma, C., He, K., and Xu, J. (2019). Paleoenvironmental context of the evolution of the Baodun Culture at Chengdu Plain, Sichuan Province, China. *Holocene* 29, 1731–1742. doi: 10.1177/0959683619862031

Huo, W. (2022). Sanxingdui: A dialogue between eastern and western ancient bronze civilizations. *J.Tsinghua Uni.* 37, 1–8.

Jia, G., Bai, Y., Yang, X., Xie, L., Wei, G., Ouyang, T., et al. (2015). Biogeochemical evidence of Holocene East Asian summer and winter monsoon variability from a tropical maar lake in southern China. *Quat. Sci. Rev.* 111, 51–61. doi: 10.1016/j.quascirev.2015.01.002

Jin, Z., An, Z., Yu, J., Li, F., and Zhang, F. (2015). Lake Qinghai sediment geochemistry linked to hydroclimate variability since the last glacial. *Quat. Sci. Rev.* 122, 63–73. doi: 10.1016/j.quascirev.2015.05.015

Johnsen, S. J., Clausen, H. B., Dansgaard, W., Fuhrer, K., Gundestrup, N., Hammer, C. U., et al. (1992). Irregular glacial interstadials recorded in a new Greenland ice core. *Nature* 359, 311–313. doi: 10.1038/359311a0

Kang, S., Du, J., Wang, N., Dong, J., Wang, D., Wang, X., et al. (2020). Early Holocene weakening and mid-to late Holocene strengthening of the East Asian winter monsoon. *Geology* 48, 1043–1047. doi: 10.1130/G47621.1

Kido, Y., Koshikyrwa, T., and Tada, R. (2006). Rapid and quantitative major element analysis method for wet fine-grained sediments using an XRF microscanner. *Mar. Geol.* 229, 209–225. doi: 10.1016/j.margeo.2006.03.002

Lamb, A. L., Wilson, G. P., and Leng, M. J. (2006). A review of coastal palaeoclimate and relative sea-level reconstructions using $\delta^{13}C$ and C/N ratios in organic material. *Earth Sci. Rev.* 75, 29–57. doi: 10.1016/j.earscirev.2005.10.003

Lawrence, F. W., and Upchurch, S. B. (1982). Identification of recharge areas using geochemical factor analysis. *Ground Water* 20, 680–687. doi: 10.1111/j.1745-6584.1982.tb01387.x

Lei, G., Zhu, Y., Jiang, X., Li, Z., Jin, J., Fang, K., et al. (2014). Climate Variations over the past 1400 Years Inferred from an α-cellulose $\delta^{13}C$ Record from Xianshan Peat in Southeast China. *Sci. Geogeaph. Sin.* 34, 1018–1024.

Li, K., Tan, B., Ni, J., and Liao, M. N. (2018). Hydroclimate changes since Last Glacial Maximum: Geochemical evidence from Yilong Lake, Southwestern China. *Acta Ecol. Sin.* 38, 8973–8982. doi: 10.5846/stxb201806011228

Liang, L., Sun, Y., Yao, Z., Liu, Y., and Wu, F. (2012). Evaluation of high-resolution elemental analyses of Chinese loess deposits measured by X-ray fluorescence core scanner. *Catena* 92, 75–82. doi: 10.1016/j.catena.2011.11.010

Liu, B., Sheng, E., Lan, J., and Yu, K. (2022). Peat development in the Napahai wetland and its response to variations in the intensity of the Indian summer monsoon, southwestern China, since the last deglaciation. *Palaeogeogr. Palaeoclimatol. Palaeoecol.* 598:111026. doi: 10.1016/j.palaeo.2022.111026

Liu, G. (2016). Formation and evolution mechanism of ecological security pattern in Southwest China. *Acta Ecol. Sin.* 36, 7088–7091. doi: 10.5846/stxb201611212364

Liu, L., Chen, H., Yu, Z., Zhu, D., He, Y., Liu, J., et al. (2020). Peatland development and carbon dynamics since the Last Glacial Maximum in the Hengduan Mountains Region. *Catena* 190:104525. doi: 10.1016/j.catena.2020.104525

Loring, D. H., and Asmund, G. (1996). Geochemical factors controlling accumulation of major and trace elements in Greenland coastal and fjord sediments. *Environ. Geol.* 28, 2–11. doi: 10.1007/s002540050072

Luo, C. (2003). Geomorphological study on Jinkou Grand Canyon and Dawa mountain area. *J. Leshan Nom. Coll.* 18, 84–88.

Ma, X., Chen, D., Yang, Y., Zhang, Y., and Zhang, J. (2014). Statistical analysis of XRF scanned elements and their environmental significance in Hala lake, Qinghai, China. *J. Saltlake Res.* 22, 1–10.

Meng, Q., Niu, R., Zheng, X., Zhou, L., Sun, C., and Wang, L. (2018). Geochemical characteristics of the peat profile in the Yangbajing basin, Tibetan, China and its paleoenvironmental implications. *J. East China Norm. Univ.* 151–159.

Meyers, P. A. (1994). Preservation of elemental and isotopic source identification of sedimentary organic matter. *Chem. Geol.* 114, 289–302. doi: 10.1016/0009-2541(94)90059-0

Meyers, P. A. (1997). Organic geochemical proxies of paleoceanographic, paleolimnologic, and paleoclimatic processes. *Org. Geochem.* 27, 213–250. doi: 10.1016/S0146-6380(97)00049-1

Meyers, P. A., and Ishiwatari, R. (1993). Lacustrine organic geochemistryman overview of indicators of organic matter sources and diagenesis in lake sediments. *Org. Geochem.* 20, 867–900. doi: 10.1016/0146-6380(93)90100-P

Meyers, P. A., and Lallier-Vergès, E. (1999). Lacustrine sedimentary organic matter records of Late Quaternary paleoclimates. *J. Paleolimnol.* 21, 345–372. doi: 10.1023/A:1008073732192

Mohtadi, M., Prange, M., Oppo, D. W., De Pol-Holz, R., Merkel, U., Zhang, X., et al. (2014). North Atlantic forcing of tropical Indian Ocean climate. *Nature* 509, 76–80. doi: 10.1038/nature13196

Mohtadi, M., Prange, M., and Steinke, S. (2016). Palaeoclimatic insights into forcing and response of monsoon rainfall. *Nature* 533, 191–199. doi: 10.1038/nature17450

Morrill, C., Overpeck, J. T., Cole, J. E., Liu, K. B., Shen, C., and Tang, L. (2006). Holocene variations in the Asian monsoon inferred from the geochemistry of lake sediments in central Tibet. *Quat. Res.* 65, 232–243. doi: 10.1016/j.yqres.2005.02.014

O'Leary, M. H. (1981). Carbon isotope fractionation in plants. *Phytochemistry* 20, 553–567. doi: 10.1016/S0016-7037(60)80006-3

O'Leary, M. H. (1988). Carbon Isotopes in Photosynthesis: Fractionation techniques may reveal new aspects of carbon dynamics in plants. *Bioscience* 38, 328–336. doi: 10.2307/1310735

Overpeck, J., Anderson, D., Trumbore, S., and Prell, W. (1996). The southwest Indian Monsoon over the last 18000 years. *Clim. Dynam.* 12, 213–225. doi: 10.1007/BF00211619

Peng, H., Bao, K., Yuan, L., Uchida, M., Cai, C., Zhu, Y., et al. (2021). Abrupt climate variability since the last deglaciation based on a high-resolution peat dust deposition record from southwest China. *Quat. Sci. Rev.* 252:106749. doi: 10.1016/j.quascirev.2020.106749

Peros, M., Collins, S., G'Meiner, A. A., Reinhardt, E., and Pupo, F. M. (2017). Multistage 8.2 kyr event revealed through high-resolution XRF core scanning of Cuban sinkhole sediments. *Geophys. Res. Lett.* 44, 7374–7381. doi: 10.1002/2017GL074369

Qu, H., and Huang, B. (2019). Paleoclimate change reflected by element ratios of terrigenous sediments from deep-sea Oxygen isotope MIS6 to MIS5 at MD12-3432 stationinnorthern South China Sea. *Earth Sci. Front.* 26, 236–242.

Reimer, P. J., Bard, E., Bayliss, A., Beck, J. W., Blackwell, P. G., Ramsey, C. B., et al. (2013). IntCal13 and Marine13 radiocarbon age calibration curves 0-50,000 Years cal BP. *Radiocarbon* 55, 1869–1887. doi: 10.2458/azu_js_rc.55.16947

Shakun, J. D., and Carlson, A. E. (2010). A global perspective on Last Glacial Maximum to Holocene climate change. *Quat. Sci. Rev.* 29, 1801–1816. doi: 10.1016/j.quascirev.2010.03.016

Shen, J. (2013). Spatiotemporal variations of Chinese lakes and their driving mechanisms since the Last Glacial Maximum: A review and synthesis of lacustrine sediment archives. *Chin. Sci. Bull* 58, 17–31. doi: 10.1007/s11434-012-5510-7

Shen, J., and Xiao, X. (2018). Evolution of the South Asian monsoon during the last 20 kyr recorded in lacustrine sediments from Southwestern China. *Quat. Sci.* 38, 799–820.

Stuiver, M., and Grootes, P. M. (2000). GISP2 oxygen isotope ratios. *Quat. Res.* 53, 277–284. doi: 10.1006/qres.2000.2127

Talbot, M. R., and Laerdal, T. (2000). The Late Pleistocene-Holocene palaeolimnology of Lake Victoria, East Africa, based upon elemental and isotopic analyses of sedimentary organic matter. *J. Paleolimnol.* 23, 141–164. doi: 10.1023/A:1008029400463

Wang, D., and Chen, X. (2014). The Development and Control of Geohazards in Jinkouhe Town. *Leshan. Acta Geol. Sichuan* 34, 416–420.

Wang, H., Hong, Y., Lin, Q., Hong, B., Zhu, Y., Wang, Y., et al. (2010). Response of humification degree to monsoon climate during the Holocene from the Hongyuan peat bog, eastern Tibetan Plateau. *Palaeogeogr. Palaeoclimatol. Palaeoecol.* 286, 171–177. doi: 10.1016/j.palaeo.2009.12.015

Wang, Q., Yang, X., Anderson, N. J., Zhang, E., and Li, Y. (2014). Diatom response to climate forcing of a deep, alpine lake (Lugu Hu, Yunnan, SW China) during the Last Glacial Maximum and its implications for understanding regional monsoon variability. *Quat. Sci. Rev.* 86, 1–12. doi: 10.1016/j.quascirev.2013.12.024

Wang, Y. J., Cheng, H., Edwards, R. L., An, Z. S., Wu, J. Y., Shen, C. C., et al. (2001). A High-resolution absolute-dated late pleistocene monsoon record from Hulu Cave, China. *Science* 294, 2345–2348. doi: 10.1126/science.1064618

Weltje, G. J., and Tjallingii, R. (2008). Calibration of XRF core scanners for quantitative geochemical logging of sediment cores: Theory and application. *Earth Planet. Sci. Lett.* 274, 423–438. doi: 10.1016/j.epsl.2008.07.054

Wersin, P., Hohener, P., Giovanoli, R., and Stumm, W. (1991). Early diagenetic influences on iron transformations in a freshwater lake sediment. *Chem. Geol.* 90, 233–252. doi: 10.1016/0009-2541(91)90102-W

Wu, D., Zhou, A., Chen, X., Yu, J., Zhang, J., and Sun, H. (2015). Hydrological and ecosystem response to abrupt changes in the Indian monsoon during the last glacial, as recorded by sediments from Xingyun Lake, Yunnan, China. *Palaeogeogr. Palaeoclimatol. Palaeoecol.* 421, 15–23. doi: 10.1016/j.palaeo.2015.01.005

Wu, X., Shen, J., and Wang, Y. (2011). Holocene paleoenvironmental evolution of the Huguangyan maar lake. *Mar. Geol. Quat. Geol.* 31, 155–162. doi: 10.3724/SP.J.1140.2011.04155

Xiao, X., Haberle, S. G., Shen, J., Yang, X., Han, Y., Zhang, E., et al. (2014a). Latest Pleistocene and Holocene vegetation and climate history inferred from an alpine lacustrine record, northwestern Yunnan Province, southwestern China. *Quat. Sci. Rev.* 86, 35–48. doi: 10.1016/j.quascirev.2013.12.023

Xiao, X., Haberle, S. G., Yang, X., Shen, J., Han, Y., and Wang, S. (2014b). New evidence on deglacial climatic variability from an alpine lacustrine record in northwestern Yunnan Province, Southwestern China. *Palaeogeogr. Palaeoclimatol. Palaeoecol.* 406, 9–21. doi: 10.1016/j.palaeo.2014.04.008

Xiao, X., Shen, J., Haberle, S. G., Han, Y., Xue, B., Zhang, E., et al. (2015). Vegetation, fire, and climate history during the last 18 500 cal a BP in southwestern Yunnan Province, China. *J. Quat. Sci.* 30, 859–869. doi: 10.1002/jqs.2824

Xing, W., Bao, K. S., Gallego-Sala, A. V., Charman, D. J., Zhang, Z., Gao, C., et al. (2015) . Climate controls on carbon accumulation in peatlands of Northeast China. Quat. Sci. Rev. 115, 78Ű88. doi: 10.1016/j.quascirev.2015.03.005

Xu, H., Hong, Y., Lin, Q., Zhu, Y., Hong, B., and Jiang, H. (2006). Temperature responses to quasi-100-yr solar variability during the past 6000 years based on $\delta^{18}O$ of peat cellulose in Hongyuan, eastern Qinghai–Tibet plateau, China. *Palaeogeogr. Palaeoclimatol. Palaeoecol.* 230, 155–164. doi: 10.1016/j.palaeo.2005.07.012

Xue, J., Zhong, W., and Cao, J. (2014). Changes in C3 and C4 plant abundances reflect climate changes from 41,000 to 10,000yr ago in northern Leizhou Peninsula, South China. *Palaeogeogr. Palaeoclimatol. Palaeoecol.* 396, 173–182. doi: 10.1016/j.palaeo.2014.01.003

Yan, Q. (2022). Climate change and the associated glacier response in High-Mountain Asia during the mid-Holocene: Amodeling study. *Earth Sci. Front.* 29, 372–381.

Yang, S., and Li, C. (1999). Multiple statistic study of element geochemical characteristics-element geochemical study on the Changjiang and Huanghe sendiments. *J. Mineral Petrol.* 19, 63–67.

Yu, X., Zhou, W., Franzen, L. G., Xian, F., Cheng, P., and Jull, A. J. T. (2006). High resolution peat records for Holocene monsoon history in the eastern Tibetan Plateau. *Sci. China Ser. D Earth Sci.* 49, 615–621. doi: 10.1007/s11430-006-0615-y

Zhang, E., Sun, W., Chang, J., Ning, D., and Shulmeister, J. (2018). Variations of the Indian summer monsoon over the last 30 000 years inferred from a pyrogenic carbon record from south-west China. *J. Quat. Sci.* 33, 131–138. doi: 10.1002/jqs.3008

Zhang, W., Zhang, J., and Fan, G. (2015b). Evaluation and projection of dry- and wet-season precipitation in southwestern China using CMIP5 models. *Chin. J. Atmos. Sci.* 39, 559–570.

Zhang, E., Sun, W., Zhao, C., Wang, Y., Xue, B., and Shen, J. (2015a). Linkyrges between climate, fire and vegetation in southwest China during the last 18.5kyr based on a sedimentary record of black carbon and its isotopic composition. *Palaeogeogr. Palaeoclimatol. Palaeoecol.* 435, 86–94. doi: 10.1016/j.palaeo.2015.06.004

Zhang, X., Zhang, C., Wu, D., and Zhou, A. (2015c). Element geochemistry of lake deposits measured by X-ray fluorescencecore scanner in northwest China. *Mar. Geol. Quat. Geol.* 35, 163–174.

Zhang, E., Wang, Y., Sun, W., and Shen, J. (2016). Holocene Asian monsoon evolution revealed by a pollen record from an alpine lake on the Southeastern margin of the Qinghai–Tibetan Plateau, China. *Clim. Past.* 12, 415–427. doi: 10.5194/cp-12-415-2016

Zhang, E., Zhao, C., Xue, B., Liu, Z., Yu, Z., Chen, R., et al. (2017). Millennial-scale hydroclimate variations in southwest China linked to tropical Indian Ocean since the Last Glacial Maximum. *Geology* 45, 435–438. doi: 10.1130/G38309.1

Zhang, J. (1988). Basic climatic features in Southwest China and their causes. *J. Southwest Norm. Univ.* 153–164. doi: 10.13718/j.cnki.xsxb.1988.01.025

Zhang, W. C. (2017). *Peatland sediments and Asian summer monsoon evolution in Dajiuhu Basin since the Last Glacial Maximum*. Ph.D. dissertation. Xi,an: Institute of Earth Environment, Chinese Academy of Sciences.

Zhao, L., Ma, C., Tang, L., Liu, K. B., Mao, L., Zhang, Y., et al. (2016). Investigation of peat sediments from Daiyun Mountain in southeast China: Late Holocene vegetation, climate and human impact. *Veg. Hist. Archaeobot.* 25, 359–373. doi: 10.1007/s00334-016-0554-2

Zhao, Y., Yu, Z., and Zhao, W. (2011). Holocene vegetation and climate histories in the eastern Tibetan Plateau: Controls by insolation-driven temperature or monsoon-derived precipitation changes? *Quat. Sci. Rev.* 30, 1173–1184. doi: 10.1016/j.quascirev.2011.02.006

Zheng, D., and Li, B. (1990). Evolution and differentation of the physico-geographical environment of Qinghai-Xizang Plateau. *Geogr. Res.* 9, 1–10.

Zhou, B., Wali, G., Peterse, F., and Bird, I. M. (2016). Organic carbon isotope and molecular fossil records of vegetation evolution in central Loess Plateau since 450 kyr. *Sci. China Earth. Sci.* 59, 1–10. doi: 10.1007/s11430-016-5276-x

Zhou, W., Lu, X., Wu, Z., Deng, L., Jull, A. J. T., Donahue, D., et al. (2002). Peat record reflecting Holocene climatic change in the Zoigê Plateau and AMS radiocarbon dating. *Chin. Sci. Bull.* 47, 66–70.

Zhu, L., Lu, X., Wang, J., Peng, P., Kyrsper, T., Daut, G., et al. (2015). Climate change on the Tibetan Plateau in response to shifting atmospheric circulation since the LGM. *Sci. Rep.* 5:13318. doi: 10.1038/srep13318

Zhu, Z., Mo, J., Zhang, W., Chen, J., and Zeng, Y. (2010). Oxygen isotopic composition of cellulose in sediments from lake Caohai, and its paleoenvironmental implications. *Earth Environ.* 38, 8–13.

frontiers | Frontiers in Ecology and Evolution

TYPE Original Research
PUBLISHED 01 December 2022
DOI 10.3389/fevo.2022.1046076

OPEN ACCESS

EDITED BY
Adriana Aránguiz-Acuña,
Universidad de Tarapacá,
Chile

REVIEWED BY
Shijun Jiang,
Hohai University,
China
Shailesh Agrawal,
Birbal Sahni Institute of Palaeosciences,
India

*CORRESPONDENCE
Bolong Wen
BolongWen@iga.ac.cn
Kunshan Bao
ksbao@scnu.edu.cn

SPECIALTY SECTION
This article was submitted to Paleoecology, a section of the journal Frontiers in Ecology and Evolution

RECEIVED 16 September 2022
ACCEPTED 08 November 2022
PUBLISHED 01 December 2022

CITATION
Luo N, Wen B, Bao K, Yu R, Sun J, Li X and Liu X (2022) Centennial records of Polycyclic aromatic hydrocarbons and black carbon in Altay Mountains peatlands, Xinjiang, China.
Front. Ecol. Evol. 10:1046076.
doi: 10.3389/fevo.2022.1046076

Centennial records of Polycyclic aromatic hydrocarbons and black carbon in Altay Mountains peatlands, Xinjiang, China

Nana Luo[1], Bolong Wen[1]*, Kunshan Bao[2]*, Rui Yu[2], Jing Sun[1,3], Xiujun Li[1] and Xingtu Liu[1]

[1]Key Laboratory of Wetland Ecology and Environment, Northeast Institute of Geography and Agroecology, Chinese Academy of Sciences, Changchun, China, [2]School of Geographic Sciences, South China Normal University, Guangzhou, China, [3]University of Chinese Academy of Sciences, Beijing, China

Black carbon (BC) is an important inert carbon component in the cycling process of surface carbon. Polycyclic aromatic hydrocarbons (PAHs) are a kind of thick cyclic organic compounds with carcinogenic, teratogenic, and mutagenic effects. The incomplete burning process of biomass and carbolic fuel is the important source of their co-occurrence. This study collected a 60-cm peat core from the Jiadengyu (JDY), Altay Mountain. The core was dated using the ^{210}Pb and ^{137}Cs methods. The results showed BC, total organic carbon, and PAHs of the JDY peat core to be 1.14–72.6 mgg^{-1}, 17.09–47.2%, and 260.58–1,610.77 ng·g^{-1}, respectively. $\delta^{13}C_{BC}$ was between −31.5 and −29.4‰ (mean of −30.56‰). The results of scanning electron microscopy (SEM) indicated irregular or lumpy peat BC particles, retaining a plant fiber structure. $\delta^{13}C_{BC}$, ratios of PAHs, and the SEM revealed that the BC to be the dominant source of biomass combustion in the peatland. BC showed an increasing trend between 1950 and 1980, after which it decreased. The discrepancy between the change in BC and $\delta^{13}C_{BC}$ from the national pattern of BC emission likely reflects the effect of local agricultural exploration, and thus an increase in crop burning.

KEYWORDS

peatlands, black carbon, PAHs, δ^{13} C_{BC}, Altay Mountains

Introduction

Black carbon (BC) is produced by incomplete combustion of fossil fuels or biomass in environment and plays an important role in the carbon biogeochemical process of ecosystem (Hammes et al., 2007; Ambade and Sankar, 2021; Ambade et al., 2021a). Total global BC can be broken down into residues of vegetation fires of 50–270 Tg C year $^{-1}$ (Kuhlbusch, 1995) and from the consumption of fossil fuel of 4.4 Tg C a^{-1}, showing a linear increasing trend (Bond et al., 2007). In recent years, the increased industrial and agricultural activities have significantly changed the global carbon cycle through the emission of greenhouse gases and BC particles (Kuhlbusch, 1995; Hu et al., 2020). For example, atmospheric contents of BC reached as high as 2 μg C m^{-3} in Shanghai and Beijing (China),

exceeding that in Gosan (Korea) by a factor of almost 2.5 (Chen et al., 2013).

The identification of BC sources can improve understanding of the relative effects of anthropogenic activities and regional climate change on fluxes of BC fluxes (Lehndorff et al., 2015; Sun et al., 2017).The formation and morphological structure of BC is related to the type of fuel, the temperature and duration of combustion (Preston and Schmidt, 2006). Previous methods for identifying soil BC sources included potassium dichromic oxidation, 375°C thermal oxidation, Thermal-light transmission carbon analyzer (TOT), and Thermoscopic carbon analyzer (TOT/RT), ratio between BC and total organic carbon (TOC) analysis, stable carbon isotope analysis ($\delta^{13}C_{BC}$), and scanning electron microscope observation (SEM; Gao et al., 2014; Li et al., 2019; Neupane et al., 2020). The $\delta^{13}C_{BC}$ analysis technology has been widely used in soil BC traceability analysis (Chen et al., 2013; Qi and Wang, 2019), because terrestrial plants have different stable $\delta^{13}C$ compositions, −->between −20 and −32‰ for C3 plants, and between −10 and −17‰ for C4 plants (Bird and Ascough, 2012; Kawashima and Haneishi, 2012) due to their different photosynthesis pathways of C3, C4, and CAM (Sage and Wedin, 1999). In addition, polycyclic aromatic hydrocarbons (PAHs) were usually used to identify burning sources and then indicate pyrolysis carbon sources of BC due to their co-emission from burning process (Pontevedra-Pombal et al., 2012; Ba et al., 2021). PAH ratios can act as indicators of PAH sources, with the dominant ratios being Ant/(Ant+Phe) and Fla./(Fla + Pyr), Flt/pyr (Yunker et al., 2002; Gao et al., 2018).

Black carbon is capable of absorbing and transporting PAHs, and thus forms a potential pollution source (Lohmann and Lammel, 2004; Ambade et al., 2021b). Recently, fluxes of PAHs and BC in sediment archives (e.g., peat bog and lake sediment) have been commonly utilized to reconstruct the history of regional environmental pollution and for assessing the contributions of anthropogenic and natural sources (Gao et al., 2014; Ruppel et al., 2015; Shen et al., 2020). Altay Mountain is located in the mid-high latitudes in the Alpine region, where the peat resources are abundant due to the cold and wet climate. This region is sensitive to climate change and it is gradually affected by human activities, especially with the increasing tourism. However, the research on anthropogenic impact on the wetland environment is quite limited.

The present study dated a 30-cm peat profile from Jiadengyu (JDY), Altay Mountain using the ^{210}Pb and ^{137}Cs methods, and multi-proxies including BC, 16 priorities of PAHs and $\delta^{13}C_{BC}$ were measured. The main objectives are: (1) to characterize the history of BC and PAHs fluxes in the JDY peat core; (2) to primarily reveal the main sources of BC fluxes in the Altay Mountain in China.

Materials and methods

Site description and sampling

The JDY peatland (48°30′18.72″, 87°8′27.59″; 1,600 m above the sea level) is located in the Altay Mountains Kanas Nature Reserve of the northwestern Xinjiang Uygur Autonomous Region, China (Figure 1). It is an intermontane depression with an area of about 3 km^2, and is characterized by poor drainage. It belongs to the temperate continental cold climate, with annual average temperature of −0.2°C and annual precipitation of 1065.4 mm (Zhang et al., 2018). The mountain intercepts a lot of moist air transported by westerly winds originating from the North Atlantic Ocean. The peatland receives water predominantly from glacial surface runoff and snowmelt, with a minor contribution from rainfall. Modern vegetation on the peatland is dominated by Carex and *Sphagnum* spp. The current vegetation of the study area has a meadow steppe and taiga composition and structure, respectively, and vegetation is at an altitude of between 1,500 and 2,600 m in the Altay Mountains. *Picea obovate* (spruce) and *Larix sibirica* (larch) are the dominant plant species in the taiga belt, whereas sedges and mixed grass dominate the meadow steppe belt (Forestry Bureau of Altay Mountains in Xinjiang, 2003).

In August 2019, a large block was dug up in the Jiadengyu peatland (marked as JDY). We sectioned in-site at 1-cm intervals by stainless steel knife, wrapped the sample separately with aluminum foil, and placed it in a separate polyethylene bag and then brought back to the laboratory for cryopreservation.

Physicochemical analysis

Dry bulk density, water content, and ash content analyses

The peat samples were put into the aluminum box of fixed volume, dried at 105°C over 12 h, and then weighed to obtain the water content (WC, %) and dry bulk density (DBD, $g{\cdot}cm^{-3}$). The dry samples were transferred into muffle furnace at 550°C over 4 h for complete combustion. The ash content (Ash, %) was calculated through the loss on ignition method. These physicochemical measurements and the geochemical analyses below were conducted in the Analysis and Test Center of Northeast Institute of Geography and Agroecology, Chinese Academy of Sciences (CAS).

Total organic carbon

About 1 g of dry peat samples were ground to pass 200 meshes and were digested sufficiently by 3 mol/l of HCl to fully remove the carbonate. Then, they were washed to neutral with deionized water, and dried after centrifugation. The dry samples were ground and weighed for TOC analysis by the element analyzer (Italy Euro Vector Company, EA 3000 type).

^{210}Pb and ^{137}Cs dating

Approximate 5 g dry samples of each slice were ^{210}Pb- and ^{137}Cs- dated by a γ-ray spectrometer with a low-background and high pure Ge semiconductor (ORTEC Instruments Ltd., United States). The dating was conducted at the State Key

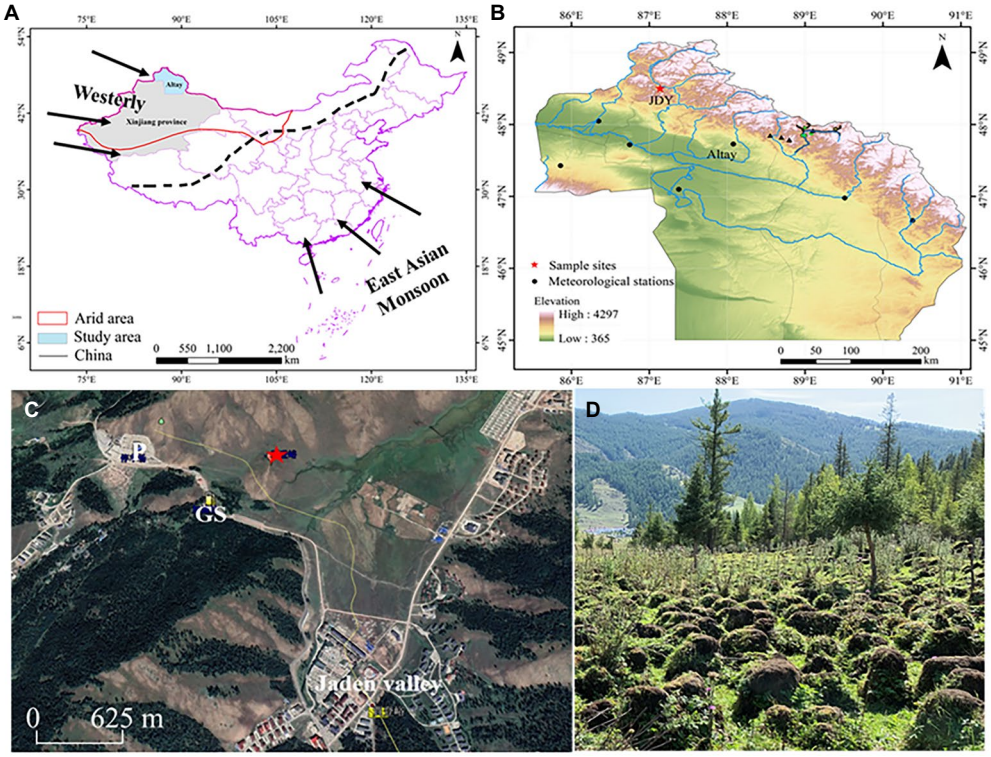

FIGURE 1
(A) China map showing the location of Jiadengyu in Northwest China and the Asian Monsoon and the Westerly; **(B)** Satellite image of the Jiadengyu valley (Google Earth) showing the location of JDY peatland (Red five pointed star) and of a car park and gas station; **(C)** Geographical map showing the sampling site in Altay Mountains, northwest China; and **(D)** Photo showing the summer scene in the studied peatland (photo in August 2019). Please refer to the Online version for the color figure.

Laboratory of Lake Science and Environment, Nanjing Institute of Geography and Limnology, CAS. Bao et al. (2010) provides a detailed explanation of the techniques of radiometric dating and equations used for calculating the peat accumulation rate (PAR) and sedimentation rate (SR).

Black carbon, $\delta^{13}C_{BC}$, and SEM- ENERGY spectrum analysis

About 1 g dry samples were treated in 10-ml HCl (1 mol/L) for 20 h to remove inorganic carbon. Then, the contents were centrifuged and the residue was digested for 20 h with 10 ml acid mixture (3 mol/L HCl + 22 mol/L HF, volumetric ratio = 1:2). Then, after centrifuging samples, the residue was soaked for 10 h in 10-ml HCl. The residue is regarded to consist of organic matter, kerogen, and BC. NaOH (30 ml, 0.1 mol/L) was applied twice for 12 h, to remove humid acid, whereas kerogen was removed by a mixed solution of 0.1 mol/L $K_2Cr_2O_7$ and 2 mol/L H_2SO_4 applied for 60 h, during which the color of the mixture was maintained as yellow. A 55°C bath was used in all steps. Residual carbon as $\delta^{13}C$ and BC was quantified using a continuous-flow isotope ratios mass spectrometer (*CF*-IRMS), comprising an EA (Flash, 2000 series) combined with a mass spectrometer (Finnigan MAT 253; Gao et al., 2014). Measurements of BC were verified against BC reference material (charred wood) manufactured by the Department of Geography, University of Zurich (Hammes et al., 2006) was used to verify the BC measurement. The particle size, morphology, and porous structure of BC were analyzed by JSM–IT 500 HR microscope (Hitachi, Tokyo, Japan), which can perfectly combine the large field optical CCD images and SEM images until the smooth operation of high magnification observation, real-time analysis, and integration of SEM and EDS. Before the observation, it is necessary to remove the carbonate and silicate in the sample (Zhan et al., 2016; Liu et al., 2019).

PAHs analysis

A 5-g sample mixed with Na_2SO_4 (20 g) was extracted using 200-ml hexane acetone (1:1, v/v) through ultra-sonication at a temperature of 35°C. Then, after concentrating the extract, the solvent was exchanged with hexane using a rotary evaporator. Separation was conducted using a Na_2SO_4-silica gel-Na_2SO_4 column under leaching of 40-mL pentane solvent. After removing aliphatic ethers with pentane, hexane dichloromethane (2:3, v/v) was used to elute PAHs. Concentration of the elution solution was repeated, the solvent was exchanged with hexane, and the solution was increased to 1 ml. The analyses were conducted using GC/MS (QP5050A). The present study adopted the standard samples of 16 priority PAHs standard mixtures of the of the SEPA Institute as

external standards for quantitative analysis, and rates of recovery rates of 80–110% were achieved (Cong et al., 2016). In order to guarantee of data quality, we have evaluated blank evolution. The mean value of Flt is 9.49 and Ant mean value is 15.48, the other 14 kinds of PAHs were not detected.

Statistical analyses

The present study calculated averages, standard deviations, and ranges of peat variables. Moreover, linear regression analysis was used to investigate the relationship between BC content in JDY peat core and TOC, PAHs, respectively. All statistical analyses were conducted in SPSS 22. $p < 0.05$ was assumed to indicate statistical significance.

Results

Physicochemical properties of peat samples

The DBD and Ash showed similar variation with depth. They had a major peak in 7–11 cm section. The WC and TOC were correlated and their depth variations were contrast with the DBD and Ash (Figure 2). The DBD value varied from 0.12 to 0.29 g cm^{-3}, and the mean value was 0.17 g cm^{-3} of the whole peat core. The DBD at 18–60 cm (mean: 0.16 g cm^{-3}) were lower than those at 1–11 cm (mean: 0.21 g cm^{-3}). The Ash ranged between 11.9 and 65.31%, with an average of 33.73% of the whole peat core. In addition, Ash (mean: 28.96%) at 18–60 cm were lower than those at 1–11 cm (mean: 55.45%). The TOC of whole peat core ranged from 17.09 to 47.2%, with an average value of 35.3% and the highest value was 47.2% at 18 cm and the lowest value (17.09%) at 11 cm. The WC ranged between 47.09 and 72.95% and the average was 62.51% of the whole peat core.

Lithological characteristics of peat section and main plant residues

According to the change of peat color, residue type, and decomposition degree, the 60 cm continuous peat core lithology was roughly divided into three layers from top to bottom as follows. The first layer is grass cortex at 0–7 cm, with vegetation coverage of about 80%. The grass roots are dense and contain green plants. The second is humus layer (7–18 cm), which is characterized by the poor decomposition, mainly in the incomplete decomposition of liverworts and mosses, modern plants with dense roots, dark brown loam soil, granular structure, loose, more roots. The third is the peat layer: 18–30 cm, dark brown, loamy to clay, granular or blocky, with more capillarity; 30–48 cm, dark brown silty clay, slightly compact, less root system; and below 48 cm, brown clay, and almost no roots.

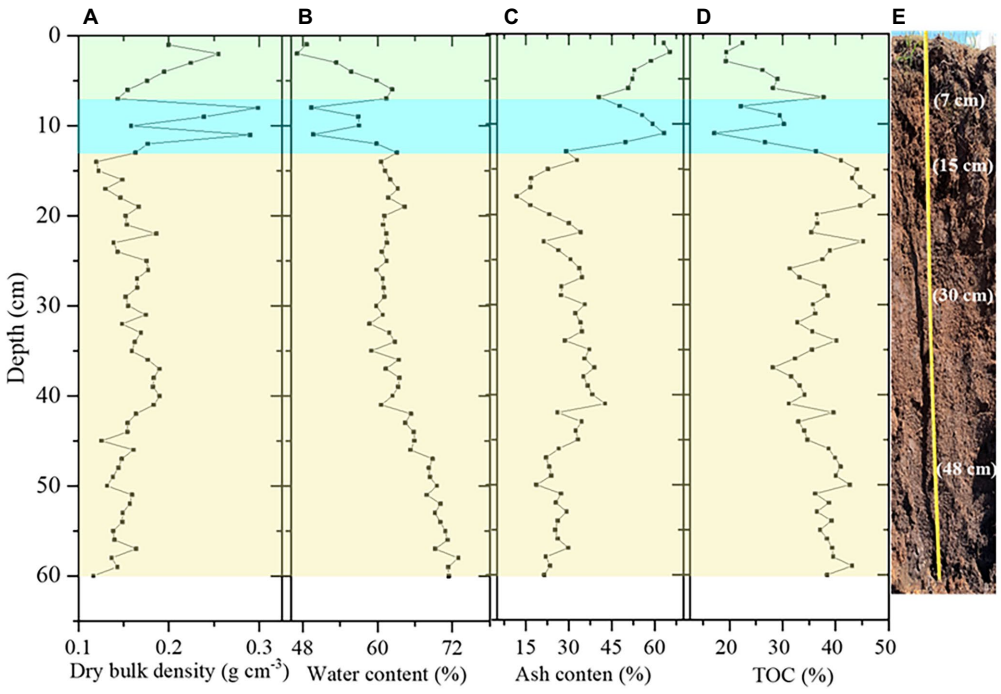

FIGURE 2
The depth profiles of dry bulk density **(A)**, water content **(B)**, ash content **(C)**, TOC **(D)** and the core section of the peat column **(E)** in the JDY peat core in Altay Mountains, NW China.

Peat chronology

The ^{210}Pb activity decreased with depth in JDY peat profile (Figure 3). Rates of sedimentation and sediment ages were calculated utilizing the CRS Model in MATLAB 2012a. The activities of ^{210}Pb decreased with depth downward. The peat record extended back by 134 years to A.D. 1883. The mean SR was 0.15 cm y^{-1} and the PAR is 0.025 g·cm^{-2} y^{-1}.

Temporal variation of BC, $\delta^{13}C_{BC}$, and PAHs

The average BC content was 25.55 mg g^{-1}, with a range of 1.14–72.6 mg g^{-1} in the JDY peat core. The range of $\delta^{13}C_{BC}$ was from −31.5 to −29.4‰ with a mean of −30.6‰. During 1880–1950, the BC and $\delta^{13}C_{BC}$ consistently showed a trend of fluctuation change with first increase and then decrease (Figures 4A,B). From 1950 to 1980, the BC and $\delta^{13}C_{BC}$ showed an obviously decrease trend.

During the period of 1980–2000, the BC and $\delta^{13}C_{BC}$ showed an obviously increase trend. After 2000, the BC decreased obviously with time but the $\delta^{13}C_{BC}$ did not show consistent variation with the BC. The total PAHs in JDY peat core were 260.59–1610.77 ng g^{-1}, and showed similar variation trend with the BC (Figures 4A,C). After 2000, the PAHs showed a decreased trend.

PAHs composition

The PAHs was mainly composed of low molecular weight compounds (2–3 rings), and the content of Nap, Any, Flu, and Phe content was the highest (Figure 5). In general, the period of 1950–1980 had the highest values. The content of Nap, Phe, Flu, and Any prior to the 1950 ($n = 10$) was lower than that during 1950–1980 ($n = 16$), and the content of Nap and Any was the lowest after 1980 ($n = 34$). The concentration of high molecular weight PAHs (IcP, BaP, and DhA) prior to the 1950 ($n = 10$) was lower than the periods 1950–1980 ($n = 16$), after 1980 ($n = 34$), the content was the lowest. For middle molecular weight PAHs (BaA, Chr), BaA value was the lowest in the three periods, and Chr value was the highest in the period from 1950 to 1980. whereas for the Flt and Pyr higher content during 1950–1980 was compared to those before 1950 and after 1980.

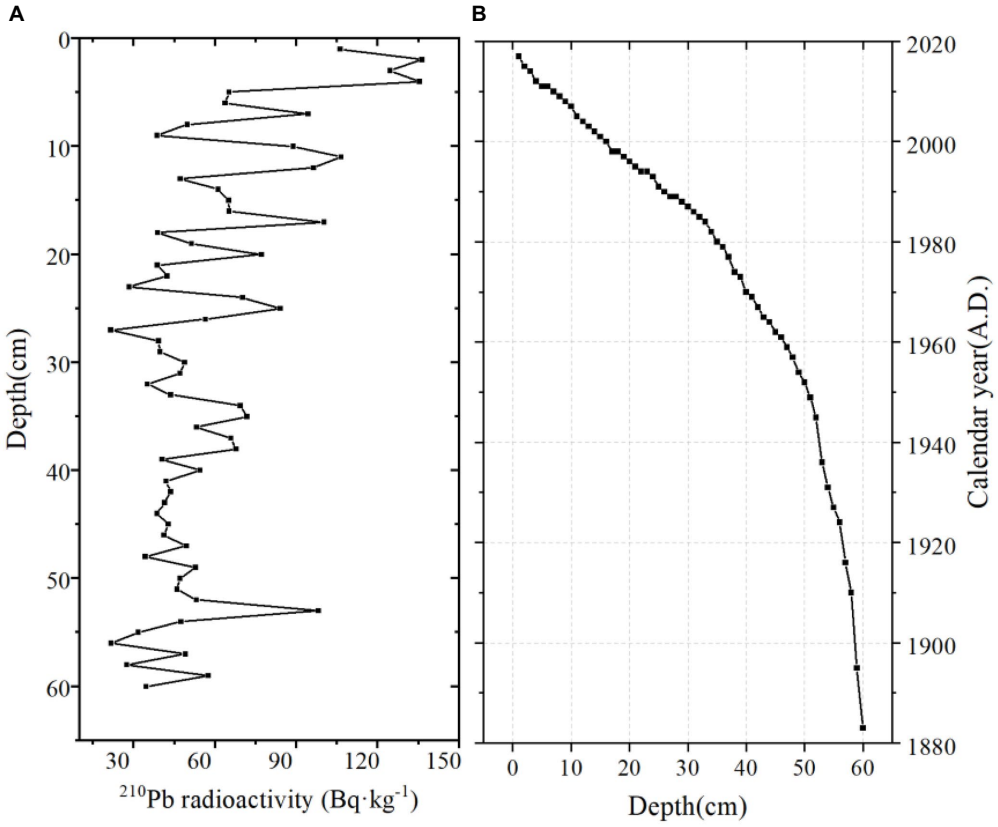

FIGURE 3
Radioactivity results for ^{210}Pb **(A)**, and the CRS calculated age **(B)**, of the JDY peat core in Altay Mountains, NW China.

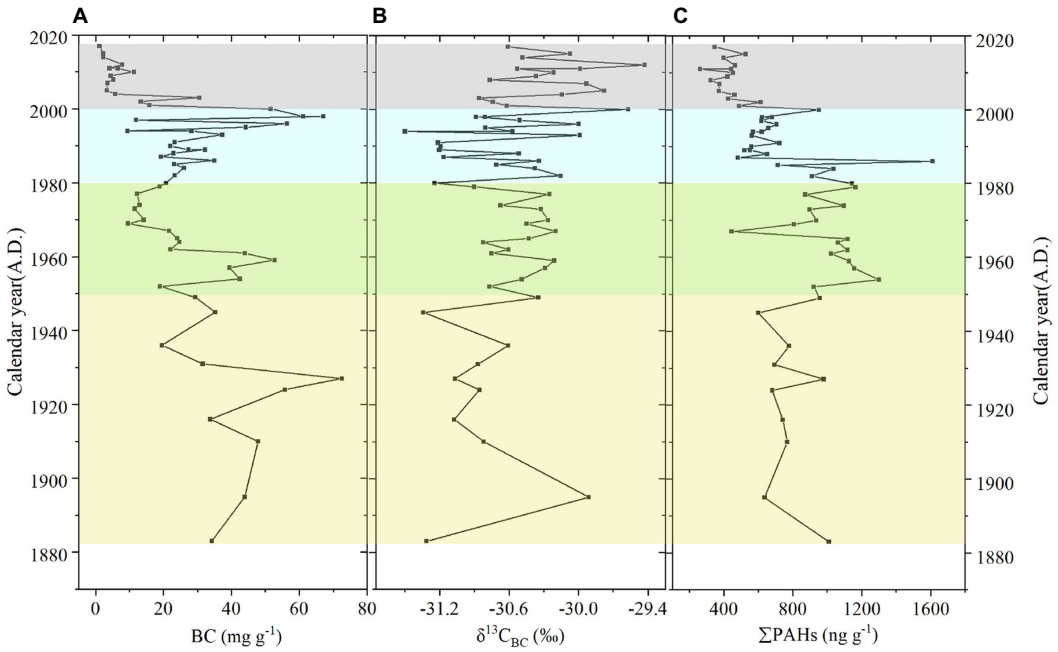

FIGURE 4
The contents of BC **(A)**, $\delta^{13}C_{BC}$ **(B)**, ratios, and the total PAHs content **(C)**, in the core of JDY.

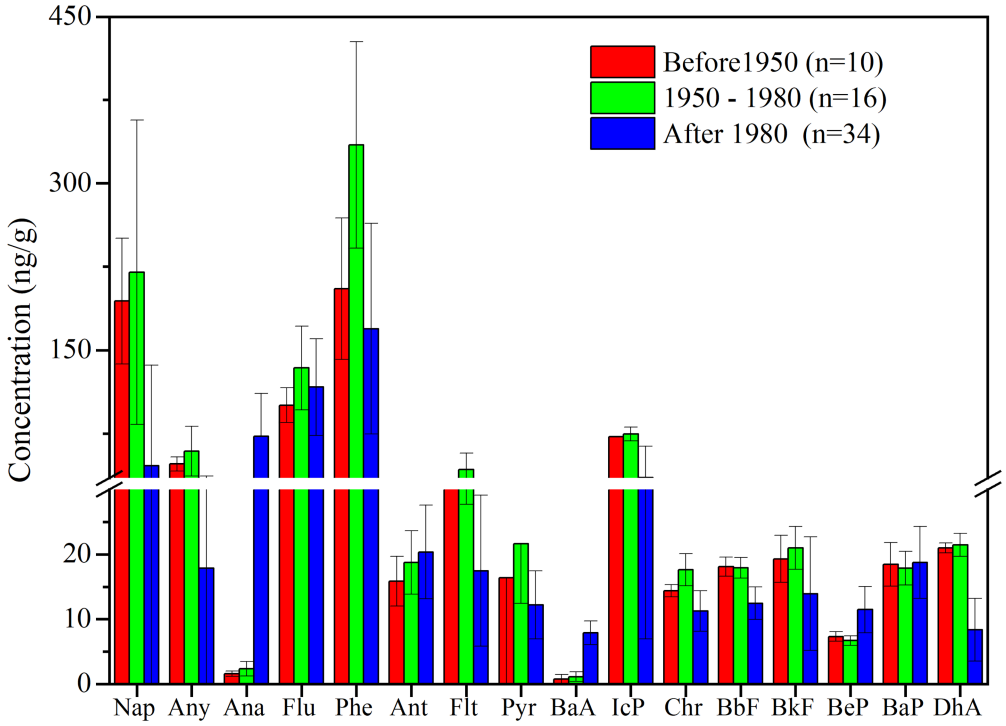

FIGURE 5
Profiles of PAHs in sediments from the JDY peat core, grouped according to the three periods. Nap, Naphthalene; Any, Acenaphthylene; Ana, Acenaphthene; Flu, Fluorene; Phe, Phenanthrene; Ant, Anthracene; Flt, Fluoranthene; Pyr, Pyrene; Chr, Chrysene; BaA, Benzo(a) anthracene; BbF, Benzo(b)fluoranthene; BkF, Benzo(k)fluoranthene; BeP, Benzo(e)pyrene; BaP, Benzo(a)pyrene; DhA, Dibenz[a,h] anthracene; and IcP, Ideno(1,2,3-cd) pyrene.

Discussion

Comparison of black carbon over the world

The mean BC content in the JDY peat profile was 21.06 mg g^{-1}, which was similar with the average BC content of 24.85 mg g^{-1} in Tuqiang peat in Great Hinggan Mountains, China (Cong et al., 2016). In order to better explain the deposition characteristics and sources of BC we compared to other soils (e.g., forest soil and loess) and sediments (e.g., lake sediment and coastal sediment), contents of BC in the peats were the highest (Table 1), and represented a key stable part of the Earth's soil carbon pool. The BC content in Nam Co Lake region (Tibetan Plateau, China) was most likely influenced by economic development in South Asia (Wang et al., 2005). In Changbai Mountain (Northeastern of China), local BC emission strongly influences the level and gradient of BC in the snowpack. Peatland, with slow degradation in anaerobic environment and continuous deposition process, is an ideal archive for recording the BC deposition history. Historical anthropogenic sources (e.g., residential and biomass burning) and natural sources (e.g., wildfire) caused more BC emitted and raised BC deposition fluxes. While, land drained and smoldering might lead BC modified in peat soils. It is necessary to study historical BC deposition progress and its influence factors in peatland, while, few studies had been reported.

TABLE 1 The black carbon contents (mg g^{-1}) for different deposition archives.

Types	Region	Contents (mg g^{-1})	Reference
Peatland	Altay Mountain, China	1.14–67.13	This study
Peatland	Sanjiang Plain, China	3.2–61.2	Gao et al. (2014)
Forest soil	Amazon, Brazilian	1–27	Cordeiro et al. (2002)
Loess	Loess Plateau, China	1–5	Wang et al. (2005)
Lake sediments*	Taihu, China	0.43–1.95	Han et al. (2010)
Lake sediments	Tibetan Plateau, China	0.49–1.09	Cong et al. (2013)
Continentals shell*	Palos Verdes Shelf, United States	1.2	Gustafsson and Gschwend (1998)
Continentals shell	Gulf of Marine, England	0.3–1.7	Gustafsson and Gschwend (1998)
Pelagic sediments	Global	0.02–1	Smith et al. (1973)

*The lake is near urban.

TABLE 2 Source discrimination indicators of PAHs in Jiadengyu peatlands in the Altay Mountains.

Discrimination indicators	Value	Possible sources
Fla/(Fla + Pyr)	<0.4	Petroleum
	0.4–0.5	Fossil fuel combustion
	>0.5	Wood and biomass burning
Ant/(Ant+Phe)	>0.1	Fuel, coal, and wood burning
	<0.1	Petroleum
Flt/Pyr	>1	Combustion source
	<1	Petroleum

Black carbon source identified by multi-proxies

The $\delta^{13}C_{BC}$ values of C3 plant combustion are generally lower than −27‰, and those of fossil fuel combustion range from −23 to −26‰ (Bird and Ascough, 2012; Saiz et al., 2015) and the $\delta^{13}C$ values in automobile exhaust gas range from −22 to −25‰ (Glaser et al., 2005). Here the $\delta^{13}C_{BC}$ in the JDY peat core varied from −29.4 to −31.5‰, with an average of −30.52‰, which is in the range of C3 plant burning type (−27 to −33‰). Therefore, the BC in the JDY peatland is dominantly from C3 plants burning.

The same pyrolysis sources always concurrently emit PAHs and BC. Therefore, the proportion contributions of different sources of PAHs can be utilized to calculate the proportion of BC sources (Yunker et al., 2002; Bucheli et al., 2004; Cao et al., 2020). It can be obtained from Table 2, the ratios of Flt/Pyr > 1, Fla./(Fla + Pyr) > 0.5, and Ant/(Ant+Phe) > 0.1 indicate that PAHs are mainly from biomass combustion (Yunker et al., 2002; Gao et al., 2018). In this study, the Flt/Pyr ratio, Fla./(Fla + Pyr), and Ant/(Ant+Phe) averages were 1.73, 0.56, and 0.13, respectively (Figure 6). Therefore, the main source of PAHs is biomass combustion in JDY profile, which is consistent with the main source revealed by the $\delta^{13}C_{BC}$ values.

Previous studies found that the BC particles emitted by diesel vehicle combustion were less than 50 nm and spherical in shape, with an agglomeration and long chain (Accardidey, 2003; Wang et al., 2015). The particle size and morphology of BC particles derived from gasoline vehicles are similar to those of diesel vehicles, but the polymerization is more obvious. BC particles emitted by coal burning are generally porous and not spherical in shape (Zhan et al., 2016). BC particles from biomass combustion releases have an irregular or lumpy shape and retain a plant fiber structure (porous or tubular; Masiello, 2004). The BC of samples at depths of 18 and 28 cm was lumpy or irregular in shape, which retained the structure of plant fibers (porous or tubular; Figure 7A,B), and indicated the effects of biomass combustion.

Black carbon temporal variation

Compared with the regional background of China's BC emissions (Gao et al., 2014), this study attempts to analyze the BC emission pattern in the Altay region during the last 150 years. The concentration of BC emissions in China has been increasing, especially after 1980, which is mainly controlled by the increase of

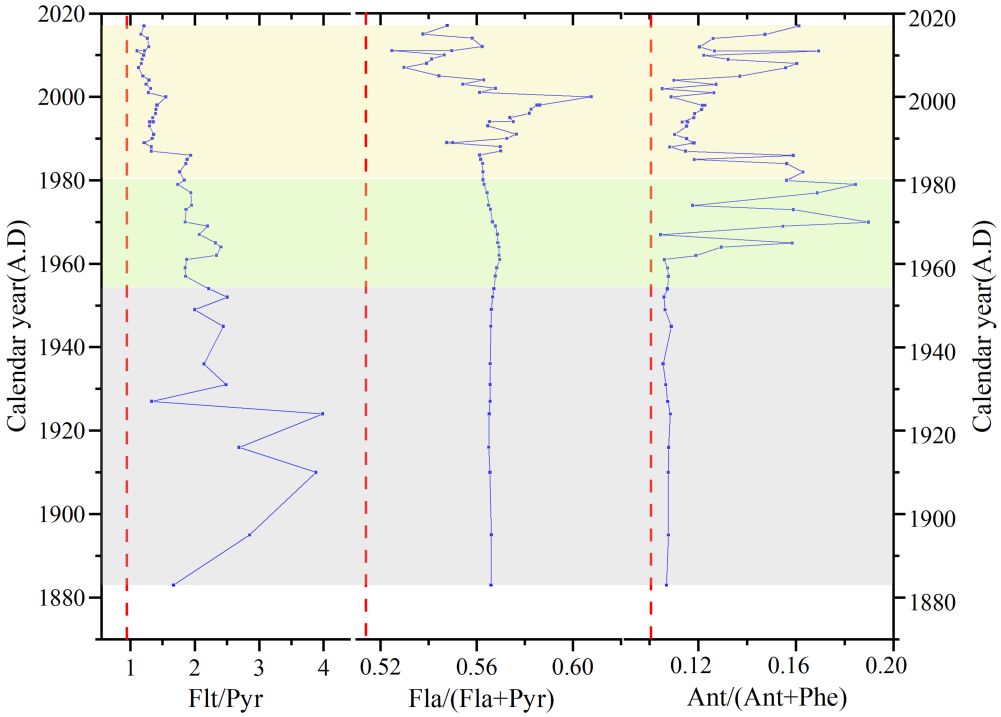

FIGURE 6
Variation of ratios of Flt/Pyr, Fla/(Fla+Pyr), and Ant/(Ant+Phe) in JDY peat core. The dashed lines indicated the boundaries for source assignments of PAHs after (Yunker et al., 2002).

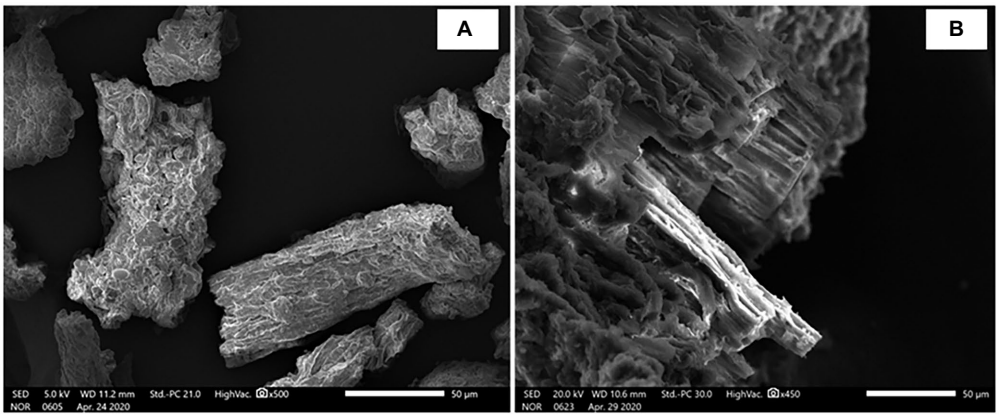

FIGURE 7
SEM images of BC examples from different samples. All scale bars represent 50 μm. **(A)** represents BC from biomass burning particles (BBP); **(B)** represents wood burning.

industrial emissions (Figure 8A; Gao et al., 2014). However, the changes of BC content and BC flux in JDY show an increasing trend before 1980 but a decreasing trend after 1980 (Figure 8B). This is because the BC in JDY peat profile is mainly from biomass combustion, as discussed above. It was reported that the cultivated land area in 1949 from 9.43 km^2 increased to 115.29 km^2 in 1980 in Altay area (Statistics XUARBo, 2018). As a result, BC content in the JDY peatland significantly increased from 1950 to 1980. The decrease in the BC record in the peat is probably a response to the increasing regional environmental protection.

Conclusion

The average accumulation rate of BC in JDY peatland was 0.025 $g \cdot cm^{-2}$ $year^{-1}$ since the 1880s. The range of $\delta^{13}C_{BC}$ was from

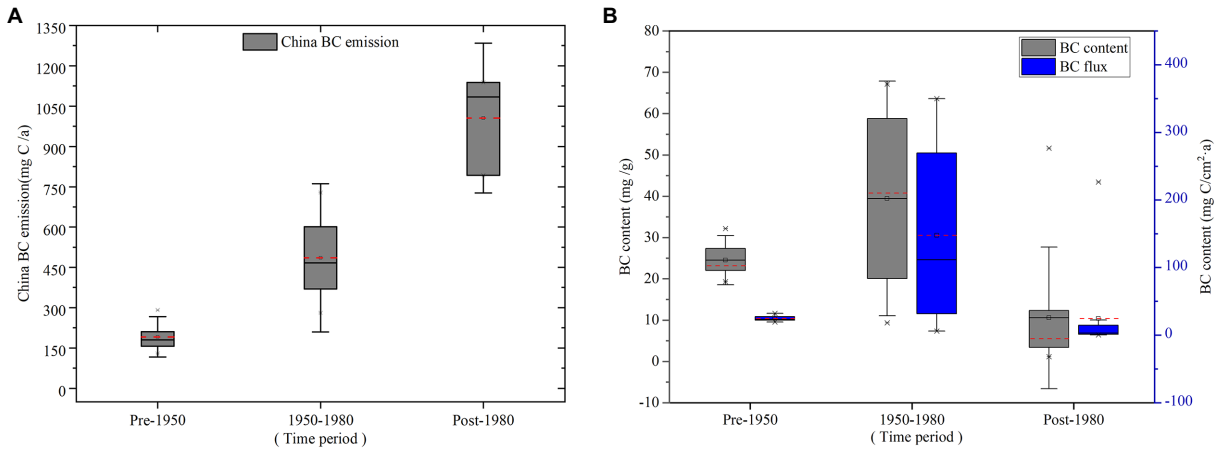

FIGURE 8
(A) Variation of China BC emission from different period, **(B)** BC content and BC flux from 1860 to 2019 in JDY peat core.

31.5 to −29.4‰. The results of SEM, $\delta^{13}C_{BC}$, and the ratios of PAHs indicated that the dominant source of BC was the burning of C3 plants. The historical variations in BC content and flux were different from the national BC emission pattern in China. The JDY peat recorded an increase of BC emission in 1950–1980 probably due to the agricultural exploration and thus increasing crop burning. The decrease in the peat BC record after 1980 would be related to the increasing environmental protection.

Data availability statement

The original contributions presented in the study are included in the article/supplementary material, further inquiries can be directed to the corresponding authors.

Author contributions

NL and KB: writing—original draft and writing—review. BW and XL: conceptualization, methodology, and supervision. RY and JS: methodology and investigation. All authors contributed to the article and approved the submitted version.

Funding

This research was funded by the National Basic Research Program of China (no. 2013FY111800), National Nature Science Foundation of China (no. 41971113), the Science and Technology Development Program of Jilin Province (Support Xinjiang), National Natural Science Foundation of China (no. 41701372), and Natural Science Foundation of Jilin Province (no. 20190103161JH).

Acknowledgments

The authors gratefully acknowledge the assistance of the Analysis and Test Center of the Northeast Institute of Geography and Agroecology, CAS.

Conflict of interest

The authors declare that the research was conducted in the absence of any commercial or financial relationships that could be construed as a potential conflict of interest.

Publisher's note

References

Accardidey, A. M. (2003). Black carbon in marine sediments: quantification and implications for the sorption of polycyclic aromatic hydrocarbons. *Massach. Instit. Technol.* 20, 171–177. doi: 10.1111/j.1748-1090.1980.tb00961.x

Ambade, B., Kurwadkar, S., Sankar, T. K., and Kumar, A. (2021a). Emission reduction of black carbon and polycyclic aromatic hydrocarbons during COVID-19 pandemic lockdown. *Air Qual. Atmos. Health* 14, 1–15. doi: 10.1007/s11869-021-01004-y

Ambade, B., and Sankar, T. K. (2021). Source apportionment and health risks assessment of black carbon aerosols in an urban atmosphere in East India. *J. Atmos. Chem.* 78, 177–191. doi: 10.1007/s10874-021-09418-9

Ambade, B., Sankar, T. K., Kumar, A., Gautam, A. S., and Gautam, S. (2021b). COVID-19 lockdowns reduce the black carbon and polycyclic aromatic hydrocarbons of the Asian atmosphere: source apportionment and health hazard evaluation. *Environ. Dev. Sustain.* 23, 12252–12271. doi: 10.1007/s10668-020-01167-1

Ba, A., Sss, A., Sk, B, Ak, A., and Tks, A. (2021). Toxicity and health risk assessment of polycyclic aromatic hydrocarbons in surface water, sediments and groundwater vulnerability in Damodar River basin. *Groundw. Sustain. Dev.* 13, 1–12. doi: 10.1016/j.gsd.2021.100553

Bao, K., Jia, L., Lu, X., and Wang, G. (2010). Grain-size characteristics of sediment in Daniugou peatland in Changbai Mountains, Northeast China: implications for atmospheric dust deposition. *Chin. Geogr. Sci.* 20, 498–505. doi: 10.1007/s11769-010-0427-z

Bird, M. I., and Ascough, P. L. Isotopes in pyrogenic carbon: a review. *Org. Geochem.* 42, 1529–1539. doi: 10.1016/j.orggeochem.2010.09.005

Bond, T. C., Bhardwaj, E., Dong, R., Jogani, R., Jung, S., Roden, C., et al. (2007). Historical emissions of black and organic carbon aerosol from energy-related combustion, 1850-2000. *Glob. Biogeochem. Cycles* 21. doi: 10.1029/2006GB002840

Bucheli, T. D., Blum, F., Desaules, A., and Gustafsson, O. (2004). Polycyclic aromatic hydrocarbons, black carbon, and molecular markers in soils of Switzerland. *Chemosphere* 56, 1061–1076. doi: 10.1016/j.chemosphere.2004.06.002

Cao, W., Geng, SY., Zou, J., Wang, Y. Y., Guo, Y. Q., Zhu, Y., et al. (2020). Post relocation of industrial sites for decades: ascertain sources and human risk assessment of soil polycyclic aromatic hydrocarbons. *Ecotoxicol. Environ. Saf.* 198, 1–9. doi: 10.1016/j.ecoenv.2020.110646

Chen, B., Andersson, A., Lee, M., Kirillova, E. N., Xiao, Q. F., Krusa, M., et al. (2013). Source forensics of black carbon aerosols from China. *Environ. Sci. Technol.* 47, 9102–9108. doi: 10.1021/es401599r

Cong, J. X., Gao, C. Y., Zhang, Y., Zhang, S. Q., He, J. B., and Wang, G. P. (2016). Dating the period when intensive anthropogenic activity began to influence the Sanjiang plain, *Sci. Rep.* 6, 1–9. doi: 10.1038/srep22153

Cong, Z., Kang, S., Gao, S., Zhang, Y., Li, Q., and Kawamura, K. (2013). Historical trends of atmospheric black carbon on Tibetan plateau as reconstructed from a 150-year Lake sediment record. *Environ. Sci. Technol.* 47, 2579–2586. doi: 10.1021/es3048202

Cordeiro, R. C., Turcq, B., Ribeiro, M. G., Lacerda, L. D., Capitaneo, J., da Silva, A. O., et al. (2002). Forest fire indicators and mercury deposition in an intense land use change region in the Brazilian Amazon (Alta Floresta, MT). *Sci. Total Environ.* 293, 247–256. doi: 10.1016/s0048-9697(02)00045-1

Forestry Bureau of Altay Mountains in Xinjiang (2003). *Comprehensive scientific investigation of two river sources in Xinjiang Altai mountain nature reserve of China*. Urumqi: Xinjiang Science and Technology Press.

Gao, C., Lin, Q., Zhang, S., He, J., and Wang, G. (2014). Historical trends of atmospheric black carbon on Sanjiang plain as reconstructed from a 150-year peat record. *Sci. Rep.* 4:5723

Gao, C., Liu, H., Cong, J., Han, D., Zhao, W., Lin, Q., et al. (2018). Historical sources of black carbon identified by PAHs and delta C-13 in Sanjiang plain of northeastern China. *Atmos. Environ.* 181, 61–69. doi: 10.1016/j.atmosenv.2018.03.026

Glaser, B., Dreyer, A., Bock, M., Fiedler, S., Mehring, M., and Heitmann, T. (2005). Source apportionment of organic pollutants of a highway-traffic-influenced urban area in Bayreuth (Germany) using biomarker and stable carbon isotope signatures. *Environ. Sci. Technol.* 39, 3911–3917. doi: 10.1021/es050002p

Gustafsson, O., and Gschwend, P. M. (1998). The flux of black carbon to surface sediments on the New England continental shelf. *Geochim. Cosmochim. Acta* 62, 465–472. doi: 10.1016/S0016-7037(97)00370-0

Hammes, K., Schmidt, M. W. I., Smernik, R. J., Currie, L. A., Ball, W. P., Nguyen, T. H., et al. (2007). Comparison of quantification methods to measure fire-derived (black/elemental) carbon in soils and sediments using reference materials from soil, water, sediment and the atmosphere. *Glob. Biogeochem. Cycles* 21, 1–18. doi: 10.1029/2006gb002914

Hammes, K., Smernik, R. J., Skjemstad, J. O., Herzog, A., Vogt, U. F., and Schmidt, M. W. I. (2006). Synthesis and characterisation of laboratory-charred grass straw (Oryza saliva) and chestnut wood (Castanea sativa) as reference materials for black carbon quantification. *Org. Geochem.* 37, 1629–1633. doi: 10.1016/j.orggeochem.2006.07.003

Han, Y., Cao, J., Jin, Z., Liu, S., and An, Z. (2010). Comparison of char and soot variations in sediments from Daihai and Taihu Lakes. *Q. Sci.* 30, 550–558. doi: 10.3969/j.issn.1001-7410.2010.03.13

Hu, K., Zhao, D. L, Liu, D. T, Ding, S., Tian, P., Yu, C. J, et al. (2020). Estimating radiative impacts of black carbon associated with mixing state in the lower atmosphere over the northern North China plain. *Chemosphere* 252, 1–13. doi: 10.1016/j.chemosphere.2020.126455

Kawashima, H., and Haneishi, Y. (2012). Effects of combustion emissions from the Eurasian continent in winter on seasonal δ~(13)C of elemental carbon in aerosols in Japan. *Atmos. Environ.* 46, 568–579. doi: 10.1016/j.atmosenv.2011.05.015

Kuhlbusch, T. A. J. (1995). Method for determining black carbon in residues of vegetation fires. *Environ. Sci. Technol.* 29, 2695–2702. doi: 10.1021/es00010a034

Lehndorff, E., Brodowski, S., Schmidt, L., Haumaier, L., Grootes, P. M., Rethemeyer, J., et al. (2015). Industrial carbon input to arable soil since 1958. *Org. Geochem.* 80, 46–52. doi: 10.1016/j.orggeochem.2015.01.003

Li, R., Han, Y., Wang, L., Shang, Y., and Chen, Y. J. (2019). Differences in oxidative potential of black carbon from three combustion emission sources in China. *J. Environ. Manag.* 240, 57–65. doi: 10.1016/j.jenvman.2019.03.070

Liu, H., Meng, Z.-H., Lv, Z.-F., Wang, X.-T., Deng, F.-Y., Liu, Y., et al. (2019). Emissions and health impacts from global shipping embodied in US-China bilateral trade. *Nat. Sustain.* 2, 1027–1033. doi: 10.1038/s41893-019-0414-z

Lohmann, R., and Lammel, G. (2004). Adsorptive and absorptive contributions to the gas-particle partitioning of polycyclic aromatic hydrocarbons:? State of knowledge and recommended Parametrization for modeling. *Environ. Sci. Technol.* 38, 3793–3803. doi: 10.1021/es035337q

Masiello, C. A. (2004). New directions in black carbon organic geochemistry. *Mar. Chem.* 92, 201–213. doi: 10.1016/j.marchem.2004.06.043

Neupane, B., Wang, J., Kang, S., Zhang, Y., Chen, P., Rai, M., et al. (2020). Black carbon and mercury in the surface sediments of Selin co, central Tibetan plateau: Covariation with total carbon. *Sci. Total Environ.* 721, 1–10. doi: 10.1016/j.scitotenv.2020.137752

Pontevedra-Pombal, X., Rey-Salgueiro, L., Garcia-Falcon, M. S., Martinez-Carballo, E., Simal-Gandara, J., and Martinez-Cortizas, A. (2012). Pre-industrial accumulation of anthropogenic polycyclic aromatic hydrocarbons found in a blanket bog of the Iberian Peninsula. *Environ. Res.* 116: 36–43. doi: 10.1016/j.envres.2012.04.015

Preston, C. M., and Schmidt, M. W. I. (2006). Black (pyrogenic) carbon: a synthesis of current knowledge and uncertainties with special consideration of boreal regions. *Biogeosciences* 3: 397–420. doi: 10.5194/bg-3-397-2006

Qi, L., and Wang, S. X. (2019). Fossil fuel combustion and biomass burning sources of global black carbon from GEOS-Chem simulation and carbon isotope measurements. *Atmos. Chem. Phys.* 19, 11545–11557. doi: 10.5194/acp-19-11545-2019

Ruppel, M. M., Gustafsson, O., Rose, N. L., Pesonen, A., Yang, H. D., Weckstrom, J., et al. (2015). Spatial and temporal patterns in black carbon deposition to dated Fennoscandian Arctic Lake sediments from 1830 to 2010. *Environ. Sci. Technol.* 49, 13954–13963. doi: 10.1021/acs.est.5b01779

Sage, R. F., and Wedin, D. A. (1999). The biogeography of C4 photosynthesis: Patterns and controlling factors.

Saiz, G., Wynn, J. G., Wurster, C. M., Goodrick, I., Nelson, P. N., and Bird, M. I. (2015). Pyrogenic carbon from tropical savanna burning: production and stable isotope composition. *Biogeosciences* 12, 1849–1863. doi: 10.5194/bg-12-1849-2015

Shen, X., Wang, P., Zhang, X., Cao, X., Shi, Y., Li, X., et al. (2020). Real-time measurements of black carbon and other pollutant emissions from residential biofuel stoves in rural China. *Sci. Total Environ.* 727:138649. doi: 10.1016/j.scitotenv.2020

Smith, D. M, Griffin, J. J., and Golderg, E. D. (1973). Elemental carbon in marine sediments: a baseline for burning. *Nature* 241, 268–270. doi: 10.1038/241268a0

Statistics XUARBo (2018). Xinjiang statistical yearbook.

Sun, W. W., Zhang, E. L., Liu, E. F., Ji, M., Chen, R., Zhao, C., et al. (2017). Oscillations in the Indian summer monsoon during the Holocene inferred from a stable isotope record from pyrogenic carbon from Lake Chenghai, Southwest China. *J. Asian Earth Sci.* 134, 29–36. doi: 10.1016/j.jseaes.2016.11.002

Wang, H. L., Nie, L., Liu, D., Gao, M. P., Wang, M. Y., and Hao, Z. P. (2015). Physico-chemical characterization and source tracking of black carbon at a suburban site in Beijing. *J. Environ. Sci.* 33, 188–194. doi: 10.1016/j.jes.2015.05.001

Wang, X., Peng, P. A., and Ding, Z. L. (2005). Black carbon records in Chinese loess plateau over the last two glacial cycles and implications for paleofires. *Palaeogeogr. Palaeoclimatol. Palaeoecol.* 223: 9–19. doi: 10.1016/j.palaeo.2005.03.023

Yunker, M. B., Macdonald, R. W., Vingarzan, R., Mitchell, R. H., Goyette, D., and Sylvestre, S. (2002). PAHs in the Fraser River basin: a critical appraisal of PAH ratios as indicators of PAH source and composition. *Org. Geochem.* 33, 489–515. doi: 10.1016/S0146-6380(02)00002-5

Zhan, C., Wan, D., Zhang, J., Han, Y., Cao, J., and Liu, X. (2016). Source apportionment of black carbon in the environment: a review of methods. *Ecol. Environ. Sci.* 25, 1575–1583. doi: 10.16258/j.cnki.1674-5906.2016.09.023

Zhang, Y., Ma, X., Liu, X., Tong, C., and Yang, P. (2018). Preliminary study on the morphology, development process and peat accumulation rate of palsas during the holocene in the Altai mountains, northern Xinjiang autonomous region, Northwest China. *Q. Sci.* 38, 1221–1232. doi: 10.11928/j.issn.10017410.2018.05.16

frontiers | Frontiers in Ecology and Evolution

TYPE Erratum
PUBLISHED 13 February 2023
DOI 10.3389/fevo.2023.1152271

OPEN ACCESS

APPROVED BY
Frontiers Editorial Office,
Frontiers Media SA, Switzerland

*CORRESPONDENCE
Frontiers Production Office
✉ production.office@frontiersin.org

SPECIALTY SECTION
This article was submitted to Paleoecology, a section of the journal Frontiers in Ecology and Evolution

RECEIVED 27 January 2023
ACCEPTED 27 January 2023
PUBLISHED 13 February 2023

CITATION
Frontiers Production Office (2023) Erratum: Centennial records of polycyclic aromatic hydrocarbons and black carbon in Altay Mountains peatlands, Xinjiang, China. *Front. Ecol. Evol.* 11:1152271. doi: 10.3389/fevo.2023.1152271

Erratum: Centennial records of polycyclic aromatic hydrocarbons and black carbon in Altay Mountains peatlands, Xinjiang, China

Frontiers Production Office*

Frontiers Media SA, Lausanne, Switzerland

KEYWORDS

peatlands, black carbon, PAHs, $\delta^{13}C_{BC}$, Altay Mountains

An Erratum on
Centennial records of polycyclic aromatic hydrocarbons and black carbon in Altay Mountains peatlands, Xinjiang, China

by Luo, N., Wen, B., Bao, K., Yu, R., Sun, J., Li, X., and Liu, X. (2022). *Front. Ecol. Evol.* 10:1046076. doi: 10.3389/fevo.2022.1046076

Due to a production error, there was a mistake in Figure 4 as published. An incorrect image was published as Figure 4. The corrected Figure 4 appears below.

The publisher apologizes for this mistake. The original version of this article has been updated.

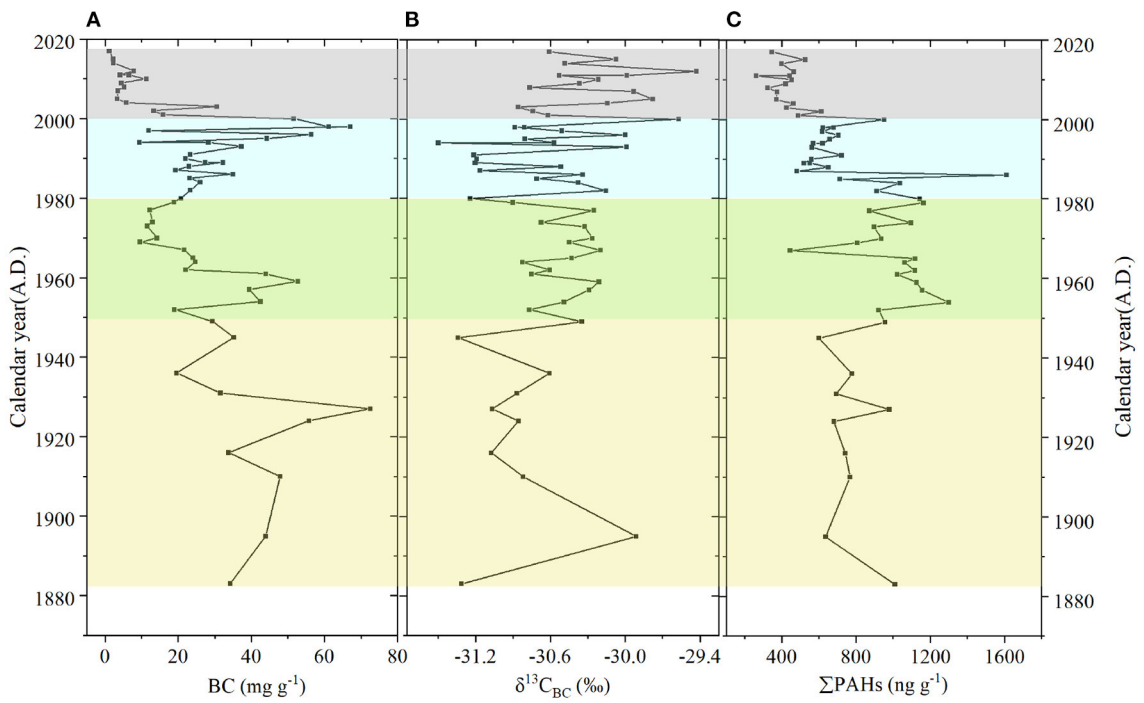

FIGURE 4
The contents of BC **(A)**, $\delta^{13}C_{BC}$ **(B)**, ratios, and the total PAHs content **(C)**, in the core of JDY.

frontiers | Frontiers in Ecology and Evolution

TYPE Original Research
PUBLISHED 24 January 2023
DOI 10.3389/fevo.2023.1119840

OPEN ACCESS

EDITED BY
Kunshan Bao,
South China Normal University,
China

REVIEWED BY
Yuxin He,
Zhejiang University,
China
Xuhui Dong,
Guangzhou University,
China

*CORRESPONDENCE
Xiangzhen Kong
✉ xzkong@niglas.ac.cn
Longjuan Cheng
✉ longjuan822@ntu.edu.cn

SPECIALTY SECTION
This article was submitted to Paleoecology, a section of the journal Frontiers in Ecology and Evolution

RECEIVED 09 December 2022
ACCEPTED 06 January 2023
PUBLISHED 24 January 2023

CITATION
Zhang C, Kong X, Xue B, Zhao C, Yang X, Cheng L, Lin Q, Zhang K and Shen J (2023) Synergistic effects of climate warming and atmospheric nutrient deposition on the alpine lake ecosystem in the south-eastern Tibetan Plateau during the Anthropocene. *Front. Ecol. Evol.* 11:1119840. doi: 10.3389/fevo.2023.1119840

Synergistic effects of climate warming and atmospheric nutrient deposition on the alpine lake ecosystem in the south-eastern Tibetan Plateau during the Anthropocene

Can Zhang[1], Xiangzhen Kong[1,2]*, Bin Xue[1], Cheng Zhao[3], Xiangdong Yang[1], Longjuan Cheng[4]*, Qi Lin[1], Ke Zhang[1] and Ji Shen[3]

[1]State Key Laboratory of Lake Science and Environment, Nanjing Institute of Geography and Limnology, Chinese Academy of Sciences, Nanjing, China, [2]Department of Lake Research, UFZ - Helmholtz Centre for Environmental Research, Magdeburg, Germany, [3]School of Geography and Marine Science, Nanjing University, Nanjing, China, [4]School of Geographical Science, Nantong University, Nantong, Jiangsu Province, China

Alpine lakes on the Tibetan Plateau are highly sensitive to global change and have been recognized as the sentinel of climate warming. However, anthropogenic impacts in populated area are migrating to these remote areas *via* transporting particulate nutrients by atmospheric deposition. Whether warming and nutrient deposition would impose additive or synergistic effects on the lake ecosystem remains largely unknown. Here, we present multi-proxy (sediment pigment and geochemistry) records during the past two centuries at the Cuoqia Lake in the southeast Tibetan Plateau. We found that the lake exhibited rapid ecological changes since 1980 AD characterized by an increase in primary productivity due to algal proliferation, with more rapid growth of green algae and diatoms. These findings are in concert with many other lakes (e.g., Moon Lake and Shade Co) in the same area, suggesting a consistent pattern of ecosystem evolution at the region scale. Statistical analyses suggested that nutrient deposition and climate warming were strongly associated with the variations in primary productivity and algae composition, exerting both individual and interactive effects. In addition, scenario analyses with a well-established process-based ecosystem model further revealed that the two factors not only individually, but also synergistically promoted the algal proliferation and community succession. Such synergy is evident in that the effect of lake warming would be more pronounced under higher nutrient deposition scenario, which is potentially due to higher temperature-driven mineralization in warmer conditions, and higher efficiency of nutrient utilization under enhanced light availability attributing to declining ice thickness and duration in cold seasons. Overall, our study proposes the existence and quantifies the synergistic impacts of climate warming and anthropogenic activities in driving the ecological changes in remote alpine lakes on the Tibetan Plateau. The lake ecological consequences driven by individual factor would be worsen by such synergy, so that we cannot predict the lake ecosystem trajectory in the future based on each factor separately, and more efforts than previously expected would be needed for the lake restoration and management.

KEYWORDS

lacustrine ecosystem, climate warming, atmospheric deposition, paleolimnology, ecosystem modeling

1. Introduction

The Tibetan Plateau, as the "Third Pole" of the Earth (Qiu, 2008), is one of the most sensitive areas to climate changes at a rate twice warming than the global average from meteorological observations (Immerzeel et al., 2020). Lakes are sentinel of global changes and sensitive to unprecedented climate warming and pervasive human activities (Adrian et al., 2009). Evidence from paleolimnological investigations suggests that aquatic ecosystems of montane lakes have correspondingly experienced rapid and pronounce changes in recent decades on the plateau (Hu et al., 2014, 2017). Climate warming can stimulate changes in primary producer communities through directly heating surface lake water, shortening the duration, thinning the ice-cover, and altering thermal stratification, or indirectly affects ecological changes by interaction with nutrient recycling (Catalan et al., 2013; Woolway et al., 2020). Recent studies indicate algal communities and diatom compositions display a trend towards long-term warming over the past century (Hu et al., 2017; Kong, L. et al., 2017). Specifically, reduced ice cover and enhanced thermal stratification caused by climate warming induce the diatom shifts from benthic Fragilaria taxa to planktonic Cyclotella with a preference of warm condition (Smol et al., 2005; Hu et al., 2014; Rühland et al., 2015).

Anthropogenic impacts in populated area are migrating to these remote areas *via* transporting particulate nutrients by atmospheric deposition (Wolfe et al., 2003). Tibetan Plateau region is now a hotpot of atmospheric nitrogen (N) deposition, transporting from lower latitude southeast Asia by monsoon circulation, with the N deposition rate of up to 20–40 kg ha^{-1} yr.$^{-1}$ (Chen et al., 2004; Zhang et al., 2012). Furthermore, nitrate concentration recorded in Himalayan ice cores revealed a long-term increase in N pollution since 1850 AD (Thompson et al., 2000). Previous study suggests that increased N deposition is indeed an important nutrient source, promoting primary productivity and driving ecological changes when N deposition rate exceeds ~10 kg ha^{-1} yr.$^{-1}$ at remote montane lakes (Bergstrom and Jansson, 2006; Hu et al., 2014). Such a high N deposition rate in the southeast of Tibetan Plateau should be close to or above the estimated critical load for ecological changes (Liu et al., 2011; Zhang et al., 2012). Furthermore, lake primary productivity enhancement and phytoplankton composition alternation driven by N deposition are also reported especially for N-limited alpine lakes in the Tibetan Plateau region (Hu et al., 2014).

Ecological dynamics of aquatic system are not only driven by a single stressor such as climate change, human activity, or nutrient supply, but more often by multiple stressors (Birk et al., 2020), which have been increasingly recognized as the joint drivers of lake ecological changes (Ormerod et al., 2010). A recent study from 33 freshwater mesocosm experiments indicates that more than 60% of the cases are subject to additive effects and interactive (synergistic or reversal) effects by the paired-stressor combinations (Birk et al., 2020). Furthermore, a modern survey based on more than 1,000 lakes in U.S. suggests that the synergistic effects of climate changes and nutrients supply are indeed widespread in determining lake primary productivity and algal community shifts, especially for eutrophic lakes (Rigosi et al., 2014). In addition, *in situ* experiments in Rocky Mountain lakes also reveal small planktonic species respond to lake thermal structure changes only with adequate nutrient availability, which also supports the interactive effects of lake warming and nutrient availability for mesotrophic-oligotrophic alpine lakes (Saros et al., 2012). However, whether warming and atmospheric deposition would impose additive or even synergistic effects on the lake ecosystem in the Tibetan Plateau region are rarely investigated and remains unknown. Therefore, in-depth research on the synergistic effects of multiple stressors is warranted for improved understanding the response mechanisms of lake ecosystem on the Tibetan Plateau.

The long-term perspective is crucial for understanding the nature and timing of the lake ecological evolution, and its feedback mechanism responding to external multiple stressors (Smol, 2010). Paleolimnological approaches are widely used to reconstruct the long-term dynamics of environmental changes and ecological evolution based on multi-proxy data over decadal to centennial timescales (Zhang et al., 2019; Fordham et al., 2020), exemplified by numerous studies in European, North American, Arctic, and Tibetan Plateau region (Smol et al., 2005; Rühland et al., 2015). For example, fossil pigment proxy can reflect the pelagic algal community succession of the lake, and the tempting outcomes from sediment pigment shed lights on exploring the phytoplankton community exemplified from our study and others in more eutrophic lakes (Leavitt et al., 1997; Leavitt and Hodgson, 2002; McGowan, 2013). However, the key drivers and underlying mechanisms of such dynamics remains difficult to quantify based on the sediment records alone. On the other hand, process-based ecosystem modelling offers the opportunity to hindcast the lake evolution history and to identify the key drivers (climate and human activities). Yet such approach is constantly restricted by lack of external forcing (climate, nutrient loading etc.,) and field data, particularly in those understudied lakes without a routine monitoring program (Kong, X. et al., 2017). Combining the modelling and paleolimnological approach is therefore promising to improve our understanding of the long-term lake evolution, which calls for more investigations including the Tibetan Plateau region (Seddon et al., 2014).

In this study, a representative subalpine lake (Cuoqia Lake) in the southeast of Tibetan Plateau was chosen as a monitor of regional environmental and ecological changes. We use high-resolution paleolimnological records to (1) investigate the regional environmental changes and lake ecological evolution (primary productivity and algal biomass) over the past two centuries based on ^{210}Pb/^{137}Cs dated multiproxy data including geochemistry, stable isotopes and sedimentary pigments, (2) disentangle its response mechanisms to climate warming and atmospheric nutrient deposition using ecosystem modelling, and (3) explore the synergistic effects of multiple external stressors in regulating primary productivity and algae abundance changes through statistical analyses and comparative scenario modelling.

2. Study site

Cuoqia Lake (CQ Lake, 27°24′ N, 99°46′ E, 3960 m a.s.l.) is located in the hinderland of Hengduan Mountains in the southeast margin of Tibetan Plateau, ~20 km southwest of Shangri-la country, Yunnan province (Figure 1A). It is a small subalpine ice-scour lake with the maximum water depth and average water depth of ~26.4 m and ~13.2 m, respectively. CQ Lake have a surface area of ~0.07 km^2 and a catchment area of ~0.44 km^2 with a small catchment and lake area ratio of 6.3 (Figures 1B,C). It is a semi-closed lake without visible surface inflows and outflows, and is mainly fed by seasonal rainfall and snowmelt water. The lake is surrounded by forest vegetation on three sides and steep rock walls on one side. There are no visible aquatic plants in lake water with a pH of ~6.7 and dissolved organic carbon (DOC) of 5.15 mg/l in May 2014. The watercolor is close to sauce-brown with a Secchi depth of 3.7 m. Field survey indicates that it is an oligo-trophic lake with total phosphorus (TP) and total nitrogen (TN) of ~10 μg L^{-1} and ~80 μg L^{-1}, and is N-limited with TN:TP of ~8 (Hu et al., 2017; Li et al., 2021).

Currently, the study site belongs to highland humid monsoon climate region, and has distinct rainy and dry seasons with wet in

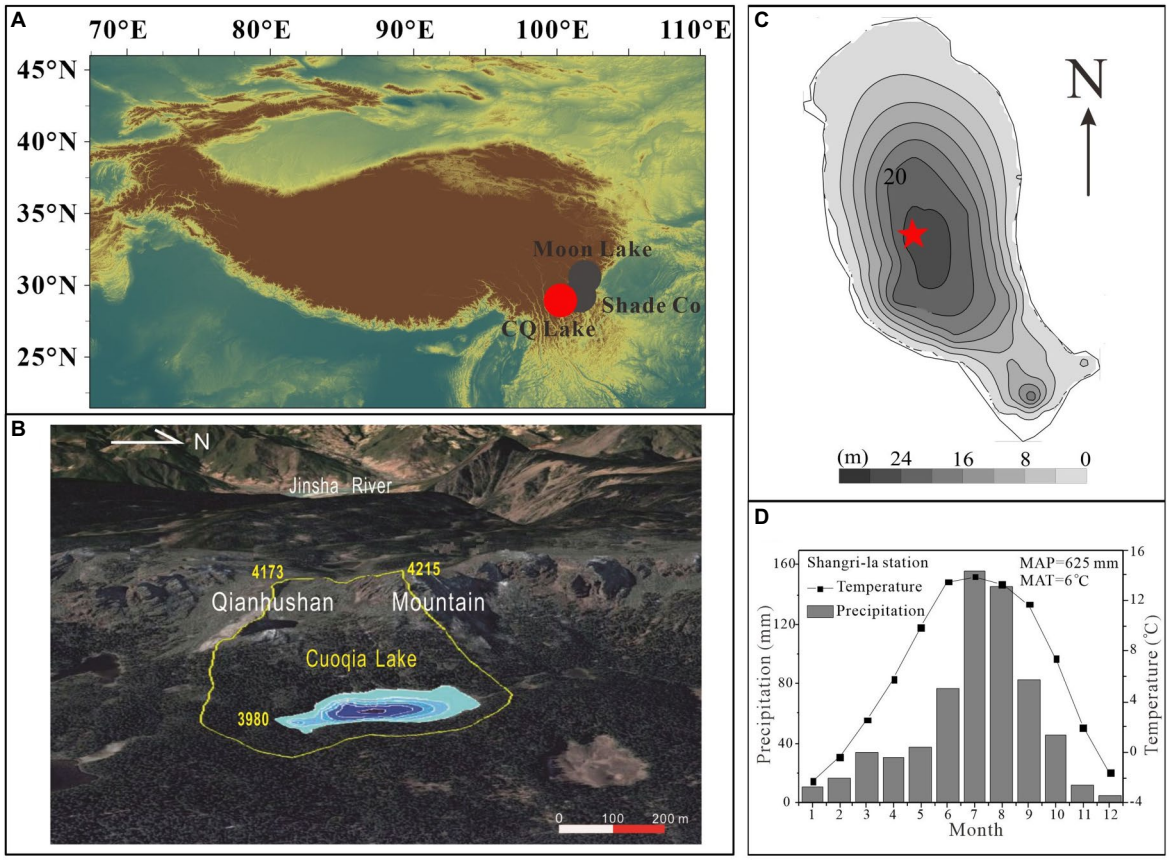

FIGURE 1
Location and setting. **(A)** Map showing the location of the study site Cuoqia Lake (CQ Lake, red dots) and nearby Moon Lake and Shade Co (gray dots) in the southeast Tibetan Plateau. **(B)** topography and catchment (circled by yellow line) of CQ Lake, base map from Google Earth [modified from Li et al. (2021)]. **(C)** Bathymetry of the CQ Lake and locations of the sediment cores (red asterisks). **(D)** Mean monthly temperature and precipitation at the Shangri-la Meteorological Station, Yunnan Province, China (data retrieved from the Meteorological Administration of China, http://data.cma.cn/).

summer and dry in winter. It is mainly influenced by the interaction of Indian summer monsoon, the southern branch of the Westerly wind, and local Tibetan Plateau climate (Zhang et al., 2022). There is no weather station around the lake, and the nearest Shangri-la meteorological station (3276.7 m a.s.l.) shows that the mean annual precipitation (MAP) is ~651.1 mm with more than 81.3% of precipitation falling during monsoon season from April to September over the period of 1958–2020. The mean annual temperature (MAT) ~6.3°C with a maximum monthly mean of ~13.9°C in July and a minimum of ~ − 2.3°C in January, and the relative humidity is ~68% (Figure 1D). At present, the lake lies below the tree line and surrounded by forest vegetation on three sides and steep rock walls on one side. Primary vegetation around the lake appears to be undisturbed in the historic past, dominated by cold temperate conifer forest such as *Abies* and *Picea*, shrub such as *azalea*, Yunnan wormwood such as *Kobresia yunnanensis* and miscellaneous grass meadow (Xiao et al., 2014; Li et al., 2021).

3. Materials and methods

3.1. Sample collection and age control

In May 2014, two parallel sediment cores (CQ1: 37 cm and CQ2: 30 cm) through the sediment–water interface, were retrieved from the deepest site of the lake at a water depth of ~26 m using a gravity corer (Figure 1C; Chai et al., 2018; Zhang et al., 2022). In the field, both sediment cores were sub-sectioned by extruding vertically at every 0.5-cm interval immediately and the sedimentary lithology is mainly dominated by humus black clay. The sediment samples were transported to the laboratory and stored in the freezer before freeze-drying. The CQ2 is used for dating analysis and the CQ1 for proxy analysis including sedimentary pigment, total organic carbon (TOC), TN, carbon isotope ($\delta^{13}C$), nitrogen isotope ($\delta^{15}N$), and TP. The chronology is determined by ^{210}Pb and ^{137}CS activities analysis using a gamma spectrometer (Hyperpure Ge detector) at 46.5 KeV and 661.6 KeV, respectively. Chronology of CQ2 were established based on ^{210}Pb and ^{226}Ra activities using the constant rate of supply (CRS) model and the chronology of core CQ1 was obtained from core CQ2 through the correlation of loss-on-ignition profiles (Chai et al., 2018).

3.2. Proxy analysis

Sedimentary pigments (0.2–0.5 g dry sample) were extracted using organic solvents of acetone: methanol: water (80:15:5, v/v/v) by leaving in a -20°C freezer for 24 h. Extracts were filtered with a 0.22 μm-pore PTFE filter, concentrated to dry with N_2 gas, and re-dissolved with organic solvents of acetone: ion-pairing reagent: methanol (70:25:5, v/v/v; Chen et al., 2001). Note that sedimentary pigments were measured at 0.5-cm resolution for upper 10 cm and 1-cm resolution for the lower. Pigments were measured *via* an Agilent 1200 series high performance

liquid chromatography unit (HPLC, Agilent, United States) with quaternary pump, autosampler, 120EC-C18 Hypersil column (3.0 × 150 mm; 2.7 μm particle size), and photo-diode array detector (PAD). Pigments were identified and quantified based on the retention time and absorption spectra and authentic standards (DHI, Denmark; Leavitt and Hodgson, 2002; McGowan, 2013). The identified pigments included all algae (Chl α, pheophytin α), chlorophytes (Chl *b*, pheophytin *b*, lutein), siliceous algae (diatoxanthin), and cyanobacteria (canthaxanthin). The concentration of all pigments was expressed in nmol g TOC^{-1}. TOC, TN and TP were previously published in Chai et al. (2018). $\delta^{13}C$ and $\delta^{15}N$ were measured at 0.5-cm resolution using a Thermo Scientific MAT253 Delta V mass spectrometer coupled with a Flash elemental analyzer (Thermo Fisher, United States). The $\delta^{13}C$ and $\delta^{15}N$ is presented in δ notation as the per mil deviation (‰) from standards relative to Vienna PeeDee Belemnite (VPDB) and atmospheric N_2, respectively. Replicate analyses indicate that the analytical precision was better than 0.1‰ for the $\delta^{13}C$ and 0.3‰ for the $\delta^{15}N$.

3.3. Data analysis

Principal components analysis (PCA) was used to summarise the major ecological trends of primary producer communities inferred from sedimentary pigment dataset. Redundancy analysis (RDA) was conducted to reveal the correlations between primary producer communities and multiple environmental factors. The response variables are sedimentary pigment concentration of the total algal community and specific algal group including chlorophytes, siliceous algae, and cyanobacteria. The explanatory variables include nutrient factors (TOC, TN, C/N, and TP), climate factors (temperature and precipitation), and atmospheric N deposition factors ($\delta^{15}N$ and N_2O emission). Note that N_2O emission in the study region was obtained from grid monitoring data from EDGAR-Emissions Database for Global Atmospheric Research[1]. In addition, variation partitioning analyses was further performed to investigate the synergistic effect of two main forcing factors on algal community dynamics. The climate changes (temperature) and atmospheric N deposition ($\delta^{15}N$) were selected as driving variables, while sedimentary pigment concentration of the total algal community and specific taxonomic groups as the response variables. All the variables were log-transformed prior to analysis, performed by the program Canoco 5 (Šmilauer and Lepš, 2014).

3.4. Lake ecosystem modelling configuration

We further implemented a process-based lake ecosystem modeling approach for CQ Lake for a mechanistic understanding of the long-term ecological dynamics. Here we used the GOTM-WET model (Schnedler-Meyer et al., 2022), which included both General Ocean Turbulence Model (GOTM) and Water Ecosystem Tool (WET) for lake hydrodynamic and ecological modeling, respectively. GOTM is originally a 1D hydrodynamic model for ocean and its lake branch includes the hypsographic structure of the lake water and sediment, so that the model could simulate water temperature, ice cover, turbulence and mixing along the lake vertical dimension (Umlauf and Lemmin, 2005). WET is developed from the PCLake model (Janse et al., 2010), and can simulate the mass-balanced closed nutrient cycling and ecological processes with a customizable food web structure. Here we focused on the phytoplankton community and applied the 'default' setting that which includes three algae groups (diatoms, green algae, cyanobacteria) that are the dominant groups in CQ Lake. The model can simulate the lake dynamics at hourly basis. Considering that we primarily investigated the long-term lake ecosystem dynamic, we aggregated the model outputs from hourly to annually basis to better compare with the sedimentary data which are in annual time-resolution.

We collected the meteorological data (including wind speed, wind direction, air pressure, air temperature, relative humidity, cloud cover, solar radiation and precipitation) at hourly basis from the ERA5 global meteorological reanalysis data (from European Centre for Medium-Range Weather Forecasts, ECMWF) at the grid cell of CQ Lake (Supplementary Figure S2). In addition, we collected daily air temperature at the national meteorology station (CMA) 'Shangrila' (3,277 m a.s.l., ~20 km northeast of CQ Lake) from 1957 to 2020 AD, which is elevation-corrected with a reduction of ~5.2°C for CQ Lake. The Shangrila data is used for bias-correction of the ERA5 data (Supplementary Figure S3). Furthermore, the meteorological data without anthropogenic climate change were provided by the Inter-Sectoral Impact Model Inter-comparison Project (ISI-MIP) database as the 'piControl' scenario (Supplementary Figure S4), which were projected by four Global Climate Models (GCMs; Warszawski et al., 2014). The ISIMIP data were downscaled from daily to hourly basis following the method by Shatwell et al. (2019), except for wind speed and direction which were provided along the Eastward and Northward direction at sub-daily resolution (Frieler et al., 2017).

The annual discharge to the lake was estimated using the SCS-CN model (Kong et al., 2015) driven by annual precipitation data from ERA5. For nutrient loading from the drainage area (TN and TP), an export coefficient model (Johnes, 1996) was used considering vegetation (subalpine conifers and shrubs) as the land use type. We further incorporated annual atmospheric N deposition as part of the TN loading, based on the field observations in 1999 AD (2.22 kg hm^{-2} $yr.^{-1}$; Zhang et al., 2013) and 2012 AD (20.0 kg hm^{-2} $yr.^{-1}$; Zhu et al., 2015). The long-term data were estimated by the linear interpolation assuming a zero deposition in 1947 AD from the sediment N isotope peak (2.79‰; Supplementary Figure S5).

The hydrodynamic model (GOTM) was calibrated against the daily water temperature data from a neighboring Moon Lake at 1 m depth during 2013 (Supplementary Figure S6). The calibration was performed using the auto-calibration program PARSAC with several successful applications with GOTM (Ayala et al., 2020; Kong et al., 2022). For the ecological model WET, the initial parameter values were based on the default values calibrated to 40+ lakes (Janse et al., 2010), serving as a starting point for calibration. The initial values for state variables of nutrient (TN and TP) in the sediments were determined based on the sediment records at the corresponding layer.

3.5. Model hindcast and scenario analyses

We designed a model scenario analysis including both the TN loading and meteorological conditions as the two-factorial experimental simulations. For TN loading, there are two levels (N −/+) representing the scenarios of constantly low TN loading after 1980s AD, and the factual TN loading with an increase after 1980s AD and much rapidly

1 https://edgar.jrc.ec.europa.eu

after 2000s AD (Supplementary Figures S4, S5). For meteorological variables, two scenarios including the 'piControl' (PIC, or C−) and the 'historical' (HIST, or C+) were used representing the climate without and with anthropogenic impacts, respectively. In summary, the scenario analyses including four model scenarios (N −/+ and C −/+), while for C −/C+ there are four GCMs, resulting in 16 model runs in total.

Among the model runs, the scenario of TN+ and C+ represents the factual condition, which was considered as the 'hindcast' simulation. Due to lack of recent field observations for biogeochemical and ecological variables, we performed a model calibration during the hindcasting, by using the sediment records including the geochemical (TN and TP) and the pigment records of the three algal groups. A trial-and-error method was utilized to fit the model outputs from 1900 to 2020 AD to the sediment records. All the parameter values that were optimized during the calibration were documented in the Supplementary Table S1.

Next, we tested the hypotheses that the rapid increasing atmospheric N deposition and the climate change since the 1980s together dictated the ecological dynamics in CQ Lake, particularly in the succession of algal community. We evaluated if there are additive and/or synergistic effects of TN loading and climate change on the ecological dynamics. Relevant processes of the causal effects between the TN loading and climate change and ecological dynamics were provided by the process-based modelling with GOTM-WET. All statistical analyses were performed in R (R Core Team, 2021). Long-term trends and change rate in time series of model outputs were calculated based on the Mann-Kendall test and Sen's slope by the R package 'trend' (Pohlert, 2020).

4. Results

4.1. Sedimentary records

The chronology of CQ1 and CQ2 cores were previously reported in Chai et al. (2018) and Zhang et al. (2022), covering the past two centuries from 1800 to 2014 AD (Supplementary Figure S1). The sedimentary pigment records exhibited a two-stage pattern with relatively stable and low value before ~1980 AD and thereafter started distinctly increasing to the highest value in the top, expect for the cyanobacteria pigment (Figures 2, 3). In the interval of 1800–1980 AD, the pigments of siliceous algae (diatoxanthin) and cyanobacteria (canthaxanthin) were present in quite low abundances, while the pigments of total algae (Chl *a* and pheophytin *a*) and chlorophytes (Chl *b* and lutein) were relative moderate. Note that the concentrations of pheophytin *a* and pheophytin *b* are quite high and show a high value between 1800 and 1850 AD and shift to a low relative value afterward. In the interval of 1980–2014 AD, the total algae pigments began to increase rapidly until 2000 AD with a low value before. The chlorophytes pigments show a gradually increasing trend and an abrupt increase from the siliceous algae pigments, whereas the canthaxanthin pigment remains low in the whole profile.

For the pigment data, PCA axis 1 (PCA1) explained 71.9% of the total variance in the pigment assemblages and was positively correlated with all primary producers (Chl *a* and pheophytin *a*) and chlorophylls and their derivatives from chlorophytes (Chl *b* and pheophytin *b*; Figure 4A). PCA axis 2 (PCA2) explained a further 14.3% of the total variation and was positively correlated with cyanobacteria (canthaxanthin) and negatively correlated with chlorophytes (lutein) and siliceous algae (diatoxanthin). RDA results revealed that variations in pigment composition were significantly correlated with temperature and atmospheric N deposition ($\delta^{15}N$ and N_2O). In contrast, other factors such as TN, TOC, TP, C/N, and precipitation show weak correlation with pigment composition changes (Figure 4B). The results of variation partitioning analyses reveal that climate warming and N deposition can independently explain 9.9 and 46.8% of the explained variables, respectively. In contrast, synergistic effects of climate warming and N deposition contribute anther 43.3% for the variability in algal community (Figure 4C). In contrast, climate warming, N deposition, and synergistic effects can explain 5.9, 27.7, and 25.6% of the total variables, respectively, with another 40.9% unexplained variables which may be due to the unconsidered additive or synergistic effects of multi-factors and the uncertainty of analytical method.

4.2. Model calibration and hindcast

The ecosystem model GOTM-WET well captures the daily surface water temperature during 2013 ($RMSE = 1.31$°C, $R = 0.92$), with the seasonal variations of summer peaks (~15°C) and winter minimum (0°C; Supplementary Figure S6). The model also predicts an ice coverage from November to March, and the maximum ice thickness ranged 0.1–0.2 m, which are all in concert with field observations (Supplementary Figure S6). The model predicts that the lake stratifies from May to October with a mean thermocline depth of 3.11 m and a maximum of 9.49 m. The calibration during 2013 proves that the physic model (GOTM) is valid for the lake, so that the model could accurately predict the lake thermal dynamics for the years beyond 2013. The model hindcast from 1900 to 2020 AD provides the predictions of the lake physical dynamics driven by the factual climate and nutrient loading (Figure 5). The results suggest that the physic condition including water temperature, light in the epilimnion, and maximum ice thickness were rather stable before the 1970s. Light intensity started to increase from late 1970s AD, and temperature and ice started to change rapidly after the 2000s. From 2000 to 2020 AD, annual average water temperature increased at a rate of 0.017°C $yr.^{-1}$, while maximum ice thickness decreased at −0.07 cm $yr.^{-1}$. Annual average light in the epilimnion decreased at a rate of 0.1 W m^{-2} $yr.^{-1}$.

The ecological model (WET) is calibrated during the hindcast against the long-term sediment records, in particular to the phytoplankton community indicated by the pigment data (Figure 6). The results show that the model nicely captures the long-term patterns of Chl *a* concentration and the biomass of two major algal groups (green and diatom). In specific, the rapid increase of Chl *a* and green algae since the 2000s are both represented, while the increase in diatom biomass since the 1980s are also well simulated. Though the absolute Chl *a* and biomass are difficult to quantify by the pigment data, the consistent patterns between pigment and model imply that the model has grasped the key succession features of the phytoplankton community over the historical period since 1900 AD. The model predicts the rather stable TN concentration in the water column before 2000 AD, and a rapid increase TN afterwards (Supplementary Figure S5), associated with the rapid increase TN atmospheric deposition. Taken together, the model calibration during 2013 AD and the hindcast since 1900 AD as described above provide evidence for reliable outcomes from the model scenario and mechanistic analyses below.

4.3. Model scenario analyses

The model scenario analyses reveal that the increasing TN enrichment *via* atmospheric deposition and lake warming caused by climate change are the two main factors promoting the algal proliferation

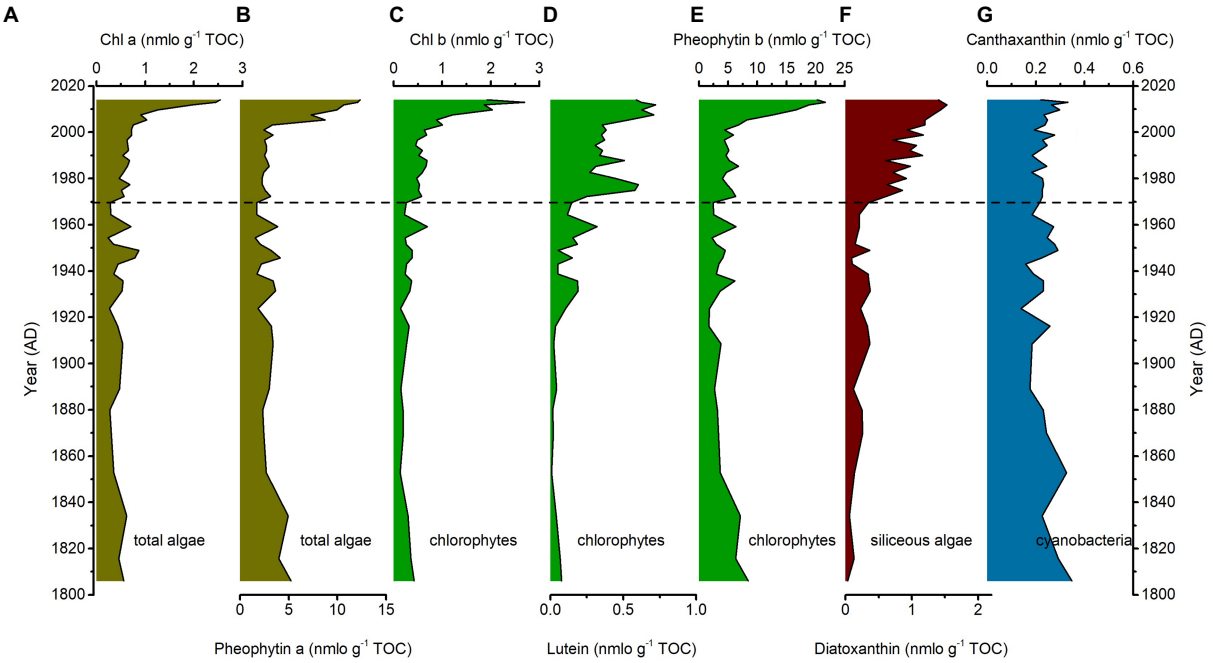

FIGURE 2
Sediment pigment. The concentration (nmolg^{-1} TOC) of main pigment including **(A)** Chl α, **(B)** pheophytin α, **(C)** Chl *b*, **(D)** lutein, **(E)** pheophytin b, **(F)** diatoxanthin, and **(G)** canthaxanthin in the sediments at the CQ Lake.

and the community succession, not only individually but also synergistically (Figure 6). Model results suggest that without the two factors (scenario 'C-/N-'), algal proliferation would not occur, while the community would maintain a persistence and constant biomass of green algae and the secondary dominating diatom. With the TN enrichment alone (scenario 'C-/N+'), Chl *a* is enhanced by 51%, green algae would flourish from the 2000s (+43%), while diatom also increases (+10%) but starts earlier around 1980s. This pattern is highly consistent with the sediment pigment data (Figure 6). This result implies that the increasing atmospheric N deposition acts as the key role in driving the phytoplankton succession, featured by the increasing biomass of green algae and diatom. Note that cyanobacteria abundance remains low in both sediment records and model predictions. On the other hand, under the lake warming alone (scenario 'C+/N-'), however, the change is less visible compared to 'C-/N+', but still effective in the way that Chl *a* (+5%), green algae (+3%) and diatom (+2%) are slightly promoted in biomass. This result suggests that lake warming acts as a secondary role in driving the algae proliferation. Finally, when the two factors are simultaneously effective (scenario 'C+/N+'), the phytoplankton community depicts the factual pattern as the historical succession, and the increases in Chl *a* (+77%), green algae (+67%), and diatom biomass (+19%) are even higher than the additive effects of each factor separately, indicating the existence of synergistic effects from both factors.

5. Discussion

5.1. Ecological and environmental changes at the CQ Lake over the past two centuries

CQ Lake is located in the southeast of Tibetan Plateau, which belongs to one of the most sensitive areas to climate changes with twice as much warming as the global average (Immerzeel et al., 2020). Over the past century, meteorological data for CQ Lake from ECMWF reveals that this study region has experienced large-magnitude warming with a rapid increase of 1.5°C since 1980 AD (Figure 3A). Regional annual precipitation shows a gradual decrease trend between 1860 and 1990 AD, followed by an increase afterwards (Figure 3B), which can be supported by reconstructed regional precipitation and relative humidity records from tree ring and speleothem (An et al., 2013; Tan et al., 2016; Xu et al., 2019). Although the catchments of remote subalpine lakes in the Tibetan Plateau are rarely affected by anthropogenic activities directly, reactive N deposition rate in the mountains is high with a value of 20–40 kg N ha^{-1} yr.$^{-1}$ (Liu et al., 2011; Zhang et al., 2012), which is mainly due to increased use of synthetic nitrogen fertilizer and fossil fuel combustion after 1980s (Liu et al., 2013). In the CQ lake, δ^{15}N data display a distinct decline towards to 0‰ since 1980 AD (Figure 3C), which can be interpreted as a signal of enhanced atmospheric N deposition (Holtgrieve et al., 2011). Although δ^{15}N in the sediments is affected by N inputs from different sources such as catchment sources, atmospheric deposition and in-lake cycling (Catalan et al., 2013), catchment vegetation and soil should contribute enrichment of δ^{15}N in lake sediments (Bartrons et al., 2010). The effect of bacterial process on δ^{15}N cannot explain the long-term significant depletion trend since 1980 AD (Talbot, 2001). Furthermore, monitoring data of global greenhouse gas emissions demonstrated a remarkable increase of N deposition at our study area inferred from N_2O concentration (Figure 3C). The consistent variations can also be observed in nearby Moon lakes with obvious depletion of δ^{15}N (Hu et al., 2014) and in Himalayan ice cores with increased nitrate concentration (Thompson et al., 2000). Therefore, all lines of these evidence support that our study area has experienced unprecedented climate warming and high atmospheric N deposition over the past several decades.

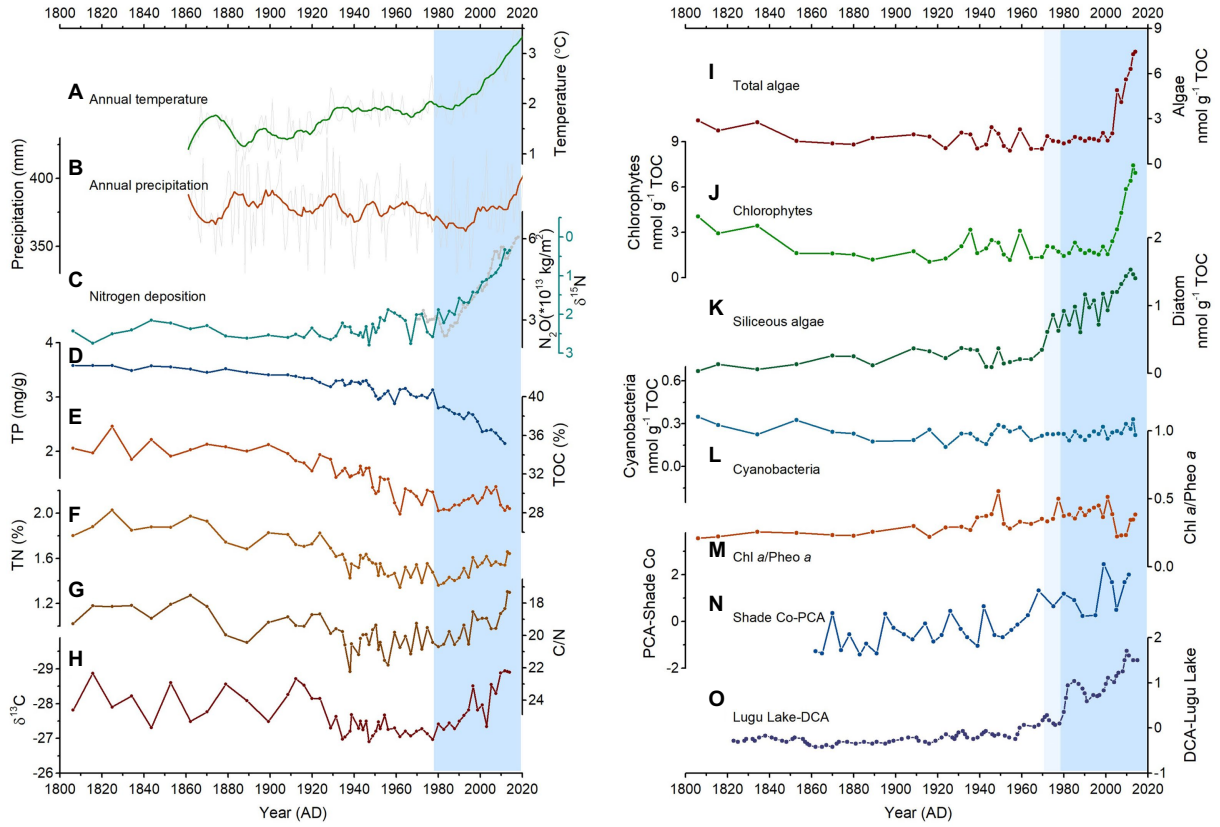

FIGURE 3
Historical environmental and ecological changes around the CQ Lake. **(A)** temperature and **(B)** precipitation changes, **(C)** sedimentary $\delta^{15}N$ and N_2O emission in the study region, **(D)** the concentration of sediment TP (Chai et al., 2018), **(E)** %TOC (Chai et al., 2018), **(F)** %TN (Chai et al., 2018), **(G)** the ratio of C/N (Chai et al., 2018), **(H)** $\delta^{13}C$; The biomass of different algae (average concentration from sediment pigments) including **(I)** total algae (Chl α and pheophytin α), **(J)** chlorophytes (Chl *b*, lutein, and pheophytin b), **(K)** siliceous algae (diatoxanthin), **(L)** cyanobacteria (canthaxanthin); **(M)** The ratio of Chl α/Pheo α, **(N)** pigment-based PCA at the Shade Co, and **(O)** diatom-based DCA at the Lugu Lake.

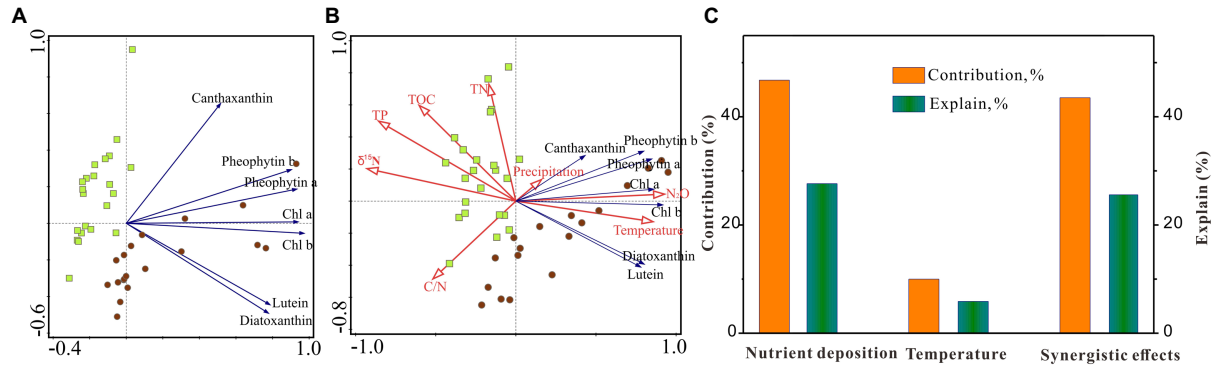

FIGURE 4
(A) Principal components analysis of pigments and **(B)** redundancy analysis between pigments and significant explanatory variables including temperature, precipitation, $\delta^{15}N$, N_2O emission, TOC, TN, C/N, and TP. **(C)** Variation partitioning analyses was further performed to investigate the synergistic effects of two main forcing factors (climate warming and atmospheric nutrient deposition) on algal community dynamics.

Previous studies show TOC and TN can indicate the variation in primary productivity within the lake and catchment basin (Meyers and Ishiwatari, 1993; Chai et al., 2018). At 1800–1980 AD, the consistent decreasing TOC and TN indicates a long-term decline in productivity in the CQ Lake and its catchment (Figures 3E,F; Chai et al., 2018), which may be related to regional precipitation changes (Meyers and Ishiwatari, 1993; Zhang et al., 2019). Decreased precipitation may limit vegetation and soil development and further diminish the input of catchment organic matter into the lake (Chen et al., 2018), resulting in the gradual decline of TOC and TN. Similar trend can be observed in the total phosphorus of lake sediments (Figure 3D). After 1980 AD, the slight increase in TOC and TN indicates the increased inputs of allochthonous

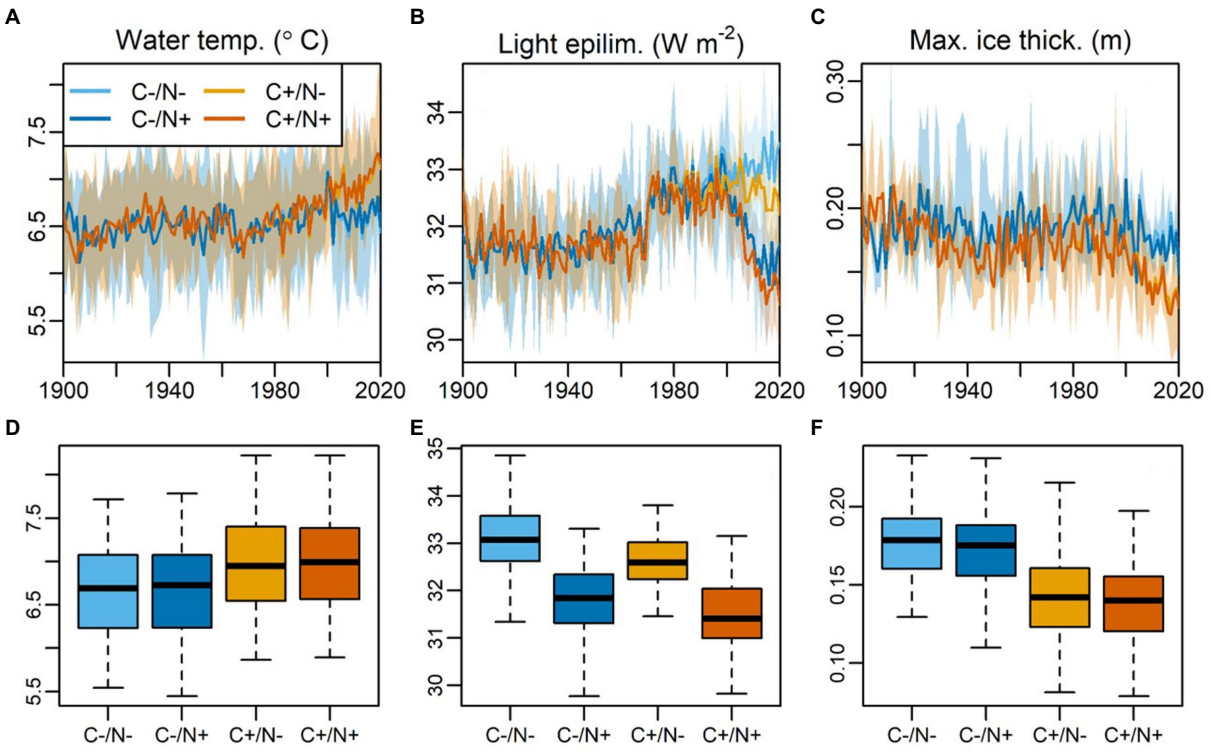

FIGURE 5
Model simulated annual averaged data for **(A)** epilimnetic water temperature volume-weighted across the epilimnion, **(B)** light intensity in the lake epilimnion weighted by the area of the water–sediment interface in each modeled layer, **(C)** maximum ice thickness from 1900 to 2020 under different scenarios. The scenarios are composed for a two-factorial approach. 'C' denotes the climate factor ('C-' is the 'piControl' climate scenario without anthropogenic change, and 'C+' is the 'historical' with climate change). 'N' denotes the nutrient loading factor ('N-/N+' represents the scenarios without and with the rapid increase of atmospheric N deposition after *ca.* 2000s). The shade area represents the modeling range derived from the four Global Climate Models (GCMs) from the ISIMIP project. **(D–F)** The corresponding boxplots of the variable above during 2000 to 2020 under various modeling scenarios.

organic matter and/or enhanced primary productivity in the lake (Figures 3E,F; Chai et al., 2018). Nevertheless, the decoupling between total phosphorus and regional precipitation points to the main contribution from enhanced primary productivity rather than allochthonous organic matter inputs at this interval. In addition, evidence of enhanced primary productivity can be observed from the proxies of C/N ratio and $\delta^{13}C$ (Figures 3G,H), because enhanced primary productivity within the lake can lead to decreased C/N ratio and depleted $\delta^{13}C$.

Cluster analysis of pigment assemblages in the CQ Lake reveals a remarkable shift in algal communities in ~1980 AD and ~2000 AD (Figures 3I–L, 4A). The concentration of most pigments showed a relatively stable low value before 1980 AD, and then siliceous algae started to increase to maximum value toward to present, and total algae and chlorophytes remained relatively stable followed by rapid proliferation until 2000 AD. In contrast, the concentration of cyanobacteria still kept stable and low value over the whole period (Figures 3I–L). Serving as dominant producers in aquatic ecosystems, algae can reflect variations of primary productivity and nutrient level (Reynolds, 2006). The remarkable increase in pigment indicates accelerating algae growth and enhanced primary productivity since 1980 AD. Although sedimentary pigment can be influenced by degradation effects downcore, the relatively stable ratio of Chl *a* and its degradation product Pheophytin *a* indicate stable preservation conditions in the CQ Lake (Figure 3M), similar to many other deep lakes (McGowan, 2013; Chen et al., 2018). The unambiguous increase in primary productivity and ecological changes can be widely observed in neighboring subalpine lakes from pigment and diatom proxies (Hu et al., 2014, 2017; Kong, L. et al., 2017; Wang et al., 2020). For example, the pigment PCA1 in nearby Shade Co shows consistent increase in primary productivity in the last few decades (Figure 3N), and similar trend can also be recorded in diatom composition (Figure 3O). Therefore, our multi-proxy paleolimnological records indicates that CQ Lake experienced remarkable environmental and ecological variations including intensified primary productivity and shift in algal community composition especially after 1980 AD.

5.2. Nutrient deposition driving ecological evolution at the CQ Lake

Nutrient supply has been widely recognized as dominate drivers of lake ecosystem dynamics (McGowan, 2013; Yang et al., 2017). Our RDA results suggest that atmospheric N deposition ($\delta^{15}N$ and N_2O emission) was strongly positively associated with the variations in primary productivity and algae abundance, while sediment phosphorus and TN show a slight negative correlation (Figure 4B). As a small subalpine lake without direct human disturbance, nutrient supply of CQ Lake mainly derives from catchment natural inputs of nitrogen and phosphorus, atmospheric N deposition, and altered in-lake nutrient

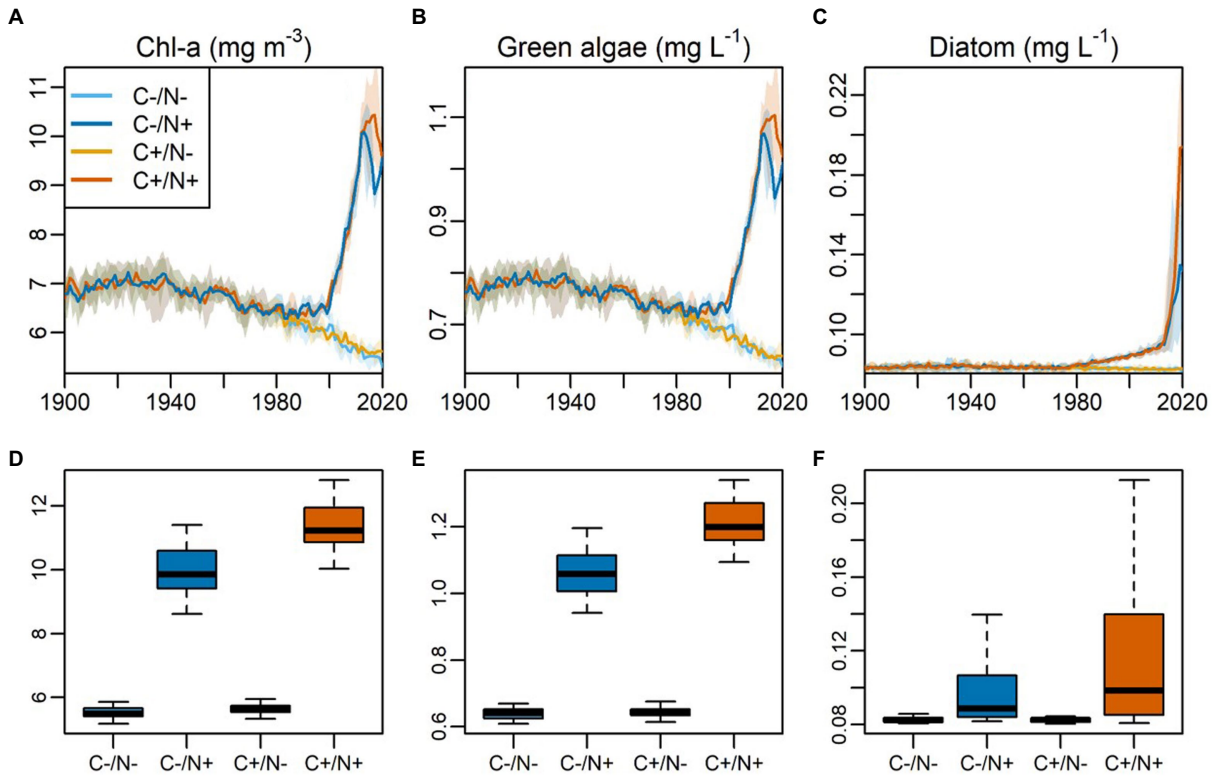

FIGURE 6
Model simulated annual averaged, volume-weighted data across the water column for **(A)** Chl *a* concentration **(B)** biomass of green algae, **(C)** biomass of diatom, from 1900 to 2020 under different scenarios. The scenarios are composed for a two-factorial approach. 'C' denotes the climate factor ('C-' is the 'piControl' climate scenario without anthropogenic change, and 'C+' is the 'historical' with climate change). 'N' denotes the nutrient loading factor ('N-/N+' represents the scenarios without and with the rapid increase of atmospheric N deposition after *ca.* 2000s). The shade area represents the modeling range derived from the four Global Climate Models (GCMs) from the ISIMIP project. **(D–F)** The corresponding boxplots of the variable above during 2000–2020 under various modeling scenarios.

cycling such as phosphorus sediment release (Hu et al., 2014). On the other land, the long-term decline in sediment phosphorus concentration plays a limited effect for algae proliferation especially since 1980 AD (Figure 3), although sediment phosphorus cannot be completely equivalent to soluble phosphorus in lake, which may be affected by sediment release and atmospheric deposition (Catalan, 2000). Modern monitoring shows atmospheric phosphorus deposition is very low compared with regional atmospheric N deposition (Wang et al., 2017). Although phosphorus can be release from sediments and catchment weathering, the amounts is generally neglectable comparing to catchment inputs in small oligotrophic lakes such as CQ Lake (Catalan, 2000).

Assuming that sediment phosphorus is dominated by catchment inputs, the nitrogen content form catchment should show a similarly reduced trend. Whereas the slightly increase in sediment TN after 1980 AD in the CQ Lake mainly reflects the contributions of other sources such as atmospheric deposition and in-lake cycling (Figure 3; Thompson et al., 2000). Previous study suggests that increased N deposition is indeed an important factor for changes in nutrient sources (Hobbs et al., 2011; Hu et al., 2014). Our model results supported a long-term increase of TN loading after 1980 AD (Figure 3F) when accounting for additional atmospheric deposition inputs even under the condition of reducing catchment inputs (Supplementary Figure S5). In addition, atmospheric N deposition can stimulate increase in primary productivity especially in subalpine lakes. Further quantitative investigation reveals that N deposition with more than 10 kg ha^{-1} yr.$^{-1}$ would cause significant ecological changes for the remote lakes (Bergstrom and Jansson, 2006). In the southeast of Tibetan Plateau, the deposition rate is 20–40 kg N ha^{-1} yr.$^{-1}$, which is close to or above the estimated critical load of N deposition for ecological changes (Liu et al., 2011; Zhang et al., 2012). At present, CQ Lake has relatively high phosphorus and low nitrogen concentration with TN:TP of ~8 and belongs to a N-limited lake. The N-limited condition may be more significantly considering the gradually declining sediment phosphorus and increasing nitrogen concentration over the past several decades (Figure 3).

Under N-limited conditions, remote lakes are quite susceptible to the enrichment effect of atmospheric N deposition, especially when deposition rates exceed the critical load (Baron et al., 2011). After1980 AD, increased active N deposition largely promotes primary productivity in the CQ Lake charactered by increase in the abundance of total algae, diatom and chlorophytes (Figure 3). Note that stable concentration of canthaxanthin pigment at this interval shows that the lake nutrient level remains too low to support the growth of cyanobacteria. Furthermore, model scenario analysis suggests nutrient loading is indeed critical factor to the variations of primary productivity and algal abundance in the CQ Lake (Jeppesen et al., 2005; Kong X. et al., 2017). Enhanced nutrient supply, caused by the rapid increase of atmospheric N deposition, stimulates algae proliferation characterized by remarkable

increase in the biomass of Chl *a*, green algae, and diatom despite the changes in climate conditions (Figure 6). Likewise, enhanced primary productivity over the past several decades can also be observed in neighboring other lakes such as Jiren Lake (29°43′ N, 100°48′ E), Tiancai Lake (26°38′ N, 99°43′ E) and Wuxu Lake (29°09′ N, 101°24′ E; Wischnewski et al., 2011; Hu et al., 2017). Overall, our results further approve that the influence of atmospheric N deposition on alpine lakes is magnificent in the Tibetan region.

5.3. Synergistic effects of climate warming and nutrient deposition

Our RDA results suggest that climate warming also play a positive role in algae abundance and community succession in the CQ Lake (Figure 4). Climate warming can stimulate changes in primary producer communities by direct physics process such as heating surface lake water, shortening the duration of ice-cover, and altering thermal stratification (Catalan et al., 2013; Woolway et al., 2020). Generally, lake warming and enhanced lake stratification due to climate changes provide more stable and suitable conditions for the growth of primary producers (Hébert et al., 2021), and prolonged growing season due to shortened ice-cover periods also provides more time for algae proliferation (Rühland et al., 2015). However, our model results reveal a limited sole contribution of climate warming to the increase in lake primary productivity and algal proliferation over the past several decades in the CQ Lake (Figure 6). The low contribution may be due to relative low warming extent by ~0.6°C increase in water temperature since 1980 AD (Figure 5A). This limited variable amplitude is insufficient to trigger detectable changes in the ecological process (Hébert et al., 2021; Kong et al., 2021). Nevertheless, our model shows that the effects of climate warming on lake primary productivity and algae proliferation are more pronounced under increasing atmospheric N deposition (N+; Figure 6), suggesting a synergistic effect of climate warming and N deposition on lake ecological changes. Meanwhile, variation partitioning analyses was performed to investigate the synergistic effect of two main forcing factors on algal community succession. The results suggest that climate warming and N deposition can independently explain 9.9% and 46.8% of the explain variables respectively, while their synergistic effects contribute anther 43.3% for the algae growth and community succession (Figure 4C). Such agreement in analytic results from two independent approaches (statistical analysis and model simulation) points to the reliability of the findings that the major role of atmospheric N deposition and the synergy with lake warming driving the long-term ecological dynamics in the CQ Lake.

Furthermore, the process-base modeling further unravels the potential mechanisms that may formulate such synergy. On the one hand, lake warming may increase the nutrient availability due to higher flux of temperature-driven mineralization, which may exacerbate the impacts of excessive nutrient after atmospheric deposition especially after 2000s AD. Similarly, *in situ* experiments in Rocky Mountain lakes revealed that small planktonic species respond to lake thermal structure changes only with adequate nutrient availability (Saros et al., 2012), suggesting that the effect of lake warming depends on the nutrient availability that cycling between dissolved and particulate forms. On the other hand, the declining maximum ice thickness in the lake since 1980 AD due to warming may increase the light availability under ice (Figures 5B,C), which may act as another indirect effect of lake warming and further promote the synergistic effects with excessive nutrient. Previous studies have implied that global warming leads to mild winter and increased light intensity related with thinner ice coverage, which may promote algae proliferation *via* more intensive photosynthesis and higher efficiency of nutrient utilization (Kong et al., 2021). Furthermore, increasing light intensity in water may also promote algae proliferation *via* more intensive photosynthesis and expansion of benthic habitat. Thus, winter is not a dormant period and may even dictate ecological processes in other seasons (Hébert et al., 2021; Hrycik et al., 2021). In addition, our sediment pigment also indicates an earlier diatom growth than other algae since 1980 AD (Figures 3I–L), and this can also be observed in the model result (Figure 6C), which is in coincidence with a rapid increase in light intensity (Figure 5B). This is because diatom is highly sensitive to light changes in lake. The 'light switch' after lake stratification has been conventionally considered as the trigger of spring diatom blooms (Sommer et al., 2012). We further hypothesize that the increasing in light after 1980 AD was because of thinner ice coverage driven by lake warming, which further enhance the synergy with nutrients. However, such hypothesis needs to be tested in future studies with more reliable field data on ice and light availability from the lake.

6. Conclusion

Our high-resolution paleolimnological records reveal the environmental and ecological variations at the CQ Lake in the southeast Tibetan Plateau over the past two centuries based on $^{210}Pb/^{137}Cs$ dated multiproxy data, including geochemistry, stable isotopes and sedimentary pigments. The most remarkable ecological changes indicated by sedimentary pigments at the CQ Lake have occurred since 1980 AD, manifested by a substantial increase in primary productivity and algae biomass. Our RDA results suggest that atmospheric nutrient deposition and climate warming were positively associated with the variations in primary productivity and algae abundance, indicating the underlying driver-response relation between both factors.

Ecosystem modelling, established based on contemporary data and paleolimnological records, was applied to disentangle the driving mechanisms of lake ecosystem dynamics. Scenario analysis revealed that nutrient deposition is the critical factor in driving the increase in lake primary productivity and algal proliferation over the past several decades in the CQ Lake, whereas the contribution of climate warming is limited under low nutrient conditions. Nevertheless, the effect of climate warming on lake ecological changes exhibits more pronounced effects under increased nutrient supply, indicating a synergistic effect of climate warming and nutrient deposition, which can also be supported by the results of the variation partitioning analyses with 43.3% contribution for synergistic effect of climate warming and N deposition. The modeling approach provides the unique opportunity to interpret the potential mechanisms shaping the synergistic effects between lake warming and atmospheric nutrient deposition, which was conventionally difficult with data analyses alone. Our results highlight that multiple environmental stressors under global changes could not only additively, but also synergistically, affect lake ecosystems, which may possibly worsen the negative impact on remote, subalpine lakes as

CQ Lake. Thus, more attention on such synergy is warranted to evaluate the impacts of global changes on aquatic ecosystems.

Data availability statement

The raw data supporting the conclusions of this article will be made available by the authors, without undue reservation.

Author contributions

CZ and XK conceptualization, data analysis, preparation of figures and tables, and writing. CZ, QL, and KZ developing methods. CZ, BX, LC, KZ, XY, and JS conducting the research and data interpretation. All authors contributed to the article and approved the submitted version.

Funding

This study is supported by the National Natural Science Foundation of China (42007401 and 42177062), the National Key Research and Development Program of China (2019YFA0607100), the Strategic Priority Research Program of Chinese Academy of Sciences (XDB40000000), and the Science and Technology Planning Project of NIGLAS (NIGLAS2022TJ02, NIGLAS2022GS02 and NIGLAS2022GS09).

Acknowledgments

We thank Yifan Chai, Lingyang Kong, Qian Wang for field and laboratory assistance.

Conflict of interest

The authors declare that the research was conducted in the absence of any commercial or financial relationships that could be construed as a potential conflict of interest.

Publisher's note

Supplementary material

The Supplementary material for this article can be found online at: https://www.frontiersin.org/articles/10.3389/fevo.2023.1119840/full#supplementary-material

References

Adrian, R., O'Reilly, C. M., Zagarese, H., Baines, S. B., Hessen, D. O., Keller, W., et al. (2009). Lakes as sentinels of climate change. *Limnol. Oceanogr.* 54, 2283–2297. doi: 10.4319/lo.2009.54.6_part_2.2283

An, W., Liu, X., Leavitt, S. W., Xu, G., Zeng, X., Wang, W., et al. (2013). Relative humidity history on the Batang–Litang plateau of western China since 1755 reconstructed from tree-ring $\delta^{18}O$ and δD. *Clim. Dyn.* 42, 2639–2654. doi: 10.1007/s00382-013-1937-z

Ayala, A. I., Moras, S., and Pierson, D. C. (2020). Simulations of future changes in thermal structure of Lake Erken: proof of concept for ISIMIP2b lake sector local simulation strategy. *Hydrol. Earth Syst. Sci.* 24, 3311–3330. doi: 10.5194/hess-24-3311-2020

Baron, J. S., Driscoll, C. T., Stoddard, J. L., and Richer, E. E. (2011). Empirical critical loads of atmospheric nitrogen deposition for nutrient enrichment and acidification of sensitive US lakes. *Bioscience* 61, 602–613. doi: 10.1525/bio.2011.61.8.6

Bartrons, M., Camarero, L., and Catalan, J. (2010). Isotopic composition of dissolved inorganic nitrogen in high mountain lakes: variation with altitude in the Pyrenees. *Biogeosciences* 7, 1469–1479. doi: 10.5194/bg-7-1469-2010

Bergstrom, A. K., and Jansson, M. (2006). Atmospheric nitrogen deposition has caused nitrogen enrichment and eutrophication of lakes in the northern hemisphere. *Glob. Chang. Biol.* 12, 635–643. doi: 10.1111/j.1365-2486.2006.01129

Birk, S., Chapman, D., Carvalho, L., Spears, B. M., Andersen, H. E., Argillier, C., et al. (2020). Impacts of multiple stressors on freshwater biota across spatial scales and ecosystems. *Nat. Ecol. Evol.* 4, 1060–1068. doi: 10.1038/s41559-020-1216-4

Catalan, J. (2000). Primary production in a high mountain lake: an overview from minutes to kiloyears. *Att. Assoc. Ital. Oceanol. Limnol.* 13, 1–21.

Catalan, J., Pla-Rabes, S., Wolfe, A. P., Smol, J. P., Rühland, K. M., Anderson, N. J., et al. (2013). Global change revealed by palaeolimnological records from remote lakes: a review. *J. Paleolimnol.* 49, 513–535. doi: 10.1007/s10933-013-9681-2

Chai, Y., Zhang, C., Kong, L., and Zhao, C. (2018). Climatic changes and heavy metal pollution over the past 200 years recorded by Lake Cuoqia, southwestern Yunnan Province (in Chinese). *J. Lake Sci.* 30, 1732–1744. doi: 10.18307/2018.0624

Chen, N., Bianchi, T. S., McKee, B. A., and Bland, M. J. (2001). Historical trends of hypoxia on the Louisiana shelf: application of pigments as biomarkers. *Org. Geochem.* 32, 543–561. doi: 10.1016/S0146-6380(00)00194-7

Chen, X., McGowan, S., Xiao, X. Y., Stevenson, A. M., Yang, X. D., Li, Y. L., et al. (2018). Direct and indirect effects of Holocene climate variations on catchment and lake processes of a treeline lake, SW China. *Palaeogeogr. Palaeoclimatol. Palaeoecol.* 502, 119–129. doi: 10.1016/j.palaeo.2018.04.027

Chen, X., Mulder, J., Wang, Y., Zhao, D., and Xiang, R. (2004). Atmospheric deposition, mineralization and leaching of nitrogen in subtropical forested catchments, South China. *Environ. Geochem. Health* 26, 179–186. doi: 10.1023/B:EGAH.0000039580.79321.1a

Fordham, D. A., Jackson, S. T., Brown, S. C., Huntley, B., Brook, B. W., Dahl-Jensen, D., et al. (2020). Using paleo-archives to safeguard biodiversity under climate change. *Science* 369:eabc5654. doi: 10.1126/science.abc5654

Frieler, K., Lange, S., Piontek, F., Reyer, C. P. O., Schewe, J., and Warszawski, L. (2017). Assessing the impacts of 1.5 °C global warming – simulation protocol of the inter-Sectoral impact model Intercomparison project (ISIMIP2b). *Geosci. Model Dev.* 10, 4321–4345. doi: 10.5194/gmd-10-4321-2017

Hébert, M. P., Beisner, B. E., Rautio, M., and Fussmann, G. F. (2021). Warming winters in lakes: later ice onset promotes consumer overwintering and shapes springtime planktonic food webs. *Proc. Natl. Acad. Sci. U. S. A.* 118:e2114840118. doi: 10.1073/pnas.2114840118

Hobbs, W. O., Vinebrooke, R. D., and Wolfe, A. P. (2011). Biogeochemical responses of two alpine lakes to climate change and atmospheric deposition, Jasper and Banff national parks, Canadian Rocky Mountains. *Can. J. Fish. Aquat. Sci.* 68, 1480–1494. doi: 10.1139/F2011-058

Holtgrieve, G. W., Schindler, D. E., Hobbs, W. O., Leavitt, P. R., Ward, E. J., Bunting, L., et al. (2011). A coherent signature of anthropogenic nitrogen deposition to remote watersheds of the northern hemisphere. *Science* 118, 11545–11548. doi: 10.1073/pnas.2114840118

Hrycik, A. R., Isles, P. F., Adrian, R., Albringt, M., Bacon, L. C., Berger, S. A., et al. (2021). Earlier winter/spring runoff and snowmelt during warmer winters lead to lower summer chlorophyll-a in north temperate lakes. *Glob. Chang. Biol.* 27, 4615–4629. doi: 10.1111/gcb.15797

Hu, Z., Anderson, N. J., Yang, X., and McGowan, S. (2014). Catchment-mediated atmospheric nitrogen deposition drives ecological change in two alpine lakes in SE Tibet. *Glob. Chang. Biol.* 20, 1614–1628. doi: 10.1111/gcb.12435

Hu, Z., Yang, X., Anderson, J. N., and Li, Y. (2017). The landscape–atmosphere continuum determines ecological change in Alpine Lakes of SE Tibet. *Ecosystems* 21, 839–851. doi: 10.1007/s10021-017-0187-z

Immerzeel, W. W., Lutz, A. F., Andrade, M., Bahl, A., Biemans, H., Bolch, T., et al. (2020). Importance and vulnerability of the world's water towers. *Nature* 577, 364–369. doi: 10.1038/s41586-019-1822-y

Janse, J. H., Scheffer, M., Lijklema, L., Liere, L. V., Sloot, J. S., and Mooij, W. M. (2010). Estimating the critical phosphorus loading of shallow lakes with the ecosystem model PCLake: sensitivity, calibration and uncertainty. *Ecol. Model.* 221, 654–665. doi: 10.1016/j.ecolmodel.2009.07.023

Jeppesen, E., Sondergaarrd, M., Jensen, J. P., Havens, K. E., Anneville, O., Carvalho, L., et al. (2005). Lake responses to reduced nutrient loading-an analysis of contemporary long-term data from 35 case studies. *Freshw. Biol.* 50, 1747–1771. doi: 10.1111/j.1365-2427.2005.01415.x

Johnes, P. J. (1996). Evaluation and management of the impact of land use change on the nitrogen and phosphorus load delivered to surface waters: the export coefficient modelling approach. *J. Hydrol.* 183, 323–349. doi: 10.1016/0022-1694(95)02951-6

Kong, X., Dong, L., He, W., Wang, Q., Mooij, W. M., and Xu, F. (2015). Estimation of the long-term nutrient budget and thresholds of regime shift for a large shallow lake in China. *Ecol. Indic.* 52, 231–244. doi: 10.1016/j.ecolind.2014.12.005

Kong, X., Ghaffar, S., Determann, M., Friese, K., Jomaa, S., Mi, C., et al. (2022). Reservoir water quality deterioration due to deforestation emphasizes the indirect effects of global change. *Water Res.* 221:118721. doi: 10.1016/j.watres.2022.118721

Kong, X., He, Q., Yang, B., He, W., Xu, F., Janssen, A. G., et al. (2017). Hydrological regulation drives regime shifts: evidence from paleolimnology and ecosystem modeling of a large shallow Chinese lake. *Glob. Chang. Biol.* 23, 737–754. doi: 10.1111/gcb.13416

Kong, X., Seewald, M., Dadi, T., Friese, K., Mi, C., Boehrer, B., et al. (2021). Unravelling winter diatom blooms in temperate lakes using high frequency data and ecological modeling. *Water Res.* 190:116681. doi: 10.1016/j.watres.2020.116681

Kong, L., Yang, X., Kattel, G., Anderson, N. J., and Hu, Z. (2017). The response of Cladocerans to recent environmental forcing in an alpine Lake on the SE Tibetan Plateau. *Hydrobiologia* 784, 171–185. doi: 10.1007/s10750-016-2868-6

Leavitt, P. R., and Hodgson, D. A. (2002). "Sedimentary pigments" in *Tracking Environmental Change Using Lake Sediments. Developments in Paleoenvironmental Research*, eds. J. P. Smol H. J. B. Birks W. M. Last R. S. Bradley and K. Alverson vol. *3* (Dordrecht: Springer), 295–325.

Leavitt, P. R., Vinebrooke, R. D., Donald, D. B., Smol, J. P., and Schindler, D. W. (1997). Past ultraviolet radiation environments in lakes derived from fossil pigments. *Nature* 388, 457–459. doi: 10.1038/41296

Li, Y., Wang, Q., Anderson, N. J., and Yang, X. (2021). Cladocera responses to climate changes and treeline shifts in an alpine lake-catchment since the last glacial maximum. *Palaeogeogr. Palaeoclimatol. Palaeoecol.* 577:110547. doi: 10.1016/j.palaeo.2021.110547

Liu, X., Duan, L., Mo, J., Du, E., Shen, J., Lu, X., et al. (2011). Nitrogen deposition and its ecological impact in China: an overview. *Environ. Pollut.* 159, 2251–2264. doi: 10.1016/j.envpol.2010.08.002

Liu, X., Zhang, Y., Han, W., Tang, A., Shen, J., Cui, Z., et al. (2013). Enhanced nitrogen deposition over China. *Nature* 494, 459–462. doi: 10.1038/nature11917

McGowan, S. (2013). "Pigments studies" in *The Encyclopedia of Quaternary Science*. ed. S. Elias, vol. *3. 2nd* ed (Amsterdam: Elsevier), 326–338.

Meyers, P. A., and Ishiwatari, R. (1993). Lacustrine organic geochemistry-an overview of indicators of organic matter sources and diagenesis in lake sediments. *Org. Geochem.* 20, 867–900. doi: 10.1016/0146-6380(93)90100-P

Ormerod, S. J., Dobson, M., Hildrew, A. G., and Townsend, C. R. (2010). Multiple stressors in freshwater ecosystems. *Freshw. Biol.* 55, 1–4. doi: 10.1111/j.1365-2427.2009.02395.x

Pohlert, T. (2020). Trend: Non-Parametric Trend Tests and Change-Point Detection. R Package Version 1.4. Available at: https://CRAN.R-project.org/package=trend.

Qiu, J. (2008). China: the third pole. *Nature* 454, 393–396. doi: 10.1038/454393a

R Core Team, (2021). *R: A Language and Environment for Statistical Computing*. R Foundation for Statistical Computing, Vienna, Austria.

Reynolds, C. S. (2006). *The Ecology of Phytoplankton*, Cambridge: Cambridge University Press.

Rigosi, A., Carey, C. C., Ibelings, B. W., and Brookes, J. D. (2014). The interaction between climate warming and eutrophication to promote cyanobacteria is dependent on trophic state and varies among taxa. *Limnol. Oceanogr.* 59, 99–114. doi: 10.4319/lo.2014.59.1.0099

Rühland, K., Paterson, A., and Smol, J. (2015). Lake diatom responses to warming: reviewing the evidence. *J. Paleolimnol.* 54, 1–35. doi: 10.1007/s10933-015-9837-3

Saros, J. E., Stone, J. R., Pederson, G. T., Slemmons, K. E., Spanbauer, T., Schliep, A., et al. (2012). Climate-induced changes in lake ecosystem structure inferred from coupled neo- and paleo-ecological approaches. *Ecology* 93, 2155–2164. doi: 10.1890/11-2218.1

Schnedler-Meyer, N. A., Andersen, T. K., Hu, F. S., Bolding, K., Nielsen, A., and Trolle, D. (2022). Water ecosystems tool (WET) 1.0 - a new generation of flexible aquatic ecosystem model. *Geosci. Model Dev.* 15, 3861–3878. doi: 10.5194/gmd-15-3861-2022

Seddon, A. R., Mackay, A. W., Baker, A. G., Birks, J. B., Breman, E., Buck, C. E., et al. (2014). Looking forward through the past: identification of 50 priority research questions in palaeoecology. *J. Ecol.* 102, 256–267. doi: 10.1111/1365-2745.12195

Shatwell, T., Thiery, W., and Kirillin, W. (2019). Future projections of temperature and mixing regime of European temperate lakes. *Hydrol. Earth Syst. Sci.* 23, 1533–1551. doi: 10.5194/HESS-23-1533-2019

Šmilauer, P., and Lepš, J. (2014). *Multivariate Analysis of Ecological Data Using CANOCO 5, 2nd Edn*. Cambridge University Press, Cambridge.

Smol, J. P. (2010). The power of the past: using sediments to track the effects of multiple stressors on lake ecosystems. *Freshw. Biol.* 55, 43–59. doi: 10.1111/j.1365-2427.2009.02373.x

Smol, J. P., Wolfe, A. P., Birks, J. B., Douglas, M. S., Jone, V. J., and Korhola, A. (2005). Climate-driven regime shifts in the biological communities of arctic lakes. *Proc. Natl. Acad. Sci. U. S. A.* 102, 4397–4402. doi: 10.1073/pnas.0500245102

Sommer, U., Adrian, R., Domis, S. L., Elser, J. J., Gaedke, U., Ibelings, B., et al. (2012). Beyond the plankton ecology group (PEG) model: mechanisms driving plankton succession. *Annu. Rev. Ecol. Evol. Syst.* 43, 429–448. doi: 10.1146/annurev-ecolsys-110411-160251

Talbot, M.R. (2001). Nitrogen isotopes in palaeolimnology. In: *Trackingenvironmental Change Using Lake Sediments. Volume 2: Physical and Geochemical Methods* (Eds.) Last, WM, and Smol, JP), pp. 401–439. Kluwer Academic Publishers, New York, Boston, Dordrecht, London, Moscow.

Tan, L., Cai, Y., An, Z., Cheng, H., Shen, C., Gao, Y., et al. (2016). Decreasing monsoon precipitation in Southwest China during the last 240 years associated with the warming of tropical ocean. *Clim. Dynam.* 48, 1769–1778. doi: 10.1007/s00382-016-3171-y

Thompson, L. G., Yao, T., Mosley-Thompson, E., Davis, M. E., Henderson, K. A., and Lin, P. N. (2000). A high-resolution millennial record of the south Asian monsoon from Himalayan ice cores. *Science* 289, 1916–1919. doi: 10.1126/science.289.5486.1916

Umlauf, L., and Lemmin, U. (2005). Interbasin exchange and mixing in the hypolimnion of a large lake: the role of long internal waves. *Limnol. Oceanogr.* 50, 1601–1611. doi: 10.4319/lo.2005.50.5.1601

Wang, R., Goll, D., Balkanski, Y., Hauglustaine, D., Boucher, O., Ciais, P., et al. (2017). Global forest carbon uptake due to nitrogen and phosphorus deposition from 1850 to 2100. *Glob. Chang. Biol.* 23, 4854–4872. doi: 10.1111/gcb.13766

Wang, R., Hu, Z., Wang, Q., Xu, M., Zheng, W., Zhang, K., et al. (2020). Discrepancy in the responses of diatom diversity to indirect and direct human activities in lakes of the southeastern Tibetan Plateau, China. *Anthropocene* 30:100243. doi: 10.1016/j.ancene.2020.100243

Warszawski, L., Frieler, K., Huber, V., Piontek, F., Serdeczny, O., and Schewe, J. (2014). The inter-sectoral impact model intercomparison project (ISI–MIP): project framework. *P. Natl. Acad. Sci. U. S. A.* 111, 3228–3232. doi: 10.1073/pnas.1312330110

Wischnewski, J., Kramer, A., Kong, Z., Mackay, A. W., Simpson, G. L., Mischke, S., et al. (2011). Terrestrial and aquatic responses to climate change and human impact on the southeastern Tibetan Plateau during the past two centuries. *Glob. Chang. Biol.* 17, 3376–3391. doi: 10.1111/j.1365-2486.2011.02474.x

Wolfe, A. P., Van Gorp, A. C., and Baron, J. S. (2003). Recent ecological and biogeochemical changes in alpine lakes of Rocky Mountain National Park (Colorado, USA): a response to anthropogenic nitrogen deposition. *Geobiology* 1, 153–168. doi: 10.1046/j.1472-4669.2003.00012.x

Woolway, R. I., Kraemer, B. M., Lenters, J. D., Lenters, J. D., Merchant, C. J., O'Reilly, C. M., et al. (2020). Global lake responses to climate change. *Nat. Rev. Earth. Environ.* 1, 388–403. doi: 10.1038/s43017-020-0067-5

Xiao, X., Haberleb, S. G., Shen, J., Yang, X., Han, Y., Zhang, E., et al. (2014). Latest Pleistocene and Holocene vegetation and climate history inferred from an alpine lacustrine record, northwestern Yunnan Province, southwestern China. *Quat. Sci. Rev.* 86, 35–48. doi: 10.1016/j.quascirev.2013.12.023

Xu, C., An, W., Wang, S., Yi, L., Ge, J., Nakatsuka, T., et al. (2019). Increased drought events in Southwest China revealed by tree ring oxygen isotopes and potential role of Indian Ocean dipole. *Sci. Total Environ.* 661, 645–653. doi: 10.1016/j.scitotenv.2019.01.186

Yang, J., Lv, H., Isabwe, A., Liu, L., Yu, X., Chen, H., et al. (2017). Disturbance-induced phytoplankton regime shifts and recovery of cyanobacteria dominance in two subtropical reservoirs. *Water Res.* 120, 52–63. doi: 10.1016/j.watres.2017.04.062

Zhang, Y., Song, L., Liu, X., Li, W., Lv, S., Zheng, L., et al. (2012). Atmospheric organic nitrogen deposition in China. *Atmos. Environ.* 46, 195–204. doi: 10.1016/j.atmosenv.2011.09.080

Zhang, B. Q., Wu, P. T., Zhao, X. N., Wang, Y., and Gao, X. (2013). Changes in vegetation condition in areas with different gradients (1980-2010) on the Loess Plateau, China. *Environ. Earth Sci.* 68, 2427–2438. doi: 10.1007/s12665-012-1927-1

Zhang, C., Zhao, C., Yu, S., Yang, X., Cheng, J., Zhang, X., et al. (2022). Seasonal imprint of Holocene temperature reconstruction on the Tibetan plateau. *Earth-Sci. Rev.* 226:103927. doi: 10.1016/j.earscirev.2022.103927

Zhang, C., Zhao, C., Zhou, A., Zhang, K., Wang, R., and Shen, J. (2019). Late Holocene lacustrine environmental and ecological changes caused by anthropogenic activities in the Chinese loess plateau. *Quat. Sci. Rev.* 203, 266–277. doi: 10.1016/j.quascirev.2018.11.020

Zhu, J., He, N., Wang, Q., Yuan, G., Wen, D., Yu, G., et al. (2015). The composition, spatial patterns, and influencing factors of atmospheric wet nitrogen deposition in Chinese terrestrial ecosystems. *Sci. Total Environ.* 511, 777–785. doi: 10.1016/j.scitotenv.2014.12.038

frontiers | Frontiers in Ecology and Evolution

TYPE Original Research
PUBLISHED 14 February 2023
DOI 10.3389/fevo.2023.1119869

OPEN ACCESS

EDITED BY
Kunshan Bao,
South China Normal University,
China

REVIEWED BY
Yongdong Zhang,
South China Normal University,
China
Xiaonan Zhang,
Yunnan University,
China

*CORRESPONDENCE
Can Zhang
✉ czhang@niglas.ac.cn
Haixia Zhang
✉ hxzhang@niglas.ac.cn

SPECIALTY SECTION
This article was submitted to Paleoecology, a section of the journal Frontiers in Ecology and Evolution

RECEIVED 09 December 2022
ACCEPTED 23 January 2023
PUBLISHED 14 February 2023

CITATION
Yan T, Zhang C, Zhang H, Sun X, Liu Y, Liu R, Zhang W and Zhao C (2023) Quantitative temperature and relative humidity changes recorded by the Lake Cuoqia in the southeastern Tibetan Plateau during the past 300 years.
Front. Ecol. Evol. 11:1119869.
doi: 10.3389/fevo.2023.1119869

Quantitative temperature and relative humidity changes recorded by the Lake Cuoqia in the southeastern Tibetan Plateau during the past 300 years

Tianlong Yan[1], Can Zhang[2]*, Haixia Zhang[2]*, Xiaoshuang Sun[3], Yilan Liu[2], Ruikun Liu[1], Wei Zhang[1] and Cheng Zhao[2,4]

[1]School of Geography, Liaoning Normal University, Dalian, China, [2]State Key Laboratory of Lake Science and Environment, Nanjing Institute of Geography and Limnology, Chinese Academy of Sciences, Nanjing, China, [3]School of Civil Architectural Engineering, Shandong University of Technology, Zibo, Shandong, China, [4]School of Geography and Ocean Science, Nanjing University, Nanjing, China

High-elevation lakes on the Tibetan Plateau have the advantage of sensitive response to climate changes. Multiple proxy records in lake sediments can provide a large amount of extractable information for paleoclimate reconstructions and assessing the position of recent global warming within the context of natural climate variability. In this study, we reconstruct the climatic and environmental changes over the past 300 years from a remote alpine lake (Lake Cuoqia) in the southeastern Tibetan Plateau using multiple proxies including branched glycerol dialkyl glycerol tetraethers (brGDGTs), *n*-alkanes, elements, fatty acids and their hydrogen isotopes. Due to ice-cover nature of lake surface during winter, brGDGTs mainly reflect the variation in warm-season temperature from March to October, supported by nearby instrumental data. Our reconstructed high-resolution temperature showed a continuous cooling trend between 1700 and 1950AD, followed by a rapid warming afterward, in parallel with other proxies such as *n*-alkanes and fatty acids in the same core, which is also consistent with previously published regional temperature records. The hydrogen isotope (δD) of fatty acids, similar to regional tree-ring $\delta^{18}O$, can record the history of atmospheric precipitation isotope and further indicate the variations of regional relative humidity. Our record exhibited a long-term decrease since 1700AD, in accord with the decreasing lake level inferred from the ratio of Fe/Mn. The combined pattern of reconstructed temperature and relative humidity showed consistent changes before 1950AD toward to a gradually cold-dry trend, whereas started to decouple afterward. Before 1950AD, the declined temperature and relative humidity are mainly driven by insolation and thermal contrast between the Indian-Pacific Ocean and south Asian continent. After 1950AD, decoupling of temperature and relative humidity may be related to the increased regional evaporation and human-induced emission of greenhouse gases and aerosol.

KEYWORDS

quantitative temperature, relative humidity, brGDGTs, hydrogen isotopes, past 300 years

Introduction

The southeastern Tibetan Plateau is the source of many large rivers in Asia, which is crucial to the atmospheric circulation and hydrological cycle from the regional to global scale (Ding, 1992). The meteorological data since 1950 AD showed that the heating rate of the Tibetan Plateau is twice the global average and relative humidity shows a downward trend (Chen et al., 2015). However, the

scarcity of meteorological stations and the lack of paleoclimate records limit us to perceive the mechanism of long-term climate changes (Yao et al., 2019). Thus, in order to obtain the pattern of long-term climate change, proxy-based climate researches are necessary. Moreover, this region is a refuge for many animals and plants with high biodiversity (Tan et al., 2018). Climate change in this region has an important impact on the socio-economic development and ecosystem of Southwest China. The past 300 years has been an important period for understanding the transition from nature-led to human-induced environmental changes, as well as for understanding the interaction between humans and nature. Understanding the characteristics and mechanisms of temperature and humidity changes over the past 300 years in the southeastern Tibetan Plateau is very important for assessing the climate change trend in the future.

Lake sediments have the advantages of good continuity, high resolution, climate sensitivity and large amount of extractable information. They have irreplaceable advantages in reconstructing climatic and environmental changes (Shen et al., 2010). In recent years, many records of quantitative temperature and precipitation/relative humidity have been reconstructed based on lake sediments in southeastern Tibetan Plateau (An et al., 2014; Liu X. et al., 2014; Zhang et al., 2017, 2022; Tan et al., 2018; Feng et al., 2019; Xu et al., 2019; Sun et al., 2021; Zhao et al., 2021a). Quantitative temperature reconstruction can not only understand the trend of temperature change in a long-time scale, but also obtain the absolute value and change amplitude of temperature more clearly. It is of great significance for providing more accurate future climate prediction (Kaufman et al., 2004). In addition, the reconstruction of relative humidity can increase the understanding of hydroclimatic changes in the southeastern Tibetan Plateau.

Glycerol dialkyl glycerol tetraethers (GDGTs) are a kind of membrane-spanning lipids with two C_{28} alkyl chains, 4–6 methyl substituents and 0–2 cyclopentyl moieties from bacteria and archaea (Sinninghe Damste et al., 2009; Schouten et al., 2013), which are common in lakes (Sun et al., 2011; Russell et al., 2018; Zhao et al., 2021a). Previous studies have shown that the bacterial-sourced branched GDGTs (brGDGTs) responses to temperature changes *via* producing more/less methyl branches to adjust to colder/warmer conditions (Peterse et al., 2011; Schouten et al., 2013). With the development of chromatographic separation, previous study successfully separated 5- and 6- methyl brGDGTs, further improving the reliability of temperature reconstructions (De Jonge et al., 2014). Hydrogen isotopes of fatty acids is a proxy which can well record the isotopic changes of atmospheric precipitation (Eglinton and Eglinton, 2008; Sachse et al., 2012). At present, there are few studies on precipitation/relative humidity reconstruction using hydrogen isotopes of fatty acids in southwestern China. In this study, we use multiple proxies to (1) quantitatively reconstruct temperature changes and precipitation/relative humidity over the past 300 years including brGDGTs, hydrogen isotope (δD), *n*-alkane, fatty acids and element, and (2) assess combined pattern of temperature and precipitation/relative humidity and the possible driving mechanisms.

Materials and methods

Study site

Lake Cuoqia is located in Hengduan Mountains in the southeastern Tibetan Plateau, ~20 km southwest of Shangri La County, Diqing Autonomous Prefecture, Yunnan Province (27°24′18.72″ N, 99°46′19.87″ E; elevation: 3960 m; Figure 1A). Hengduan Mountain is an important geographical boundary between the first and second steps of China, with obvious vertical zonality and dramatic changes in geomorphology and climate. Marine glaciers are developed in this area, and many glacial lakes are developed between 3,900 and 4,000 m above sea level (Zhang et al., 2012). Lake Cuoqia is lower than the forest line, with an area of 0.07 km^2, an average depth of 13.2 m and a maximum depth of 26 m (Figure 1B, Chai et al., 2018). The lake is hydrologically closed with no visible surface inflow and outflow. It is mainly supplied by atmospheric precipitation and ground melting snow water (Zhang et al., 2022). The vegetation around the lake is almost undisturbed by human activities, mainly subalpine low temperature coniferous trees, such as *Abies* and *Rhododendron* shrubs (Xiao et al., 2014).

The region is mainly affected by the Indian monsoon, with the same period of rain and heat. The region belongs to the temperate continental monsoon climate, with abundant solar radiation throughout the year and small annual temperature difference. According to the modern meteorological data of Shangri La Meteorological Station (27°30′0″ N, 99°25′12″ E; elevation: 3276.7 m), the nearest meteorological station to Lake Cuoqia, mean annual air temperature is 6.01°C, and mean annual precipitation is 624.72 mm. The temperature in this area is the highest in July (average monthly temperature 13.9°C) and the lowest in January (average monthly temperature - 2.3°C). The precipitation is mainly concentrated in June to September (Figure 1C). The monthly average humidity changes are between 58% (December) and 79% (August). From 1958 to 2015 AD, the mean annual precipitation has no obvious change, while the mean annual air temperature shows an obvious upward trend with 0.03°C/year (Figure 1D).

Sample collection and age control

In May 2014, a pair of sediment core (CQ1 and CQ2) were obtained using Hon Kajak large-diameter (9 cm) gravity sampler in the center of the Lake Cuoqia (Figure 1B). The two cores are 37 cm and 30 cm, respectively, and composed of humus black mud. The cores were sampled at an interval of 0.5 cm in the field. The samples were stored in self-sealing bags and refrigerated at 4°C for analysis. We also collected plant samples from trees, shrubs, grasses and surface soil around the lake.

CQ1 is used for proxy analysis of brGDGTs, fatty acids and its hydrogen isotopes, *n*-alkanes, total organic carbon (TOC), total nitrogen (TN) (Chai et al., 2018) and elements. CQ2 is used for $^{210}Pb/^{137}Cs$ dating to further calibrate the age model based on the CRS (Constant Rate of ^{210}Pb Supply) model (Appleby and Oldfeld, 1978). The depth-age sequence of both cores was previously published in Chai et al. (2018) and Zhang et al. (2022).

Biomarkers proxy analysis

About 1–3 g freeze-dried samples were extracted 4 times through ultrasonic shaker using organic solvents (dichloromethane: methanol = 9:1, v/v), ensuring complete extraction of organic matter from samples. After drying with N_2 gas, extracted total lipids were hydrolyzed using 6% KOH in Methyl alcohol solution for 12 h. Then, the supernatant was obtained after adding NaCl and *n*-hexane and

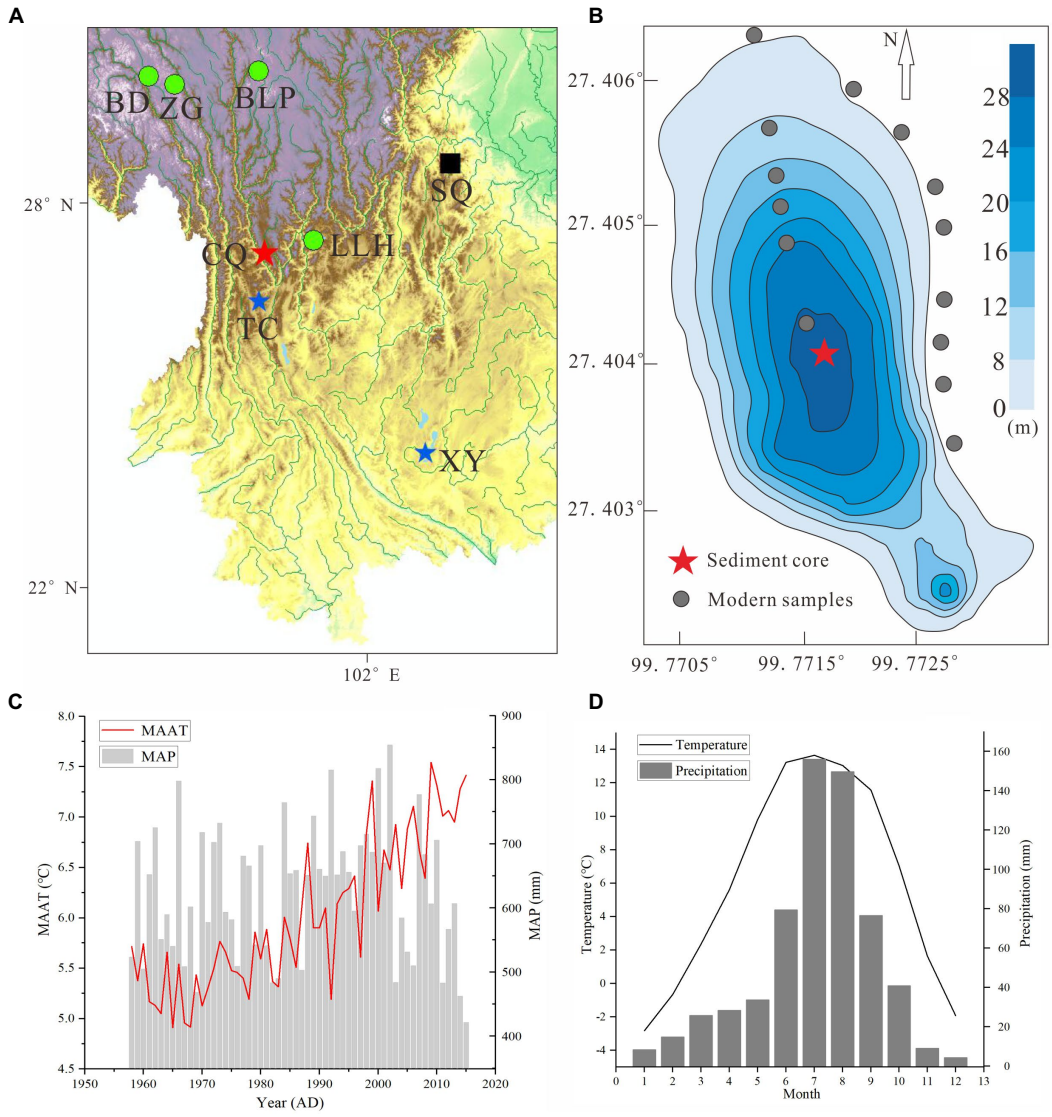

FIGURE 1
Location map and core sampling. **(A)** The map showing location of the Lake Cuoqia (CQ, red asterisks) and other paleoclimate records mentioned in this study. Blue asterisks are paleotemperature record from lakes [TC: Lake Tiancai (Zhang et al., 2017; Feng et al., 2019); XY: Lake Xingyun (Wu et al., 2018)]. Black block is stalagmite record from Shenqi cave (Tan et al., 2018). Green circle is tree ring records. [LLH: Larix trees in the low-latitude highlands (Xu et al., 2019); BLP: Batang-Litang Plateau (An et al., 2014); BD, ZG: Bangda and Zuogong (Duan and Zhang, 2014)]. **(B)** Bathymetry of the Lake Cuoqia and locations of the sediment cores (asterisks), surface sediment samples and soil samples on the catchment (grey dots). **(C)** The temperature and precipitation changes from Shangri La Meteorological Station during 1958–2015years. **(D)** Mean monthly temperature and precipitation at the Shangri-la Meteorological Station, Yunnan Province, China (data retrieved from the Meteorological Administration of China, http://data.cma.cn/). (For interpretation of the references to color in this figure legend, the reader is referred to the web version of this article).

centrifuging. Add 1.5 mL HCl (6 Mol) and 1.5 mL *n*-hexane to the bottle containing the sample solution to obtain the component of fatty acids. Finally, the neutral supernatant containing *n*-alkanes and GDGTs were further extracted through silica gel column chromatography using *n*-hexane and MeOH, respectively.

A total of 30 samples are determined for the fatty acids and δD values using Delta-V isotope ratio mass spectrometry (IRMS) instrument (Thermo Finnigan) *via* a high-temperature pyrolysis reactor at 1430°C. The instrument parameter settings and data analysis methods were referred to Liu and Liu, 2019. A total of 52 samples are analyzed for the *n*-alkanes *via* an Agilent 7,890 Gas Chromatography and the conditions for the Gas Chromatography following the previous research (Zhang et al., 2019).

A total of 68 samples are analyzed for the brGDGTs *via* UPLC-APCI-MS (the ACQUITY I-Class plus/Xevo TQ-S system) equipped with two coupled UPLC silica columns (BEH HILIC columns, 3.0 × 150 mm, 1.7 μm; Waters) in series, fitted with a pre-column and maintained at 30°C. The instrument can fully separate of 5- and 6-methyl isomers with improved chromatographic procedure. The samples were dissolved in 1000 μL *n*-hexane and injected for 4 μL for analysis. BrGDGTs were eluted at a constant flow rate of 0.4 mL/min for 80 min. The mobile phases of A and B, where A = hexane and B = hexane: isopropanol (9:1, v/v), were run isocratic ally with 82% A and 18% B for 25 min, followed by a linear gradient to 65% A and 35% B for 25–50 min, then to 100% B for 50–60 min with another 20 min re-equilibration. BrGDGTs were ionized in the APCI source at a probe temperature of

550°C, voltage corona of 5.0 μV, voltage cone of 110 V, gas flow desolvation of 1,000 L/h, gas flow cone of 150 L/h and collision gas flow of 0.15 mL/min. BrGDGTs isomers were detected using the selective ion monitoring (SIM) mode *via* $[M+H]^+$ ions at m/z 744 for the C_{46} standard, m/z 1,050, 1,048, 1,046, 1,036, 1,034, 1,032, 1,022, 1,020, and 1,018 for brGDGTs compounds (Hopmans et al., 2016). The modern samples were analyzed with the C_{46} standard and the relative concentrations of brGDGTs were calculated according to the integrated peak areas. Lipid preparation, *n*-alkanes and brGDGTs analysis were performed at the State Key Laboratory of Lake Science and Environment, Nanjing Institute of Geography and Limnology, Chinese Academy of Science. The fatty acids and its hydrogen isotopes were analyzed at State Key Laboratory of Loess and Quaternary Geology, Institute of Earth Environment, Chinese Academy of Sciences.

Parameters of average chain length (ACL) associated with *n*-alkanes and fatty acids were calculated as follow, respectively (Ficken et al., 2000; Liu and Liu, 2019).

$$\mathrm{ACL}_{n-\mathrm{alkanes}} = \begin{pmatrix} 21\times C_{21} + 23\times C_{23} \\ +\ldots+ 33\times C_{33} \end{pmatrix} / \begin{pmatrix} C_{21} + C_{23} \\ +\ldots+ C_{33} \end{pmatrix} \quad (1)$$

$$\mathrm{ACL}_{\mathrm{fatty\ acids}} = \begin{pmatrix} 20\times C_{20} + 22\times C_{22} \\ +\ldots+ 30\times C_{30} \end{pmatrix} / \begin{pmatrix} C_{20} + C_{22} \\ +\ldots+ C_{30} \end{pmatrix} \quad (2)$$

Where the C*i* is the abundance of the *i*th *n*-alkanes and fatty acids.

Reconstructions of quantitative temperature and relative humidity

The site-specific calibration of Lake Cuoqia was established using a stepwise regression method between brGDGTs fractional abundance of short-core CQ1 and the instrumental temperature record during the warm season (from March to October, $T_{M\text{-}O}$; Zhang et al., 2022). Such calibration has also been verified by reconstructed temperature record of another pair core (CQ2) since 1950 AD. Thus, the equation was further used to quantitatively reconstruct the temperature sequences of both cores over the past 300 years.

$$\begin{aligned} T_{M-O} = {} & 4.29 - 0.57\times f(IIIa) + 24.38\times f(IIa) \\ & - 3.44\times f(IIb) - 28.84\times f(Ia) \\ & - 34.19\times f(Ib) \begin{pmatrix} R^2 = 0.89, \\ RMSE = 0.24°\mathrm{C}, \\ n = 22 \end{pmatrix} \end{aligned} \quad (3)$$

Methanol correction formula is as follow (Yang and Huang, 2003):

$$\delta D_{n-\mathrm{Fas}} = \left[(2n+2)\,\delta D_{n-\mathrm{FAMEs}} - 3\delta D_{\mathrm{methanol}}\right] / (2n-1) \quad (4)$$

$\delta D_{n-\mathrm{Fas}}$, $\delta D_{n-\mathrm{FAMEs}}$ and $\delta D_{\mathrm{methanol}}$ represent value of fatty acids, fatty acid methyl ester and methanol δD, respectively. The value of $\delta D_{\mathrm{methanol}} = -123‰$.

For better discuss the driving mechanisms of climatic change, we calculated the temperature difference obtained by subtracting the average temperature of the Indian-Pacific Ocean from our reconstructed temperature. The specific method is firstly to normalize the difference between our reconstructed temperature and the temperature of the Indian-Pacific Ocean before interpolating to the same resolution.

Results

Our modern results show that the *n*-alkanes in lake surface sediments are mainly composed of long chains of C_{29} and C_{31} (Supplementary Figure S1). This is consistent with carbon chain distribution of catchment terrestrial plants (trees and shrubs) and top soils, but different from those of herbaceous plants dominated by medium chains (C_{27}) in the basin, indicating that the *n*-alkanes in the sediments of Lake Cuoqia are mainly derived from exogenous terrestrial arbors. The carbon chain distribution pattern of fatty acids showed that C_{16} and C_{22} were the main fraction in all periods (Supplementary Figure S2). C_{22} of fatty acids was applied for δD analysis due to the unclear source of C_{16} from microorganisms or terrestrial plants (Hou et al., 2006).

The reconstructed temperature shows consistent in two cores from Lake Cuoqia, showing a decline trend before 1950 AD and an increase after 1950 AD (Figure 2A). ACL values of *n*-alkanes and fatty acids changed almost same before 1930 AD, showing a continuous downward trend. After 1930, although ACL of both *n*-alkanes and fatty acids showed an upward trend, the growth rate of fatty acids was more obvious (Figure 2C). The ACL values of *n*-alkanes and fatty acids were consistent with the temperature results, both showing a change pattern of first falling and then rising. In addition, the change pattern of TOC and TN are also consistent with the temperature (Figure 2D). The δD of C_{22} from fatty acids showed a continuous decline pattern in the past 300 years (Figure 2E). The change pattern is consistent with the values of Fe/Mn (Figure 2F). The Rb/Sr. increased continuously before 1980 AD and began to decrease after 1980 AD (Figure 2G).

Discussion

Quantitative temperature reconstruction at Lake Cuoqia since 1700AD

Previous study shows that the brGDGTs in Lake Cuoqia mainly come from autochthonous sources, which are supported by multiple lines of evidence including comparison of brGDGTs distribution between surface sediments and down-core samples, ternary plots analysis (tetra-, penta-, and hexamethylated brGDGTs), relationship between the concentration of brGDGTs in surface sediments and water depth and ∑IIIa/∑IIa calculation (Zhang et al., 2022). The brGDGTs can well capture the temperature changes during the instrumental period at Lake Cuoqia with high correlation ($R^2 = 0.89$) to nearby meteorological data (Zhang et al., 2022). Using the same correction equation, we further quantitatively reconstructed the temperature changes in the past 300 years. The reconstructed temperature dropped continuously before 1950 AD and rose rapidly afterwards (Figure 2A). BIT (Branched Isoprenoid Tetraether index) values are the ratio of branched GDGTs to all fractional abundance of GDGTs (including branched and isoprenoid tetraether) and have been widely used as a proxy to evaluate the stability of the sedimentary environment (Zhang et al., 2019, 2022; Yan et al., 2021; Zhao et al., 2021a). The change of the BIT values was quite stable varying from 0.95 to 1 (Figure 2B), indicating

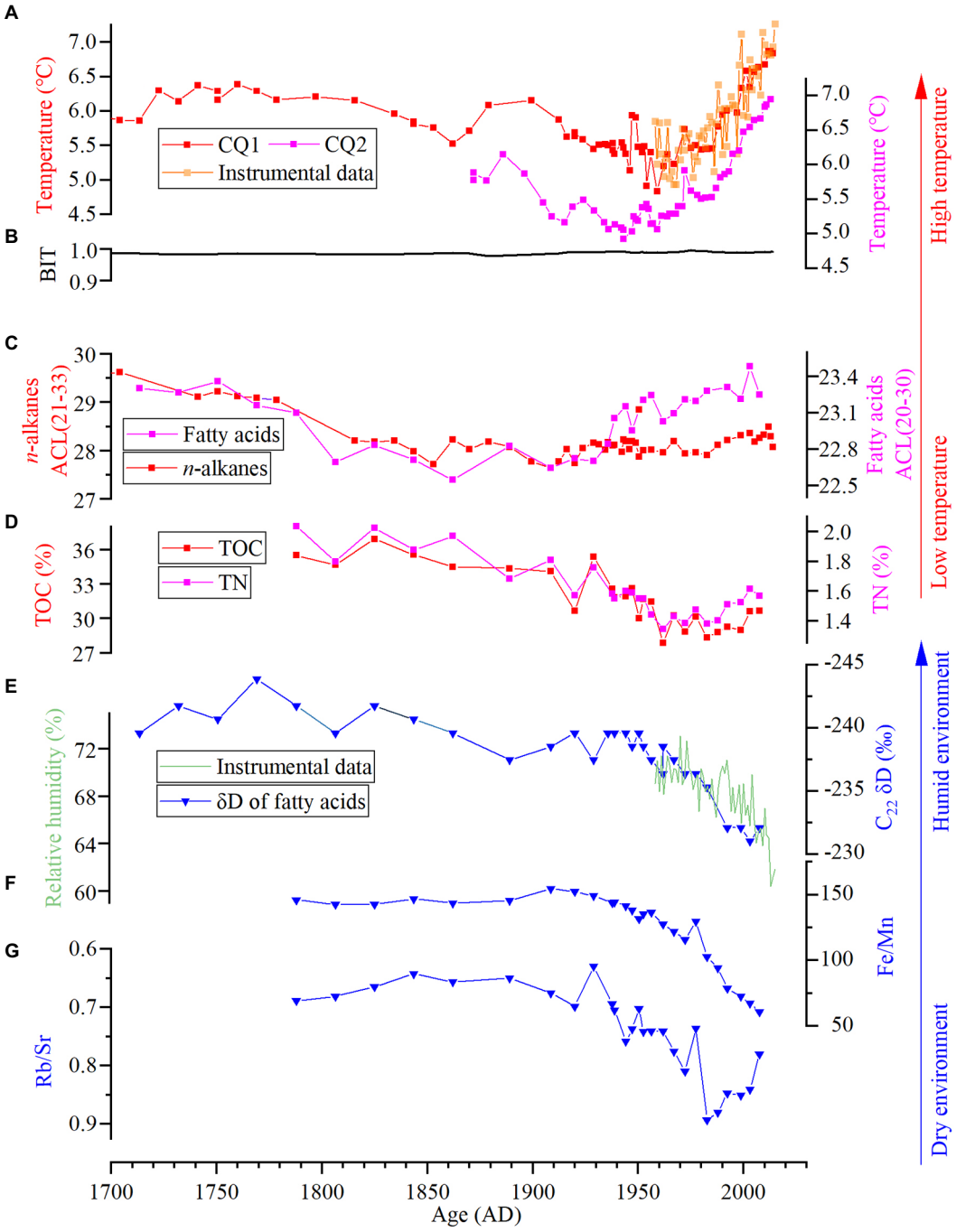

FIGURE 2
Results of multiple proxies from Lake Cuoqia. **(A)** The reconstructed temperature using brGDGTs from core CQ1 (red line) and CQ2 (magenta line). The orange line represents the warm season temperature (3–10month) from Shangri La Meteorological Station. Elevation correlation was made using a lapse rate of ~0.53°C/100m (He and Wang, 2020). **(B)** BIT values. **(C)** ACL values of fatty acids and *n*-alkanes. **(D)** TOC and TN (Chai et al., 2018). **(E)** δD of fatty acids (C_{22}, blue line) and relative humidity (green line) from instrumental data. **(F)** Fe/Mn ratio. **(G)** Rb/Sr. ratio. (For interpretation of the references to color in this figure legend, the reader is referred to the web version of this article).

stable sedimentary environment and the applicability of the calibration to the whole core. Our temperature results are supported by warm-season temperature (from March to October) from regional meteorological station data during 1958–2015 AD for both long-term trend and amplitude of variation (Figure 2A).

The reconstructed temperature shows consistent with other proxies from the same core such as ACL values of both *n*-alkanes and fatty acids, TOC and TN (Figures 2C, D). Previous study shows that the mid- and long-chains of leaf wax mainly from terrestrial plants, which is sensitive to temperature changes and can be used as an indicator of temperature changes (Zhou et al., 2005). Although the overall pattern of temperature changes is consistent, the slight discrepancy between them is possibly due to different responses to climate change. TOC and TN are two fundamental proxies for describing organic matter content in sediments, mainly reflecting the primary production of biomass which is related with regional climate changes (Meyers and Ishiwatari, 1993). The decline

of TOC and TN may indicate the gradually cold-dry climate conditions, in accord with the variation of our reconstructed temperature.

Our reconstructed temperature is also consistent with previously limited regional temperature records (Duan and Zhang, 2014; Zhang et al., 2017; Wu et al., 2018). For instance, July temperature based on subfossil chironomids from Lake Tiancai showed an overall decrease with a rapid increase after 1970 AD, albeit with an abnormal value at 1950 AD and quite low resolution (Figure 3B; Zhang et al., 2017). Our absolute temperature has lower values than Lake Tiancai for the past 300 years, which can attribute to differences of reconstructed season and elevation (higher ~60 m). Moreover, the similar long-term trend can also be observed from pollen-based July temperature record at the Lake Xingyun (Figure 3C; Wu et al., 2018). The higher-resolution warm-season (from April to September) temperature from tree ring showed a slight decrease trend before 1920 AD with a reverse afterwards (Figure 3D; Duan and Zhang, 2014). The low temperatures centered at 1870 AD and 1980 AD corresponded with our reconstructed temperature (Figure 3D). The mismatch in the warming time may be attributed to dating uncertainty. It is worth noting that our temperature shows obvious discrepancy with the trend of mean annual air temperature reconstructed by brGDGTs from Lake Tiancai and sea surface temperature from Indian-Pacific Ocean (Tierney et al., 2015; Feng et al., 2019), both showing a continuous warming (Figures 3E, F). This may be attributed to seasonal difference between warm-season and mean annual temperature, which is confirmed to be present at longer Holocene scales (Sun et al., 2021; Zhang et al., 2022). In conclusion, our reconstructed 300 years quantitative temperature is reliable and agrees well with regional limited temperature records.

Relative humidity changes over the past 300 years

Previous studies suggest that the hydrogen isotopes of fatty acids and *n*-alkanes from terrestrial plants can well record the isotopic changes of atmospheric precipitation (Eglinton and Eglinton, 2008; Sachse et al., 2012). δD of C_{22} from fatty acids has similar fraction process of *n*-alkanes δD from precipitation isotope in hydrological cycles (Hou et al., 2006; Contreras-Rosales et al., 2014). However, the controlled factors of leaf wax δD include local rainfall, soil evaporation, vegetation fractionations, etc. (Dansgaard, 1964; Cai et al., 2012; Sachse et al., 2012; Zhang et al., 2020). The water required for plants in the lake catchment mainly derived from soil water which is influenced by monsoon precipitation and soil evaporation effect (Sachse et al., 2004, 2012; Zhao et al., 2021b). Thus, leaf wax δD should mainly reflect the variations in the relative humidity. The isotopic fractionations may also exist during lipid biosynthesis in plant, and possible evapotranspiration between soil and lipid leaf wax water (Sachse et al., 2012). Some studies from southwestern China demonstrate that the isotope (δD and $\delta^{18}O$) of tree ring indeed indicates the changes of relative humidity on centennial time scale (An et al., 2014), and has been verified by the regional instrumental data. Note that the effect of vegetation fractionation also exists in tree-ring δD with little influence, similar to our leaf wax δD of fatty acid (An et al., 2014). Therefore, our isotope records the changes of regional relative humidity with positive δD of C_{22} indicating dry environment, and vice versa.

In the past 300 years, the gradually enriched δD of C_{22} from the Lake Cuoqia indicates a continuously dry condition, which shows good relation with the relative humidity measured by instrument data over the past decades (Figure 2E). Our δD-based relative humidity is also consistent with the ratio of Fe/Mn from the same core (Figure 4B). Fe/Mn can indicate redox state and further indicate the rise and fall of lake level with high ratio of Fe/Mn corresponding to high lake level, and vice versa (Mackereth, 1966). Similar changes can also be observed in another proxy of Rb/Sr. ratio in the same core (Figure 2G), which is widely used to reflect the intensity of chemical weathering with low values for intense chemical weathering related to humid environment, and vice versa (Chen et al., 2008; Liu J. et al., 2014).

The consistent changes of the relative humidity can also be recorded by other geological archives including tree ring, stalagmite and lake (An et al., 2014; Xiao et al., 2014; Tan et al., 2018; Xu et al., 2018, 2019). For example, the relative humidity, reconstructed by high-resolution tree ring $\delta^{18}O$ from Batang-Litang Plateau (BLP) of southeastern Tibetan Plateau (Figure 1A), showed a long-term drying trend in the past 300 years (Figure 4C; An et al., 2014). Also, similar trend can be observed in another $\delta^{18}O$ of tree ring from low-latitude highlands (LLH) of southwestern China (Figure 1A), revealing an apparent drying trend especially after 1840 AD (Figure 4D; Xu et al., 2018, 2019), which can be supported by the reconstructed cloud cover records using composite $\delta^{18}O$ of three tree-ring chronologies from southeastern Tibetan Plateau (Figure 4E; Liu X. et al., 2014). Similarly, many $\delta^{18}O$ records of stalagmite in nearby regions also show consistent changes with our reconstructed relatively humidity. For instance, the precipitation index and $\delta^{18}O$ of stalagmite from Shenqi Cave (SQ) in southwestern China (Figures 4F, G; Tan et al., 2018) showed a persistent positive trend, indicating a drying environment. In addition, the gradually drying environment is also supported by pollen data in sediments of Lake Tiancai, in which the tree pollen of *Tsuga* gradually decreases (Xiao et al., 2014). In summary, the reconstructed relative humidity is consistent with proxies from same core and is supported by instrumental data and regional precipitation/relative humidity records.

Combined pattern of temperature and relative humidity and driving mechanisms

Our reconstructed temperature and relative humidity showed consistent changes between 1700 AD and 1950 AD toward to gradually cold-dry trend, whereas started to decouple after 1950 AD, manifested as increasing temperature and decreasing relative humidity (Figures 2A,E). The combined pattern of reconstructed temperature and relative humidity is characterized with decoupling at 1950 AD, when the reason has not yet completely recorded and discussed by regional archives. Here, we focus on analyzing and explaining the underlying causes and driving factors of decoupling before and after 1950 AD.

The continuous decrease of temperature and relative humidity before 1950 AD was in accord with the decreasing warm-season insolation (from March to October) at 26° N (Figure 3H; Laskar et al., 2004; Sun et al., 2021). The decreasing insolation reduced total energy received at the earth surface, resulting into the decline in regional temperature. The decreasing insolation also weakened the intensity of Indian summer monsoon and further reduced the precipitation and/or relative humidity in our study area (Tan et al., 2018). Moreover, the persistent decline of relative humidity may be related to the decreasing thermal contrast between sea surface temperatures of the tropical Indian-Pacific Ocean and land temperature in our region (Figure 3G), which determines the intensity of water-vapor transports dominated by the Indian summer monsoon (Bansod et al., 2003; Feng and Hu, 2005;

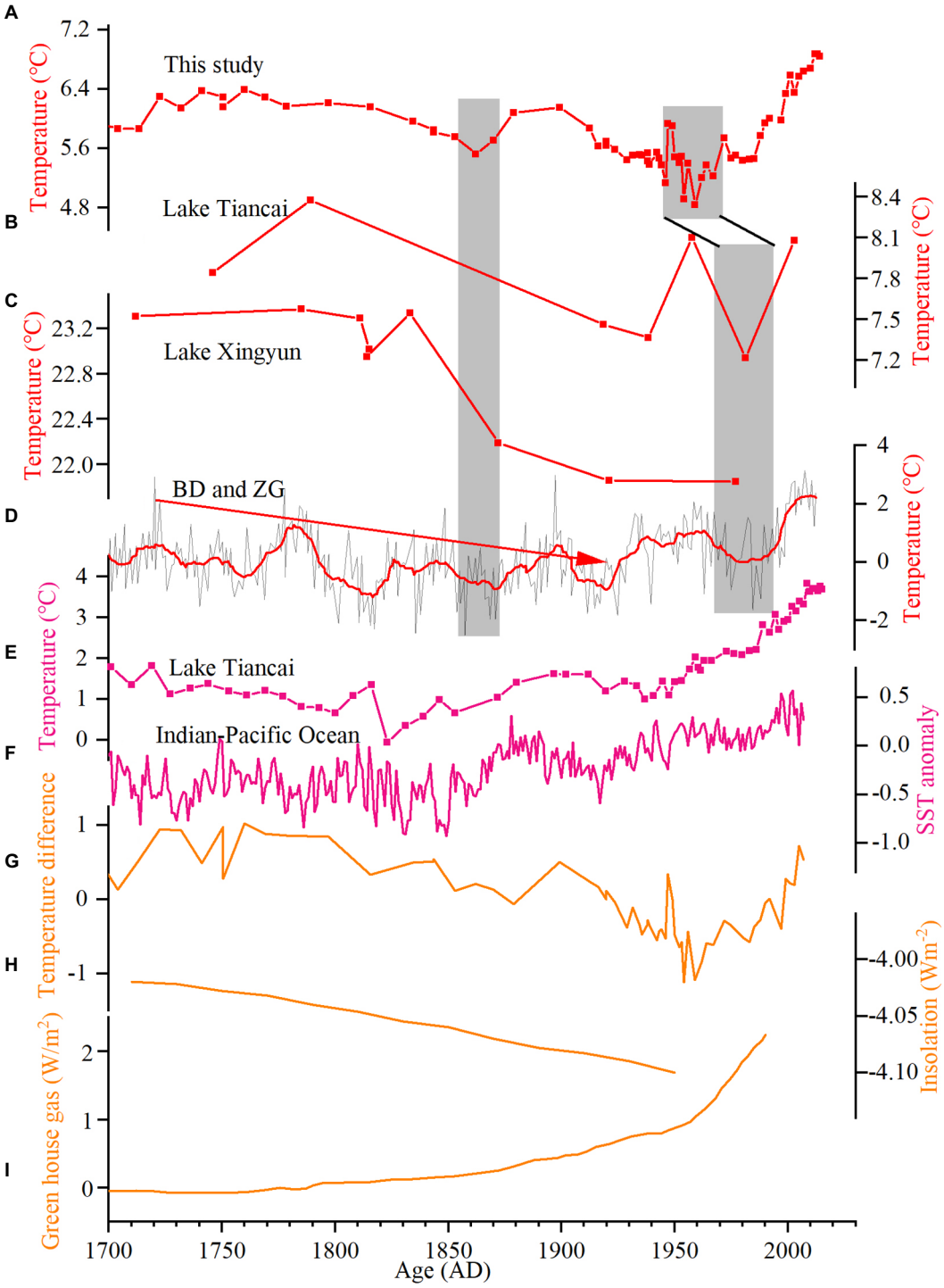

FIGURE 3
Comparison with regional temperature records and driving mechanisms. **(A)** Quantitative temperature reconstruction from Lake Cuoqia in this study. The gray shadows indicate period of low temperature. **(B)** Quantitative mean July temperature reconstruction based on subfossil chironomids from Lake Tiancai (Zhang et al., 2017). **(C)** Pollen-based mean July temperature record from Lake Xingyun (Wu et al., 2018). **(D)** The Apr-Sep mean temperature reconstruction using tree ring from Bangda (BD) and Zuogong (ZG) in the southeastern Tibetan Plateau (Duan and Zhang, 2014). **(E)** Quantitative mean annual air temperature using brGDGTs from Lake Tiancai (Feng et al., 2019). **(F)** The temperature reconstruction of Indian-Pacific Ocean based on coral records (Tierney et al., 2015). **(G)** Temperature difference between our reconstructed temperature anomaly and SST from Indian-Pacific Ocean (Tierney et al., 2015). **(H)** Warm-season insolation anomaly at 26°N (Laskar et al., 2004). **(I)** GHG-driven forcing (Crowley, 2000). (For interpretation of the references to color in this figure legend, the reader is referred to the web version of this article).

An et al., 2014). Furthermore, the pressure difference between Tibetan Plateau and tropical Ocean may also affect the monsoon precipitation and relative humidity in the southeastern Tibetan Plateau (Rashid et al., 2011). Previous studies suggest that the years with high relative humidity are related to the low-pressure conditions on the southeastern Tibetan Plateau, while the pressure field on the Indian Ocean is opposite

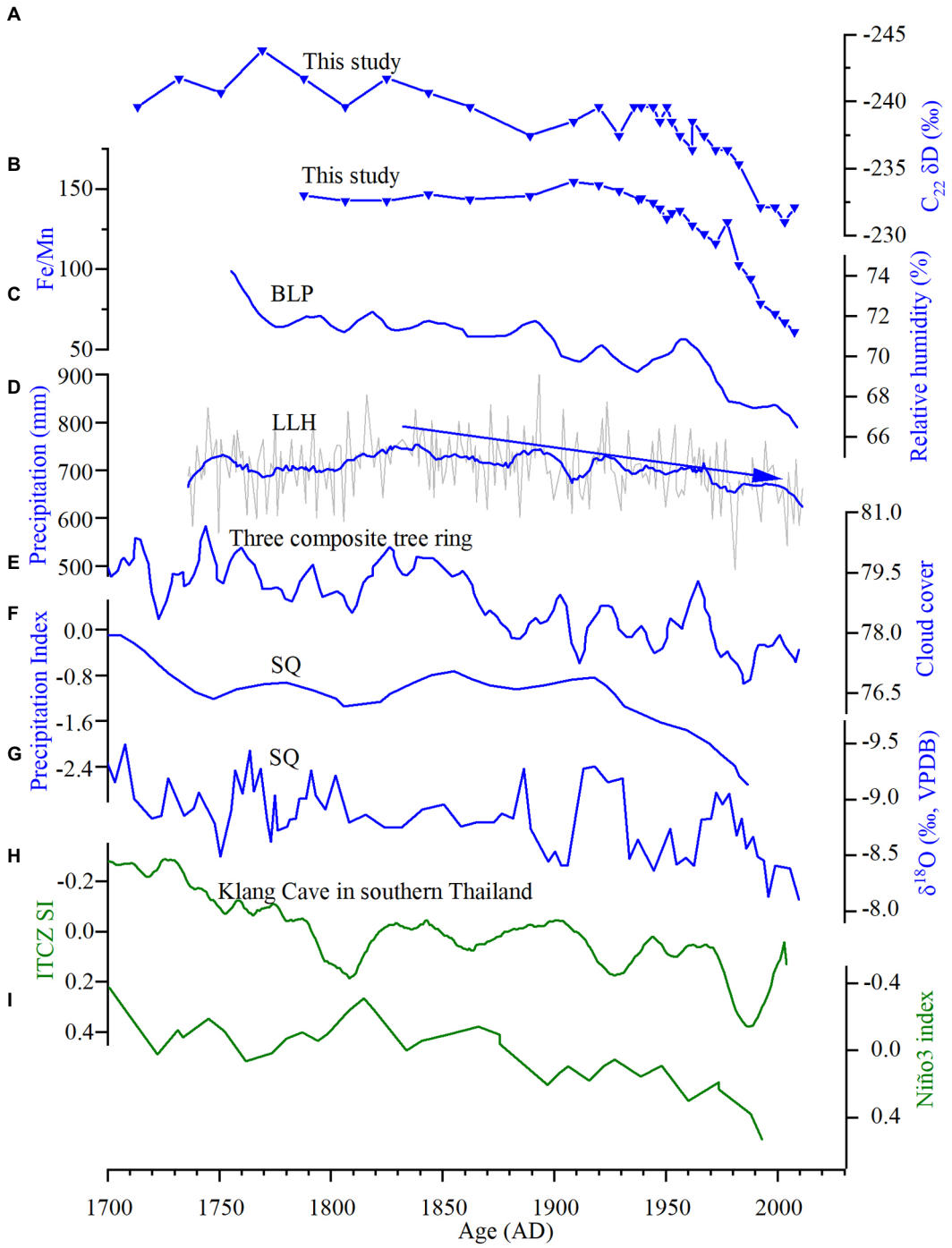

FIGURE 4
Comparison with regional relative humidity records and driving mechanisms. **(A)** δD of C_{22} from fatty acids (this study). **(B)** Changes of lake level inferred from Fe/Mn (this study). **(C)** Reconstructions of relative humidity from June to August based on tree-ring δD chronologies (An et al., 2014). **(D)** Record of $\delta^{18}O$ from regional tree ring (Xu et al., 2019). **(E)** Reconstructed cloud cover using composite $\delta^{18}O$ of three tree-ring chronologies (Liu X. et al., 2014). **(F)** Precipitation index inferred from stalagmite (Tan et al., 2018). **(G)** Stalagmite $\delta^{18}O$ of Shenqi cave (Tan et al., 2018). **(H)** Shift index of Intertropical Convergence Zone inferred from stalagmite (Tan et al., 2019). **(I)** Model simulated Niño3.4 sea surface temperatures variability (Man and Zhou, 2011). (For interpretation of the references to color in this figure legend, the reader is referred to the web version of this article).

(An et al., 2014). When the Tibetan Plateau maintains a high-pressure ridge in summer, the intensity of Indian summer monsoon weakens, reducing the movement of ocean air mass from the Indian Ocean to the plateau (Charles et al., 1997; Xu et al., 2009). Therefore, the path of rain storms will move southward, resulting in low relative humidity. In addition, the decreasing relative humidity over the past 300 years has high coherence with overall southward shift of Intertropical Convergence Zone (Figure 4H; Tan et al., 2019) and intensified EI Niño-like conditions (Figure 4I; Man and Zhou, 2011), indicating a pivotal role of low-latitude driving force to southeastern Tibetan Plateau.

After 1950, our reconstructed temperature record showed consistent changes to the rapid increase in greenhouse gases emission caused by

human activity (Figure 3I), indicating a close connection between them (Crowley, 2000). Although increased temperature can lead to more water-vapor supply and larger temperature difference between sea and land, the relative humidity showed an overall decrease trend during this period (Figure 4A). The decreased relative humidity may be caused by enhanced evaporation associated with unprecedented warming. In addition, the decreasing relative humidity was possibly related to the aerosol-affected Anthropocene warming as well which can lead to a weakening of summer monsoon intensity and thus result into dry environment (Liu et al., 2017). In the future, the continued and rapid warming would further decrease the relative humidity, and more attention should be taken for extreme climate changes in the Tibetan Plateau region.

Conclusion

We reconstruct quantitative warm-season temperature and relative humidity from Lake Cuoqia over the past 300 years, using multiple proxies of brGDGTs, *n*-alkanes, fatty acids and δD of C_{22}. The result of temperature showed decreased trend before 1950 AD and increased trend thereafter, which was consistent with the changes in ACL values of *n*-alkanes and fatty acids in the same core. Our temperature data was also in accord with regional warm-season and/or summer temperature records. The reconstructed relative humidity using C_{22} δD of fatty acids showed gradually dry trend over the past 300 years, which is consistent with the results of lake level inferred from Fn/Mn in the same core and regional $\delta^{18}O$ records from tree ring. Before 1950 AD, temperature and relative humidity were coupled, showing a cold-dry trend. After 1950 AD, the temperature and relative humidity were decoupled, and the temperature began to rise while the relative humidity continued to decline. The temperature is possibly affected by warm-season insolation before 1950 AD. The continuous drying is related to monsoon intensity and water-vapor input caused by the temperature difference between the lake Cuoqia and the Indian-Pacific Ocean. After 1950 AD, the decoupling of temperature and relative humidity may be related to the enhanced evaporation and increased emission of human-induced greenhouse gases and aerosol. The continued and rapid warming would further decrease the relative humidity, and more attention should be taken for extreme climate changes in the Tibetan Plateau region in the future.

Data availability statement

The original contributions presented in the study are included in the article/Supplementary material, further inquiries can be directed to the corresponding author.

Author contributions

TY, CZhang, and HZ designed the conceptualization, conducted data interpretation, drawing and writing. CZhang, HZ, XS, and YL participate in experiments analysis. CZhao, XS, RL, and WZ conducted the research and data interpretation. All authors contributed to the article and approved the submitted version.

Funding

This work was supported by the Jiangsu Special Fund on Technology Innovation of Carbon Dioxide Peaking and Carbon Neutrality (BK20220016), the National Natural Science Foundation of China (42007401), the Strategic Priority Research Program of Chinese Academy of Sciences (XDB40000000), the Laboratory opening project of Liaoning Normal University (#CX202201030), and the Science and Technology Planning Project of NIGLAS (NIGLAS2022TJ02).

Acknowledgments

We thank Yifan Chai, Lingyang Kong, Qian Wang, Xiangdong Yang for field and laboratory assistance.

Conflict of interest

The authors declare that the research was conducted in the absence of any commercial or financial relationships that could be construed as a potential conflict of interest.

Publisher's note

Supplementary material

The Supplementary material for this article can be found online at: https://www.frontiersin.org/articles/10.3389/fevo.2023.1119869/full#supplementary-material

References

An, W., Liu, X., Leavitt, S. W., Xu, G., Zeng, X., Wang, W., et al. (2014). Relative humidity history on the Batang-Litang plateau of western China since 1755 reconstructed from tree-ring $\delta^{18}O$ and δD. *Clim. Dynam.* 42, 2639–2654. doi: 10.1007/s00382-013-1937-z

Appleby, P. G., and Oldfeld, F. (1978). The calculation of lead-210 dates assuming a constant rate of supply of unsupported ^{210}Pb to the sediment. *Catena* 5, 1–8. doi: 10.1016/S0341-8162(78)80002-2

Bansod, S. D., Yin, Z., Lin, Z., and Zhang, X. (2003). Thermal field over Tibetan plateau and Indian summer monsoon rainfall. *Int. J. Climatol.* 23, 1589–1605. doi: 10.1002/joc.953

Cai, Y., Zhang, H., Cheng, H., An, Z., Lawrence Edwards, R., Wang, X., et al. (2012). The Holocene Indian monsoon variability over the southern Tibetan plateau and its teleconnections. *Earth Planet. Sci. Lett.* 335-336, 135–144. doi: 10.1016/j.epsl.2012.04.035

Chai, Y. F., Zhang, C., Kong, L. Y., and Zhao, C. (2018). Climatic changes and heavy metal pollution over the past 200 years recorded by Lake Cuoqia，southwestern Yunnan Province. *J. Lake Sci.* 30, 1732–1744. (in Chinese with English abstract). doi: 10.18307/2018.0624

Charles, C. D., Hunter, D. E., and Fairbanks, R. G. (1997). Interaction between the ENSO and the Asian monsoon in a coral record of tropical climate. *Science* 277, 925–928. doi: 10.1126/science.277.5328.925

Chen, L., Shen, H., Jia, Y., Wu, J., Li, X., Wei, L., et al. (2008). Environmental change inferred from Rb and Sr of lacustrine sediments in Huangqihai Lake, Inner Mongolia. *J. Geogr. Sci.* 18, 373–384. doi: 10.1007/s11442-008-0373-1

Chen, D., Xu, B., Yao, T., Guo, Z., Cui, P., Chen, F., et al. (2015). Assessment of past, present and future environmental changes on the Tibetan Plateau. *Chin. Sci. Bull.* 60, 3025–3035. doi: 10.1360/N972014-01370

Contreras-Rosales, L. A., Jennerjahn, T., Tharammal, T., Meyer, V., Lückge, A., Paul, A., et al. (2014). Evolution of the Indian summer monsoon and terrestrial vegetation in the Bengal region during the past 18 ka. *Quat. Sci. Rev.* 102, 133–148. doi: 10.1016/j.quascirev.2014.08.010

Crowley, T. J. (2000). Causes of climate change over the past 1000 years. *Science* 289, 270–277. doi: 10.1126/science.289.5477.270

Dansgaard, W. (1964). Stable isotopes in precipitation. *Tellus* 16, 436–468. doi: 10.1111/j.2153-3490.1964.tb00181.x

De Jonge, C., Hopmans, E. C., Zell, C. I., Kim, J., Schouten, S., and Sinninghe Damsté, J. S. (2014). Occurrence and abundance of 6-methyl branched glycerol dialkyl glycerol tetraethers in soils: implications for palaeoclimate reconstruction. *Geochim. Cosmochim. Acta* 141, 97–112. doi: 10.1016/j.gca.2014.06.013

Ding, Y. (1992). Effects of the Qinghai-Xizang (Tibetan) plateau on the circulation features over the plateau and its surrounding areas. *Adv. Atmos. Sci.* 9, 112–130. doi: 10.1007/BF02656935

Duan, J., and Zhang, Q. (2014). A 449-year warm season temperature reconstruction in the southeastern Tibetan plateau and its relation to solar activity. *J. Geophys. Res. Atmos.* 119, 11,578–11,592. doi: 10.1002/2014JD022422

Eglinton, T. I., and Eglinton, G. (2008). Molecular proxies for paleoclimatology. *Earth Planet Sc. Lett.* 275, 1–16. doi: 10.1016/j.epsl.2008.07.012

Feng, S., and Hu, Q. (2005). Regulation of Tibetan Plateau heating on variation of Indian summer monsoon in the last two millennia. *Geophys. Res. Lett.* 32:L02702. doi: 10.1029/2004GL021246

Feng, X., Zhao, C., D'Andrea, W. J., Liang, J., Zhou, A., and Shen, J. (2019). Temperature fluctuations during the common era in subtropical southwestern China inferred from brGDGTs in a remote alpine lake. *Earth Planet. Sci. Lett.* 510, 26–36. doi: 10.1016/j.epsl.2018.12.028

Ficken, K. J., Li, B., Swain, D. L., and Eglinton, G. (2000). An n-alkane proxy for the sedimentary input of submerged/floating freshwater aquatic macrophytes. *Org. Geochem.* 31, 745–749. doi: 10.1016/S0146-6380(00)00081-4

He, Y., and Wang, K. (2020). Contrast patterns and trends of lapse rates calculated from near-surface air and land surface temperatures in China from 1961 to 2014. *Sci. Bull.* 65, 1217–1224. doi: 10.1016/j.scib.2020.04.001

Hopmans, E. C., Schouten, S., and Sinninghe Damste, J. S. (2016). The effect of improved chromatography on GDGT-based palaeoproxies. *Org. Geochem.* 93, 1–6. doi: 10.1016/j.orggeochem.2015.12.006

Hou, J., Huang, Y., Wang, Y., Shuman, B., Oswald, W. W., Faison, E., et al. (2006). Postglacial climate reconstruction based on compound-specific D/H ratios of fatty acids from blood pond, New England. *Geochem. Geophys. Geosyst.* 7:1076. doi: 10.1029/2005GC001076

Kaufman, D. S., Ager, T. A., Anderson, N. J., Anderson, P. M., Andrews, J. T., Bartlein, P. J., et al. (2004). Holocene thermal maximum in the western Arctic (0–180°W). *Quat. Sci. Rev.* 23, 529–560. doi: 10.1016/j.quascirev.2003.09.007

Laskar, J., Robutel, P., Joutel, F., Gastineau, M., Correia, A. C. M., and Levrard, B. (2004). A long-term numerical solution for the insolation quantities of the earth. *Astron. Astrophys.* 428, 261–285. doi: 10.1051/0004-6361:20041335

Liu, J., Chen, J., Selvaraj, K., Xu, Q., Wang, Z., and Chen, F. (2014). Chemical weathering over the last 1200 years recorded in the sediments of Gonghai Lake, Lvliang Mountains, North China: a high-resolution proxy of past climate. *Boreas* 43, 914–923. doi: 10.1111/bor.12072

Liu, H., and Liu, W. (2019). Hydrogen isotope fractionation variations of n-alkanes and fatty acids in algae and submerged plants from Tibetan plateau lakes: implications for palaeoclimatic reconstruction. *Sci. Total Environ.* 695:133925. doi: 10.1016/j.scitotenv.2019.133925

Liu, J., Rühland, K. M., Chen, J., Xu, Y., Chen, S., Chen, Q., et al. (2017). Aerosol-weakened summer monsoons decrease lake fertilization on the Chinese loess plateau. *Nat. Clim. Chang.* 7, 190–194. doi: 10.1038/nclimate3220

Liu, X., Xu, G., Grießinger, J., An, W., Wang, W., Zeng, X., et al. (2014). A shift in cloud cover over the southeastern Tibetan plateau since 1600: evidence from regional tree-ring d18O and its linkages to tropical oceans. *Quat. Sci. Rev.* 88, 55–68. doi: 10.1016/j.quascirev.2014.01.009

Mackereth, F. J. H. (1966). Some chemical observations on post-glacial lake sediments. *Phil. Trans. R. Soc. Lond. B* 250, 165–213. doi: 10.1098/rstb.1966.0001

Man, W., and Zhou, T. (2011). Forced response of atmospheric oscillations during the last millennium simulated by a climate system model. *Chin. Sci. Bull.* 56, 3042–3052. doi: 10.1007/s11434-011-4637-2

Meyers, P. A., and Ishiwatari, R. (1993). Lacustrine organic geochemistry-an overview of indicators of organic matter sources and diagenesis in lake sediments. *Org. Geochem.* 20, 867–900. doi: 10.1016/0146-6380(93)90100-P

Peterse, F., Prins, M. A., Beets, C. J., Troelstra, S. R., Zheng, H., Gu, Z., et al. (2011). Decoupled warming and monsoon precipitation in East Asia over the last deglaciation. *Earth Planet. Sci. Lett.* 301, 256–264. doi: 10.1016/j.epsl.2010.11.010

Rashid, H., England, E., Thompson, L., and Polyak, L. (2011). Late glacial to Holocene Indian summer monsoon variability based upon sediment records taken from the bay of Bengal. *Terr. Atmos. Ocean. Sci.* 22, 215–228. doi: 10.3319/TAO.2010.09.17.02(TibXS)

Russell, J. M., Hopmans, E. C., Loomis, S. E., Liang, J., and Sinninghe Damsté, J. S. (2018). Distributions of 5- and 6-methyl branched glycerol dialkyl glycerol tetraethers (brGDGTs) in east African lake sediment: effects of temperature, pH, and new lacustrine paleotemperature calibrations. *Org. Geochem.* 117, 56–69. doi: 10.1016/j.orggeochem.2017.12.003

Sachse, D., Billault, I., Bowen, G. J., Chikaraishi, Y., Dawson, T. E., Feakins, S. J., et al. (2012). Molecular Paleohydrology: interpreting the hydrogen-isotopic composition of lipid biomarkers from photosynthesizing organisms. *Annu. Rev. Earth Planet. Sci.* 40, 221–249. doi: 10.1146/annurev-earth-042711-105535

Sachse, D., Radke, J., and Gleixner, G. (2004). Hydrogen isotope ratios of recent lacustrine sedimentary n-alkanes record modern climate variability. *Geochim. Cosmochim. Acta* 68, 4877–4889. doi: 10.1016/j.gca.2004.06.004

Schouten, S., Hopmans, E. C., and Sinninghe Damsté, J. S. (2013). The organic geochemistry of glycerol dialkyl glycerol tetraether lipids: a review. *Org. Geochem.* 54, 19–61. doi: 10.1016/j.orggeochem.2012.09.006

Shen, J., Xue, B., Wu, J. L., Wu, Y. H., Liu, X. Q., Yang, X. D., et al. (2010). *Lake Sedimentation and Environmental Evolution*. Beijing: Science Press.

Sinninghe Damste, J. S., Ossebaar, J., Abbas, B., Schouten, S., and Verschuren, D. (2009). Fluxes and distribution of tetraether lipids in an equatorial African lake: constraints on the application of the TEX_{86} palaeothermometer and BIT index in lacustrine settings. *Geochim. Cosmochim. Acta* 73, 4232–4249. doi: 10.1016/j.gca.2009.04.022

Sun, Q., Chu, G., Liu, M., Xie, M., Li, S., Ling, Y., et al. (2011). Distributions and temperature dependence of branched glycerol dialkyl glycerol tetraethers in recent lacustrine sediments from China and Nepal. *J. Geophys. Res. Biogeosci.* 116:1365. doi: 10.1029/2010JG001365

Sun, X., Zhao, C., Zhang, C., Feng, X., Yan, T., Yang, X., et al. (2021). Seasonality in Holocene temperature reconstructions in southwestern China. *Paleoceanogr. Paleoclimatol.* 36:e2020PA004025. doi: 10.1029/2020PA004025

Tan, L., Cai, Y., Cheng, H., Edwards, L. R., Lan, J., Zhang, H., et al. (2018). High resolution monsoon precipitation changes on southeastern Tibetan plateau over the past 2300 years. *Quat. Sci. Rev.* 195, 122–132. doi: 10.1016/j.quascirev.2018.07.021

Tan, L., Shen, C., Löwemark, L., Chawchai, S., Edwards, R. L., Cai, Y., et al. (2019). Rainfall variations in central indo-Pacific over the past 2,700 y. *P. Natl. Acad. Sci. U.S.A.* 116, 17201–17206. doi: 10.1073/pnas.1903167116

Tierney, J. E., Abram, N. J., Anchukaitis, K. J., Evans, M. N., Giry, C., Kilbourne, K. H., et al. (2015). Tropical Sea surface temperatures for the past four centuries reconstructed from coral archives. *Paleocean* 30, 226–252. doi: 10.1002/2014PA002717

Wu, D., Chen, X., Lv, F., Brenner, M., Curtis, J., Zhou, A., et al. (2018). Decoupled early Holocene summer temperature and monsoon precipitation in Southwest China. *Quat. Sci. Rev.* 193, 54–67. doi: 10.1016/j.quascirev.2018.05.038

Xiao, X., Haberleb, S. G., Shen, J., Yang, X., Han, Y., Zhang, E., et al. (2014). Latest Pleistocene and Holocene vegetation and climate history inferred from an alpine lacustrine record, northwestern Yunnan Province, southwestern China. *Quat. Sci. Rev.* 86, 35–48. doi: 10.1016/j.quascirev.2013.12.023

Xu, C., An, W., Wang, S. Y. S., Yi, L., Ge, J., Nakatsuka, T., et al. (2019). Increased drought events in Southwest China revealed by tree ring oxygen isotopes and potential role of Indian Ocean dipole. *Sci. Total Environ.* 661, 645–653. doi: 10.1016/j.scitotenv.2019.01.186

Xu, H., Hong, Y. T., Hong, B., Zhu, Y. X., and Wang, Y. (2009). Influence of ENSO on multi-annual temperature variations at Hongyuan, NE Qinghai-Tibet plateau: evidence from d13C of spruce tree rings. *Int. J. Climatol.* 30, 120–126. doi: 10.1002/joc.1877

Xu, C., Sano, M., Dimri, A. P., Ramesh, R., Nakatsuka, T., Shi, F., et al. (2018). Decreasing Indian summer monsoon on the northern Indian sub-continent during the last 180 years: evidence from five tree-ring cellulose oxygen isotope chronologies. *Clim. Past* 14, 653–664. doi: 10.5194/cp-14-653-2018

Yan, T., Zhao, C., Yan, H., Shi, G., Sun, X., Zhang, C., et al. (2021). Elevational differences in Holocene thermal maximum revealed by quantitative temperature reconstructions at ~30° N on eastern Tibetan plateau. *Palaeogeo. Palaeoclim. Palaeoec.* 570:110364. doi: 10.1016/j.palaeo.2021.110364

Yang, H., and Huang, Y. (2003). Preservation of lipid hydrogen isotope ratios in Miocene lacustrine sediments and plant fossils at clarkia, northern Idaho, USA. *Org. Geochem.* 34, 413–423. doi: 10.1016/S0146-6380(02)00212-7

Yao, T., Xue, Y., Chen, D., Chen, F., Thompson, L. G., Cui, P., et al. (2019). Recent third Pole's rapid warming accompanies cryospheric melt and water cycle intensification and interactions between monsoon and environment: multidisciplinary approach with observations, modeling, and analysis. *Bull. Am. Meteorol. Soc.* 100, 423–444. doi: 10.1175/BAMS-D-17-0057.1

Zhang, E., Chang, J., Cao, Y., Sun, W., Shulmeister, J., Tang, H., et al. (2017). Holocene high-resolution quantitative summer temperature reconstruction based on subfossil chironomids from the southeast margin of the Qinghai-Tibetan plateau. *Quat. Sci. Rev.* 165, 1–12. doi: 10.1016/j.quascirev.2017.04.008

Zhang, W., Liu, B. B., Li, Y. H., Feng, J., Zhang, B., Wang, Z. L., et al. (2012). Quaternary glacier development and environmental evolution in Qianhu Mountain, North-Western Yunnan Province. *Acta Geogra. Sinica* 67, 657–670. doi: 10.11821/xb201205008

Zhang, C., Zhao, C., Yu, S., Yang, X., Cheng, J., Zhang, X., et al. (2022). Seasonal imprint of Holocene temperature reconstruction on the Tibetan plateau. *Earth-Sci. Rev.* 226:103927. doi: 10.1016/j.earscirev.2022.103927

Zhang, C., Zhao, C., Yu, Z., Zhang, H., Zhou, A., Zhang, X., et al. (2020). Western Pacific Ocean influences on monsoon precipitation in the southwestern Chinese loess plateau since the mid-Holocene. *Clim. Dyn.* 54, 3121–3134. doi: 10.1007/s00382-020-05159-9

Zhang, C., Zhao, C., Zhou, A., Zhang, K., Wang, R., and Shen, J. (2019). Late Holocene lacustrine environmental and ecological changes caused by anthropogenic activities in the Chinese loess plateau. *Quat. Sci. Rev.* 203, 266–277. doi: 10.1016/j.quascirev.2018.11.020

Zhao, C., Cheng, J., Wang, J., Yan, H., Leng, C., Zhang, C., et al. (2021b). Paleoclimate significance of reconstructed rainfall isotope changes in Asian monsoon region. *Geophy. Res. Lett.* 48:e92460. doi: 10.1029/2021GL092460

Zhao, C., Rohling, E. J., Liu, Z., Yang, X., Zhang, E., Cheng, J., et al. (2021a). Possible obliquity-forced warmth in southern Asia during the last glacial stage. *Sci. Bull.* 66, 1136–1145. doi: 10.1016/j.scib.2020.11.016

Zhou, W., Xie, S., Meyers, P. A., and Zheng, Y. (2005). Reconstruction of late glacial and Holocene climate evolution in southern China from geolipids and pollen in the Dingnan peat sequence. *Org. Geochem.* 36, 1272–1284. doi: 10.1016/j.orggeochem.2005.04.005

frontiers | Frontiers in Ecology and Evolution

TYPE Original Research
PUBLISHED 02 March 2023
DOI 10.3389/fevo.2023.1121632

OPEN ACCESS

EDITED BY
Kunshan Bao,
South China Normal University,
China

REVIEWED BY
Yuan Li,
Chinese Academy of Sciences, China
Xu Chen,
China University of Geosciences Wuhan,
China

*CORRESPONDENCE
Bin Xue
✉ bxue@niglas.ac.cn
Can Zhang
✉ czhang@niglas.ac.cn

SPECIALTY SECTION
This article was submitted to Paleoecology, a section of the journal Frontiers in Ecology and Evolution

RECEIVED 12 December 2022
ACCEPTED 08 February 2023
PUBLISHED 02 March 2023

CITATION
Cheng L, Gao X, Wang G, Ding Z, Xue B, Zhang C, Liu J and Jiang Q (2023) Intensified sensitivity and adaptability of zooplankton Bosminidae in subtropical shallow freshwater lakes with increasing trophic level. *Front. Ecol. Evol.* 11:1121632. doi: 10.3389/fevo.2023.1121632

Intensified sensitivity and adaptability of zooplankton Bosminidae in subtropical shallow freshwater lakes with increasing trophic level

Longjuan Cheng[1], Xinyuan Gao[1], Guangwei Wang[1], Zhou Ding[1], Bin Xue[2]*, Can Zhang[2]*, Jinliang Liu[3] and Qingfeng Jiang[1]

[1]School of Geographical Science, Nantong University, Nantong, Jiangsu, China, [2]State Key Laboratory of Lake Science and Environment, Nanjing Institute of Geography and Limnology, Chinese Academy of Sciences, Nanjing, Jiangsu, China, [3]School of Environmental Science, Nanjing Xiaozhuang University, Nanjing, Jiangsu, China

The deterioration in lake water environments, especially increasing lake eutrophication, is prevalent all over the world, which has seriously affected the balance and stability of the internal ecosystem of lakes. In this study, modern water and sediment samples were collected from three subtropical freshwater lakes with significant differences in nutrient levels to analyze the concentration of the zooplankton Cladocera Bosminidae and its relationship with lakes' ecological changes. The results show that the deterioration in lake water environments caused by increasing eutrophication limits the survival of most zooplankton. However, the Bosminidae shows a positive adaptability to eutrophication and high sensitivity to the changes in the lake environment. In addition, the lake eutrophication process caused by the intensification of human activities enhances the survival advantage of Bosminidae with more food sources, which is more conducive to its rapid reproduction.

KEYWORDS

subtropical shallow freshwater lake, zooplankton, Bosminidae, eutrophication, ecological changes

1. Introduction

Crustacean zooplankton Cladocera are highly abundant in freshwater bodies worldwide. These Cladocera communities are sensitive to changes in the environment and climate (Korhola and Rautio, 2001; Szeroczyńska and Sarmaja-Korjonen, 2007; Pawłowski et al., 2015; Cheng et al., 2020a). The Bosminidae family belongs to Cladocera communities and is characterized by small body sizes (0.2–1.0 mm). They are ubiquitous on lake surfaces where the concentration of nutrients is relatively high (Zaret and Kerfoot, 1975; Jiang and Du, 1979; Zaret and Kerfoot, 1980; Threlkeld, 1981; De Melo and Hebert, 1994). The different species of the Bosminidae family exhibit unique adaptability to different nutritional environments (Jiang and Du, 1979; Szeroczyńska and Sarmaja-Korjonen, 2007). For example, *Bosmina longirostris* is commonly reported in eutrophic lakes, warming waters, and metal-contaminated lakes (Boucherle and Züllig, 1983; Balcer et al., 1984; Labaj et al., 2015; Adamczuk, 2016). *Bosmina* (E.) *longispina* can be used to indicate oligotrophic and mesotrophic environment changes (Deevey, 1942;

Boucherle and Züllig, 1983; Miroslaw-Grabowska et al., 2015). However, due to the destruction of Bosminidae chitin fossils in the process of deposition, it is difficult to distinguish all the specific species of Bosminidae. Recent studies showed that the total number of Bosminidae, including both the eutrophic species *Bosmina longirostris* and oligotrophic and mesotrophic species *Bosmina* (E.) *longispina*, shows clear survival advantages in lakes with high trophic levels (Cheng et al., 2019, 2020b). For example, a large number of Bosminidae (a relative abundance greater than 80% in the total concentration of Cladocera) have been found in shallow eutrophic lakes in the subtropical zone (Liu et al., 2008; Wang et al., 2019; Cheng et al., 2020b). Furthermore, the abundance of *Bosmina longirostris* is usually greater than that of the species *Bosmina* (E.) *longispina* (Cheng et al., 2019, 2021) in eutrophic lakes. Therefore, we studied whether the Bosminidae can be used as a new indicator of the evolution of eutrophication in freshwater lakes in a subtropical region.

Since entering the Anthropocene, the impact of human activities on freshwater environments such as lakes has been increasing (Lin et al., 2020). Under the combined effects of anthropogenic activities (such as rapid industrialization and urbanization) and climate change, lakes in the middle and lower reaches of the Yangtze River in eastern China, which is located in a subtropical region with a relatively dense population and developed economy, have undergone drastic deterioration over a few decades (Qin et al., 2013; Zhu et al., 2019). Currently, these freshwater shallow lakes in the middle and lower reaches of the Yangtze River are a prominent area of environmental deterioration in China (Qin et al., 2013; Zhu et al., 2019). Furthermore, most lakes in this area have entered either a mesotrophic stage or a eutrophic stage, or in between, and are suffering serious cyanobacteria outbreaks that the stability and balance in the lake ecosystem are seriously disturbed (Zhu et al., 2019). For example, the biological composition of lakes has changed significantly, including the miniaturization of fishery structure, the reduction of aquatic plant area, cyanobacteria outbreaks, and a significant decline in biodiversity (Mao et al., 2012; Zhang K. et al., 2018; Jenny et al., 2020).

Taihu Lake (severe eutrophication), Nanyi Lake (transition from mesotrophication to eutrophication), and Shengjin Lake (mesotrophication) are located in the middle and lower reaches of the Yangtze River. They show significant differences in trophic level, area, and local economic development level and are representative of the research on the relationship between the evolution of zooplankton community and eutrophication. Therefore, in this study, we chose the three shallow freshwater lakes as our research object. Based on the research methods of paleolimnology and limnology, we focused on the indicative significance of Bosminidae in lake eutrophication in the three lakes since the 1950s. We analyzed the temporal and spatial changes in Bosminidae density and focused on revealing the adaptability and sensitivity of Bosminidae to lake eutrophication.

2. Materials and methods

2.1. Study area and field sampling

Taihu Lake, Nanyi Lake, and Shengjin Lake are located in the middle and lower reaches of the Yangtze River (Figure 1). The annual temperature and precipitation in the lower reaches of the Yangtze River Basin are 15–16°C and 1,010–1,600 mm, respectively (Qin et al., 2007; Wang et al., 2015; Yao and Xue, 2016; Zhang M. et al., 2018). Taihu Lake (mean depth = 1.89 m, area = 2,338 km^2) is socioeconomically important and is the third largest freshwater lake in the Yangtze Delta. It supplies drinking water to some of the large cities in the delta, including Shanghai, Suzhou, and Wuxi (Qin et al., 2007). Taihu Lake is divided into different ecological types (Qin et al., 2007). The eastern area of Taihu Lake (called the East Taihu Lake) has an average water depth of < 1 m. As opposed to the western and central lake areas, it is a grass lake dominated by large areas of aquatic plants (Cheng et al., 2020a). More than 200 rivers flow into Taihu Lake with a combined total length of ~120,000 km (Zhong et al., 2014). The lake has been experiencing prolonged eutrophication over the past 40 years, with increased cyanobacterial (Microcystis) blooms mostly during summer, reducing both water quality and biodiversity (Qin et al., 2007; Yang et al., 2008; Li and Chen, 2010; Dai et al., 2016).

Nanyi Lake (31°03′-31°10′N, 118°50′-119°02′ E) is located in the Shuiyangjiang River Basin, which belongs to the lower reaches of the Yangtze River. The lake's surface area is 203 km^2 with a mean depth of approximately 2 m (Wang et al., 2013). The Langchuan River and the New Langchuan River flow into the northeastern part of Nanyi Lake (Yao and Xue, 2016). Since the 1970s, significant increases in the trophic level and water level of Nanyi Lake have been observed, and currently, it is in a critical period of ecosystem transformation from mesotrophic to eutrophic status (Cheng et al., 2021).

Shengjin Lake (116° 55′–117° 15′ E and 30° 15′–30° 30′ N), which is an important national nature reserve, has a surface area of 133 km^2 and consists of three parts: upper, middle, and lower (Wang et al., 2015). Shengjin Lake serves as a habitat for more than 70,000 wintering water birds each year (Yang, 2011). It also joined the East Asian–Australasian Waterfowl Reserve Network in 2005 and was added to the list of Wetlands of International Importance in 2015 (Cao et al., 2018; Peng et al., 2019; Yang et al., 2019). With the increase in human activities, the trophic state of Shengjin Lake has also been increasing since the 1980s (Cheng et al., 2020c).

2.2. Materials and methods

Modern zooplankton samples were collected in October 2017 and in April and July 2018. Sedimentary cores were collected in October 2016 and 2017 (Table 1). The number of zooplankton in a unit volume of water was counted and the individuals were counted under the microscope at 100–200x magnification. The pretreatment process for subfossil Cladocera and geochemical indices (TN, TP, and $\delta^{13}C$ in the Bosminidae ($\delta^{13}C_{bos}$)) have been described in detail in previous studies (Cheng et al., 2020b,c, 2021). The subsamples for subfossil Cladocera were treated with 100 ml of 10% potassium hydroxide (KOH) solution, heated at 60°C for 45 min, sieved through a 38-μm mesh under running deionized water, and transferred into 15-ml centrifuge tubes (Frey, 1986; Korhola and Rautio, 2001). Most Cladocera remains were identified by their shell, headshield, postabdomen, and claw, and at least 100 individuals from each Cladocera (species) were counted in each sample (Jiang and Du, 1979; Szeroczyńska and Sarmaja-Korjonen, 2007). For the data on dating results and subfossil Bosminidae in the sedimentary cores, we refer to published literature and Supporting Information (Cheng et al., 2019, 2020c, 2021). Bosminidae (*Bosmina* spp.) includes unidentified *Bosmina* spp., *Bosmina longirostris*, *Bosmina* (E.) *longispina*, and *Bosmina* (E.) *coregoni*.

10.3389/fevo.2023.1121632

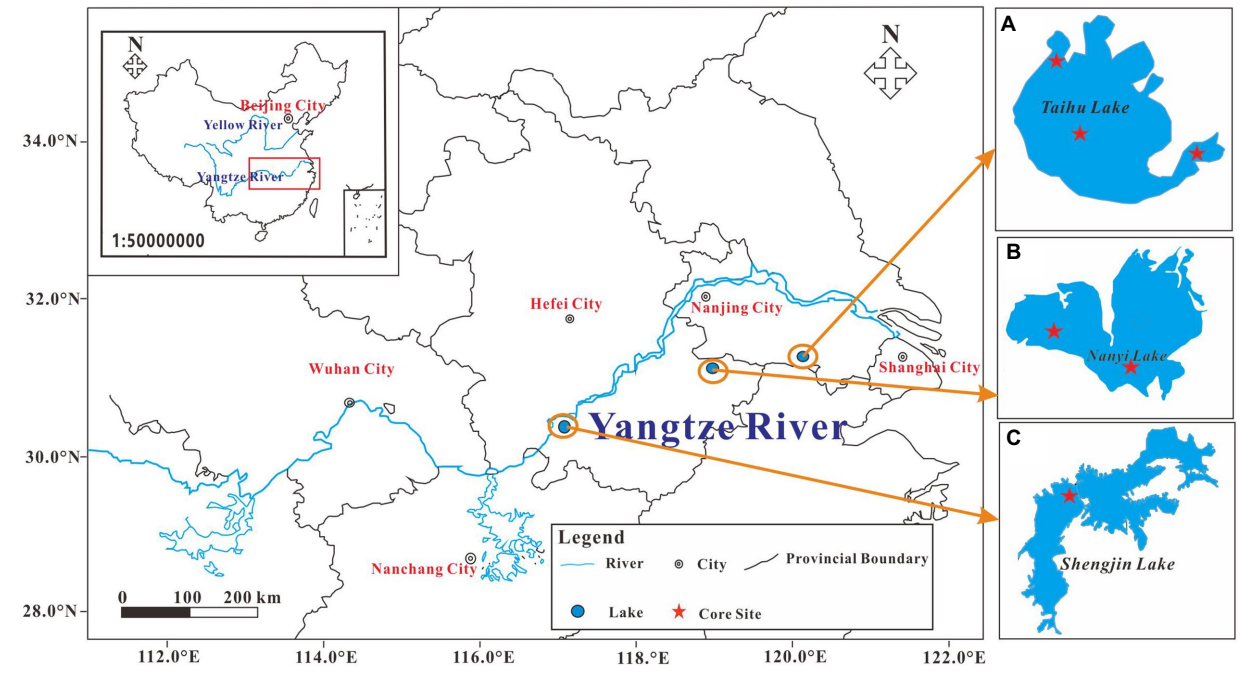

FIGURE 1
The location of the study area and the sample site. **(A)** Taihu Lake; **(B)** Nanyi Lake; and **(C)** Shengjin Lake.

TABLE 1 The physical and chemical water parameters noted in the sample sites.

Lake	Site	Season	Water depth (m)	Water temperature (°C)	pH	Transparency (cm)
Taihu lake	TH-2 (31.40890°N, 120.04118°E)	Spring	2.2	19.3	8.49	73
		Summer	2.8	28.9	8.9	25
		Autumn	2.8	15	7.24	60
	TH-7 (31.15603°N, 120.05130°E)	Spring	2.8	17	8.5	25
		Summer	3.5	31.9	9.09	23
		Autumn	4	15	7.68	15
	TH-5 (31.08744°N, 120.51746°E)	Spring	1.5	18.9	8.77	41
		Summer	1.7	30.5	8.66	28
		Autumn	1.8	15	7.58	60
Nanyi lake	NYH (31.11354°N, 118.97826°E)	Spring	1.8	19.4	8.21	18
		Summer	2.8	37.4	8.54	20
		Autumn	2.6	27	8.79	40
	NY-2 (31.06560°N, 118.95933°E)	Autumn	2.7	26	8.22	66
	NY-3 (31.10030°N, 118.90244°E)	Autumn	2.4	26	8.07	67
Shengjin lake	SJH (30.38942° N, 117.04160° E)	Spring	0.6	20.5	7.38	17
		Summer	2.1	33	7.5	38
		Autumn	1.3	19	7.44	40

2.3. Statistical analysis

Graphical representations of modern zooplankton, Bosminidae, and $\delta^{13}C_{bos}$ records were generated using Origin 8.0 and CorelDRAW 2018. Pearson's correlation analysis was conducted by IBM SPSS 19.0 (Statistical Graphics Corp, Princeton, United States) and Origin 8.0 using TN, TP, and Bosminidae to investigate the relationships between the biological indicator (Cladocera) and trophic indicators (TN and TP).

3. Results

3.1. Variability in modern Bosminidae abundance

We identified the modern zooplankton in Taihu Lake, Nanyi Lake, and Shengjin Lake. The results showed that Cladocera were the dominant zooplankton species in the three lakes, with the exception of the total number of Copepoda in Shengjin Lake in summer (52 ind./L) exceeding that of Cladocera (44 ind./L) and Rotifera (5 ind./L) (Figure 2). There were higher proportions of Cladocera in zooplankton in the Nanyi Lake (NYH: mean 320 ind./L). Values in the western area of the Taihu Lake (TH-2: mean 127 ind./L) and central area (TH-7: mean 198 ind./L) were much higher than in the Shengjin Lake (SJH: mean 24 ind./L). In spring, the total number of Cladocera identified in TH-7 and NYH reached the maximum values of 478 ind./L and 805 ind./L, respectively (Figure 2). The abundance of zooplankton in the eastern area (TH-5) of the Taihu Lake was far lower than those in the western and central areas (Figure 2). Only the abundance of Cladocera in summer was greater than 50 ind./L in TH-5, while the abundances of Cladocera, Copepoda, and Rotifera in spring and autumn were relatively low and balanced. The total number of zooplankton in SJH was similar to that in TH-5 with a low abundance in each season (Figure 2).

The dominant species of the zooplankton composition in different seasons in the three lakes was Cladocera, which mainly consisted of Bosminidae (Figure 2). The composition characteristics of Bosminidae concentrations in each lake and season were consistent with the distribution of the total number of Cladocera. The total abundance of Bosminidae in TH-2 and TH-7 with severe eutrophication and in NYH in the transitional stage from the mesotrophic to the eutrophic status exceeded 400 ind./L, with a relative proportion of more than 95% in spring. The peak values for Bosminidae in other lake areas mostly reached in summer and autumn.

3.2. Changes in trophic levels (TN and TP) and subfossil Bosminidae abundances since the 1950s

Information about species and abundances of subfossil Cladocera and trophic indices (TN and TP) has been described in detail elsewhere (Cheng et al., 2020a,b,c, 2021). For data on Bosminidae, total Cladocera, and chronology, we refer to the "Supporting Information." The trophic levels (TN-% and TP-mg/g) remained at a high level since the 1950s, with average values of 0.11% and 0.68 mg/g in the TH-2 core, 0.97% and 0.42 mg/g in the TH-5 core, 0.07% and 0.43 mg/g in the TH-7 core, 0.13% and 0.50 mg/g in the NY-2 core, 0.16% and 0.53 mg/g in the NY-3 core, and 0.28% and 0.59 mg/g in the SJH core (Figures 3, 4). The values of TN and TP in the west (TH-2 core) and central (TH-7 core) areas of the Taihu Lake significantly increased, while the values of TN in the east (TH-5 core) tended to decline but were kept at a higher level (0.92% ~ 1.0%) than in the TH-2 core (0.08% ~ 0.18%) and TH-7 core (0.06% ~ 0.10%). The values of TP in the cores of TH-2, TH-7, and TH-5 ranged from 0.12 to 0.48 mg/g, 0.35 to 0.51 mg/g, and 0.40 to 0.45 mg/g, respectively. The abundance of Bosminidae in the Taihu Lake changed consistently with TN and TP in the western and central areas, but there was a significant decreasing trend in the eastern Taihu Lake (Figures 3, 4). The values of TN and TP in the Nanyi Lake and Shengjin Lake clearly increased. The values of TN in the cores of NY-2, NY-3, and SJH ranged from 0.08 to 0.20%, 0.10 to 0.21%, and 0.23 to 0.31%, respectively. The values of TP in the cores of NY-2, NY-3, and SJH changed from 0.31 to 0.69 mg/g, 0.37 to 0.68 mg/g, and 0.45 to 0.64 mg/g, respectively. The abundance of Bosminidae also increased corresponding to the increase in nitrogen and phosphorus concentrations in the Nanyi Lake and Shengjin Lake.

The abundances of Cladocera sum and Bosminidae in the cores of TH-2 and TH-7 remained at a high level. Among them, the abundances of total Cladocera and Bosminidae in the TH-2 core ranged from 1,080 ~ 5,295 ind./g with a mean value of 3,048 ind./g, i.e., 94% ~ 98% with a mean value of 96%, respectively, while those in the TH-7 core ranged from approximately 2,507 ~ 9,373 ind./g with a mean value of 5,140 ind./g, i.e., 90% ~ 96% with a mean value of 94%, respectively (Figure 5). After the 1950s, the Cladocera sum decreased in the TH-2 core, but the abundance of Bosminidae increased significantly. The change in Cladocera sum and Bosminidae abundances in the TH-7 core was similar to that in the TH-2 core; that is, the fluctuation in Bosminidae increased after the 1950s (Figure 5). The change in Cladocera sum in the TH-5 core corresponding to that of Bosminidae decreased after the 1950s and their changed ranges were 463 ~ 1,127 ind./g with a mean value of 758 ind./g, i.e., 12% ~ 86% with a mean value of 44%, respectively. The change in the abundance of Bosminidae was consistent with that of the Cladocera sum that increased gradually with time in Nanyi Lake and Shengjin Lake (Figure 5). The ranges for Cladocera sum and Bosminidae in the NY-2 core were 111 ~ 901 ind./g with a mean value of 444 ind./g, i.e., 71% ~ 95% with a mean value of 86%, respectively. Values in the NY-3 core were 101 ~ 639 ind./g with a mean value of 400 ind./g, i.e., 53% ~ 89% with a mean value of 77%, respectively. The abundances of Cladocera sum and Bosminidae in Shengjin Lake (SJH core) were relatively lower than those of in the other two lakes, which changed from 241 ~ 487 ind./g with a mean value of 366 ind./g, i.e., 13% ~ 69% with a mean value of 48%, respectively (Figure 5).

3.3. Changes in the $\delta^{13}C$ values of subfossil Bosminidae in Taihu Lake since the 1950s

To accurately track the flow characteristics of carbon sources in primary consumers, the results of the stable carbon isotope analysis of subfossil Bosminidae ($\delta^{13}C_{bos}$) in the cores of TH-2 and TH-7 from the heavily eutrophic area in Taihu Lake after the 1950s are shown in Figure 6. The mean values of $\delta^{13}C_{bos}$ in the cores of TH-2 and TH-7 showed relatively consistent mean values of −22.45‰ and − 22.51‰, respectively. However, the variation range in the $\delta^{13}C_{bos}$ value of the TH-2 core was higher than that of

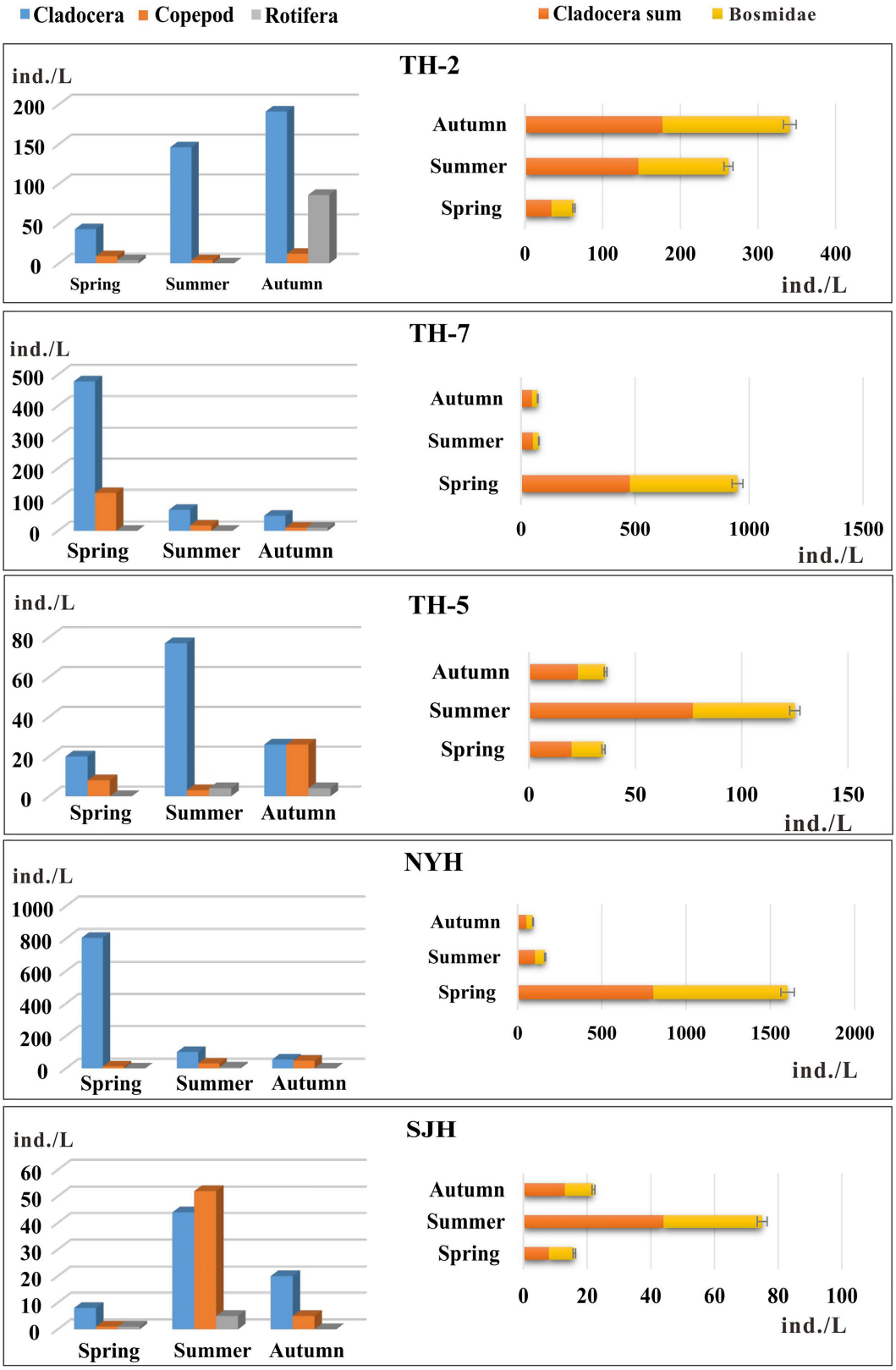

FIGURE 2
Modern zooplankton and Bosminidae from the Taihu Lake (TH-2, TH-7, and TH-5), Nanyi Lake (NYH), and Shengjin Lake (SJH) in the main living seasons.

the TH-7 core (Figure 6A). The $\delta^{13}C_{bos}$ values in the TH-2 core varied in the range of −25.77‰ ~ −19.54‰, while the $\delta^{13}C_{bos}$ values in the TH-7 core changed from −23.40‰ to −20.80‰. After the 1980s, with intensified eutrophication of Taihu Lake, the $\delta^{13}C_{bos}$ values of the two cores shared a common downward trend that was lower than the mean values (Figure 6B).

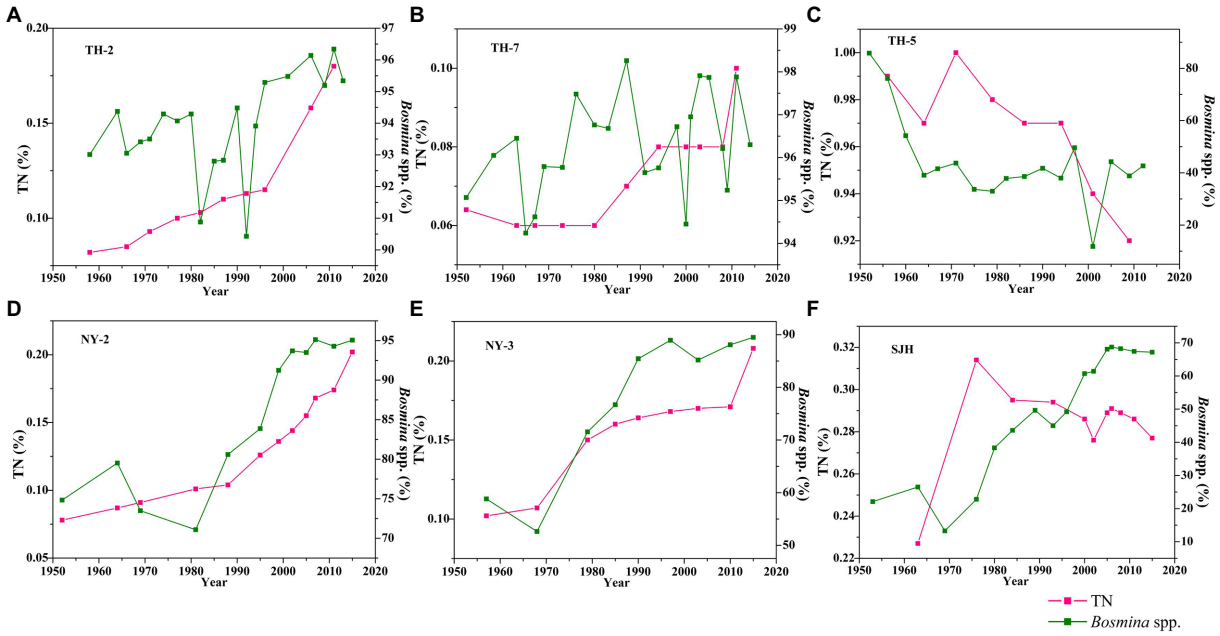

FIGURE 3
Changes in TN and Bosminidae (*Bosmina* spp.) in the Taihu Lake **(A–C)**, Nanyi Lake **(D,E)**, and Shengjin Lake **(F)** since the 1950s.

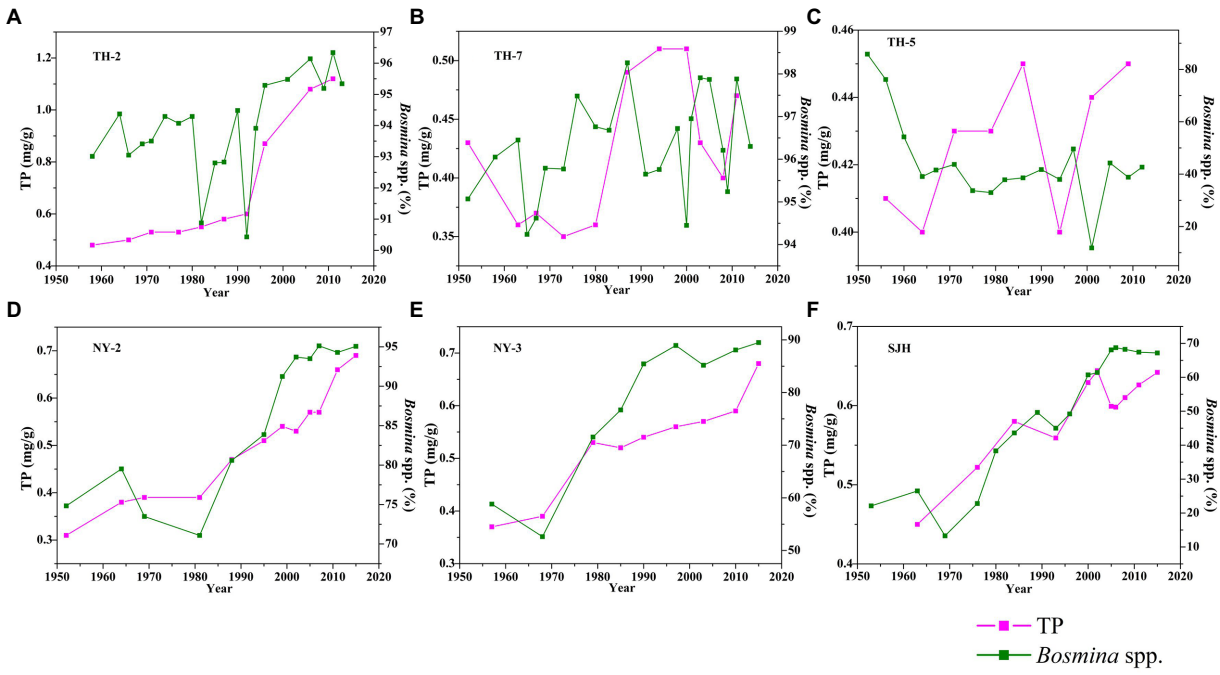

FIGURE 4
Changes in TP and Bosminidae (*Bosmina* spp.) in the Taihu Lake **(A–C)**, Nanyi Lake **(D,E)**, and Shengjin Lake **(F)** since the 1950s.

3.4. Pearson's correlation analysis between Bosminidae abundance change and trophic level

The Pearson correlation analysis between Bosminidae and trophic indices showed that the abundance of Bosminidae, including *B. longirostris* and *B* (E.) *longispina*, were significantly correlated with TN and TP (Table 2; Cheng et al., 2020a,b,c, 2021). There were significant positive correlations between Bosminidae and TN in the cores of TH-2, NY-2, and NY-3. The Bosminidae were positively correlated with TP in all cores except TH-5, which had a significant negative correlation. In addition, there were

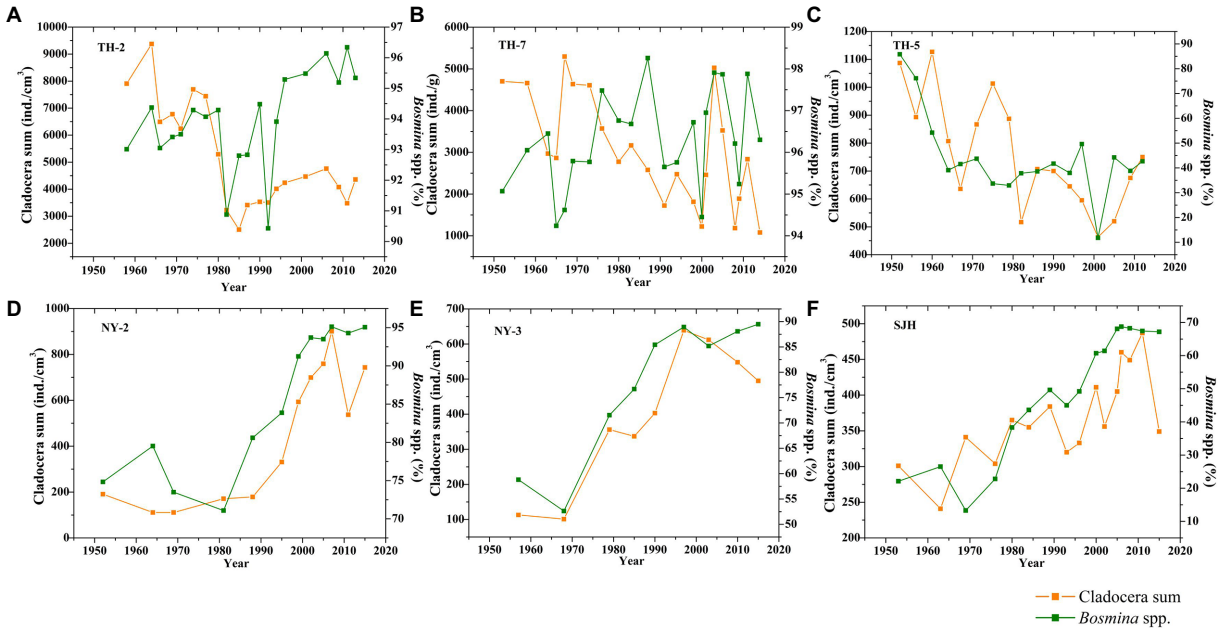

FIGURE 5
Changes in Cladocera sum and Bosminidae (*Bosmina* spp.) in the Taihu Lake **(A–C)**, Nanyi Lake **(D,E)**, and Shengjin Lake **(F)** since the 1950s.

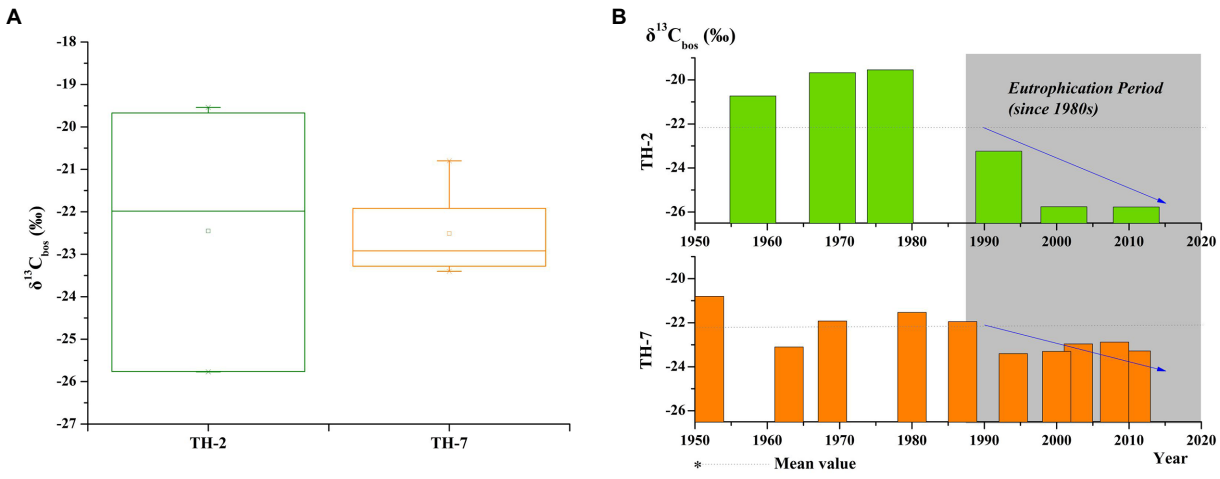

FIGURE 6
Changes in the $\delta^{13}C$ values of subfossil Bosminidae in the Taihu Lake after the 1950s. **(A)** Statistical distribution of $\delta^{13}C_{bos}$ in the cores of TH-2 and TH-7 and **(B)** temporal distribution of $\delta^{13}C_{bos}$ in the cores of TH-2 and TH-7.

significant positive correlations between Bosminidae and TP in the cores of Nanyi Lake and Shengjin Lake. The eutrophic species *B. longirostris* in the three lakes was significantly positively correlated with TN, except in the TH-5 core. There were significant positive correlations between *B. longirostris* and TP in the cores of TH-2, NY-2, NY-3, and SJH. The oligotrophic species *B* (E.) *longispina* had a significant negative correlation with TN in the cores of TH-2 and TH-7 but a significant positive correlation in the two cores of Nanyi Lake. *B* (E.) *longispina* was negatively correlated with TP in the cores of TH-2 and TH-5 and was positively correlated with TP in the cores of NY-2 and NY-3.

4. Discussion

The lake trophic status in the lower reaches of the Yangtze River from a recent study showed that most of the lakes have been categorized into the mesotrophic or the eutrophic status (Cheng and Li, 2006; Qin et al., 2013). The trophic levels of the three lakes, located in the middle and lower reaches of the Yangtze River, have also reached the mid-eutrophic level and above and are increasing from Shengjin Lake to Nanyi Lake and then to Taihu Lake, which is closely related to the distribution of economic development, population, and urbanization in each region (Qin et al., 2013;

TABLE 2 Pearson's correlation analysis between the trophic indices TN and TP with the species of Bosminidae. Data sources of TH-2, TH-7, TH-5, NY-2, NY-3, and SJH cores were taken from Cheng et al. (2020a,b,c, 2021).

	TN/Bosminidae	TN/*B. longirostris*	TN/*B* (E.) *longispina*	TP/Bosminidae	TP/*B. longirostris*	TP/*B* (E.) *longispina*
TH-2 ($n = 13$)	0.673*	0.819**	−0.794**	0.493	0.630*	−0.718**
TH-7 ($n = 13$)	0.279	0.651*	−0.764**	0.195	0.345	−0.291
TH-5 ($n = 12$)	0.376	0.154	0.33	−0.720**	−0.176	−0.646*
NY-2 ($n = 15$)	0.853**	0.747**	0.799**	0.851**	0.726**	0.851**
NY-3 ($n = 14$)	0.897**	0.842**	0.855**	0.926**	0.867**	0.875**
SJH ($n = 15$)	0.294	0.665**	−0.484	0.715**	0.907**	−0.064

*Correlation is significant at the $p < 0.05$ level. **Correlation is significant at the $p < 0.01$ level.

Zhang M. et al., 2018; Shi et al., 2019; Cheng et al., 2020c, 2021). An analysis of modern zooplankton compositions showed that Cladocera was dominant in the three lakes and that the abundance was gradually increasing from Shengjin Lake through Nanyi Lake to Taihu Lake (Figure 2). Furthermore, the abundances of Bosminidae in the Nanyi Lake and in the western and central areas of the Taihu Lake were greater than 90% (Figure 2). This showed that Bosminidae abundance increased corresponding to the increasing trophic level (Li et al., 2016; Cheng et al., 2020b; Li et al., 2021). However, a higher Copepod density was recorded in summer than that of Cladocera and there was a low abundance of Bosminidae in the composition of modern zooplankton in the Shengjin Lake, which might indirectly suggest that the Bosminidae did not have a reproductive advantage under low trophic levels. The subfossil Cladocera in the sedimental cores of the three lakes also showed that the Bosminidae was a broadly dominant species (Figure 5). Especially in Taihu Lake, the density of Bosminidae subfossils was close to 10,000 ind./cm^3 (Cheng et al., 2019). In Nanyi Lake and Shengjin Lake, where trophic levels had increased significantly since the 1950s, the abundance of subfossil Bosminidae also increased (Figure 5). In addition, among the modern Cladocera in the three lakes, Bosminidae was the dominant species, which was consistent with the Cladocera subfossil results at the same location and also indirectly proved that Bosminidae subfossils were well preserved in lakes of the middle and lower reaches of the Yangtze River.

In terms of space, there were huge differences in the economic development level, the urbanization level, and population along the Yangtze River from west to east. Taihu Lake is located in the eastern delta of the Yangtze River, which has an extremely developed economy and a very large population (Qin et al., 2007). Because Taihu Lake is located near many developed cities such as Shanghai, Suzhou, and Wuxi, a large quantity of nutrients such as nitrogen and phosphorus flow into Taihu Lake on account of human activities, which are far greater in Taihu Lake than in Nanyi Lake and Shengjin Lake in the Anhui Province (Dai et al., 2016). Agricultural and fisheries development in Nanyi Lake is more adequate than in Shengjin Lake (Wang et al., 2013). As a national nature reserve, Shengjin Lake has a relatively good environment and low nutrient level compared with the other two lakes (Wang et al., 2015). The spatial gradient distributions of Bosminidae abundance in the three lakes were in line with the different economic development levels (Figure 5). Thus, it could be inferred that there were different types of interference of human activities around the three lakes.

The significant positive relationship between Bosminidae and eutrophic species *B. longirostris* with TN and TP further proved that Bosminidae had an advantage in the eutrophic process (Table 2). In particular, *B. longirostris* demonstrated strong adaptability and sensitivity in a wide range of water environments, such as the eutrophic status, warming waters, and metal-contaminated lakes in previous studies (Boucherle and Züllig, 1983; De Kluijver et al., 2012; Labaj et al., 2015; Kong et al., 2017; Cheng et al., 2020b). Our study showed that Bosminidae abundance increased with the increase in the outbreak intensity of cyanobacteria in eutrophic lake areas (Figures 3, 4). Especially in the west and central lake areas of Taihu Lake with serious eutrophication, the concentration of Bosminidae has increased to a relatively stable state. While Nanyi Lake and Shengjin Lake are in the stage of rising trophic levels, and the abundance of Bosminidae is also showing a synchronous rising trend (Figure 3). Although previous studies suggested that Bosminidae were too small to feed on Microcystis directly with a large size (Jiang and Du, 1979; Li and Chen, 2010), more studies showed that Microcystis tended to form large suspended aggregates with materials after cell death including dissolved organic carbon, dissolved inorganic carbon, and dissolved inorganic nitrogen and phosphorus in the water column and then were likely the main diet of Bosminidae (De Kluijver et al., 2012; Agasild et al., 2019; Cheng et al., 2020b). It could be speculated that cyanobacteria blooms might change the food preference of the zooplankton Bosminidae. At the same time, the water environment also changed greatly due to excessive reproduction of cyanobacteria; thus, Bosminidae made timely adaptive adjustments to the original living environment and food source changes (Agasild et al., 2019). For example, Cladocera's size gradually became smaller to better escape the predation of zooplankton-feeding fish (Shurin, 2001; Jeppesen et al., 2003; Liu et al., 2009). Accordingly, in lake areas where cyanobacteria blooms were stronger, the density of small-size species of Bosminidae was greater and other species of zooplankton may have decreased or even gone extinct (Jiang et al., 2013; Li et al., 2016).

The present study revealed that Bosminidae could accelerate reproduction under rich food sources, resulting in excessive abundance (accounting for more than 90% of the total number of Cladocera) (Figure 2). However, water temperature also impacts the body size and community trophic structure of zooplankton (Gao et al., 2021). The three shallow freshwater lakes located in the middle

and lower reaches of the Yangtze River in a subtropical zone had suitable temperature conditions that produced a favorable habitat for most lake creatures, including the zooplankton. However, a strong disturbance can easily occur in these shallow freshwater lakes, which can result in the release of sediment nitrogen and phosphorus and a large amount of exogenous nitrogen and phosphorus inputs from catchment by increasing human activities (Zhu et al., 2019). Excessive nitrogen and phosphorus inputs caused cyanobacteria blooms that seriously threatened the survival of most aquatic organisms such as fish. Large aquatic plants and other biodiversity significantly decreased, and this finally led to the imbalance of lake ecosystems (Qin et al., 2013). Surprisingly, the cyanobacteria outbreak provided favorable conditions for the expansion of the Bosminidae (De Kluijver et al., 2012; Cheng et al., 2020b). The changes in $\delta^{13}C_{bos}$ values after 1950s also revealed the flow characteristics of carbon sources in the Bosminidae (Figure 6). In particular, after the 1980s (after China's Reform and Open Policy), with increasing lake eutrophication, the $\delta^{13}C_{bos}$ values exhibited a significant negative trend (Figure 6), which was consistent with the change in organic carbon isotopes in sediments ($\delta^{13}C_{org}$; Cheng et al., 2020b). The $\delta^{13}C$ value of algae in Taihu Lake was similar to the value of $\delta^{13}C$ in modern Bosminidae during the cyanobacteria bloom (Cheng et al., 2020b). This further indicated that the cyanobacteria outbreak provided a rich food source for Bosminidae. Bosminidae propagation in large numbers due to the outbreak of cyanobacteria also showed that Bosminidae had its own unique adaptability to the eutrophic environment and strong competitiveness compared with other zooplankton. The high adaptive ability of Bosminidae to eutrophication could indicate that it is more competitive than other larger Cladocera species.

Our data on subfossil Cladocera in the TH-5 core of East Taihu Lake showed that the total Cladocera and Bosminidae abundances were lower than those found in the core of other lake areas and tended to decrease after the 1950s (Figure 2). This was due to intensification of the swamping trend in East Taihu Lake, the water level reduction, aquatic macrophyte development, and water stagnation for prolonged periods of time caused by enclosed fish cultures and crab farming practices. These are extremely detrimental to the survival of the planktonic species Bosminidae but provide a more suitable habitat for the littoral Cladocera species (Yang et al., 2003; Li, 2004; Cheng et al., 2020a). The significant negative correlation between Bosminidae and TP also indirectly proved that the environment of the East Taihu Lake was not conducive to the survival of Bosminidae (Table. 2). It could be seen that the trophic level was not the only factor limiting the growth of Bosminidae, but it was the key factor behind the rapid expansion of Bosminidae, once certain restrictive conditions were exceeded. As shown in the western and central areas of Taihu Lake, Bosminidae reproduction expanded and abundance increased once the trophic level was enriched and the water level depth met the living conditions of the planktonic species Bosminidae (Figures 2, 5). Additionally, the significant positive correlations between oligotrophic species Bosminidae with TN and TP in Nanyi Lake were opposite of those in Taihu Lake, which was closely related to the fact that Nanyi Lake was in a critical period of transition from the mesotrophic to the eutrophic status (Cheng et al., 2021). Research by Dodson (1992) showed that the abundance of zooplankton usually increased with increasing nutritional levels within a certain range. The current trophic level of the Nanyi Lake is still increasing, but it has not reached the eutrophic level as in the central and western areas of Taihu Lake. Therefore, the abundance of oligotrophic species increased significantly with the increase in trophic level.

5. Conclusion

The spatial distribution of the three subtropical shallow freshwater lakes in the middle and lower reaches of the Yangtze River was characterized by gradually increasing nutrient levels from west to east. An analysis of the composition of zooplankton in the modern lake water of the three lakes and Cladocera subfossils from the sedimental cores revealed that the Cladocera planktonic species Bosminidae changed relatively consistently with the temporal and spatial distributions of the nutrient levels in the three lakes, indicating that the small planktonic Bosminidae species had unique sensitivity and adaptability during lake eutrophication. In addition, the significant correlation between Bosminidae and nutrient indicators such as TN and TP, as well as the gradually negative $\delta^{13}C_{bos}$ values under increasing eutrophication, further proved that the abundance of Bosminidae changed with the change in eutrophication level. This reflected the change in food source preference of the Bosminidae and its strong adaptability to harsh environments during lake eutrophication. Bosminidae was more adaptive to the change in this environment, which showed that the genus was highly sensitive to changes in the lake environment and can indicate the evolution of the lake. This study offered a new alternative index for paleoecology research and also provided a new idea for mechanism research on modern lake eutrophication environments.

Data availability statement

The original contributions presented in the study are included in the article/Supplementary material, further inquiries can be directed to the corresponding authors.

Author contributions

LC: writing–original draft, validation, resources, and formal analysis. XG, GW, and JL: visualization and investigation. ZD: investigation and field work. BX: supervision, project administration, and funding acquisition. CZ: supervision, visualization, investigation, and writing–editing. QJ: software and resources. All authors contributed to the article and approved the submitted version.

Funding

This research was supported by grants from the Natural Science Foundation of China project (42002204 and 42177426), the National Key Research and Development Program of China (2019YFA0607100), and the Jiangsu Special Fund on Technology Innovation of Carbon Dioxide Peaking and Carbon Neutrality (BK20220016).

Conflict of interest

The authors declare that the research was conducted in the absence of any commercial or financial relationships that could be construed as a potential conflict of interest.

Publisher's note

All claims expressed in this article are solely those of the authors and do not necessarily represent those of their affiliated organizations, or those of the publisher, the editors and the reviewers. Any product that may be evaluated in this article, or claim that may be made by its manufacturer, is not guaranteed or endorsed by the publisher.

Supplementary material

The Supplementary material for this article can be found online at: https://www.frontiersin.org/articles/10.3389/fevo.2023.1121632/full#supplementary-material

References

Adamczuk, M. (2016). Past, present, and future roles of small cladoceran *Bosmina longirostris* (O. F. Müller, 1785) in aquatic ecosystems. *Hydrobiologia* 767, 1–11. doi: 10.1007/s10750-015-2495-7

Agasild, H., Panksep, K., Tõnno, I., Blank, K., Kõiv, T., Freiberg, R., et al. (2019). Role of potentially toxic cyanobacteria in crustacean zooplankton diet in a eutrophic lake. *Harmful Algae* 89:101688. doi: 10.1016/j.hal.2019.101688

Balcer, M. D., Korda, N. L., and Dodson, S. I.. (1984). *Zooplankton of the Great Lakes: A Guide to the Identification and Ecology of the Common Crustacean Species*. Madison: University of Wisconsin Press.

Boucherle, M. M., and Züllig, H. (1983). Cladoceran remains as evidence of change in trophic state in three Swiss lakes. *Hydrobiologia* 103, 141–146. doi: 10.1007/BF00028442

Cao, L., Pan, C., and Wang, X. (2018). Study on environmental protection and ecological construction in Shengjinhu lake basin. *Guangdong Chem. Ind.* 45, 198–199. doi: 10.3969/j.issn.1007-1865.2018.05.091

Cheng, L. J., Giri, K., Xue, B., Yao, S., Li, L., and Liu, J. (2020b). Application of subfossil Bosmina and its $\delta^{13}C$ values in tracing the long-term food web dynamics of shallow eutrophic lakes: a case in Taihu Lake, Southeast China. *Sci. Total Environ.* 730:138909. doi: 10.1016/j.scitotenv.2020.138909

Cheng, X. Y., and Li, S. J. (2006). An analysis on the evolvement processes of lake eutrophication and their characteristics of the typical lakes in the middle and lower reaches of Yangtze River (in Chinese). *Chin. Sci. Bull.* 51, 1603–1613. doi: 10.1007/s11434-006-2005-4

Cheng, L. J., Xue, B., Yao, S., and Liu, J. (2020c). Response of Cladocera fauna to environmental change based on sediments from Shengjin Lake, a Yangtze River-connected Lake in China. *Quat. Int.* 536, 52–59. doi: 10.1016/j.quaint.2019.11.044

Cheng, L. J., Xue, B., Zawisza, E., Yao, S., Liu, J., and Li, L. (2020a). Effects of environmental change on subfossil Cladoceran in the subtropical shallow freshwater East Taihu Lake, China. *Catena* 188:104446. doi: 10.1016/j.catena.2019.104446

Cheng, L. J., Xue, B., Zawisza, E., Yao, S., Liu, J., and Li, S. (2021). Specific species response of Cladocera to the trophic and hydrological environments of lakes: a case study of a typical shallow mesotrophic lake. *Catena* 207:105630. doi: 10.1016/j.catena.2021.105630

Cheng, L. J., Yao, S., Xue, B., Liu, J., and Li, L. (2019). Long-term change of the assemblages and abundance of cladocerans in different ecotypes of Lake Taihu. *J. Lake Sci.* 31, 1670–1684. doi: 10.18307/2019.0607

Dai, X. L., Qian, P. Q., Ye, L., and Song, T. (2016). Changes in nitrogen and phosphorus concentrations in Lake Taihu, 1985–2015. *J. Lake Sci.* 28, 935–943. doi: 10.18307/2016.0502

De Kluijver, A., Yu, J., Houtekamer, M., Middelurg, J. J., and Liu, Z. (2012). Cyanobacteria as a carbon source for zooplankton in eutrophic Lake Taihu, China, measured by ^{13}C labeling and fatty acid biomarkers. *Limnol. Oceanogr.* 57, 1245–1254. doi: 10.4319/lo.2012.57.4.1245

De Melo, R., and Hebert, P. (1994). A taxonomic reevaluation of north-American Bosminidae. *Can. J. Zool.* 72, 1808–1825. doi: 10.1139/z94-245

Deevey, E. S. J. (1942). Studies on Connecticut lake sediments. III. The Biostratonomy of Linsley pond. *Am. J. Sci.* 240, 233–264. doi: 10.2475/ajs.240.4.233

Dodson, S. (1992). Predicting crustacean zooplankton species richness. *Limnol. Oceanogr.* 37, 848–856. doi: 10.4319/lo.1992.37.4.0848

Frey, D. G. (1986). "Cladocera analysis" in *Handbook of Holocene Palaeoecology and Palaeohydrology*. ed. B. E. Berglund (New York: John Whiley & sons), 667–692.

Gao, X., Tõnno, I., Vrede, T., Freiberg, R., Nilsson, J. L., and Goedkoop, W. (2021). Both climate trends and short-term fluctuations affected algae–zooplankton interactions in a boreal lake during the late Holocene. *Freshw. Biol.* 66, 2076–2085. doi: 10.1111/fwb.13815

Jenny, J. P., Anneville, O., Arnaud, F., Baulaz, Y., and Weyhenmeyer, G. A. (2020). Scientists' warning to humanity: rapid degradation of the world's large lakes. *J. Great Lakes Res.* 46, 686–702. doi: 10.1016/j.jglr.2020.05.006

Jeppesen, E., Jensen, J. P., Lauridsen, T. L., Amsinck, S. L., Christoffersen, K., Sondergaard, M., et al. (2003). Sub-fossils of cladocerans in the surface sediment of 135 lakes as proxies for community structure of zooplankton, fish abundance and lake temperature. *Hydrobiologia* 491, 321–330. doi: 10.1023/A:1024488525225

Jiang, X., and Du, N.. (1979). *Fauna of China Arthropod Phylum Crustacean Freshwater Cladocera*. Beijing: Science Press, 41–42.

Jiang, X., Li, Q., Liang, H., Zhao, S., Zhang, L., Zhao, Y., et al. (2013). Clonal variation in growth plasticity within a *Bosmina longirostris* population: the potential for resistance to toxic cyanobacteria. *PLoS One* 8:e73540. doi: 10.1371/journal.pone.0073540

Kong, L., Yang, X., Kattel Anderson, G. N. J., and Hu, Z. (2017). The response of Cladocerans to recent environmental forcing in an alpine Lake on the SE Tibetan plateau. *Hydrobiologia* 784, 171–185. doi: 10.1007/s10750-016-2868-6

Korhola, A., and Rautio, M. (2001). "Cladoceran and other branchiopod crustaceans" in *Tracking Environmental Change Using Lake Sediments: Volume 4. Zoological Indicators*. eds. J. P. Smol, H. J. B. Birks and W. M. Last (New York: Kluwer Academic Publishers), 5–41.

Labaj, A. L., Kurek, J., Jeziorski, A., and Smol, J. P. (2015). Elevated metal concentration inhibit biological recovery of Cladocera in previously acidified Boral lakes. *Freshw. Biol.* 60, 347–359. doi: 10.1111/fwb.12496

Li, W. (2004). "Tendency and reason for evolution toward mash in the east Taihu" in *Process and Mechanism of Environmental Changes of Lake Taihu*. eds. B. Qin, W. Hu and W. Chen (Beijing: Science Press), 33–51.

Li, J., and Chen, F. (2010). Preliminary analysis on population declines of daphnia in summer and autumn in Lake Taihu. *J. Lake Sci.* 22, 552–556. doi: 10.18307/2010.0411

Li, Y., Hu, L., Zhao, Y., Wang, H., Huang, X., Chen, G., et al. (2021). Meltwater-driven water-level fluctuations of Bosten lake in arid China over the past 2,000 years. *Geophys. Res. Lett.* 48:2020GL090988. doi: 10.1029/2020GL090988

Li, Y., Xie, P., Zhao, D., Zhu, T., Guo, L., and Zhang, J. (2016). Eutrophication strengthens the response of zooplankton to temperature changes in a high-altitude lake. *Ecol. Evol.* 6, 6690–6701. doi: 10.1002/ece3.2308

Lin, Q., Zhang, K., Liu, E., Sabatier, P., Arnaud, F., and Shen, J. (2020). Deciphering centurial anthropogenic pollution processes in large lakes dominated by socio-economic impacts. *Anthropocene* 32:100269. doi: 10.1016/j.ancene.2020.100269

Liu, G., Chen, F., and Liu, Z. (2008). Preliminary study on cladoceran microfossils in the sediments of Lake Taihu. *J. Lake Sci.* 20, 470–476. doi: 10.18307/2008.0410

Liu, G., Liu, Z., Li, Y., Chen, F., Gu, B., and Smoak, J. M. (2009). Effects of fish introduction and eutrophication on the cladoceran community in Lake Fuxian, a deep oligotrophic lake in Southwest China. *J. Paleolimnol.* 42, 427–435. doi: 10.1007/s10933-008-9286-3

Mao, Z., Gu, X., Zeng, Q., Zhou, L., and Sun, M. (2012). Food web structure of a shallow eutrophic Lake (lake Taihu, China) assessed by stable isotope analysis. *Hydrobiologia* 683, 173–183. doi: 10.1007/s10750-011-0954-3

Miroslaw-Grabowska, J., Zawisza, E., Jaskolka, A., and Obremska, M. (2015). Natural transformation of the Romoty paleolake (NE Poland) during the late glacial and Holocene based on isotopic, pollen, cladoceran and geochemical data. *Quat. Int.* 386, 171–185. doi: 10.1016/j.quaint.2015.06.040

Pawłowski, D., Płóciennik, M., Brooks, S. J., Luoto, T. P., Milecka, K., Nevalainen, L., et al. (2015). A multiproxy study of younger Dryas and early Holocene climatic conditions from the Grabia River paleo-oxbow lake (Central Poland). *Palaeogeogr. Palaeoclimatol. Palaeoecol.* 438, 34–50. doi: 10.1016/j.palaeo.2015.07.031

Peng, L., Dong, B., Wang, P., Sheng, S., Sun, L., Fang, L., et al. (2019). Liping Liu research on ecological risk assessment in land use model of Shengjin Lake in Anhui province. *China. Environ. Geochem. Health* 1:15. doi: 10.1007/s10653-019-00322-6

Qin, B. Q., Gao, G., Zhu, G. W., Zhang, Y. L., Song, Y. Z., Tang, X. M., et al. (2013). Lake eutrophication and its ecosystem response. *Sci. Bull.* 58, 961–970. doi: 10.1007/s11434-012-5560-x

Qin, B. Q., Xu, P., Wu, Q., Luo, L., and Zhang, Y. (2007). Environmental issues of Lake Taihu, China. *Hydrobiol* 581, 3–14. doi: 10.1007/s10750-006-0521-5

Shi, K., Zhang, Y., Zhang, Y., Li, N., Qin, B., Zhu, G., et al. (2019). Phenology of phytoplankton blooms in a trophic lake observed from long-term MODIS data. *Environ. Sci. Technol.* 53, 2324–2331. doi: 10.1021/acs.est.8b06887

Shurin, J. B. (2001). Interactive effects of predation and dispersal on zooplankton communities. *Ecology* 82, 3404–3416. doi: 10.1890/0012-9658(2001)082[3404:IEOPAD]2.0.CO;2

Szeroczyńska, K., and Sarmaja-Korjonen, K.. (2007). *Atlas of Subfossil Cladoceran from Central and Northern Europe*. Swiecie: Friends of the Lower Vistula Society. 10–11.

Threlkeld, S. (1981). The recolonization of Lake Tahoe by *Bosmina-longirostris-evaluating* the importance of reduced Mysis-relicta population. *Limnol. Oceanogr.* 26, 433–444. doi: 10.4319/lo.1981.26.3.0433

Wang, L., Wang, C., Deng, D., Zhao, X., and Zhou, Z. (2015). Temporal and spatial variations in phytoplankton: correlations with environmental factors in Shengjin Lake. *China. Environ. Sci. Pollut. Res.* 22, 14144–14156. doi: 10.1007/s11356-015-4640-2

Wang, Z., Yan, Z., Xu, L., Lu, X., Winemiller, K. O., and Lei, G. (2013). Effects of hydrologic regulation on icefish population dynamics, assemblage structure and fishery yield in Lake Nanyi, China. *Ecol. Freshw. Fish* 22, 637–644. doi: 10.1111/eff.12068

Wang, L., Zhuang, H., Zhang, Y., and Wei, W. (2019). Diversity of the Bosmina (Cladocera: Bosminidae) in China, revealed by analysis of two genetic markers (mtDNA 16S and a nuclear ITS). *BMC Evol. Biol.* 19:145. doi: 10.1186/s12862-019-1474-4

Yang, X.. (2011). *Research on the Numbers, Distribution, Feeding Behavior and Diet of Great white Fronted Geese at Shengjin Lake, the National Natural Reserves in Anhui Province*. Dissertation, University of Science and Technology of China, Hefei, China.

Yang, Y., Li, W., Zhou, Z., and Li, C. (2019). The study on the relationship between wetland landscape pattern and water level in Shengjin Lake. *J. Biol.* 36, 61–64. doi: 10.3969/j.issn.2095-1736.2019.02.061 (In Chinese)

Yang, G., Pan, H., Liu, Z., Wang, W., and Qin, B. (2008). A comparative study on seasonal variations of crustaceans in the different Lake areas in Lake Taihu. *China Environ. Sci.* 28, 27–32.

Yang, Z. F., Shi, W. G., Chen, L. Q., Chen, Y., and Zhou, Z. L. (2003). Ecological environment succession and countermeasure of east Taihu Lake. *China Environ. Sci.* 23, 64–68. (In Chinese)

Yao, S., and Xue, B.. (2016). *The Evolution of Lake Environment in the Qingyi River in the Shuiyangjiang River Valley in the Lower Reaches of the Yangtze River*. Nanjing: Nanjing University Press, 7–202.

Zaret, R., and Kerfoot, C. (1975). Fish predation on *Bosmina-longirostris*-body-size selection versus visibility selection. *Ecology* 56, 232–237. doi: 10.2307/1935317

Zhang, M., Shi, X., Yang, Z., Yu, Y., Shi, L., and Qin, B. (2018). Long-term dynamics and drivers of phytoplankton biomass in eutrophic Lake Taihu. *Sci. Total Environ.* 645, 876–886. doi: 10.1016/j.scitotenv.2018.07.220

Zhang, K., Yang, X., Xu, M., Lin, Q., Kattel, G., and Shen, J. (2018). Confronting challenges of managing degraded lake ecosystems in the Anthropocene, exemplified from the Yangtze River basin in China. *Anthropocene* 24, 30–39. doi: 10.1016/j.ancene.2018.11.001

Zhong, J., Liu, M., Wang, Y., Yang, X., Jiang, X., and Xu, C. (2014). Spatial correlation of major water quality indices between the Lake and rivers in Lake Taihu basin. *Chinese J. Ecol.* 33, 2176–2182.

Zhu, G. W., Xu, H., Zhu, M. Y., Zou, W., Guo, C. X., Ji, P. F., et al. (2019). Changing characteristics and driving factors of trophic state of lakes in the middle and lower reaches of Yangtze River in the past 30 years. *J. Lake. Sci.* 31, 1510–1524.

frontiers | Frontiers in Ecology and Evolution

TYPE Original Research
PUBLISHED 10 May 2023
DOI 10.3389/fevo.2023.1177638

OPEN ACCESS

EDITED BY
Kunshan Bao,
South China Normal University, China

REVIEWED BY
Xiangzhen Kong,
Chinese Academy of Sciences (CAS), China
John Birks,
University of Bergen, Norway

*CORRESPONDENCE
Kaarina Weckström
✉ kaarina.weckstrom@helsinki.fi

RECEIVED 01 March 2023
ACCEPTED 18 April 2023
PUBLISHED 10 May 2023

CITATION
Weckström K, Weckström J, Wischnewski J, Davidson TA, Lauridsen TL, Landkildehus F, Christoffersen KS and Jeppesen E (2023) Unlocking environmental archives in the Arctic—insights from modern diatom-environment relationships in lakes and ponds across Greenland.
Front. Ecol. Evol. 11:1177638.
doi: 10.3389/fevo.2023.1177638

Unlocking environmental archives in the Arctic—insights from modern diatom-environment relationships in lakes and ponds across Greenland

Kaarina Weckström[1,2]*, Jan Weckström[1], Juliane Wischnewski[3], Thomas A. Davidson[3], Torben L. Lauridsen[4], Frank Landkildehus[4], Kirsten S. Christoffersen[5] and Erik Jeppesen[3,6,7,8]

[1]Ecosystems and Environment Research Programme (ECRU), University of Helsinki, Helsinki, Finland, [2]Department of Glaciology and Climate, Geological Survey of Denmark and Greenland, Copenhagen, Denmark, [3]Department of Ecoscience—Lake Ecology and Arctic Research Centre, Aarhus University, Aarhus, Denmark, [4]Department of Biology—Aquatic Biology, Aarhus University, Aarhus, Denmark, [5]Department of Biology—Freshwater Biology, University of Copenhagen, Copenhagen, Denmark, [6]Sino-Danish Centre for Education and Research, Beijing, China, [7]Department of Biological Sciences, Middle East Technical University, Ankara, Türkiye, [8]Institute for Ecological Research and Pollution Control of Plateau Lakes, School of Ecology and Environmental Science, Yunnan University, Kunming, China

Given the current rate of Arctic warming, the associated ecological changes need to be put into a longer-term context of natural variability. Palaeolimnology offers tools to explore archives stored in the sediments of Arctic lakes and ponds. The interpretation of these archives requires a sound knowledge of the ecology and distribution of the sedimentary proxy organisms used. Here we explored the relationship between diatoms, a widely used proxy group of siliceous algae, and the environmental drivers defining their assemblages and diversity in 115 lakes and ponds in Greenland, a markedly understudied arctic region covering extensive climate and environmental gradients. The main environmental drivers of diatom communities were related to climate and lake ontogeny, including both measured and unmeasured (spatially structured) environmental variables. The lakes and ponds in the northern study regions showed a distinctive dominance of small benthic fragilarioid species, while diatom communities in the South(west) of Greenland were more varied, including many epiphytes, owing to the longer growing season and higher habitat diversity of these lakes and ponds. The newly established lakes in the Ilulissat region host markedly different communities compared to all other sites. Species diversity followed an overall clear latitudinal decline towards the North. Despite the large distances between our study regions, diatom dispersal appeared not to be limited. Based on our results, diatoms are an excellent proxy for climate-mediated lake ecosystem change in the Arctic and thus a valuable tool for climate reconstructions in the region. Particular consideration should be given to often unmeasured climate-related drivers, such as in-lake habitat availability, due to their apparent importance in defining Arctic diatom communities.

KEYWORDS

palaeolimnology, diatoms, diversity, dispersal, lakes and ponds, climate change, Greenland

Introduction

To understand fully current climate and environmental change, driven by the Great Acceleration since the mid-20th century (Steffen et al., 2015), we need to place observed change into the context of long-term natural environmental variability. However, data from environmental monitoring programmes commonly cover only the past decades, and in remote regions like the Arctic, monitoring and field studies are spatially and temporally patchy (Metcalfe et al., 2018; Kahlert et al., 2021). In the absence of long-term instrumental and biomonitoring, lake sediment archives containing a wealth of microfossils and biogeochemical tracers can offer a valuable tool for assessing past environmental change over relevant time scales.

The Arctic has warmed nearly four times faster than the globe over the recent decades (Rantanen et al., 2022), a rate that is unprecedented over decades to millennia (Miller et al. 2013). Simultaneously, dramatic ecosystem change has been reported throughout the Arctic (Overpeck et al., 1997; Smith et al., 2005; Kaufman et al., 2009; Post et al., 2009; Wrona et al., 2016), as studies show that changes in temperature, and snow and ice cover alter limnological boundary conditions (e.g., light and mixing regime, nutrient cycling, length of growing season) and influence biological dynamics (Douglas et al., 2004; Schindler and Smol, 2006; Callaghan et al., 2010; Rautio et al., 2011).

To give these ongoing changes perspective, palaeolimnological studies (analysing sedimentary archives) are now commonly used as an alternative for missing long-term monitoring data in remote arctic regions to assess the rate, speed, magnitude and direction of environmental change (e.g., Douglas et al., 2004; Smol et al., 2005; Rühland et al., 2008; Hobbs et al., 2010; Medeiros et al., 2012; Saros and Anderson, 2015). Interpreting palaeolimnological archives requires a sound understanding of the microfossils and biogeochemical tracers (or proxies) found in the sediments. Lake surface-sediment surveys or "training sets," i.e., a large number of lakes from which both surface-sediment proxies and measured environmental variables are analysed for the purpose of quantitative environmental reconstructions, offer a very good tool to investigate the links between proxy distribution, abundance, diversity and environmental setup.

Many palaeolimnological studies use diatoms as a proxy indicator. A premise for using diatoms, a key component of Arctic freshwater ecosystems, as a reliable proxy of environmental change over time is a sound understanding of their ecological and biogeographical characteristics (e.g., Smol et al., 2002; Bouchard et al., 2004). While this is the case for several common and abundant taxa, the ecology and distribution of a much larger number of species are still rather poorly known.

Lake surface-sediment surveys investigating diatom distribution and taxa-environment relationships exist for much of Arctic Canada (Douglas and Smol, 1995; Rühland et al., 2003; Bouchard et al., 2004; Antoniades et al., 2005; Michelutti et al., 2007; Keatley et al., 2008; Hadley et al., 2013) and also to a lesser extent for arctic Russia (Laing and Smol, 2000; Weckström et al., 2003; Pla-Rabes et al., 2016; Dulias et al., 2017), arctic Lapland (Korhola et al., 1999; Rosén et al., 2000; Weckström and Korhola, 2001; Bigler and Hall, 2002) and Spitzbergen (Jones and Birks, 2004; Zgrundo et al., 2017). For Greenland however, which stretches over 26 latitudes (59° and 83°N) and captures long environmental and climate gradients (Table 1), studies that investigate surface-sediment diatom assemblages in relation to environmental variables in a larger number of lakes are sparse (Ryves et al., 2002; McGowan et al., 2018). Other Greenland studies have used diatoms to primarily reconstruct environmental/climate change over the recent past and Holocene (McGowan et al., 2003; Perren et al., 2009, 2012; Law et al., 2015), but so far no comprehensive study on diatom distribution and abundance exists that captures the vast environmental gradients and spatial heterogeneity of Greenland.

Here we explored surface-sediment diatom taxa-environment relationships from 115 lakes and ponds, located in five different regions along the ice-free margin of Greenland, covering an exceptionally large latitudinal (*ca.* 60°−83° N) and longitudinal gradient (*ca.* −72°− −19° E). The large geographical scale of our sampling regime provides us with the opportunity to assess the overriding drivers of diatom community structure in the Arctic and to investigate the relative roles of spatial vs. environmental factors. The five different study regions are effectively isolated from each other, and diatoms can therefore only disperse overland passively via air or actively by water birds (Kristiansen, 1996). The lake communities of each region may therefore to some extent be defined by low degree of interchange (dispersal) between the regions. Several studies have underlined the importance of spatial gradients in addition or sometimes over environmental gradients in shaping diatom community structure in streams and lakes (Soininen and Weckström, 2009; Sweetman et al., 2010; Smucker and Vis, 2011; Virtanen and Soininen, 2012; Liu et al., 2016), and the discussion over dispersal influencing diatom species distribution is still ongoing (Keck et al., 2018; Falasco et al., 2019; Leboucher et al., 2020 and reference therein).

The objectives of this study are to investigate diatom distribution and abundance across Greenlandic lakes and ponds and to determine which environmental factors are important in influencing diatom communities and to what degree they are spatially structured in this climatically and environmentally varied region. As such, this study contributes valuable and hard-to-obtain information on ecological and biogeographical characteristics of Arctic freshwater diatoms, vital for ecologist and palaeoecologist alike, adding important basis knowledge for future palaeoclimatic and palaeoenvironmental interpretations in a yet poorly investigated and climatically sensitive region.

Methods

Study area & sites

The 115 investigated lakes and ponds are located along the ice-free margins in five different regions of Greenland (Figure 1). Forty eight sites are embedded in the unreworked Archaean gneiss of the southern West, in the region of Nuuk, Godhåbsfjord, where the annual mean temperature is −1.4°C, with 752 mm annual mean precipitation (Nuuk weather station). Fourteen sites are located in the central West, east of Ilulissat, at the foot of the inland ice and are embedded in reworked Archaean gneiss in early Proterozoic fold belts. The annual mean air temperature here is −3.9°C, and the annual mean precipitation is 266 mm (Ilulissat weather station). The sites in this region are further divided into young lakes/ponds ($n = 7$) that have emerged under the Greenland Ice Sheet since 1850 and into lakes/ponds ($n = 7$) significantly older than this date (Jeppesen et al., 2023). Seventeen sites are embedded in Proterozoic and lower

TABLE 1 Measured environmental variables for 115 Greenlandic lakes and ponds with means, medians, and ranges.

(A)												
Variable	Daneborg/Zackenberg (*n*=23)			Pearyland (*n*=13)			Nunatarsuaq (*n*=11)			Pituffik (*n*=6)		
	Range	Mean	Median	Range	Mean	Median	Range	Mean	Median	Range	Mean	Median
Lon (°E)	(−20.09)–(−21.48)			(−29.27)–(−29.99)			(−65.55)–(−65.70)			(−68.49)–(−68.67)		
Lat (°N)	74.31–74.51			82.16–82.2			77.41–77.44			76.54–76.58		
Area (ha)	0.2–69.3	8.85	3.50	1.16–19.48	6.11	5.01	0.78–206.97	32.63	8.42	2.85–26.31	8.14	4.99
Alt (m asl)	9–300	159.30	108.00	67–455	167.69	180.00	649–702	680.91	685.00	131–252	176.83	173.00
Depth (m)	0.3–19.8	3.88	2.70	0.4–18	5.95	4.90	0.7–35	8.38	4.00	1.5–4.3	2.52	2.40
TP (mg/l)	0.002–0.029	0.01	0.01	0.001–0.01	0.00	0.00	0.003–0.006	0.00	0.00	0.004–0.004	0.00	0.00
TN (mg/l)	0.04–0.71	0.25	0.20	0.06–0.23	0.13	0.13	0.06–0.39	0.14	0.12	0.004–0.004	0.00	0.00
Cond (mS/cm)	4–77	16.55	14.00	65–1.393	367.23	208.00	6–15	8.00	7.00	53–133	90.83	96.00
pH (units)	6.5–9.37	7.67	7.64	7.37–7.37	7.37	7.37	6.6–7.4	6.95	6.90	6.6–7.8	7.40	7.55
Chla	0.218–3.09	0.98	0.71	0.14–0.52	0.34	0.38	0.09–0.33	0.22	0.22	0.39–0.89	0.60	0.61
AT (°C)	1.14–3.75	2.65	2.95	0–1.62	0.97	1.09	1.92–2.16	2.04	2.02	4.41–4.78	4.53	4.51
EVI	0.97–1.07	1.01	1.00	1.02–1.04	1.03	1.03	0.96–1.01	0.98	0.97	1.01–1.05	1.03	1.03

(B)									
Variable	Ilulissat old (*n* =7)			Ilulissat young (*n* =7)			Nuuk (*n* =48)		
	Range	Mean	Median	Range	Mean	Median	Range	Mean	Median
Lon (°E)	(−49.89)–(−49.95)			(−49.77)–(−49.08)			(−50.04)–(−51.59)		
Lat (°N)	69.05–69.08			69.09–69.11			64.13–65.3		
Area (ha)	0.26–28.7	10.68	5.50	0.21–15	4.21	2.60	0.3–180.5	19.12	3.80
Alt (m asl)	267–306	291.00	293.00	304–339	324.14	326.00	12–775	344.71	266.00
Depth (m)	4.8–49.7	18.71	12.00	4–13.7	8.64	9.00	0.39–90	16.37	9.50
TP (mg/l)	0.006–0.016	0.01	0.01	0.002–0.01	0.01	0.01	0–0.028	0.01	0.01
TN (mg/l)	0.1–0.56	0.30	0.26	0.09–0.42	0.22	0.20	0.03–0.9	0.30	0.25
Cond (mS/cm)	37–178	82.55	59.00	119.92–561.67	339.22	322.00	3.6–65	24.88	20.32
pH (units)	7.36–8.18	7.80	7.85	7.95–8.36	8.20	8.22	5.29–8.6	6.92	6.91
Chla	0.4–1.5	0.93	1.00	0.3–1.1	0.57	0.60	0.06–2.04819281	0.65	0.53
AT (°C)	6.61–7.02	6.85	6.85	5.62–5.81	5.68	5.65	5.73–8.35	7.18	7.39
EVI	1.03–1.06	1.04	1.04	0.95–0.99	0.97	0.96	0.97–1.15	1.06	1.05

A = the general North, B = the general South.

Cambrian carbonate rocks (Pituffik) and siliciclastic sedimentary rocks (Nunatarsuaq) in the Northwest, with −11.1°C annual mean air temperature and 127 mm annual mean precipitation (Pituffik weather station). In the central North on Pearyland, 13 sites were investigated. The geology here is characterised by Lower Cambrian and Lower Silurian carbonate rocks, the annual mean air temperature is −16.9°C with 188 mm annual mean precipitation (St. Nord weather station), typical for polar deserts. Twenty three sites are embedded in the Northeast (Zackenberg/Daneborg), with a geology dominated by Early Proterozoic gneiss and migmatites from the Caledonian fold belt. The annual mean air temperature is −10.5°C and annual mean precipitation is 231 mm (Daneborg weather station; Henriksen and Higgins, 2009; Cappelen et al., 2011). Apart from the climatic differences between the regions, a climatic gradient also exists within each of the five regions from the more maritime outer coast to the continental ice-free inland. The study sites range in size from large proglacial lakes (*ca*. 2 km^2) to small bedrock catchment ponds (0.002 km^2) and their maximum

10.3389/fevo.2023.1177638

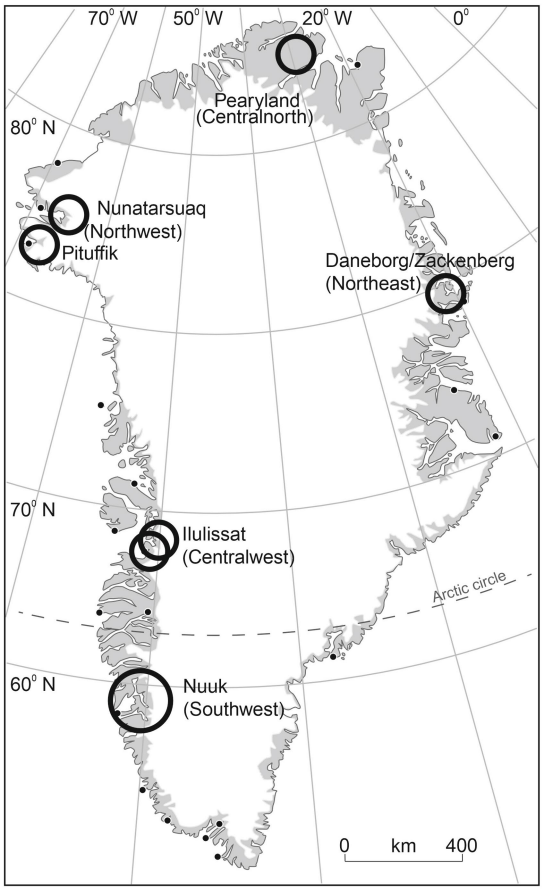

FIGURE 1
Location of study areas.

depth varies between 0.3 and 90 m. Due to their remoteness, human impact is low.

Sample collection and environmental data

The surface sediments were retrieved between 1998 and 2013, during the arctic summer (July–August) from the deepest area of each site using a Kajak corer (KC Denmark) or, in shallow lakes and ponds, with a tube on a rod. The cores were sliced into 0.25–0.5 cm intervals, with an exception of the 1998 samples from the Zackenberg/Daneborg region; here the cores were sliced in 1 cm intervals. The top half-centimetre was used for diatom sample preparation. Sampling regions and sites were chosen to cover wide environmental and spatial gradients across Greenland and to cover lakes and ponds from all depths, with approximately half between 2 and 10 m depth.

Lake water was collected for chemical analysis (total phosphorus (TP), total nitrogen (TN), specific conductivity, chlorophyl-*a* (chl *a*), and acidity (pH)) at the same time as the surface sediment was retrieved. From each site, a composite sample was collected with a 5 l Schindler sampler at 0.5–3 m intervals (depending on depth) from the surface to 0.5 m above the bottom in the deepest part of each site. The discrete samples were mixed and used for subsampling. For chemical analyses, a subsample of 250 ml was frozen, and for chl *a* a duplicate 1 l sample was filtered on a GF/C filter (Whatman) using vacuum and stored in snow/ice fans until arrival at the lab where it was frozen until analysis. TP was determined as molybdate reactive phosphorus (Murphy and Riley, 1962) following persulphate digestion (Koroleff, 1970) and TN as nitrite + nitrate after potassium (K) persulphate digestion (Solórzano and Sharp, 1980). Chl *a* was determined spectrophotometrically after ethanol extraction for approx 24 h (Jespersen and Christoffersen, 1987). Specific conductivity and pH in the surface water (0.5 m) was obtained using an YSI multiprobe recorder.

For information on fish absence or presence, multi-mesh sized monofilament survey gillnets were placed in the lakes/ponds in the afternoon and left overnight. Depending on the size and depth of the sites, the number of nets varied from one to five, covering the littoral, profundal and pelagic zone (Jeppesen et al., 2017).

Lake/pond area and altitude were extracted from Google Earth Pro (V 7.1.2.2041) to avoid error from the use of different (older) GPS technologies. To estimate vegetation cover in the catchment areas the enhanced vegetation index (EVI) was used. We extracted EVI, using a 250 m resolution, 16 day EVI band, compiled as an annual mean between 2000 and 2013. For EVI extraction, site coordinates were placed approx 250 m away from the water body where possible without interfering with neighbouring water bodies to avoid false EVI extraction due to water surfaces. All EVI data were downloaded from the NASA USGS website via the Modistool package in R (Tuck et al., 2014).

August mean air temperature for 1998–2013 was downloaded and extracted for our specific sites from WorldClim-Global Climate data in the highest resolution possible (30 arc-seconds /~1 km; http://www.worldclim.org/; Hijmans et al., 2005) using the rgdal and raster package in R.

Diatom analysis

Surface-sediment samples were prepared for diatom analysis, following standard procedures using the water bath technique (Renberg, 1990; Battarbee et al., 2001). Slides were mounted using the mounting medium Naphrax®. The target total count for each of the 115 samples was 300–500 diatom valves. In 65 samples diatom valve concentrations were low, and the total count in these samples was 100–300 valves (26 samples: 100–200; 39 samples: 201–300). The samples were analysed at 1,000 × magnification under oil immersion using a Zeiss AXIO phase contrast microscope. A complete list of identified taxa is provided in Supplementary Table 1.

Statistical analysis

Environmental data were checked for homogeneity of variance and log-transformed where necessary. Principal Components Analysis (PCA) using a correlation matrix was subsequently applied to explore the patterns across the different sampling regions. Diatom species abundance data was log- and Hellinger-transformed. PCA using a covariance matrix was subsequently applied to explore patterns in diatom composition. Despite relatively long floristic gradients revealed in Detrended Component Analysis (DCA; 3.8 SD), the linear response model PCA, in combination with Hellinger transformation, was

chosen as the more appropriate model (Legendre and Gallagher, 2001) to explore patterns of variation in the diatom assemblage.

Diatom species diversity was calculated for each site using the inverse Simpson index and species richness on rarefied count data to account for different sample size. Correlations between richness, diversity and selected environmental and spatial variables were calculated using the Pearson correlation coefficient. The significance of the difference (or similarity) between species diversity in the different sampling regions was tested using the Welch Two Sample t-test, which accounts for unequal variance in the objects being compared.

To test for the importance of the spatial structure in our data set, spatial vectors (Principal Coordinates of Neighbour Matrices, PCNMs) were produced as a proxy for space and consequently added as spatial predictors in redundancy analysis (RDA). PCNMs are based on basic coordinates and produce a numerical expression of a range of possible spatial correlation in the data set. The vectors with small numbers (e.g., V1, V5) capture broad-scale spatial patterns across Greenland, whereas vectors with higher numbers (e.g., V42, V59) capture local-scale spatial patterns (variation in a single region).

To evaluate the respective importance of spatial and environmental factors for structuring diatom communities in our study sites, we used partial RDA on diatom abundance and presence/absence (PA) data. This was done under the assumption that PA data will be stronger shaped by spatial factors than environmental factors (compared to the proportion explained using diatom abundance data) if dispersal was to be a significant driver.

All statistical analyses were analysed in R (R Development Core Team, 2011), version 3.4, using the vegan (Oksanen et al., 2022), labdsv (Roberts, 2019) and analogue (Simpson, 2007) packages. C2 was used to compile the diatom summary plot (Juggins, 2007).

Results

Environmental characteristics of the lakes and ponds

The 115 Greenland lakes and ponds range from ultra-oligotrophic to mesotrophic (TP = below detection limit-29 µl/L, mean = 6.3 µl/L, median = 5.0 µl/L), from acidic to strongly alkaline (pH = 5.3–9.4, mean = 7.3, median = 7.3), and from extremely dilute to relatively high conductivity waters (specific conductivity = 4–1,393 µS/cm, mean = 86 µS/cm, median = 23 µS/cm; Table 1).

The first two PCs extracted from PCA of the environmental variables explain 44% of the variation (PC1 = 24%, PC2 = 20%). PCA clearly separates the lakes and ponds into the generally warmer, deeper, larger and more nutrient-enriched sites with higher amount of catchment vegetation in the Southwest (Nuuk area), and the shallower, colder, ultra-oligotrophic, higher conductivity and more alkaline sites in the North and Northeast (Supplementary Figure 1; Table 1).

Diatom assemblages and distribution

In total, 284 diatom taxa were found. Those identified to either species or subspecies/variety/forma level are shown in Supplementary Table 1. Most common are fragilarioid, monoraphid (*Achnanthidium* spp., *Achnanthes* spp. and *Psammothidium* spp.), and nitzschoid taxa, contributing to the diatom assemblage with 29, 16 and 10% relative abundance, respectively. Also eunoid (8%) and cymbelloid (*Cymbella* spp., *Cymbopleura* spp., *Encyonema* spp., *Encyonopsis* spp.; 7%) taxa and *Cyclotella* spp. including newly separated genera (7%) form a significant part of the diatom assemblages. Figure 2 summarises the most common taxa found and reveals the general shift from a dominance of small benthic *Fragilaria* (e.g., *Staurosirella pinnata*, *Staurosira pseudoconstruens*, *Staurosira venter*) and *Nitzschia* (*Nitzschia alpina*) species in sites located in the Pearyland, Pituffik and Zackenberg/Daneborg area (the general North), to more periphytic and acidophilous species from the genera *Cymbella*, *Cymbopleura*, *Pinnularia* (e.g., *Pinnularia mesolepta*), *Eunotia*, *Brachysira*, *Frustulia* (*Frustulia saxonica*, *Frustulia quadrisinuata*) and planktic species (e.g., *Pantocsekiella ocellata*, *Discostella stelligera*) in the Southwest (Nuuk area), also evident in the PCA analysis of diatom assemblages (Supplementary Figure 2). The young lakes in the Ilulissat region stand out, with marked abundances of *Odontidium mesodon*, *Nitzschia perminuta* and *Encyonopsis microcephala*. Unlike other sites in the North, Nunatarsuaq lakes in the Northwest display higher abundances of periphytic, acidophilous and planktic taxa, similar to the assemblages in the Southwest.

Richness and diversity

The diatom species richness and diversity overall (with the exception of the Nunatarsuaq region) decrease from South to North, strongly correlating with latitude ($r = -0.65$, -0.55, respectively, $p < 0.001$) and mean August air temperature ($r = 0.59$, 0.51, respectively, $p < 0.001$; Figure 3). There is no significant relationship between species diversity and lake/pond area ($r = 0.008$) or depth ($r = 0.06$), but generally deeper lakes are amongst the more species-rich sites from the Southwest (Nuuk region). A weak, but statistically significant, relationship was found between richness/diversity and EVI ($r = 0.29/0.27$, $p < 0.001$). On the local scale, relationships between species diversity and the environment are less clear. The Nunatarsuaq lakes exhibit a diversity that is more similar to the species diversity range of the Nuuk region (Welch *t*-test: $t = 2.2$, $p = 0.04$; Figure 4A). The comparison of species diversity between same latitude sites on the west coast versus the east coast of Greenland reveals no significant differences (Welch *t*-test: $t = 0.46$, $p = 0.65$; compare old Ilulissat lakes vs. Zackenberg/Daneborg Figure 4A). For the three regions Nuuk, Zackenberg/Daneborg and Pearyland, where sites follow a quasi-coast—inland—ice margin transect, species diversity decreases from the sites closest to the coast or fjord towards the sites closest to the inland ice, but no statistically significant relationship with our measured environmental variables is found (Figures 4B,D).

Environmental predictors

The RDA, with forward selection (999 Monte Carlo permutations) reveals that eight out of the 11 environmental variables contribute significantly to the species-sites relationships of the data set, accounting for 29% of the variance (TP, area and fish insignificant). Mean August temperature, EVI and lake depth have the strongest correlation with axis 1, whilst specific conductivity and pH correlate

10.3389/fevo.2023.1177638

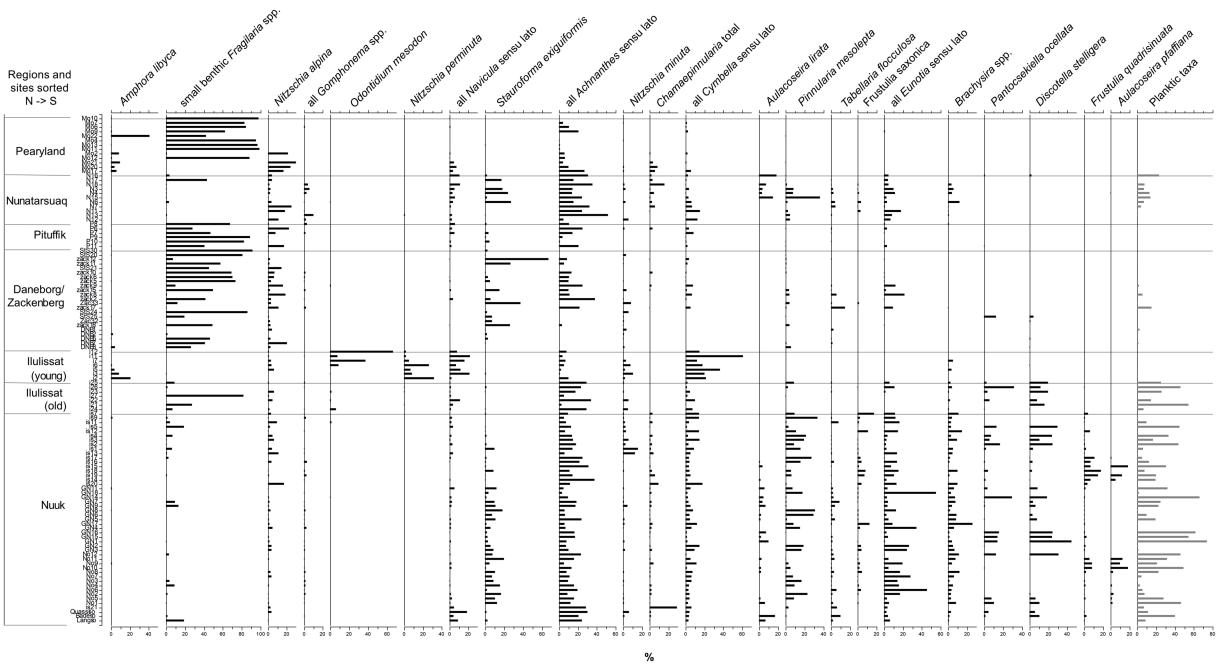

FIGURE 2
Distribution of the most common diatom taxa found in the 115 lakes and ponds, sorted by decreasing latitude. Taxa are expressed as relative abundance. Small benthic *Fragilaria* species (*Pseudostaurosira brevistriata*, *Staurosira pseudoconstruens*, *Staurosira venter*, and *Staurosirella pinnata*), *Navicula sensu* lato (*Navicula* spp., *Naviculadicta* spp.), *Achnanthes sensu* lato (*Achnanthes* spp., *Achanthidium* spp., *Planothidium* spp., *Psammothidium* spp., *Rossithidium* spp.), *Cymbella sensu* lato (*Cymbella* spp., *Cymbopleura* spp., *Encyonema* spp., *Encyonopsis* spp.) and *Eunotia sensu* lato (*Cystopleura faba*, *Eunotia* spp.) are displayed as groups as they showed similar trends in abundance. Planktic taxa include all centric taxa and *Tabellaria flocculosa*.

with axis 2 (Figure 5). The seven investigated areas show distinct clusters in the ordination plot. The Nuuk region (Southwest) plots on the positive side of the first axis, whilst the Zackenberg/Daneborg region (Northeast), Pearyland (North) and Pituffik (Northwest) plot on the opposite end. The Nunatarsuaq region (Northwest) is located in between. The older lakes in the Ilulissat region (West) and some Pearyland sites plot on the positive side of the second axis, with the young lakes in the Ilulissat region clustering closely together at the positive end of the axis. Each region hosts relative well-defined diatom communities. Dominantly acidophilous and periphytic taxa (*Brachysira* spp., *Frustulia* spp., *Cymbella sensu* lato spp., *Pinnularia* spp.), and planktic/tychoplanktic taxa (*Pantocsekiella*, *Discostella* spp., *Aulacoseira* spp., *Tabellaria* spp.) plot together with the warmer, deeper, nutrient-enriched lakes in the Southwest. Small fragilariod taxa (e.g., *S. venter*, *S. pseudoconstruens*, *S. pinnata*) are closely linked to the shallower, cooler, nutrient-poor lakes and ponds in the North, Northeast and Northwest. The intermediate region in the Northwest (Nunatarsuaq) hosts a combination of taxa from the Southwest (Nuuk) and the northern sites. The lakes from the Ilulissat region and Pearlyland with higher alkalinity and conductivity are dominated by *Nitzschia* spp., *O. mesodon*, *E. microcephala* and *Amphora libyca*.

Spatial predictors

To test for the influence of the spatial factors on the diatom species distribution, PCNM's were used. In total, 59 spatial vectors (PCNMs) captured the spatial structure of the 115 locations across Greenland. In the RDA with Monte Carlo forward selection, 15 of these spatial vectors significantly explained patterns in diatom species communities. Combining these 15 significant spatial vectors with the 11 measured environmental variables, the RDA with Monte Carlo forward selection revealed that all 15 spatial vectors and lake depth, EVI, specific conductivity, chl *a*, TN and TP were statistically significant in shaping the diatom communities ($p \leq 0.01$). Mean August air temperature was marginally significant, depending on the permutation run. In combination with spatial vectors (e.g., V4, V59—vectors capturing the regional and local spatial structure of the Ilulissat region, respectively), specific conductivity still remained strongly associated with community patterns along axis 2, whilst axis 1 was now more strongly associated with spatial vectors (e.g., V1, V5—vectors effectively capturing the degree in spatial structuring between all northern and all southern sites), while measured environmental variables were less important (Figure 6).

The partial RDA (variance partitioning) using diatom species abundance data revealed that all environmental factors explain independently 5%, while space explains 14%. The conditional effect relating to the covariance between environment and space explains 17% of the variance. Together they explain 36% of the total variation ($p < 0.001$). The partial RDA using PA data revealed a similar proportion of explanatory power (environmental factors 3%, space 12%, conditional effect 15%; together explaining 30% of the total variance, $p < 0.001$; Figures 7A,B). The variance explained is relatively low, but it is typical of data sets containing many taxa and many zero values in the species matrix. Important, however, are the associated

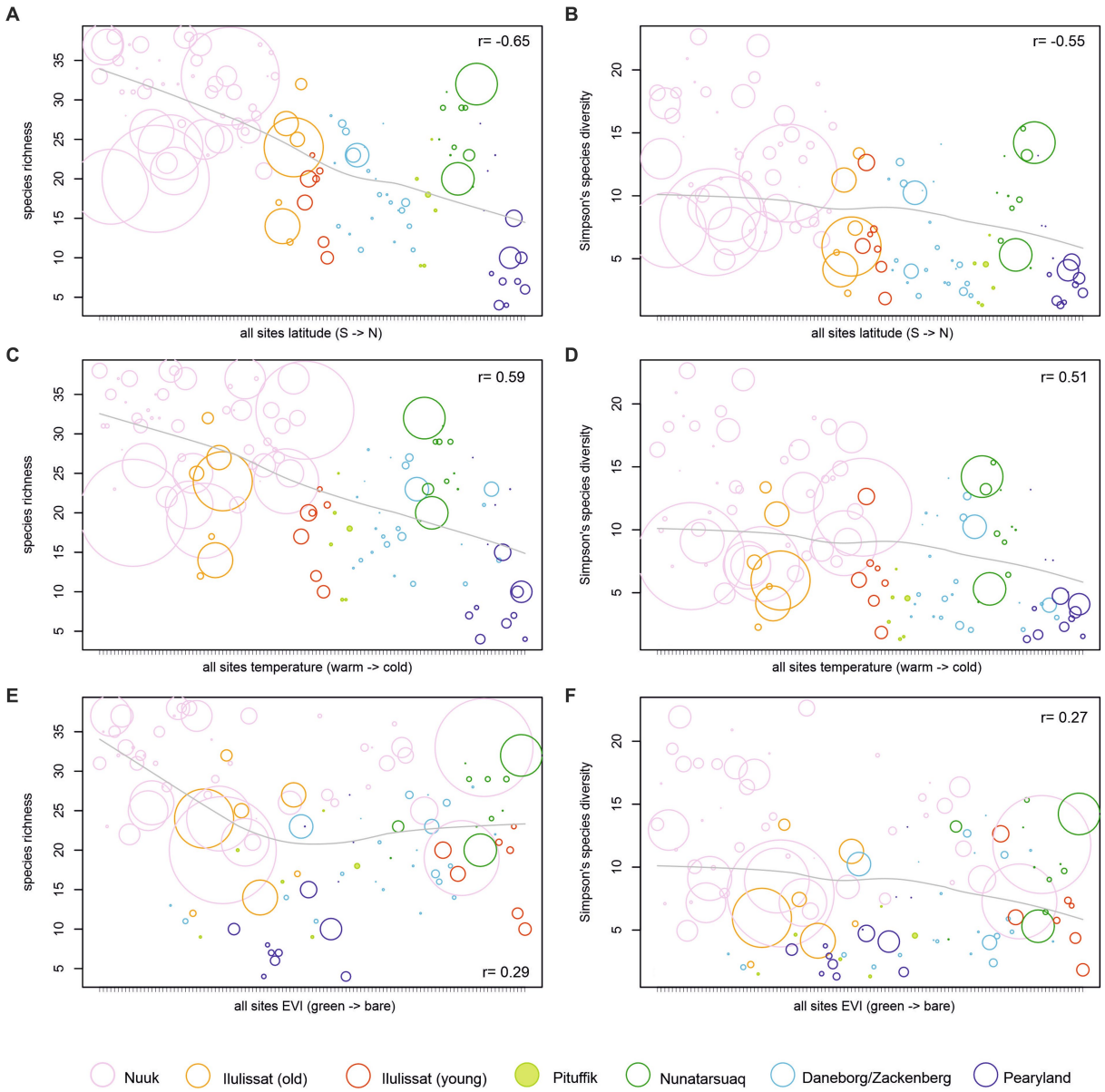

FIGURE 3
Species richness and diversity on a regional scale vs. latitude Species richness and diversity on a regional scale vs. latitude **(A,B)**, mean August air temperature **(C,D)**, and enhanced vegetation index (EVI) **(E,F)**. Sites are colour-coded by region and scaled by lake depth.

permutation tests showing the statistical significance of the explanatory variables.

Discussion

Environmental gradients

Typical for high latitude freshwaters, the majority of our lakes and ponds are ultra-oligotrophic to oligotrophic (Ryves et al., 2002; Bouchard et al., 2004; Cremer and Wagner, 2004). The distribution of trophy is associated with mean August air temperature. Warmer summer temperatures, characteristic for the southwestern region of Greenland, lead to increased terrestrial plant growth and hence catchment inputs (Normand et al., 2013), which affect the trophic state of the lakes and ponds: sites in the Southwest are more nutrient enriched (up to mesotrophic), while ultra-oligotrophic in the North and Northwest (Table 1). High specific conductivity sites are closely linked to carbonate bedrock geology and silty soil type (vs. rocky catchments) in the Pituffik and Pearyland regions. More dilute and acidic lakes are located in Southwest Greenland, embedded in gneiss bedrock and associated with more established soil and vegetation development binding base cations (Law et al., 2015). Dilute and acidic lakes are also found in the Nunatarsuaq region (Table 1), which, unlike the Pituffic lakes are embedded in siliciclastic bedrock. Some sites in recently deglaciated areas, here the newly established lakes from the Ilulissat region, had high conductivity (Jeppesen et al., 2023) despite the gneiss bedrock

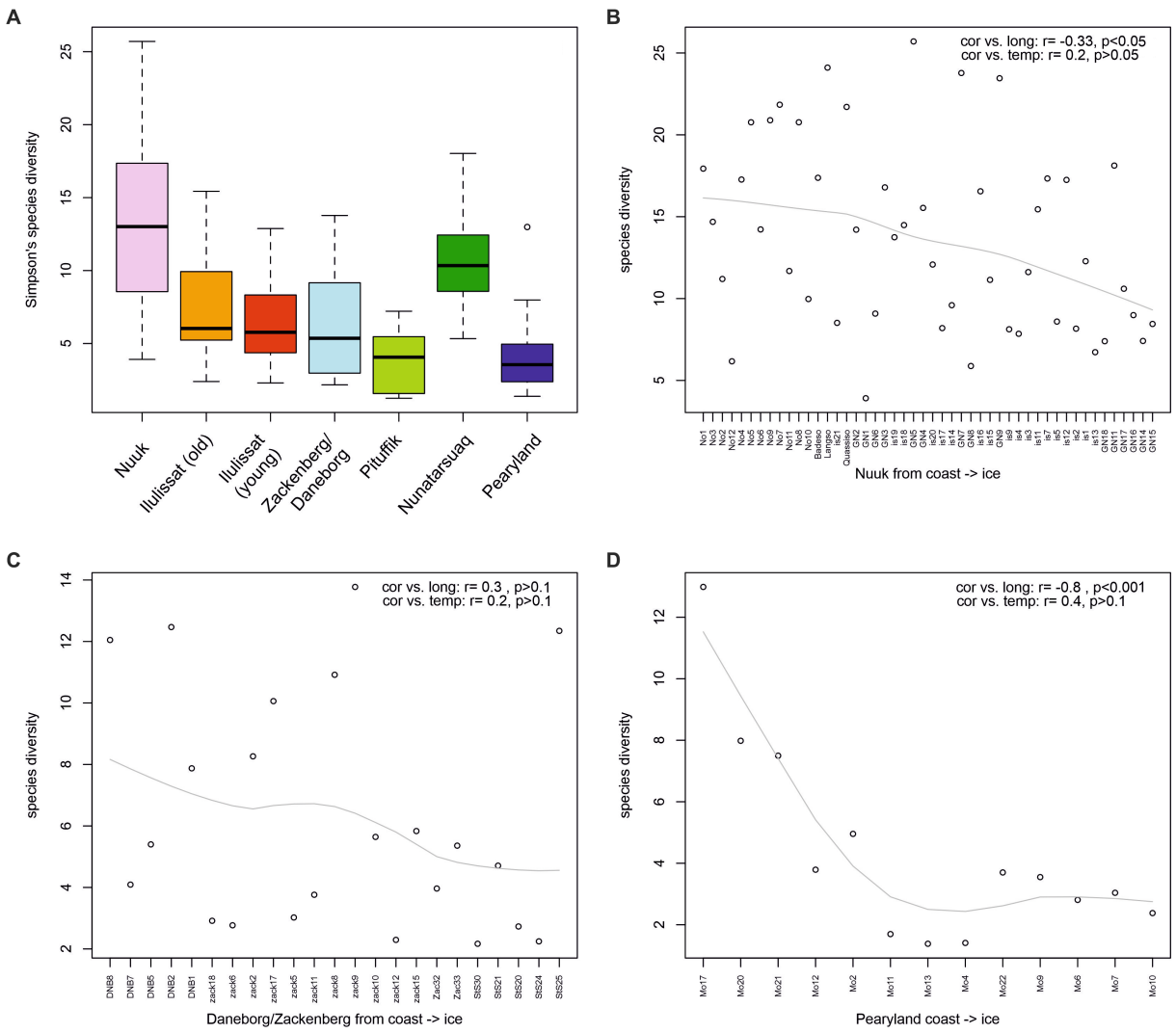

FIGURE 4
Species diversity of study regions **(A)**, and three local-scale examples of a "coast->ice margin" transect **(B-D)**.

geology. These high values are linked to the recent retreat of the inland ice, as inwash to these lakes from the newly emerged catchments is rich in nutrients and base-rich solutes (Law et al., 2015; Jeppesen et al., 2023).

Diatom communities and species ecology

Many of the taxa encountered in our Greenland lake surface-sediment data set, including dominantly benthic species, have been previously reported in studies from the high Artic. These taxa are typical for slightly acidic to circumneutral, oligotrophic, electrolyte-poor lakes (Bouchard et al., 2004; Jones and Birks, 2004; Antoniades et al., 2005; Keatley et al., 2008; Hadley et al., 2013; McGowan et al., 2018). The low abundance of planktic taxa has been observed in most high Arctic surveys and is linked to the shallowness of sites, extended ice-cover period and low nutrient concentration of the lake water (e.g., Smol, 1988; Weckström et al., 1997a,b; Weckström and Korhola, 2001; Teittinen et al., 2018). We found consistently higher abundances of planktic *Pantocsekiella ocellata* and *Discostella stelligera* in the deeper lakes of the Southwest (Nuuk region), indicating a longer open water season, sufficient depth and nutrient supply enabling planktic growth (Reynolds et al., 2002; Rühland et al., 2015; Saros and Anderson, 2015; Ossyssek et al., 2020). Higher abundances of planktic species were also observed in the deeper lakes of the regions Ilulissat (*Cyclotella* and *Discostella*) and Nunatarsuaq (*Aulacoseira*, especially *A. lirata*; Figure 2; Table 1). The difference in the dominant planktic species is likely related to temperature stratification, with more stratified lakes in the warmer Southwest. Heavily silicified *Aulacoseira* taxa require turbulent (mixed) conditions to thrive, whereas small *Cyclotella* (*sensu* lato) species dominate in a temperature-stratified water column (Rühland et al., 2003, 2015).

The high compositional species turnover in our survey identified by DCA (3.8 SD) was expected and indicates relatively large differences in diatom assemblages amongst regions and sites due to the wide range of habitats across Greenland. Species of mostly alkaliphilous *Staurosirella*, *Staurosira* and *Staurosira* are typical for the Pearyland, Pituffik and Zackenberg/Daneborg regions. These taxa are often described as pioneers in fast changing environments, and are known to be competitive in shallow, hard-substrate, low-productivity cold sites, where they thrive

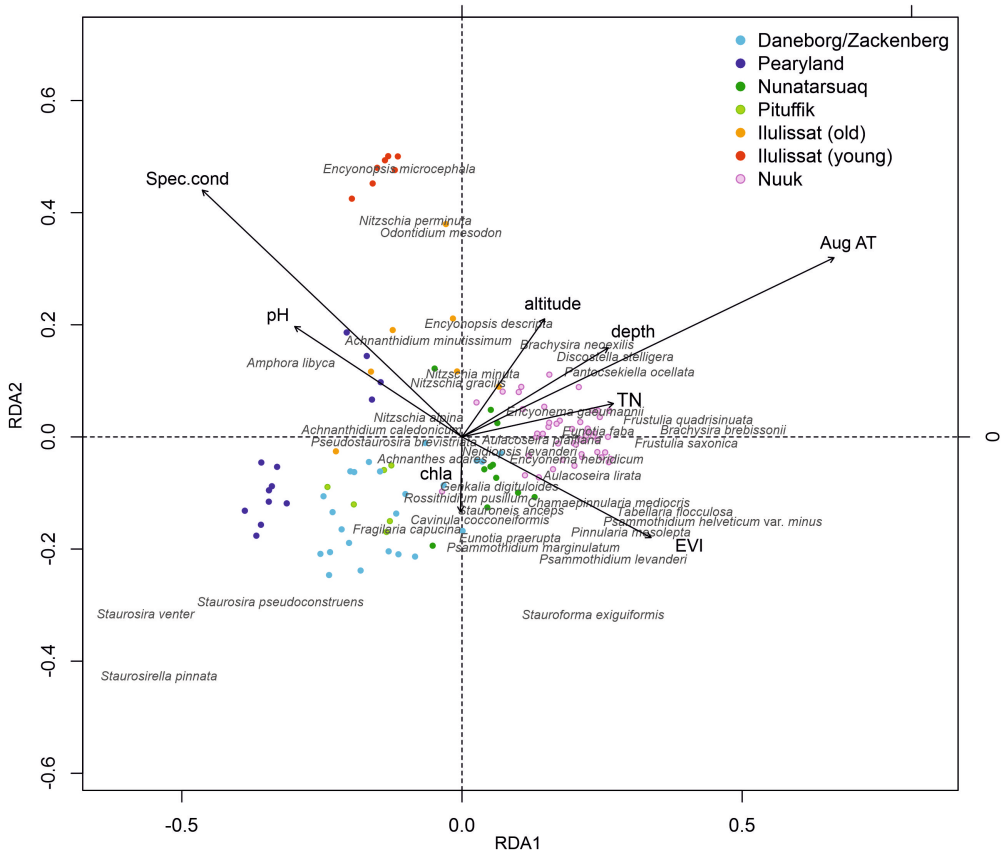

FIGURE 5
Redundancy analysis (RDA) (includes measured environmental variables only) with Monte Carlo forward selection. Regions are colour-coded, and the 40 most abundant taxa are shown.

under prolonged ice-cover and the resulting short growing season (Lotter and Bigler, 2000; Rühland et al., 2003; Pla-Rabes et al., 2016).

While pioneer species and generalists with wider niches (e.g., *Achnanthes sensu* lato) dominate Greenland's northerly sites, southerly sites host more complex communities and life forms. A succession along a gradient of increasing temperature, from relatively simple diatom assemblages (adnate benthic small *Fragilaria*) to more diverse and complex assemblages has been observed in other lake surface-sediment studies in the Canadian Arctic (e.g., Michelutti et al., 2003) and in palaeolimnological studies, where it was suggested to be an indication of climate warming (Smol, 1988; Douglas and Smol, 1999). The southerly sites in Greenland host generalist *Achnanthes sensu* lato Achnanthes sensu lato (*Achnanthes* spp., *Achanthidium* spp., *Planothidium* spp., *Psammothidium* spp., *Rossithidium* spp) along with high abundances of *Eunotia* spp. and larger epiphytic species like *F. quadrisinuata*, *F. saxonica*, *Brachysira brebissonii*, *B. neoexilis* and *P. mesolepta*, which are acidophilous taxa (Weckström et al., 2003) reflecting the dilute and slightly acidic waters of the Southwest. Here they also reflect a higher abundance of mosses and submerged macrophytes than in the northern sites due to the longer growing season and higher temperatures, as these epiphytic taxa have often been found in moss-rich Artic freshwaters (Douglas and Smol, 1995; Michelutti et al., 2007; McGowan et al., 2018). Apart from the absence of *Frustulia* species, diatom communities in Nunatarssuaq are dominated by these same taxa, likely owing to the dilute and slightly acidic lake waters in this region (Table 1) and the presence of mosses also in the deeper sites. Many of the lakes here have very clear water (Secchi depth ≥ lake depth) due to stony catchment areas with little soil. As the Nunatarsuaq area is located at a higher elevation close to the inland ice, the number of sunny days is higher than near the coast, favouring benthic macrophytes.

Encyonopsis microcephala was encountered at high abundances together with the cold-water *O. mesodon* (Potapova, 2009) and the generalist *N. perminuta* in the newly established lakes and ponds at the foreland of the fast-retreating Ilulissat glacier (Figure 2; *E. microcephala*, which in Figure 2 is grouped together with *Cymbella* spp., was found at 20% on average). Also, *A. libyca* was abundant in several of these lakes and ponds. It was found at marked abundances only here and at the higher conductivity of the Pearyland sites. Despite their classification as pioneers, small fragilariod taxa were scarce (Figure 2). As such, these sites, established after 1850 and some after 1960 (Jeppesen et al., 2023), host very different diatom communities compared with any other sites investigated in this study. They are high-conductivity and vegetation-free (both submerged and terrestrial) systems, characterised by a rocky lake bottom, with clay and a thin layer of lake sediment deposition. Species of *Amphora* and *Diatoma* (*Odontidium*) have been shown to prefer high-conductivity environments (Ryves et al., 2002; Weckström and Juggins, 2005). This could explain their occurrence in such glacier-proximal lakes, which are known to be ion-enriched and alkaline (Engstrom et al., 2000). *Nitzschia perminuta* was also observed at high abundances in Svalbard ponds, which were recently formed after glacier retreat (30–40 yr. old), and which are similar to our sites in being hydrologically isolated from

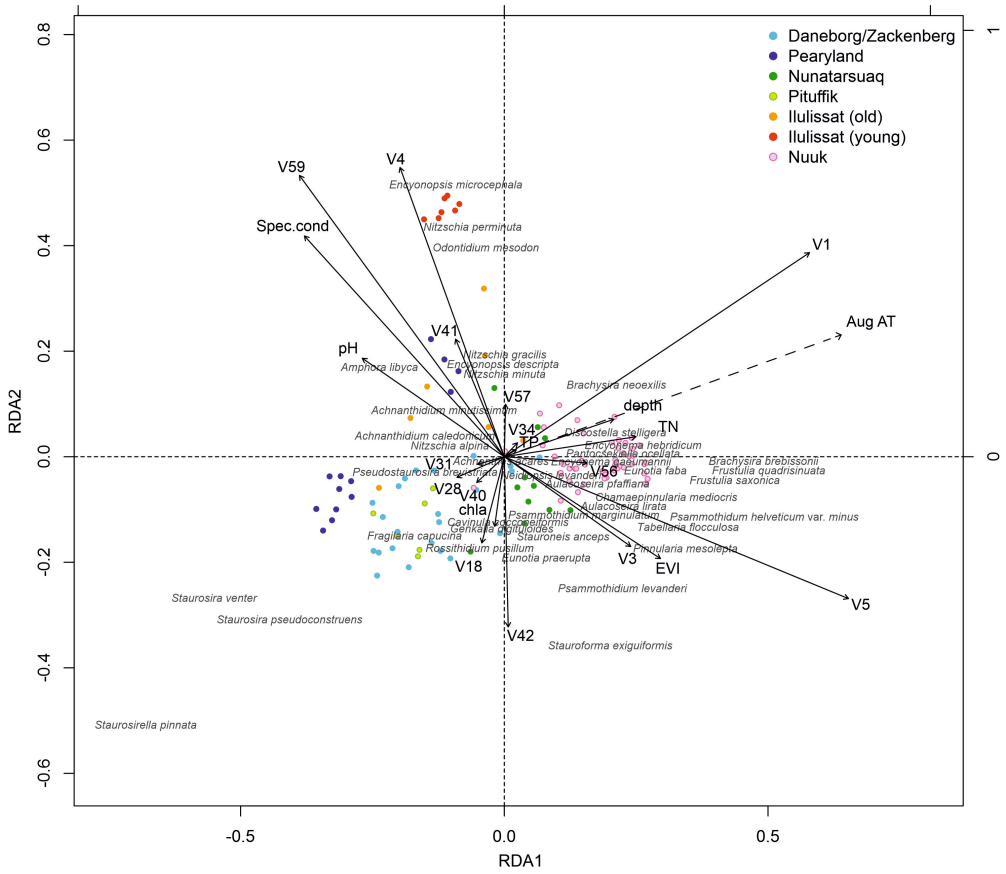

FIGURE 6
Redundancy analysis (RDA) with significant spatial vectors (PCNMs) included, under Monte Carlo forward selection. Regions are colour-coded, and the 40 most abundant taxa are shown.

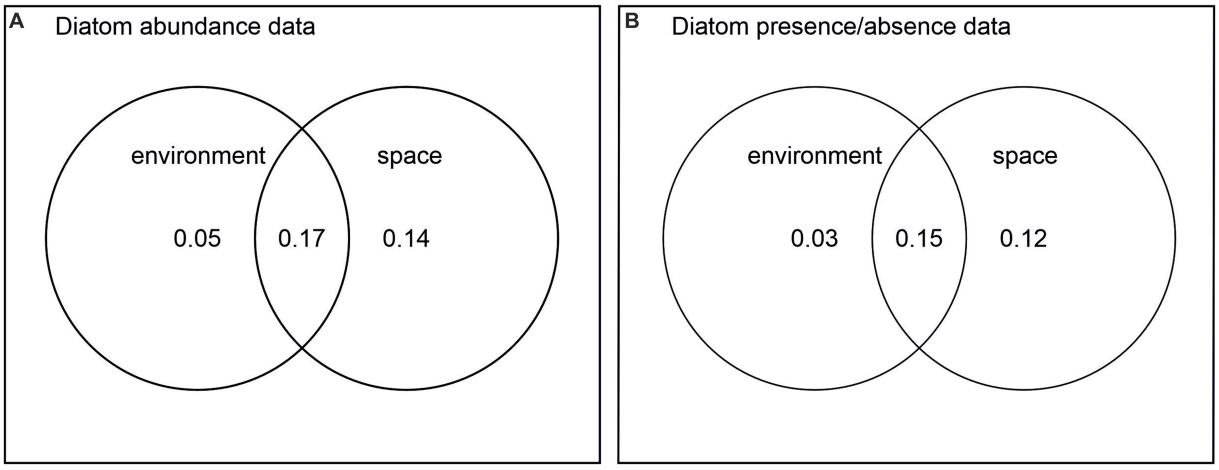

FIGURE 7
Variance partition on **(A)** diatom abundance data, environmental variables, and spatial vectors and **(B)** diatom presence/absence data, environmental variables, and spatial vectors.

the retreating glacier (Pinseel et al., 2017). In the Kangerlusuaq region, 250 km south of Ilulissat, McGowan et al. (2018) found *Encyonopsis* (*Cymbella*) *microcephala* at high abundances co-dominant with different species of *Nitzschia* in the investigated inland lakes, whilst the abundance of small fragilariod taxa was low. These taxa are known to inhabit microbial biofilms (McGowan et al., 2018). In addition to these more motile species, also prostrate forms, such as *O. mesodon* (Spaulding et al., 2010, as *Diatoma mesodon*) are suited to grow as epiphytes on algal

filaments in complex microbial mats (McGowan et al., 2018, and references therein). Cyanobacteria-dominated microbial mats are highly common in cold polar waters and are known to be primary colonisers after glacier/ice sheet retreat, offering a suitable habitat for other algal groups (Vincent, 2000).

Diatom richness and diversity

With the exception of the Nunatarssuaq region, diatom diversity and species richness showed a decline with latitude, aligning with earlier studies encompassing the North American, European and Russian Arctic (Michelutti et al., 2003; Kahlert et al., 2021). Bouchard et al. (2004) further found a strong correlation between species diversity and lake area, which they attributed to a higher heterogeneity in habitats. Their study covered a much smaller region compared with our Greenland-wide lake survey, where other environmental gradients override the importance of lake area. Mean August temperature, which decreases from south to north, is strongly correlated with diversity and richness in our data set, emphasising that the duration of the growing season directly or indirectly strongly controls diatom diversity in the High Arctic. A longer and warmer summer in the southern sites will lead to earlier ice breakup and a longer growing season, creating a wider range of habitats. Diversity increases due to the development of more complex assemblages as the season progresses (Smol, 1988; Douglas and Smol, 1999; Smol et al., 2005; Keatley et al., 2008; Weckström et al., 2014). In addition, the terrestrial vegetation is generally denser (or present) at southern sites, promoting diatom abundance and diversity indirectly via additional nutrient input (Bouchard et al., 2004; Wrona et al., 2016). The surprisingly high species richness and diversity in the Nunatarsuaq region in comparison to all other northerly sampling regions (Figure 4A) could at least partly be explained by the presence of aquatic mosses in the majority of the sites, translating into a greater potential for diverse micro-habitats for benthic taxa (Bouchard et al., 2004). Additionally, half of the sites in the region are deep (Table 1), allowing for a planktic community to develop, adding to the species diversity.

In the regions with a wider ice-free margin (Nuuk, Daneborg/Zackenberg and Pearyland, Figure 1) the within-region diversity and richness decreased from the coastal and fjord lakes towards the inland and ice margin lakes (Figure 4), weakly correlating with decreasing mean August air temperature along an altitudinal gradient (the temperature range within each region varied from 1.6°C in Pearlyland to 2.6°C in Zackenberg/Daneborg and Nuuk). This tentatively aligns with the above-discussed dependency of diatom diversity on the length of the growing season.

Diatoms—environment vs. space

The physical and chemical components in the RDA (without spatial vectors) explained 29% of the variation in the diatom community, a figure that is similar to other studies in the Arctic (e.g., Ryves et al., 2002; Lim et al., 2007; Keatley et al., 2008). Mean August temperature, specific conductivity, and vegetation cover (EVI) were most significant in driving the diatom community composition, indicating that climate, geology, and lake/catchment age determine (indirectly) species distribution along the extensive environmental gradients in Greenland.

The presence and abundance of fish has been suspected as a potential driver of diatom species distribution via controlling the direct grazing pressure on planktic diatom communities (e.g., McGowan et al., 2018). Indeed, fish presence has shown strong cascading effects on zooplankton and macroinvertebrate communities in arctic and boreal regions (Jeppesen et al., 2003, 2017; Milardi et al., 2016) and on the dominance of planktic or benthic diatom production (Milardi et al., 2017). In this study, however, we could not show a significant effect of fish presence on diatom species community distribution, similar to results from Jeppesen et al. (2017), who did not find cascading effects of fish on the phytoplankton biomass in low and high arctic lakes in Greenland.

When environmental and spatial components were analysed together in RDA (using diatom abundance data), the environment uniquely explained only 5% of the variation, whereas space, captured as spatial vectors (PCNMS) based on basic coordinates, appears to have a stronger impact on the patterns in the diatom community composition, uniquely accounting for 14% of the variation. Together, environmental components and space accounted for 36% of the variation (including the conditional effect relating to their covariance, Figure 7). Results using diatom presence/absence data were almost identical. We hypothesised that if space explained a markedly larger portion of diatom variability using P/A data, this would indicate dispersal as a significant driver over the large distances between our study regions. As this was not the case, we conclude that spatial factors relating to the varying environmental settings/long environmental gradients covered by our extensive study area are likely at play. As further support, there was no difference in species diversity between the sites on the east and west coast located at the same latitude; if diatom communities were affected by dispersal limitation over larger distances, we would have expected the more isolated east coast diatom communities to display lower species diversity. Many of the diatom species encountered were found in several of the study regions (see Supplementary Table 1). The most significant spatial vectors were those separating the southern sites in Nuuk from all northern study regions along a climate (temperature, EVI) gradient and those separating Ilulissat sites (and a few Pearyland lakes) from all other regions along a conductivity gradient, but also separating the old and new sites within the Ilulissat region relating to lake ontogeny.

For a much smaller regional-scale surface diatom data set in the Kangerlussuaq area, West Greenland, McGowan et al. (2018) found that space accounted for 9–20% of variation in the diatom community, depending on sampling season. Likewise, Virtanen and Soininen (2012) concluded that spatial structure was more important than local environmental variables for defining diatom communities in boreal streams, suggesting that large-scale processes related to climate, history and dispersal may play a significant role in community distribution, while Sweetman et al. (2010) observed a similar pattern for zooplankton in Canadian Arctic lakes. However, for lakes in the Canadian High Arctic, Keatley et al. (2008) found only environmental variables to be important in structuring diatom communities, although they conclude that this may only be true at the landscape level explored. Our study covers a significantly larger geographical area, where distance between study areas was hypothesised to increase in importance as a factor

explaining spatial structure following findings by, for example, Verleyen et al. (2009).

The spatial separation of the subset of young Ilulissat sites may be explained by these lakes having appeared recently (after 1850 and many after 1960) due to glacier retreat (Jeppesen et al., 2023). They are characterised by bare catchment ground and poor lake habitat development. The markedly different environmental conditions of these lakes, which were not fully captured by our measured environmental variables, is reflected as very distinct diatom communities. Hence, spatial structure may become more important in shaping species communities when relevant spatially linked environmental variables are not captured by the environmental data collected. Potential unmeasured variables contributing to the higher explanatory power of space in our study setting could be, for example, duration of lake ice cover, length of the growing season, abundance of aquatic macrophytes, topography of the catchment, wind conditions, lake shape, and trophic interactions between zoo- and phytoplankton (not related to fish presence). Looking at the positions between the main spatial and environmental vectors in Figure 6, the unmeasured spatially structured environmental variables are largely linked to the latitudinal climate gradient and to lake ontogeny. Future climate warming is hence likely affecting several of the measured and non-measured spatially structured environmental variables in this study, and potentially marked changes in Greenlandic (and Arctic-wide) diatom communities regarding their species composition and diversity may be expected.

Conclusion

One of the key requirements for the use of organisms as palaeoecological proxies, is a sufficient understanding of their ecology (which modern environments are species found in and what changes in their environment are they responding to). Exploring modern calibration data sets, which combine information on species assemblages and their surrounding environment, allows such critical information to be gained. Here we used a large 115-lake data set of remote Greenlandic lakes, covering extensive geographical, climatic and environmental gradients to improve our knowledge on the ecological and biogeographical characteristics of Arctic freshwater diatoms.

There were marked differences in the diatom community structure between sites, although a number of species were found in all regions. The lakes and ponds in the northern regions showed a distinctive dominance of small benthic fragilarioid species, linked to their extensive ice-cover period and poor habitat diversity. Diatom communities in the Southwest of Greenland were more varied, including many epiphytes, expressing the longer growing season, more complex successional development, and higher habitat diversity of these lakes and ponds. The main environmental drivers of diatom communities in Greenland were summer (August) air temperature, catchment vegetation and lake conductivity. However, a larger part of diatom variability was explained by spatially structured (unmeasured) environmental variables that aligned with the identified main explanatory variables into climate-related and bedrock/lake development—related drivers. Species diversity was most strongly driven by climate (temperature), following an overall clear latitudinal decline towards the North. Regionally, diversity declined along an altitudinal gradient from the coast to the ice margin. Despite the large distances between our study regions, diatom dispersal appeared not to be limited.

Diatoms provide an excellent tool for (long-term) assessments of climate change in the Arctic and its effects on lake ecosystems, as they appear to be most strongly driven by climate-related variables over Arctic-wide scales. However, several of these drivers, such as in-lake habitat availability, are often left unmeasured in Arctic field campaigns, similarly to non-climatic (trophic interactions) parameters, but should nevertheless be carefully considered due to their apparent importance, when using diatoms as a proxy for reconstructing past and present climate change in the Arctic.

Data availability statement

The original contributions presented in the study are included in the article/Supplementary material, further inquiries can be directed to the corresponding author.

Author contributions

KW and JaW wrote the paper, developing the paper from an earlier draft written by JuW. JuW generated the diatom data and analysed the data. TD, TL, FL, KC, and EJ conducted numerous logistically complicated field trips to collect the samples and commented on the manuscript. All authors contributed to the article and approved the submitted version.

Funding

The work was supported by the Global Climate Change Programme (no. 9700195), the Commission for Scientific Research in Greenland, the North Atlantic Research Programme 1998–2000, the Arctic Programme, 1998–2002, the Nordic Council of Ministers, the Research in the North by the National Research Council, and the Carlsberg Foundation and the EU project Eurolimpacs. In the writing phase EJ was supported by the TÜBITAK programme BIDEB2232 (project 118C250) and KW was supported by Arctic Avenue (spearhead research project between the University of Helsinki and Stockholm University).

Conflict of interest

The authors declare that the research was conducted in the absence of any commercial or financial relationships that could be construed as a potential conflict of interest.

Publisher's note

be made by its manufacturer, is not guaranteed or endorsed by the publisher.

Supplementary material

The Supplementary material for this article can be found online at: https://www.frontiersin.org/articles/10.3389/fevo.2023.1177638/full#supplementary-material

SUPPLEMENTARY TABLE S1
List of all taxa found in this study and their occurrence in the different study regions.

SUPPLEMENTARY FIGURE 1
PCA of environmental variables. Regions are colour-coded.

SUPPLEMENTARY FIGURE 2
PCA of diatom taxa. Regions are colour-coded, and the 40 most abundant taxa are shown.

References

Antoniades, D., Douglas, M. S. V., and Smol, J. P. (2005). Quantitative estimates of recent environmental changes in the Canadian high Arctic inferred from diatoms in lake and pond sediments. *J. Paleolimnol.* 33, 349–360. doi: 10.1007/s10933-004-6611-3

Battarbee, R. W., Jones, V. J., Flower, R. J., Cameron, N. G., Bennion, H., Carvalho, L., et al. (2001). "Diatoms," in *Tracking environmental change using Lake sediments. Developments in Paleoenvironmental research*. eds. J. P. Smol, H. J. B. Birks, W. M. Last, R. S. Bradley and K. Alverson, vol. *3* (Dordrecht: Springer) doi: 10.1007/0-306-47668-1_8

Bigler, C., and Hall, R. I. (2002). Diatoms as indicators of climatic and limnological change in Swedish Lapland: a 100-lake calibration set and its validation for paleoecological reconstructions. *J. Paleolimnol.* 27, 97–115. doi: 10.1023/A:1013562325326

Bouchard, G., Gajewski, K., and Hamilton, P. B. (2004). Freshwater diatom biogeography in the Canadian Arctic archipelago. *J. Biogeogr.* 31, 1955–1973. doi: 10.1111/j.1365-2699.2004.01143.x

Callaghan, T. V., Bergholm, F., Christensen, T. R., Jonasson, C., Kokfelt, U., and Johansson, M. (2010). A new climate era in the sub-Arctic: accelerating climate changes and multiple impacts. *Geophys. Res. Lett.* 37. doi: 10.1029/2009GL042064

Cappelen, J., ed. (2011). DMI monthly climate data collection1768–2010, Denmark, The Faroe Islands and Greenland. Danish Meteorological Institute Technical Report 11-05 (Copenhagen: DMI) (www.dmi.dk/dmi/tr11-05.pdf (report).

Cremer, H., and Wagner, B. (2004). Planktonic diatom communities in high Arctic lakes (store Koldewey, Northeast Greenland). *Can. J. Bot.* 82, 1744–1757. doi: 10.1139/B04-127

Douglas, M. S., and Smol, J. P. (1995). Periphytic diatom assemblages from high arctic ponds. *J. Phycol.* 31, 60–69. doi: 10.1111/j.0022-3646.1995.00060.x

Douglas, M. S. V., and Smol, J. P. (1999). "Freshwater diatoms as indicators of environmental change in the high Arctic," in *The diatoms: Applications for the environmental and earth sciences*. eds. E. F. Stoermer and J. P. Smol (Cambridge: Cambridge University Press), 227–244.

Douglas, M. S. V., Smol, J. P., Pienitz, R., and Hamilton, P. (2004). "Algal indicators of environmental change in arctic and antarctic lakes and ponds," in *Long-Term Environmental Change in Arctic and Antarctic Lakes*. eds. R. Pienitz, M. S. V. Douglas and J. P. Smol (Dordrecht: Springer), 117–157.

Dulias, K., Stoof-Leichsenring, K. R., Pestryakova, L. A., and Herzschuh, U. (2017). Sedimentary DNA versus morphology in the analysis of diatom-environment relationships. *J. Paleolimnol.* 57, 51–66. doi: 10.1007/s10933-016-9926-y

Engstrom, D. R., Fritz, S. C., Almendinger, J. E., and Juggins, S. (2000). Chemical and biological trends during lake evolution in recently deglaciated terrain. *Nature* 408, 161–166. doi: 10.1038/35041500

Falasco, E., Bona, F., Monauni, C., Zeni, A., and Piano, E. (2019). Environmental and spatial factors drive diatom species distribution in alpine streams: implications for biomonitoring. *Ecol. Indic.* 106:105441. doi: 10.1016/j.ecolind.2019.105441

Hadley, K. R., Douglas, M. S. V., Lim, D., and Smol, J. P. (2013). Diatom assemblages and limnological variables from 40 lakes and ponds on Bathurst Island and neighboring high Arctic islands. *Int. Rev. Hydrobiol.* 98, 44–59. doi: 10.1002/iroh.201201449

Henriksen, N., and Higgins, A. K. (2009). Descriptive text to the geological map of Greenland, 1:500000, dove Bukt, sheet 10. *Geol. Surv. Den Green. Map Series* 4:32.

Hijmans, R. J., Cameron, S. E., Parra, J. L., Jones, P. G., and Jarvis, A. (2005). Very high resolution interpolated climate surfaces for global land areas. *Int. J. Climatol.: J. Royal Meteorol. Soc.* 25, 1965–1978. doi: 10.1002/joc.1276

Hobbs, W. O., Telford, R. J., Birks, H. J. B., Saros, J. E., Hazewinkel, R. R., Perren, B. B., et al. (2010). Quantifying recent ecological changes in remote lakes of North America and Greenland using sediment diatom assemblages. *PLoS One* 5:e10026. doi: 10.1371/journal.pone.0010026

Jeppesen, E., Davidson, T. A., Meerhoff, M., DeMeester, L., González-Bergonzoni, I., Vidal, N., et al. (2023). Differences in food web structure and composition between new and nearby older lakes in West Greenland suggest succession trajectories driven by glacier retreat. *Hydrobiologia*. doi: 10.1007/s10750-023-05189-4

Jeppesen, E., Jensen, J. P., Jensen, C., Faafeng, B., Hessen, D. O., Søndergaard, M., et al. (2003). The impact of nutrient state and lake depth on top-down control in the pelagic zone of lakes: a study of 466 lakes from the temperate zone to the arctic. *Ecosystems* 6, 313–325. doi: 10.1007/PL00021503

Jeppesen, E., Lauridsen, T. L., Christoffersen, K. S., Landkildehus, F., Geertz-Hansen, P., Amsinck, S. L., et al. (2017). The structuring role of fish in Greenland lakes: an overview based on contemporary and paleoecological studies of 87 lakes from the low and the high Arctic. *Hydrobiologia* 800, 99–113. doi: 10.1007/s10750-017-3279-z

Jespersen, A. M., and Christoffersen, K. (1987). Measurements of chlorophyll-a from phytoplankton using ethanol as extraction solvent. *Arch. Hydrobiol.* 109, 445–454. doi: 10.1127/archiv-hydrobiol/109/1987/445

Jones, V. J., and Birks, H. J. B. (2004). Lake-sediment records of recent environmental change on Svalbard: results of diatom analysis. *J. Paleolimnol.* 31, 445–466. doi: 10.1023/B:JOPL.0000022544.35526.11

Juggins, S. (2007). *C2 Version 1.5 User Guide. Software for Ecological and Palaeoecological Data Analysis and Visualisation*. Newcastle University, Newcastle upon Tyne, UK. 73

Kahlert, M., Bailet, B., Chonova, T., Karjalainen, S. M., Schneider, S. C., and Tapolczai, K. (2021). Same same, but different: the response of diatoms to environmental gradients in Fennoscandian streams and lakes–barcodes, traits and microscope data compared. *Ecol. Indic.* 130:108088. doi: 10.1016/j.ecolind.2021.108088

Kaufman, D. S., Schneider, D. P., McKay, N. P., Ammann, C. M., Bradley, R. S., Briffa, K. R., et al. (2009). Recent warming reverses long-term arctic cooling. *Science* 325, 1236–1239. doi: 10.1126/science.1173983. Erratum in: Science 2010, 327(5966):644

Keatley, B. E., Douglas, M. S. V., and Smol, J. P. (2008). Prolonged ice cover dampens diatom community responses to recent climatic change in high Arctic lakes. *Arct. Antarct. Alp. Res.* 40, 364–372. doi: 10.1657/1523-0430(06-068)

Keck, F., Franc, A., and Kahlert, M. (2018). Disentangling the processes driving the biogeography of freshwater diatoms: a multiscale approach. *J. Biogeogr.* 45, 1582–1592. doi: 10.1111/jbi.13239

Korhola, A., Weckström, J., and Nyman, M. (1999). Predicting the long-term acidification trends in small subarctic lakes using diatoms. *J. Appl. Ecol.* 36, 1021–1034. doi: 10.1046/j.1365-2664.1999.00461.x

Koroleff, F. (1970). Determination of total phosphorus in natural waters by means of persulfate oxidation. International Council for the Exploration of the Sea (ICES). Report No. 3.

Kristiansen, J. (1996). 16. Dispersal of freshwater algae — a review. *Hydrobiologia* 336, 151–157. doi: 10.1007/BF00010829

Laing, T. E., and Smol, J. P. (2000). Factors influencing diatom distributions in circumpolar treeline lakes of northern Russia. *J. Phycol.* 36, 1035–1048. doi: 10.1046/j.1529-8817.2000.99229.x

Law, A. C., Anderson, N. J., and McGowan, S. (2015). Spatial and temporal variability of lake ontogeny in South-Western Greenland. *Quat. Sci. Rev.* 126, 1–16. doi: 10.1016/j.quascirev.2015.08.005

Leboucher, T., Tison-Rosebery, J., Budnick, W. R., Jamoneau, A., Vyverman, W., Soininen, J., et al. (2020). A metacommunity approach for detecting species influenced by mass effect. *J. Appl. Ecol.* 57, 2031–2040. doi: 10.1111/1365-2664.13701

Legendre, P., and Gallagher, E. (2001). Ecologically meaningful transformations for ordination of species data. *Oecologia* 129, 271–280. doi: 10.1007/s004420100716

Lim, D. S. S., Smol, J. P., and Douglas, M. S. V. (2007). Diatom assemblages and their relationships to lakewater nitrogen levels and other limnological variables from 36 lakes and ponds on Banks Island, NWT, Canadian Arctic. *Hydrobiologia* 586, 191–211. doi: 10.1007/s10750-007-0623-8

Liu, S., Xie, G., Wang, L., Cottenie, K., Liu, D., and Wang, B. (2016). Different roles of environmental variables and spatial factors in structuring stream benthic diatom and macroinvertebrate in Yangtze River Delta. *China. Ecol. Indic.* 61, 602–611. doi: 10.1016/j.ecolind.2015.10.011

Lotter, A. F., and Bigler, C. (2000). Do diatoms in the Swiss Alps reflect the length of ice-cover? *Aquat. Sci.* 62, 125–141. doi: 10.1007/s000270050002

McGowan, S., Gunn, H. V., Whiteford, E. J., Anderson, N. J., Jones, V. J., and Law, A. C. (2018). Functional attributes of epilithic diatoms for palaeoenvironmental interpretations in south-West Greenland lakes. *J. Paleolimnol.* 60, 273–298. doi: 10.1007/s10933-017-9968-9

McGowan, S., Ryves, D. B., and Anderson, N. J. (2003). Holocene records of effective precipitation in West Greenland. *The Holocene* 13, 239–249. doi: 10.1191/0959683603hl610rp

Medeiros, A. S., Biastoch, R. G., Luszczek, C. E., Wang, X. A., Muir, D. C., and Quinlan, R. (2012). Patterns in the limnology of lakes and ponds across multiple local and regional environmental gradients in the eastern Canadian Arctic. *Inland Waters* 2, 59–76. doi: 10.5268/IW-2.2.427

Metcalfe, D. B., Hermans, T. D. G., Ahlstrand, J., Becker, M., Berggren, M., Björk, R. G., et al. (2018). Patchy field sampling biases understanding of climate change impacts across the Arctic. *Nat. Ecol. Evol.* 2, 1443–1448. doi: 10.1038/s41559-018-0612-5

Michelutti, N., Douglas, M. S. V., and Smol, J. P. (2003). Diatom response to recent climatic change in a high arctic Lake (char lake, Cornwallis Island, Nunavut). *Glob. Planet. Chang.* 38, 257–271. doi: 10.1016/S0921-8181(02)00260-6

Michelutti, N., Douglas, M. S. V., and Smol, J. P. (2007). Evaluating diatom community composition in the absence of marked limnological gradients in the high Arctic: a surface sediment calibration set from Cornwallis Island (Nunavut, Canada). *Polar Biol.* 30, 1459–1473. doi: 10.1007/s00300-007-0307-x

Milardi, M., Lappalainen, J., McGowan, S., and Weckström, J. (2017). Can fish introductions alter nutrient cycles in previously fishless high-latitude lakes? *J. Limnol.* 76, 1–14. doi: 10.4081/jlimnol.2016.1364

Milardi, M., Siitonen, S., Lappalainen, J., Liljendahl, A., and Weckström, J. (2016). The impact of trout introductions on macro-and micro-invertebrate communities of fishless boreal lakes. *J. Paleolimnol.* 55, 273–287. doi: 10.1007/s10933-016-9879-1

Miller, G. H., Lehman, S. J., Refsnider, K. A., Southon, J. R., and Zhong, Y. (2013). Unprecedented recent summer warmth in Arctic Canada. *Geophys. Res. Lett.* 40, 5745–5751. doi: 10.1002/2013GL057188

Murphy, J., and Riley, J. P. (1962). A modified single solution method for the determination of phosphate in natural waters. *Anal. Chim. Acta* 27, 31–36. doi: 10.1016/S0003-2670(00)88444-5

Normand, S., Randin, C., Ohlemüller, R., Bay, C., Høye, T. T., Kjær, E. D., et al. (2013). A greener Greenland? Climatic potential and long-term constraints on future expansions of trees and shrubs. *Philos. Trans. R. Soc. B* 368:20120479. doi: 10.1098/rstb.2012.0479

Oksanen, J., Simpson, G.L., Blanchet, F.G., Kindt, R., Legendre, P., Minchin, P.R., O'Hara, R.B., Solymos, P., Stevens, M.H.H., and Szoecs, E. (2022). Package 'vegan'.

Ossyssek, S., Geist, J., Werner, P., and Raeder, U. (2020). Identification of the ecological preferences of *Cyclotella comensis* in mountain lakes of the northern European Alps. *Arct. Antarct. Alp. Res.* 52, 512–523. doi: 10.1080/15230430.2020.181393

Overpeck, J. K., Hughen, D., Hardy, R., Bradley, R., Case, R., Douglas, M., et al. (1997). Arctic environmental change of the last four centuries. *Science* 278, 1251–1256. doi: 10.1126/science.278.5341.1251

Perren, B. B., Douglas, M. S. V., and Anderson, N. J. (2009). Diatoms reveal complex spatial and temporal patterns of recent limnological change in West Greenland. *J. Paleolimnol.* 42, 233–247. doi: 10.1007/s10933-008-9273-8

Perren, B. B., Massa, C., Bichet, V., Gauthier, E., Mathieu, O., Petit, C., et al. (2012). A paleoecological perspective on 1450 years of human impacts from a lake in southern Greenland. *The Holocene* 22, 1025–1034. doi: 10.1177/0959683612437865

Pinseel, E., Van de Vijver, B., Kavan, J., Verleyen, E., and Kopalová, K. (2017). Diversity, ecology and community structure of the freshwater littoral diatom flora from Petuniabukta (Spitsbergen). *Polar Biol.* 40, 533–551. doi: 10.1007/s00300-016-1976-0

Pla-Rabes, S., Hamilton, P. B., Ballesteros, E., Gavrilo, M., Friedlander, A. M., and Sala, E. (2016). The structure and diversity of freshwater diatom assemblages from Franz Josef Land archipelago: a northern outpost for freshwater diatoms. *Peerj* 4:e1705. doi: 10.7717/peerj.1705

Post, E., Forchhammer, M. C., Bret-Harte, M. S., Callaghan, T. V., Christensen, T. R., Elberling, B., et al. (2009). Ecological dynamics across the Arctic associated with recent climate change. *Science* 325, 1355–1358. doi: 10.1126/science.1173113

Potapova, M. (2009). Odontidium mesodon. In diatoms of North America. Retrieved January 23, 2023. Available from: https://diatoms.org/species/odontidium_mesodon.

R Development Core Team. (2011). R: A language and environment for statistical computing. R foundation for statistical computing. Vienna, Austria.

Rantanen, M., Karpechko, A. Y., Lipponen, A., Nordling, K., Hyvärinen, O., Ruosteenoja, K., et al. (2022). The Arctic has warmed nearly four times faster than the globe since 1979. *Commun. Earth Environ.* 3:168. doi: 10.1038/s43247-022-00498-3

Rautio, M., Dufresne, F., Laurion, I., Bonilla, S., Vincent, W. F., and Christoffersen, K. F. (2011). Shallow freshwater ecosystems of the circumpolar Arctic. *Écoscience* 18, 204–222. doi: 10.2980/18-3-3463

Renberg, I. (1990). A procedure for preparing large sets of diatom slides from sediment cores. *J. Paleolimnol.* 4, 87–90. doi: 10.1007/BF00208301

Reynolds, C. S., Huszar, V., Kruk, C., Naselli-Flores, L., and Melo, S. (2002). Towards a functional classification of the freshwater phytoplankton. *J. Plankton Res.* 24, 417–428. doi: 10.1093/plankt/24.5.417

Roberts, D.W. (2019). Labdsv: ordination and multivariate analysis for ecology. R package version 2.0-1.

Rosén, P., Hall, R., Korsman, T., and Renberg, I. (2000). Diatom transfer-functions for quantifying past air temperature, pH and total organic carbon concentration from lakes in northern Sweden. *J. Paleolimnol.* 24, 109–123. doi: 10.1023/A:1008128014721

Rühland, K., Paterson, A. M., and Smol, J. P. (2008). Hemispheric-scale patterns of climate-related shifts in planktonic diatoms from north American and European lakes. *Glob. Chang. Biol.* 14, 2740–2754. doi: 10.1111/j.1365-2486.2008.01670.x

Rühland, K. M., Paterson, A. M., and Smol, J. P. (2015). Lake diatom responses to warming: reviewing the evidence. *J. Paleolimnol.* 54, 1–35. doi: 10.1007/s10933-015-9837-3

Rühland, K., Priesnitz, A., and Smol, J. P. (2003). Paleolimnological evidence from diatoms for recent environmental changes in 50 lakes across Canadian Arctic treeline. *Arct. Antarct. Alp. Res.* 35, 10–123. doi: 10.1657/1523-0430(2003)035[0110:PEFDFR]2.0.CO;2

Ryves, D., McGowan, S., and Anderson, N. J. (2002). Development and evaluation of a diatom-conductivity model from lakes in West Greenland. *Freshw. Biol.* 47, 995–1014. doi: 10.1046/j.1365-2427.2002.00832.x

Saros, J. E., and Anderson, N. (2015). The ecology of the planktonic diatom Cyclotella and its implications for global environmental change studies. *Biol. Rev.* 90, 522–541. doi: 10.1111/brv.12120

Schindler, D. W., and Smol, J. P. (2006). Cumulative effects of climate warming and other human activities on freshwaters of Arctic and subarctic North America. *Ambio* 35, 160–168. doi: 10.1579/0044-7447(2006)35[160:ceocwa]2.0.co;2

Simpson, G. L. (2007). Analogue methods in Palaeoecology: using the analogue package. *J. Stat. Softw.* 22, 1–29.

Smith, L. C., Sheng, Y., Macdonald, G. M., and Hinzman, L. D. (2005). Disappearing Arctic lakes. *Science* 308:1429. doi: 10.1126/science.11081

Smol, J. P. (1988). Paleoclimate proxy data from freshwater arctic diatoms. *Verh. Internat. Verein. Limnol.* 23, 837–844. doi: 10.1080/03680770.1987.11899722

Smol, J. P., Birks, H. J. B., and Last, W. M. (2002). *Tracking Environmental Change Using Lake Sediments: Volume 3: Terrestrial, Algal, and Siliceous Indicators*. New York, Boston, Dordrecht, London, Moscow: Kluwer Academic Publishers.

Smol, J. P., Wolfe, A. P., Birks, H. J. B., Douglas, M. S., Jones, V. J., Korhola, A., et al. (2005). Climate-driven regime shifts in the biological communities of arctic lakes. *PNAS* 102, 4397–4402. doi: 10.1073/pnas.0500245102

Smucker, N. J., and Vis, M. L. (2011). Spatial factors contribute to benthic diatom structure in streams across spatial scales: considerations for biomonitoring. *Ecol. Indic.* 11, 1191–1203. doi: 10.1016/j.ecolind.2010.12.022

Soininen, J., and Weckström, J. (2009). Diatom community structure along environmental and spatial gradients in lakes and streams. *Fundam. Appl. Limnol.* 174, 205–213. doi: 10.1127/1863-9135/2009/0174-0205

Solórzano, L., and Sharp, J. H. (1980). Determination of total dissolved phosphorus and particulate phosphorus in natural waters 1. *Limnol.Oceanogr.* 25, 754–758. doi: 10.4319/lo.1980.25.4.0754

Spaulding, S. A., Van de Vijver, B., Hodgson, D. A., McKnight, D. M., Verleyen, E. L. I. E., and Stanish, L. (2010). "Diatoms as indicators of environmental change in Antarctic and subantarctic freshwaters," in *The Diatoms: Applications for the Environmental and Earth Sciences*. eds. J. P. Smol and F. E. Stoermer (Cambridge: Cambridge University Press), 267–283.

Steffen, W., Broadgate, W., Deutsch, L., Gaffney, O., and Ludwig, C. (2015). The trajectory of the Anthropocene: the great acceleration. *Anthropol. Rev.* 2, 81–98. doi: 10.1177/2053019614564785

Sweetman, J. N., Rühland, K. M., and Smol, J. P. (2010). Environmental and spatial factors influencing the distribution of cladocerans in lakes across the Central Canadian Arctic treeline region. *J. Limnol.* 69, 76–87. doi: 10.3274/JL10-69-1-07

Teittinen, A., Weckström, J., and Soininen, J. (2018). Cell size and acid tolerance constrain pond diatom distributions in the subarctic. *Freshw. Biol.* 63, 1569–1578. doi: 10.1111/fwb.13186

Tuck, S. L., Phillips, H. R., Hintzen, R. E., Scharlemann, J. P., Purvis, A., and Hudson, L. N. (2014). MODISTools–downloading and processing MODIS remotely sensed data in R. *Ecol. Evol.* 4, 4658–4668. doi: 10.1002/ece3.1273

Verleyen, E., Vyverman, W., Sterken, M., Hodgson, D. A., De Wever, A., Juggins, S., et al. (2009). The importance of dispersal related and local factors in shaping the taxonomic structure of diatom metacommunities. *Oikos* 118, 1239–1249. doi: 10.1111/j.1600-0706.2009.17575.x

Vincent, W. F. (2000). "Cyanobacterial dominance in the polar regions" in *The Ecology of Cyanobacteria*. eds. B. A. Whitton and M. Potts (Dordrecht: Springer)

Virtanen, L., and Soininen, J. (2012). The roles of environment and space in shaping stream diatom communities. *Eur. J. Phycol.* 47, 160–168. doi: 10.1080/09670262.2012.682610

Weckström, J., Hanhijärvi, S., Forsström, L., Kuusisto, E., and Korhola, A. (2014). Reconstructing lake ice cover in subarctic lakes using a diatom-based inference model. *Geophys. Res. Lett.* 41, 2026–2032. doi: 10.1002/2014GL059474

Weckström, K., and Juggins, S. (2005). Coastal diatom–environment relationships from the Gulf of Finland, Baltic Sea. *J. Phycol.* 42, 21–35. doi: 10.1111/j.1529-8817.2005.00166.x

Weckström, J., and Korhola, A. (2001). Patterns in the distribution, composition and diversity of diatom assemblages in relation to ecoclimatic factors in Arctic Lapland. *J. Biogeogr.* 28, 31–45. doi: 10.1046/j.1365-2699.2001.00537.x

Weckström, J., Korhola, A., and Blom, T. (1997a). The relationship between diatoms and water temperature in thirty subarctic Fennoscandian lakes. *Arct. Alp. Res.* 29, 75–92. doi: 10.2307/1551838

Weckström, J., Korhola, A., and Blom, T. (1997b). Diatoms as quantitative indicators of pH and water temperature in subarctic Fennoscandian lakes. *Hydrobiologia* 347, 171–184. doi: 10.1023/A:1003091923476

Weckström, J., Snyder, J. A., Korhola, A., Laing, T. E., and MacDonald, G. M. (2003). Diatom inferred acidity history of 32 lakes on the Kola peninsula, Russia. *Water Air Soil Poll.* 149, 339–361. doi: 10.1023/A:1025682801187

Wrona, F. J., Johansson, M., Culp, J. M., Jenkins, A., Mård, J., Myers-Smith, I. H., et al. (2016). Transitions in Arctic ecosystems: ecological implications of a changing hydrological regime. *J. Geophys. Res. Biogeosci.* 121, 650–674. doi: 10.1002/2015JG003133

Zgrundo, A., Wojtasik, B., Convey, P., and Majewska, A. (2017). Diatom communities in the high Arctic aquatic habitats of northern Spitsbergen (Svalbard). *Polar Biol.* 40, 873–890. doi: 10.1007/s00300-016-2014-y

frontiers | Frontiers in Ecology and Evolution

TYPE Original Research
PUBLISHED 15 May 2023
DOI 10.3389/fevo.2023.1120460

OPEN ACCESS

EDITED BY
Luo Chuanxiu,
Chinese Academy of Sciences (CAS), China

REVIEWED BY
Veronica Rossi,
University of Bologna, Italy
Thomas Mark Cronin,
United States Department of the Interior,
United States

*CORRESPONDENCE
Michael E. Meadows
✉ michael.meadows@uct.ac.za

†These authors share first authorship

RECEIVED 10 December 2022
ACCEPTED 26 April 2023
PUBLISHED 15 May 2023

CITATION
Kirsten KL, Pretorius L, Meadows ME, Weij R, Aquino-López M, Antonopoulos HG, Dubazana Y, Qadeer A, Finch J and Bao K (2023) The depositional history of the Knysna estuary since European colonization in the context of sea level and human impacts. *Front. Ecol. Evol.* 11:1120460. doi: 10.3389/fevo.2023.1120460

The depositional history of the Knysna estuary since European colonization in the context of sea level and human impacts

Kelly L. Kirsten[1,2†], Lauren Pretorius[3†], Michael E. Meadows[4,5*], Rieneke Weij[1,2], Marco Aquino-López[6], Helen G. Antonopoulos[5], Yakhuluntu Dubazana[5], Abdul Qadeer[7], Jemma Finch[3] and Kunshan Bao[8]

[1]Department of Geological Sciences, University of Cape Town, Rondebosch, South Africa, [2]Human Evolution Research Institute, University of Cape Town, Rondebosch, South Africa, [3]Discipline of Geography, School of Agricultural, Earth and Environmental Sciences, University of KwaZulu-Natal, Pietermaritzburg, South Africa, [4]School of Geography and Ocean Sciences, Nanjing University, Nanjing, China, [5]Department of Environmental and Geographical Science, University of Cape Town, Rondebosch, South Africa, [6]Centro de Investigacion en Matemáticas, Guanajuato, Mexico, [7]National Engineering Laboratory for Lake Pollution Control and Ecological Restoration, State Environmental Protection Key Laboratory of Drinking Water Source Protection, Chinese Research Academy of Environmental Sciences, Beijing, China, [8]School of Geography, South China Normal University, Guangzhou, China

Introduction: Estuaries are highly vulnerable systems and increasingly exposed to a number of environmental, climatic and human-induced stressors. The Knysna estuary and lagoon complex, on the south coast of South Africa, is regarded as environmentally and economically important, yet faces regional impacts resulting from ongoing urbanisation and land use change as well as the significant global threats of rising sea levels and changing climate. Although the estuary has been reasonably well studied in terms of modern ecological processes, little is known of how the system has responded to changes in the longer term, not least the impact of European colonization and subsequent population growth and economic development.

Methods: In order to address this shortcoming, a series of shallow (<1 m) cores was extracted from a range of representative habitats and marine influences in the estuary and three of these (namely KNY-19A, KNY-19B, KNY-19G) selected for detailed analysis, including organic matter content, magnetic susceptibility, selected elemental analysis and particle size.

Results and Discussion: Notwithstanding the challenges of dating estuarine sediments due to the possibility of erosion and resuspension, combined modelling of 210Pb and 14C ages is successfully deployed to develop an age-depth relationship for each core, providing a chronological framework for late Holocene environmental changes. Sedimentary characteristics of the three cores, taken in contrasting estuarine conditions, yield insights as to how different parts of the estuary responded to changes in sea level and anthropogenic activities in and around the Knysna basin, as well as in the wider catchment.

KEYWORDS

^{210}pb, ^{14}C, grain size, magnetic susceptibility, loss-on-ignition, estuarine sediments, human impact, sedimentation rate

1. Introduction

Estuaries are dynamic, turbulent and extremely productive systems that provide a multitude of ecosystem services, including nutrient regulation, storm protection, food provision, recreation and education (Warwick et al., 2018). The estuarine zone is spatially and temporally variable in response to, *inter alia*, changes in mixing regimes and a range of other environmental processes (Hayton, 1991). As such, estuaries are susceptible to an assortment of perturbations related to hydroclimate, tidal regime and human activities (Warwick et al., 2018). Sediments, and the processes by which they accumulate or erode, represent key elements of the estuarine system, and offer important opportunities to explore the longer-term system behavior in response to environmental, climate, sea-level and anthropogenic changes (Newton et al., 2020). Indeed, the relationship between people and environment in coastal wetlands globally has deteriorated rapidly (Kirwan and Megonigal, 2013) and there is a clear need for their protection.

Sediments in these dynamic systems are subject to a high degree of reworking that makes obtaining a chronology of the sediment profile extremely challenging and, thereby, hindering potentially valuable environmental reconstructions (Andersen, 2017). The Knysna Estuary, a microtidal system on the south coast of South Africa [Figure 1; tidal range 0.4–2.0 m (Largier et al., 2000)], is widely regarded for its scientific and socioeconomic importance owing to, among other attributes, its exceptional biodiversity (Marker, 2003). Although the Knysna Estuary is a functioning estuary from an ecological perspective, it is already significantly threatened by anthropogenic activities, including urban expansion, tourism development and land use change (Marker and Miller, 1993; CES, 2007). Instances of high nutrient influx, sourced from surface runoff and catchment inflow which raises inorganic nitrogen and phosphorus concentrations, are noted across the system but particularly in the Ashmead Channel (Human et al., 2020). The rise in nutrients has led to algal blooms, notably in the lower reaches, that are indicative of eutrophication (Human et al., 2016). Seagrass patches are continuously disturbed in the search for bait by subsistence and recreational fishers (Claassens et al., 2020; Barnes, 2021).

With contemporary dynamics mind, several representative localities in the estuary were selected with a view to resolve system response to long-term environmental dynamics, both natural and anthropogenic, in the geologically recent past. Therefore, the aim of this study is to investigate the depositional history of the Knysna estuary based on its recent sedimentary history and to interpret the observed changes in the context of environmental and anthropogenic factors. The aim is achieved through the following objectives: (a) to obtain a series of shallow (<1 m) sediment cores from a selected range of habitats and geomorphic settings in the estuary; (b) to obtain age estimates using radiometric methods based on ^{14}C, ^{210}Pb, and ^{137}Cs and, through the application of appropriate chronological modelling, develop age models for the selected cores and determine the robustness of each model; (c) to analyze, on three cores selected representing contrasting estuarine habitats, a range of physico-chemical characteristics, including organic matter content, magnetic susceptibility, particle size and selected elements; (d) to provisionally interpret the physico-chemical parameters and chronology in the context of reconstructed environmental changes of the late Holocene/Anthropocene in the Knysna estuary. The study highlights the problems and prospects for dating and interpretation of sedimentary sequences from estuarine environments.

2. Materials and methods

2.1. Physiographic setting

The Knysna estuarine system is a biologically diverse, permanently open estuarine bay on the south coast of South Africa (Reddering and Esterhuysen, 1987; Claassens et al., 2020). The catchment is approximately 400 km^2, arising in the Cape Fold Mountain range, draining through primarily quartzitic sandstones of the Table Mountain Group (Grindley, 1985; Reddering and Esterhuysen, 1987).

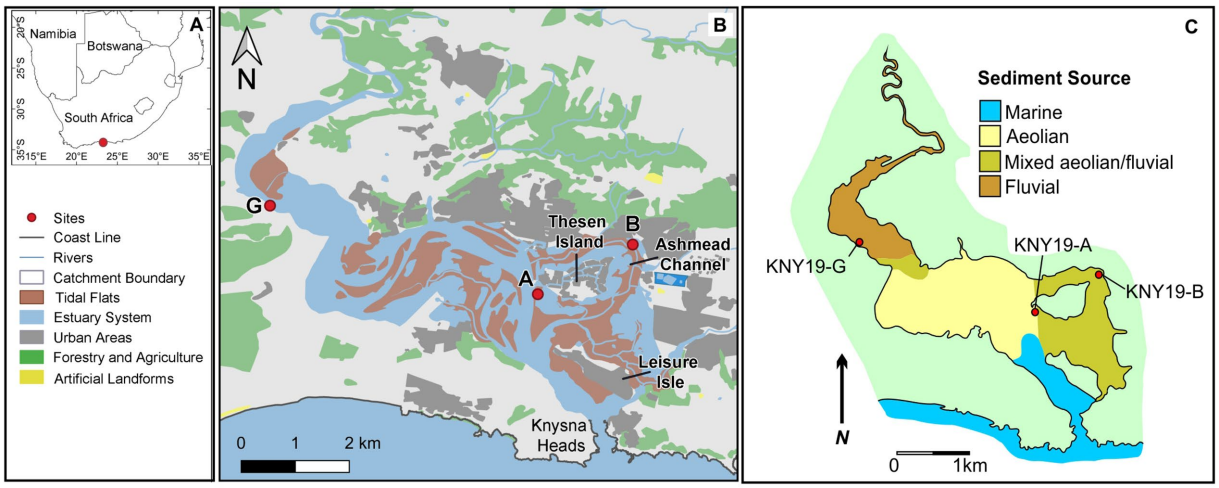

FIGURE 1
(A) The south coast of South Africa, **(B)** The Knysna Estuary and surrounding land-use practices, also indicated are the three core sites in the middle and upper reaches of the system, located along **(C)** Sediment sources of the Knysna Estuary after Reddering and Esterhuysen (1987).

The Outeniqua Mountains, which form the northernmost boundary, are characterized by steep, rugged terrain to a maximum elevation of ±1,500 m (Helgren and Butzer, 1977; Marker, 2003; Figure 1A). The valley is deeply incised into resistant Cape Supergroup rocks, before transitioning into the coastal platform of 200–240 m altitude (Marker and Miller, 1993; Marker, 2003). To the south of the estuary, a substantial coastal dune complex is an important source of sediment, although it has been stabilised by vegetation (Reddering and Esterhuysen, 1987).

Sediments in the system are therefore of aeolian, marine and fluvial origin. Cover sands in the middle catchment area are very easily mobilised, especially when disturbed by human activities, such as construction and quarrying activities (Grindley, 1985; Marker, 2000). Sediment loads are elevated during rainfall events causing higher levels of silt and sand to enter the basin (Marker, 2000; Human et al., 2020). Sediments of a marine origin typically do not extend much beyond the distal reaches of the estuary (Cooper, 2001). However, the estuary acts as a sediment trap as a slow ebb tide hinders terrestrial sediment loss (Grindley, 1985; Marker, 2000) and they also build-up at the rock-bound headlands as the tidal inlet is constrained by the absence of accommodation space (Cooper, 2001). The catchment geology is a relatively minor contributor to the sediment load due to the fact that the sandstones are highly resistant to weathering, producing quartz sand and quartzite pebbles, and only the Cederberg Formation is fine-grained (Reddering and Esterhuysen, 1987). The primary rivers draining the catchment are the Knysna and Gouna Rivers and their tributaries (Marker and Miller, 1993; Marker, 2000). The freshwater springs and the sediment-laden Salt River are additional sources (Russell, 1996). Water flows through an S-shaped channel of shallow depth ranging between 2 and 5 m below mean low water, which is flanked by extensive sandy intertidal and supratidal flats (Reddering and Esterhuysen, 1987; Largier et al., 2000). The Knysna River waters are clear, low in both nutrients and sediment load (Grindley, 1985; Allanson et al., 2000). The estuarine part of the system is characterized by three hydrographical regimes, *viz.* the lower bay regime, the middle lagoon regime and the upper estuary regime, with the boundaries being transitional in terms of fluvial and marine water inputs (Largier et al., 2000). A shallow, tidal branch of the estuary, the Ashmead Channel, surrounds Thesen Island (Human et al., 2016; Claassens et al., 2020; Figure 1B). Tidal influence can reach 19 km upstream and results in consistent flushing of the system (Reddering and Esterhuysen, 1987; Petermann et al., 2018). The local tidal gauge record is limited to the past 43 years (Rautenbach et al., 2019).

2.2. Coring locations

Initially, eight shallow (<1 m) cores were obtained using aluminum pipes forced manually into the surface, which resulted in good sediment recovery, from sites representing different estuarine regimes and habitats. Three of these cores (KNY19-A, KNY19-B, and KNY19-G) were selected for more detailed analysis of sediments at sites representing distinct environmental settings, namely direct exposure to marine influences, tidal flats and wetlands, respectively. The remaining five cores retrieved from the system were either duplicates to the cores presented here or sediment retrieval depth was minor. The lower bay regime would have been a desirable coring location, however marine inflow and sediment re-circulation makes the area highly disturbed. The cores were transported to the Department of Environmental and Geographical Sciences, University of Cape Town (UCT), split lengthwise and documented according to established standard protocols. Lithology was described using the Troels-Smith sediment classification scheme (Troels-Smith, 1955), and a Munsell Soil Color chart was used to describe colouration. Sub-samples at 1 cm intervals were taken for subsequent analysis.

KNY19-A (34.05 S; 23.05 E) was recovered from the tidal flats west of Thesen Island, in the vicinity of the main channel. The sediment core penetrated to a depth of 100 cm, while the retrieved sediment measured 44 cm, with a compaction factor of 55%. KNY19-B (34.04 S; 23.07 E) was recovered from the outer bend of the lower section of the Ashmead Channel on mudflats. The sediment core penetrated to a depth of 60 cm while the retrieved sediment measured 57 cm, thus experiencing a compaction factor of <5%. The site of core KNY19-G (34.03 S; 22.99 E) lies at the distal end of the estuary, where the river widens considerably, and was extracted from an area vegetated with *Phragmites australis*. The sediment core penetrated to a depth of 48 cm, while the retrieved sediment measured 37 cm, indicating a compaction factor of approximately 20%.

2.3. Measurement of physicochemical parameters

Dry bulk density (g/cm^3) of the samples was determined by weighing a volumetric subsample of each 1 cm interval of the sediment cores prior and post overnight freeze drying. Loss on ignition (LOI), as an estimate of total organic matter content (OM; %), was measured by weighing dry subsamples before and after ashing at 550°C for 6 h. Mass magnetic susceptibility was quantified from the homogenised, dried samples using a Bartington Instruments MS2 sensor. The particle size spectra were determined using a Malvern automated laser-optical particle-size analyzer (Mastersizer-2000; Malvern Instruments Ltd., Worcestershire, United Kingdom) after the removal of organic matter by 10% hydrogen peroxide (H_2O_2) and of carbonate by 10% hydrochloric acid (HCl). This instrument has a measurement range of 0.02 to 2,000 µm and an error of <3% with repeated measurement (Bao et al., 2017).

The Calcium (Ca) and Strontium (Sr) bulk concentrations were evaluated to determine marine influences on the system. The elements we measured using a Spectro Xepos XRF spectrophotometer at the Department of Biological Sciences, at UCT, and were expressed as a percentage of composition when they are in their oxidised condition. To achieve homogeneity, the samples were pulverised using a mortar and pestle. The powder was collected through a < 200 µm sieve mesh. A standard 32 mm XRF sample cup was used to hold around 4–5 g of the sample. As per standard practices, Ca is stated in percentage, while Sr concentrations were reported in mg kg-1, which is equivalent to parts per million (ppm).

2.4. Chronology

2.4.1. Radiocarbon

A total of six radiocarbon samples, near the base and mid-core, were submitted for AMS radiocarbon analysis (Beta Analytic Inc.,

Miami) (Supplementary Table S1). Plant macrofossil samples were dated where available, but the majority of samples were based on bulk sediments. For calibration purposes, the Marine20 calibration curve was employed for the five bulk samples (Heaton et al., 2020), withthe SHCal20 calibration curve employed for the one plant macrofossil sample (Hogg et al., 2020). The regional marine reservoir correction for the south coast of South Africa was applied to the bulk radiocarbon samples, namely $\Delta R = 187 \pm 18$ ^{14}C yr (Maboya et al., 2018). In an estuarine setting, there remains uncertainty regarding carbon source pathways contributing to bulk sediment samples, hence we applied the marine reservoir correction to account for marine offsets. Where plant and bulk sample ages were available from the same depth, the plant samples were considered more reliable in constructing the age model (see Supplementary Table S1).

2.4.2. ^{210}Pb and ^{137}Cs

Weighed, dry samples (approximate 5 g) were sealed in plastic test tubes and sent to the State Key Laboratory of Lake Science and Environment, Nanjing Institute of Geography and Limnology, Chinese Academy of Sciences, for ^{210}Pb and ^{137}Cs dating. Total ^{210}Pb, ^{226}Ra, and ^{137}Cs radioactivities were measured using a low-background ɣ-ray spectrometer with a high pure Ge semiconductor (ORTEC Instruments Ltd., United States). Total ^{210}Pb was determined at 46.5 keV, and ^{226}Ra was determined at 295 keV and 352 keV by its daughter nuclide ^{214}Pb after 3 weeks storage in sealed containers to allow radioactive equilibrium, ^{137}Cs was determined at 662 keV. The standard sources and sediment samples of known activity were provided by the China Institute of Atomic Energy and used to calibrate the absolute efficiencies of the detectors. Counting times of ^{210}Pb and ^{137}Cs typically ranged from 50,000 to 86,000 s, and measurement precision was between ±5 and ± 10% at the 95% confidence level. The unsupported ^{210}Pb activity was determined from the difference between the total ^{210}Pb and supported ^{210}Pb activity which was assumed to be in equilibrium with *in situ* ^{226}Ra.

2.4.3. Plum-Py modelling

^{210}Pb, in combination with the radiocarbon ages were calibrated using the Bayesian age-depth modelling of cores dated by ^{210}Pb and ^{14}C in the Python package Plum v.0.8.5 (Aquino-López et al., 2018). Plum is a Bayesian forward model that simultaneously integrates two different processes: (1) the behavior of the $^{210}Pb_{flux}$ and the variation of $^{210}Pb_{sup}$ with depth and (2) an age-depth function which incorporates a Bayesian piece-wise linear model constrained by prior information on accumulation rate and variability (Aquino-López et al., 2020). This is in contrast to the Constant Rate of Supply (CRS) model, which is based on $^{210}Pb_{ex}$ flux being constant. Plum can model the ^{210}Pb and ^{14}C simultaneously, avoiding multiple calibration and modelling of data. Therefore, radiocarbon ages can be incorporated during the analysis to guide the model output. Sediment accumulation rates (SAR) were also determined for all three cores at a 1 cm resolution.

2.5. Quantitative analyses

Grain size measurement outputs from the laser diffractometer were analyzed using the G2Sd package (Fournier et al., 2014) in the R Software environment. Grain size statistics were calculated using the logarithmic (Folk and Ward, 1957) Method (phi scale) with outputs of mean, standard-deviation, skewness, and kurtosis. A combined dataset was collated using the grain size statistic outputs, LOI, dry bulk density, and magnetic susceptibility of cores A, B, and G. The final stratigraphic plots were produced using the tidypaleo, ggplot2 and patchwork packages in the R software environment.

3. Results

3.1. Chronology

3.1.1. Pb-210 activities

Activities for the three Knysna cores range from 37.13 to 168.4 Bq/kg for $^{210}Pb_{tot}$, from 22.62 to 64.10 Bq/kg for ^{226}Ra (equivalent to the supported ^{210}Pb) and from 1.72 to 122.7 Bq/kg for $^{210}Pb_{xs}$ (unsupported ^{210}Pb) (Figure 2). ^{226}Ra is assumed to be in equilibrium with the supported ^{210}Pb portion inherited from the sediments themselves. The unsupported ^{210}Pb, or $^{210}Pb_{xs}$, is derived from subtracting the supported ^{210}Pb portion from $^{210}Pb_{tot}$. $^{210}Pb_{xs}$ forms the basis for the ^{210}Pb age-depth models. $^{210}Pb_{tot}$ and $^{210}Pb_{xs}$ should generally decrease exponentially with depth (Andersen et al., 2000; Barsanti et al., 2020) due to the natural decay of ^{210}Pb. KNY19-A and B display a decreasing trend in $^{210}Pb_{tot}$, but not obviously exponential. The $^{210}Pb_{tot}$ in KNY19-G, on the other hand, does decrease exponentially downcore. In none of the cores does $^{210}Pb_{tot}$ decrease monotonically (Figure 2). In KNY19-A and B, the decrease in $^{210}Pb_{tot}$ results from both ^{226}Ra and $^{210}Pb_{xs}$ decreasing downcore. In KNY19-G, $^{210}Pb_{xs}$ decreases exponentially with depth, while ^{226}Ra remains relatively constant. The $^{210}Pb_{tot}$ in the Knysna estuary sediments results from the rainout of ^{210}Pb in the atmosphere, *in situ* ingrowth of ^{210}Pb by the decay of ^{222}Rn, and possibly from marine sediment supply due to the tidal hydrodynamics. The ^{137}Cs activities were zero along the depth profiles of all three cores.

3.1.2. Age-depth models

Age-depth models (ADM) for the Knysna Estuary system show deposition occurred from the Holocene, as early as 4,050 cal yr BP to present, based on ^{210}Pb and radiocarbon ages. Because ^{137}Cs was not detectable in this area, the ^{210}Pb age-depth models were supported by radiocarbon dates. The radiocarbon ages from bulk samples in Supplementary Table S1, with the exception of the plant sample at the base of KNY19-G, were corrected for the marine reservoir effect, which is greater in the case of the more recent sediments.

Core KNY19-A sediments accumulated from 4,050 cal yr BP to present. Three corrected radiocarbon ages (Supplementary Table S1) are in good agreement with the ^{210}Pb age-depth model (Figure 3). A hiatus occurs at 31 cm depth, identified by an erosional surface, and introduces uncertainty in the age-depth model. Core KNY19-B sediments accumulated from ~700 to 0 cal yr BP. The single radiocarbon age at the base of the core (Supplementary Table S1) is consistent with the ^{210}Pb age-depth model (Figure 3). The upper portion, however, cannot be validated fully due to the lack of a radiocarbon age. The age-depth model for Core KNY19-G suggests these sediments were deposited from ~125 cal yr BP. Two bulk sample radiocarbon ages, at 36 cm and 16 cm are supplemented by a separate

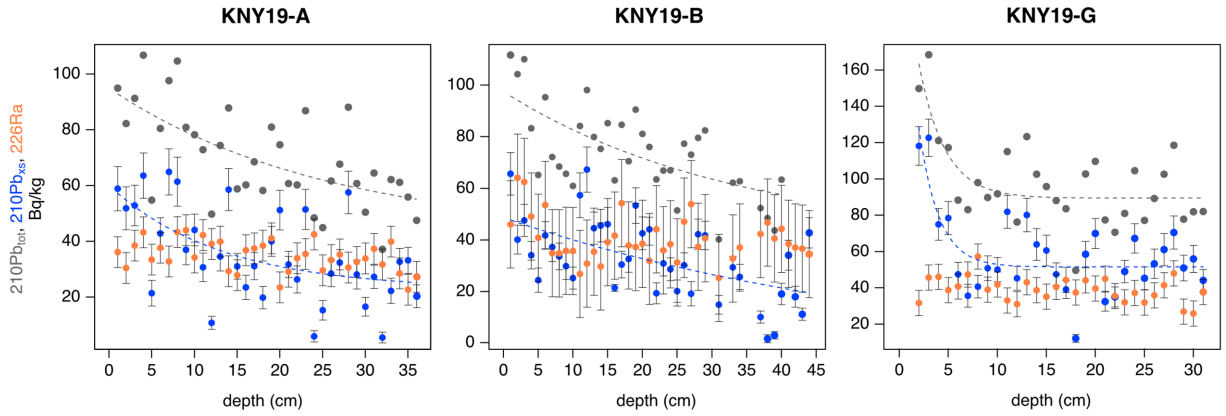

FIGURE 2
Activities of $^{210}Pb_{tot}$ (gray), $^{210}Pb_{xs}$ (blue), and ^{226}Ra (orange) for cores KNY19-A, KNY19-B, and KNY19-G. Stippled lines are exponential fits of $^{210}Pb_{tot}$ and $^{210}Pb_{xs}$. Note independent scaling of *x* and *y* axes.

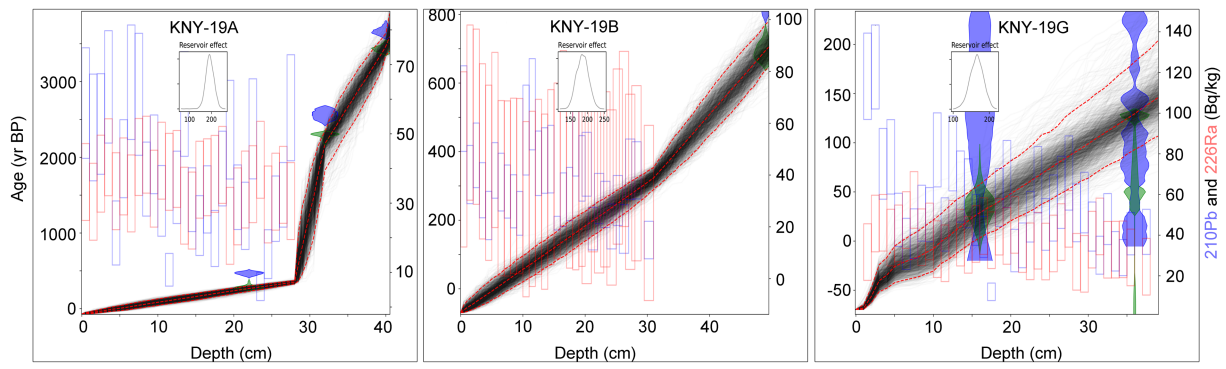

FIGURE 3
Age-depth models for cores KNY19-A, KNY19-B, and KNY19-G as produced by Plum, showing the ^{210}Pb (blue rectangles), ^{226}Ra (red rectangles), calibrated radiocarbon ages (blue distribution), and marine reservoir corrected, calibrated ages (green distribution) against depth (cm). KNY19-A experiences a loss and reworking of sediments defined by unit A2 and represented by the orange rectangle.

plant sample at the base (36 cm). The basal bulk sample radiocarbon age was excluded in favor of the plant sample; the two radiocarbon ages incorporated into the model are in good agreement with the ^{210}Pb age-depth model (Figure 3).

3.2. Sedimentology

3.2.1. Core KNY19-A

Core KNY19-A can be subdivided into four lithological units based on changes in sedimentary characteristics and spans 4,050 years. Given the likely presence of a hiatus or condensed section, the chronology of this record should be treated with caution. Two anomalies occur and are evident in all sedimentological parameters at 14–11 cm (150–100 cal yr BP) and 30–27 cm (1275–340 cal yr BP) depth, although the effect on magnetic susceptibility is most pronounced. Core KNY19-A exhibits a relatively uniform grain size distribution (GSD) with sand being the dominant grain size (Figure 4). Bulk density generally remains stable throughout the sedimentary sequence, with the exception of a decline between 30 and 27 cm. A sharp increase in the sediment accumulation rate (SAR) occurs at 27 cm (~340 cal yr BP) from 0.002 to 0.075 cm/yr, which represents sedimentation accelerated markedly above this depth (Figure 4). The increase in SAR is associated with an increase in the sand size fraction and corresponding reduction in silt and clay content.

3.2.1.1. Unit A1 (44–31cm; 4,050–1750calyr BP)

Unit A1 is characterized by low levels of organic matter ranging from 1 to 6%, with a mean of 3%. Sediments are classified as medium sand (2 Phi), strongly fine skewed and very poorly sorted. This unit has a weak overall magnetic susceptibility signal. The core lithology shows the presence of intact marine molluscan shells, primarily *Dosinia hepatica* (Lamarck, 1818) and *Loripes clausus* (Philippi, 1849), lying horizontally in a sandy matrix.

3.2.1.2. Unit A2 (30–27cm; 1,275–340calyr BP)

The transition between Unit A1 and A2, is marked by an abrupt increase in magnetic susceptibility, peaking at 380 × 10^{-8} m^3/kg. Similarly, LOI peaks, reaching a maximum of 5% at 26 cm within this unit. Dry bulk density decreases from 1.4 to 1.3 g/cm^3. The observed core lithology for this unit shows sandy material with an increasing frequency of marine shell fragments.

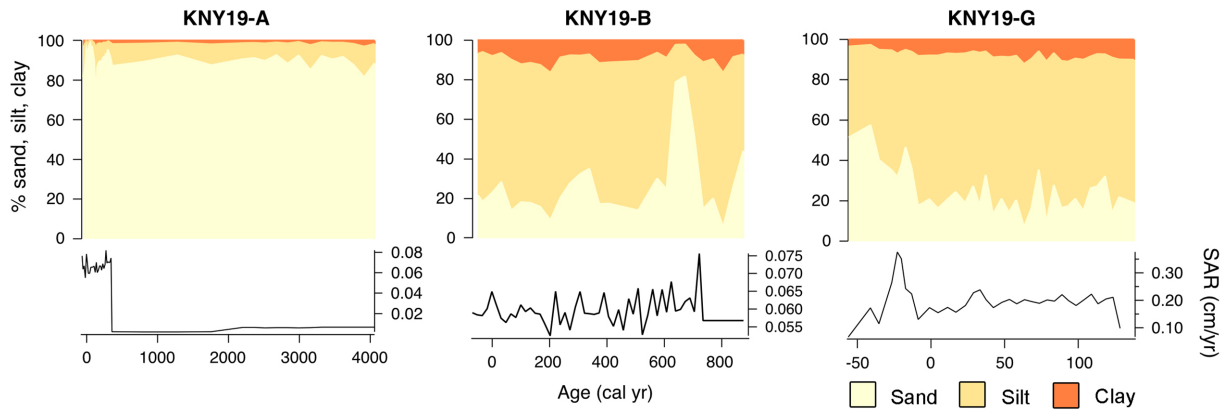

FIGURE 4
Grain size distribution (%) and sediment accumulation rate (cm/yr) versus age (calyr BP) for KNY19-A, KNY19-B, and KNY19-G.

3.2.1.3. Unit A3 (26–12cm; 320–115calyr BP)

Unit A3 is characterized by poorly to very poorly sorted medium sand with a low but stable magnetic susceptibility signal. LOI remains relatively low, fluctuating around 6%. The lithology is predominantly medium sand with little shell debris and the occasional presence of more organic rich material.

3.2.1.4. Unit A4 (11–0cm; 100calyr BP to present)

The base of Unit A4 is marked by a distinct peak in magnetic susceptibility (83 $\times 10^{-8}$ m^3/kg), as well as a shift to very well sorted, near-symmetrical grain size distribution. LOI (~4%) and mean grain size (medium sand) are consistent, except for the top 2 cm (about −40 cal yr BP) where grain size decreases and LOI increases.

3.2.2. Core KNY19-B

The core features two distinct changes in sediment characteristics, thereby forming three distinct sedimentary units referred to here as B1, B2 and B3 at intervals 57–40 cm, 39–19 cm and 18–0 cm, respectively. The core spans the last 900 years. Sediments are of variable grain size distribution but are dominated by silt. Bulk density remains relatively stable throughout the sedimentary sequence. The SAR is relatively constant (~0.058 cm/yr), except for a peak at 47 cm (~720 cal yr BP) of ~0.076 cm/yr This peak in SAR coincides with a peak in the sand-sized fraction at the expense of silt and clay. The SARs for this core are similar to the youngest section (<310 cal yr BP) of core KNY19-A (Figure 4).

3.2.2.1. Unit B1 (57–40cm; 900–610calyr BP)

LOI fluctuates between 4 and 11%, averaging 6%. Mean grain size fluctuates between medium and fine silt (5–6 φ) from 48 to 44 cm (~735–675 cal yr BP) where a coarsening upwards to fine sand (2–3 φ) towards the top of the unit. In parallel, grain size distribution transitions from finely skewed to strongly finely skewed. The magnetic susceptibility signal remains low but also gradually increases upwards. Lithology is relatively homogeneous throughout the unit.

3.2.2.2. Unit B2 (39–19cm; 590–250calyr BP)

The base of Unit B2 is marked by a peak in magnetic susceptibility and an abrupt decrease in LOI at 39–37 cm (590–560 cal yr BP), whereafter the sediments are high in organic content, fluctuating between ~7 and 24%, and averaging 13.4%, although gradually decreasing towards the top of the unit. Mean grain size coarsens upwards from fine silt (6 φ) to medium silt (5 φ), remaining finely skewed throughout. Sediments are consistently poorly sorted, even more so towards the boundary with the overlying unit. Magnetic susceptibility is low, and rather constant, above 37 cm (from 250 cal yr BP onwards). Overall, the unit is homogeneous, with no clear sedimentary structures or evidence of bioturbation present.

3.2.2.3. Unit B3 (18–0cm; 235calyr BP to present)

LOI decreases from 9% at the base of unit B3, to 2% in the upper 2 cm (from ~ −35 cal yr BP). Mean grain size coarsens upward from very fine silt (7 φ) to medium silt (5 φ), decreasing to fine silt at the surface (2–0 cm; from ~ −35 cal yr BP to present). Skewness shifts from being almost symmetrical at the base to strongly finely skewed at the top. Sorting is poor throughout, becoming very poorly sorted near the surface, while lithology is again basically homogeneous.

3.2.3. Core KNY19-G

Core KNY19-G covers the last 210 years and has a consistently low magnetic susceptibility signal throughout, ranging from 5.1–13.5 $\times 10^{-8}$ m^3/kg with a mean of 7.5 $\times 10^{-8}$ m^3/kg. The core is subdivided into three units, units, G1 – G3 at 36–19 cm, 18–6 cm and 5–0 cm, respectively. The sediments are in general dominated by silt, and relatively constant until 5 cm (−25 cal yr BP). Similarly, the SAR is constant (~0.19 cm/yr) but increases towards the top. This increase coincides with an increase in sand at the expense of silt. The SAR in KNY19-G is an order of magnitude higher than in KNY19-B and the top of KNY19-A (Figure 4).

3.2.3.1. Unit G1 (36–19cm; 140–40calyr BP)

Unit G1 is characterized by low LOI content, ranging from 6.2 to 14.5%, averaging 9%. LOI gradually increases upwards, while mean grain size fluctuates between medium and fine silt (5–6 φ) for poorly- to very poorly sorted sediments. The grain size distribution is near-symmetrical at the base, trending toward a finely skewed distribution

towards the top of the unit. Bulk density is higher on average here than in the other units, fluctuating around an average of 1.1 g/cm^3.

3.2.3.2. Unit G2 (18–6cm; 37 to −23calyr BP)

LOI fluctuates between 12 and 14%, but falls to 8.4% at 9 cm, whereafter it increases to 16% at the top of the unit. Bulk density exhibits an inverse relationship with LOI, peaking at 1.13 g/cm^3 at 8 cm depth. Mean grain size lies within the medium silt size class (5–6 φ) to 9 cm (~ −13 cal yr BP), at which point it increases to coarse silt (4–5 φ) at 7 cm (~ −20 cal yr BP). Sediment sorting varies between poorly to very poorly sorted. Grain size distribution is finely skewed throughout but increases from 8 cm upwards.

3.2.3.3. Unit G3 (5–0cm; −27calyr BP to present)

LOI achieves maximum values in Unit G3, increasing from 22% at the base to 27% at the core surface. Mean grain size coarsens upwards from medium silt to coarse silt (5–4 φ) and on the whole the sediments are very poorly sorted. Grain size is less finely skewed towards the top of the core where it is near-symmetrically distributed. Bulk density increases to 0.91 g/cm^3 at 3 cm (~ −40 cal yr BP), before decreasing to 0.86 g/cm^3 at the surface.

3.3. Sr and Ca characteristics

Sr and Ca are strongly correlated with each other in all cores (KNY19-A = 0.97, KNY19-B = 0.78, KNY19-G = 0.86). Ca and Sr concentrations are initially high with values over 10% and 300 ppm, respectively, in KNY19-A, before sharply declining at 39 cm (Figure 5). Moderate concentrations are maintained until 27 cm. Upcore of 27 cm, concentrations are low although higher than at the other two sites. Concentrations at site KNY19-B remain relatively low, fluctuating between 0.25 and 0.09% for Ca and 32.5 and 14.6 ppm for Sr At KNY19-G, concentrations appear to be steadily increasing from the base of the core until ~8 cm, after which a sharp rise in both elements are recorded to the surface.

4. Discussion

4.1. Site location and age model reliability

Carbon-14 samples were taken from the bottom of the core to provide a basal limit for the depositional period. Basal ages of the three cores appear to be highly dependent on local site conditions. Deposition at Core KNY19-A covers the last 4,000 years; however, it is evident here that sediment reworking has occurred with a possible condensed section. Such situations are to be expected in coastal systems where the combined effects of fluvial discharge and tidal forcing are dynamic in nature. The initial phase, between 4,050 and 1750 cal yr BP, exhibits a slow sedimentation rate before an apparent hiatus/condensed section in the sedimentary sequence occurs. This is likely due to the location of the site proximal to the mouth and the entering marine waters leading to erosion or redistribution of sediments in response to changing sea levels and tidal regimes. Two additional samples were taken above and below the fragmented shell layer to constrain the discontinuity in deposition. Continuous sedimentation is initiated again from 340 cal yr BP, and at a much higher rate of accumulation. The position of core KNY19-B is more protected from wave action and deposition and appears to be continuous from 900 cal yr BP to present, although surface sediments do appear to have been bioturbated. Core KNY19-G spans only the last 200 years and has by far the highest sediment accumulation rate. The basal sample from KNY19-G is the sole sample with sufficient plant material for analysis. This age is seen as more reliable than the bulk sample at this site. Since the core site lies further up the estuary, it is reasonable to suppose that sediment dynamics may be more strongly influenced by fluvial processes (Reddering and Esterhuysen, 1987) and the declines in transport energy of the river as it reaches the estuarine basin.

The reliability of ^{210}Pb activity, and thus the quality of the age-depth models, depends on several factors (Sanchez-Cabeza and Ruiz-Fernández, 2012), including the conceptual model used, validation with an independent chronometer, mobility of Pb within the sediment, grain size variation and the extent of sediment reworking by biological (bioturbation) and physical (waves and currents) processes. The degree of compaction, particularly in KNY19-A, may provide some uncertainty to the age model by disturbing the ^{210}Pb profile as well as affecting calculated SAR (Barsanti et al., 2020). The inclusion of radiocarbon samples within the modelling approach supports the age-depth model and validates the ^{210}Pb data, thus contributing to the reliability of the age model and given reasonable margins of error, broadly supports our interpretation of the ^{210}Pb ages (Figure 3). In addition, the modelling approach employed in this study, the recently developed Plum package for R and Python (Aquino-López et al., 2020), is more flexible using a forward modelling approach that is able to handle potentially disturbed ^{210}Pb profiles. The Knysna Estuary system is dominated by marine water influx due to the large tidal prism. KNY19-A and KNY19-B are located in the lower reaches of the system and experience a mix water regime, whereas KNY19-G is closer to the fluvial inflow, leading to brackish water conditions depending on the state of tide and discharge from the Knysna River. Thus, there is some potential of lead mobility within a saline system, but this is limited to generally <0.02% (Zhao et al., 2013) and therefore, lead mobility can be considered negligible in this instance. Grain size variation may be an influencing factor on the reliability of the models, however there is no clear correlation between $^{210}Pb_{xs}$ and the clay content of each core, suggesting that the influence of preferential absorption of lead onto fine particles is not a crucial factor in the Knysna system.

Considering the dynamic and highly productive nature of estuarine systems, reworking and bioturbation that disturb the sedimentary column are highly likely. Much of the estuary is generally protected from strong marine wave action, but currents are present due to river flow and tidal influences, which may indeed rework or resuspend sediments over time. Cores KNY19-B and KNY19-G were retrieved from relatively low energy environments, while KNY19-A is adjacent to the main channel, which may have altered its course at various stages in the past. Nevertheless, analysis of each core reveals generally homogeneous sedimentary structures, with little evidence of disturbance. An exception to this is unit A2 in core KNY19-A, where it is related to the marine shells found in this unit but does not seem to have influenced the sedimentation very much (3 cm perhaps). Samples for dating, including those subsampled for ^{210}Pb analysis, were not taken from potentially disturbed sediments. Furthermore, the radiocarbon age for unit A2 indicates that these sediments are

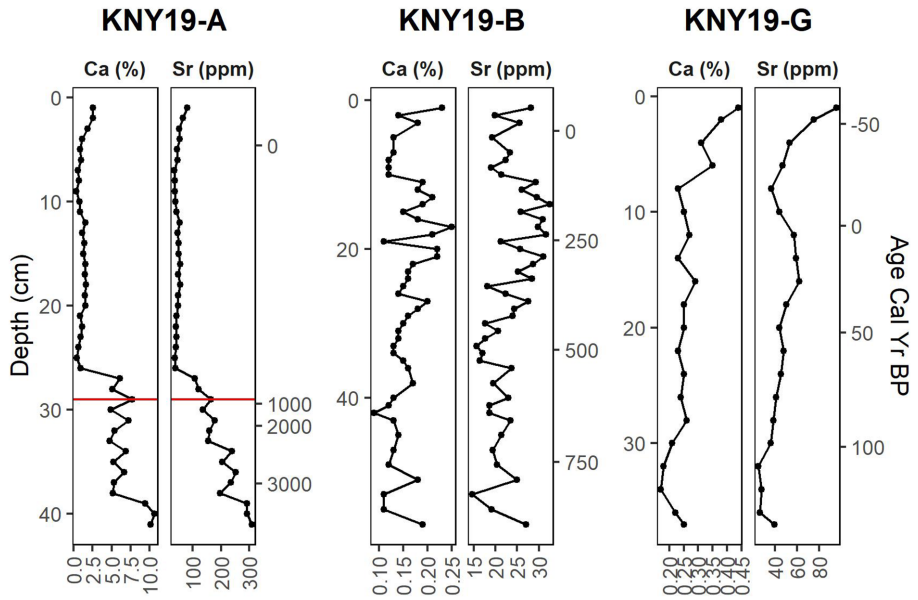

FIGURE 5
Variations in Ca (%) and Sr (ppm) concentrations at each core location against Depth (cm) and age (calyr BP).

younger than the equilibrium depth of $^{210}Pb_{xs}$. This unit therefore does not affect the ^{210}Pb component of the age-depth model.

4.2. Depositional history and associated palaeoenvironments

4.2.1. Post mid-Holocene sea level highstand

Core KNY19-A, located on the western shore of Thesen Island, is the most proximal of the three sites and is exposed to stronger marine influences in being most proximal to the inlet of the estuary with little shielding from geomorphological features (Figure 1). The basal unit spans the interval 4,050–1750 cal yr BP (Figures 5, 6), and is characterized by medium sand, prevalent whole marine bivalve shells and gastropods, suggesting a shallow marine environment (Figure 7A), and supported by elevated Sr and Ca concentrations (Figure 6). The concentration of Ca and Sr are globally and regionally recognised as marine indicators (Peterson et al., 2000; Wündsch et al., 2016, 2018). The decline in marine influences is in temporal agreement with lakes along the coast of South Africa, e.g. Eilandvlei (Kirsten et al., 2018; Wündsch et al., 2018), Verlorenvlei (Kirsten et al., 2020), Lake St Lucia (Benallack et al., 2016; Gomes et al., 2017). When placed in the context of the sea-level history for the southern African coastline, this unit corresponds to a highstand of up to 2 m above present mean sea level (Cooper et al., 2018). Marker and Miller (1993) traced shell deposits of what they concluded to be a product of the mid-Holocene highstand and determined that during that interval, the shoreline of the lagoon would have extended 400 m inland from the present day. Miller et al. (1995) constrained the mid-Holocene highstand to be approximately 2.4–2.8 m above present mean sea level between 6,000–4,000 cal yr BP, this would imply higher wave energy during the mid-Holocene highstand followed by a rapid regression.

Surface deposits (Units A3 and A4) at KNY19-A are separated from the basal unit (Unit A1) by an undulating, erosional/reworked shell lag package (Unit A2) which has a lower bulk density than Unit A1 (Figures 7B,C). This unit consists of similar bioclastic material as recorded in Unit A1; however, it has undergone fragmentation likely due to reworking or transportation under changing marine energy conditions associated with relative sea-level change. When considered relative to the underlying unit (A1) and the association with higher than present sea level, followed by a period of regression and transgression, this interval most likely represents a period of shoreface retreat (Bruun, 1962; Swift, 1968). When the base of a shoreface translates landward in response to transgression, it truncates pre-existing deposits due to wave and tidal processes producing a ravinement surface draped with lag deposits (Cattaneo and Steel, 2003). Given the proximity of KNY19-A to the mouth of the estuary, the overlying high-energy reworked deposits (Unit A2) are followed by tidally influenced sediment (Units A3 and A4), this depositional unit likely represents a tidal ravinement surface produced as an effect of steady sea level rise between 500 cal yr BP to present (Figure 7D). Cores KNY19-A and KNY19-B capture different portions of sea-level history with KNY19-B recording a larger duration record of the latest transgression due to availability of accommodation space created by underlying antecedent topography. KNY19-A captures older records due to its proximal position within the basin however less of the overlying equivalent tidal sediment due less accommodation space created by the underlying topography (Figure 7).

4.2.2. Environmental conditions during the late Holocene

The falling sea level following the Holocene highstand would have exposed subaerially many parts of the estuary previously submerged, particularly in the intertidal zone, possibly resulting in reworking by aeolian processes before an increase in source waters could sustain

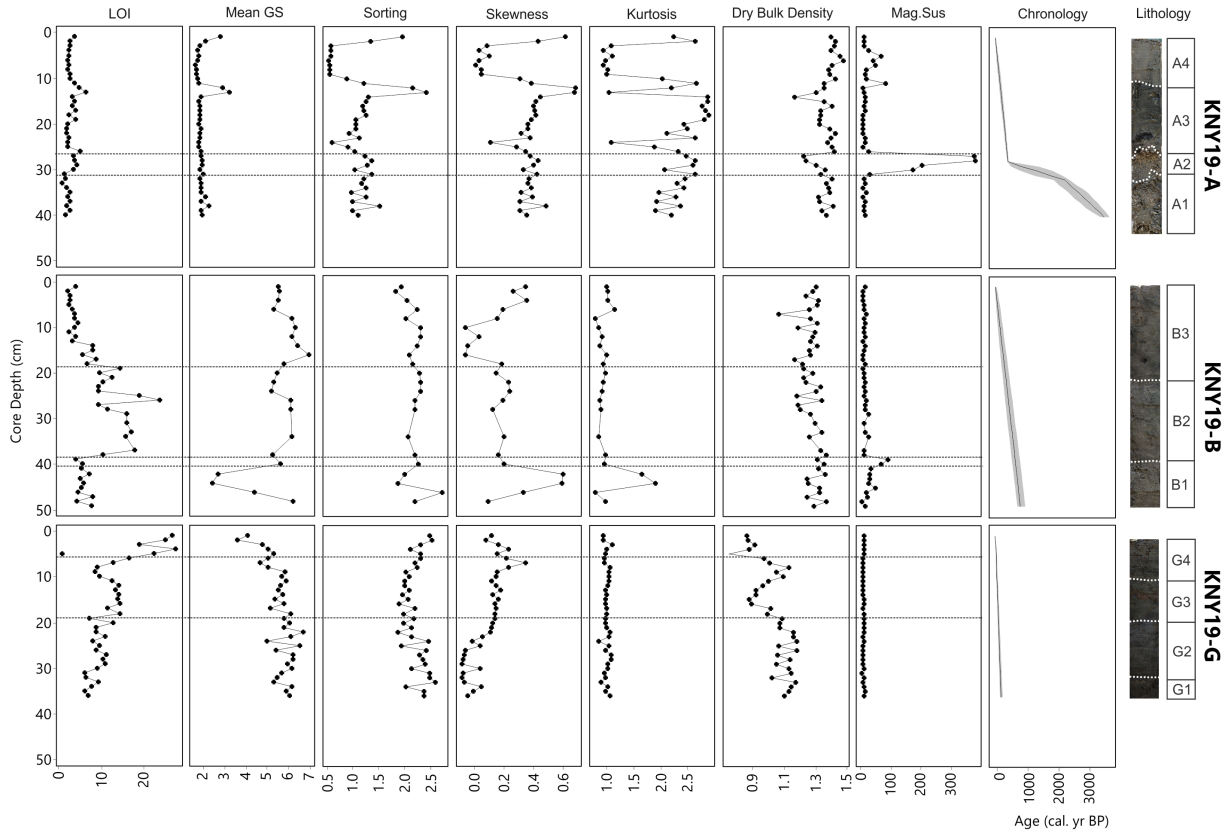

FIGURE 6
Sediment profile for KNY19-A, KNY19-B and KNY19-G against depth indicating sedimentary horizons and associated sediment characteristics, from left to right, loss-on-ignition (%), the mean, sorting, and skewness of grain size, kurtosis, the bulk density (g/cm^3), magnetic susceptibility (83×10^{-8} m^3/kg). Dotted horizontal lines indicate changes in sedimentary character.

open water conditions. A period of lower sea level, up to 2 m below modern mean sea level (Miller et al., 1995) occurred between 900 and 500 cal yr BP and would have had a substantial impact on the Knysna estuary system. Thesen Island would have been somewhat larger at the time and the greater expanse of subaerially exposed sediments may have been subject to erosion and reworking. An increase in coarser grained sediment in the Ashmead Channel (Core KNY19-B) is also noted during this interval and is also likely related to reworking of relict marine sands from the mid-Holocene highstand. From 900 to 600 cal yr BP, the channel transitions from very platykurtic to less platykurtic indicating a brief evolution from less mobile sand sheet deposits to more mobile dune deposits (Marker and Holmes, 2002; Holmes et al., 2007).

The geology of the catchment comprises primarily quarzitic sandstones with a high silicate composition of the Table Mountain Group (Grindley, 1985). These lithologies are therefore diamagnetic in nature (Tite, 1972) implying that variations in magnetic susceptibility, especially along the shore of Thesen Island (KNY19-A), are unexpected. Sediment sources in the system are either fluvial, aeolian or marine in origin (Figure 1C), therefore either one or a combination of the latter must supply the magnetisable material. The Enon formation, which is composed of thickly bedded conglomerates, sandstone lenses and mudstone units within a sandy clay matrix, surrounds the southern perimeter of the Knysna Estuary (Muir et al., 2017). There are also outcrops of shale in the upper catchment that may also have trace deposits of magnetisable materials, implying that the catchment is indeed a potential source. Negligible sediments of marine origin are delivered into the estuary, and only in the very lower reaches of the estuary, although wave energy is not completely dissipated due to the lack of barrier development at the mouth (Cooper, 2001) so that marine inputs cannot be excluded. The southern Cape coast is highly susceptible to large swells along its wave-dominated coastline, and, under storm conditions, marine inputs of sediment may increase. Neighbouring systems to the west and east drain through Gneissic granite and bentonite deposits, which could be a source of trace deposits of magnetisable material into Knysna should wave propagation transport the material into the estuary during more turbulent seas. The supply of aeolian deposits is generally from the coastal dunes but these have the least potential for magnetisable materials. Highest magnetic susceptibility values occur closer to the mouth (KNY19-A and KNY19-B) decreasing in magnitude towards the upper reaches.

Analysis of surface samples reveals that sites near Leisure Isle and the Heads (Figure 1) have higher concentrations of cadmium, copper, nickel, cobalt and chromium, attributed to a localised source of heavy metals (Watling and Watling, 1982), which is primarily governed by anthropogenic impacts on the system. However, the elevated magnetic susceptibility signal between 700 and 590 cal yr BP (unit B1) occurs at a time that pre-dates any probable major human influences in the area, suggesting a natural phenomenon may be the underlying mechanism

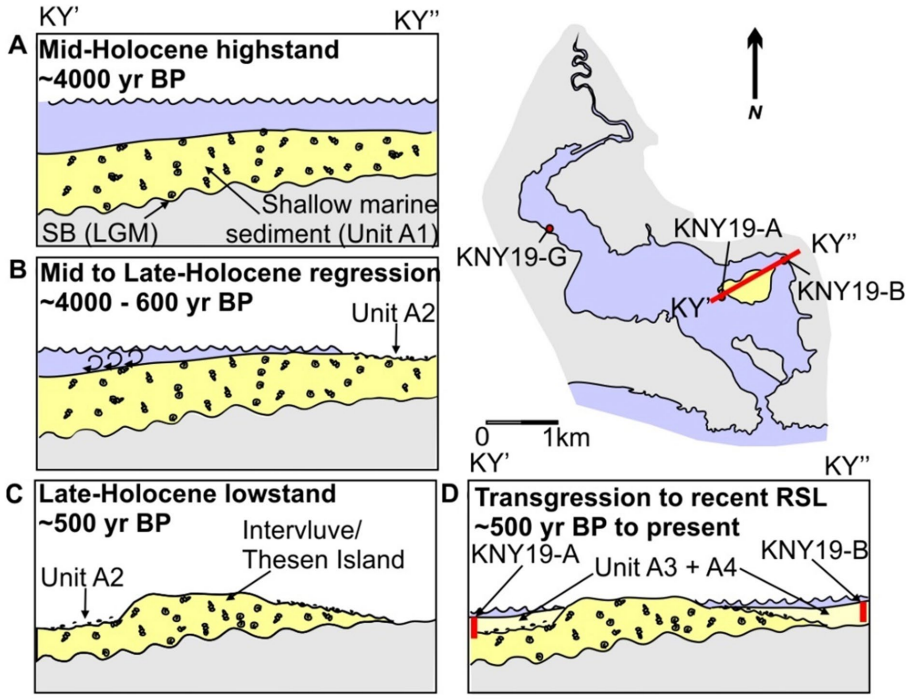

FIGURE 7
Conceptual figure describing the depositional history of the Knysna estuary from the late Holocene to present. Cross-sectional profile KY'-KY" is depicted in insets **(A–D)** showing different stages of sea-level history and associated sediment depositional and erosional processes. **(A)** Shallow marine sediment (Unit A1) is deposited on top of the Last-Glacial Maximum (LGM) Pleistocene deposits (grey) under higher than present sea level conditions. **(B)** Sea level falls in the mid to late Holocene. Interaction with receding wave base results in minor reworking of underlying unit A1, producing a shell lag (unit A2) composed of unit A1 material. **(C)** As regression continues to a lowstand, a drop in base level causes incision/channelisation of Unit A1, forming a relative topographical high (presently known as Thesen Island) and further stripping of sediment. **(D)** Transgression from ~500 yr. BP resulted in further reworking of Unit A2 by tidal ravinement processes, and subsequent deposition of estuarine sediment (Units A3 and A4).

for this trend. Thus, a potential combination of augmented inputs both from the wider catchment, possibly from greater runoff under higher precipitation, and from a marine source during a period of more turbulent oceanic conditions may underlie this observation. The influx of turbulent source waters would have made for an unstable environment and limit submerged and emergent vegetation growth (Adams, 2016), an interpretation consistent with the rather low OM%. Palaeoflooding evidence is recorded all along the southern Cape coast between 650 and 300 cal yr BP. Sediments deposited on the continental shelf near the Gouritz River, 110 km to the west, reveal torrential rains and flash flooding in the catchment after 650 cal yr BP under more humid climatic conditions (Hahn et al., 2016). Additionally, high energy floods and higher lake levels occurred in the Wilderness and Groenvlei catchments, 35 km, and 11 km to the west, respectively, between 700 and 500 cal yr BP (Reinwarth et al., 2013; Wündsch et al., 2018).

The period between 660 and 250 cal yr BP appears to have been relatively stable across the lower reaches of the system (KYN19-A and KNY19-B), as the higher LOI values suggests a phase of vegetation colonization and expansion, particularly in the area of Ashmead Channel (KNY19-B). The presence of organic matter suggests that this environment may have been partially vegetated. The structure of the middle and lower reaches of the estuary and the vegetation it hosts are governed by the large tidal prism (Maree, 2000). Currently, Knysna has one of the most extensive *Zostera* beds of all estuaries in South Africa and the community is widespread in the Ashmead Channel. *Zostera* is unable to withstand turbulent water (Adams, 2016). Expansion of salt marsh vegetation, which is especially productive (Maree, 2000), on the landward limits of the intertidal zones would be expected under stable environmental conditions. The characteristics of the sediments accumulating at this time are consistent with a period of relative equilibrium where water levels in the estuary are either stable or rising but at a rate that does not exceed sedimentation. The environmental conditions in this phase contrast markedly with prior conditions when sediments were clearly intertidal. The lower reaches of the estuary around Thesen Island (KNY19-A and KNY19-B) show a notable reduction in LOI and productivity accompanied by a sharp increase in the sediment accumulation rate (SAR) at ~340 cal yr BP, along with a rise in sand. The decline in organic matter and changes in sediment characteristics, namely fluctuations in bulk density, magnetic susceptibility and a coarsening of mean grain size at KNY19-B, may indicate a transition from marsh back to tidal flat deposits following a rise in water levels. Between 320 and 150 cal yr BP, sediments in the Ashmead Channel (KNY19-B) exhibit a rapid decrease in grain size, which suggests a shift to a period of lower overall environmental energy. Regional records from Wilderness and the Gouritz River, suggest relatively humid conditions and rising lake levels at this time (Hahn et al., 2016; Wündsch et al., 2016, 2018; Kirsten et al., 2018; Quick et al., 2018).

4.2.3. Human influences on system functionality

During the last 200 years or so, there are notable trends in sediment characteristics, particularly around Thesen Island and the Ashmead channel. A marked decline in organic matter accumulation is recorded to levels not previously evident at those sites. There is evidence also of increases in magnetisable material, as coarser grained sediments in the Ashmead Channel occur at approximately the same time as the expansion of human activity in the region (Russell, 1996). The early European settlers engaged, *inter alia* in felling forests in the catchment, along with constructing a harbour, causeways, roads and bridges. Mining operations, which included alluvium, lignite and gold, began in the late 1800s and continued until 1950 (Grindley, 1985). Gold mining began in the upper reaches of the catchment in the 1860s before collapsing in 1894, such activities greatly impact water quality and can lead to a greater concentration of metals contaminants (Abdul-Wahab and Marikar, 2011). Both Leisure Isle and Thesen Island have been considerably modified over the last 250 years through reclamation and stabilisation (Reddering and Esterhuysen, 1987). The land-use changes associated with the expansion of the urban areas under a growing population and deforestation in the greater Knysna Basin would increase the area of impermeable surfaces and enhance surface runoff, while the construction itself would lead to accelerated erosion (Reddering and Esterhuysen, 1987; Marker, 2000). Fire-induced erosion has contributed to the transference of finer sediments into the Knysna estuary channel through aeolian processes. The Knysna Basin has inherited a high degree of landscape sensitivity as a consequence of its geomorphological history and anthropogenic pressures (Marker, 2003). All of these processes potentially increase the rate of erosion, remobilisation of sediments and lead to a higher sediment load in the rivers. The resulting higher inputs of magnetisable material from the industries established in the estuary since the late 1880s. In fact, Thesen Island hosted a sawmill and boat building factory in the 1920s before being converted into a residential marina estate in 2005, while Leisure Isle was converted to a residential development in the 1930s (Reddering and Esterhuysen, 1987; Claassens et al., 2020; Human et al., 2020).

Sediment accumulation rates in the lower reaches of the estuary remain relatively consistent over time. However, at core site KNY19-G, which represents only the last 125 years or so of the record, SAR is an order of magnitude higher than elsewhere in the system. The position of this site and its greater exposure to fluvial processes reflects changes in the river catchment more broadly. Notably, the exponential increase in organic matter indicates an expansion of the wetlands in the upper reaches of the estuary. Wetland encroachment is controlled by factors associated with vegetation productivity, sediment supply and subsurface processes (Reed, 1990). Accordingly, the observed changes in sediment supply and discharge arising through the construction of the Charlesford Weir upstream of the Knysna River may have played a vital role in the establishment of wetland at this locality (Chmura and Hunt, 2004; Switzer, 2008). In addition, the increased use of urea-based fertilizer in the catchment may contribute to the increased organic content of downstream sediments (Switzer, 2008). The coarsening of mean grain size at KNY19-G implies either an increase in energy, or anthropogenic disturbance. Residential developments on the flanking Brenton dune along the western shores and in the upper catchment, increased erosion of significant natural sediment sources to the system leading to greater deposition of sandy silt in the estuary (Reddering and Esterhuysen, 1987; Marker, 2000). All things considered, human activities since the arrival of colonial settlers in the 1700s to present have greatly modified the system.

5. Conclusion

Multi-proxy evidence from three sediment cores reveals that the microtidal environment of the Knysna Estuary has been heavily influenced by marine transgressions and regressions, but also suggests changes in character that may be linked to human activities in the geologically recent past. Although sediment accumulation rates have not changed dramatically since the European colonization of the region in the late 1700s, rapid changes in organic matter content are recorded. The study demonstrates the feasibility and value of combined age-depth modelling of ^{210}Pb and ^{14}C, that underpins the comparison of environmental conditions across the estuary basin and provides greater chronological control when attributing possible causes for the changes observed. Sites selected for the three sediment cores provide a window into past environmental conditions in a range of geomorphological settings. Core KNY19-A, for example, yields insights into past sea level changes and its impacts on the system, although such high energy environments are more prone to erosion and consequently the sedimentary sequence is less continuous. KNY19-B was sampled from the mudflats of the Ashmead channel, a low energy environment additionally protected by the sandy-silt deposition zone of Thesen Island, and the sediments here offer a glimpse into changing conditions in the estuary and the impact of storm events over time. The low energy environment of the wetland of the upper estuary (KNY19-G) yield a record of catchment dynamics, including increased anthropogenic impacts. The upper reaches are likely to experience higher sedimentation rates, as fluvial inputs enter the system and settle, offering an opportunity for future high-resolution sedimentological and physicochemical studies to further unravel the evolution of this vulnerable and valuable estuarine system.

Data availability statement

The raw data supporting the conclusions of this article will be made available by the authors, without undue reservation.

Author contributions

KK: conceptualisation, methodology, investigation, writing, project administration, drafting and revising, analysis, and interpretation of data. MM: conceptualisation, methodology, investigation, writing, project administration, drafting and revising, and fund acquisition. LP: conceptualisation, methodology, investigation, writing, drafting and revising, analysis, and interpretation of data. RW and MA-L: methodology, investigation, writing, drafting and revising, analysis, and interpretation of data. HA and YD: investigation, writing, drafting, and revising. AQ: writing, drafting, and revising. JF: drafting and revising, writing, and interpretation of data. KB: methodology, investigation, writing, project administration, drafting and revising, funds acquisition,

analysis, and interpretation of data. All authors contributed to the article and approved the submitted version.

Funding

This study was funded by the National Natural Science Foundation of China (41761144062, 41730646, 41725002, and 41771506) and by the National Research Foundation of South Africa (Grant no: 110776) under SANParks Permit Number: MEAD-ME/2018–007. KK acknowledges the DSI-NRF Centre of Excellence in Palaeosciences (Grant Ref#: COE2021NGP-KD), the NRF CPRR (Grant Ref#: 120806), the UCT #AdvancingWomxn funding for HERI and the UCT VC2030 Leadership grant scheme. LP acknowledges the support from the NRF (Grant ID: 129531). RW was funded by the Oppenheimer Memorial Trust and VC2030 Scholar Postdoctoral Fellowship awards.

Acknowledgments

Field assistance of S. Hess, M. Armitage and numerous students is gratefully acknowledged.

Conflict of interest

The authors declare that the research was conducted in the absence of any commercial or financial relationships that could be construed as a potential conflict of interest.

Publisher's note

Supplementary material

The Supplementary material for this article can be found online at: https://www.frontiersin.org/articles/10.3389/fevo.2023.1120460/full#supplementary-material

References

Abdul-Wahab, S., and Marikar, F. (2011). The environmental impact of gold mines: pollution by heavy metals. *Open Eng.* 2, 304–313. doi: 10.2478/s13531-011-0052-3

Adams, J. B. (2016). Distribution and status of Zostera capensis in South African estuaries — a review. *S. Afr. J. Bot.* 107, 63–73. doi: 10.1016/j.sajb.2016.07.007

Allanson, B. R., Maree, B., and Grange, N. (2000). An introduction to the chemistry of the water column of the Knysna estuary with particular reference to nutrients and suspended solids. *Trans. R. Soc. South Africa* 55, 141–162. doi: 10.1080/00359190009520440

Andersen, T. J. (2017). "Some practical considerations regarding the application of 210Pb and 137Cs dating to estuarine sediments" in *Applications of Paleoenvironmental techniques in estuarine studies*. eds. K. Weckström, K. M. Saunders, P. A. Gell and C. G. Skilbeck (Dordrecht, The Netherlands: Springer Nature), 121–140.

Andersen, T. J., Mikkelsen, O. A., Moller, A. L., and Pejrup, M. (2000). Deposition and mixing depths on some European intertidal mudflats based on 210Pb and 137Cs activities. *Cont. Shelf Res.* 20, 1569–1591. doi: 10.1016/S0278-4343(00)00038-8

Aquino-López, M. A., Blaauw, M., Christen, J. A., and Sanderson, N. K. (2018). Bayesian analysis of 210 Pb dating. *J. Agric. Biol. Environ. Stat.* 23, 317–333. doi: 10.1007/s13253-018-0328-7

Aquino-López, M. A., Ruiz-Fernández, A. C., Blaauw, M., and Sanchez-Cabeza, J. A. (2020). Comparing classical and Bayesian 210Pb dating models in human-impacted aquatic environments. *Quat. Geochronol.* 60:101106. doi: 10.1016/j.quageo.2020.101106

Bao, K., Shen, J., and Sapkota, A. (2017). High-resolution enrichment of trace metals in a west coastal wetland of the southern Yellow Sea over the last 150 years. *J. Geochem. Explor.* 176, 136–145. doi: 10.1016/j.gexplo.2015.09.010

Barnes, R. S. K. (2021). Patterns of seagrass macrobenthic biodiversity in the warm-temperate Knysna estuarine bay, Western cape: a review. *Aquat. Ecol.* 55, 327–345. doi: 10.1007/s10452-021-09848-3

Barsanti, M., Garcia-Tenorio, R., Schirone, A., Rozmaric, M., Ruiz-Fernández, A. C., Sanchez-Cabeza, J. A., et al. (2020). Challenges and limitations of the 210Pb sediment dating method: results from an IAEA modelling interlaboratory comparison exercise. *Quat. Geochronol.* 59:101093. doi: 10.1016/j.quageo.2020.101093

Benallack, K., Green, A. N., Humphries, M. S., Cooper, J. A. G., Dladla, N. N., and Finch, J. M. (2016). The stratigraphic evolution of a large back-barrier lagoon system with a non-migrating barrier. *Mar. Geol.* 379, 64–77. doi: 10.1016/j.margeo.2016.05.001

Bruun, P. (1962). Sea level rise as a cause of shore erosion. *J. Waterways Harb. Division* 88, 117–130. doi: 10.1061/JWHEAU.0000252

Cattaneo, A., and Steel, R. J. (2003). Transgressive deposits: a review of their variability. *Earth Sci. Rev.* 62, 187–228. doi: 10.1016/S0012-8252(02)00134-4

CES (2007). *Knysna estuary management plan – Volume I: situation assessment*. Grahamstown: CES.

Chmura, G. L., and Hunt, G. A. (2004). Controls on salt marsh accretion: a test in salt marshes of eastern Canada. *Estuaries* 27, 70–81. doi: 10.1007/BF02803561

Claassens, L., Barnes, R. S. K., Wasserman, J., Lamberth, S. J., Miranda, N. A. F., van Niekerk, L., et al. (2020). Knysna estuary health: ecological status, threats and options for the future. *Afr. J. Aquat. Sci.* 45, 65–82. doi: 10.2989/16085914.2019.1672518

Cooper, J. (2001). Geomorphology of tide-dominated and river-dominated, barred, microtidal estuaries: a contrast. *J. Coast. Res.* 34, 428–436. doi: 10.2307/25736309

Cooper, J. A. G., Green, A. N., and Compton, J. S. (2018). Sea-level change in southern Africa since the last glacial maximum. *Quat. Sci. Rev.* 201, 303–318. doi: 10.1016/j.quascirev.2018.10.013

Folk, R. L., and Ward, W. C. (1957). Brazos River bar [Texas]; a study in the significance of grain size parameters. *J. Sediment. Res.* 27, 3–26. doi: 10.1306/74D70646-2B21-11D7-8648000102C1865D

Fournier, J., Gallon, R. K., and Paris, R. (2014). G2Sd: a new R package for the statistical analysis of unconsolidated sediments. *Geomorphol. Relief Process. Environ.* 20, 73–78. doi: 10.4000/geomorphologie.10513

Gomes, M., Humphries, M. S., Kirsten, K. L., Green, A. N., Finch, J. M., and de Lecea, A. M. (2017). Diatom-inferred hydrological changes and Holocene geomorphic transitioning of Africa's largest estuarine system, Lake St Lucia. *Estuar. Coast. Shelf Sci.* 192, 170–180. doi: 10.1016/j.ecss.2017.03.030

Grindley, J. R. (1985). "Estuaries of the cape: Knysna (CMS 13)" in *CSIR research*. eds. H. J. Heydorn and J. R. G. Stellenbosch (Pretoria: Council for Scientific and Industrial Research)

Hahn, A., Schefuß, E., Andó, S., Cawthra, H. C., Frenzel, P., Kugel, M., et al. (2016). Linking catchment hydrology and ocean circulation in late Holocene southernmost Africa. *Clim. Past Discuss.* 13, 649–665. doi: 10.5194/cp-2016-100

Hayton, R. D. (1991). Reflections on the estuarine zone. *Nat. Resour. J.* 31, 123–138.

Heaton, T. J., Köhler, P., Butzin, M., Bard, E., Reimer, R. W., Austin, W. E. N., et al. (2020). Marine20 - the marine radiocarbon age calibration curve (0-55,000 cal BP). *Radiocarbon* 62, 779–820. doi: 10.1017/RDC.2020.68

Helgren, D. M., and Butzer, K. W. (1977). Paleosols of the southern Cape Coast, South Africa: implications for laterite definition, genesis, and age. *Geogr. Rev.* 67, 430–445. doi: 10.2307/213626

Hogg, A. G., Heaton, T. J., Hua, Q., Palmer, J. G., Turney, C. S. M., Southon, J., et al. (2020). SHCal20 southern hemisphere calibration, 0-55,000 years cal BP. *Radiocarbon* 62, 759–778. doi: 10.1017/RDC.2020.59

Holmes, P., Marker, M., Bateman, M., and Carr, A. (2007). The place of aeolian coversands in the geomorphic evolution of the southern Cape coast, South Africa. *S. Afr. J. Geol.* 110, 125–136. doi: 10.2113/gssajg.110.1.125

Human, L. R. D., Adams, J. B., and Allanson, B. R. (2016). Insights into the cause of an *Ulva lactuca* Linnaeus bloom in the Knysna estuary. *S. Afr. J. Bot.* 107, 55–62. doi: 10.1016/j.sajb.2016.05.016

Human, L. R. D., Weitz, R., Allanson, B. R., and Adams, J. B. (2020). Nutrient fluxes from sediments pose management challenges for the Knysna estuary, South Africa. *Afr. J. Aquat. Sci.* 45, 1–9. doi: 10.2989/16085914.2019.1671787

Kirsten, K. L., Haberzettl, T., Wündsch, M., Frenzel, P., Meschner, S., Smit, A. J. J., et al. (2018). A multiproxy study of the ocean-atmospheric forcing and the impact of sea-level changes on the southern cape coast, South Africa during the Holocene. *Palaeogeogr. Palaeoclimatol. Palaeoecol.* 496, 282–291. doi: 10.1016/j.palaeo.2018.01.045

Kirsten, K. L., Kasper, T., Cawthra, H. C., Strobel, P., Quick, L. J., Meadows, M. E., et al. (2020). Holocene variability in climate and oceanic conditions in the winter rainfall zone of South Africa—inferred from a high resolution diatom record from Verlorenvlei. *J. Quat. Sci.* 35, 572–581. doi: 10.1002/jqs.3200

Kirwan, M. L., and Megonigal, J. P. (2013). Tidal wetland stability in the face of human impacts and sea-level rise. *Nature* 504, 53–60. doi: 10.1038/nature12856

Largier, J. L., Attwood, C., and Harcourt-Baldwin, J. L. (2000). The hydrographic character of the Knysna estuary. *Trans. R. Soc. South Africa* 55, 107–122. doi: 10.1080/00359190009520437

Maboya, M. L., Meadows, M. E., Reimer, P. J., Backeberg, B. C., and Haberzettl, T. (2018). Late Holocene marine radiocarbon reservoir correction for the south and east coast of South Africa. *Radiocarbon* 60, 571–582. doi: 10.1017/RDC.2017.139

Maree, B. (2000). Structure and status of the intertidal wetlands of the Knysna estuary. *Trans. R. Soc. South Africa* 55, 163–176. doi: 10.1080/00359190009520441

Marker, M. E. (2000). A descriptive account of sand movement in the Knysna estuary. *Trans. R. Soc. South Africa* 55, 129–139. doi: 10.1080/00359190009520439

Marker, M. E. (2003). The Knysna Basin, South Africa: geomorphology, landscape sensitivity and sustainability. *Geogr. J.* 169, 32–42. doi: 10.1111/1475-4959.04971

Marker, M. E., and Holmes, P. J. (2002). The distribution and environmental implications of coversand deposits in the southern cape, South Africa. *S. Afr. J. Geol.* 105, 135–146. doi: 10.2113/105.2.135

Marker, M. E., and Miller, D. E. (1993). A Mid-Holocene high stand of the sea at Knysna. *S. Afr. J. Sci.* 89, 100–101.

Miller, D. E., Yates, R. J., Jerardino, A., and Parkington, J. E. (1995). Late Holocene coastal change in the southern cape. *South Africa. Quat. Int.* 29–30, 3–10. doi: 10.1016/1040-6182(95)00002-Z

Muir, R. A., Bordy, F. M., Reddennng, J. S. V., and Viljocn, J. H. A. (2017). Lithostratigraphy of the enon formation (Uitenhage group) South Africa. *S. Afr. J. Geol.* 120, 273–280. doi: 10.25131/gssajg.120.2.273

Newton, A., Icely, J., Cristina, S., Perillo, G. M. E., Turner, R. E., Ashan, D., et al. (2020). Anthropogenic, direct pressures on coastal wetlands. *Front. Ecol. Evol.* 8:e00144. doi: 10.3389/fevo.2020.00144

Petermann, E., Knöller, K., Rocha, C., Scholten, J., Stollberg, R., Weiß, H., et al. (2018). Coupling end-member mixing analysis and isotope mass balancing (222-Rn) for differentiation of fresh and recirculated submarine groundwater discharge into Knysna estuary, South Africa. *J. Geophys. Res. Oceans* 123, 952–970. doi: 10.1002/2017JC013008

Peterson, L. C., Haug, G. H., Hughen, K. A., and Röhl, U. (2000). Rapid changes in the hydrologic cycle of the tropical Atlantic during the last glacial. *Science* 290, 1947–1951. doi: 10.1126/science.290.5498.1947

Quick, L. J., Chase, B. M., Wündsch, M., Kirsten, K. L., Chevalier, M., Mäusbacher, R., et al. (2018). A high-resolution record of Holocene climate and vegetation dynamics from the southern cape coast of South Africa: pollen and microcharcoal evidence from Eilandvlei. *J. Quat. Sci.* 33, 487–500. doi: 10.1002/jqs.3028

Rautenbach, C., Barnes, M. A., and de Vos, M. (2019). Tidal characteristics of South Africa. Deep Sea res 1 Oceanogr res pap 150. doi: 10.1016/j.dsr.2019.103079,

Reddering, J. S. V., and Esterhuysen, K. (1987). Sediment dispersal in the Knysna estuary: environmental management considerations. *S. Afr. J. Geol.* 90, 448–457.

Reed, D. J. (1990). The impact of sea-level rise on coastal salt marshes. *Prog. Phys. Geogr.* 14, 465–481. doi: 10.1177/030913339001400403

Reinwarth, B., Franz, S., Baade, J., Haberzettl, T., Kasper, T., Daut, G., et al. (2013). A 700-year record on the effects of climate and human impact on the southern cape coast inferred from lake sediments of Eilandvlei, wilderness embayment, South Africa. *Geogr. Ann. Ser. B* 95, 345–360. doi: 10.1111/geoa.12015

Russell, I. A. (1996). Water quality in the Knysna estuary. *Koedoe* 39, 1–8. doi: 10.4102/koedoe.v39i1.278

Sanchez-Cabeza, J. A., and Ruiz-Fernández, A. C. (2012). 210Pb sediment radiochronology: an integrated formulation and classification of dating models. *Geochim. Cosmochim. Acta* 82, 183–200. doi: 10.1016/j.gca.2010.12.024

Swift, D. J. P. (1968). Coastal erosion and transgressive stratigraphy. *J. Geol.* 76, 444–456. doi: 10.1086/627342

Switzer, T. (2008). Urea loading from a spring storm-Knysna estuary, South Africa. *Harmful Algae* 8, 66–69. doi: 10.1016/j.hal.2008.08.005

Tite, M. S. (1972). The influence of geology on the magnetic susceptibility of soils on archaeological sites. *Archaeometry* 14, 229–236. doi: 10.1111/j.1475-4754.1972.tb00065.x

Troels-Smith, J. (1955). Characterization of unconsolidated sediments. *Dan. Geol. Unders.* 3, 38–71.

Warwick, R. M., Tweedley, J. R., and Potter, I. C. (2018). Microtidal estuaries warrant special management measures that recognise their critical vulnerability to pollution and climate change. *Mar. Pollut. Bull.* 135, 41–46. doi: 10.1016/j.marpolbul.2018.06.062

Watling, R. J., and Watling, H. R. (1982). Metal surveys in south African estuaries II. *Knysna River. Water SA* 8, 36–44.

Wündsch, M., Haberzettl, T., Cawthra, H. C., Kirsten, K. L., Quick, L. J., Zabel, M., et al. (2018). Holocene environmental change along the southern cape coast of South Africa – insights from the Eilandvlei sediment record spanning the last 8.9 kyr. *Glob. Planet Change* 163, 51–66. doi: 10.1016/j.gloplacha.2018.02.002

Wündsch, M., Haberzettl, T., Kirsten, K. L., Kasper, T., Zabel, M., Dietze, E., et al. (2016). Sea level and climate change at the southern cape coast, South Africa, during the past 4.2 kyr. *Palaeogeogr. Palaeoclimatol. Palaeoecol.* 446, 295–307. doi: 10.1016/j.palaeo.2016.01.027

Zhao, S., Feng, C., Wang, D., Liu, Y., and Shen, Z. (2013). Salinity increases the mobility of cd, cu, Mn, and Pb in the sediments of Yangtze estuary: relative role of sediments' properties and metal speciation. *Chemosphere* 91, 977–984. doi: 10.1016/j.chemosphere.2013.02.001

frontiers | Frontiers in Ecology and Evolution

TYPE Original Research
PUBLISHED 30 June 2023
DOI 10.3389/fevo.2023.1179176

OPEN ACCESS

EDITED BY
Olga Solomina,
Institute of Geography (RAS), Russia

REVIEWED BY
Abdelazim Negm,
Zagazig University, Egypt
Jorge Mongil-Manso,
Universidad Católica de Ávila, Spain

*CORRESPONDENCE
Hector Pizarro
✉ hpizarro@ing.uchile.cl

†These authors share first authorship

RECEIVED 03 March 2023
ACCEPTED 29 May 2023
PUBLISHED 30 June 2023

CITATION
Jaque J, Melo Pinochet N, Aránguiz-Acuña A and Pizarro H (2023) Analysis of sediment from an irrigation dam in an agricultural valley impacted by the mega-drought in central Chile. *Front. Ecol. Evol.* 11:1179176. doi: 10.3389/fevo.2023.1179176

Analysis of sediment from an irrigation dam in an agricultural valley impacted by the mega-drought in central Chile

Jennery Jaque[1,2†], Naveska Melo Pinochet[1,2†], Adriana Aránguiz-Acuña[2,3] and Héctor Pizarro[4*]

[1]Departamento de Ciencias Geológicas, Universidad Católica del Norte, Antofagasta, Chile, [2]Laboratorio de Ecología Acuática, Departamento de Recursos Ambientales, Facultad de Ciencias Agronómicas, Universidad de Tarapacá, Arica, Chile, [3]Millennium Nucleus in Andean Peatlands (AndesPeat), Universidad de Tarapacá, Arica, Chile, [4]Departamento de Geología, FCFM, Universidad de Chile, Santiago, Chile

Central Chile has been affected since 2010 by an increasing mega-drought accompanied by a historically low precipitation rate, as a probable consequence of climate change. Additionally, the increasing pressure exerted by the withdrawals of human activities, such as agriculture and metal mining, promotes conditions of hydric scarcity. Despite this intensive use of the watersheds and the sustained and increasing aridity, it has not been explored whether an artificial sedimentary record can trace these changes in the agricultural valleys of the region. To unravel and evaluate the recent environmental/climatic variability, the effects of the mega-drought that has pertained since 2010, extractivist pressures on a Mediterranean valley in central Chile, and sediment records were obtained from an irrigation dam and studied through a multi-proxy analysis. The dam was built and has been in operation since 1975 and is located in the Aconcagua River Valley, Valparaíso, Chile. Magnetic properties, carbon content, mineral composition, and metal content were analyzed from sediments of a 120 cm long core. Changes in vegetation cover from 1990 to 2020 were analyzed through NDVI filters. Horizons associated with drier conditions were observed in the upper zone of the core, which corresponded from the year 2001 to the present, assuming a constant sedimentation rate of 2.72 cm·yr^{-1}. Additionally, the characteristic alternation of dry–wet conditions was observed in the deep horizon of the dam sediments. The concentrations of Cu, Pb, Al, and As have increased over the years, while the concentration of Mo has decreased. Some of these elements are associated with copper mining, existing in the valley. Analysis of Landsat images from the year 2000 to the present has identified a significant decrease in vegetation cover associated with dry/wet periods, which may be related to cycles of El Niño/La Niña events. Although not all the proxies analyzed were sensitive enough to detect changes at the desired resolution, since the dam is very recent, the results shed light on the effects of the interaction between industrial activities and the decrease of water availability in multiple-use watersheds, suggesting variations in metals concentrations and changes in water availability, probably promoted by anthropic activities, climatic events, and increasing aridity in the Aconcagua River Valley.

KEYWORDS

Aconcagua River Valley, environment/climatic variability, dam sediments, magnetic properties, metals concentrations, multi-proxy analysis

1. Introduction

The Mediterranean area of central Chile is currently suffering from a long and intense period of drought that has not been seen in recent history (Garreaud et al., 2017), which has caused a decrease in the budgets of the lake and highland aquatic ecosystems, with dramatic consequences for local agriculture, livestock, and water supply for human consumption (Muñoz et al., 2020). During the mega-drought, the surface area of lakes in the Andes of central Chile has decreased between 7 and 28.34% (Fuentealba et al., 2021), and these changes have been associated with regional climate trends involving a decrease in precipitation and an increase in temperature (Garreaud et al., 2017). Moreover, the interaction with the increasing pressure of withdrawals from human activities, especially those at the industrial level, has created conditions of scarcity, where the water demand may exceed the recharge capacities of the hydrological systems (Le Goff et al., 2022). The combination of these water stress factors has put Chile in a condition of high risk among the countries of the Americas (Muñoz et al., 2020).

The Aconcagua River Basin is of transverse exorheic type, with an approximate area of 7,337 km^2, which originates in the Cordillera de Los Andes and flows into the Concón Bay in the Valparaíso Region, Chile (Dirección General de Aguas, 2004; Soto Bäuerle et al., 2011). The Valparaíso Region is one of the most densely populated regions at the national level (1.8 million inhabitants), and the Aconcagua River Basin hosts a great variety of economic activities. These activities are mainly associated with the exploitation of natural resources, such as copper mining, industries, water treatment plants, and important agricultural activities (Aguilar et al., 2011; Instituto Nacional de Estadísticas, 2014; Dirección General de Aguas, 2019). Metallic mining in the area has focused on the exploitation of fine copper and its by-products, traces of which have been previously detected in different points of the basin (Fe, Mg, Cu, As, and SO_4^{-2}, among others), and industrial activities in the manufacture, treatment, and sale of food, preservatives, cement, and industrial chemicals, among others. Agricultural activities have also impacted the natural basins, mainly through the extraction of water for irrigation and the use of agrochemicals and pesticides in their crops, such as Carbofuran and Chlorothalonil (Dirección General de Aguas, 2004). The area of the watershed allocated for agricultural use is equivalent to 12%. The largest avocado crops are found there, accounting for 41% of the total production of avocado trees in the country with high water demand. The most commercially appreciated cultivars require >500 mm of water per season to reach their highest relative production (Lahav and Whiley, 2007) and well-drained soils. These requirements allow avocado crops to cause an increase in soil erosion and loss of natural vegetation (Soto Bäuerle et al., 2011).

Many watersheds in the Valparaíso region have been impacted by the current climatic conditions and the consequent land use changes. An extreme example of these interacting factors is the La Ligua and Petorca watersheds. After suffering from high levels of aquifer exploitation, the Petorca province was declared a water scarcity zone in 1997 (Muñoz et al., 2020) and a groundwater restriction zone in 2014 (Dirección General de Aguas, 2019). In Petorca, the quality of life of the population and the availability of water for small farmers have been seriously affected due to the lack of water for irrigation (Bolados-García and Sánchez-Cuevas, 2017; Duran-Llacer et al., 2020). This has increased due to drought and climate change, and also to water theft by large growers, a result of the Chilean private management model of water that establishes the water market, which has triggered various social conflicts in the area (Bolados-García and Sánchez-Cuevas, 2017; Panez-Pinto et al., 2017). Such socio-environmental and economic conflicts could potentially occur in all regions where the frequency and magnitude of aridity periods are increasing. Therefore, it is important to quantify and study the impacts of environmental/climatic variability, the mega-droughts that currently affect the area, and the effects of extractivism resulting from the economic activities in the valley. In this context, multiproxy studies have been focused on the study of lake sediments to understand climate variability and the effects of extractivism in Chile (e.g., Bertrand et al., 2008; Von Gunten et al., 2009; Aránguiz-Acuña et al., 2020; Gayo et al., 2022). However, these sedimentary records usually reflect changes on the Holocene time scale. Meanwhile, sediments from an irrigation dam are time-constrained, meaning they can better archive the recent-past environmental conditions and current transformations of land use.

This study aimed to check the use of different proxies measured (magnetic properties, geochemical analysis, loss on ignition, satellite image processing, and reflectance spectrum) on a short sediment record from an irrigation dam in the Aconcagua River Valley to unravel the environmental and/or climatic history in central Chile between 1975 and 2019. In addition, this study seeks to link the magnetic and geochemical variations recorded in the sediments with the severe mega-drought that started in 2010 and polluting industrial activities.

2. Methodology

2.1. Study site and sampling

The Aconcagua Valley is located in the Aconcagua River basin in the Valparaiso region, which is 88 km east of the city of Valparaiso, Chile (Figure 1). The study area, known as the central valley, is a semi-arid region located at 800 m.a.s.l. and is mainly composed of volcanic, volcanic sedimentary, and intermediate acidic intrusive units (Rivano et al., 1993; Escribano, 2008; Naranjo, 2014; Figure 1). This valley is home to cities such as San Felipe and Los Andes, and its primary economic activities include mining, industry, and agricultural development (Gaete et al., 2007; Dirección General de Aguas, 2009). This valley, like others in the area, has been impacted by water scarcity since 2010, alternating between wet periods and agricultural growth (Maturana et al., 1997; Dirección General de Aguas, 2009; Garreaud et al., 2017).

The sampling site is specifically located in the town of Calle Larga at 806 m.a.s.l and corresponds to an artificial irrigation dam constructed for agricultural use. One sediment core 120 cm long and 10 cm in diameter was extracted from the bottom of the artificial irrigation reservoir in February 2019. The

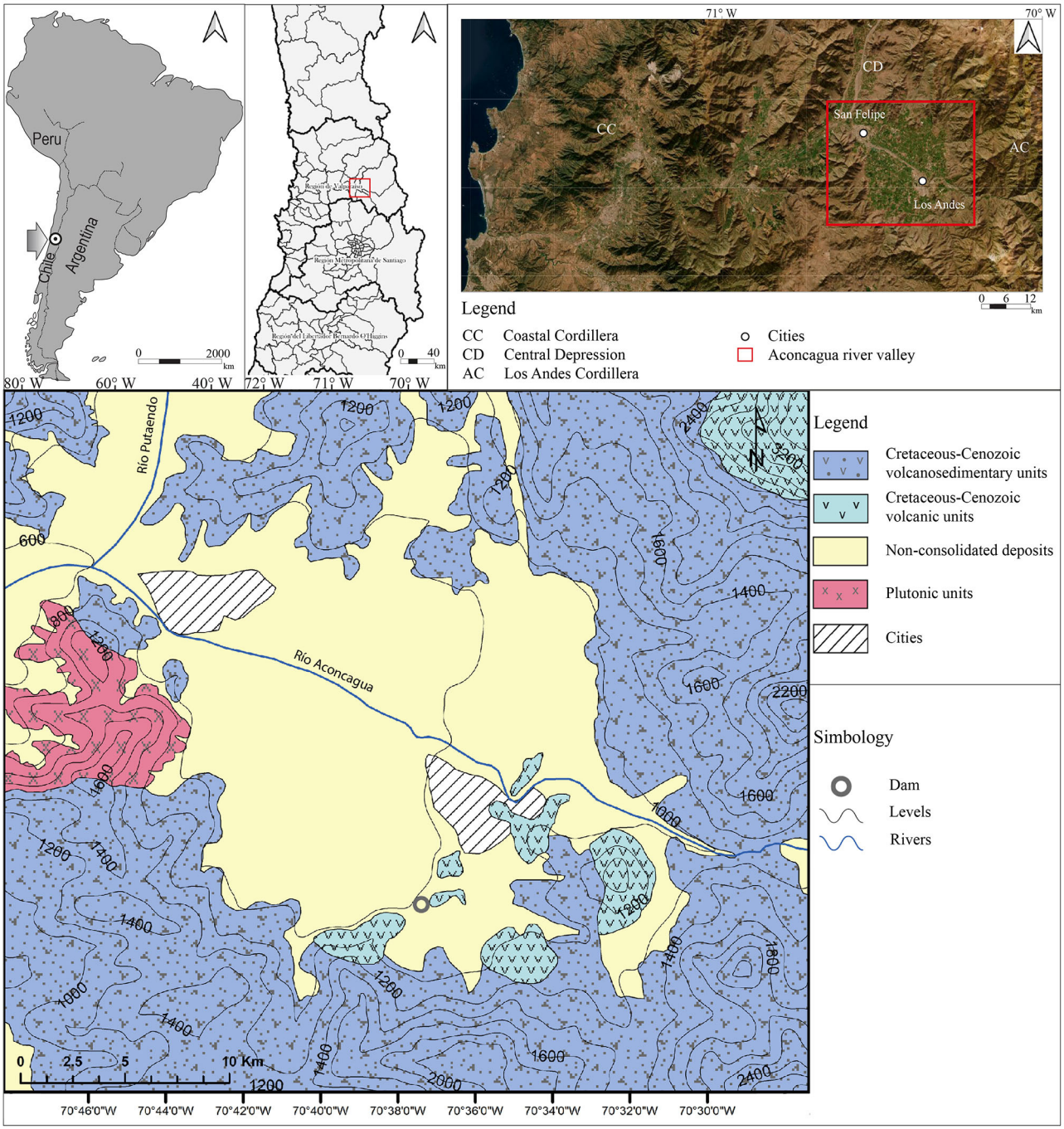

FIGURE 1
Location of the study site. Aconcagua River Valley, Calle Larga town, Valparaíso Region, Central Chile (modified from Rivano et al., 1993).

sedimentary core was extracted during a period of extreme drought when the reservoir was dry, using a trench to obtain the core (Supplementary Figure 1). The core was sliced every 1 cm, and a total of 120 samples of approximately 15 g each were collected for magnetic, petrographic, and geochemical analyses (Supplementary Figure 1). Samples were coded as TP+ depth (in cm) and sorted at 4 °C. In addition, Figure 2 shows the different techniques used and the parameters to be calculated.

The first step was to perform a macroscopic description of the whole core, and then, X-ray images of the sedimentary core were taken. To radiograph the complete core (120 cm in total), we used a conventional radiograph and the ADAM software to obtain and improve the quality of the photographs. This allowed us to observe and analyze alternation patterns and changes in color and thickness (Mena et al., 2011).

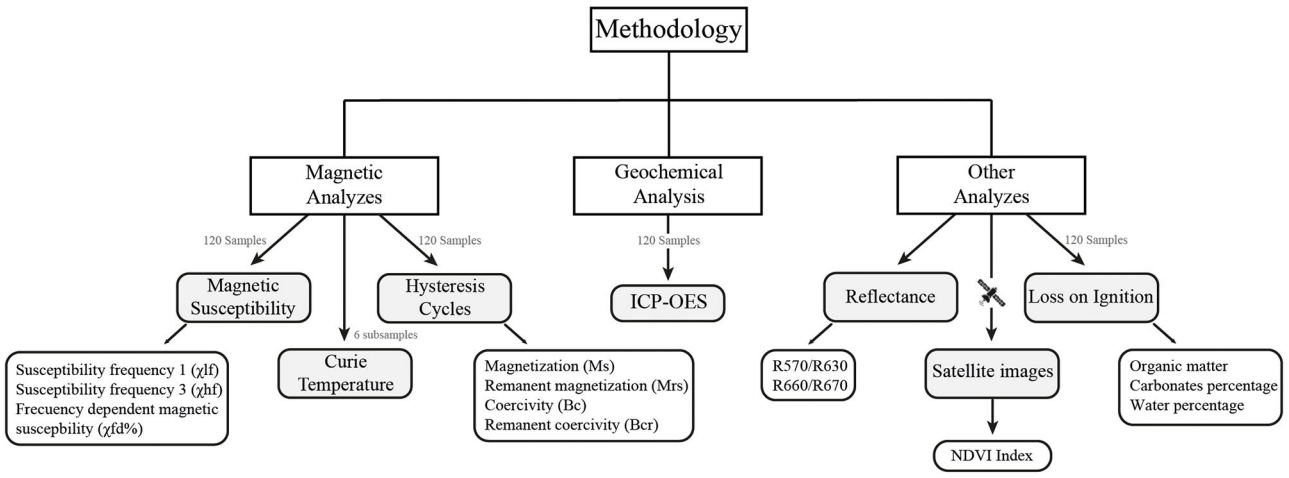

FIGURE 2
Flowchart of the methodologies used in this study: magnetic, geochemical, and other analyses performed with their respective measured parameters.

2.2. Analysis of magnetic properties

To identify potential changes in the distribution of magnetic particles throughout the core, wet sediment samples were mounted on 8 cm^3 standard-size paleomagnetic cubes for mass magnetic susceptibility (χ) measurements. The χ was measured using a Kappabridge MFK1-FA susceptibility bridge (AGICO Co.) under normal ambient conditions (22–24°C) and a 200 A/m field at Maini Equipment Center (Universidad Católica del Norte, UCN, Antofagasta, Chile). Measurements were performed at two different frequencies of 976 Hz (χlf) and 15.616 Hz (χhf), corresponding to low and high frequencies, respectively. This method allowed us to calculate the frequency-dependent magnetic susceptibility (Figure 2; Dearing et al., 1996)

$$([\chi fd\% = ((\chi lf - \chi hf)/\chi lf)^{*}100]) \quad (1)$$

where, χfd% is a widely used parameter to reflect the content of the particles close to the superparamagnetic/single domain (SP/SD) boundary (Maher et al., 2003; Yang et al., 2023).

Additionally, the same samples were subjected to hysteresis experiments at room temperature using a MicroMag AGM 2900-2 alternating gradient force magnetometer at UCN (Princeton Measurements Corp., Princeton, NJ, USA) with the purpose of determining magnetic mineral content and grain size. Magnetic hysteresis parameters were calculated using PmagPy routines (available at https://earthref.org/PmagPy/cookbook/; Tauxe, 1998, 2005).

Finally, six sub-samples (TP001, TP007, TP043, TP052, TP088, and TP097) were used to determine Curie temperatures by thermomagnetic experiments using a CS4 MFK1-FA (AGICO). Powdered samples were heated from room temperature to 700°C (and then cooled to room temperature) under a weak magnetic field (300 A/m) and 1 atm pressure in a non-inert (oxygen) atmosphere. Curie points were calculated using the method proposed by Hodel et al. (2017).

$$(grad = |(\chi Tn+1 - \chi Tn)/(Tn+1 - Tn)|) \quad (2)$$

2.3. Chemical analysis

The sediment core samples were subjected to various analyses at different facilities. At the Center for Advanced Studies in Arid Zones (CEAZA), loss on ignition measurements were conducted on 1 cm^3 cubes per sample. The cubes were heated in a muffle to 550°C for 4 h to obtain the percentage of organic matter and then to 950°C for 7 h to determine the percentage of carbonate.

The reflectance in the visible spectrum (380 to 750 nm) of the entire core was measured in the STS-VIS optical spectrometer. Two spectral indices were calculated: the ratio of clay detection of reflectance at wavelengths of 570 nm and 630 nm (R_{570}/R_{630}) and the relative absorption band depth 660–670 nm ($RABD_{660;670}$) as an indicator of total chlorine (diagenetic products of chlorophyll) (Rein and Sirocko, 2002; Von Gunten et al., 2012; De Jong et al., 2013).

All samples (120) were analyzed by Inductively Coupled Plasma Optical Emission Spectrometry (ICP-OES, model OPTIMA 8000). Total concentrations of copper, zinc, cadmium, nickel, iron, aluminum, vanadium, molybdenum, and arsenic were measured for each sample. For this, the samples were disaggregated according to the EPA 3052 method with hydrochloric and hydrofluoric acid (Remeteiová et al., 2020).

2.4. Analysis of satellite images

Vegetation cover changes were analyzed using satellite images obtained from the Earth Explorer platform (USGS) of the Landsat 5 and 8 satellites for the period between 1990 and 2020 (every 5 years). The images were georeferenced to the UTM WGS 84 South Zone19 projection and vegetation cover filters were applied. The Normalized Difference Vegetation Index (NDVI) filters were obtained with the ERDAS IMAGINE 2014 software using the following formula:

$$NDVI = (ICR - R)/(ICR + R) \quad (3)$$

In the above formula, ICR corresponds to the near-infrared reflectance (Band 4), while R corresponds to the red reflectance (Band 3). The numerical value given by the previous expression ranges from −1 to 1, with the value 0 indicating the approximate threshold of vegetation absence (Rouse et al., 1974). The numerical values are translated into the images with two colors: red for values close to −1 (loss of vegetation) and green for values close to 1 (increase of vegetation). A 25% variation in vegetation cover was used to visualize inter-period differences (Muñoz, 2013).

2.5. Data analysis

Chemical and magnetic data zones were identified by performing the CONISS analysis (Grimm, 1987) with TILIA software. For combinations of chemical and magnetic proxies that showed high and significant correlation coefficients, Spearman's rank correlation was used to calculate R, and *p*-values were also calculated for linearly detrended data. All analyses were conducted using ioGAS 64 software.

3. Results

3.1. Macroscopic sedimentary characteristics

The mineralogical composition of the sediment consisted mainly of feldspar, lithics, quartz, calcite, and magnetite. The grains were silt and clay-sized, and they were mainly spherical and elongated. Additionally, remnants of organic matter were observed in the bottom of the core.

Based on the macroscopic characteristics, the sedimentary core was divided into two sections. On the bottom section (between 120 and 48 cm), the sedimentary core was identified as a section, characterized by alternating light brown and gray (2 and 3 cm thick) and dark brown (1 and 1.5 cm thick) Horizons. The upper section (from the top to 48 cm depth) had a massive structure and millimeter parallel lamination with a variable contribution of vegetation remains. Another subsection was identified in the upper section, characterized by a reddish-brown color with no pattern or defined horizons and apparently poor in organic matter.

3.2. Magnetic properties of sediments

Magnetic susceptibility (χ) values varied slightly along the sedimentary core, ranging from 3.77×10^{-3} to 7.94×10^{-3} m^3kg^{-1}, with a mean value of 5.47×10^{-3} m^3kg^{-1} (Figure 3). The frequency-dependent magnetic susceptibility (χfd%) values varied between 1.76 and 3.91%, with a mean value of 2.62% (Figure 3G). Although the curve was relatively homogeneous, some middle (42–64 cm) and bottom (81–99 cm) sections had χfd% values of > 3%. If the χfd% values were > 3%, this could be used as an indicator of the presence and concentration of small ferromagnetic particles that have magnetic sizes near the superparamagnetic (SP)/single (SD) magnetic limit (Maher and Taylor, 1988; Dearing et al., 1996). Their presence suggests that the number of very small ferromagnetic particles is significant in some samples from the middle and bottom of the sedimentary core.

The measured thermomagnetic experiments showed irreversible behavior for all samples analyzed in all curves (Supplementary Figure 2). Two clear sections could be described: first, a smooth progressive increase up to approximately 580°C, and then a drastic change in the slope of the curve at approximately 580°C. This suggests the presence of nearly pure magnetite (Tc1) and a progressive decrease, indicated by a gentle slope between 580 and 680°C, which is an indicator of a mixture of Ti-rich and Ti-poor titanohematite-titanomaghemite (Tc3; Supplementary Figure 2; Tauxe, 1998).

This last magnetic phase is associated with a more oxidizing environment. Additionally, the top of the sediments (from 7 cm depth to the top) showed a progressive decrease in susceptibility from 500 to 570°C. This is probably associated with the presence of Ti-poor titanomagnetites. At the bottom of the sediments (97 cm depth), an abrupt increase was observed just before ∼580 °C during heating (Hopkinson peak), which could indicate the presence of superparamagnetic grain (fine grain) magnetite within this slice (Dunlop and Özdemir, 2001). This is confirmed by a value of χ fd% > 3%, which is an indicator of the presence of magnetic particles of SP magnetic size.

All samples exhibited similar behavior in the hysteresis curves, as follows: (1) a strong ferromagnetic behavior and a weak paramagnetic behavior, which are clearly observed in the shape of the curves; (2) low coercivity values (Bc and Bcr), and (3) high magnetization values (Ms and Mr). The curves generated by the coercive force (Bc) and remaining coercivity force (Bcr) were relatively homogeneous along the core. Conversely, the saturation magnetization (Ms) and saturation remanence (Mr) curves were heterogeneous along the core. Similar behavior was observed in the curves generated by low-field magnetic susceptibility (χ lofi), high-field magnetic susceptibility (χ hifi), and ferrimagnetic susceptibility (χ ferry) values (Supplementary Figure 3).

The hysteresis values were plotted in the Theoretical Day Plot (Day et al., 1977; Dunlop, 2002a) to discriminate the magnetic size (and possible size mixtures) of the Fe-bearing minerals. The measured values were plotted close to the pseudo-single-domain (PSD) field, between the single domain (SD) + multi-domain (MD) mixing curves and the single domain (SD) + superparamagnetic (SP) (10 nm) domain mixing curves (Supplementary Figure 4). This finding could be the result of a mixture of PSD and SP magnetic grains or a ternary mixture of SP+SD+MD (i.e., Dunlop, 2002b). This observation could be the result of an SP + PSD mixture dominated by PSD and MD magnetic grains. This interpretation is consistent with the shape of the hysteresis loops, the values calculated from these, and the low χfd% values (< 3%) obtained, likely indicating a detrital origin of magnetic minerals (magnetite and titanomagnetite).

3.3. Chemical concentration of sediments

The concentration of quantified elements along the sediment core showed variable depth patterns. Arsenic concentration in the sedimentary core was more abundant in the upper section but

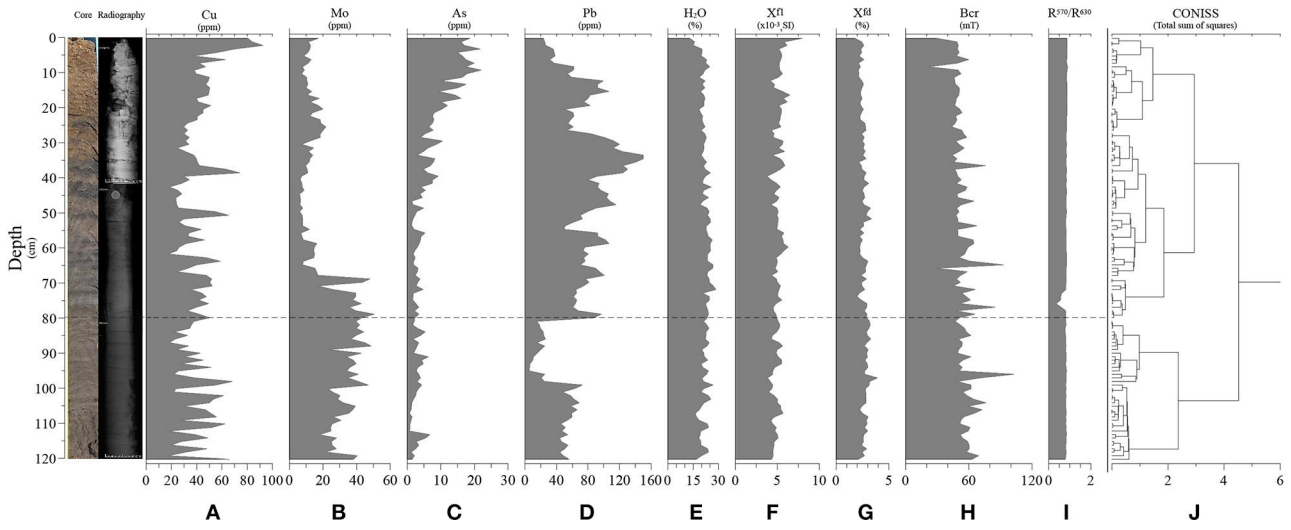

FIGURE 3
Geochemical analysis of sedimentary core. **(A)** Copper concentration (ppm); **(B)** molybdenum concentration; **(C)** arsenic concentration; **(D)** lead concentration; **(E)** water percentage; **(F)** magnetization; **(G)** frequency susceptibility dependence; **(H)** remanent coercivity; **(I)** R570/R630 ratio; **(J)** environmental relationship identified by CONISS analysis.

decreased from 30 cm to the bottom. Molybdenum was present in low concentrations in recent sediments but increased from 70 cm in the older sediments (Figures 3B, C). Lead was low in the top sediments but reached high concentrations with peaks at medium depths (15 cm, 35 cm, 60 cm, and 80 cm), followed by a gap between 80 and 100 cm (Figure 3D). Copper had its maximum concentration in the top sediments and had other peaks at 40 cm, 50 cm, and around 70 cm, while deeper sediments had varying copper concentrations (Figure 3A). The Al concentration in the core was more abundant at the top, showing some peaks (7 cm, 12 cm, and 13 cm), which indicated an increasing concentration of aluminum toward the top. The other potentially toxic metals analyzed, such as nickel, iron, cadmium, and zinc, did not show significant variations over the years. There was only an abrupt increase in iron at the top of the sedimentary core associated with the years 2016 to 2019.

The water percentage was relatively homogeneous throughout the sedimentary core and did not present significant variations, with values ranging from 12 to 28%. Only in the sediments at the top of the core was a decrease in water percentage observed (Figure 3E), mainly due to direct exposure to air and heat when the dam went dry in 2019.

The percentage of carbonate, measured by loss on ignition at 925°C (LOI_{925}), did not exceed 3% throughout the whole sediment core. However, in the case of organic matter (LOI_{550}), concentrations varied between 2.3 and 4.4%. This variation could be associated with the observed lamination of light/gray and dark brown horizons, where the highest values of organic matter are related to dark brown horizons, and low organic matter values are associated with light brown/gray horizons. The percentage of organic matter decreased moving upward.

Regarding the reflectance ratio, R_{660}/R_{670}, only one point showed a deviation value of 1, with a single break at 43 cm. No variations were observed for the $RABD_{660;670}$ index, suggesting constancy in lithogenic and diagenetic content during the analyzed period.

3.4. Satellite images of the central valley

According to the NDVI, there has been a change and growth in the density and arrangement of vegetation cover over the past 30 years (1990 to 2020). This change was concentrated in periods after the year 2000, as shown in Figure 4, where there was a significant increase in sectorized vegetation. This increase was mainly due to the expansion of agricultural livestock in the valley, as illustrated by the shape of the polygons in Figures 4B, C, especially between the years 2005 and 2010. During this period, the vegetation cover increased by 7,954 hectares (Figure 4D). However, since 2010, there has been a considerable loss of vegetation cover of 15,027 hectares (Figure 4E), with a slight recovery since 2015 equivalent to 3,479 hectares. Nevertheless, the net balance remains negative (Figure 4F).

4. Discussion

Paleoenvironmental studies commonly use multi-proxy analyses, including both organic and inorganic variables, of lake and marine sediments to unravel past environmental and climatic conditions over thousands of years. However, identifying proxies that are sensitive enough to account for inter-annual changes. In this study, a sediment core was obtained from a short-dated irrigation dam in a region heavily affected by the current mega-drought. The core reflects climatic and anthropogenic events that have impacted the area from 1975 to 2019.

Since then, there have been no removals identified from the beginning of the dam to the date of sampling, it is plausible to

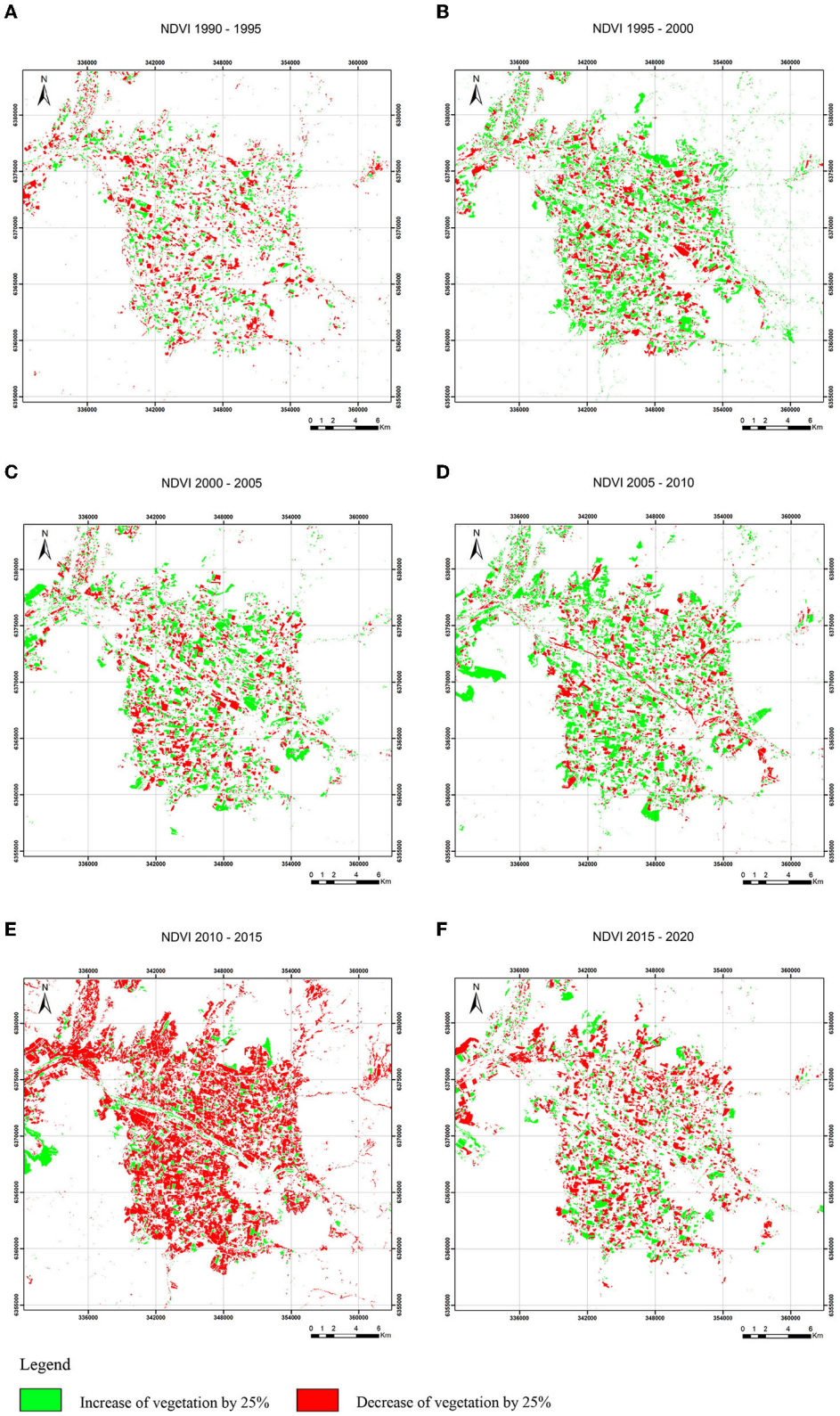

FIGURE 4
Linear regressions of Normalized Difference Vegetation Index (NDVI) made in the central valley between 1990 and 2020, divided into five annual windows: **(A)** 1990–1995; **(B)** 1995–2000; **(C)** 2000–2005; **(D)** 2005–2010; **(E)** 2010–2015; and **(F)** 2015–2020.

assume a constant sedimentation rate for the period, calculated as 2.73 cm·yr^{-1} (120 cm of sediments in the 44 years between 1975 and 2019). Analyses and observations have allowed for the identification of proxies that were sensitive to changes that have occurred during the last four decades in central Chile. These proxies describe two different depositional environments and are related to water availability and other events.

The upper sediments up to 48 cm of the core (from 2019 to 2001, considering the constant assumed rate) could be related to drier conditions, with a massive structure and millimeter parallel lamination and a scarce contribution of vegetation remains. Another subsection was characterized by a reddish-brown color without lamination and poor organic matter. Ti-poor titanomagnetites are also recognized from thermomagnetic experiments in this region. Additionally, very small ferromagnetic particles were recorded in the break generated between 48 and 62 cm, which may be linked to authigenic processes over magnetic minerals (Dearing et al., 1996; Evans and Heller, 2003; Hao et al., 2008). The copper curve showed high values at depths of approximately 7 cm, 38 cm, and 51 cm, which corresponded to the years 2016, 2005, and 2000, respectively. In addition, from 41 cm to the top, the concentration of copper began to rise, reaching its highest concentration of 20 ppm.

In the bottom section, between 120 and 48 cm (corresponding to the period 1975–2001, considering the assumed constant rate), a section characterized by alternating light brown and gray (2 and 3 cm thick) and dark brown (1 and 1.5 cm thick) horizons was identified. This arrangement of horizons could be related to the alternation of dry/wet periods, in agreement with the cyclic behavior of the Mediterranean template climate of the valley (Naranjo, 2014; Garreaud et al., 2020). In addition, the intercalation of light/gray and dark brown horizons is consistent with the organic matter content measured by LOI_{550}, with the highest organic matter values related to dark brown horizons. In contrast, low organic matter values are associated with light brown/gray horizons. The CONISS analysis defined a break at 80 cm (corresponding to 1990), primarily due to the strong break in the lead curve.

The upper horizon is well explained by drier environmental conditions. Higher metal concentrations measured, especially of Cu, Pb, and As, could be linked to contamination produced by the expansion of the surrounding mining and/or agricultural industries. Upstream in the basin is the Miocene Rio Blanco-Los Bronces copper–molybdenum deposit, among other mines near the sampling sites.

In general, the concentration of Cu in the sediments (40 ppm on average) is lower than the background concentrations of the Farellones Formation (120 ppm on average; Hollings et al., 2005) and the Abanic Formation (Hollings et al., 2005; Muñoz et al., 2006; between 28 and 80 ppm), which compose the substratum of the Aconcagua River. However, observed peaks of > 60 ppm could be associated with specific events that concentrate salts in the basin, such as a decrease in flow, or systematic inputs of these elements into the basin. High values associated with the years 2016, 2005, 2001, and 1996, respectively, could be related to specific natural disasters that occurred, such as debris flows and El Niño episodes (Higueras et al., 2004). Additionally, there are several peaks of similar magnitude below 96 cm, which corresponds to 1984. These peaks, such as the one that occurred in 2016, could be related to the break of a pipeline that transported copper concentrate, which resulted in a discharge of 50,000 liters of material into the river, which was documented in the press (Radio Cooperativa, 2016).

The current molybdenum concentration (17 ppm on the surface) is lower than that recorded in the Rio Blanco-Los Bronces Cu-Mo deposit, which is approximately 200 ppm on average (Crespo Mena, 2019). However, it is higher than the concentrations recorded in the substrate from the Aconcagua River (<5 ppm on average; Hollings et al., 2005). High concentrations of Cu and Mo have been reported in the upper basin (Gaete et al., 2007; Fierro et al., 2021); nevertheless, the relative mobility of some metals, such as Mo, is dependent on redox conditions, and oxidizing conditions increase the mobility in lacustrine sediments.

The arsenic concentration was lower than that measured in rocks from the Rio Blanco-Los Bronces deposit (61.66 ppm on average; Crespo Mena, 2019), where it is possible to recognize sulfides rich in As, such as arsenopyrite, tennantite, and enargite. The values were similar to those recorded in fluvial sediments of other intensively managed watersheds, such as the Maipo River (12 ppm on average; Tapia et al., 2022) and the Cachapoal River (10 ppm on average; Duran-Llacer et al., 2020).

In contrast, the lead concentration measured in the sediments was higher than that recorded in the rocks of the Rio Blanco-Los Bronces Cu-Mo deposit, Farellones, and Abanicos formations, where the average values are 26 ppm, 8 ppm, and 7 ppm, respectively, while in the sediments, it is 66 ppm, on average. The concentration curve is variable, with a high concentration from 80 cm and above and a peak value of 140 ppm at 35 cm (2006), mainly associated with intensive industrial activities and the use of fossil fuels.

The concentration of Al in the sediments ranges between 0.07 and 0.62 ppm, which is lower than the concentration in the rocks of the Aconcagua substrate. For the Farellones Formation, the concentration ranges from 14.98 to 19.66 ppm, and for Abanico Formation, it ranges from 13.43 to 20.0 ppm (Hollings et al., 2005). The highest Al values tend to be associated with periods of lower precipitation, such as the La Niña phase. This is similar to the relationship found by Tapia et al. (2022) between the As concentration in sediments and precipitation, where the concentration of this metal decreases during periods of greater rainfall. The value of $R^2 > 0.3$ between Al and As concentration could indicate that part of the As concentration in the sediments could be linked to a climatic component (Supplementary Figure 5).

An exploratory analysis of the relation between climate data (Dirección General de Aguas, 2009) and hydric availability in the sampling area was performed. Monthly temperature series from 1979 to 2019 (NOOA Physical Sciences Laboratory, https://www.psl.noaa.gov/enso/mei/; Figure 5A) were used, where positive anomalies were considered indicators of the El Niño phase and negative anomalies of the La Niña phase. This same procedure was applied to the Pacific Decadal Oscillation (PDO) data series (data from the NOOA Physical Sciences Laboratory, https://www.ncei.

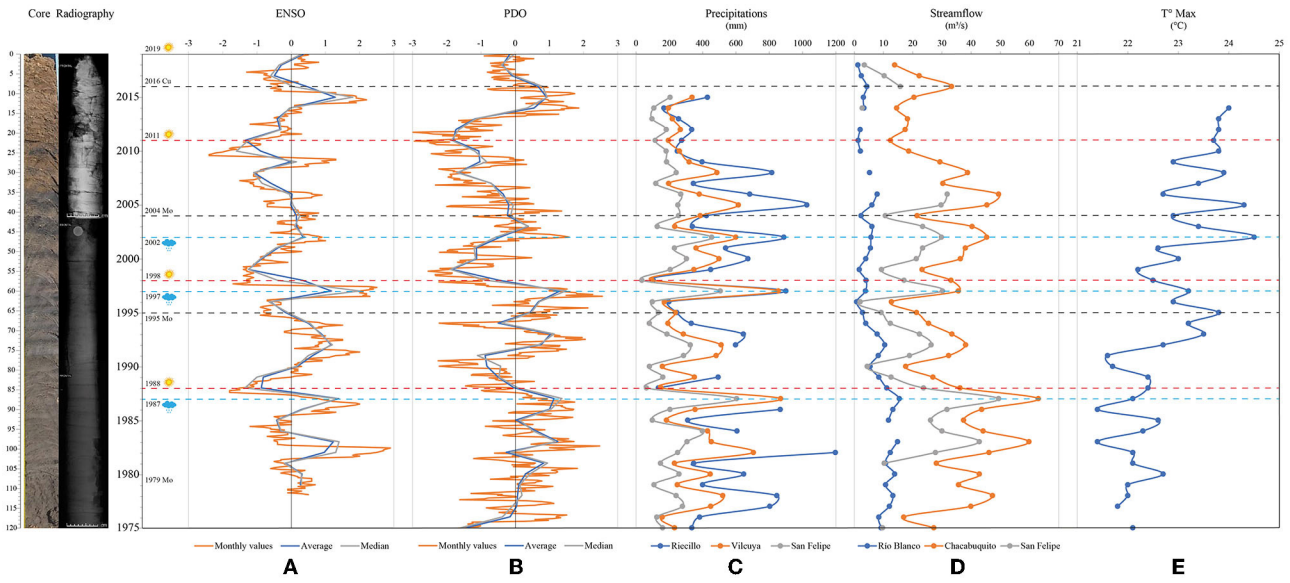

FIGURE 5
The meteorological database (https://climatologia.meteochile.gob.cl). **(A)** MEI index from www.esrl.noaa.gov/psd/enso/mei/ for the period of 1976–2010; **(B)** MEI index from https://www.ncei.noaa.gov/access/monitoring/pdo/ for the period of 1976–2020; **(C)** precipitation from Riecillos, Vilcuya, and San Felipe stations; **(D)** streamflow from Río Blanco, Chacabuquito, and San Felipe stations; **(E)** maximum temperature (°C).

noaa.gov/access/monitoring/pdo/; Figure 4B). The temperature series were positively correlated with the El Niño phases and negatively correlated with the La Niña phases, with precipitation and river flow values, such as the Rio Blanco and Chacabuquito (Figures 5C, D; Supplementary Figure 5), suggesting an influence of inter-annual climatic variability on water availability in the watersheds of the Valparaíso region.

These variations in water availability could be related to changes in vegetation cover. NDVI images from 2000 to 2010 showed an increase in coverage, mainly due to the expansion of agricultural livestock in the valley, while between 2010 and 2015, there was a significant loss of vegetation, which could be explained by the mega-drought (Garreaud et al., 2020). Although there has been a slight recovery in coverage, the trend continues to be negative. Between 1990 and 2010, there was an alternation between El Niño and La Niña phases, with a significant El Niño event occurring in 1998 (Figures 4A, B), while from 2010 to date, the predominance of La Niña begins, which is consistent with different NDVI images (Figures 4E, F).

5. Conclusions and recommendations

From the analysis carried out in a sedimentary core reflecting a short period of time associated with the current mega-drought in central Chile, it was possible to identify sufficiently sensitive variables that allowed us to visualize changes in the geochemical and loss of ignition (water percentage) results, triggered by the reduced hydric availability and decreasing vegetation cover detected by the NDVI index. However, in the case of magnetic properties, the accumulation time was too brief for the results to be conclusive.

The variations in the Cu and Mo concentrations and the high values of this last element measured along the sedimentary core in the Aconcagua Valley can be linked to pollution, mainly associated with the mining industry that is located upstream of the valley. The high Pb concentration recorded in the sediments can be linked to pollution associated with the agricultural industry and/or burning of fossil fuels. We also identify variations in the concentration of Al and As in the sediments, which could be linked to a climatic component that has been recognized in other basins of the central valley.

This region hosts complex and productive ecosystems of global relevance, which are especially vulnerable in the face of unpromising climate change scenarios. Future studies in this valley could complement the results obtained. The study of biological components could be applied to reconstruct the changes in organic markers associated with the use of agrochemicals and the effect of the proxies analyzed on the functioning of ecological communities. This is to help to complete an adequate evaluation of the risk generated by the drought on the agroecological systems and the availability of food and water for the ecological and human communities. In addition, the magnetic techniques used in this study could be applied to different types of sedimentary cores with longer residence times to obtain more conclusive results.

Data availability statement

The raw data supporting the conclusions of this article will be made available by the authors, without undue reservation.

Author contributions

JJ, NM, AA-A, and HP: conceptualization, writing—original draft, and writing—review and editing. JJ, NM, and HP: formal analysis and visualization. AA-A: funding acquisition and project administration. JJ and NM: methodology. AA-A and HP: supervision. All authors contributed to the article and approved the submitted version.

Acknowledgments

We would like to thank the ANID-FONDECYT 1200423 and ANID-FODECYT Postdoctorado 3210291 projects for their support. We also thank Agricola Brown Ltd., for its support with sampling. The chemical analysis was carried out with the technical assistance of Sue Ellen Vega, while the XRD images were provided by the Blanco Laboratory. Magnetic analysis was carried out at the MAINI Laboratory of the Universidad Católica del Norte, while LOI and reflectance analyses were conducted with the help of Dr. Antonio Maldonado of CEAZA.

Conflict of interest

The authors declare that the research was conducted in the absence of any commercial or financial relationships that could be construed as a potential conflict of interest.

Publisher's note

All claims expressed in this article are solely those of the authors and do not necessarily represent those of their affiliated organizations, or those of the publisher, the editors and the reviewers. Any product that may be evaluated in this article, or claim that may be made by its manufacturer, is not guaranteed or endorsed by the publisher.

Supplementary material

The Supplementary Material for this article can be found online at: https://www.frontiersin.org/articles/10.3389/fevo.2023.1179176/full#supplementary-material

SUPPLEMENTARY FIGURE 1
Process of sedimentary core extraction, and storage, of sedimentary core and sampling. **(A)** In 2019, a trench was made excavated during a period when the irrigation dam was dry (3 m length × 1 m width × 1.20 m depth). This sedimentary section represents the entire sedimentation history of the dam. **(B)** The sedimentary core was extracted from one of the walls of the irrigation dam. **(C)** Sedimentary core extracted. Subsequently, It it was stored in a refrigerated chamber at about 8°C. Then, in the CEAZA laboratory the sedimentary core was sliced at the CEAZA laboratory every 1 cm, and a total of 120 samples of approximately 15 g each were collected for different analysisanalyses. **(D)** Crucibles with 1 cm^3 of sediment used for Loss loss on ignition; **(E)** paleomagnetic boxes with 8 g of sediment each, one used for magnetic techniques and non-magnetic techniques.

SUPPLEMENTARY FIGURE 2
Curie temperature (Tc) of 6 subsamples. In red color: heating curve and in blue color: cooling curve. Tc1: magnetite Tc calculated using the method proposed by Hodel et al. (2017). grad = | (KTn+1 −KTn)/(Tn+1 −Tn). **(A)** Curie temperature of sample TP001; **(B)** Curie temperature of sample TP007; **(C)** Curie temperature of sample TP043; **(D)** Curie temperature of sample TP052; **(E)** Curie temperature of sample TP088; **(F)** Curie temperature of sample TP097.

SUPPLEMENTARY FIGURE 3
6 representative curves of hysteresis cycles from a total of 120 samples. This parameter was calculated using the program PmagPy program (Tauxe, 1998, 2005), **(A)** Hysteresis hysteresis cycle of the TP006 sample; **(B)** Hysteresis hysteresis cycle of the TP010 sample; **(C)** Hysteresis hysteresis cycle of the TP037 sample; **(D)** hysteresis of the TP047 sample; **(E)** Hysteresis hysteresis loop of the TP069 sample; **(F)** Hysteresis hysteresis loop of the TP115 sample.

SUPPLEMENTARY FIGURE 4
Hysteresis ratios plotted on a Day plot diagram (Day et al., 1977 after Dunlop, 2002a,b) for 120 samples.

SUPPLEMENTARY FIGURE 5
Relationship between the annual average of the ENSO measurements and other climatic parameters. **(A)** Al concentration vs. As concentration; **(B)** ENSO average vs. annual surface water flow record at the San Felipe meteorological station; **(C)** ENSO average vs. annual precipitation at the San Felipe meteorological station; **(D)** ENSO average vs. annual maximum temperature measured in the area. R2: Correlation coefficient, red circles: El Niño phase, and blue circles: La Niña phase. ENSO and PDO data taken are taken from the NOOA Physical Sciences Laboratory. Annual surface water flow, temperature, and precipitation data taken are taken from the DGA.

References

Aguilar, R., Hormazábal, C., Gaete, H., and Neaman, A. (2011). Spatial distribution of copper, organic matter and pH in agricultural soils affected by mining activities. *J. Soil Sci. Plant Nutr.* 11, 125–145. doi: 10.4067/S0718-95162011000300010

Aránguiz-Acuña, A., Luque, J. A., Pizarro, H., Cerda, M., Heine-Fuster, I., Valdés, J., et al. (2020). Aquatic community structure as sentinel of recent environmental changes unraveled from lake sedimentary records from the Atacama Desert, Chile. *PloS ONE* 15, e0229453. doi: 10.1371/journal.pone.0229453

Bertrand, S., Charlet, F., Charlier, B., Renson, V., and Fagel, N. (2008). Climate variability of southern chile since the last glacial maximum: a continuous sedimentological record from lago Puyehue (40 S). *J. Paleolimnol.* 39, 179–195. doi: 10.1007/s10933-007-9117-y

Bolados-García, P., and Sánchez-Cuevas, A. (2017). Una ecología política feminista en construcción: EL caso de las"Mujeres de zonas de sacrificio en resistencia", Región de Valparaíso, Chile. *Psicoperspectivas*. 16, 33–42. doi: 10.5027/psicoperspectivas-Vol16-Issue2-fulltext-977

Crespo Mena, J. A. (2019).Origen y distribución de plata en el yacimiento tipo pórfido de Cu-Mo Río Blanco, Chile Central.

Day, R., Fuller, M., and Schmidt, V. A. (1977). Hysteresis properties of titanomagnetites: grain-size and compositional dependence. *Physics Earth Planet. Int.* 13, 260–267. doi: 10.1016/0031-9201(77)90108-X

De Jong, D., von Gunten, R., Maldonado, L. A., and Grosjean, M. (2013). Late Holocene summer temperatures in the central Andes reconstructed from the sediments of high-elevation Laguna Chepical, Chile (32 S). *Climate Past* 9, 1921–1932. doi: 10.5194/cp-9-1921-2013

Dearing, J. A., Hay, K. L., Baban, S. M., Huddleston, A. S., Wellington, E. M., Loveland, P., et al. (1996). Magnetic susceptibility of soil: an evaluation of

conflicting theories using a national data set. Geophys. *J. Int Geophys.* 127, 728–734. doi: 10.1111/j.1365-246X.1996.tb04051.x

Dirección General de Aguas (2004). *Diagnóstico y Clasificación de Cursos y Cuerpos de Agua según Objetivos de calidad en la Cuenca del Río Aconcagua*. Gobierno de Chile.

Dirección General de Aguas. (2009). Diagnóstico y Clasificación de Sectores Acuíferos, Volumen 1. Gobierno de Chile. 23. Dirección General de Aguas. (2009). Diagnóstico y Clasificación de Sectores Acuíferos, Volumen 2. Gobierno de Chile Dirección General de Aguas. (2009). Diagnóstico y Clasificación de Sectores Acuíferos, Volumen 1. Gobierno de Chile.

Dirección General de Aguas. (2019). *Proyecto de Actualización de la modelación hidrológica integrada del Aconcagua*. Resumen Ejecutivo. Gobierno de Chile.

Dunlop, D. J. (2002a). Theory and application of the Day plot (Mrs/Ms versus Hcr/Hc) 1. Theoretical curves and tests using titanomagnetite data. *J. Geophys. Res. Solid Earth* 107, EPM-4. doi: 10.1029/2001JB000486

Dunlop, D. J. (2002b). Theory and application of the Day plot (Mrs/Ms versus Hcr/Hc) 2. Application to data for rocks, sediments, and soils. *J. Geophys. Res. Solid Earth* 107(B3), EPM-5. doi: 10.1029/2001JB000487

Dunlop, D. J., and Özdemir, Ö. (2001). *Rock Magnetism: Fundamentals and Frontiers*. Cambridge: Cambridge university press.

Duran-Llacer, I., Munizaga, J., Arum,í, J. L., Ruybal, C., Aguayo, M., Sáez-Carrillo, K., et al. (2020). Lessons to be learned: Groundwater depletion in Chile's Ligua and Petorca watersheds through an Interdisciplinary approach. *Water* 12, 2446. doi: 10.3390/w12092446

Escribano, J. (2008). *Superficies de Bajo Relieve en la Cordillera de Chile Central Entre Los 32°30's y los 33°30's, y su Relación con el Alzamiento Andino*. Chile: Universidad de Chile.

Evans, M. E., and Heller, F. (2003). *Environmental Magnetism: Principles and Applications of Enviromagnetics*. Amsterdam: Elsevier.

Fierro, P., Valdovinos, C., Lara, C., and Saldías, G. S. (2021). Influence of intensive agriculture on benthic macroinvertebrate assemblages and water quality in the Aconcagua River Basin (Central Chile). *Water* 13, 492. doi: 10.3390/w13040492

Fuentealba, M., Bahamóndez, C., Sarricolea, P., Meseguer-Ruiz, O., and Latorre, C. (2021). The 2010–2020 'megadrought drives reduction in lake surface area in the Andes of central Chile (32°-36°S). *J. Hydrol. Reg. Stu.* 38, 100952. doi: 10.1016/j.ejrh.2021.100952

Gaete, H., Aránguiz, F., Cienfuegos, G., and Tejos, M. (2007). Metales pesados y toxicidad de aguas del río Aconcagua en Chile. *Química Nova* 30, 885–891. doi: 10.1590/S0100-40422007000400023

Garreaud, R. D., Alvarez-Garreton, C., Barichivich, J., Boisier, J. P., Christie, D., Galleguillos, M., et al. (2017). The 2010–2015 megadrought in central Chile: Impacts on regional hydroclimate and vegetation. *Hydrol. Earth Syst. Sci.* 21, 6307–6327. doi: 10.5194/hess-21-6307-2017

Garreaud, R. D., Boisier, J. P., Rondanelli, R., Montecinos, A., and Sepúlveda, H. H., and Veloso-Aguila, D. (2020). The central Chile mega drought (2010–2018): a climate dynamics perspective. *Int. J. Climatol.* 40, 421–439. doi: 10.1002/joc.6219

Gayo, E. M., Muñoz, A. A., Maldonado, A., Lavergne, C., Francois, J. P., Rodríguez, D., et al. (2022). A cross-cutting approach for relating anthropocene, environmental injustice and sacrifice zones. *Earth's Future* 10, e2021EF. doi: 10.1029/2021EF002217

Grimm, E. C. (1987). CONISS: a FORTRAN 77 program for stratigraphically constrained cluster analysis by the method of incremental sum of squares. *Comput. Geosci.* 13, 13–35. doi: 10.1016/0098-3004(87)90022-7

Hao, Q., Oldfield, F., Bloemendal, J., and Guo, Z. (2008). The magnetic properties of loess and paleosol samples from the Chinese Loess Plateau spanning the last 22 million years. *Palaeogeography Palaeoecol.* 260, 389–404. doi: 10.1016/j.palaeo.2007.11.010

Higueras, P., Oyarzun, R., Oyarzún, J., Maturana, H., Lillo, J., and Morata, D. (2004). Environmental assessment of copper-gold-mercury mining in the Andacollo and Punitaqui districts, northern Chile. *Appl. Geochem.* 19, 1855–1864. doi: 10.1016/j.apgeochem.2004.04.001

Hodel, F., Macouin, M., Triantafyllou, A., Carlut, J., Berger, J., Rousse, S., et al. (2017). Unusual massive magnetite veins and highly altered Cr-spinels as relics of a Cl-rich acidic hydrothermal event in Neoproterozoic serpentinites (Bou Azzer ophiolite, Anti-Atlas, Morocco). *Precambrian Res.* 300, 151–167. doi: 10.1016/j.precamres.2017.08.005

Hollings, P., Cooke, D., and Clark, A. (2005). Regional geochemistry of Tertiary igneous rocks in central Chile: implications for the geodynamic environment of giant porphyry copper and epithermal gold mineralization. *Economic Geol.* 100, 887–904. doi: 10.2113/gsecongeo.100.5.887

Instituto Nacional de Estadísticas. (2014). *Anuario Estadístico Regional*. 90pp

Lahav, E., and Whiley, A. W. (2007). *Riego y Nutrición Mineral. Botánica, Producción y Usos. (Título Original: The Avocado, Botany, Production and Uses, pp 241-274. Ediciones Universitarias de Valparaíso*. Valparaíso: Pontificia Universidad Católica de Valparaíso.

Le Goff, L., Blot, F., Peltier, A., Laffont, L., Becerra, S., Henríquez Ruiz, C., et al. (2022). From uncertainty to environmental impacts: reflection on the threats to water in Chacabuco Province (Chile): a combined approach in social sciences and geochemistry. *Sust. Sci.* 4, 1–19. doi: 10.1007/s11625-022-01127-w

Maher, B. A., MengYu, H., Roberts, H. M., and Wintle, A. G. (2003). Holocene loess accumulation and soil development at the western edge of the Chinese Loess Plateau: implications for magnetic proxies of palaeorainfall. *Quaternary Sci. Rev.* 22, 445–451. doi: 10.1016/S0277-3791(02)00188-9

Maher, B. A., and Taylor, R. M. (1988). Formation of ultrafine-grained magnetite in soils. *Nature* 336, 368–370. doi: 10.1038/336368a0

Maturana, J., Bello, M., and Manley, M. (1997). Antecedentes históricos y descripción del fenómeno El Niño, Oscilación del Sur. *El Niño-La Niña* 2000, 13–27.

Mena, A., Aguiar, P., Barreiro, J. D., Francés, G., Pérez Arlucea, M., Barreiro Lois, A., et al. (2011). *El uso de la Tomografía Computarizada (TC) Como Técnica Sedimentaria: Aplicación en Testigos Oceánicos de la Cuenca Interior de Galicia* (NW margen Ibérico).

Muñoz, A. A., Klock-Barría, K., Alvarez-Garreton, C., Aguilera-Betti, I., González-Reyes, Á., Lastra, J. A., et al. (2020). Water crisis in Petorca Basin, Chile: The combined effects of a mega-drought and water management. *Water* 12, 648. doi: 10.3390/w12030648

Muñoz, M., Fuentes, F., Vergara, M., Aguirr, L., Olov Nyström, J., Féraud, G., et al. (2006). Abanico East Formation: petrology and geochemistry of volcanic rocks behind the Cenozoic arc front in the Andean Cordillera, central Chile (33 50'S). *Revista geológica de Chile* 33, 109–140. doi: 10.4067/S0716-02082006000100005

Muñoz, P. (2013). *Apuntes de Teledetección: índices de vegetación. Centro de Información de Recursos Naturales.*

Naranjo, K. (2014). *Evolución Geomorfológica asociada a la sedimentación 108 de LaCordillera de la Costa entre los Ríos Aconcagua y Cachapoal/Rapel*. Chile: Universidad de Chile.

Panez-Pinto, A., Faúndez-Vergara, R., and Mansilla-Quiñones, C. (2017). Politización de la crisis hídrica en Chile: análisis del conflicto por el agua en la provincia de Petorca. *Water Landscape*. 10, 131–148. doi: 10.17561/at.10.3614

Radio Cooperativa. (2016). *Empresa determinó causas del derrame de concentrado de cobre en Los Andes*. (2016) Available online at: https://cooperativa.cl/noticias/pais/medioambiente/contaminacion/empresa-determino-causas-del-derrame-de-concentrado-de-cobre-en-los-andes/2016-02-28/141004.html (accessed February 28, 2016).

Rein, B., and Sirocko, F. (2002). In-situ reflectance spectroscopy–analyzing techniques for high-resolution pigment logging in sediment cores. *Int. J. Earth Sci.* 91, 950–954. doi: 10.1007/s00531-002-0264-0

Remeteiová, D., Ružičková, S., Mičková, V., Laubertová, M., and Slezáková, R. (2020). Evaluation of US EPA method 3052 microwave acid digestion for quantification of majority metals in waste printed circuit boards. *Metals* 10, 1511. doi: 10.3390/met10111511

Rivano, S., Sepúlveda, P., Boric, R., and Espiñeira, D. (1993). Hojas Quillota y Portillo, V Región. Servicio Nacional de Geología y Minería, Carta Geológica de Chile, 73.

Rouse, J. W., Haas, R. H., Schell, J. A., Deering, D. W., and Harlan, J. C. (1974). *Monitoring the Vernal Advancement and Retrogradation (Green Wave Effect) of Natural Vegetation NASA/GSFC type III Final Report*. Greenbelt, MD, USA.

Soto Bäuerle, M. V., Arriagada González, J., Castro Correa, C. P., Maerker, M., and Rodolfi, G. (2011). Relación entre el cambio de uso del suelo en la cuenca del Aconcagua y su litoral arenoso correlativo: Chile central. *Revista de Geografía Norte Grande*. 50, 187–202. doi: 10.4067/S0718-34022011000300011

Tapia, J., Mukherjee, A., Rodríguez, M. P., Murray, J., and Bhattacharya, P. (2022). Role of tectonics and climate on elevated arsenic in fluvial systems: Insights from surface water and sediments along regional transects of Chile. *Environ. Pollut.* 314, 120151. doi: 10.1016/j.envpol.2022.120151

Tauxe, L. (1998). *Paleomagnetic Principles and Practice*. London: Kluwer Academic Publisher

Tauxe, L. (2005). *Paleomagnetic Principles and Practice, Vol. 17*. Cham: Springer Science and Business Media.

Von Gunten, L., Grosjean, M., Kamenik, C., Fujak, M., and Urrutia, R. (2012). Calibrating biogeochemical and physical climate proxies from non-varved 110 lake sediments with meteorological data: methods and case studies. *J. Paleolimnol.* 47, 583–600. doi: 10.1007/s10933-012-9582-9

Von Gunten, L., Grosjean, M., Rein, B., Urrutia, R., and Appleby, P. (2009). A quantitative high-resolution summer temperature reconstruction based on sedimentary pigments from Laguna Aculeo, central Chile, back to AD 850. *The Holocene* 19, 873–881. doi: 10.1177/0959683609336573

Yang, J., Xia, D., Chen, Z., Wang, S., Gao, F., Liu, X., et al. (2023). Differentiating detrital and pedogenic contributions to the magnetic properties of aeolian deposits in the southern Tibetan Plateau: implications for paleoclimatic reconstruction. *Catena* 220, 106736. doi: 10.1016/j.catena.2022.106736

frontiers | Frontiers in Ecology and Evolution

TYPE Original Research
PUBLISHED 08 December 2023
DOI 10.3389/fevo.2023.1227020

OPEN ACCESS

EDITED BY
Laura Parducci,
Sapienza University of Rome, Italy

REVIEWED BY
Keely Mills,
The Lyell Centre, United Kingdom
Neal Michelutti,
Queen's University, Canada
Thomas A. Minckley,
University of Wyoming, United States

*CORRESPONDENCE
Antonio Maldonado
antonio.maldonado@ceaza.cl

RECEIVED 22 May 2023
ACCEPTED 17 November 2023
PUBLISHED 08 December 2023

CITATION
Martel-Cea A, Maldonado A, de Porras ME, Muñoz P, Maidana NI, Massaferro J and Schittek K (2023) A multiproxy approach to reconstruct the Late Holocene environmental dynamics of the semiarid Andes of central Chile (29°S). *Front. Ecol. Evol.* 11:1227020. doi: 10.3389/fevo.2023.1227020

A multiproxy approach to reconstruct the Late Holocene environmental dynamics of the semiarid Andes of central Chile (29°S)

Alejandra Martel-Cea[1,2], Antonio Maldonado[1,3]*, María Eugenia de Porras[4], Praxedes Muñoz[3], Nora I. Maidana[5,6], Julieta Massaferro[7] and Karsten Schittek[8]

[1]Laboratorio de Paleoecología y Paleoclimatología, Centro de Estudios Avanzados en Zonas Áridas (CEAZA), La Serena, Chile, [2]Laboratorio de Palinología y Reconstrucciones Ambientales, Instituto Ciencias de la Tierra, Universidad Austral de Chile, Valdivia, Chile, [3]Departamento de Biología Marina, Universidad Católica del Norte, Coquimbo, Chile, [4]Instituto Argentino de Nivología, Glaciología y Ciencias Ambientales – Consejo Nacional de Investigaciones Científicas y Técnicas de Argentina (IANIGLA-CONICET), Mendoza, Argentina, [5]Laboratorio de Diatomeas Continentales, Facultad de Ciencias Exactas y Naturales, Departamento de Biodiversidad y Biología Experimental, Universidad de Buenos Aires, Buenos Aires, Argentina, [6]Laboratorio de Diatomeas Continentales, Consejo Nacional de Investigaciones Científicas y Técnicas de Argentina (CONICET) – Universidad de Buenos Aires, Instituto de Biodiversidad y Biología Experimental y Aplicada (IBBEA), Buenos Aires, Argentina, [7]Programa de Estudios Aplicados a la Biodiversidad del Parque Nacional Nahuel Huapi – Consejo Nacional de Investigaciones Científicas y Técnicas de Argentina (CENAC-CONICET), Bariloche, Argentina, [8]Institute of Geography Education, University of Cologne, Cologne, Germany

Mountain ecosystems located in the Andes cordillera of central Chile (29–35°S) have been strongly affected by the ongoing Mega Drought since 2010, impacting the snow cover, the surficial water resources (and thereby water storage), as well as the mountain biota and ecosystem services. Paleoenvironmental records in this part of the semiarid Andes are key to estimating the effects of past climate changes on local communities helping to forecast the ecological and biological responses under the aridification trend projected during the 21st century. Here we present a 2400-year multiproxy paleoenvironmental reconstruction based on pollen, diatoms, chironomids, sedimentological and geochemical data (XRF and ICP-MS data) of Laguna El Calvario (29°S; 3994 m a.s.l), a small and shallow Andean lake. Four main hydrological phases were established based on changes in the lithogenic and geochemical results associated with allochthonous runoff input and the subsequent response of the biological proxies. Between 2400 and 1400 cal yrs BP, wetter than present conditions occurred based on the intense weathering of the lake basin and the dominance of upper Andean vegetation. A decrease in moisture along with sub-centennial discrete wet pulses and lake-level changes occurred until ~800 cal yrs BP followed long-term stable climate conditions between 1850 and 1950 AD as suggested by a drop in vegetation productivity and low lake levels. From 1950 AD to the present, a decline in moisture with a severe trend to drier conditions occurring in the last decades occurred as reflected by an upward vegetation belt displacement around Laguna El Calvario along with a turnover of diatom assemblages and high productivity in the water column.

KEYWORDS

semiarid Andes, climate change, multiproxy analysis, mountain ecosystems, lake sediments, Late Holocene

1 Introduction

Low water availability and uncontrolled changes in land use and cover are becoming the main stressors in semiarid western Andes (29°–34°S) ecosystems under the ongoing scenario of climatic change. In this regard, the desertification process is critical in the northernmost area (especially in the Coquimbo region; 29°–32°S) (Emanuelli et al., 2016; Pizarro-Tapia et al., 2021) given that it has negatively affected the biodiversity and the ecosystem services (e.g., socioeconomic activities). The Andes cordillera acts as a water reservoir of solid/liquid precipitation falling during a few rainy months and therefore, its role has taken key relevance under the decline of precipitation and rise of temperatures in the past decades (Falvey and Garreaud, 2009; Quintana and Aceituno, 2012; Barria et al., 2019; Garreaud et al., 2019). Given that those trends will be accentuated during the 21st century causing a reduction in the snow cover as well as in glacier extension and mass balance, the projected decrease in streamflow (water supply) to the lowlands is critical (Vicuña et al., 2011).

To have a deep comprehension of how climate-sensitive high mountain ecosystems in the semiarid Andes will respond to future climate change in the mid-to-long term scale, it is necessary to understand past environmental dynamics. Despite the scarce high-elevation paleoenvironmental records in the semiarid Andes, those published in the last decade have helped to infer hydrological changes associated with the latitudinal dynamics of the northern border of the Southern Westerly Winds (SWW) and its interaction with the Southeast Pacific Subtropical Anticyclone (SEPSA) (Martel-Cea et al., 2016; Tiner et al., 2018; Mayta and Maldonado, 2022). Pollen records from central Chile (33°–36°S) suggested a high short-term variability during the Late Holocene attributed to an increased frequency of El Niño Southern Oscillation (ENSO) events (Jenny et al., 2002a; Maldonado and Villagrán, 2006; Frugone-Álvarez et al., 2020; Muñoz et al., 2020). The establishment of the modern semiarid conditions occurred around 600–700 calibrated years before the present (hereafter cal yrs BP) in the semiarid Andes (Martel-Cea et al., 2016; Mayta and Maldonado, 2022).

This work therefore presents a new Late Holocene environmental reconstruction from a high-altitude lacustrine record in the semiarid Andes (29°S) based on a multiproxy approach. Sedimentological and geochemical proxies such as organic/inorganic matter content and trace elements along with biological proxies such as pollen, diatoms, and chironomids were analyzed. Specifically, Laguna El Calvario was chosen because of its high sensitivity to changes in the snow cover (the main source of water input to the lake) which further allows for the reconstruction of long-term changes in the past 2400 years in hydrology and limnological conditions.

2 Study area

Laguna El Calvario (29°34'7.63" S; 70°21'8.63" W, 3994 m a.s.l., depth ca. 1 m, 0.8 ha area) is a small closed shallow lake located at the head of a west–east oriented valley called Quebrada Matancilla in the semiarid Andes of central Chile (Figure 1). The lake is flanked by Pleistocene-Holocene glacier deposits. The surrounding hills and basal bedrock consist of K-rich intrusive plutonic rocks of the Permian period [Guanta plutonic complex Peg(t) and Peg(gd)] which are mainly composed of tonalite and granodiorite (Nasi et al., 1985; Murillo et al., 2017). Indeed, industrial mining activities for the exploitation of Cu, Au, and Fe have been developed during the last 100 years in the semiarid Andes of central Chile (SERPLAC, 1986) having important effects on high Andean ecosystems (e.g., on natural water reservoirs; Oyarzún et al., 2006).

The climate of the study area is cold semiarid with Mediterranean influence characterized by cold/wet winters and dry/warm summers. Annual precipitation reaches 130 mm (JJA:

FIGURE 1
(A) South America and central Chile map showing the location of Laguna El Calvario (LCA) and some of the sites mentioned in the text; **(B)** 3D image of the Laguna El Calvario valley (DEM ALOS PALSAR SRTM 12.5 m JAXTA); and **(C)** photograph of Laguna El Calvario from the west.

60%) while the mean annual temperature is 3.8°C (DJF: 7.7°C; JJA: 0°C) (CRU 1980–2016). Winter precipitation originates from frontal systems associated with the northern border of the Southern Westerlies belt and is modulated by its interaction with the subtropical Anticyclone. While the frontal systems migrate in the NW-SE direction, they are intercepted by the Andes cordillera causing a strong rainfall gradient along the west side of the Andes (orographic enhancement) (Falvey and Garreaud, 2007). As the mean annual altitude of the 0°C isotherm at 29°S is located at ~4300 m a.s.l. (Carrasco et al., 2005; Barria et al., 2019), most of the precipitation around Laguna El Calvario falls as snow. During summertime, rainfall events are less frequent and correspond to convective storms coming from the eastern side of the Andes Cordillera accounting for less than 10% of the annual precipitation (Garreaud and Rutllant, 1997; Viale and Garreaud, 2014). However, summer storms bring fresh snow and cloud cover that reduce the albedo (and therefore sublimation), diminishing glacier melting in the semiarid Andes (Abermann et al., 2014). The climate interannual-to-quasidecadal variability in the area is strongly influenced by the El Niño Southern Oscillation (ENSO; positive phase), which is responsible for higher-than-average amounts of winter precipitation (Aceituno, 1988; Montecinos and Aceituno, 2003; Garreaud, 2009; Quintana and Aceituno, 2012). The high correlation between the warm ENSO phase and above-average accumulation of snowpack, increased streamflow, and positive glacier mass balance have relieved the arid trend observed in the last decades in the subtropical semiarid Andes (Masiokas et al., 2006; Gascoin et al., 2011). On the other hand, the Southern Annular Mode (SAM) in its negative (positive) phase promotes higher(lower)-than-average precipitation in south-central Chile (Quintana and Aceituno, 2012).

The vegetation composition and distribution follow the steep gradient of the semiarid Andes (so-called vegetation belts) linked to the abrupt changes in temperature, precipitation, topography (such as slope orientation), and soil characteristics. Both species diversity and plant cover decline with elevation due to the extreme conditions in the high Andean environments (Villagrán et al., 1983; Arroyo et al., 1988; Squeo et al., 1993; López-Angulo et al., 2018). On the other hand, the length of the growing season also shortens with elevation and the maximum primary productivity is recorded from the late spring (Nov–Dec) to late summer (March) (Squeo et al., 1994; Rudloff et al., 2021). Following the biogeographic data provided by Luebert and Pliscoff (2017) and the terminology of Squeo et al. (1994), it is possible to differentiate three main vegetation belts:

Pre-Andean belt (<2700m a.s.l.), characterized by major life forms such as shrubs, cacti, perennial and annual herbs. The most common species are *Ephedra chilensis, Colliguaja odorifera*, *Adesmia confusa*, *A. microphylla, Haplopappus angustifolius, Cumulopuntia sphaerica.* Tree species are restricted to azonal areas (meadows in ravines). This vegetation belt is strongly disturbed by anthropic activities and the vegetation cover reaches up to 40%.

Sub-Andean belt (2700–3500 m a.s.l.), the major life forms are shrubs and perennial herbs such as *Senecio proteus, Haplopappus baylahuen, Ephedra breana, Chuquiraga ulicina, Adesmia parviflora, A. hystrix. Atriplex imbricata, Chaetanthera limbate, Fabiana viscosa, F. imbricata, Viviania marifolia*, and *Cristaria andicola*. Tree species may appear in meadows up to 2900 m. This belt also has a cover ca. 40%.

Andean belt (3500–4450 masl) dominated by shrubs, perennial herbs, and cushion plants can be further divided into the lower and upper Andean belt. The lower Andean belt (up to 4250 m; cover ca. 27%) is characterized by *Adesmia subterranea, A. echinus, A. aegiceras*, *Azorella madreporica, Stipa chrysophylla, S. frigida*, *Cistanthe picta, Chaetanthera minuta*, and *C. sphaeroidalis.* The upper Andean belt (4250–4450 m: cover ca. 0.7%) is mainly composed of perennial herbs and grasses and a few dwarf shrubs such as *Chaetanthera sphaeroidalis*, *C. pulvinate, Stipa frigida, Adesmia subterranea, A. capitellata, Senecio pissisii*, and *S. socompae.*

3 Methodology

3.1 Coring and sedimentological, chronological, and geochemical analyses

Four short cores of Laguna El Calvario (LCA) were retrieved in 2017 using a UWITEC© gravity corer. All the cores were lithologically characterized through X-radiographs and visual descriptions. The LCA SHC-4 core was selected for performing the multiproxy analysis given it was the longest (33 cm long; Figure 1 Supplementary Material). The sedimentological analysis included a loss on ignition, X-ray fluorescence analysis (XRF), and inductively coupled plasma mass spectrometry (ICP-MS). Loss-on ignition was assessed at a contiguous 1 cm interval to estimate organic, inorganic, and carbonate contents (Heiri et al., 2001). The chronology of the Laguna El Calvario record was established through ^{210}Pb and ^{14}C dating techniques. The ^{210}Pb activities (dpm g^{-1}) were estimated for the first 15 cm through its daughter radionuclide ^{210}Po which is in secular equilibrium (Table 1 Supplementary Material). The chemical procedure included the acid digestion of sediment samples with the addition of ^{209}Po as a yield tracer and the deposition of the ^{210}Po onto ultrapure silver discs (Flynn, 1968). Activities were quantified in a Canberra Quad Alpha Spectrometer until a 1 σ error was achieved. Additionally, five bulk sediment samples were analyzed for AMS radiocarbon dating in the Direct AMS laboratory, USA. Levels 0–1 cm and 6–7 cm were analyzed for the ^{14}C measurements in order to check any ^{14}C reservoir effect, a common issue in high Andean lakes. According to the ^{210}Pb model these levels correspond to the second half of the 20th century, −60 and −9 cal yrs BP, respectively. To estimate the reservoir effect in the Laguna El Calvario, the ^{14}C ages from levels 0–1 cm and 6–7 cm were averaged resulting in a reservoir age of 1041 ^{14}C yrs BP (950 cal yrs BP), which was subtracted from the remaining three older radiocarbon ages (Table 1). Then, the radiocarbon ages were calibrated with the SHCal20 curve (Hogg et al., 2020) and the age-depth model was computed using Plum (Aquino-López et al., 2018) with the rPlum R package (Blaauw et al., 2020). rPlum is a recently developed Bayesian approach that permits computing integrated

TABLE 1 AMS radiocarbon dates of Laguna El Calvario record for the core LCA SHC4 core.

Laboratory ID	Sample ID	Depth (cm)	Material	^{14}C age	Corrected cal. ages	^{210}Pb ages (mid-point)
D-AMS 021485	LCA SHC4 0–1cm	0–1	Bulk sediment	544 ± 28	–	−60
D-AMS 021486	LCA SHC4 6–7cm	6–7	Bulk sediment	1598 ± 21	–	−9
D-AMS 021487	LCA SHC4 18–19cm	18–19	Bulk sediment	2008 ± 31	937	
D-AMS 021488	LCA SHC4 28–29cm	28–29	Bulk sediment	2549 ± 51	1478	
D-AMS 021489	LCA SHC4 32–32.5cm	32–32.5	Bulk sediment	3765 ± 49	2694	

chronologies without pre-modeling the ^{210}Pb ages but combining other chronostratigraphic markers such as the ^{14}C ages.

The XRF scanning was employed to measure the variability of geochemical elements on unprocessed sediments using an ITRAX core scanner (Cox Analytical Systems, Croudace et al., 2006) at the GEOPOLAR laboratory of the University of Bremen, Germany. Measures of the XRF series were established at each 2 mm interval and then a molybdenum tube at 40 kV and 10 mA was applied with an exposure time of 5 s for every measurement. The concentration of the different minerals was expressed in total counts (cnts) and elements over 100 cnts were selected. To support XRF data, continuous and discrete sediment samples were analyzed using an ICP-MS at UC-Davis facilities, from total digested sediment samples. The chemical procedure briefly consists of digesting ~250 mg of sediment with a mix of strong high-purity acids (HNO_3, HCl, $HCLO_4$, HF; Suprapure®Merck) in several steps until total dissolution, using screw-top PFA-Teflon™ vials and a hotplate Teflon™ PFA coating.

3.2 Inorganic proxies

Water content, organic matter, and grain size influence the scanning densities on XRF analysis (Zhang et al., 2020; Mondal et al., 2021), therefore ICP-MS was used to verify the trends of the measured elements included in this work. The elements Ti, K, Sr, and Rb can be associated with allochthonous detrital input into the lake (Guyard et al., 2007; Davies et al., 2015). The Ti/coh ratio was used as a proxy of clastic input (Ohlendorf et al., 2014; Schittek et al., 2016). The Zr/Ti ratio was used to infer the grain size given that Zr is highly abundant in the coarse silt fraction whereas Ti can be found in the clay to fine-silt fraction (Oldfield et al., 2003). Therefore, high Zr/Ti ratio values indicate increased coarse silt influx (Shala et al., 2014). The Si, P, Cd, U, and Cu elements were standardized by Titanium deposition.

3.3 Biological proxies

Pollen, diatom, and chironomid records were analyzed at 2 cm discrete intervals so each biological proxy record consisted of 17 samples. For the pollen analysis, 1 cm^3 of these sediment samples were processed following the standardized methods outlined by Faegri and Iversen (1989), including KOH treatment, sieving, acids (HCl and HF for carbonate and silicate removal), and acetolysis. In levels with low pollen concentration, an additional 2 cm^3 of sediment was processed. For the estimation of pollen concentration (grains cm^{-3}), tablets of *Lycopodium clavatum* were added to each sediment sample (Stockmarr, 1971). The palynomorphs were determined at the most detailed taxonomic level under a microscope (400–1000×) aided by pollen taxonomic keys (Heusser, 1971; Markgraf and D'Antoni, 1978) and reference samples from the Laboratorio de Paleoecología y Paleoclimatología of the Centro de Estudios Avanzados en Zonas Áridas (CEAZA). The basic pollen sum includes a minimum of 300 terrestrial pollen grains per sample while paludal, aquatic, and/or non-pollen taxa such as zygospores (Zygnemataceae) and microalgae were incorporated in a separate sum. Relative abundances were calculated for each taxon. Pollen accumulation rates (grains cm^{-2} yr^{-1}) were calculated employing the pollen concentration values and sedimentation rate derived from the age-depth model.

Two (2) grams of sediment were processed for diatom analysis following the methodology outlined by Battarbee (1986). Each sample was dried, oxidized with H_2O_2, and heated for 2 minutes in a microwave. Finally, permanent preparations were mounted using Naphrax®. A minimum of 600 valves were counted to determine the relative abundances. For absolute abundances, the aliquot method (Battarbee, 1986) was used, following random transects. Results are expressed in valves per gram of dry sediment. The taxonomic literature on diatom determination included the monographic works of Metzeltin and Lange-Bertalot (1998); Metzeltin and Lange-Bertalot (2007), Rumrich et al. (2000), and Lange-Bertalot et al. (2017), among others.

Five (5) grams of wet sediment were processed for chironomid analysis. The sediment samples were deflocculated using 10% KOH solution at 50–70°C for 30 minutes and sieved through 100 and 200 um mesh sizes. Larval head capsules (HC) were hand-sorted from the residual sediment and mounted on permanent slides with Hidromatrix® mounting media. Taxonomic identification was performed under a Nikon Phase optic microscope at a magnification of 100–1000× with reference to available taxonomic literature (Massaferro and Brooks, 2002; Massaferro et al., 2013; Cranston, 2019).

Given the nature of each of the analyzed proxies in the Laguna El Calvario record, their sensitivity and response time to a given environmental/climatic change may differ from one to another. So we decided to analyze each of them separately and therefore integrate their signal in the discussion section taking into account the different spatial/temporal scales represented by each other.

4 Results

4.1 Chronology, lithology, organic and inorganic content, XRF and ICP-MS analyses

The retrieved core of Laguna El Calvario spans the last 2400 cal yrs BP (Figure 2). The part of the age–depth model based on the three radiocarbon dates is the most accurate possible concerning the given ages (Table 1). The ^{210}Pb radioactive activities showed good exponential decay and the unsupported activities occurred in the first 15 cm reaching the age of 1833 AD (Figure 2, Table 1 Supplementary Material), determining a supported activity of 0.85 ± 0.17 dpm g^{-1}. The mean sedimentation rate ranges around 0.13 ± 0.01 cm year^{-1} in the first 5 cm.

The lithological description and organic content of the sedimentological record of Laguna El Calvario (LCA-SHC4; 33 cm) are summarized in Figure 3. Between 33 and 28 cm the sediment is composed of a porous dark brownish silty sand with gravel-sized clasts. The organic matter and carbonate contents are around 25% and 3%, respectively, while the inorganic density exhibits its highest values (0.21–0.33 g cm^{-3}). The sediment composition shifts to clayey silt from 28 cm to the top of the core. Intercalated light–dark brown and green laminated layers are present around 20–28 cm and 2–8 cm whereas a brown homogeneous layer is present between 20 and 8 cm. The content of organic matter and clasts fluctuates around 22–42%, and 2.6–3.9%, respectively. Inorganic density ranged between 0.1 and 0.2 g cm^{-3}.

Regarding the geochemical results, changes in XRF-Molybdenum Incoherent/Coherent ratio (inc/coh) follow the LOI organic matter (%) and water content (%) (Figure 3). The elements Ti, K and Sr show similar trends throughout the core according both, XRF and ICP-MS data (Figure 4; Tables 2, 3 Supplementary Material), which validates the data obtained with XRF. Indeed, the strong coherence among these curves suggests the same origin of variability (Table 2 Supplementary Material). The sparse plant cover in the surroundings and the hydrological changes associated with the precipitation regime dynamics can modulate the terrigenous input into the lake therefore, the Ti/coh ratio was applied as an indirect indicator of precipitation. Thus, high values of Ti/coh ratio along with Ti, K, and Sr in the ICP-MS were recorded between 32 and 28 cm (Figure 4). Between 28 and 20 cm, Ti/coh ratio shows highly variable values with maxima around 27 and 21 cm concomitant with the occurrence of a dark layer (Figure 4). Between 20 and 8 cm, these ratio values are more stable but show a rising trend. Ti, K, and Sr and the Ti/coh ratio values display a

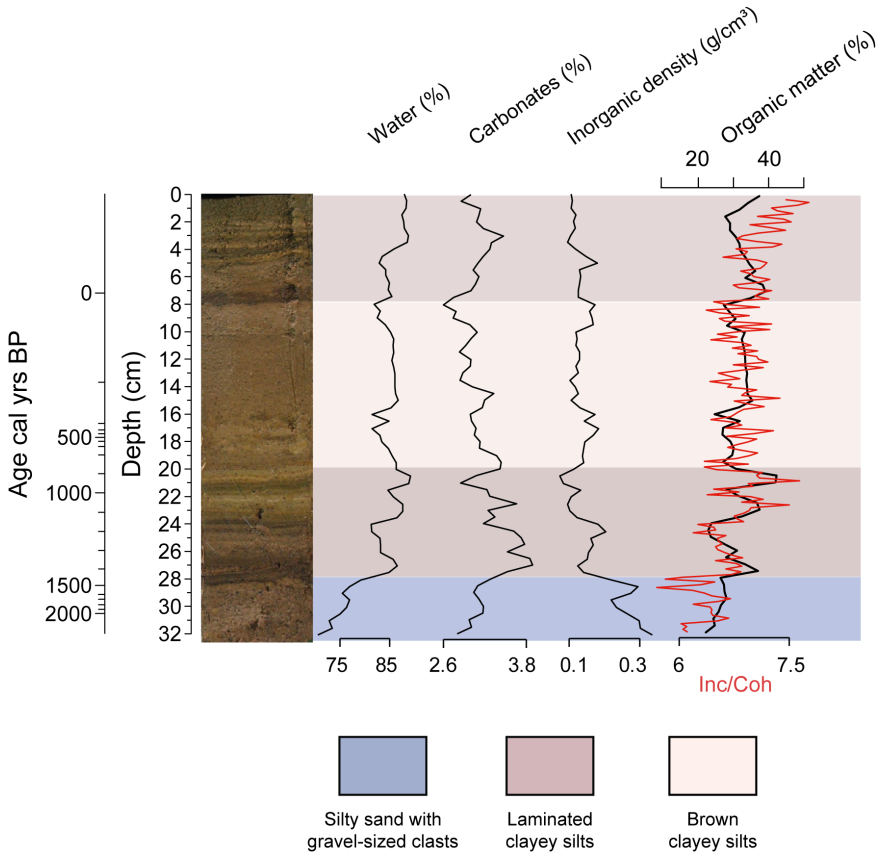

FIGURE 2
Bayesian age *vs* depth model constructed in rplum R package (Blaauw et al., 2020) based on the ^{210}Pb and radiocarbon ages of the LCA SH4 core. The weighted mean of the model is represented in the red dashed line where the black shadow shows the 95% confidence interval. Blue rectangles indicate the depth position and ^{210}Pb activities (dpm g^{-1}) (axis labels at the right) and ^{14}C samples correspond to the purple figures.

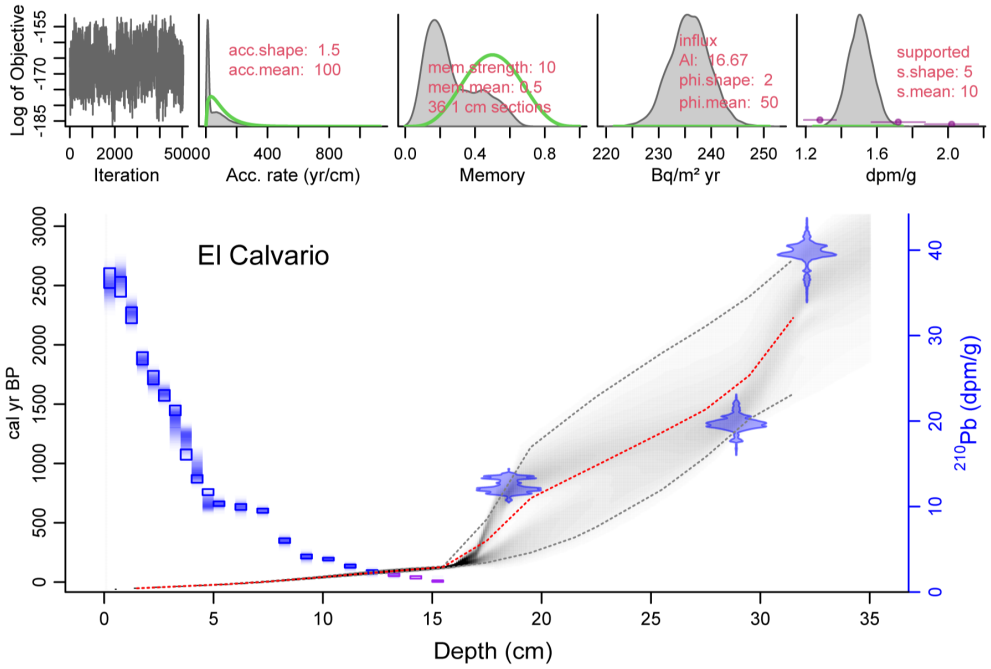

FIGURE 3
Lithology, water content and loss on ignition of the Laguna El Calvario record.

declining trend in the last 8 cm. Additionally, XRF data including Rb showed similar trends (Figure 4).

The Zr/Ti ratio, a proxy of grain size changes, shows peak values and high variability that are concomitant with laminated sediments between 28 and 20 cm and then, in the last 8 cm (Figure 4). The silica data based on the XRF analysis were not included in the results due to the low counts. In this regard, the Si/Ti ratio in the ICP_MS analysis shows different trends of the detrital-related elements since increases are observed in the topmost 6 cm of the record (Figure 4). So, the variation of silica in the record could be attributed to intra-lake processes such as productivity. The P/Ti ratio from the ICP-MS data also shows the highest values in the topmost 6 cm supporting the silica interpretation. The ICP-MS Cd/Ti and U/Ti ratios were considered as proxies of sulfidic conditions and organic sedimentation given that the U content is normally well correlated with organic fluxes reaching the bottom of the lake. In fact, Cd/Ti and U/Ti ratios present their highest values in the topmost 8 cm. Finally, the ICP-MS Cu/Ti is considered an indicator of mining activity in the region, which displays the highest concentrations in the uppermost 6 cm.

4.2 Biological proxy analyses

The palynological record shows a high plant diversity with pollen taxa defining the three main vegetation belts in the western semiarid Andean region: Poaceae, *Adesmia*-type, and *Nassauvia*-type (high and lower Andean); *Ephedra* (sub-Andean), and Chenopodiaceae and arboreal taxa (pre-Andean) (Figure 5A).

Between 32 and 22 cm (2400–1000 cal yrs BP; Figure 5A), the pollen record is dominated by Poaceae (up to 22%), *Chaethantera/Oriastrum* (6–17.3%), *Senecio*-type (6–12%), *Oxalis* (3–11%), *Ephedra* (<10%), Chenopodiaceae (9–14%) and *Arenaria* (4–13%). The cold-tolerant pollen types such as *Nassauvia*-type (up to 3.6%), *Adesmia*-type (up to 6.2%), *Laretia*-type (up to 5%) reach their highest values at the top of the zone (1500–1000 cal yrs BP) whereas Poaceae percentages gradually decline (8.5%). *Arenaria values* increase from 4 to 12% since 1300 cal yrs BP. Cyperaceae and *Myriophyllum*, paludal and aquatic taxa, display low frequencies (<2%) while the non-pollen palynomorph *Pediastrum* presents maximum values of ~28 cm. Pollen accumulation rates (PAR) for local terrestrial taxa are relatively low ranging between 9 and 25 pollen grains cm^{-2} yr^{-1}.

Between 22 and 12 cm (1000–75 cal yrs B; Figure 5A), the pollen assemblages are characterized by the slight recovery of Poaceae values up to 14.5% along with the decline of *Chaethantera/Oriastrum*, *Nassauvia*-type and *Adesmia*-type. *Ephedra* (up to 21.6%), Montiaceae (4–17%) and Verbenaceae (2–7%) values increase during this period. Cyperaceae percentages remain under 2% while *Pediastrum* values strongly decline to almost zero. *Spirogyra* spores display a mild increment and the *Zygnema* spores percentages increase at 16 cm (100 cal yrs BP). PAR values are the lowest for the whole record (total terrestrial pollen ca. 2 grains cm^{-2} yr^{-1}) increasing towards the end of this period (up to 40 grains cm^{-2} yr^{-1}).

Between 12 and 0 cm (75 cal yrs BP to present; Figure 5A), shrubs such as *Ephedra*, Chenopodiaceae, and *Senecio*-type percentages declined at the expenses of Poaceae (10–37%) and herbs values such as *Arenaria* (12–28%) and Montiaceae (13–21.6%). Other taxa percentages such as Verbenaceae (5–10%) and *Plantago* (1–2.5%) increase during this period similar to Cyperaceae percentages that show an increment towards the top of the record (2.6–12.8%). The non-pollen palynomorphs (NPPs), such as the

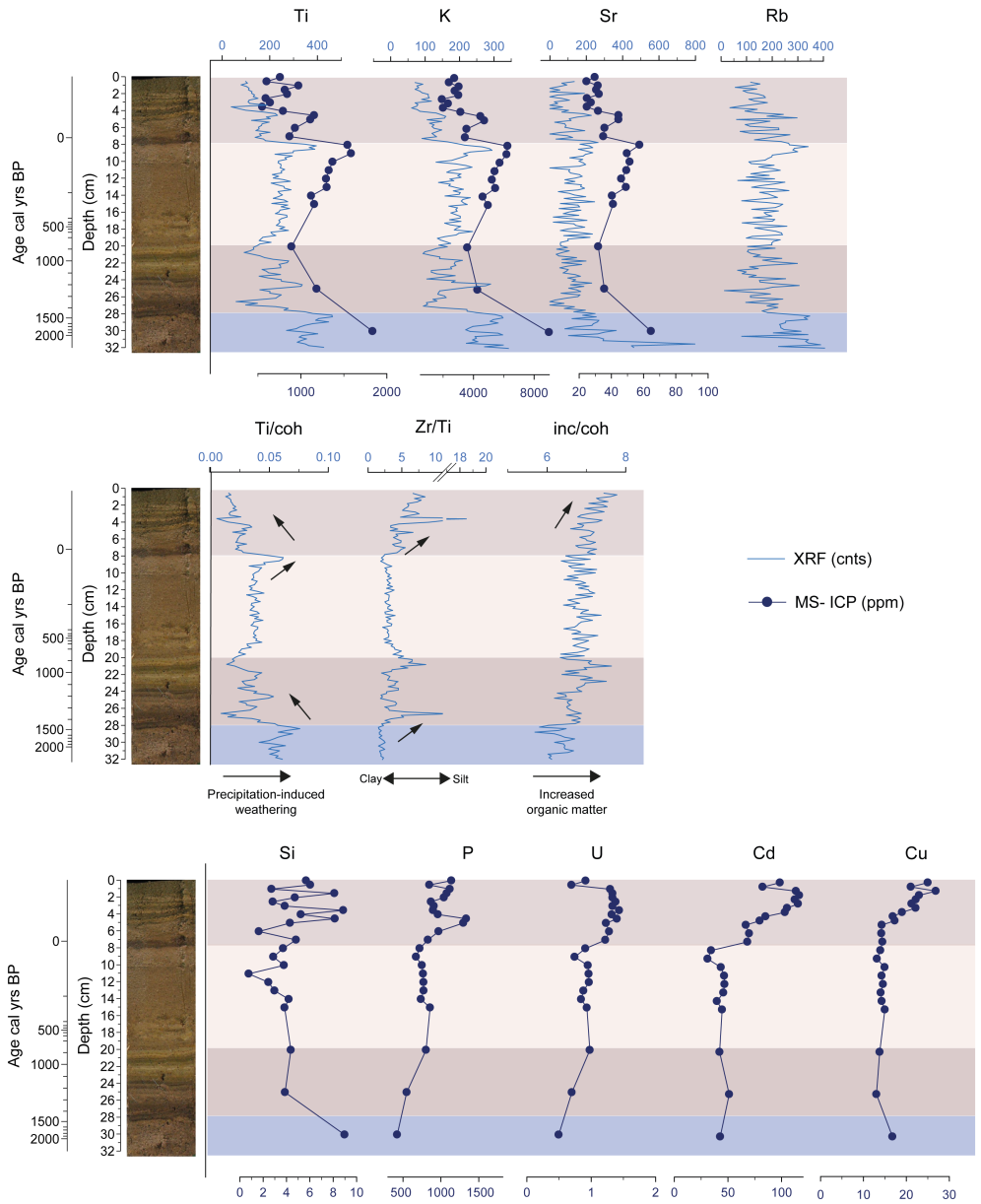

FIGURE 4
XRF and MS-ICP data of trace elements of the Laguna El Calvario.

algae *Pediastrum* and the *Zygnema* spores, values also show a significant increase whereas *Spyrogyra* spores are absent in this zone. PAR values are the highest for the whole sequence reaching up to 126 grains cm^{-2} yr^{-1}.

The diatom record of the Laguna El Calvario includes 15 taxa that have relative abundances over 5% (Figure 5B). Between 32 and 19 cm (2400–700 cal yrs BP), diatom assemblages are characterized by a high frequency of *Cymbella* spp. (20–42%), *Halamphora veneta* (15–25%) and *Gomphonema* spp. (20–50%). Associated taxa include *Planothidium aff. biporomum* (0–5%), *Pinnularia aff. brebissonii* (1–6%), *Craticula pampeana* (1–11.6% at 25–27 cm), *Craticula halophila* (0–7%), *Caloneis silicuta* (0–3%) and *Nitzchia* spp. (0–4%). Small fragilariods, including *Pseudostaurosira pseudoconstruens*, display a short-lived peak at the top of the period (ca. 1000 cal yrs BP). Diatoms abundance fluctuates between 60 and 130 × 10^7 valves per gram of dry sediment (Figure 5B). Between 19 and 5 cm (700 cal yrs BP to 1970 AD), *Gomphonema* spp. (up to 45%) and the small fragilarioids (with more than 45% at the top of the period) dominate while *Cymbella* spp. and *Halamphora veneta* values decline. Other secondary taxa such as *Fragilaria capucina* var., *Amphora copulata*, *Ulnaria ulna*, and *Encyonema silesiacum* showed minor increments. The diatom record presents a major diatom assemblage change in the last 5 cm (1970 AD to present) when most of the taxa values decline at expenses of the small fragilarioids (82–92%; Figure 5B). *Ulnaria ulna* exhibited a minor increase in the most surficial sample (5.6%).

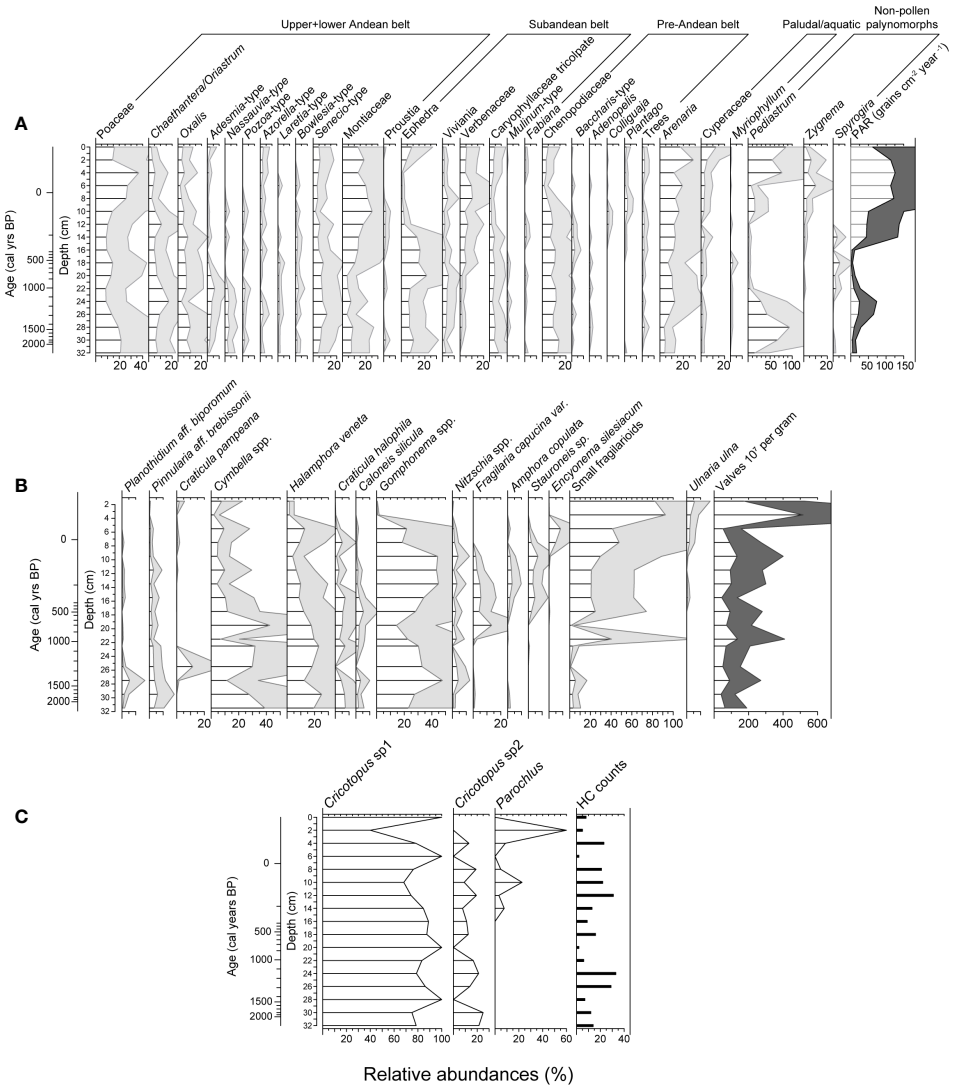

FIGURE 5
(A) Pollen record; **(B)** Diatom record; **(C)** Chironomid record of the Laguna El Calvario. The grey shadows in the pollen and diatom records correspond to exaggeration at 3x.

The chironomid record is characterized by the presence of 3 morphotypes (Figure 5C). The dominant morphotype is *Cricotopus* sp1 with ca. 80% of the total relative abundance associated with *Cricotopus* sp 2 (ca.15%) and *Parochlus* < 5%. From 32 to 14 cm (2400–120 cal yrs BP), the chironomid assemblages are dominated by the morphotypes *Cricotopus* sp1 and *Cricotopus* sp2. The Head Capsules (HC) counts are highly variable ranging between 2 and 33 (Figure 5C). Between 14 and 0 cm (from 120 cal yrs BP to 2014 AD), the chironomid record shows a clear alternation of *Cricotopus* and *Parochlus* abundance whereas the HC counts ranged from 31 and 2. *Cricotopus* sp1 dominates the whole record except for a peak of *Parochlus* at 2 cm. *Cricotopus* sp 2 co-dominates the records but disappears in the topmost 2 cm (Figure 5C). Given the low counts of HC, we interpreted with caution the chironomid record which was supported with the other proxies.

5 Discussion

5.1 Past environmental changes in Laguna El Calvario

The multiproxy analysis of Laguna El Calvario allows us to have a broad perspective of the past environmental changes during the last 2400 years in the western semiarid Andes (29°S). Following the lithological and biological changes in the sedimentary record (Figures 3–5) four main phases can be distinguished.

5.1.1 Phase 1: from 2400 to 1400 cal yr BP

Between 2400 and 1400 cal yrs BP the sedimentary record of Laguna El Calvario is characterized by the presence of sands with gravel-sized clasts (Figure 2) with high inorganic density and high values of Ti/coh ratio (particularly between 2400–2000 cal yrs BP) as

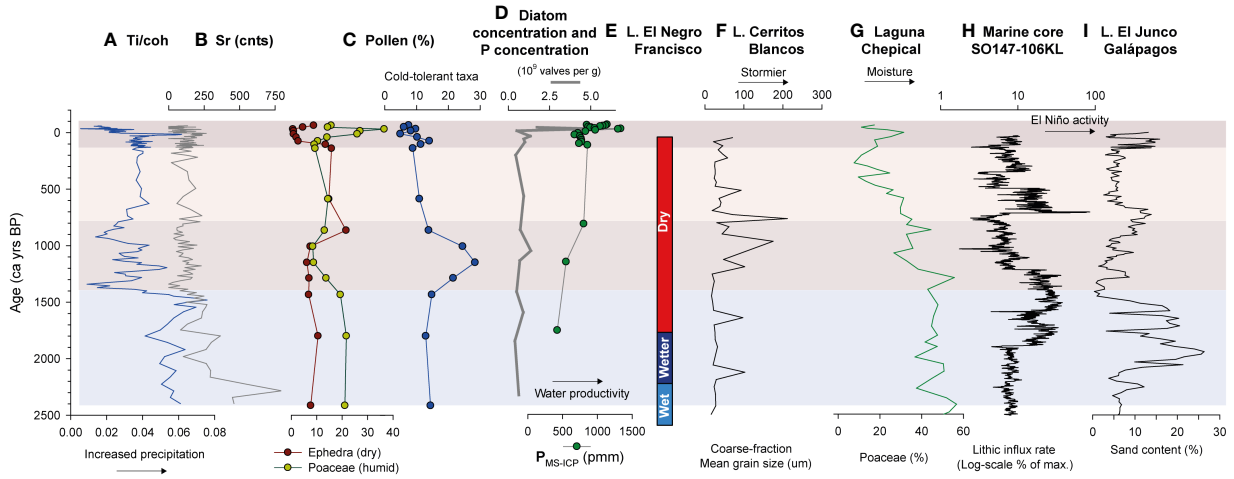

FIGURE 6
(A) Titanium/Molybdenum coherent ratio (XRF); **(B)** Sr (XRF); **(C)** Pollen; **(D)** Diatom and Phosphorus concentrations of the Laguna El Calvario; **(E)** Hydrological changes in the Andean lake Laguna El Negro Francisco (27°S; 4125 m a.s.l., Grosjean et al., 1997); **(F)** Storm activity in the Andean lake Laguna Cerritos Blancos (30°S, 3850 m a.s.l., Tiner et al., 2018); **(G)** Moisture changes in the Andean lake Laguna Chepical (32°S, 3050 m a.s.l., Martel-Cea et al., 2016); **(H)** El Niño activity inferred by Lithic influx in a sediment core located in the Peruvian offshore (Rein et al., 2005) and **(I)** Sand content in the Laguna El Junco, Galápagos archipelago, Ecuador (Conroy et al., 2008). Shadows bars correspond to the phases discussed in text.

well other elements (Figures 4, 6A, B). These sedimentological and geochemical features suggest a relatively high-energy deposition together with intense allochthonous sediment input that might be associated with high precipitation by this time (Haberzettl et al., 2005; Haberzettl et al., 2007; Schittek et al., 2016). The latter may also indicate glacial activity or increased runoff of detrital material after glacial retreatment in the basin. A similar situation has been observed in the glacial sediments from an Andean lake in Perú, where a high concentration of Sr was associated with erosion of granodiorite bedrock triggered by active glaciers (Stansell et al., 2013). More humid and colder than today conditions are reflected by the pollen record until 1400 cal yrs BP, supporting the latter. High Poaceae frequency and cold-tolerant taxa (*Chaetanthera/Oriastrum*, *Nassauvia*-type, *Adesmia*-type, *Azorella*-type, *Laretia*-type, *Senecio*-type, and Oxalis) percentages along with low pollen accumulation rates (PAR) before 1500 cal yrs BP (Figure 5A) reflect the upper Andean belt currently located 250 m above the Laguna El Calvario. However, the vegetation cover of the lower Andean belt that currently surrounds the lake catchment (4000 m a.s.l.; Figure 1) is low due to very low growth rates promoted by cold temperatures, even during the warmest months (Rudloff et al., 2021).

The diatom richness is characterized by the presence of the epiphytic diatoms *Planothidium* aff. *biporomum*, *Cymbella* spp. and *Gomphonema* spp. along with the benthic *Halamphora veneta* and *Craticula* spp. between 2400 to 1400 cal yrs BP. These assemblages reveal a shallow, vegetated, and saline-prone (particularly by the presence of *Gomphonema* spp. and *Halamphora veneta)* lacustrine environment (Figure 5B) (e.g., Jenny et al., 2002a; Jenny et al., 2002b; Hassan et al., 2013) but also the occurrence of oxygenated and shallow freshwater evidenced by the high frequency of the planktonic green algae *Pediastrum* sp. (Figure 5A) (Innes and Zong, 2021). The presence of the littoral cold-adapted *Cricotopus* as the dominant taxa in this part of the chironomid record (Figure 5C) also supports the cold and shallow conditions (Matthews-Bird et al., 2016; Motta and Massaferro, 2019; Martel-Cea et al., 2021). Additionally, the lowest values of Phosphorus and diatom concentrations may evidence low primary productivity in the water column (Figures 5B and 6D). Wet years before 1400 cal yrs BP may have increased the water input to the lake via snowmelt and/or upslope fluvio-glacial flow triggering the temporary rise of the lake level and promoting the increment of habitat opportunities for the aquatic biota (e.g., Innes and Zong, 2021).

5.1.2 Phase 2: from 1400 and 800 cal yr BP

After 1400 cal yrs BP, a shift from sand to laminated clayey silts characterized the sedimentary sequence until 800 cal yrs BP reflecting the onset of typical lacustrine-type sedimentation. The rise and fluctuation of the Zr/Ti ratio peaking around 1400–1300 and 1000–850 cal yrs BP (Figure 4) indicate an increased input of the coarser silt fraction to the lake (Oldfield et al., 2003). This might be associated with an increase in torrential rainfall, an upward displacement of the zero isotherm, or rapid melting of the snowpack as stated for the previous period. This is supported by the drop and variations of Ti/coh ratio values (Figure 6A) that imply a decrease of precipitation under a centennial-scale variability with moderate magnitude wet spells around 1200 and 1100 cal yrs BP. The pollen record shows the increment of cold-tolerant taxa (*Chaethantera/Oriastrum, Adesmia*-type, *Azorella*-type), *Arenaria* (Figure 5A), and a slight decline of Poaceae (Figure 6C) between 1400 and 800 cal yrs BP, suggesting the occurrence of cold conditions. The mild increment of PAR values (Figure 5A) can be related to an increase in temperature during the growing season (i.e., an amelioration of climatic conditions allowing the expansion of the plant cover; Squeo et al., 2006; Rudloff et al., 2021). *Arenaria* together with the persistence of *Cricotopus* spp. pointed out a decline in the lake level and/or expansion of the riparian/coastal zone (Riedemann et al., 2008; Markgraf et al., 2009; Teillier et al., 2011; Martel-Cea et al., 2016). This could be associated with a seasonal retraction of the lake that should have been constant over time in order to be recorded at sub-centennial time scales. The

aquatic taxa also point out the decline of the lake level given the sustained drop of *Pediastrum* sp. (Figure 5A). In this context, Shala et al. (2014) recorded increased Zr/Ti ratio when silt deposits in the littoral zone were eroded after the decline of the water column in a Finnish glacial lake. Therefore, the Zr/Ti increase occurred around 1350 and ca. 900 cal yrs BP in the Laguna El Calvario record could be related to an increase of detrital material by erosion and/or transport. To sum up, increased or sustained precipitation associated with cold conditions under a more pronounced seasonality occurred between 1400 and 800 cal yrs BP, compared to the previous phase.

5.1.3 Phase 3: from 800 cal yrs BP to 1850 AD

A shift from laminated to homogenous clayey silt sediment, a decline of silt influxes (low Zr/Ti ratio, Figure 4), a mild increase and stabilization of Ti/coh (Figure 6A) and other detrital input indicators (Ti, K, Sr, Ca) trends may indicate stable climatic conditions regarding the previous phase. On the other hand, the pollen record shows a minor increase of Montiaceae and *Arenaria* along with the decline of cold-tolerant taxa (*Chaethantera/ Osriastrum, Nassauvia*-type, and *Adesmia*-type) from the Andean belt associated with an expansion of shrubs from Sub-Andean (*Ephedra*, Verbenaceae) and the Pre-Andean belt pollen types (*Baccharis*) to a lesser extent (Figure 5A). This may imply an upward displacement of vegetation belts even PAR values decrease would still indicate very sparse vegetation. The increase of spores of *Spirogyra*, the absence of *Pediastrum* sp. (Figure 5A) along with the increase of the small fragilarioids between 800 and 250 cal yrs BP (Figure 5B) reveals the persistence of a shallow lake environment under dry conditions. Particularly, *Spirogyra* is common in standing water that experiences seasonal desiccation, regressive stage, and/or very shallow freshwater (Hoshaw and McCourt, 1988; Medeanic, 2006; van Geel et al., 2020). To sum up, the multiproxy record of Laguna El Calvario reflects a phase of increased aridity with an upward expansion of vegetation belts, low lake levels, and stable low precipitation between 800 cal yrs BP and 1850 AD.

5.1.4 Phase 4: from 1850 to 2014 AD

From 1850 AD to 1940 AD, the Ti/coh ratio and the allochthonous elements (Ti, K, Sr, Rb) present important peaks and then show a two-step decline during the last 50 years (Figures 4, 6A, B). In the first half of the 20th century, the PAR reached maximum values with pollen assemblages dominated by Poaceae, Montiaceae, Verbenaceae, and *Arenaria* (Figures 4A, 5C) which reflect the establishment of wetter conditions in the Laguna El Calvario basin regarding the previous phase. However, a vegetation turnover occurred in the early 2000s when lowland taxa such as Chenopodiaceae and *Ephedra* increased relative to Poaceae, Montiaceae, and *Arenaria*. This vegetation shift implies a transition from wetter than present to the current semiarid conditions that may be associated with a decrease in precipitation and a rise in temperature as recorded by instrumental records in the semiarid Andes of central Chile (Morales et al., 2020). The same trend has previously been recorded at a regional scale resulting in the glacier equilibrium line altitude, an upward shift of the zero-isotherm altitude (Carrasco et al., 2005; Barria et al., 2019), and reduction of the glacier-covered area (~35%) (Hess et al., 2020) that ultimately have directly affected the primary productivity and phenology of the Andean communities (Rudloff et al., 2021). The increment of the Zr/Ti ratio since 1940 AD (Figure 4) can be linked to the decline of the water level causing an increment of coarser silts in the sedimentary sequence accumulated in the catchment during the previous wetter decades. During the 20th century, the aquatic assemblages display the increment of *Pediastrum* sp. along with Cyperaceae and *Zygnema* (whose habitat preferences are associated with marsh environments, Figure 5A; Innes and Zong, 2021). On the other hand, the diatom assemblages display a complete dominance of the tychoplanktonic small fragilarioids and *Ulnaria ulna* (Figure 5B) whereas the chironomid record shows the establishment and increment of *Parochlus* sp., a cold-stenothermal (and an oxy-conformer) littoral taxon (Figure 5C). All the proxies together suggest a shift from a saline-prone to a cold freshwater lake probably associated with an increase of the rock glacier/snow melting along with an oxygenated (during springs) and oligo-mesotrophic water column possibly with the occurrence of ice cover during wintertime (Lotter and Bigler, 2000; Alvial et al., 2008; Hassan et al., 2013; Martel-Cea et al., 2016; Martel-Cea et al., 2021).

Recent human activity is also evident in the pollen record around Laguna El Calvario. A major increase of the palatable *Plantago* genera occurred around 1900–1920 AD (Figure 5A) synchronous to the intense transhumant livestock farming (mainly goats) that began during the first part of the 20th century (Castillo, 2003). On the other hand, even with the persistence of *Ephedra* and Chenopodiaceae throughout the record, both taxa exhibit minima values around 1900–1980 AD. *Ephedra* and Chenopodiaceae have been commonly and/or extensively used as fodder plants and/or fuel resources in the region (e.g. Meneses, 2017; Muñoz and Villaseñor, 2018) which may explain their low percentages in the pollen record during the 20th century.

High values of Ti/coh ratio, P/Ti and Si/Ti ratios (ICP-MS data), organic matter (Figures 2, 4), and diatom concentrations (Figure 6D) in the second half of the 20th century pinpoint an important increment of primary productivity. High rates of U accumulation (Figure 4) have been normally related to reducing conditions in marine and lacustrine environments which would be related to the reduction of the soluble phase of U(VI) to U(IV) in the vicinity of Fe(III) and SO_4 reduction (Klinkhammer and Palmer, 1991; Francois et al., 1993; Zheng et al., 2002; Tribovillard et al., 2006). This could explain the high concentration of U/Ti and Cd/Ti ratios, both increasing under reducing environmental conditions and in the presence of sulfides. These would have happened during periods characterized by high organic sedimentation rates which agrees with P/Ti ratio values and diatom concentration increase, reflecting the organic production in the column water or in the benthic zone. Notwithstanding, in some cases, the particulate U sedimentation overcomes the accumulation by diagenetic reactions (Chappaz et al., 2010). Instead, the Cu forms organic complexes with dissolved organic matter in superficial waters and is rapidly removed from natural waters (Rader et al., 2019). In sediments, it binds with clays, oxides, sulfides, and organic

matter (Bryan et al., 2002; Tribovillard et al., 2006) increasing the concentrations of lake bottoms when anoxic conditions prevail (Sundelin and Eriksson, 2001). In this context, the increase of Cu (shown as Cu/Ti ratio; Figure 2 Supplementary Material) would be caused by increased organic compounds in the water column derived from primary productivity within the lake and the basin. However, this coupled Cu-primary productivity increase was not observed earlier in the record. An alternative explanation could be that the metal increases could be caused by anthropogenic impact, due to in the last century mining activities, 50 km close to the lake, that has had an enormous influence on air pollution, as has been recorded both on the coast and in the Andes (von Gunten et al., 2009a; Gayo et al., 2022).

5.2 Comparing the Laguna El Calvario record at the regional scale

In order to compare the long-term environmental changes of the Laguna El Calvario (LCA) record with other paleorecords of western South America, (1) the Ti/coh ratio was selected as a proxy of runoff-induced basin erosion (Figure 6A); (2) the high Andean grassland taxa Poaceae and lowland xerophytic *Ephedra* as a moisture availability proxy while *Chaetanthera/Oriastrum*, *Adesmia* type, *Azorella* type, *Nassauvia* type as a proxy of cold conditions (Figure 6B) and; (3) the P/Ti ratio (ICP-MS) and diatom concentration as a lake productivity proxies (Figure 6C).

The relative high persistence and dominance of humid taxa throughout the pollen record of the Laguna El Calvario are consistent with the establishment of a wet Late Holocene inferred by several paleorecords in central Chile (30–35°S). Increased winter precipitation has been recorded from 4000 cal yrs BP on in the subtropical Andes (Veit, 1996; Grosjean et al., 1997; Espizua, 2005; Martel-Cea et al., 2016; Tiner et al., 2018; Frugone-Álvarez et al., 2020; Mayta and Maldonado, 2022), the lowlands (Jenny et al., 2002b; Jenny et al., 2003; Villa-Martínez et al., 2003 and Frugone-Álvarez et al., 2017) and the coastal areas (Maldonado and Villagrán, 2002 and Maldonado and Villagrán, 2006). Intense glacial activity in El Encierro valley (29°S; Figure 1A) located northwards of Laguna El Calvario was recorded before 2600 cal yrs BP (Grosjean et al., 1998; Zech et al., 2006). So after this period of glacial advance (3000–2600 yrs cal BP; Grosjean et al., 1998), the Laguna El Calvario basin could have been formed when ice retreated around 2600 cal yrs BP. High lake levels in the Laguna El Negro Francisco in the Andes at 27°S (4125 m a.s.l., Figure 6D) (Grosjean et al., 1997) and a smooth trend to wet conditions in small lakes at 30°S (3900–3800 m a.s.l.) (Mayta and Maldonado, 2022) were recorded after 2700 cal yr BP. This chronology is almost consistent with the high erosion around the lake basin (Figures 6A, B) and the downward distribution of the vegetation belts in Laguna El Calvario before 1500 cal yrs BP (Figures 4, 6C). On the other hand, grain size and geochemical analysis from two lakes located further south (Laguna El Cepo and Laguna Cerritos Blancos, 30°S, 2900–3800 m a.s.l.; Figure 1A) suggest an increment of storm frequency since 2200 cal yrs BP (Figure 6F) (Tiner et al., 2018) whereas the pollen assemblages of Laguna Quebrada Parada and Laguna Corralito (Figure 1A) pinpoint the establishment of wetter conditions from 1900 cal yrs BP (Mayta and Maldonado, 2022). Synchronous wet conditions inferred Laguna El Calvario record around 2400–1600 cal yrs BP were recorded in Laguna Chepical (32°S; Figures 1B, 6G) that shows wetter than present conditions between 2700–1300 cal yrs BP (Martel-Cea et al., 2016). Coastal and lowland records reflect wetter conditions after 3000 cal yrs BP peaking after 1800 cal yrs BP that were associated with an equatorward position/migration of the northern border of the SWW (Jenny et al., 2002a; Maldonado and Villagrán, 2002; Jenny et al., 2003).

Between 1500 and 800 cal yrs BP, the Laguna El Calvario record reflects a high variability of precipitation at the centennial scale along with the persistence of cold conditions as recorded by the dominance of high-altitude pollen types. The other paleorecords from the Elqui valley (30°S; Figure 1A) also show wetter conditions coupled with an increase in storm frequency (Tiner et al., 2018; Mayta and Maldonado, 2022). However, the Laguna Chepical record (33°S) reflects a decrease of moisture by this time but an extended ice cover season (Figure 5G) (Martel-Cea et al., 2016). In the lowlands, the Laguna Aculeo (33°S; Figure 1A) record pinpoints wet conditions between 2500–700 cal yrs BP (Villa-Martínez et al., 2003) while Palo Colorado (32°S; Figure 1A), a coastal record, displays a retraction of wet indicators around 700 cal yrs BP (Maldonado and Villagrán, 2006).

After 800–750 cal yrs BP, a marine core record located at 41°S inferred a less humid interval as a result of the southward displacement of SWW (Lamy et al., 2001) in concordance with an increase of pollen types indicating drier conditions in Laguna El Calvario, Laguna Quebrada Parada and Laguna Corralito (Mayta and Maldonado, 2022). Superimposed on these long-term conditions, a high frequency of ENOS-modulated storms was recorded by different proxies in Laguna Aculeo (33°S) and Laguna del Maule (36°S; Figure 1A) (Jenny et al., 2002a; Frugone-Álvarez et al., 2020, respectively). So, dry general climatic conditions under a high variability associated with the ENSO may have prevailed north of 32°S but more marked southwards of 33°S.

After 1800 AD, the higher temporal resolution of the Laguna El Calvario record, increasing from 0.02 to 0.13 cm yr^{-1}, provides quite detailed data for the last two centuries (Figure 2 Supplementary Material). Drier than present conditions were replaced by colder ones as reflected by the increase in upper Andean belt elements (cold-tolerant taxa) around 1850 AD. This is synchronous to the last part of the Little Ice Age, recorded in central Chile lowlands as lower spring-summer temperatures (von Gunten et al., 2009b), glacial expansion in the high Andes at 35°S (Espizua and Pitte, 2009) and increased precipitation in central Chile (33–34.5°S; LeQuesne et al., 2006). Between 1900 and 1950 AD, wet pollen indicators (Poaceae) abundance increased at the expense of cold tolerant taxa pollen. Besides, a synchronous higher variability of runoff indicators related to an upward shift of the zero-isotherm altitude might suggest an increase in liquid precipitation. This increasing trend of precipitation was also recorded by the low-frequency signal of three ring chronologies of central Chile (33°–34.5°; LeQuesne et al., 2006).

During the last part of the 20th century, similar to modern dry conditions established in Laguna El Calvario synchronously to the

mediterranean Andes (Martel-Cea et al., 2016) and the Altiplano (Morales et al., 2012). The recent decline of Poaceae and the increase of lowland shrubs (*Ephedra* and Chenopodiaceae) may represent an ongoing upward displacement of plant communities in the subtropical Andes. This process can be directly linked to the ongoing climate change characterized by the establishment of extreme drought conditions (also called Mega Drought; Garreaud et al., 2019) that broadly affects the Andean lake basins in central Chile (Fuentealba et al., 2021). Regarding regional warming, warmer autumns and springs (Burger et al., 2018) may have influenced the nutrient enrichment (high productivity, OM, and P) in Laguna El Calvario (Figure 6D; Figure 2 Supplementary Material) but may have led in a drastic decline of primary productivity in the plant communities at the same time (Rudloff et al., 2021).

Climate variability in the subtropical Andes during the late Holocene, mainly after ~2000 cal yrs BP has been attributed to El Niño Southern Oscillation, whose positive phase (El Niño) originates rainy winters in central Chile (Jenny et al., 2002a; Maldonado and Villagrán, 2006; Martel-Cea et al., 2016; Frugone-Álvarez et al., 2020). Wetter than present conditions around 2400 and 1500 cal yrs BP as well as colder conditions until 800 cal yrs BP in Laguna El Calvario is near concomitant with the increased El Niño activity inferred by several tropical records from the Eastern Pacific with a range of ca. 2000 to ca. 1000 cal yrs BP (Figures 6G, I) (Moy et al., 2002: 2000–1000 cal yrs BP; Rein et al., 2005: 2000–1300 cal yrs BP; Conroy et al., 2008: 2000–1500 cal yrs BP). Therefore, ENSO may have played a key role in the hydrological dynamics in the Laguna El Calvario at least between 2000 and 1500 cal yrs BP. Most ENSO paleorecords show a more weakened activity or La Niña-like phase in the past 800 years that may explain the stable dry conditions displayed by the Laguna El Calvario record (Moy et al., 2002; Rein et al., 2005; Conroy et al., 2008). Some discrepancies among records of central Chile and the subtropical Andes during the last millennium (i.e., Laguna Aculeo, Laguna del Maule, and neoglacial advances) could be attributed to other large atmospheric anomalies such as Southern Annular Mode (SAM) that also could have played a key role in the past at the interannual scale (Vuille and Milana, 2007; Dätwyler et al., 2020). However, further studies are needed to elucidate the implications of the coupling SAM and ENSO modes of variability in the past by evaluating the sensibility of paleorecords of the semiarid Andes of central Chile.

6 Conclusions

The Laguna El Calvario record reflects significant climate-driven changes at millennial to sub-centennial timescales during the past 2400 years in the semiarid Andes of central Chile based on sedimentological, geochemical, pollen, diatoms and chironomids data. The sediment deposition onset in Laguna El Calvario might have occurred after ice retreatment around 2600 cal yrs BP. Geochemical analyses provided a good approximation of the allochthonous clastic input where the Ti/coh ratio allowed us to estimate the long-term changes in the precipitation regime along with the pollen record. Maximum values of Ti/coh ratio evidenced an intense runoff period before 1400 cal yrs BP. Increased precipitation and colder than present conditions may have triggered a 200 m downward shift of the Andean vegetation belts whereas the aquatic biota records (algae, diatoms, and chironomids) suggested cold and shallow waters in El Calvario. Between 1500 and 800 cal yrs BP, the Laguna El Calvario record reflects wetter and colder conditions under a high centennial-to-multidecadal variability (wetter pulses) of precipitation. After 800 yrs BP, an increase of lowland pollen types in Laguna El Calvario suggests the establishment of drier conditions under a high variability associated with ENSO until 1850 AD when the dominance of upper Andean belt elements (cold tolerant taxa) indicates colder conditions synchronous to the last part of the Little Ice Age. Between 1900 and 1950 AD, an increase of wet pollen indicators at expenses of cold-tolerant taxa pollen synchronous to higher variability of runoff indicators might be related to an upward shift of the zero-isotherm altitude, and therefore a major proportion of liquid precipitation. The modern establishment of the drought regime and the increment of temperature have been shown since 1950 AD and accentuated in the last decade (Mega Drought). In addition, higher lake productivity, the presence of exotic plants, and the heavy metal enrichment of the sediments of Laguna El Calvario may be associated with transhumance practices and the establishment of the industrial mining companies in the area (Anthropocene) which have played a key role in the mid-to-long-term resilience of mountain communities.

The sedimentary record of Laguna El Calvario is not just the northernmost Andean record in central Chile but is unique in that it provides such a high temporal resolution for the last two centuries. The agreement between the Laguna El Calvario climatic trends during this period and the dendrochronological and instrumental data is surprising and confirms the robustness of this record for the whole 2400 cal yrs BP. Indeed, the regional comparison with other paleorecords allows us to confirm that even though there is a quite robust pattern of the dynamics of the northern edge of the SWW at the millennial-to-centennial scale, there are temporal (at shorter times scales)/latitudinal asynchronies that need to be further analyzed.

Data availability statement

The raw data supporting the conclusions of this article will be made available by the authors, without undue reservation.

Author contributions

All authors have approved the final version of the manuscript and the individual contributions of each co-author to the article are: AM-C analyzed the pollen, diatom, chironomid, and sedimentological data and age-depth model, wrote and edited the manuscript with contributions from all coauthors. AM designed the study, retrieved the cores, obtained the funding and participated in writing and editing the manuscript. MdP retrieved the cores, obtained the funding and participated in writing and editing the manuscript. PM carried out the ^{210}Pb chronology, the analysis of ICP-MS data and participated in writing the manuscript. NM

carried out the diatom analysis and participated in writing the manuscript. JM carried out the chironomid analysis and participated in writing the manuscript. KS carried out the XRF analysis and participated in writing the manuscript.

Funding

The author(s) declare financial support was received for the research, authorship, and/or publication of this article. The funding for this work was provided by the ANID-FONDECYT #1180413, ANID-Millennium Science Initiative Program-NCN19_153, and ANID-R20F0008.

Acknowledgments

We thank Andres Zamora for his assistance during the coring collection campaign, Leonardo D. Rios for assistance with Figure 1, Marigen Heise and Claudia Alcaíno for their assistance with laboratory analysis, Alexander Rhein for the sedimentological description, and the Hospital Público San Juan de Dios de La Serena for the digital X-ray images of the core.

Conflict of interest

The authors declare that the research was conducted in the absence of any commercial or financial relationships that could be construed as a potential conflict of interest.

Publisher's note

All claims expressed in this article are solely those of the authors and do not necessarily represent those of their affiliated organizations, or those of the publisher, the editors and the reviewers. Any product that may be evaluated in this article, or claim that may be made by its manufacturer, is not guaranteed or endorsed by the publisher.

Supplementary material

The Supplementary Material for this article can be found online at: https://www.frontiersin.org/articles/10.3389/fevo.2023.1227020/full#supplementary-material

References

Abermann, J., Kinnard, C., and MacDonell, S. (2014). Albedo variations and the impact of clouds on glaciers in the Chilean semi-arid Andes. *J. Glaciology* 60 (219), 183–191. doi: 10.3189/2014JoG13J094

Aceituno, P. (1988). On the functioning of the southern oscillation in the south american sector. Part 1: surface climate. *Monthly Weather Rev.* 116, 505–524. doi: 10.1175/1520-0493(1988)116<0505:OTFOTS>2.0.CO;2

Alvial, I., Cruces, F., Araneda, A., M., G., and R., U. (2008). Estructura comunitaria de diatomeas contenidas en el estrato superficial de ocho lagos andinos de Chile Central. *Rev. Chil. Hist. Natural* 81, 83–94. doi: 10.4067/S0716-078X2008000100007

Arroyo, M. T. K., Squeo, F. A., Armesto, J. J., and Villagrán, C. (1988). Effects of aridity on plant diversity in the northern Chilean Andes: results of a natural experiment. *Ann. Missouri Botanical Garden* 75, 55–78. doi: 10.2307/2399466

Aquino-López, M. A., Blaauw, M., and Christen, J. A. (2018). Bayesian analysis of ^{210}Pb dating. *J. Agric. Biol. Environ. Stat.* 23, 317–333. doi: 10.1007/s13253-018-0328-7

Barria, I., Carrasco, J., Casassa, G., and Barria, P. (2019). Simulation of long-term changes of the equilibrium line altitude in the central Chilean andes mountains derived from atmospheric variables during the 1958–2018 period. *Front. Environ. Sci.* 7 (161). doi: 10.3389/fenvs.2019.00161

Battarbee, R. W. (1986). "Diatoms analysis," in *Handbook of Holocene palaeoecology and palaeohydrology* (New York: John Wiley & Sons).

Blaauw, M., Christen, J. A., and Aquino-López, M. A. (2020). "rplum: bayesian age-depth modelling of '^{210}Pb'-dated cores," in *R package version 0.1.4*. Available at: https://CRAN.R-project.org/package=rplum.

Bryan, S. E., Tipping, E., and Hamilton-Taylor, J. (2002). Comparison of measured and modelled copper binding by natural organic matter in freshwaters. *Comp. Biochem. Physiol. Part C: Toxicol. Pharmacol.* 133 (1), 37–49. doi: 10.1016/S1532-0456(02)00083-2

Burger, F., Brock, B., and Montecinos, A. (2018). Seasonal and elevational contrasts in temperature trends in Central Chile between 1979 and 2015. *Global Planetary Change* 162, 136–147. doi: 10.1016/j.gloplacha.2018.01.005

Carrasco, J. F., Casassa, G., and Quintana, J. (2005). Changes of the 0°C isotherm and the equilibrium line altitude in central Chile during the last quarter of the 20th century. *Hydrological Sci. J.* 50 (6), 933–948. doi: 10.1623/hysj.2005.50.6.933

Castillo, G. (2003). "La vuelta de los años: reseñas y perspectivas sobre las comunidades, el pastoreo y la tranhumancia en la región semiárida de Chile," in *Dinámicas de los sistemas agrarios en el Chile árido: la Región de Coquimbo. Santiago*. Eds. P. Livenais and X. Aranda (Santiago de Chile: LOM Ediciones), 65–116.

Chappaz, A., Gobeil, C., and Tessier, A. (2010). Controls on uranium distribution in lake sediments. *Geochimica Cosmochimica Acta* 74 (1), 203–214. doi: 10.1016/j.gca.2009.09.026

Conroy, J. L., Overpeck, J. T., Cole, J. E., Shanahan, T. M., and Steinitz-Kannan, M. (2008). Holocene changes in eastern tropical Pacific climate inferred from a Galápagos lake sediment record. *Quaternary Sci. Rev.* 27 (11), 1166–1180. doi: 10.1016/j.quascirev.2008.02.015

Cranston, P. S. (2019). Identification guide to genera of aquatic larval Chironomidae (Diptera) of Australia and New Zealand. *Zootaxa* 4706 (1), 071–102. doi: 10.11646/zootaxa.4706.1.3

Croudace, I. W., Rindby, A., Rothwell, R. G., and Rothwell, R. G. (2006). "ITRAX: description and evaluation of a new multi-function X-ray core scanner," in *New techniques in sediment core analysis*. Ed. R. G. Rothwell (London: Geological Society of London), 51–63.

Dätwyler, C., Grosjean, M., Steiger, N. J., and Neukom, R. (2020). Teleconnections and relationship between the El Niño–Southern Oscillation (ENSO) and the Southern Annular Mode (SAM) in reconstructions and models over the past millennium. *Clim. Past* 16 (2), 743–756. doi: 10.5194/cp-16-743-2020

Davies, S. J., Lamb, H. F., and Roberts, S. J. (2015). "Micro-XRF core scanning in palaeolimnology: recent developments," in *Micro-XRF Studies of Sediment Cores: Applications of a non-destructive tool for the environmental sciences*. Eds. I. W. Croudace and R. G. Rothwell (Dordrecht: Springer Netherlands), 189–226.

Emanuelli, P., Milla, F., Duarte, E., Torrealba, J., Garrido Ruiz, C., Colmenares, M., et al. (2016). "Diagnóstico de la desertificación en Chile y sus efectos en el desarrollo sustentable. Technical report 03," (Santiago, Chile: Corporación Nacional Forestal (CONAF)) 33 pp. Available at: https://bibliotecadigital.ciren.cl/handle/20.500.13082/32893. (Accessed November 23, 2023).

Espizua, L. E. (2005). Holocene glacier chronology of Valenzuela Valley, Mendoza Andes, Argentina. *Palaeogeogr., Palaeoclimatol., Palaeoecol.* 15 (7), 1079–1085. doi: 10.1191/0959683605hl866rr

Espizua, L. E., and Pitte, P. (2009). The Little Ice Age glacier advance in the Central Andes (35°S), Argentina. *Palaeogeography, Palaeoclimatology, Palaeoecology* 281, 345–350. doi: 10.1016/j.palaeo.2008.10.032

Faegri, K., and Iversen, J. (1989). *Textbook of pollen analysis* (Londres: John Wiley & Sons Ld).

Falvey, M., and Garreaud, R. D. (2007). Wintertime precipitation episodes in central Chile: associated meteorological conditions and orographic influences. *J. Hydrometeorology* 8, 171–193. doi: 10.1175/JHM562.1

Falvey, M., and Garreaud, R. D. (2009). Regional cooling in a warming world: Recent temperature trends in the southeast Pacific and along the west coast of subtropical South America, (1979-2006). *J. Geophysical Res.* 114 (D4), D04102. doi: 10.1029/2008jd010519

Flynn, W. (1968). The determination of low levels of polonium-210 in environmental materials. *Analytica chimica Acta* 43, 221–226. doi: 10.1016/S0003-2670(00)89210-7

Francois, R., Bacon, M. P., Altabet, M. A., and Labeyrie, L. D. (1993). Glacial/interglacial changes in sediment rain rate in the SW Indian Sector of subantarctic Waters as recorded by 230Th, 231Pa, U, and δ15N. *Paleoceanography* 8 (5), 611–629. doi: 10.1029/93PA00784

Frugone-Álvarez, M., Latorre, C., Barreiro-Lostres, F., Giralt, S., Moreno, A., Polanco-Martínez, J., et al. (2020). Volcanism and climate change as drivers in Holocene depositional dynamic of Laguna del Maule (Andes of central Chile – 36° S). *Clim. Past* 16 (4), 1097–1125. doi: 10.5194/cp-16-1097-2020

Frugone-Álvarez, M., Latorre, C., Giralt, S., Polanco-Martínez, J., Bernárdez, P., Oliva-Urcia, B., et al. (2017). A 7000-year high-resolution lake sediment record from coastal central Chile (Lago Vichuquén, 34°S): implications for past sea level and environmental variability. *J. Quaternary Sci.* 32 (6), 830–844. doi: 10.1002/jqs.2936

Fuentealba, M., Bahamóndez, C., Sarricolea, P., Meseguer-Ruiz, O., and Latorre, C. (2021). The 2010–2020 'megadrought' drives reduction in lake surface area in the Andes of central Chile (32° - 36°S). *J. Hydrology: Regional Stud.* 38, 100952. doi: 10.1016/j.ejrh.2021.100952

Garreaud, R. D. (2009). The Andes climate and weather. *Advanced Geosciences* 22, 3–11. doi: 10.5194/adgeo-22-3-2009

Garreaud, R. D., Boisier, J. P., Rondanelli, R., Montecinos, A., Sepúlveda, H. H., and Veloso-Aguila, D. (2019). The central Chile mega drought (2010–2018): A climate dynamics perspective. *Int. J. Climatology* 40 (1), 421–439. doi: 10.1002/joc.6219

Garreaud, R. D., and Rutllant, J. (1997). Precipitación estival en los Andes de Chile central: Aspectos climatológicos. *Atmósfera* 10, 191–211. Available at: https://www.revistascca.unam.mx/atm/index.php/atm/article/view/8418.

Gascoin, S., Kinnard, C., Ponce, R., Lhermitte, S., MacDonell, S., and Rabatel, A. (2011). Glacier contribution to streamflow in two headwaters of the Huasco River, Dry Andes of Chile. *Cryosphere* 5 (4), 1099–1113. doi: 10.5194/tc-5-1099-2011

Gayo, E. M., Muñoz, A. A., Maldonado, A., Lavergne, C., Francois, J. P., Rodríguez, D., et al. (2022). A cross-cutting approach for relating Anthropocene, environmental injustice and sacrifice zones. *Earth's Future* 10, e2021EF002217. doi: 10.1029/2021EF002217

Grosjean, M., Geyh, M. A., Messerli, B., Schreier, H., and Veit, H. (1998). A late-Holocene (<2600 BP) glacial advance in the south-central Andes (29°S), northern Chile. *Holocene* 8 (4), 473–479. doi: 10.1191/095968398677627864

Grosjean, M., Valero-Garcés, B. L., Geyh, M. A., Messerli, B., Schotterer, U., Schreier, H., et al. (1997). Mid- and late-Holocene limnogeology of Laguna del Negro Francisco, northern Chile, and its palaeoclimatic implications. *Holocene* 7 (2), 151–159. doi: 10.1177/095968369700700203

Guyard, H., Chapron, E., St-Onge, G., Anselmetti, F. S., Arnaud, F., Magand, O., et al. (2007). High-altitude varve records of abrupt environmental changes and mining activity over the last 4000 years in the Western French Alps (Lake Bramant, Grandes Rousses Massif). *Quat. Sci. Rev.* 26 (19), 2644–2660. doi: 10.1016/j.quascirev.2007.07.007

Haberzettl, T., Corbella, H., Fey, M., Janssen, S., Lücke, A., Mayr, C., et al. (2007). Lateglacial and Holocene wet—dry cycles in southern Patagonia: chronology, sedimentology and geochemistry of a lacustrine record from Laguna Potrok Aike, Argentina. *Holocene* 17 (3), 297–310. doi: 10.1177/0959683607076437

Haberzettl, T., Fey, M., Lücke, A., Maidana, N., Mayr, C., Ohlendorf, C., et al. (2005). Climatically induced lake level changes during the last two millennia as reflected in sediments of Laguna Potrok Aike, southern Patagonia (Santa Cruz, Argentina). *J. Paleolimnology* 33 (3), 283–302. doi: 10.1007/s10933-004-5331-z

Hassan, G. S., De Francesco, C. G., and Dieguez, S. (2013). The significance of modern diatoms as paleoenvironmental indicators along an altitudinal gradient in the Andean piedmont of central Argentina. *Palaeogeography Palaeoclimatology Palaeoecol.* 369 (0), 349–360. doi: 10.1016/j.palaeo.2012.11.002

Heiri, O., Lotter, A., and Lemcke, G. (2001). Loss on ignition as a method for estimating organic and carbonate content in sediments: reproducibility and comparability of results. *J. Paleolimnology* 25, 101–110. doi: 10.1023/A:1008119611481

Hess, K., Schmidt, S., Nüsser, M., Zang, C., and Dame, J. (2020). Glacier changes in the semi-arid huasco valley, Chile, between 1986 and 2016. *Geosciences* 10 (11), 429. doi: 10.3390/geosciences10110429

Heusser, C. J. (1971). *Pollen and spores of Chile: Modern types of the Pteridophyta, Gymnospermae, and Angiospermae* (Tucson: University of Arizona Press).

Hogg, A. G., Heaton, T. J., Hua, Q., Palmer, J. G., Turney, C. S. M., Southon, J., et al. (2020). SHCal20 southern hemisphere calibration, 0–55,000 years cal BP. *Radiocarbon* 62 (4), 759–778. doi: 10.1017/RDC.2020.59

Hoshaw, R. W., and McCourt, R. M. (1988). The Zygnemataceae (Chlorophyta): a twenty-year update of research. *Phycologia* 27 (4), 511–548. doi: 10.2216/i0031-8884-27-4-511.1

Innes, J. B., and Zong, Y. (2021). History of mid- and late holocene palaeofloods in the yangtze coastal lowlands, east China: evaluation of non-pollen palynomorph evidence, review and synthesis. *Quaternary* 4 (3), 21. doi: 10.3390/quat4030021

Jenny, B., Valero-Garcés, B. L., Urrutia, R., Kelts, K., Veit, H., Appleby, P. G., et al. (2002a). Moisture changes and fluctuations of the Westerlies in Mediterranean Central Chile during the last 2000 years: The Laguna Aculeo record (33°50'S). *Quaternary Int.* 87 (1), 3–18. doi: 10.1016/s1040-6182(01)00058-1

Jenny, B., Valero-Garcés, B. L., Villa-Martínez, R., Urrutia, R., Geyh, M., and Veit, H. (2002b). Early to mid-holocene aridity in central Chile and the southern westerlies: the laguna aculeo record (34°S). *Quaternary Res.* 58 (2), 160–170. doi: 10.1006/qres.2002.2370

Jenny, B., Wilhelm, D., and Valero-Garcés, B. L. (2003). The Southern Westerlies in Central Chile: Holocene precipitation estimates based on a water balance model for Laguna Aculeo (33°50'S). *Climate Dynamics* 20 (2), 269–280. doi: 10.1007/s00382-002-0267-3

Klinkhammer, G. P., and Palmer, M. R. (1991). Uranium in the oceans: Where it goes and why. *Geochimica Cosmochimica Acta* 55 (7), 1799–1806. doi: 10.1016/0016-7037(91)90024-Y

Lamy, F., Hebbeln, D., Röhl, U., and Wefer, G. (2001). Holocene rainfall variability in southern Chile: a marine record of latitudinal shifts of the Southern Westerlies. *Earth Planetary Sci. Lett.* 185 (3-4), 369–382. doi: 10.1016/s0012-821x(00)00381-2

Lange-Bertalot, H., Hofmann, G., Werum, M., and Cantonati, M. (2017). "Freshwater Benthic Diatoms of Central Europe. Over 800 common species used in ecological assessment. English edition with updated taxonomy and added species," Schmitten-Oberreifenberg (Germany): Koeltz Botanical Books.

LeQuesne, C., Stahle, D. W., Cleaveland, M. K., Therrell, M. D., Aravena, J. C., and Barichivich, J. (2006). Ancient austrocedrus tree-ring chronologies used to reconstruct central Chile precipitation variability from A.D. 1200 to 2000. *J. Clim.* 19, 5731-5744. doi: 10.1175/jcli3935.1

López-Angulo, J., Pescador, D. S., Sánchez, A. M., Mihoč, M. A. K., Cavieres, L. A., and Escudero, A. (2018). Determinants of high mountain plant diversity in the Chilean Andes: From regional to local spatial scales. *PloS One* 13 (7), e0200216. doi: 10.1371/journal.pone.0200216

Lotter, A. F., and Bigler, C. (2000). Do diatoms in the Swiss Alps reflect the length of ice-cover? *Aquat. Sci.* 62 (2), 125–141. doi: 10.1007/s000270050002

Luebert, F., and Pliscoff, P. (2017). *Sinopsis bioclimática y vegetacional de Chile.* (Santiago, Chile: Editorial Universitaria).

Maldonado, A., and Villagrán, C. (2002). Paleoenvironmental Changes in the Semiarid Coast of Chile (~32°S) during the Last 6200 cal Years Inferred from a Swamp-Forest Pollen Record. *Quaternary Res.* 58 (2), 130–138. doi: 10.1006/qres.2002.2353

Maldonado, A., and Villagrán, C. (2006). Climate variability over the last 9900 cal yr BP from a swamp forest pollen record along the semiarid coast of Chile. *Quaternary Res.* 66 (2), 246–258. doi: 10.1016/j.yqres.2006.04.003

Markgraf, V., and D'Antoni, H. L. (1978). *Pollen Flora of Argentina. Modern Spores and Pollen Types of Pteridophyta, Gymnospermae and Angiospermae.* (Tucson: The University of Arizona Press).

Markgraf, V., Whitlock, C., Anderson, R. S., and Garcia, A. (2009). Late Quaternary vegetation and fire history in the northernmost Nothofagus forest region: Mallin Vaca Lauquen, Neuquen Province, Argentina. *J. Quaternary Sci.* 24 (3), 248–258. doi: 10.1002/jqs.1233

Martel-Cea, A., Astorga, G. A., Hernández, M., Caputo, L., and Abarzúa, A. M. (2021). Modern chironomids (Diptera: Chironomidae) and the environmental variables that influence their distribution in the Araucanian lakes, south-central Chile. *Hydrobiologia* 848 (10), 2551–2568. doi: 10.1007/s10750-021-04575-0

Martel-Cea, A., Maldonado, A., Grosjean, M., Alvial, I., de Jong, R., Fritz, S. C., et al. (2016). Late Holocene environmental changes as recorded in the sediments of high Andean Laguna Chepical, Central Chile (32°S; 3050 m a.s.l.). *Palaeogeography Palaeoclimatology Palaeoecol.* 461, 44–54. doi: 10.1016/j.palaeo.2016.08.003

Masiokas, M., Villalba, R., Luckman, B. H., Le Quesne, C., and Aravena, J. C. (2006). Snowpack variations in the central andes of Argentina and Chile 1951 2005: large-scale atmospheric influences and implications for water resources in the region. *J. Climate* 19, 6634–6352. doi: 10.1175/JCLI3969.1

Massaferro, J., and Brooks, S. J. (2002). Response of chironomids to Late Quaternary environmental change in the Taitao Peninsula, southern Chile. *J. Quaternary Sci.* 17 (2), 101–111. doi: 10.1002/jqs.671

Massaferro, J., Ortega, C., Fuentes, R., and Araneda, A. (2013). Guia Para la Identificación de Tanytarsini Subfosiles (Diptera: Chironomidae: Chironominae) de la Patagonia. *Ameghiniana* 50 (3), 319–334. doi: 10.5710/amgh.05.03.2013.566

Matthews-Bird, F., Gosling, W. D., Coe, A. L., Bush, M., Mayle, F. E., Axford, Y., et al. (2016). Environmental controls on the distribution and diversity of lentic Chironomidae (Insecta: Diptera) across an altitudinal gradient in tropical South America. *Ecol. Evol.* 6 (1), 91–112. doi: 10.1002/ece3.1833

Mayta, C., and Maldonado, A. (2022). Climatic and ecological changes in the subtropical high Andes during the last 4,500 years. *Front. Earth Sci.* 10, 833219. doi: 10.3389/feart.2022.833219

Medeanic, S. (2006). Freshwater algal palynomorph records from Holocene deposits in the coastal plain of Rio Grande do Sul, Brazil. *Rev. Palaeobotany Palynology* 141 (1), 83–101. doi: 10.1016/j.revpalbo.2006.03.012

Meneses, R. (2017). Manual de produccion caprina [en línea]. In: *Boletin INIA - Instituto de Investigaciones Agropecuarias*. Available at: https://hdl.handle.net/20.500.14001/6672 (Accessed 18-07-2022).

Metzeltin, D., and Lange-Bertalot, H. (1998). Tropical diatoms of South America I. About 700 predominantly rarely known or new taxa representative of the neotropical flora. *Iconogr Diatomol* 5, 1–695.

Metzeltin, D., and Lange-Bertalot, H. (2007). Tropical diatoms of South America II. Special remarks on biogeographic disjunction. *Iconogr Diatomol* 18, 1–877.

Mondal, M. N., Horikawa, K., Seki, O., Nejigaki, K., Minami, H., Murayama, M., et al. (2021). Investigation of adequate calibration methods for X-ray fluorescence core scanning element count data: A case study of a marine sediment piston core from the Gulf of Alaska. *J. Mar. Sci. Eng.* 9 (5), 540. doi: 10.3390/jmse9050540

Montecinos, A., and Aceituno, P. (2003). Seasonality of the ENSO-related rainfall variability in central Chile and associated circulation anomalies. *J. Climate* 16 (2), 281–296. doi: 10.1175/1520-0442(2003)016<0281:SOTERR>2.0.CO;2

Morales, M. S., Christie, D. A., Villalba, R., Argollo, J., Pacajes, J., Silva, J. S., et al. (2012). Precipitation changes in the South American Altiplano since 1300 AD reconstructed by tree-rings. *Clim. Past* 8 (2), 653–666. doi: 10.5194/cp-8-653-2012

Morales, M. S., Cook, E. R., Barichivich, J., Christie, D. A., Villalba, R., LeQuesne, C., et al. (2020). Six hundred years of South American tree rings reveal an increase in severe hydroclimatic events since mid-20th century. *PNAS* 117 (29), 16816–16823. doi: 10.1073/pnas.2002411117

Motta, L., and Massaferro, J. (2019). Climate and site-specific factors shape chironomid taxonomic and functional diversity patterns in northern Patagonia. *Hydrobiologia* 839 (1), 131–143. doi: 10.1007/s10750-019-04001-6

Moy, C. M., Seltzer, G. O., Rodbell, D. T., and Anderson, D. M. (2002). Variability of El Nino/Southern Oscillation activity at millennial timescales during the Holocene epoch. *Nature* 420 (6912), 162–165.

Muñoz, P., Rebolledo, L., Dezileau, L., Maldonado, A., Mayr, C., Cárdenas, P., et al. (2020). Reconstructing past variations in environmental conditions and paleoproductivity over the last ~8000 years off north-central Chile (30° S). *Biogeosciences* 17 (22), 5763–5785. doi: 10.5194/bg-17-5763-2020

Muñoz, E. J., and Villaseñor, R. (2018). Uso de las plantas nativas por una comunidad de cabreros de Las Vegas de la quebrada de Tulahuén, Región de Coquimbo, Chile. *Idesia (Arica)* 36 (2), 243–258. doi: 10.4067/S0718-34292018005000201

Murillo, I., Velásquez, R., and Creixell, T. (2017). *Geología de la Áreas Guanta - Los Cuartitos y Paso de Vacas Heladas, Regiones de Atacama y Coquimbo. Escala 1: 100.000.* (Santiago de Chile: SERNAGEOMIN).

Nasi, C., Mpodozis, C., Moscoso, R., Maksaev, V., and Cornejo, P. (1985). El Batolito Elqui-Limarí (Paleozoico Superior-Triásico): características petrográficas, geoquímicas y significado tectónico. *Rev. Geológica Chile* 25-26, 77–111. doi: 10.5027/andgeoV12n2-3-a06

Ohlendorf, C., Fey, M., Massaferro, J., Haberzettl, T., Laprida, C., Lücke, A., et al. (2014). Late Holocene hydrology inferred from lacustrine sediments of Laguna Cháltel (southeastern Argentina). *Palaeogeography Palaeoclimatology Palaeoecol.* 411, 229–248. doi: 10.1016/j.palaeo.2014.06.030

Oldfield, F., Wake, R., Boyle, J., Jones, R., Nolan, S., Gibbs, Z., et al. (2003). The late-Holocene history of Gormire Lake (NE England) and its catchment: a multiproxy reconstruction of past human impact. *Holocene* 13 (5), 677–690. doi: 10.1191/0959683603hl654rp

Oyarzún, R., Lillo, J., Oyarzún, J., Higueras, P., and Maturana, H. (2006). Strong metal anomalies in stream sediments from semiarid watersheds in Northern Chile: When geological and structural analyses contribute to understanding environmental disturbances. *Int. Geology Rev.* 48 (12), 1133–1144. doi: 10.2747/0020-6814.48.12.1133

Pizarro-Tapia, R., Ibáñez-Córdova, A., García-Chevesich, P., Vallejos-Carrera, C., Sangüesa-Pool, C., and Mendoza-Mendoza, R. (2021). "The Chilean forest sector and its relationship with water resources," in *Water Resources of Chile*. Eds. B. Fernández and J. Gironás (Cham: Springer International Publishing), 301–315.

Quintana, J., and Aceituno, P. (2012). Changes in the rainfall regime along the extratropical west coast of South America (Chile): 30-43° S. *Atmosfera* 25 (1), 1–22. Available at: https://www.redalyc.org/articulo.oa?id=56523435001 (Accessed November 23, 2023).

Rader, K. J., Carbonaro, R. F., van Hullebusch, E. D., Baken, S., and Delbeke, K. (2019). The fate of copper added to surface water: field, laboratory, and modeling studies. *Environ. Toxicol. Chem.* 38 (7), 1386–1399. doi: 10.1002/etc.4440

Rein, B., Lückge, A., Reinhardt, L., Sirocko, F., Wolf, A., and Dullo, W.-C. (2005). El Niño variability off Peru during the last 20,000 years. *Paleoceanography* 20 (4), PA4003. doi: 10.1029/2004pa001099

Riedemann, P., Aldunate, G., and Teillier, S. (2008). *Flora nativa de valor ornamental: Chile zona Cordillera de Los Andes. Identificación y propagación* (Santiago, Chile: Corporación Jardín Botánico Chagual).

Rudloff, V. M., Rutllant, J. A., Martel-Cea, A., and Maldonado, A. (2021). Hydrothermal modulation of NDVI in the high-altitude semiarid Andes of Chile (30–34°S). *J. Arid Environments* 186, 104397. doi: 10.1016/j.jaridenv.2020.104397

Rumrich, U., Lange-Bertalot, H., and Rumrich, M. (2000). Diatoms of the Andes. From Venezuela to Patagonia/Tierra del Fuego. *Iconogr. Diatomol.* 9, 7–649.

Schittek, K., Kock, S. T., Lücke, A., Hense, J., Ohlendorf, C., Kulemeyer, J. J., et al. (2016). A high-altitude peatland record of environmental changes in the NW Argentine Andes (24 °S) over the last 2100 years. *Clim. Past* 12 (5), 1165–1180. doi: 10.5194/cp-12-1165-2016

SERPLAC. (1986). *La Minería en la IV región. Secretaría Regional de Planificación y Coordinación IV región*. (La Serena, Chile: Intendencia Región Coquimbo). 33 p. Available at: https://bibliotecadigital.ciren.cl/handle/20.500.13082/25817. Last access: (Accessed November 23, 2023).

Shala, S., Helmens, K. F., Jansson, K. N., Kylander, M. E., Risberg, J., and Löwemark, L. (2014). Palaeoenvironmental record of glacial lake evolution during the early Holocene at Sokli, NE Finland. *Boreas* 43 (2), 362–376. doi: 10.1111/bor.12043

Squeo, F. A., Osorio, R., and Arancio, G. (1994). *Flora de Los Andes de Coquimbo: Cordillera de Doña Ana.* (La Serena: Universidad de la Serena).

Squeo, F. A., Tracol, Y., López, D., Gutiérrez, J. R., Cordova, A. M., and Ehleringer, J. R. (2006). ENSO effects on primary productivity in Southern Atacama desert. *Advanced Geosciences* 6, 273–277. doi: 10.5194/adgeo-6-273-2006

Squeo, F. A., Veit, H., Arancio, G., Gutierrez, J. R., Arroyo, M. T. K., and Olivares, N. (1993). Spatial heterogeneity of high mountain vegetation in the andean desert zone of Chile. *Mountain Res. Dev.* 13 (2), 203–209. doi: 10.2307/3673638

Stansell, N. D., Rodbell, D. T., Abbott, M. B., and Mark, B. G. (2013). Proglacial lake sediment records of Holocene climate change in the western Cordillera of Peru. *Quaternary Sci. Rev.* 70, 1–14. doi: 10.1016/j.quascirev.2013.03.003

Stockmarr, J. (1971). Tablets with spores used in absolute pollen analysis. *Pollen spores* 13, 615–621.

Sundelin, B., and Eriksson, A.-K. (2001). *Environ. Toxicol. Chem.* 20 (4), 748–756. doi: 10.1002/etc.5620200408

Teillier, S., Marticorena, A., and Niemeyer, H. (2011). *Flora Andina de Santiago. Guía para la identificación de las especies de las cuencas del Maipo y del Mapocho.* (Santiago: Universidad de Chile).

Tiner, R. J., Negrini, R. M., Antinao, J. L., McDonald, E., and Maldonado, A. (2018). Geophysical and geochemical constraints on the age and paleoclimate implications of Holocene lacustrine cores from the Andes of central Chile. *J. Quaternary Sci.* 33 (2), 150–165. doi: 10.1002/jqs.3012

Tribovillard, N., Algeo, T. J., Lyons, T., and Riboulleau, A. (2006). Trace metals as paleoredox and paleoproductivity proxies: An update. *Chem. Geology* 232 (1), 12–32. doi: 10.1016/j.chemgeo.2006.02.012

van Geel, B., Brinkkemper, O., van Reenen, G. B. A., Van der Putten, N. N. L., Sybenga, J. E., Soonius, C., et al. (2020). Multicore study of upper holocene mire development in west-frisia, northern Netherlands: ecological and archaeological aspects. *Quaternary* 3 (2), 12. doi: 10.3390/quat3020012

Veit, H. (1996). Southern Westerlies during the Holocene deduced from geomorphological and pedological studies in the Norte Chico, Northern Chile (27-33°S). *Palaeogeography Palaeoclimatology Palaeoecol.* 123 (1-4), 107–119. doi: 10.1016/0031-0182(95)00118-2

Viale, M., and Garreaud, R. (2014). Summer precipitation events over the western slope of the subtropical Andes. *Mon. Wea. Rev.* 142, 1074–1092. doi: 10.1175/MWR-D-13-00259.1

Vicuña, S., Garreaud, R., and McPhee, J. (2011). Climate change impacts on the hydrology of a snowmelt driven basin in semiarid Chile. *Climatic Change* 105 (3), 469–488. doi: 10.1007/s10584-010-9888-4

Villagrán, C., Arroyo, M. T. K., and Marticorena, R. (1983). Efectos de la desertización en la distribución de la flora andina de Chile. *Rev. Chil. Hist. Natural* 56, 137–157.

Villa-Martínez, R., Villagrán, C., and Jenny, B. (2003). The last 7500 cal yr B.P. of westerly rainfall in Central Chile inferred from a high-resolution pollen record from Laguna Aculeo (34°S). *Quaternary Res.* 60 (3), 284–293. doi: 10.1016/j.yqres.2003.07.007

von Gunten, L., Grosjean, M., Eggenberger, U., Grob, P., Urrutia, R., and Morales, A. (2009a). Pollution and eutrophication history AD 1800–2005 as recorded in sediments from five lakes in Central Chile. *Global Planetary Change* 68 (3), 198–208. doi: 10.1016/j.gloplacha.2009.04.004

von Gunten, L., Grosjean, M., Rein, B., Urrutia, R., and Appleby, P. (2009b). A quantitative high-resolution summer temperature reconstruction based on sedimentary pigments from Laguna Aculeo, central Chile, back to AD 850. *Holocene* 19, 873–881. doi: 10.1177/0959683609336573

Vuille, M., and Milana, J. P. (2007). High-latitude forcing of regional aridification along the subtropical west coast of South America. *Geophysical Res. Lett.* 34 (23), L23703. doi: 10.1029/2007gl031899

Zech, R., Kull, C., and Veit, H. (2006). Late Quaternary glacial history in the Encierro Valley, northern Chile (29°S), deduced from 10Be surface exposure dating. *Palaeogeography Palaeoclimatol. Palaeoecol.* 234 (2), 277–286. doi: 10.1016/j.palaeo.2005.10.011

Zhang, X., Zhang, H., Chang, F., Ashraf, U., Peng, W., and Wu, H. (2020). Application of corrected methods for high-resolution XRF core scanning elements in lake sediments. *Appl. Sci.* 10 (22), 8012. doi: 10.3390/app10228012

Zheng, Y., Anderson, R. F., van Geen, A., and Fleisher, M. Q. (2002). Preservation of particulate non-lithogenic uranium in marine sediments. *Geochimica Cosmochimica Acta* 66 (17), 3085–3092. doi: 10.1016/S0016-7037(01)00632-9

frontiers | Frontiers in Ecology and Evolution

TYPE Original Research
PUBLISHED 21 December 2023
DOI 10.3389/fevo.2023.1218658

OPEN ACCESS

EDITED BY
Kunshan Bao,
South China Normal University, China

REVIEWED BY
Zhiwei Wan,
Jiangxi Normal University, China
Kun Zhang,
Huaibei Normal University, China

*CORRESPONDENCE
Bin Xue
Bxue@niglas.ac.cn

RECEIVED 07 May 2023
ACCEPTED 29 November 2023
PUBLISHED 21 December 2023

CITATION
Ling C, Xue B, Yao S, Zhang W, Pan D and Tang L (2023) High-resolution sea-level fluctuations during the Mid-Holocene in the Ningshao Coastal Plain region, eastern China. *Front. Ecol. Evol.* 11:1218658. doi: 10.3389/fevo.2023.1218658

High-resolution sea-level fluctuations during the Mid-Holocene in the Ningshao Coastal Plain region, eastern China

Chaohao Ling[1,2], Bin Xue[2]*, Shuchun Yao[2], Wenchao Zhang[3], Dadong Pan[1] and Lingyu Tang[4]

[1]School of History and Geography, Minnan Normal University, Zhangzhou, China, [2]State Key Laboratory of Lake Science and Environment, Nanjing Institute of Geography and Limnology, Chinese Academy of Sciences, Nanjing, China, [3]School of Earth Sciences and Resources, China University of Geosciences (Beijing), Beijing, China, [4]Nanjing Institute of Geology and Palaeontology, Chinese Academy of Sciences, Nanjing, China

Sea level changes during the Mid-Holocene directly influenced the Neolithic culture in the Yangtze River Delta region (YRD). However, the high-resolution sea level change characteristics for this period remain unclear. In this study, we performed a high-resolution palynological analysis, including pollen, Dinoflagellate cysts, and Foraminiferal organic linings, using a high-resolution sediment core from Shanglin Lake, in the North of Ningshao Plain (the south of Hangzhou Bay). 11 accelerator mass spectrometry ^{14}C(AMS) datings indicate the age of the sediments range from 8 cal ka B.P. to 5.6 cal ka B.P. The results show that during the Mid-Holocene, Shanglin Lake evolved from an estuary – subtidal lagoon – semi-enclosed bay – semi-enclosed lagoon – semi-enclosed bay – enclosed lagoon to a modern freshwater lake. There was a period of no, or minimal, eustatic sea-level rise between 7733 and 7585 cal yr B.P. The Mid-Holocene high sea level comes in 7253–7082 cal yr BP. Between 7000 cal yr BP and 5502 cal yr BP, the sea level is close to modern value. The sea level change during this period had a significant impact on the local Neolithic human activity.

KEYWORDS

Holocene, sea-level fluctuations, pollen, dinoflagellate cysts, foraminiferal organic linings, Ningshao coastal plain

1 Introduction

The cultivation and domestication of crops have been a revolutionary event in human history, and the origin, domestication, and cultivation of rice, a major food source for humans, is one of the major focuses of environmental archaeological investigation (Fuller, 2007; Fuller, 2011; Silva et al., 2015). The middle and lower reaches of the Yangtze River are

densely populated and widely recognized as the birthplace of rice cultivation, and studies on the origin and development of rice cultivation in this region have received increasing attention in the past decades (Zong et al., 2007; Fuller et al., 2009; Zheng et al., 2011; Zong et al., 2011; He et al., 2018; Zheng et al., 2018; Innes et al., 2019; He et al., 2020).

The Mid-Holocene Neolithic culture in the Yangtze River Delta was mainly based on rice agriculture, and it is widely regarded as the core area where rice agriculture originated (Zong et al., 2007; Fuller et al., 2009; Zheng et al., 2011; Silva et al., 2015; Liu et al., 2020), human prehistoric civilization in this region has experienced many ups and downs, and cultural faults have been found in many archaeological sites in the past half century (Zhu et al., 2003; Zhu et al., 2003; He et al., 2018; Wang et al., 2018; He et al., 2020). Rice farming is influenced by many factors such as terrain, climate, soil, and hydrology (Zhu et al., 2003; Zhao, 2010; Zhao, 2019). Which is different from the middle reaches of the Yangtze River, the hydrology change caused by sea level change in the Yangtze River Delta is one of the most important factors (Zong et al., 2011; He et al., 2018; He et al., 2020).

The Yangtze River Delta region experienced dramatic sea-level fluctuations in the Holocene, especially in the Mid-Holocene. In the Ningshao plain of eastern China, sea-level fluctuation during the Mid-Holocene is of particular interest, because it seriously affected the development of Neolithic cultures such as the Majiabang (~7000–6000 cal yr BP), Liangzhu (~5200–4000 cal yr BP), Kuahuqiao (~8000–7200 cal yr BP) and the Hemudu (~7000–5000 cal yr BP) cultures around the Hangzhou Bay area (Chen and Stanley, 1998; Sandweiss, 2003; Zong, 2004; Zong et al., 2007; Song et al., 2013; Zhu et al., 2003; Liu et al., 2016; Liu et al., 2018; Wang et al., 2018; Tang et al., 2019). However, due to the lack of high-quality chronology-controlled sequences, the sea-level fluctuations during the Mid-Holocene are still poorly cognition. As a result, the cognition of sea level change fluctuation has shown great difference (Wang et al., 2012; Zheng et al., 2018), which made the cultural interruptions were caused by marine transgression or land floods is still in dispute (Chen and Stanley, 1998; Xie and Yuan, 2012; Song et al., 2013; Liu et al., 2016; Liu et al., 2018; Wang et al., 2018; Tang et al., 2019).

In this study, we report pollen, Dinoflagellate cysts, Foraminiferal organic linings, and organic $\delta^{13}C$ analyses from a core collected in the Shanglin Lake located in a low-energy, surrounded by hill, the average altitude of the North of Ningshao Plain is less than 8 m, remote from any significant fluvial source of sediment. Multiple proxy analyses were performed to reconstruct sea level change in the Mid-Holocene to identify the cause of cultural interruptions on the Ningshao Plain.

2 Materials and methods

2.1 Study area and field sampling

The Ningshao Plain is located in a transitional zone between the Mid-subtropical to northern subtropical belts under the influence of the East Asian Monsoon. The region experiences marked seasonality in both temperature and precipitation, with an annual mean temperature of 16.2°C and a mean temperature is ~4°C in January and ~28°C in July, and annual mean precipitation is about 1600 mm (Ningbo Chorography Codification Committee, 1995). This area was covered by mixed evergreen deciduous broad-leaved forest, showing the characteristics of transition from evergreen broad-leaved forest to deciduous broad-leaved forest vegetation. The vegetation in the hills is mainly the masson pine community and Rhododendron community. Masson pine forest is mixed with Chinese fir and broad-leaved trees, showing the appearance of a mixed forest. Dominant plant species include: *Pinus massoniana*, *Aphananthe*, *Castanea*, *Castanopsis sclerophylla*, *Castanopsis*, *Cyclobalanopsis*, *Liquidambar formosana*, *Quercus aliena*, *Quercus acutissima*, *Celtis* and *Ulmus* (Wu, 1980).

Shanglin Lake is located in the Ningshao Coastal Plain area on the south bank of Hangzhou Bay. Its terrain is high in the south and low in the north, and it is spread out towards Hangzhou Bay in the shape of three steps of hills, plains, and tidal flats (Figure 1). Shanglin Lake is located in a low-energy, surrounded by hill (Figure 1), remote from any significant fluvial source of sediment. It is located about 23 kilometers north of Hangzhou Bay. The sediments are valuable archives for the reconstruction of sea-level changes.

There are few studies on the geomorphologic evolution during the Mid-Holocene sea level change in the Cixi area, south bank of Hangzhou Bay. Wang et al. (1982) reconstructed the Holocene sea-level change curve in the coastal areas of Zhejiang by combining hundreds of geomorphological survey cores with coastal stratigraphic sequence, geomorphologic features, and archaeological data. Feng and Wang (1986) further added new materials and dating to reconstruct the coastline in three periods during the Mid-Holocene in this area (Figure 1B).

We chose the lagoon Shanglin Lake located near the ancient coastline (Chen et al., 1984), which is on a hill close to the Tianluoshan site and Hemudu site, etc. (Figure 1B). The lakes in the foothills of this area were dominated by nature at the end of primitive society and were little affected by human activities.

We drilled six exploratory cores (SLH-1-SLH6) on the water platform without sampling using drilling tools in advance to facilitate the mapping of the lake bottom sedimentation and then drilled four cores with a piston seal sampler operated on the water platform according to the drilling. Details of all exploratory cores and cores are shown in Figure 2.

We split all of these cores with 1 cm intervals after completion of drilling in the State Key Laboratory of Lake Science and Environment, Nanjing Institute of Geography and Limnology, Chinese Academy of Sciences, China. After describing the lithology and photographing, we selected 16 samples, including plant fragments, shells, and wood for AMS ^{14}C dating at Beta Analytic Inc. According to the detailed stratigraphic situation (Figure 2 and Table 1) and the dating results of each cores (Table 2), we chose sampling core 18SLH4 as the focus of this paper.

2.2 Grain size testing and analysis

Cores were subsampled at the same intervals from the core for a total of 265 subsamples. These samples were firstly pretreated with

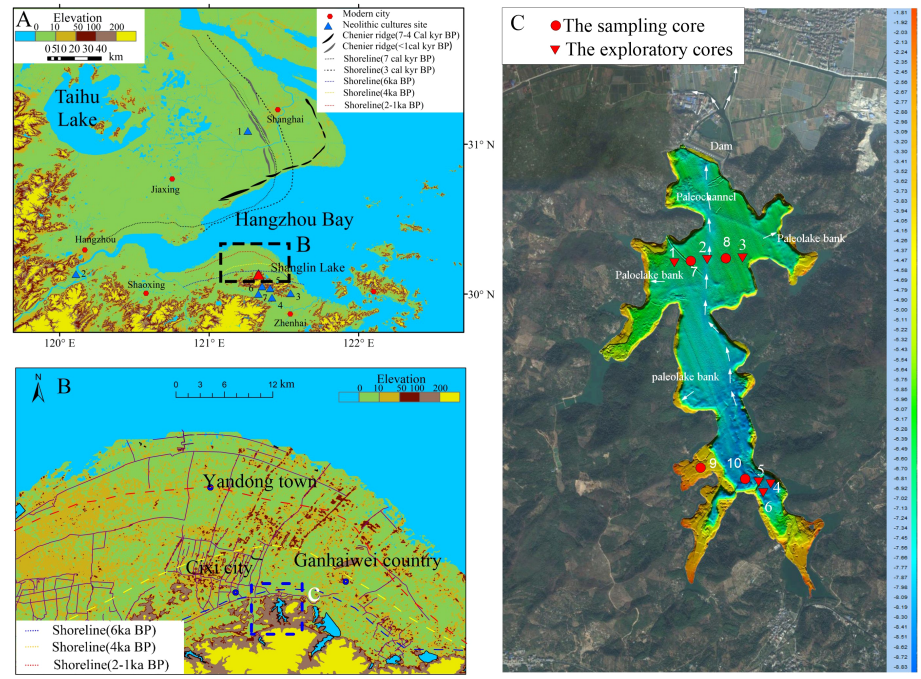

FIGURE 1
The location of the study area and the sample site. **(A)** Location of the study area, both sides of Hangzhou Bay, showing the topography, chenier ridges, and palaeo-shorelines (Wang, 1982; Feng and Wang, 1986). The seven culture sites are: 1 Beiganshan site (Chen et al., 2005; Zong et al., 2011); 2 Kuahuqiao site (Zong et al., 2007; Shu et al., 2010); 3 Yushan site (He et al., 2018; Wang et al., 2018); 4–7 Hemudu (Li et al., 2009; Wang et al., 2018). **(B)** Geographical map showing the present topographic features and the positions of cheniers and palaeo-shorelines during the Mid-Holocene. **(C)** Bottom topography of Shanglin Lake and the cores collected for this study numbered in sequence according to their distance from the Shanglin Lake (Table 1).

10% H_2O_2 and then 10% HCl to remove organic matter and carbonates respectively, and then washed in distilled water to remove residual HCl. Following this, 5 ml of 5% Calgon® (sodium hexametaphosphate) was added to each sample before shaking in an ultrasonic bath for 15 min to prevent flocculation of finegrained particles (Beuselinck et al., 1998). The grain size was measured on each subsample with a Beckman Coulter Laser Diffraction Particle Size Analyzer (Mastersize2000) in the State

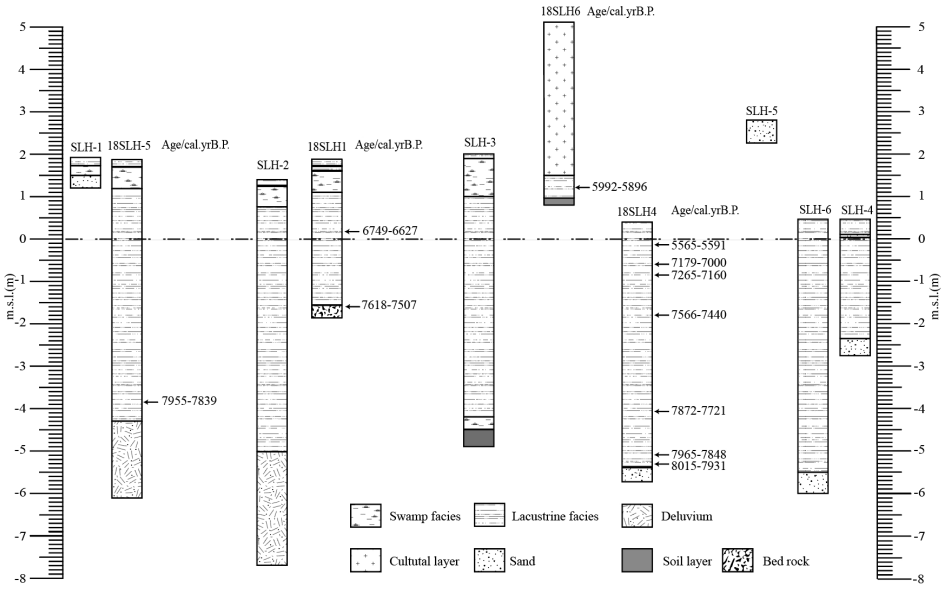

FIGURE 2
Stratigraphic of cores with calibrated mean radiocarbon ages.

TABLE 1 Details of the stratigraphic sequences recorded for all cores.

No.	Cores	Location	Lithological description
1	SLH-1	N 30°08′33.74″ E 121°19′36.11″	0–15 cm. Yellowish–gray clayey silt. Soft lacustrine sediments. 15–40 cm. Bluish gray silty clay. Compact lacustrine sediments. 40–50 cm. Gray dark clayey silt. Compact lacustrine sediments. Below 50 cm. Yellow sand with gravel. Lake bottom sediments.
2	SLH-2	N 30°08′36.86″ E 121°19′49.14″	0–10 cm. Bluish gray clay. Soft lacustrine sediments. 10–60 cm. Yellowish brown clay with plant fragments and roots. Bog sediments. 60–300 cm. Bluish gray silty clay. Compact lacustrine sediments. 300–600 cm. Yellowish–gray clay. A few plant fragments are present in this section. Soft lacustrine sediments. 600–860 cm. The gray–brown mixture of sand and mud. Some plant fragments. Alluvial facies or eluvial facies sediments.
3	SLH-3	N 30°08′36.92″ E 121°19′58.94″	0–11 cm. Bluish gray clay. Soft lacustrine sediments. 11–102 cm. Yellowish brown silty clay. A few plant fragments. Compact bog sediments. 102–625 cm. Bluish gray clayey silt. A few plant fragments. Compact lacustrine sediments. 625–650 cm. Yellowish brown clay. A few plant fragments. Compact bog sediments. 650–690 cm. Yellowish brown and light gray clay. Compact paleosols.
4	SLH-4	N 30°07′49.19″ E 121°20′03.58″	0–280 cm. Bluish gray clayey silt. Soft lacustrine sediments. Bluish gray sand with gravel at 60–70 cm. Bedrock at 280–320 cm.
5	SLH-5	N 30°07′48.62″ E 121°20′02.51″	0–40 cm. Gravel with sand. Unable to sample.
6	SLH-6	N 30°07′46.76″ E 121°20′02.67”	0–60 cm. Bluish gray clayey silt. Lacustrine sediments. Bedrock at 600–650 cm.
7	18SLH1	N 30°08′36.94″ E 121°19′55.40″	0–20 cm. Bluish gray clay. Soft lacustrine sediments. 20–30 cm. Bluish gray clayey silt. Compact lacustrine sediments. 30–80 cm. Yellowish–gray silty clay. A few plant fragments. 80–140 cm. Bluish gray clayey silt. A few plant fragments. Compact lacustrine sediments. 140–350 cm. Bluish gray clayey silt. Soft lacustrine sediments. Abundant shell fragments at 350 cm. Bedrock at 360–380 cm.
8	18SLH4	N30°07’46.71” E121°20’0.28”	0–22 cm. Yellowish–gray clay. Soft lacustrine sediments. 22–32 cm. Yellowish–gray silty clay. 32–85 cm. Yellowish–gray clayey silt. Compact lacustrine sediments. There is clear horizontal bedding. 85–100 cm. Gray clayey silt. Lacustrine sediments with clear horizontal bedding. 100–140 cm. Gray clayey silt. Some plant fragments. 140–480 cm. Bluish gray clayey silt. Soft lacustrine sediments. A small wood is present at 448 cm. 480–580 cm. Gray–brown silty clay. Some 580–610 cm.
9	18SLH5	N30°08′36.84″, E121°19′42.69″	0–20 cm. Bluish gray clay. Soft lacustrine sediments. 20–80 cm. Yellowish brown clay. Abundant plant roots. Soft bog sediments. 80–300 cm. Bluish gray clayey silt. Some plant fragments. Soft lacustrine sediments. 300–580 cm. Yellowish–gray clayey silt. Some plant fragments. 580–800 cm. The gray–brown mixture of sand and mud. Soft texture. Some plant fragments. A small wood is present at 602 cm. Spiral shell fragments present at 667 cm, 691 cm, 751 cm, and 762 cm. Alluvial/eluvial sedimentary facies.
10	18SLH6	N30°07′50.43″ E121°19′46.36″	0–360 cm. Gray dark cultural layer with abundant rock, pottery pieces, and plant fragments. 360–400 cm. Gray silty clay. Compact lacustrine sediments. 400–435 cm. Yellowish brown and light gray clay. Compact paleosols.

Key Laboratory of Lake Science and Environment, Nanjing Institute of Geography and Limnology, Chinese Academy of Sciences, China.

The EMMA end element model method (Weltje, 1997) is able to distinguish between the different components of the grain size, running the Analysize package provided by Paterson and Heslop (2015) in the MATLAB environment. Since the bottom 30 cm of the cores is riverine sand, the particle size was calculated after excluding the bottom 15 samples. We chose three components with less information lost and a better correspondence with the distribution in the samples, namely, two single peak modes and a mode with one high and one low peak, labeled as EM1, EM2, and EM3, respectively (Figure 3).

2.3 TOC, TN and $\delta^{13}C$

The stable isotope composition of organic carbon is widely used as a proxy in paleoenvironmental reconstruction and can be used to quantify the relative proportions of marine versus terrestrially derived water and carbon in a range of sample materials (Bouillon et al., 2008), thus providing information on coastline proximity and hence sea level. Subsamples were taken from the core between 0–5.8 m depth for a total of 54 samples, to measure total organic carbon (TOC), total nitrogen (TN), and organic $\delta^{13}C$. TOC and TN were analyzed using an EA3000 Elemental Analyzer and organic $\delta^{13}C$ analysis were crushed and treated with acid in Ag-capsules prior to isotope analysis using a MAT251 elemental analyzer coupled in continuous flow mode to a Finnegan Delta Plus XL mass spectrometer (± 0.1‰ V-PDB), in the State Key Laboratory of Lake Science and Environment, Nanjing Institute of Geography and Limnology, Chinese Academy of Sciences, China.

2.4 Microfossil analyses

Microfossils, especially pollen, spores, freshwater algae, dinoflagellate cysts, and Foraminiferal organic linings as the most direct indicators or proxies, provide significant information on environmental evolution. Therefore, palynological analysis played an important role in restoration and reconstruction of vegetation history and sea-level fluctuations, which provides information from the sediment cores, especially in alluvial coastal plain regions. (Nakagawa et al., 2003; Pidek et al., 2010; Zhao et al., 2011; Lowe and Walker, 2015; Hao et al., 2022).

TABLE 2 Summary of radiocarbon dates obtained from cores.

Sample No.	Beta No.	Depth/cm	Material	^{14}C age	Calibrated age (cal. yr BP, 2σ range)
18SLH4-55	543783	55	Plant Material	4910±30	5665–5591
18SLH4-100	511659	100	Plant Material	6200±30	7179–7000
18SLH4-125	536113	125	Plant Material	6270±30	7265–7160
18SLH4-221	536114	221	Plant Material	6610±30	7566–7440
18SLH4-448	511658	448	Wood	6980±30	7872–7721
18SLH4-551	511660	551	Wood	7080±30	7965–7848
18SLH4-581	484449	581	Plant Material	7140±30	8015–7931
18SLH1-165	546022	165	Plant Material	5860±30	6749–6627
18SLH1-350	514643	350	Shell	6700±30	7618–7507
18SLH6-3A-96	514637	384	Plant Material	5170±30	5992–5896
18SLH5-568	514460	568	Plant Material	7060±30	7955–7839

Distributions of modern dinoflagellate cysts (dinocysts) and planktonic Foraminiferal fauna in marine environments are directly associated with upper water masses, sea-surface temperature, salinity, nitrate, phosphate, and other oceanographic variables (Rochon et al., 1999; Dale, 2009; de Vernal et al., 2005; Pospelova and Kim, 2010; Zonneveld et al., 2013; Hao et al., 2020). Therefore, organic-walled dinoflagellate cysts and foraminifer linings being preserved in sediments are commonly used as indicators for reconstructions of past sea-level fluctuations and oceanographic conditions (de Vernal et al., 2005; Zonneveld et al., 2008; Bringué et al., 2014; Pospelova et al., 2015).

In our study, subsamples every 3 cm were taken from the core of 18SLH4 between 0 and 1m, and at 10 cm intervals elsewhere, for a total of 83 samples for biological proxy analysis (palynology, Dinoflagellate cysts Foraminiferal organic linings). Samples were prepared for palynological analysis using the standard laboratory techniques, including alkali digestion, hydrofluoric acid digestion, and acetolysis (reference for pollen method here), but we didn't sieve at 180 μm to

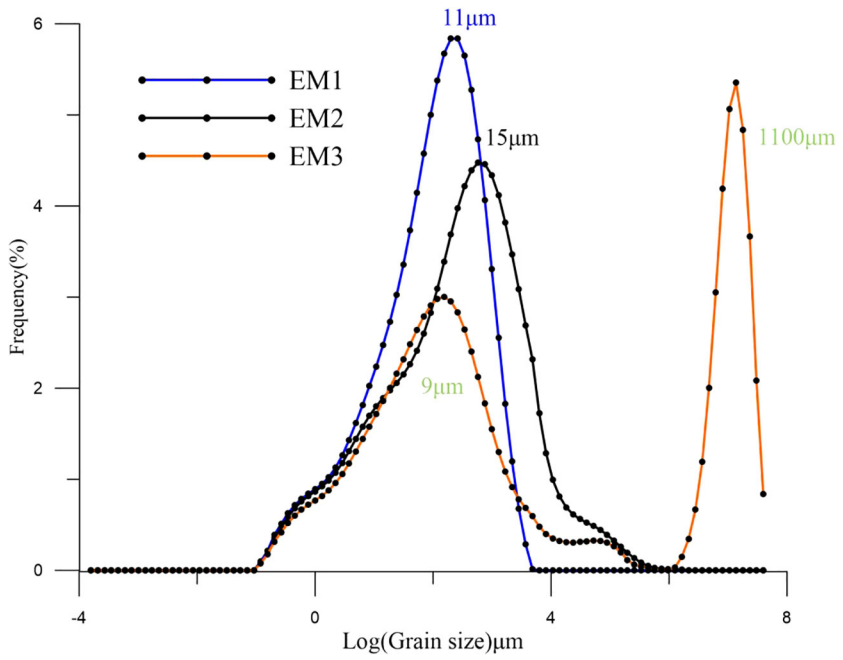

FIGURE 3
Distribution of End-Member of 18SLH4 from Shanglin Lake.

retain Foraminiferal linings. Microfossils were identified using reference keys and type slides and counted using a stereomicroscope at a magnification of ×400 for critical features. Identification of pollen grains, pteridophyte spores, and Foraminiferal organic linings followed He et al. (1965), Wang (1980), Wang et al. (1980), Wang et al. (2012) and Tang et al. (2019); Dinoflagellate cysts followed Moore et al. (1991), He et al. (2009) and Tang et al. (2013). 400 land pollen grains were counted for each sampled level, plus all aquatic pollen, pteridophyte spores, Dinoflagellate cysts and Foraminiferal organic linings.

3 Result

3.1 AMS^{14}C dating and age-depth model

The 11 ages include both original and tree-wheel corrected ages (Stuiver et al., 1993; Reimer et al., 2009) (http://calib.org, accessed in November 2016) (Table 2). A complete chronological framework was developed for the 18SLH4 core using the R package *Clam* (Figure 4).

3.2 Grain size analysis

Based on the lithological characteristics and dating results, 18SLH4 was selected for particle size testing, and a total of 265 samples were tested at equal intervals. The mean grain size of the cores was 6.93 μm, ranging from 4.22 to 7.93 μm (Figure 5).

The plural of the EM1 component is 11 μm, which is the main material input of the core, with an average value of 72.23%. The EM3, with the main peak at 1100 μm and the secondary peak at 9 μm, has a mean proportion of 3.36%, which may indicate the input of slope sediment and storm surge caused by abnormal floods.

3.3 Characteristics of TOC, TN and δ^{13}C

The records of TOC, TN, and δ^{13}C changes are given in Figure 6, and Figure 7 indicates the material sources of organic matter in the sediments for each period.

3.4 Microfossil assemblages

18SLH4 core found abundant spore pollen and microsomal paleontological fossils from nearly 100 families and genera, including regional arboreal pollen such as *Pinus, Fagus, Quercus, Cyclobalanopsis, Fagus, Betula, Carpinus, Corylus, Altingia, Ulmus, Juglans, Pterocarya*, Rosaceae, *Rhus*, etc.; pollen of endemic wet/aquatic herbs, such as *Phragmites, Suaeda*, Cyperaceae, *Typha, Nymphoides, Potamogeton*, etc.; pollen of herbs including Poaceae, Chenopodiaceae, Ranunculaceae, *Artemisia, Aster*, etc.; the spores of ferns including *Hicriopertis, Selaginella, Lycopodium, Pteris*, Sinopteridaceae, *Alsophila, Osnunda*, Hymenophyllaceae, Polypodiaceae, etc. There are also a variety of shallow marine

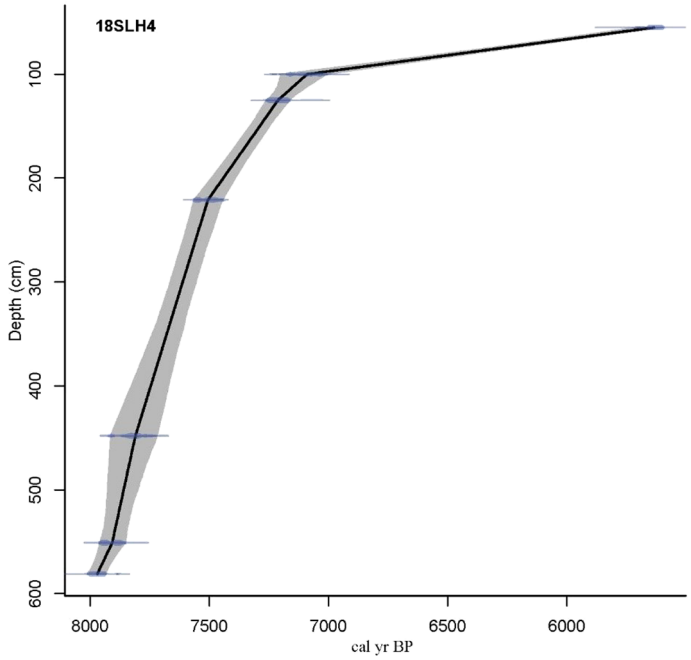

FIGURE 4
Lithology and age-depth model of 18SLH4 core from Shanglin Lake.

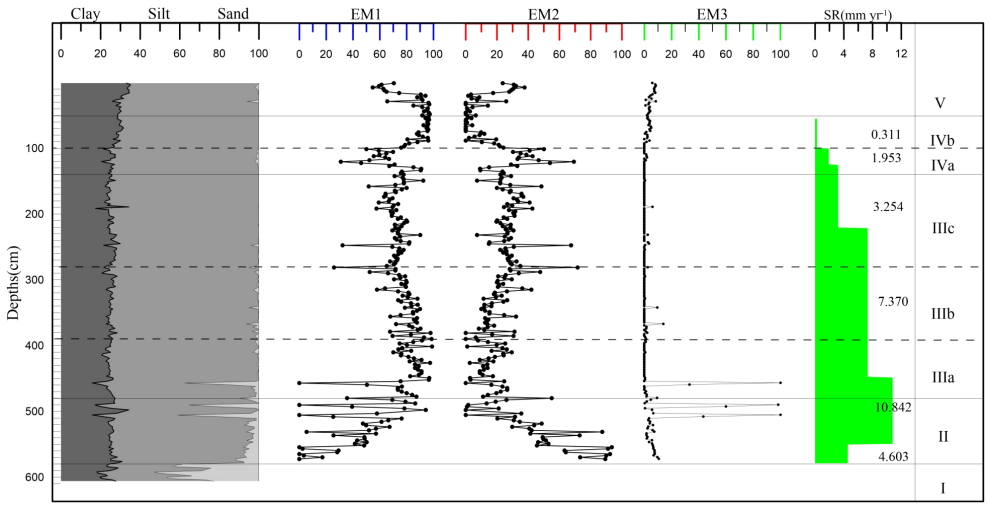

FIGURE 5
Vertical distribution of End-Member of the core 18SLH4 from Shanglin Lake.

Flagellates, such as *Multispinula, Spiniifertes, Operculodinium, Lingnlosphaeridium*, and *Selenopemphix*. *Polysphaeridium, Achomosphaera*, and a few freshwater algae such as *Zygnema, Pediastrum, Concentricyste*, etc. Two samples at 135 cm and 550 cm can be seen *Trochammina* and *Haplophragmoides* (*Trochammina* and *Haplophragmoides*, were identified under the guidance of Pro. Baohua Li, Nanjing Institute of Geology and Paleontology, Chinese Academy of Sciences), but a large number of Foraminiferal organic linings were found (Plates1–7).

Based on the comprehensive analysis of the content of the main spore pollen species and lithological characteristics combined with the clustering analysis of the terrestrial spore and pollen content, five zones can be classified from bottom to top (Figure 8, Figure 9).

Zone I (8031–7971 cal yr BP, 606–580 cm): The spore-pollen concentration is 6840 grains/ml on average. Pollen content of trees and shrubs (average 82.5%) is significantly higher than herbaceous pollen, dominated by deciduous *Quercus*, *Cyclobalanopsis*, and *Pinus*, of which, deciduous broad-leaved species accounted for about 43.7%, evergreen broad-leaved species accounted for 15.8%. The average pollen content of herbaceous plants reached 15.7%, mainly Poaceae (7.9%). The average content of fern spores was 14.6%; a small number of freshwater algae were found, no furrow flagellates were seen, and Foraminiferal organic linings were found

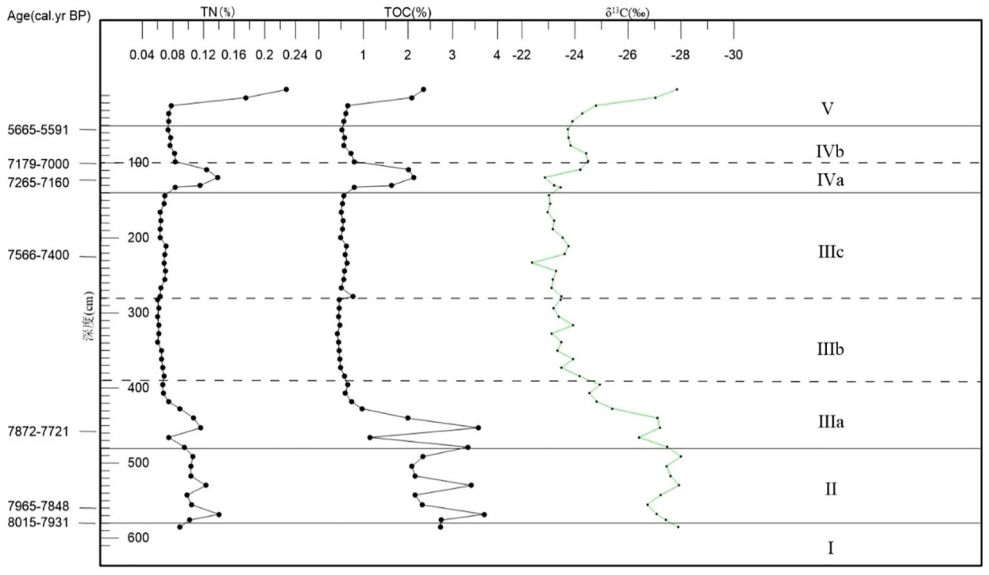

FIGURE 6
Vertical distribution of TOC, TN and $\delta^{13}C$ of the core 18SLH4 from Shanglin Lake.

10.3389/fevo.2023.1218658

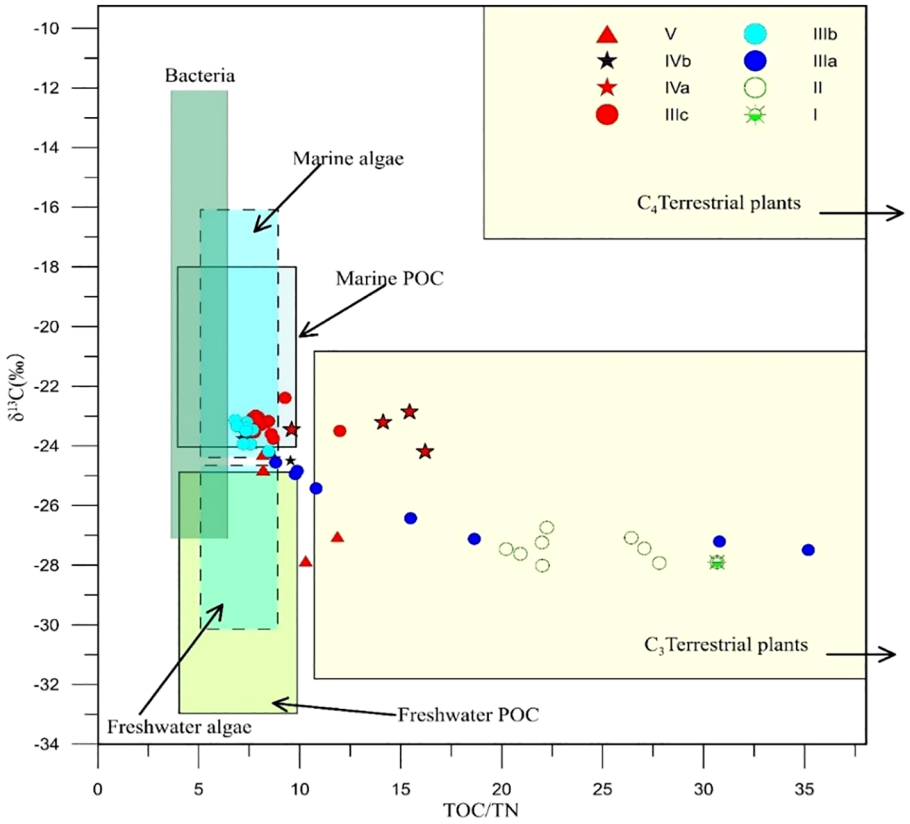

FIGURE 7
The source discrimination of organic carbon of the core 18SLH4 from Shanglin Lake (modified from Lamb et al., 2006).

with an endomorph of 363 grain/ml, mainly relatively fragmented individuals below 50 μm.

Zone II (7971–7848 cal yr BP, 580–480 cm): Spore-pollen concentration is 6704 grains/ml. Tree and shrub pollen dominates (average 80.5%), mainly deciduous *Quercus*, *Cyclobalanopsis*, and *pinus*, with 14.2% evergreen broad-leaved species. Herbaceous plants pollen accounts for an average of 16%, mainly Poaceae (8.6%). The average content of Cyperaceae is 3.6%; the average content of ferns is 15.3%, mainly in Hymenophyllaceae and Polypodiaceae, the average content of freshwater algae is less than

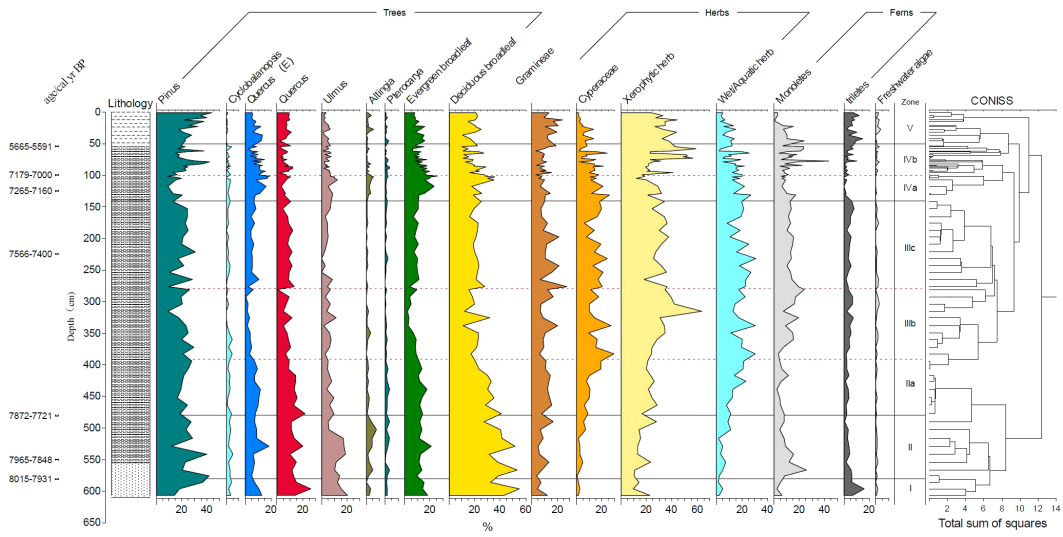

FIGURE 8
Pollen percent diagram of 18SLH4 from Shanglin Lake.

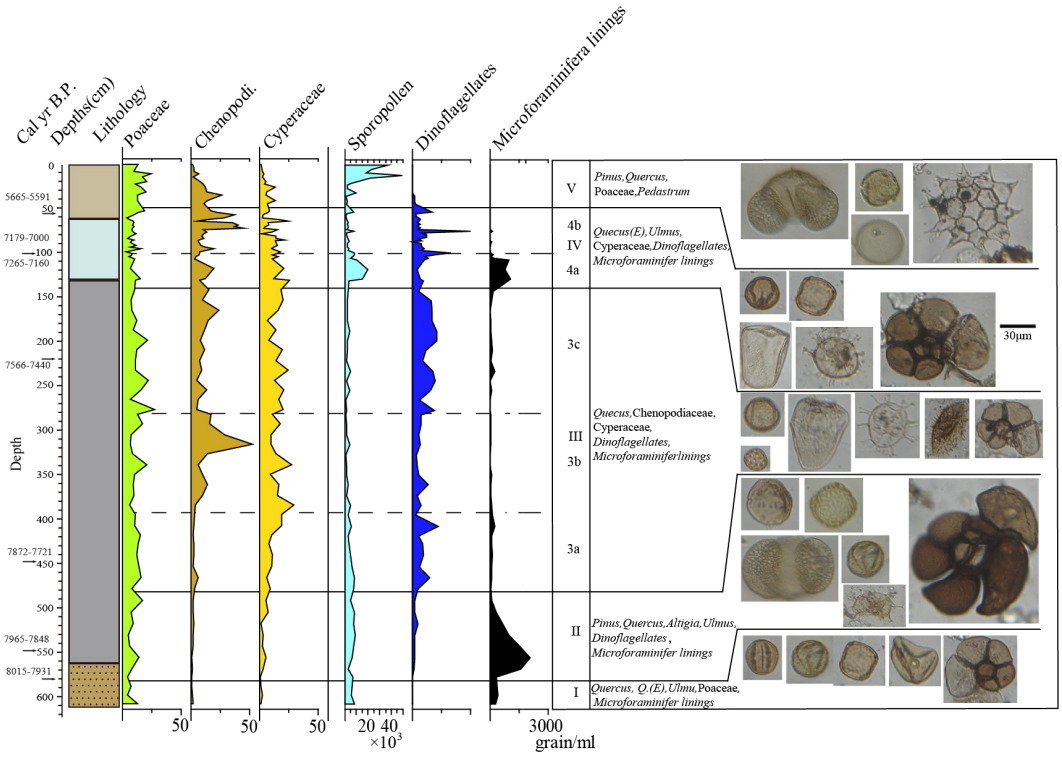

FIGURE 9
Multiproxy data of 18SLH4 from Shanglin Lake.

1%, and the average content of Dinoflagellate cysts is 37 grains/ml in the shallow/near-shore phase. At the same time, the Foraminiferal organic linings increase suddenly, with an average concentration of 1039 grains/ml, and a maximum of 2052 grains/ml. A small number of Foraminiferal shells could be seen.

Zone III (7848–7257 cal yr BP, 480–140 cm): The average concentration of spore pollen was 3960 grains/ml, which is the lowest stage of the whole core. The average pollen content of trees and shrubs was 53.64%, which dropped sharply compared with the previous two stages. The average content of Poaceae was 11.4%, Chenopodi was 10.4%, Cyperaceae was 12.6%, ferns was 15.8%, and the freshwater algae was less than 1%. The content of Dinoflagellate cysts began to increase at this stage, with an average content of 169 grains/ml. The content of Foraminiferal organic linings is extremely low, with an average of 74 grains/ml, mostly ranging in diameter from 50 to 100 μ m. At this stage, no Foraminiferal shell was found.

3a (7848–7735 cal yr BP, 480–390 cm): Pollen and spore concentration was 5343 grains/ml, which is the highest value in the whole of Zone 3, with 65% pollen content in trees and shrubs, 13.1% in Poaceae, 2.7% in Chenopodi, 11.8% in Cyperaceae with an increasing trend, reaching 19% at the end of the stage. 9% in ferns, 162 grains/ml in Dinoflagellate cysts. The concentration of Foraminiferal organic linings was 110 grains/ml.

3b (7735–7585 cal yr BP, 390–280 cm): The spore-pollen concentration was 1993 grains/ml, which is the lowest content in Zone III, with 46.78% of tree and shrub pollen, including 21% in Pinus, 10.6% in Poaceae and the average content of Chenopodiaceae is 17%, with a peak in the middle, with a maximum value of 52.3%, Cyperaceae of 16.2% with an upward trend. At the end of the stage, it reaches 19%, and ferns show a gradual upward trend. The average content is 18.4%, which is the highest content in cores. The content of Dinoflagellate cysts is 102 grains/ml, and the Foraminiferal organic linings are 46 grains/ml. Lowest for the entire Zone III.

3c (7585–7257 cal yr BP, 280–140 cm): The spore-pollen concentration was 2687 grains/ml, increasing compared to 3a, with 51.7% for arboreal pollen, 14.4% for Pinus, 10.6% for Poaceae, 17% for Chenopodi, with a peak in the middle and a maximum of 52.3%, 16.2% for Cyperaceae and 18.1% for ferns, with a relatively stable, with 236 grains/ml for the Dinoflagellate cysts, the highest stage of Zone III, and 80 grains/ml for the Foraminiferal organic linings.

Zone IV (7257–5567 cal yr BP, 140–50 cm): Spore-pollen concentration 4785 grains/ml, significantly increased compared with Zone III, pollen of trees and shrubs was 56.2%, pollen of *Pinus* was 21%, Poaceae was 8.9%, Chenopodi was 15.3%, Cyperaceae was 12.9%, fern was 15.5%, showing an increasing trend, freshwater algae was less than 1%, The content of Dinoflagellate cysts fluctuates greatly, the highest value is 161 grains/ml, was the highest stage of the whole profile, the Foraminiferal organic linings suddenly increases sharply, to the end stage of annihilation, the average is 156 grains/ml. The Foraminiferal shell is visible at this stage.

4a (7257–7082 cal yr BP, 140–100 cm): The spore-pollen concentration of 9806 grains/ml, a significant increase compared to the previous stage, pollen of tree shrubs was 66.6%, pollen of *Pinus* was 14.4%, a decrease, Poaceae was 8.9%, Chenopodi 15.3%, Cyperaceae 12.9%, ferns 15.5%, a slight increase compared to the previous stage, freshwater algae less than 1%, the concentration of Dinoflagellate cysts was 212 grains/ml, the average content of Foraminiferal organic linings in this stage was 593 grains/ml, and the highest stage was 1073 grains/ml, corresponding to the age of 7223 cal yr BP, showing a gradually decreasing trend. The spore-pollen was poorly preserved, and regional pollen of *Tsugar*, *Picea*, and *Abies* appeared.

4b (7082–5502 cal yr BP, 100–50 cm): The spore-pollen concentration 4785 grains/ml, a significant increase compared to the previous stage, tree and shrub pollen was 54.8%, *Pinus* pollen was 21%, Poaceae was 8.8%, Chenopodi was 8.5%, a significant decrease compared to 4a, Cyperaceae was 11.2%, fern was 17.2%, a slight increase compared to the previous a stage, freshwater algae was less than 1%, the concentration of Foraminiferal organic linings was 16 grains/ml on average, and the concentration was very low, but the location of 6278 cal yr BP showed a sudden change with a concentration of 151 grains/ml, and the concentration of Dinoflagellate cysts in this layer was the highest value in this stage.

Zone V (50–0 cm, 5502 cal yr BP–today): Spore-pollen concentration was 14631 grains/ml in the upper 20 cm, the average spore-pollen concentration was 30109 grains/ml, in the lower 30 cm the concentration was 3576 grains/ml, pollen of tree and shrubs was 59.6%, 64.5% in the upper part and 56.1% in the lower part, the average content of *pinus* was 29.1%, with the upper part being 35.5% in the upper part and 24.5% in the lower part. The content of Xerophytic herbs did not vary much, averaging 34.2%, Hygroscopic herbs showed a decreasing trend averaging 5.5%, with 2.3% in the upper part and 7.8% in the lower part, ferns varied more steadily, averaging 15.5%, and Poaceae varied more steadily averaging 15%.

The average content of Chenopodi was 9% and showed a decreasing trend in this zone with 2.8% in the upper part, the average content of Cyperaceae 5.5%, 2.2% in the upper part, 7.8%, and 13.4% in the lower part, showing a decreasing trend. Freshwater algae were 1.8% with less variation, no Dinoflagellate cysts was seen above the top 35 cm, and the average concentration at the bottom 15 cm was 35 grains/ml. No Foraminiferal organic linings were seen at this stage.

4 Discussions

4.1 Hydrological history of Shanglin Lake

4.1.1 Stage 1 (8031–7971 cal yr BP, 606–580 cm)

The Upper Forest Lake may be a paleo-valley during this time. The average content of sand reaches 37.36% with very poor sorting, and the sediments at the bottom of the paleo waterway SLH-2 and 18SLH5 core in the north are a mixture of silt and sand (Figure 2, Table 2), revealing strong hydrodynamics (Hori et al., 2002) TOC/TN and $\delta^{13}C$ scatter projections indicate that the source of organic matter is mainly terrestrial C3 vegetation (Lamb et al., 2006). The small amount of Foraminiferal organic linings and the absence of Dinoflagellate cysts were visible in this section, indicating sea level rise and the beginning of the Estuary stage (Zonneveld et al., 1997; Dale, 2009; Shennan, 2015).

4.1.2 Stage 2 (7971–7848 cal yr BP, 580–480 cm)

The sediment cores in this time period are gray-brown sandy silt. The EM2 is the highest stage in the whole core, with an average content of 45% and gradually decreasing from 89% at the bottom to 25% at the top, indicating strong marine wave energy. The EM3 end element indicates the possible presence of nearshore slope accumulation (Zhu, 2008). The content of Chenopodi is extremely low, averaging 1.4%, Poaceae averages 8.6%, and Cyperaceae averages 3.5%, and the combination with TOC/TN, $\delta^{13}C$ indicates that the source of organic matter is mainly terrestrial debris deposition from the watershed and ocean dynamics (Lamb et al., 2006). Dinoflagellate cysts gradually appeared but at low levels, and a large number of organic linings of varying individual sizes appeared in sediment samples, *Trochammina* were identified from this stage, revealing a relatively open marine environment with strong hydrodynamics, which was not conducive to the deposition of Dinoflagellate cysts, reflecting the rapid sea level rise at this stage (Bringué et al., 2014). Chenopodi and Cyperaceae showed a slow upward trend, indicating the development of the watershed flora towards the saline-alkali communities (Gao and Zhang, 2006; Wu et al., 2008; Tang et al., 2019). The concentrations of Foraminiferal organic linings showed a significant decreasing trend, indicating that sea level rise slowed at the end of this stage and the lagoons began to form.

4.1.3 Stage 3 (7848–7257 cal yr BP, 480–140 cm)

The grain-size characteristics of this stage are generally stable, and the physicochemical indexes are also stable, which means that the Shanglin Lake gradually enters a more stable lagoon stage, the lithology is dominated by greenish-gray muddy silt, and the TOC/TN, $\delta^{13}C$ reveals that the organic carbon is dominated by marine algae (Lamb et al., 2006); 3a (7848–7735 cal yr BP, 480–390 cm), TOC/TN, and $\delta^{13}C$ show a gradual transition from terrestrial to marine sources of organic carbon in the sediments (Lamb et al., 2006). With the influence of the gradual infiltration of seawater, the lake enters a rapid accumulation period, developing a variety of nearshore shallow marine phases of Dinoflagellate cysts, dominated by *Achomosphaera*, *Spiniifertes*, and *Operculodinium*, etc. The rapid rise in sea level makes the groundwater in the region saline and alkaline, and Wet herbaceous plants such as reeds, sedges, and suede on the lake beach were beginning to develop; 3b (7735–7585 cal yr BP, 390–280 cm), TOC/TN and $\delta^{13}C$ organic carbon are the sea source, but the concentration of flagellates appears low and seawater input decreases, at this time the sea level change was relatively stable or slightly decreasing, developing plant communities dominated by Quinoa, reeds, and sedge; 3c (7585–7257 cal yr BP, 280 cm), the sea level change is relatively stable or slightly decreasing, developing plant communities dominated by Quinoa, reeds and sedge. 7257 cal yr BP, 280–140 cm, the concentration of Dinoflagellate cysts increased, indicating sea level rise.

4.1.4 Stage 4 (7257–7082 cal yr BP, 140–100 cm)

In the early part of this stage, the sediments are black chalky silt, rich in plant remains containing woody debris, and a large number of benthic Foraminiferal organic linings (large) occur, which indicates that seawater is rapidly inundating the marsh, and thus this stage is a period of rapid sea level rise.

4.1.5 Stage 5 (7082–5502 cal yr BP, 100–50 cm)

The increase in freshwater algae, which indicates that lakeshore marshes are developing again, indicates that the sea level is in a more stable state. The presence of high levels of Chenopodi indicates the occurrence of salt marshes. At the depth of 75 cm, an abrupt change in the concentration of Dinoflagellate cysts at approximately 6278 cal yr BP was the maximum for this stage, as well as a small amount of Foraminiferal organic linings, suggesting a possible transient sea invasion at this location, as concluded in previous studies (Zheng et al., 2011; He et al., 2018; Wang et al., 2018; He et al., 2020).

4.1.6 Stage 6 (5502 cal yr BP–present day, 50–0 cm)

After ~5502 cal yr BP, the sediments have obvious horizontal stratification and are dominated by grayish-yellow chalky silt. The sporopollenin record shows the gradual disappearance of saline-tolerant plant species such as reeds, sedges, and suede, as well as the gradual disappearance of Dinoflagellate cysts, and the increase of *Typha*, along with the appearance of a small amount of Myriophyllum, which indicates that the lake of Shanglin Lake evolved into a freshwater lake.

4.2 The Mid-Holocene sea level fluctuations

Using 50 intertidal mangrove peat data and shallow marine sediments, Bird et al. (2007, 2010) reconstructed the sea level change in Singapore during 9.5–6.5 cal ka BP and concluded that sea level rose by 4 m during 7.5–7.0 cal kyr BP and slowly or stopped during 7.8 to 7.4 cal kyr BP in the Singapore area, but the rise was faster around that time. Wang et al. (2012) reconstructed the early-mid Holocene sea level change in the southern Yangtze River Delta and showed that it rose by about 2 m between 7.6 and 7.4 cal kyr BP.

The rapid rise of sea level in the early to Mid-Holocene, ~8000 cal yr BP seawater reached the foothills of the mountain slopes in the northern Ning Shao Plain (Liu et al., 2015; Zheng et al., 2018). Multiple indicators of Shanglin Lake reveal that ~8000 cal yr BP sea level reached the foothills of the Cixi area to form an estuarine bay, at which time the sediment elevation was about −5.6 m (Figure 2), and seawater began to inundate the lake connected to the ocean from this time. The period lasted until 7733 cal yr BP, after which the rate of rise slowed or even stopped. This means that the core was located near the coastal supratidal zone, and the sediment elevation at this time was −2.75 m (Figure 2). Thus, it can be inferred that the sea level rose rapidly from ~8000 cal yr BP to 7633 cal yr BP by about 3 m, and 7733–7585 cal yr BP was suitable for the survival of saline mudflats, with *Phragmites*, *Suaeda*, and Cyperaceae dominating the plant community. The low level of Dinoflagellate cysts relative to the pre-and post-phase indicates that the phase has been on the Supratidal Zone and the sea level rise stagnation lasted for nearly 150 years, after which the sea level started to enter the rising phase (7585–7082 cal yr BP), which is consistent with Bird et al. (2007) who suggested that the sea level stagnated or even slightly decreased from 7.8–7.4 cal kyr BP and the pattern of rapid sea level rise around that time is similar, but there are some differences in the timing and duration of the occurrence in this study.

From ~7585 cal yr BP, the saline plant community of Shanglin Lake started to fall, and the sea level was about −2.75 m. The sediment of ~7253 cal yr BP was deposited nearshore and shallow, and the sea level was about −1.35 m as inferred from the elevation of the sediment at this time. About 300 years later, the sea level rose about 1.4 m, and Shanglin Lake was connected to the sea again. After that, until ~7082 cal yr BP, the sea level was relatively stable and maintained a high sea level for nearly 200 years.

After ~7000 cal yr BP, the concentration of Foraminiferal organic linings fell back to low values and disappeared rapidly, and the saline plant community gradually developed to dominate again. Shanglin Lake begins to break away from the direct influence of the ocean, implying the end of the high sea level period, and drops back to close to modern sea level. Sediment elevations during this time period approached modern sea level elevations. The dominance of saline plant communities during ~7000–5500 cal yr BP indicates that coastal areas at 0–1 m elevation in the Ning Shao Plain area have been in the supratidal zone during this time period. There were also several peaks in the concentration of trench whip algae during this time, indicating the influence of sea level fluctuations, including (Figure 9) a peak in the concentration of trench whip algae at ~6278 cal yr BP at 75 cm, as well as a small amount of Foraminiferal organic linings, suggesting that a sea invasion may have occurred at this time.

Multi-indicator analysis of high-resolution sediments from the 18SLH4 core in Shanglin Lake reveals that sea level in the Ningshao Coastal Plain varies minimally or decreases slightly from ~7733–7585 cal yr BP, with a rapid sea level rise around this period and a high sea level at ~7253–7082 cal yr BP. Between ~7000–5500 cal yr BP, sea level is more stable with small fluctuations, with a brief sea intrusion at ~6280 cal yr BP.

4.3 Sea level changes and cultural history

Early rice cultivation from 7700 cal yr B.P. has recently been demonstrated from the Yangtze delta at Kuahuqiao, which site was abandoned due to renewed sea-level rise ca. 7550 cal yr BP (Zong et al., 2007; Innes et al., 2009). Several previous studies have shown that the region was detached from seawater influence at about 7600 cal yr BP, and coastal wetlands began to form in the foothills of the plains during 7500–7000 cal a BP (Dai et al., 2018; Liu et al., 2018). The plant communities revealed by the spore-pollen of Shanglin Lake show that the region developed coastal wetlands at 7733–7585 cal yr BP, with a peak at about 7600 cal B.P, after which the sea did not recede and the sea level continued

to grow. At 7253–7082 cal yr BP, sea level rose rapidly to form a semi-enclosed bay environment, appearing nearly 200 years in subtidal lagoonal phase deposition.

The sea level after 7000 cal yr BP began to fall back until 5502 cal yr BP, when supratidal ecological communities with absolute dominance of Phragmites, *Suaeda*, and Cyperaceae, indicating that the sea level maintained a stable and slightly fluctuating environment, making the early Hemudu and Tianluoshan cultures less prosperous than the Majiabang and Songze cultures in northern Hangzhou Bay. The relative survival pressure of the Hemudu and Tianluoshan people was higher (Qin et al., 2011). The extreme peak of Dinoflagellate cysts at about 6278 cal yr BP, along with a small amount of Foraminiferal organic linings, indicates a brief sea invasion during this period, which is consistent with the sea invasion event of 6400–6300 cal yr BP derived from previous studies. Seed analysis shows that the time of sea invasion from 6400 to 6300 cal yr BP was recorded (Zheng et al., 2012). The presence of moderate amounts of Dinoflagellate cysts in samples between about 6278 cal yr BP and about 5600 cal yr B.P. indicates that seawater had been influencing ancient human activities in the Ningshao Plain area during this period, and that saline plant communities were more developed at this stage, suggesting that the Hemudu people lived in relatively saline groundwater conditions for agricultural activities at that time. Multi-indicator analysis of the Yushan site (Figure 1A) by He et al. (2018) showed that the Hemudu culture 6300–5600 was interrupted by transgression, but Wang et al. (2012) infer that extreme events and flooding accompanying accelerated sea-level rise were major causes of cultural interruption. However, the sediments of this phase in Shanglin Lake have more obvious stratification and no obvious storm surge accumulation features.

5 Conclusion

We selected Shanglin Lake, which is surrounded by mountains on three sides and faces Hangzhou Bay in the back north, away from the alluvial plain and disturbed by river alluvium, to reconstruct a detailed history of sea level changes in the Cixi region of Zhejiang from 8–5.6 cal yr BP based on a well-established chronosequence and multiple proxies such as grain size, TOC/TN, $\delta^{13}C$, sporo-pollen, Dinoflagellate cysts, Foraminiferal organic, etc.

Our study indicated that the evolution of Shanglin Lake since the Mid-Holocene experienced the stages of the estuarine bay, semi-enclosed bay, semi-enclosed lagoon, semi-enclosed bay, enclosed lagoon, and modern lake.

The multiple proxies suggest that there was a period of no or minimal eustatic sea-level rise between 7733 and 7585 cal yr BP in Ningshao Coastal Plain, Yangtze River Delta region. The Mid-Holocene high sea level comes in 7253–7082 cal yr BP. Between 7000 cal yr BP and 5502 cal yr BP, the sea level is relatively stable and fluctuates around modern height.

The sea level changes may directly influence the Neolithic cultural transitions in the Mid-Holocene in the Ningshao plain, which provides warnings for predicting the possible impacts of coastal deltas in response to sea level rise in the context of global warming.

Data availability statement

The original contributions presented in the study are included in the article/Supplementary Material. Further inquiries can be directed to the corresponding author.

Author contributions

CL: writing – original draft, validation, resources, and formal analysis. LT and BX: contributed to the conceptualization of the study. CL and SY: investigation and fieldwork. BX: supervision. CL, WZ, and DP revised the manuscript. All authors contributed to the article and approved the submitted version.

Funding

This research has been supported by, the Natural Science Foundation of Fujian Province (grant no. 2022J05178) and the Natural Science Foundation of Hunan Province (grant no. 2021JJ30555).

Acknowledgments

We are very grateful to Prof. Baohua Li (Nanjing Institute of Geology and Paleontology, Chinese Academy of Sciences) for his help in the identification of foraminifera fossils. Jingkui Tao and Wei Wang from Nanjing Institute of Geography and Limnology, Chinese Academy of Sciences are thanked for their hard work during the field campaign.

Conflict of interest

The authors declare that the research was conducted in the absence of any commercial or financial relationships that could be construed as a potential conflict of interest.

Publisher's note

Supplementary material

The Supplementary Material for this article can be found online at: https://www.frontiersin.org/articles/10.3389/fevo.2023.1218658/full#supplementary-material

References

Beuselinck, L., Govers, G., Poesen, J., Degraer, G., and Froyen, L. (1998). Grain-size analysis by laser diffractometry: comparison with the sieve-pipette method. *Catena* 32, 193–208. doi: 10.1016/S0341-8162(98)00051-4

Bird, M. I., Austin, W. E. N., Wurster, C. M., Fifield, L. K., Mojtahid, M., Sargeant, C., et al. (2010). Punctuated eustatic sea-level rise in the early Mid-Holocene. *Geology* 38 (9), 803–806. doi: 10.1130/G31066.1

Bird, M. I., Fifi eld, L. K., Chang, C. H., Teh, T. S., and Lambeck, K. (2007). An infl ection in the rate of early Mid-Holocene sea-level rise: A new sea-level curve for Singapore. *Estuar Coast Shelf Sci.* 71, 523–536. doi: 10.1016/j.ecss.2006.07.004

Bouillon, S., Connolly, R., and Lee, S. Y. (2008). Organic matter exchange and cycling in mangrove ecosystems: Recent insights from stable isotope studies. *J. Sea Res.* 59, 44–58. doi: 10.1016/j.seares.2007.05.001

Bringué, M., Pospelova, V., and Field, D. B. (2014). High resolution sedimentary record of dinoflagellate cysts reflects decadal variability and 20th century warming in the Santa Barbara Basin. *Quat. Sci. Rev.* 105, 86–101. doi: 10.1016/j.quascirev.2014.09.022

Chen, Q., Lu, Y., and Le, Z. (1984). On the lacustrine fluctuation in the regions of Ningbo-Shaoxing Plain in historical periods (in Chinese with English abstract). *Geo. Res.* 3 (3), 29–43.

Chen, Z., and Stanlety, D. J. (1998). Sea-Level rise on eastern China's Yangtze delta. *J. Coast. Res.* 14 (1), 360–366. http://www.jstor.org/stable/4298785.

Chen, Z., Wang, Z., Schneiderman, J., Taol, J., and Cail, Y. (2005). Holocene climate fluctuations in the Yangtze delta of eastern China and the Neolithic response. *Holocene* 15 (6), 915–924. doi: 10.1191/0959683605hl862rr

Dai, B., Liu, Y., Sun, Q., Zhang, W., and Chen, Z. (2018). Foraminiferal evidence for the Holocene environmental transitions in the Yaojiang Valley, south Hangzhou Bay of eastern China and its Neolithic implications. *Mar. Geology* 404, 15–23. doi: 10.1016/j.margeo.2018.07.001

Dale, B. (2009). Eutrophication signals in the sedimentary record of dinoflagellate cysts in coastal waters. *J. Sea Res.* 61 (1-2), 103–113. doi: 10.1016/j.seares.2008.06.007

de Vernal, A., Eynaud, F., Henry, M., Hillaire-Marcel, C., Londeix, L., Mangin, S., et al. (2005). Reconstruction of sea-surface conditions at middle to high latitudes of the Northern Hemisphere during the Last Glacial Maximum (LGM) based on dinoflagellate cyst assemblages. *Quaternary Sci. Rev.* 24, 897–924. doi: 10.1016/j.quascirev.2004.06.014

Feng, H., and Wang, Z. (1986). Zhejiang's holocene coastline shift and sea-level change (in Chinese with English abstract). *J. Hangzhou Univ.* 13 (01), 100–107.

Fuller, D. Q. (2007). Contrasting patterns in crop domestication and domestication rates: recent archaeobotanical insights from the old world. *Ann. Bot.* 100 (5), 903–924. doi: 10.1093/aob/mcm048

Fuller, D. Q. (2011). Pathways to Asian civilizations: tracing the origins and spread of rice and rice cultures. *Rice* 4 (3-4), 78–92. doi: 10.1007/s12284-011-9078-7

Fuller, D. Q., Ling, Q., Zheng, Y. F., Zhao, Z. J., Chen, X. G., Hosoya, L. A., et al. (2009). The domestication process and domestication rate in rice: spikelet bases from the Lower Yangtze. *Science* 323, 1607–1610. doi: 10.1126/science.1166605

Gao, Z., and Zhang, L. (2006). Measuring and analyzing of the mult-i seasonal spectral characteristics for saltmarsh vegetation in shanghai (in chinese with english abstract). *Acta Ecologica Sin.* 26 (3), 793–800.

Hao, X., Li, L., Ouyang, X., Qin, L., Jiang, X., Li, J., et al. (2022). Holocene vegetation evolution, hydrologic variability and sea-level fluctuations on the south coastal plain of Laizhou Bay, Bohai Sea, China: new evidence from pollen, freshwater algae and dinoflagellate cysts. *J. Paleolimnol* 68, 155–167. doi: 10.1007/s10933-021-00229-2

Hao, X., Ouyang, X., Zheng, L., Zhuo, B., and Liu, Y. (2020). Palynological evidence for Early to Mid-Holocene sea-level fluctuations over the present-day Ningshao Coastal Plain in eastern China. *Mar. Geology* 426, 106213. doi: 10.1016/j.margeo.2020.106213

He, C., Song, Z., and Zhu, Y. (2009). *Fossil dinoflagellates of china (in chinese)* (Beijing: Science Press).

He, Y., Hu, L. Y., and Wang, K. L. (1965). Quaternary Foraminiferal in the east region of Jiang-su Province. Memoirs of Nanjing Institute of Geology and Palaeontology. *Chin. Acad. Sci.* 4, 51–162.

He, K., Lu, H., Li, Y., Ding, F., Zhang, J., and Wang, C. (2020). Cultural response to Middle Holocene sea-level fluctuations in eastern China: a multi-proxy approach. *Boreas* 49 (1), 71–88. doi: 10.1111/bor.12421

He, K., Lu, H., Zheng, Y., Zhang, J., Xu, D., Huang, X., et al. (2018). Middle-Holocene sea-level fluctuations interrupted the developing Hemudu culture in the lower Yangtze River, China. *Quaternary Sci. Rev.* 188, 90–103. doi: 10.1016/j.quascirev.2018.03.034

Hori, K., Saito, Y., and Wang, P. (2002). Evolution of the coastal depositional systems of the changjiang (Yangtze) river in response to late pleistocene-holocene sea-level changes[J]. *J. Sedimentary Res.* 2002, 72.

Innes, J. B., Zong, Y., Chen, Z., Chen, C., Wang, Z., and Wang, H. (2009). Environmental history, palaeoecology and human activity at the early neolithic forager/cultivator site at kuahuqiao, hangzhou, eastern china. *Quaternary Sci. Rev.* 28 (23-24), 2277–2294. doi: 10.1016/j.quascirev.2009.04.010

Innes, J. B., Zong, Y., Xiong, H., Wang, Z., and Chen, Z. (2019). Pollen and non-pollen palynomorph analyses of Upper Holocene sediments from Dianshan, Yangtze coastal lowlands, China: Hydrology, vegetation history and human activity. *Palaeogeogr. Palaeoclimatol. Palaeoecol.* 523, 30–47. doi: 10.1016/j.palaeo.2019.03.009

Lamb, A. L., Wilson, G. P., and Leng, M. J. (2006). A review of coastal palaeoclimate and relative sea-level reconstructions using [delta] 13c and c/n ratios in organic material. *Earth Sci. Rev.* 75 (1-4), 29–57. doi: 10.1016/j.earscirev.2005.10.003

Li, Z., Song, B., Saito, Y., and Li, J. (2009). "Sedimentary facies and geochemical characteristics of Jiangdou Core JD01 from the upper delta plain of Changjiang (Yangtze) delta, China," in *Ias Meeting of Sedimentologists*.

Liu, Y., Sun, Q., Fan, D., Lai, X., Xu, L., Finlayson, B., et al. (2016). Pollen evidence to interpret the history of rice farming at the Hemudu site on the Ningshao coast, eastern China. *Quaternary Int.* 426 (dec.28), 195–203. doi: 10.1016/j.quaint.2016.05.016

Liu, Y., Sun, Q., Fan, D., Dai, B., Ma, F., Xu, L., et al. (2018). Early to Middle Holocene sea level fluctuation, coastal progradation and the Neolithic occupation in the Yaojiang Valley of southern Hangzhou Bay, Eastern China. *Quaternary Sci. Rev.* 189, 91–104. doi: 10.1016/j.quascirev.2018.04.010

Liu, Y., Sun, Q., Thomas, I., et al. (2015). Middle holocene coastal environment and the rise of the liangzhu city complex on the yangtze delta, china. *Quaternary Res.* 84 (3), 326–334. doi: 10.1016/j.yqres.2015.10.001

Liu, X., Liu, Z., Qian, Q., Song, W., Yuan, Y., et al. (2020). Isotope chemometrics determines farming methods and geographical origin of vegetables from yangtze river delta region, china. *Food Chem.* 342, 128379. doi: 10.1016/j.foodchem.2020.128379

Lowe, J., and Walker, M. (2015). *Reconstructing quaternary environments. 3rd edn* (New York, USA: Routledge), 183–197.

Moore, P. D., Webb, J. A., and Collison, M. E. (1991). *Pollen Analysis* (London: Blackwell Scientific Publications), 127–131.

Nakagawa, T., Kitagawa, H., Yasuda, Y., Tarasov, P., Nishida, K., Gotanda, K., et al. (2003). Asynchronous climate changes in the North Atlantic and Japan during the last termination. *Science* 299, 688–691. doi: 10.1126/science.1078235

Ningbo Chorography Codification Committee (1995). *Ningbo Chorography* (Beijing: Zhonghua Book Company).

Paterson, G. A., and Heslop, D. (2015). New methods for unmixing sediment grain size data. *Geochemistry* 16 (12), 4494–4506. doi: 10.1002/2015GC006070

Pidek, I., Piotrowska, K., and Kasprzyk, I. (2010). Pollen-vegetation relationships for pine and spruce in southeast Poland on the basis of volumetric and Tauber trap records. *Gran* 49, 215–226. doi: 10.1080/00173134.2010.514006

Pospelova, V., and Kim, S. J. (2010). Dinoflagellate cysts in recent sediments from the aquaculture sites of southern South Korea. *Mar. Micropaleontol.* 76, 37–51. doi: 10.1016/j.marmicro.2010.04.003

Pospelova, V., Price, A., and Pedersen, T. (2015). Palynological evidence for late quaternary climate and marine primary productivity changes along the California margin. *Paleoceanography* 30, 877–894. doi: 10.1002/2014PA002728

Qin, J., Taylor, D., Atahan, P., Zhang, X., Wu, G., Dodson, J., et al. (2011). Neolithic agriculture, freshwater resources and rapid environmental changes on the lower Yangtze, China. *Quaternary Res.* 75 (1), 55–65. doi: 10.1016/j.yqres.2010.07.014

Reimer, P. J., Baillie, M. G. L., Bard, E., Bayliss, A., Beck, J., Blackwell, P., et al. (2009). IntCal09 and Marine09 radiocarbon age calibration curves, 0–50,000 years cal. BP. *Radiocarbon* 51, 1111–1150. doi: 10.1017/S0033822200034202

Rochon, A., de Vernal, A., Turon, J.-L., Matthiessen, J., and Head, M. J. (1999). Distribution of recent dinoflagellate cysts in surface sediments from the north atlantic ocean and adjacent areas in relation to sea-surface parameters. *Am. Assoc. Stratigraphic Palynologists Contributions Ser.* 35, 146.

Sandweiss, D. H. (2003). Terminal Pleistocene through Mid-Holocene archaeological sites as paleoclimatic archives for the Peruvian coast. *Palaeogeogr. Palaeoclimatol. Palaeoecol.* 194 (1-3), 23–40. doi: 10.1016/S0031-0182(03)00270-0

Shennan, I. (2015). *Handbook of sea-level research* (Wiley-Blackwell). doi: 10.1002/9781118452547.ch2

Shu, J., Wang, W., Jiang, L., and Takahara, H. (2010). Early Neolithic vegetation history, fire regime and human activity at Kuahuqiao, Lower Yangtze River, East China: New and improved insight. *Quaternary Int.* 227 (1), 10–21. doi: 10.1016/j.quaint.2010.04.010

Silva, F., Stevens, C. J., Weisskopf, A., Cristina, C., Ling, Q., Andrew, B., et al. (2015). Modelling the geographical origin of rice cultivation in asia using the rice archaeological database. *PLoS One*. doi: 10.1371/journal.pone.0137024

Song, B., Li, Z., Saito, Y., Okuno, J., Lu, A., Hua, D., et al. (2013). Initiation of the Changjiang (Yangtze) delta and its response to the Mid-Holocene sea level change. *Palaeogeography Palaeoclimatology Palaeoecol.* 388, 81–97. doi: 10.1016/j.palaeo.2013.07.026

Stuiver, M., Reimer, P. J., and Reimer, R. W. (1993). Extended C-14 data-base and revised Calib 7.1 C-14age calibration program. *Radiocarbon* 35, 215–230.

Tang, L., Shu, J., Chen, J., and Wang, Z. (2019). Mid to late Holocene vegetation change recorded at a Neolithic site in the Yangtze coastal plain, China. *Quaternary Int.* 59, 122–130. doi: 10.1016/j.quaint.2018.12.031

Tang, L. Y., Mao, L. M., Lu, X., Ma, Q., Zhou, Z. Z., Yang, C. L., et al. (2013). Palaeoecological and palaeoenvironmental significance of some important spores and micro-algae in quaternary deposits. *Chin. Sci. Bull.* 58, 3125–3139. doi: 10.1007/s11434-013-5747-9

Wang, P. X. (1980). *Collection of Papers on Marine Microfossil* (Beijing: China Ocean Press), 1–204.

Wang, P. X., Min, Q. B., Bian, Y. H., and Zhang, J. J. (1980). Micropaleontologic characteristics of relict sediments of the East China sea. *(in Chinese with English abstract) Acta Oceanologia Sin.* 2 (1), 67–78.

Wang, P. X. (1982). The changes of sea-level in Holocene on the coast of Zhejiang (in Chinese with English abstract). *Mar. Geo. Res.* 2 (2), 79–88.

Wang, Z., Ryves, D. B., Lei, S., et al. (2018). Middle Holocene marine flooding and human response in the south Yangtze coastal plain, East China. *Quaternary Sci. Rev.* 187, 80–93. doi: 10.1016/j.quascirev.2018.03.001

Wang, Z., Zhuang, C., Saito, Y., et al. (2012). Early Mid-Holocene sea-level change and coastal environmental response on the southern Yangtze delta plain, China: implications for the rise of Neolithic culture. *Quaternary Sci. Rev.* 35 (none), 51–62. doi: 10.1016/j.quascirev.2012.01.005

Weltje, G. J. (1997). End-member modeling of compositional data: numerical-statistical algorithms for solving the explicit mixing problem. *Math. Geology* 29 (4), 503–549. doi: 10.1007/BF02775085

Wu, Z. Y. (1980). Vegetation of China. (Beijing: Science Press).

Wu, T., Wu, M., and Xiao, J. (2008). Dynamics of community succession and species diversity of vegetations in beach wetlands of hangzhou bay (in chinese with english abstract). *Chin. J. Ecol.* 27 (8), 1284–1289.

Xie, Z. R., and Yuan, L. W. (2012). Fluctuation characteristics of Holocene sea-level change and its environmental implications. *Quaternary Sci.*

Zhao, Z. J. (2010). New data and new issues for the study of origin of rice agriculture in China. *Archaeological Anthropological Sci.* 2 (2), 99–105. doi: 10.1007/s12520-010-0028-x

Zhao, Z. J. (2019). Introduction of the origin of agriculture in China. *Res. Heritages Preserservation* 4 (1), 1–7.

Zhao, Y., Yu, Z., and Zhao, W. (2011). Holocene vegetation and climate histories in the eastern Tibetan Plateau: controls by insolation- driven temperature or monsoon-derived precipitation changes? *Quat Sci. Rev.* 30, 1173–1184. doi: 10.1016/j.quascirev.2011.02.006

Zheng, H., Zhou, Y., Yang, Q., Hu, Z., Ling, G., Zhang, J., et al. (2018). Spatial and temporal distribution of Neolithic sites in coastal China: Sea level changes, geomorphic evolution and human adaption. *Sci. China Earth Sci.* 61, 123–133. doi: 10.1007/s11430-017-9121-y

Zheng, Y. F., Sun, G. P., and Chen, X. G. (2011). Response of rice cultivation to fluctuating sea level during the Mid-Holocene. *Chin. Sci. Bull.* 56, 2888 ~ 2896. doi: 10.1007/s11434-011-4786-3

Zheng, Y., Sun, G., and Chen, X. (2012). Response of rice cultivation to fluctuating sea level during the mid-holocene. *Chin. Sci. Bull.* 57, 370–378. doi: 10.1007/s11434-011-4786-3

Zhu, C., Zheng, C. G., Ma, C. M., Yang, X., Gao, X., Wang, H., et al. (2003). On the Holocene sea-level highstand along the Yangtze Delta and Ningshao Plain, east China [J]. *Chin. Sci. Bull.* 48 (24), 2672–2683. doi: 10.1007/BF02901755

Zhu, X. (2008). *) sedimentary petrology (in chinese)* (Beijing: Petroleum Industry Press).

Zonneveld, K. F., Versteegh, G. J. M., and Lange, G. J. D. (1997). Preservation of organic-walled dinoflagellate cysts in different oxygen regimes: a 10,000 year natural experiment. *Mar. Micropaleontology* 29, 393–405. doi: 10.1016/S0377-8398(96)00032-1

Zong, Y. (2004). Mid-Holocene sea-level highstand along the Southeast Coast of China. *Quaternary Int.* 117 (1), 55–67. doi: 10.1016/S1040-6182(03)00116-2

Zong, Y., Chen, Z., Innes, J. B., Chen, C., Wang, Z., and Wang, H. (2007). Fire and flood management of coastal swamp enabled first rice paddy cultivation in east China. *Nature* 449, 459–462. doi: 10.1038/nature06135

Zong, Y., Wang, Z., Innes, J. B., and Chen, Z. (2011). Holocene environmental change and Neolithic rice agriculture in the lower Yangtze region of China: A review. *Holocene* 22 (6), 623–635. doi: 10.1177/0959683611409775

Zonneveld, K. A. F., Marret, F., Versteegh, G. J. M., Bogus, K., Bonnet, S., Bouimetarhan, I., et al. (2013). Atlas of modern dinoflagellate cyst distribution based on 2405 data points. *Rev. Palaeobot. Palynol.* 191, 1–197. doi: 10.1016/j.revpalbo.2012.08.003

Zonneveld, K., Versteegh, G., and Kodrans-Nsiah, M. (2008). Preservation and organic chemistry of late Cenozoic organicwalled dinoflagellate cysts: a review. *Mar. Micropaleontol* 68, 179–197. doi: 10.1016/j.marmicro.2008.01.015

Frontiers in
Ecology and Evolution

Ecological and evolutionary research into our natural and anthropogenic world

This multidisciplinary journal covers the spectrum of ecological and evolutionary inquiry. It provides insights into our natural and anthropogenic world, and how it can best be managed.

Discover the latest Research Topics

See more →

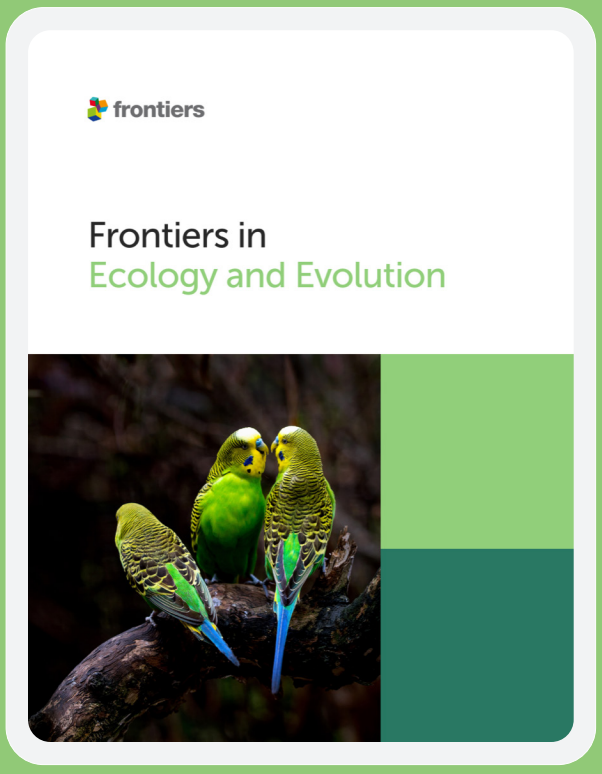

Frontiers

Avenue du Tribunal-Fédéral 34
1005 Lausanne, Switzerland
frontiersin.org

Contact us

+41 (0)21 510 17 00
frontiersin.org/about/contact